NANO- AND MICROPARTICLE-INDUCED CELL DEATH, INFLAMMATION AND IMMUNE RESPONSES

EDITED BY: Shrikant R. Mulay, Martin Herrmann, Rostyslav Bilyy, Alexander Gabibov and Hans-Joachim Anders

PUBLISHED IN: Frontiers in Immunology

frontiers Research Topics

ISSN 1664-8714
ISBN 978-2-88945-921-6
DOI 10.3389/978-2-88945-921-6

About Frontiers

Frontiers is more than just an open-access publisher of scholarly articles: it is a pioneering approach to the world of academia, radically improving the way scholarly research is managed. The grand vision of Frontiers is a world where all people have an equal opportunity to seek, share and generate knowledge. Frontiers provides immediate and permanent online open access to all its publications, but this alone is not enough to realize our grand goals.

Frontiers Journal Series

The Frontiers Journal Series is a multi-tier and interdisciplinary set of open-access, online journals, promising a paradigm shift from the current review, selection and dissemination processes in academic publishing. All Frontiers journals are driven by researchers for researchers; therefore, they constitute a service to the scholarly community. At the same time, the Frontiers Journal Series operates on a revolutionary invention, the tiered publishing system, initially addressing specific communities of scholars, and gradually climbing up to broader public understanding, thus serving the interests of the lay society, too.

Dedication to Quality

Each Frontiers article is a landmark of the highest quality, thanks to genuinely collaborative interactions between authors and review editors, who include some of the world's best academicians. Research must be certified by peers before entering a stream of knowledge that may eventually reach the public - and shape society; therefore, Frontiers only applies the most rigorous and unbiased reviews.
Frontiers revolutionizes research publishing by freely delivering the most outstanding research, evaluated with no bias from both the academic and social point of view. By applying the most advanced information technologies, Frontiers is catapulting scholarly publishing into a new generation.

What are Frontiers Research Topics?

Frontiers Research Topics are very popular trademarks of the Frontiers Journals Series: they are collections of at least ten articles, all centered on a particular subject. With their unique mix of varied contributions from Original Research to Review Articles, Frontiers Research Topics unify the most influential researchers, the latest key findings and historical advances in a hot research area! Find out more on how to host your own Frontiers Research Topic or contribute to one as an author by contacting the Frontiers Editorial Office: researchtopics@frontiersin.org

NANO- AND MICROPARTICLE-INDUCED CELL DEATH, INFLAMMATION AND IMMUNE RESPONSES

Topic Editors:
Shrikant R. Mulay, Klinikum der Universität München, Germany
Martin Herrmann, Friedrich-Alexander-Universität Erlangen-Nürnberg, Germany
Rostyslav Bilyy, Friedrich-Alexander-Universität Erlangen-Nürnberg, Germany; Danylo Halytsky Lviv National Medical University, Ukraine
Alexander Gabibov, Institute of Bioorganic Chemistry of the Russian Academy of Sciences, Russia
Hans-Joachim Anders, Klinikum der Universität München, Germany

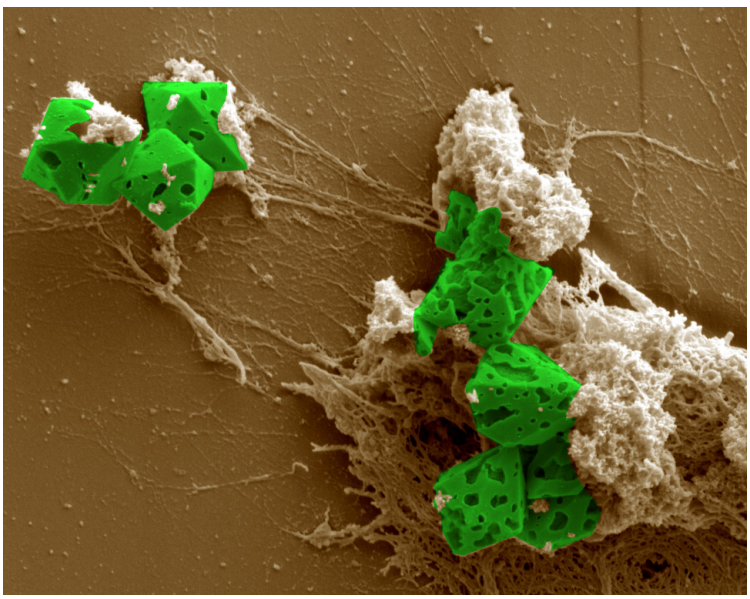

Scanning electron micrograph displaying calcium carbonate crystals entrapped within NETs like structures in neutrophil-rich eye rheum.
Image: Aparna Mahajan.

Cover image: CI Photos/Shutterstock.com

Nano- and microparticles including crystals, synthetic biomaterials, misfolded proteins or environmental particulates are involved in a wide range of biological processes and diseases. They may present as intrinsic or environmental toxins but may also be applied intentionally, e.g. as immune adjuvants, drug carriers or ion exchangers. The discovery that a wide range of nano- and microparticles share the capacity to induce IL-1ß secretion via activation of the NLRP3 inflammasome in dendritic cells and macrophages has led to the hypothesis that nano- and microparticles may contribute in a uniform mechanistic manner to different disease entities. Other molecular mechanisms triggered by a range nano- and microparticles have also

recently been identified including (i) the induction of regulated necrosis; (ii) neutrophil extracellular trap (NET) formation and (iii) foreign body granuloma formation as a mechanism of persistent tissue inflammation and scarring.

Research on the biology of nano- and microparticle handling is currently under intense investigation. The cell type-specific responses of nano- and microparticle exposure deserves careful attention as well as the related secondary responses to these particles that lead to tissue remodeling. The immune system is at the center of these processes in terms of particle clearance, particle-induced cell death and inflammation, thereby limiting particle-related inflammation and orchestrating wound healing responses.

In this Research Topic, we welcomed the submission of Original Research, Review and Mini-Review articles that addressed the significance of the immune system in particle-induced cell death, inflammation and immune responses. These findings will help facilitate new approaches to the prevention and management of particle-related diseases.

Citation: Mulay, S. R., Herrmann, M., Bilyy, R., Gabibov, A., Anders, H.-J., eds. (2019). Nano- and Microparticle-Induced Cell Death, Inflammation and Immune Responses. Lausanne: Frontiers Media. doi: 10.3389/978-2-88945-921-6

Table of Contents

frontiers in Immunology

EDITORIAL
published: 17 April 2019
doi: 10.3389/fimmu.2019.00844

Editorial: Nano- and Microparticle-Induced Cell Death, Inflammation and Immune Responses

Shrikant R. Mulay[1,2†], *Martin Herrmann*[3†], *Rostyslav Bilyy*[3,4†], *Alexander Gabibov*[5†] *and Hans-Joachim Anders*[1*†]

[1] Nephrologisches Zentrum, Medizinische Klinik und Poliklinik IV, Klinikum der Universität München, Munich, Germany, [2] Pharmacology Division, CSIR-Central Drug Research Institute, Lucknow, India, [3] Department of Internal Medicine 3, Friedrich-Alexander-Universität Erlangen-Nürnberg (FAU) and Universitätsklinikum Erlangen, Erlangen, Germany, [4] Department of Cytology Histology and Embryology, Danylo Halytsky Lviv National Medical University, Lviv, Ukraine, [5] M. M. Shemyakin and Yu. A. Ovchinnikov Institute of Bioorganic Chemistry of the Russian Academy of Sciences, Moscow, Russia

Keywords: inflammation, necrosis, apoptosis, particles, crystals

Editorial on the Research Topic

Nano- and Microparticle-Induced Cell Death, Inflammation and Immune Responses

OPEN ACCESS

Edited and reviewed by:
Pietro Ghezzi,
Brighton and Sussex Medical School, United Kingdom

***Correspondence:**
Hans-Joachim Anders
hjanders@med.uni-muenchen.de

†These authors have contributed equally to this work

Specialty section:
This article was submitted to Inflammation, a section of the journal Frontiers in Immunology

Received: *13 March 2019*
Accepted: *01 April 2019*
Published: *17 April 2019*

Citation:
Mulay SR, Herrmann M, Bilyy R, Gabibov A and Anders H-J (2019) Editorial: Nano- and Microparticle-Induced Cell Death, Inflammation and Immune Responses. Front. Immunol. 10:844. doi: 10.3389/fimmu.2019.00844

INTRODUCTION

Crystals, fibers, and other microparticles form inside the body from nutrients or metabolites but also enter the body from outside during environmental or occupational exposures. Altogether crystal and microparticle-related diseases account for numerous medical disorders (1). In some of these disorders, the crystal masses themselves cause the problem, e.g., when stones obstruct the bile ducts or the urinary draining system. In other crystal-immune responses largely account for clinical symptoms and tissue damage, e.g., in gout, silicosis, or asbestosis. This Research Topic in *Frontiers of Immunology* selected a series of articles focusing on how immune and tissue cells respond to crystals, microparticles, and nanoparticles. Our authors shed light on the recent and ongoing research efforts to unravel the molecular mechanisms underlying particle-related tissue injury, inflammation, and remodeling. We hope the readers of this Research Topic find the content useful to further develop the field, to identify common and particle-specific mechanisms of crystallopathies.

NANO- AND MICROPARTICLE-INDUCED CELL DEATH

Nano- and microparticles induce a broad range of cellular responses when exposed to immune and non-immune cells. These crystalline particles could be either of environmental origin e.g., silica, asbestos, air pollutants, or biological origin e.g., cholesterol, calcium, and monosodium urate (MSU) crystals.

In the current issue, Shu and Shi gave a systematic overview of the physical and chemical properties of solid particles and their host responses. For example, phagocytosis of solid particles is mainly governed by their size, which regulates the inflammatory and cell death responses. Crystals with sharp and pointy edges induce direct injury as compared to spherical crystals and rod-shaped crystals. Accordingly, Köppert et al. also found that primary calciprotein particles, which are spherical, amorphous and soft, were rapidly cleared by liver sinusoidal endothelial cells, whereas

secondary calciprotein particles, which are longer, more crystalline, and less soluble, are cleared by Kupffer cells and macrophages.

Cytotoxicity of crystals mainly involves lysosomal rupture, activation of multiple cathepsins, mitochondrial dysfunction leading to either apoptosis or regulated necrosis—viz. mitochondria permeability transition-related necrosis, necroptosis, and pyroptosis (Shu and Shi). In addition, MSU was reported to activate Syk and Src pathways leading to cell death and inflammation in phagocytosis-independent manner (Shu and Shi). Similarly, Shu et al. demonstrated that microscopic cholesterol crystals extract cholesterol from the cell surface upon physical interactions with the plasma membrane, which results in catastrophic plasma membrane rupture and necrosis independent of any known cell death-inducing pathway. Furthermore, in response to stress, a self-cannibalization process termed autophagy is activated, which might be associated with cell death. Frauscher et al. demonstrated that uremia-induced autophagy in vascular smooth muscle cells protects from vascular calcification. Interestingly, pharmacological activation of autophagy protected mice from vascular calcification during chronic kidney disease (CKD).

Ingestion of nano- and microparticles occurs as environmental or occupational pollutants, as well as when used as adjuvants or drug delivery systems. The first line of immune defense—neutrophils regulate immune response to these ingested foreign particles either by removing them by phagocytosis or immobilizing them by trapping with neutrophils extracellular traps (NETs). Silica nanoparticles when ingested during pregnancy cause pregnancy complications. Higashisaka et al. have highlighted the protective roles of neutrophils during pregnancy complications in a murine model of pregnancy. They observed that neutrophil depletion exacerbated silica nanoparticles-induced impairment of placental vessels and increased apoptotic cell death during pregnancy.

NANO- AND MICROPARTICLE-INDUCED INFLAMMATION

A wide range of solid particles is known to induce the formation of NETs (2), which results in the release of intracellular danger associated molecular patterns to initiate the inflammatory response. Bilyy et al. demonstrated that agglomerations of non-stabilized superparamagnetic iron oxide nanoparticles (SPIONs) induce NET formation both *in vivo* and *in vitro*. Interestingly, they observed that inert coating of SPIONs with biocompatible albumin or dextran reduced agglomeration and NET formation by neutrophils and prevented vascular occlusion *in vivo*. These findings again confirm that the physical and chemical properties of solid particles drive host response (Shu and Shi).

At their discovery NETs were considered effective weapons aimed to capture, immobilize, and kill bacteria. Later the list of targets was extended to fungi, viruses, and further pathogens. Recent discoveries have clearly demonstrated that nano-and microparticulate matter is also prone to stimulate NETs formation. The minireview of Li et al. summarizes findings related to NETs formation upon the contact of neutrophils with crystals from MSU, calcium pyrophosphate dihydrate, cholesterol, as well as calcium carbonate and silica. Hydrophobic nanoparticles cause NET formation by membrane disruption and lysosomal leakage. However, for some micro- and nanoparticles the mechanisms of action for the formation of NETs still remains elusive.

Nanocrystals e.g., those from MSU or cholesterol are prone to cluster cell surface receptors to trigger cellular responses. The inhibitory receptors for MSU-induced inflammation CLEC12A and SIRL-1, are thoroughly discussed in the minireview of Fernandes and Naccache. The data suggest that interaction with receptor not only induces mechanical grouping of these cell surface molecules but initiate more complex regulatory processes with distinct effects on leukocyte activation. Targeting inhibitory receptors is a potential therapeutic option to evaluate existing drugs and future drug candidates. However, the list of nanoparticles triggering NET formation can be quite exotic, and very selective.

Cristobalite, contained in volcanic ashes (but not other ash components), was identified as a trigger in macrophages of NLRP3 inflammasome activation with subsequent release of IL-1β (Damby et al.). Inflammasome activation through inhalation of volcanic ash again links air-born microparticles with neutrophil activation and pulmonary diseases. Interestingly, cellular uptake of ash results in lysosomal destabilization, as was reported earlier size dependently for 10 nm diamonds (3), and is followed by activation of mitochondrial responses provoking an oxidative burst.

Calcium oxalate crystals are the naturally occurring particles that reportedly trigger the formation of NETs. Unfortunately, many natural inhibitors of crystal formation like nephrocalcin, osteopontin, uropontin often fail to stop pathological crystal deposition during CKD. The disease is accompanied by fibrosis largely mediated by Transforming Growth Factor beta (TGFβ), and thus anti-TGFβ antibodies are widely used in treatment. Steiger et al. proposed that antibodies can also bind some calcium compounds and thus slow down the process of crystallization in the affected organ. They demonstrated that anti-TGFβ IgG ameliorates CKD not only directly via its influence on the target but also by the prevention of the formation of calcium oxalate crystals in the affected kidneys.

Calcium oxalate nanoparticles were also found to activate human monocyte and enhance local tissue inflammatory responses governed by the production of TNF-a, IL-1b, IL-8, and IL-10. Contact with calcium oxalate crystals but not with zinc oxide nanoparticles stimulated macrophage differentiation into the inflammatory M1-type (Dominguez-Gutierrez et al.). In addition, the properties of a putative calcium oxalate receptor are discussed in the paper.

Another natural defense mechanism against nanoparticles was reported in the work (Marschner et al.), where long pong pentraxin 3 (PTX3), an opsonin known to interact with dead cells and other extracellular microparticles, was identified as an endogenous factor inhibiting growth of calcium oxalate crystals. By limited CaOx crystal aggregation and adhesion to

tubular cell membranes it serves as one of several endogenous inhibitors of stone formation in nephrocalcinosis and potentially other crystallopathies.

NANO- AND MICROPARTICLE-INDUCED IMMUNE RESPONSES

When it comes to immune response the first task of the immune system is to recognize the invader, and micro- and nanoparticles are hard to be recognized, since usually they are the same compounds the body encounters daily in smaller concentrations or in a different soluble form (e.g., MSU). The review of Nakayama summarizes recent advances in our understanding how macrophages recognize crystals particles: some crystal particles are negatively charged and are recognized by scavenger receptor family members in a charge-dependent manner. Alternatively, a model for receptor-independent phagocytosis of crystals has also been proposed to explain their clearance by macrophages (Mahon and Dunnet). Effect of the nanoparticle engulfment can be quite different. Silver and gold nanoparticles when covered with tannic were able to induce maturation of dendritic cells and stimulate the uptake of viral particles (HCV-2) (Orlowski et al.).

Unfortunately, there are much more of them causing harmful effects. The minireview by Mahon and Dunne summarize the role of particles associated with gout, calcium pyrophosphate deposition (CPPD) disease, and osteoarthritis (OA). As well as wear-debris particles generated from prosthetic implants and contributing to joint destruction through the production of cartilage-degrading enzymes and pro-inflammatory cytokines, driving periprosthetic osteolysis which impacts on the longevity of total joint replacements. Understanding the danger of implanted material will allow us to better define molecular targets to inhibiting side effects of implantation-associated dangerous micro and nanoparticles (Chulpanova et al.; Orlowski et al.).

Some nanoparticles like silica are known for decades to cause disease and autoimmune disorder, but it is not that easy to study the conditions in experimental setup due to the fact that most established animal (mice) cell line are prone to develop only a part of the whole repertoire of interactions attributable to autoimmune conditions in human. In the work of Mayeux et al. this limitation was overcome by in-depth analysis of diversity outbred mice, revealing not only association of silicosis with lung autoimmune markers, bronchoalveolar lavage fluid cells, IL-6 and anti-ENA5, but also stronger silica-induced inflammation between mal mice. We should remember that cellular remnants and "apoptotic blebs" are also of nano- and microscale, and usually engulfment is silent and anti-inflammatory process (Tucher et al.). Apoptotic cells were known to produce different type of micro and nano extracellular vesicles (EV) they were known to be differently glycosylated and distinctly processed by macrophages (4). However, the formation of nanoparticles, like exosomes and others extracellular vesicles not related to apoptosis make their discrimination complicated. Group of Schiller have demonstrated that protein composition of apoptotic EV is quite unique and thus can serve as reliable discrimination factor; some danger signals like HMGB1 protein could be found only in apoptotic-related microvesicles (Tucher et al.). Another important finding suggests that release of large extracellular vesicles, 200 to 1,000 nm in diameter, involve proteasome action (Tucher et al.).

But when it comes to cancer, it looks that EV are becoming powerful communicating and instructing tools. In minireview "Role of macrovesicles produced by cancer cells," immune cells and mesenchymal stem cells are discussed in details, demonstrating how modification of the extracellular vesicle cargo can target specific tumor mechanisms responsible for tumor formation and progression to develop new therapeutic strategies and to increase the efficacy of antitumor therapies (Chulpanova et al.).

Immunosuppression is a key factor in silent clearance of dying cell microdebris, thus it's role in dealing with disease associated nano- and micro particles is crucial. The review by Huaux details the contribution of immunosuppressive cells and their derived immunoregulatory mediators and discusses the role of inflammatory vs. immunosuppressive mechanisms connecting micro- and nano-particles with pathogenesis of chronic diseases. The review summarizes role of immunosuppressive cytokines, involvement of regulatory T- and B lymphocytes, immunosuppressive myeloid cells and discusses how particle-related diseases can develop independently of chronic inflammation, enriches current bioassays predicting particle toxicity and suggests new clinical strategies for treating patients affected by particle-associated diseases (Marschner et al.).

PERSPECTIVES

The studies of this issue illustrate that crystals and microparticles induce diverse biological responses beyond triggering the NLRP3 inflammasome and the secretion of IL-1β from myeloid cells (5). Crystal biology just started as an interdisciplinary field and certainly holds bright promises for major discoveries also in the future. We still do not understand the full spectrum of molecular mechanisms shared across particles of different natures as well as different sizes and shapes. Often molecular machinery prone to recognize cellular debris can also react with inorganic crystals and vice versa. We lack an understanding of the particle-specific immune responses. Another unsolved issue is the functional differences between microparticle-induced neutrophil necroptosis and NET formation, a regulated form of chromatin release different from regulated neutrophil necrosis (6, 7). Only an interdisciplinary approach can address these important questions and eventually lead to new treatment modalities for patients with crystal- and microparticle-related disorders.

AUTHOR CONTRIBUTIONS

All authors listed have made a substantial, direct and intellectual contribution to the work, and approved it for publication.

FUNDING

MH, RB, AG, and H-JA were supported by the Volkswagen Foundation (grant 90 361). This work was partially supported by the Deutsche Forschungsgemeinschaft (DFG CRC1181 to MH, AN372/14-3, 16-2, 24-1, to H-JA, and MU3906/1-1 to SM). RB also received support from the Ministry of Healthcare of Ukraine, grant 0119U101338.

REFERENCES

1. Mulay SR, Anders HJ. Crystallopathies. *N Engl J Med*. (2016) 374:2465–76. doi: 10.1056/NEJMra1601611
2. Desai J, Foresto-Neto O, Honarpisheh M, Steiger S, Nakazawa D, Popper B, et al. Particles of different sizes and shapes induce neutrophil necroptosis followed by the release of neutrophil extracellular trap-like chromatin. *Sci Rep*. (2017) 7:15003. doi: 10.1038/s41598-017-15106-0
3. Munoz LE, Bilyy R, Biermann MH, Kienhofer D, Maueroder C, Hahn J, et al. Nanoparticles size-dependently initiate self-limiting NETosis-driven inflammation. *Proc Natl Acad Sci USA*. (2016) 113:E5856–E5865. doi: 10.1073/pnas.1602230113
4. Bilyy RO, Shkandina T, Tomin A, Munoz LE, Franz S, Antonyuk V, et al. Macrophages discriminate glycosylation patterns of apoptotic cell-derived microparticles. *J Biol Chem*. (2012) 287:496–503. doi: 10.1074/jbc.M111.3144
5. Franklin BS, Mangan MS, Latz E. Crystal formation in inflammation. *Annu Rev Immunol*. (2016) 34:173–202. doi: 10.1146/annurev-immunol-041015-055539
6. Boeltz S, Amini P, Anders HJ, Andrade F, Bilyy R, Chatfield S, et al. To NET or not to NET:current opinions and state of the science regarding the formation of neutrophil extracellular traps. *Cell Death Differ*. (2019) 26:395–408. doi: 10.1038/s41418-018-0261-x
7. Desai J, Mulay SR, Nakazawa D, Anders HJ. Matters of life and death. How neutrophils die or survive along NET release and is "NETosis" = necroptosis? *Cell Mol Life Sci*. (2016) 73:2211–9. doi: 10.1007/s00018-016-2195-0

Conflict of Interest Statement: The authors declare that the research was conducted in the absence of any commercial or financial relationships that could be construed as a potential conflict of interest.

frontiers in Immunology

SYSTEMATIC REVIEW
published: 28 May 2018
doi: 10.3389/fimmu.2018.01157

Systematic Overview of Solid Particles and Their Host Responses

Fei Shu[1,2] *and Yan Shi*[1,3]*

[1] *Department of Basic Medical Sciences, Institute for Immunology, Center for Life Sciences, Beijing Key Laboratory for Immunological Research on Chronic Diseases, Tsinghua University, Beijing, China,* [2] *Peking University-Tsinghua University-National Institute of Biological Sciences Joint Graduate Program, School of Life Sciences, Peking University, Beijing, China,* [3] *Department of Microbiology, Immunology and Infectious Diseases, Snyder Institute, University of Calgary, Calgary, AB, Canada*

Crystalline/particulate substances trigger a plethora of signaling events in host cells. The most prominent consequence is the inflammatory reactions that underlie crystal arthropathies, such as gout and pseudogout. However, their impact on our health was underestimated. Recent work on the role of cholesterol crystal in the development of atherosclerosis and the harm of environmental particulates has set up new frontiers in our defense against their detrimental effects. On the other hand, in the last 100 years, crystalline/particulate substances have been used with increasing frequencies in our daily lives as a part of new industrial manufacturing and engineering. Importantly, they have become a tool in modern medicine, used as vaccine adjuvants and drug delivery vehicles. Their biological effects are also being dissected in great detail, particularly with regard to their inflammatory signaling pathways. Solid structure interaction with host cells is far from being uniform, with outcomes dependent on cell types and chemical/physical properties of the particles involved. In this review, we offer a systematic and broad outlook of this landscape and a sage analysis of the complex nature of this topic.

Keywords: solid particle, host response, biological crystal, adjuvant, cell death

OPEN ACCESS

Edited by:
Hans-Joachim Anders, Ludwig-Maximilians-Universität München, Germany

Reviewed by:
Orestes Foresto-Neto, Universidade de São Paulo, Brazil
Rahul D. Pawar, The Scripps Research Institute, United States
Ramanjaneyulu Allam, Universität Bern, Switzerland

***Correspondence:**
Yan Shi
yanshi@biomed.tsinghua.edu.cn

Specialty section:
This article was submitted to Inflammation, a section of the journal Frontiers in Immunology

Received: *30 March 2018*
Accepted: *08 May 2018*
Published: *28 May 2018*

Citation:
Shu F and Shi Y (2018) Systematic Overview of Solid Particles and Their Host Responses. Front. Immunol. 9:1157. doi: 10.3389/fimmu.2018.01157

INTRODUCTION

Solid amorphous/crystalline/fibrous particles are common in our environment. Looking outward, all life forms are exposed to particles varying in size, chemistry, and the state of agglomeration in the surroundings. With the technological advancements, human populations are facing new variations related to the exposure to environmental and/or occupational pollutants/hazards/toxins. In recent times, nanotechnologies bring ultrafine particles into our lives (1). Therefore, we are in an ever-changing world of particulate substances. Looking inward, several essential biological components are in delicate balance near the point of precipitation, including nucleic acid metabolites, lipids, and ions. Some forms of solidification, such as cholesterol crystal (CC) formation and calcification of joints, are a part of aging physiology. Other precipitations, such as monosodium urate (MSU) (2), can

Abbreviations: Alum, trivalent aluminum salts, including ALOH and $AlPO_4$; BCP, basic calcium phosphate; CASR, calcium-sensing receptor; CC, cholesterol crystal; CPPD, calcium pyrophosphate dihydrate; CVD, cardiovascular disease; DC, dendritic cell; LDH, layered double hydroxides; LDL, low density lipoprotein; HDL, high density lipoprotein; LLOMe, L-leucyl-L-leucine methyl ester; MLKL, mixed lineage kinase domain-like; MSU, monosodium uric acid crystal; NADPH, nicotinamide adenine dinucleotide phosphate oxidase; NET, neutrophil extracellular traps; NLRP3, NACHT, LRR, PYD domains-containing protein 3; RIPK1/RIPK3, receptor-interacting serine/threonine-protein kinase 1/3; ROS, reactive oxygen species; SERCA, sarcoplasmic/ER Ca^{2+}-ATPase; TXNIP, thioredoxin-interacting protein; TLR, toll-like receptor; VLPs, virus-like particles.

lead to acute inflammation and tissue damage. In addition, with advancements in modern medicine, pharma-biotech companies/institutes introduce particles in formulation development for vaccination, drug delivery and cancer therapy. Compared with other areas of biomedical research, so far there has not been a discipline dedicated to studying how hosts respond to solid structures. As such, our understanding and theories are mostly fragmented, creating a hidden deficit in our effort to control and utilize this class of materials.

Host responses to solid/crystalline particles have been studied by scientists and clinicians for decades for health concerns. Historical lessons are vivid. One of the most memorable is the chrysotile and amphibole asbestos-induced respiratory deficiencies and mesothelioma (3, 4). The impact was that guidelines were imposed by regulatory bodies to strictly ban its consumer use and minimize it human exposure of occupational operators (https://www.epa.gov/asbestos). In recent years, cellular signaling events associated with crystal-triggered inflammation have become an intensely investigated topic (5). Some areas are covered with extreme depths, including inflammasome activation (6), cell death (7–9), reactive oxygen species (ROS) production (10, 11), and adjuvanticity (12, 13). However, crystals vary greatly in their geometry and chemistry. Host cells with whom they interact are also diverse. Therefore, the speedy accumulation of newly gained knowledge has not led to a sufficient number of consensuses. In addition, a solid structure/host cell response cannot be comprehended at any given cross section. It is a chain of events from crystal formation/entry, cell membrane binding, intracellular signaling cascades, cytokine release, cell death, secondary host responses, etc. In this review, we aim to integrate several less illuminated areas of cell responses to solid particles, including physiochemical properties, nanoparticles, particulate adjuvants, and ongoing debates regarding their activation mechanisms. In other words, we offer a panoramic view of this interesting topic.

PHYSICAL AND CHEMICAL PROPERTIES

While research on signaling events in host response to solid particles is currently very active, the study of their chemical and physical properties remains a widely pursued subject. As particles under analysis and experimental readouts vary, it is hard to draw a set of conclusions with any precision. The overarching observations are: (1) Size of any given solid structure has a great impact on its biological effects. (2) A given volume of a particulate substance can have different effects depending on their geometric parameters. (3) Surface chemistry, including coating, can change outcomes. (4) Different host cell types can manifest different host responses. However, if the nature and types of experimental outcomes can hypothetically be set aside, and only activation intensity (i.e., cytokine production, adjuvanticity, and cellular morphology changes) is used as the readout, some internal consistencies can be extracted from the existing literature.

Size

Generally, solid structures of size 1–100 nm are considered as nanoparticles. For these particles, the general entry into the cells is mediated by endocytosis or simple diffusion without any defined receptors. Sizes beyond 100 nm and up to 10 μm are regarded as microcrystals. Within the latter, for particles with a diameter larger than 0.5 μm, phagocytosis is the dominant form of entry (14). There have been some isolated studies (15–17) whereby the size of polylactide-co-glycolide (110 vs 800–900 nm) did not show any significant changes in the ability to induce antibody responses to protein antigens from *Neisseria meningitidis* and HIV in mice (18). However, most papers appear to offer different results (1). Early work using simple stimulation and cell proliferation index measurement suggested that larger surface area (smaller diameter) of polystyrene and TiO_2 particles seemed to block macrophage cell line proliferation *in vitro* (taken as an indicator of cell loss) (19). This finding was confirmed by another group where carbon black as well as TiO_2 particles were used *in vivo*. In that study, both particles of 250 nm in diameter and those roughly one log smaller were instilled intratracheally. In rats, the smaller ultrafine particles induced drastically higher neutrophil infiltration in the lung and greater epithelial damage (20). Using epithelial cells as an example, amounts (total volume) required for small (below 20 nm) vs large (above 100 nm) silica crystals tended to create a log difference in the efficiency of inducing cell death. In addition, smaller particles achieved the same effect much faster than the larger ones in human endothelial cells *in vitro* (21). Similar observations were made by other groups studying human endothelial cells and macrophage *in vitro* (22). One reason for this difference is that small particles enter cells more readily. Using silver nanoparticles (SNP) SNP-5, SNP-20, and SNP-50 (numbers indicate diameter in nanometer) as an example, *in vitro* cellular toxicity of smaller particles was correlated with their rapid presence inside the human epithelial cells (23). In one report that compared nano vs micro silica particles, smaller (30–1000 nm) crystals entered mouse BMDM easily and caused significant lysosomal marker loss, indicating lysosome destabilization, in comparison with the larger ones (1,000–10,000 nm) (24). An interesting contrast was another paper suggesting that silica particles 1,000 nm across were more toxic than small (30 nm) to THP-1 cells (25), a phenomenon associated with the efficient uptake of the larger particles. This study, as well as several others, suggested that phagocytes, such as J774.2 and RAW264.7 cells, were more prone to particle-induced cell damage than nonphagocytic cells (L929) (26). These results imply that efficient entry may ultimately explain the ability to trigger cellular responses. Whether additional signaling mechanisms related to particle size also account for the stimulation intensity have not been independently investigated.

Morphology and Geometry

Shape of solid structures has been implicated in some studies to be a critical factor in triggering host cell responses. The differences in crystalline symmetry, i.e., anatase vs rutile TiO_2, could result in significantly different outcomes in mouse keratinocytes *in vitro* (27). The sharp and pointy edges of many crystals, i.e., asbestos and MSU, are believed to at least partially contribute to their pathology *via* direct injury to mouse mesothelial cell membrane *in vitro* and *in vivo* (28, 29). Using non-opsonized hydroxyapatite (HA) as an example, a study was conducted to compare four types of geometries: needle, plate, sphere, and rod

and tested their ability to induce TNFα/IL-6 and ROS production as well as cytotoxicity. It was found that needle and plate shapes induced the highest rate of cell death in human bronchial epithelial cells accompanied by high IL-6 production. Interestingly, rod-shaped HA induced more ROS production. RAW264.7 cells, on the other hand, showed much less selectivity to the shape in all the parameters measured (30). A study on carbon nanotubes (CNTs) also suggested that long and needle-shaped CNTs and asbestos triggered human macrophage IL-1β secretion *in vitro* while only the former triggered IL-1α production. Carbon black and short CNTs failed to induce either (31). Interestingly, in this report, it was found that long CNTs induced a typical NACHT, LRR, PYD domains-containing protein 3 (NLRP3) inflammasome activation event that relied on ROS production, P2X7 receptor, and lysosomal destabilization. Long silver nanowires were also more inflammatory toward human epithelial and liver cells *in vitro* than the short ones (23), and spherical TiO_2 was less stimulatory than the same material in the shape of nano belts *in vivo* (32). The observations may be associated with higher area/volume ratio, although a systematic analysis is not yet available. In a study comparing crystalline nanocellulose with fibrillary cellulose, it was found in A549 cells fibrillary cellulose was more toxic than the crystalline counterpart. This was mainly due to the former's strong ability to induce oxidative stress. On the other hand, crystalline cellulose was able to induce a broad range of cytokine production including IL-6, IL-8, MCP-1, IL-12p70, and G-CSF (33). Therefore, distinct shapes with similar chemistry can lead to different profiles of cellular responses. Many crystalline structures may also exist in an amorphous state by contrast to the better known larger crystals. In a pulmonary inflammation mouse model, amorphous/colloidal silica induced only transient inflammation while the response triggered by crystals was more persistent (34). Indeed, for non-crystalline structures such as SiO_2 from nano to micro μm sizes (mono-disperse and poly-disperse), the stimulation for NLRP3 inflammasome activation in mouse macrophages was lower than the crystalline. On the other hand, the comparison between amorphous and colloidal forms did not reveal any difference in stimulation capacity (35).

Chemical Composition

Chemical properties of solid structures have been directly linked to their stimulatory ability. Under this umbrella, one consideration is the degree of solubility. It is generally considered that solubility is proportionally related to cytotoxicity (36). In several reports, slightly soluble zinc and iron oxides were more potent in inducing target cell DNA release than almost insoluble CeO_2, ZrO_2, TiO_2, and $Ca_3(PO_4)_2$. In one study, ionic metal was critical to IL-6 and IL-8 production by human airway epithelial cells which were blocked by metal chelation (37). However, mechanistic insights of the observations of this nature are not available (38, 39). In the absence of detectable solubility, chemical composition can also make a difference in cellular responses. By comparing various metal oxides, copper oxide had the highest toxicity toward airway epithelial cells (40). In that study, several metal oxides were equally potent to induce ROS in the treated cells, however, CuO had the ability to suppress the cellular antixidation effects, i.e., the activities of catalase and glutathione reductase. It should be noted that depending on cell types studied and experimental settings, results have not been consistent regarding chemical compositions of particles. In some studies, Y_2O_3 (yttrium oxide) and ZnO were found to trigger inflammatory responses (ICAM-1, MCP-1, and IL-8 expression) better than Fe_2O_3 in endothelial cells (41), by contrast with the report by Brunner et al. where iron oxides were more stimulatory in human mesothelioma and rodent fibroblast (36). Surface charge and hydrophobicity may also affect cellular responses *in vivo* (42–44). This notion was echoed by a study where unmodified silica crystals induced strong IL-1β, ROS, and NLRP3 inflammasome activation in THP-1 cells. However, surface functionalization with –COOH, $–NH_2$, $–SO_3H$, and –CHO groups significantly reduced all aspects of inflammatory responses (45). In fact, the simple presence of cell culture serum can result in significant reduction of toxicity toward fibroblast, which presumably was driven by the alteration of particle surface chemistry (46). Interestingly, the different surface chemistry can also alter their anatomic distributions. For instance, i.p. injected polymethyl methacrylate beads tended to deposit in the spleen resulting in its enlargement. Polystyrene beads of similar sizes, on the other hand, were accumulated in adipose tissues (47). Likely the different surface chemistries triggered different migration patterns in the phagocytosing macrophages.

It should be noted that the forth mentioned experimental results are small samples of the vast literature on chemical/geometric properties of host-interacting particles. Depending on cell types, readouts, and experimental settings, different and even contradictory reports are common. Ideally, the desired approach is to isolate one particular variable for extensive analysis while other parameters are meticulously controlled. Thus far, the boldest attempt to extract a set of principles underneath the surface chemistry and immune recognition was made by Williams et al. (48). In that study, they used "layered double hydroxides" (LDH) for analysis, prompted by the effect of alum in immune stimulation. The exact chemical compositions are technically challenging to understand. We can picture their setup as follows. A sheet of metal (M^+M^{2+} and M^{3+}) hydroxides is laid against pairing anions to form a stack. Each stack is laid on top of another for a multilayered structure. Because the metal ions can be chosen, M^+M^{2+} vs M^{3+} ratios and anion species can be selected, the resulting structures can be tested for their immune regulation solely as a function of various ions used in the experiment. Dendritic cell (DC) activation was measured by a set of cytokine production. $LiAl_2$-CO_3, Mg_2Al-NO_3, Mg_2Fe-Cl, Imject alum, and alhydrogel were compared. Surprisingly, this study revealed that all *in vitro* human DC responses were highly correlated with a linear combination of three LDH properties: the radius of the spherical M^+ or M^{2+} metal cations; the distance between the LDH layers (interlayer spacing); and zeta potential that defines the magnitude of the electrical charge at the interfacial double layer around the LDH particle. Newly synthesized LDHs were highly predictable by these variables in their DC stimulatory capacity. These properties were directly verified in *in vivo* mouse antibody production. These efforts were aimed to produce a set of "chemical–immunology rules". Clearly, to understand the complex nature of host responses to solid structures, undertakings like this point to a possible angle to tackle the vast unknowns of

physics and chemistry of particulate substances involved in host cell activation.

BIOLOGICAL CRYSTALS

Unlike particles that come with modern manufacturing/processing or exist in our environment, crystalline deposition has long been a part of human biology/pathology. Best known among them are uric acid, cholesterol, heme, and a list of calcium-containing crystals [calcium pyrophosphate dihydrate (CPPD), HA, calcium oxalate, and calcium phosphate family in general]. Slightly less prevalent diseases can be caused by additional crystals, such as xanthine leading to xanthinuria and arthropathy (49) and cystine (oxidized cysteine dimer) in kidney stones (50). A rare genetic disease, adenine phosphoribosyltransferase deficiency, results in the inability to produce adenosine monophosphate from adenine, 2,8-dihydroxyadenine crystal formation, and kidney failure in human and mice (51–54). In this section, we aim to illustrate the most common types and their related pathologies.

Monosodium Urate Crystals

Gout, the deposition of MSU crystals, has been recognized for over 4,000 years and extensively described in the ancient literature (55). Historically, its occurrence has been associated with excessive dietary and alcohol consumption (56). In the 18th century, crystals from a tophaceous joint were isolated and their chemical nature was reported (55). It is generally believed that high purine metabolism leads to hyperuricemia (>6.8 mg/dl), a precondition for gout and tophus. Gout is often induced by metabolic and environmental factors, such as increased Ca^{2+}, low pH, and cold weather, and occurs only in the distal extremities, never near the core of body where the temperature is more consistent (57). Interestingly, till date, we still cannot duplicate the *in vivo* crystal formation event in the lab, as at this concentration uric acid does not precipitate in standard buffers (58). Additional factors, for instance natural MSU antibodies, may be critical for this process (58, 59). Mechanistically, *in vivo* the initial nucleation of uric acid crystals is reversed due to rapid dissolution. The antibodies (IgG in human gout patients and IgM in mouse) help stabilize the nucleation core whereby the crystal growth is permitted. This notion is supported by clinical observations that MSU crystals isolated from patients are often coated with a layer of antibodies (60), with Fab pointing to the crystalline surface (61). Regarding the signaling events leading to the painful inflammatory episode of gouty arthritis, many models have been proposed. MSU typically activates NLRP3 inflammasome and IL-1β production, and the proposed signaling events pertinent to NLRP3 regulation, such as ROS, K^+ efflux, and lysosomal rupture, are all implicated in its inflammatory properties (discussion later). Specific to MSU, it has been suggested that CD11b and CD16 may directly recognize MSU crystals because antibodies for these two surface molecules reduced MSU-mediated neutrophil activation (62, 63). Interestingly, the antibody blockage also reduced neutrophil responses to CPPD, a chemically distinct structure, suggesting that these surface molecules may merely participate in the signaling rather than the specificity determinant for these crystalline surfaces. Liu-Bryan and Terkeltaub's group reported that toll-like receptor (TLR)2/TLR4 and CD14 were the functional receptors of MSU (64–66). The conclusion was mostly drawn from the reduced inflammatory responses in mice deficient in these genes. Using similar TLR-deficient mouse models as well as *in vitro* cell transfection, Chen et al. failed to see any involvement of TLR2 or TLR4 (67). While the suggestion of protein-based positive signaling receptor for MSU has not been further investigated, one paper suggested that Clec12a is an inhibitory receptor for this crystal. Binding analysis showed that Clec12a had specific affinity for MSU and mice deficient in this gene mounted increased inflammatory responses against MSU challenge (68). Our lab's results have suggested another model. The surface of MSU crystal showed substantial binding to cholesterol, a component of lipid rafts. The binding event caused the plasma membrane lipid sorting and an accumulation of ITAM-containing membrane proteins. This accumulation, in turn, recruited Syk to the inner leaflet and induced a chain reaction similar to Syk/PI3K-dependent phagocytic activation (69). This model describes a lipid-based signaling event independent of protein receptors. Whether this signaling modality is central to the general sensing of solid structures and is being actively investigated.

Calcium Crystals

While calcium salt crystals mediate inflammatory responses similar to MSU (70), the prerequisites for their formation are different. First, calcium-containing crystal generation does not require elevated levels of Ca^{2+}. Second, these crystals almost always develop on matrix surfaces, mostly cartilages (71). Inorganic pyrophosphate, produced *via* ATP metabolism, is found to induce CPPD formation. On cartilages, inorganic pyrophosphate level is regulated by several enzymatic activities including ectonucleotide pyrophosphatase (72, 73). Unlike MSU, calcium crystal deposition in joints is common and remains asymptomatic in most adults, and it is, therefore, difficult to directly link CPPD formation to the symptoms of pseudogout (74). In model systems with synthetic crystals, CPPD does stimulate strong inflammatory activation. Therefore, the prevailing proposal is that CPPD formation is an essential first step for the eventual development of the acute "gout" like symptoms (75). Signaling-wise, CPPD and basic calcium phosphate can stimulate nitric oxide and collagenase production in chondrocytes *in vitro* (76, 77). Martinon et al. found that CPPD is a strong inducer of NLRP3 inflammasome activation *in vitro* (6). In addition, CPPD crystals can inhibit neutrophil apoptosis *via* Bcl-2 (78). It is very likely that all these factors work in sync to generate the inflammatory responses to calcium salt crystals.

Cholesterol Crystals

Cholesterol clustering *in vivo* is primarily in two forms. Gallstones (cholelithiasis) are large solid structures mostly made of cholesterol in biliary duct and gallbladder. They are results of liver cholesterol accumulation, often with a genetic disposition (79). The presence of CC in atherosclerotic lesions reflects the imbalance of cholesterol homeostasis and has by far the highest impact in human health, being one of the root causes of cardiovascular disease (CVD, a third of mortality in the developed countries). *Via* the mevalonate pathway, all mammalian cells are capable of

cholesterol synthesis (80). Its metabolism is mainly in the liver in the form of biliary secretion of surplus cholesterol and bile acid. Therefore, the cholesterol transport becomes the critical regulation of its level. For the cardiovascular system, low density lipoprotein *via* its receptor transports esterified cholesterol to artery walls while high density lipoprotein mediates the reverse transport back to the liver (81). In the periphery, deposited esterified cholesterol can be converted by ester hydrolases into free cholesterol, leading to CC formation (82). In advanced CVD, accumulated CC in the plaques expand in volume and cause the rupture of the fibrous cap, leading to acute thrombosis, embolism, and clinical CVD symptoms (83, 84). More in depth analyses indicate that CC may be the culprit of the initial atherosclerotic change at the very beginning. It was found by some that cholesterol-lowering treatment was only beneficial when used early in mouse life (85). Because of their small sizes, optical imaging in tissues has not been easy. The limitation is being gradually overcome with new preparation protocols (86, 87) and imaging tools such as Raman scattering microscopy (88). A recent paper reported that endothelial cells produce CC rather quickly under cholesterol overload. The crystal deposition under endothelial cells was found as early as 1 week after feeding *Ldlr*$^{-/-}$ mice with high fat diet (89). Those improved detections strongly suggest their involvement in much of the initial atherosclerotic development. Local accumulation of CC has been recognized as an inflammatory event (90). CC can activate the complement system *in vitro* (91, 92) as well as IL-1α production *in vivo* and *in vitro* (93, 94). The central interest is undoubtedly focused on the involvement of NLRP3 inflammasome. Some reports suggested that NLRP3 inflammasome and its components were essential for the plaque formation (86, 95) while others failed to make this observation (93, 96).

Hemozoin

Malaria is a major cause of mortality in developing countries. In its life cycle, *Plasmodiu*m invades red blood cells and uses hemoglobin as its energy source. The product of this digestion, heme, forms hemozoin crystals (97). While *Plasmodium* itself can directly modulate endothelial permeability and cause circulation blockage (98, 99), hemozoin is a major activator of innate immunity (100), both leading to various degrees of mouse hepatocyte dysfunction *in vivo* (101). The surface of hemozoin crystals has been found to be highly active in mediating oxidative responses (102). Another property of hemozoin is its extensive phagocytosis by phagocytes in the circulation and in vital organs (liver, brain, etc.), particularly after RBC rupture (103). This phagocytic event is believed to be immune regulatory and the intensity of phagocytosis is an indicator of the disease severity (104). Macrophages and monocytes stimulated with hemozoin produce large amounts of cytokines *in vitro*, including TNFα, MIP1α, and β (105), chemotactic factors (106), ROS and nitric oxide (100, 107). A large panel of signaling molecules, including ERK1/2, JAK2/STAT-1, NFkb, and Syk kinases were all reportedly involved (108). The exact recognition mechanism is not clear, although in one report TLR9 was involved (109). This finding is controversial as others have suggested the contamination of *Plasmodium* DNA in the isolated hemozoin (110–112). By contrast, the activation mediated by NLRP3 is well characterized and has been supported by multiple research groups. Shio et al. found that hemozoin-induced NLRP3 inflammation and IL-1β production were downstream of Syk kinase. Importantly, deficiencies in NLRP3 components protected the host from one strain of malaria, *Plasmodium chabaudi adami* (113). Another paper around the same time suggested that hemozoin mediated inflammatory responses *in vitro* and *in vivo*, particularly NLRP3 activation, was *via* induction of uric acid release (110).

PARTICULATE ADJUVANTS

Adjuvants are used to increase host responses to otherwise low immunogenic antigens. They can be roughly divided into delivery tools and immune potentiators (12, 114). Serving both purposes, particulate adjuvants are a subcategory of immune enhancers and are the first preparation used in human vaccine. Glenny's work has been sufficiently discussed in vaccine reviews (115). However, one particular point worth noting is that while the early workers Glenny and Maschmann et al. used alum in various chemical composition to precipitate and stabilize diphtheria toxin, they did not recognize the immune stimulatory effects of this crystalline structure (116–118). In the last two decades, our understanding of particulate adjuvants has seen some dramatic revisions.

Alum usually refers to trivalent inorganic aluminum salts, including $Al(OH)_3$ and $AlPO_4$ (119, 120). For decades, it was thought that alum served as an *in vivo* depot for the associated antigens, prolonging antigen availability. This notion was proven incorrect by several experiments (121–123). In 2004, it was reported that injection of alum resulted in the accumulation of IL-4-producing monocytic Gr1$^+$ cells in the spleen (124). Till date, it is still not clear how this population mediates immune response, although it is involved in TH1/TH2 bias (125). In 2008, Eisenbarth et al. reported a deficiency in multiple antibody subtype production in response to alum in NLRP3$^{-/-}$ mice (126) suggesting that alum's immunogenicity may be related to its ability to activate NLRP3 inflammasome. A follow-up paper using similar mouse models by Tschopp's group, however, reported a reduction in IgE production only (127). In other reports, including from our own group, NLRP3/Caspase-1 axis was not found to be essential for alum-mediated antibody production (128–130). Later on, two groups reported that DNA release triggered by local alum injection might be responsible for its adjuvanticity (131, 132). Ishii's group further suggested that in the process, alum triggered activation of TBK1/IRF3, leading to IgE isotype switching (132). Whether this signaling event requires STING, a sensor for intracellular DNA is still a topic of discussion (131). In addition, a recent paper suggested that commercially available DNase may have proteolytic activities, which at least partially explained the reduced adjuvanticity following DNA removal in alum-treated mice (133). Therefore, the role of DNA release in alum's adjuvant effect still requires more carefully controlled analyses. Our group proposed an alternative mechanism. Using atomic force microscopy, we found that alum crystals bound to DC plasma membrane lipids and triggered an abortive phagocytic response. DCs thus activated showed enhanced binding to CD4$^+$ T cells *via* ICAM-1 and LFA-1 (128), leading to better T cell priming by DCs.

The notion that uric acid being a particulate immune adjuvant was not derived from its ability to trigger gouty inflammation. It was found that dead cells had strong adjuvant effect when delivered with protein antigens; the active fraction was molecularly identified by chromatography and mass spec analysis (134). It was found that soluble uric acid did not have any adjuvant effect, yet it turned stimulatory upon crystallization. It has been difficult to visualize MSU deposition *in vivo* following immunization because the microcrystals were not compatible with imaging preparation protocols. Although the ability of uric acid to serve as an adjuvant is confirmed (135) in recent years, MSU has been gradually recognized as a "cryptic" adjuvant, in that many immune responses appear to require background uric acid. We have reported that MSU crystallization requires endogenous antibodies that stabilized the initial crystal formation. In the absence of antibody as in the IgH mice, uric acid did not serve as an endogenous adjuvant (58). Several reports have found that removal of uric acid *in vivo* significantly reduced airway inflammation (136) and immune responses to antigens released from dead cells (2, 137). In addition, other groups have found that uric acid may be the conduit for the immune stimulatory effect of hemozoin and alum adjuvant (110, 138).

Virus-like particles (VLPs) are a relatively new technology and originated from the vaccine preparation with killed pathogens. They are assembled viral proteins with a resulting morphology similar to original viruses. These particles are highly stimulatory in comparison with their soluble proteins and at the same time free from the safety concerns associated with attenuated virions. With recombinant technologies, bacterial, viral, mammalian, and other expression systems have been used to successfully produce VLPs. Although VLPs can be considered adjuvants in comparison with free proteins, their efficacy can be further enhanced by other adjuvants (139). The mechanistic basis for the enhanced immunity is a concept termed geometric pathogen-associated structural pattern (140). In general, all VLPs form unique repetitive surface structures (140, 141). As these patterns bare the signature of invading pathogens, they are potent in activating antigen presenting cells and mediate efficient migration of these cells to draining lymph nodes. They are also able to bind to naturally existing antibodies and fix complement (142), further enhancing their immune stimulation.

Nanoparticle adjuvants were a product of time that started two decades ago. The term defines the size but posits no limitation on its chemical/structural details. One of the most frequently tested is polylactic-co-glycolic acid and polylactic acid, for their biodegradability and easy incorporation of antigens and drugs (143). They are known to induce antibody titers similar to those adjuvanted regimens. Other popular selections are liposome and micelle-based preparations. Overall, nanoparticles can easily enter solid tumors (144). This is likely the result of extensive pathways used for the uptake of these particles, including pinocytosis, and clathrin and caveolin-dependent endocytosis (145). These particles have been used as an efficient tool for delivery mainly due to their protection (146) and controlled release (147, 148) of associated antigens. Similar to other particulate antigens, nanoparticles can trigger cross-presentation and $CD8^+$ T cell responses (149), a feature sought in viral vaccine and tumor immune therapy.

SOLID PARTICLE-INDUCED HOST CELL RESPONSES

Inflammasome

Solid/amorphous/crystalline/fibrous structure-mediated cellular responses are a major part of inflammasome research, particularly signaling associated with NLRP3 inflammasome. In 2006, Tschopp's group reported that MSU and CPPD-induced IL-1β production was dependent on NLRP3 inflammasome components, NLRP3, ASC, and caspase-1 (6). This landmark experiment started the intense pursuit of inflammatory mechanisms associated with solid particles. Subsequently, a series of papers described the requirement for NLRP3 in IL-1β production in response to silica, asbestos, and metal oxides. With limited exceptions, it is reasonable to assume that the bulk of inflammation associated with solid structures is dependent on NLRP3 inflammasome. However, the molecular events that lead to NLRP3 activation are still being debated. Several intermediate conduits have been proposed including ROS production, lysosome rupture, K^+ efflux, and Ca^{2+} influx (150, 151).

Reactive Oxygen Species

In the process of ATP production in mitochondria, oxygen is ideally reduced to water. However, when this process is not complete, O_2^- escaped from this pathway becomes the source of a series of oxidizing chemicals, including hydrogen peroxide and hydroxyl radicals (152), collectively termed as ROS. These products become a part of cellular signaling network–redox biology. ROS signaling is also essential for both innate and adaptive immunity (153, 154). The excess of this production leads to oxidative stress, which is at the core of cellular aging and degenerative diseases such as sclerosis and neoplasm. ROS production can be readily induced by solid structures of various sizes and shapes, and to some extent of distinct chemical compositions. Many nanoparticles, copper, iron, cerium, zinc, nickel, titanium, aluminum oxides, gold, silver (155), silica (156), MSU (157), asbestos (158), and alum were found to induce ROS. ROS blockade with ROS scavenger or inhibition of nicotinamide adenine dinucleotide phosphate oxidase (NADPH) oxidase suppressed NLRP3 activation induced by MSU, asbestos (159), silica (158), and hemozoin (160). In the process, the conduit was proposed to be thioredoxin-interacting protein (TXNIP). TXNIP dissociates from thioredoxin in a ROS-sensitive manner and then binds to NLRP3 leading to its activation (157) (**Figure 1**). This proposal has not been completely satisfactory. First, a lot of stimuli induce ROS production but NLRP3 activation is not common to all of them, i.e., cytochrome P-450 oxidase uncoupling, xanthine oxidase activation, mitochondrial respiration, and various peroxisome oxidase activations (161). Inflammasome activation was not increased but suppressed in enhanced production of ROS in superoxide dismutase-1-deficient macrophages (162) while NADPH oxidase deficiency boosted the activation (163). Second, the source of ROS responsible for NLRP3 inflammasome activation remains unclear. The inhibition of mitochondrial complex I and II did not reduce asbestos-induced NLRP3 activation *in vitro* (159), arguing against mitochondria as the origin of ROS.

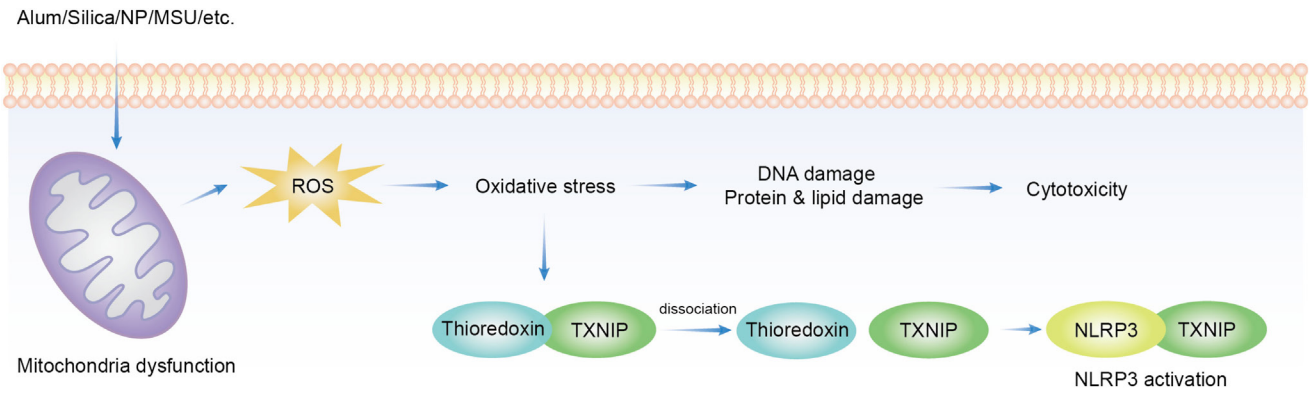

FIGURE 1 | Overview of reactive oxygen species (ROS) implicated in solid particle-induced cell death and NACHT, LRR, PYD domains-containing protein 3 (NLRP3) inflammasome activation. Solid particle treatment causes mitochondrial stress and ROS production. The oxidative stress mediates the damage of DNA, proteins, and lipids, which may be an important cause of cytotoxicity. ROS production also induces NLRP3 inflammasome activation by dissociating thioredoxin-interacting protein (TXNIP) from thioredoxin then allows its binding to NLRP3, which leads to NLRP3 activation.

Lysosomal Rupture

Another leading proposal for crystal-mediated NLRP3 inflammasome activation is *via* lysosome rupture. In this model, phagocytosis of solid particles triggers lysosome destabilization and release of cathepsin B, which activates NLRP3. Lysosome rupture blockage and cathepsin B inhibitor reduced NLRP3 activation in mouse macrophages *in vitro* induced by alum (164) and silica (165). Artificial induction of lysosome rupture with L-leucyl-L-leucine methyl ester (LLOMe) also led to NLRP3 activation that was blocked by cathepsin B inhibitor (166). However, this notion is controversial. In some reports, cathepsin B deficiency failed to reduce IL-1β production *in vitro* stimulated by MSU and silica (151, 167) or hemozoin (160). A possible explanation for this contradiction is the off-target effect of cathepsin B inhibitor as it was found to block NLRP1b inflammasome (168). Another explanation is that multiple cathepsins are involved in NLRP3 activation as the cathepsin family is highly conserved and cathepsin B inhibitor, Ca074Me, was found active toward other members (169). Furthermore, the authors found that not only NLRP3 activation but also particle-induced cell death was dependent on multiple redundant cathepsins (169, 170).

K^+ Efflux

In recent years, the role of K^+ efflux in NLRP3 activation has become the center of attention. High extracellular K^+ was reported to inhibit almost all known NLRP3 agonists *in vitro*, including hemozoin (160), silica and asbestos (159), MSU, Nigericin, and ATP (171), and bacterial pore-forming toxin, alum, CPPD, and LLOMe (151). Glyburide, a K^+ channel blocker, also inhibited NLRP3 inflammasome *in vitro* (172), which appears to confirm the role of K^+ efflux. The intracellular sensor for the reduced K^+ and how it is linked to NLRP3 activation are not clear. The idea of K^+ efflux as the upstream signal of NLRP3 came from the understanding that extracellular K^+ blocks intracellular K^+ outward motion during a typical cycle of eukaryotic membrane depolarization/repolarization (171) and assumed that particulate substances triggered a sustained drop of intracellular K^+. However, experimental high K^+ depolarizes the membrane and reduces the membrane potential (typical −40 to −80 mV) to near neutrality, and the membrane potential is a critical parameter for much of the eukaryotic biology (173–177). We recently found that both membrane depolarization and hyperpolarization were sufficient to block NLRP3 inflammasome activation without involving large amounts of K^+ moving across the plasma membrane (our own observations). Therefore, molecular details of K^+ efflux and NLRP3 inflammasome activation need to be further scrutinized. In addition to K^+, Ca^{2+} influx is induced by numerous NLRP3 activators (178). Ca^{2+} influx was suggested to be important for NLRP3 activation since thapsigargin, an inhibitor of the sarcoplasmic/ER Ca^{2+}-ATPase, incubation in Ca^{2+} free media (179), or BAPTA-AM (intracellular Ca^{2+} chelator) (180) significantly suppressed NLRP3 inflammasome activation in ATP-stimulated BMDM. Another piece of evidence was the calcium-sensing receptor activation stimulated NLRP3 inflammasome and knockdown of the receptor had the opposite effect (180). However, there are reports arguing against the Ca^{2+} influx model. One group found that extracellular Ca^{2+} activated NLRP3 through K^+ efflux (151). Another group, on the other hand, suggested that Ca^{2+} influx was neither necessary nor sufficient for NLRP3 activation during ATP, Nigericin, and LLOMe stimulation (181). In a report aiming to bridge the two ion-dependent models, K^+ and Ca^{2+} visualization sensors were used and the results suggested that K^+ efflux was necessary for sustained Ca^{2+} influx while K^+ efflux was independent of Ca^{2+} influx (182).

Cell Death

Many particles with different chemical composition, morphology, size, hydrophobicity, and ionic charge were proved to be cytotoxic. Thus a lot of efforts were made to found a common pathway. Generally, solid particle-induced cell death relies on cellular uptake, indicating that phagosome or lysosome may be important in this type of cell death (165, 183, 184). Downstream of particle phagocytosis is the lysosome rupture and ROS production, which gives rise to oxidative stress (185–187). Following oxidative stress

are mitochondrial dysfunction, DNA damage, and protein/lipid oxidation (185, 188). These factors work together to induce the eventual cytotoxicity (155). Several additional pathways have been proposed in the literature (**Figure 2**).

Silica-containing particles are ubiquitous, found in volcanic ashes (189), materials made from quartz and kaolin (190), and dusts (34). Silica dust (nano and crystalline particles) is an environmental and occupational hazard, as observed in construction, mining, ceramics, and foundries industry. This topic has been discussed in several reviews and very well documented clinically (191, 192). Silica has been found to be cytotoxic for a long time and believed to be responsible for silicosis (158, 159), and contribute to several types of cancer, infection (such as TB and Salmonella) (193–195) and autoimmune diseases (196). As we discussed earlier, crystalline silica is more potent in inducing alveolar macrophage death than colloidal and amorphous counterparts (34). Signaling-wise silica induced NLRP3 activation in LPS-primed macrophages *in vitro* (159). Some reports supported the notion that silica induced NLRP3-dependent pyroptosis, which relied on K^+ efflux and caspase-1 activation. However, others argued against the dependence on NLRP3 (151, 158, 170). A report found the reliance on receptor-interacting serine/threonine-protein kinase 3 (RIPK3)-mixed lineage kinase domain-like (MLKL)-driven necroptosis (9) while another group suggested the importance of redundant cathepsins (170). Furthermore, some groups reported that silica promoted cell death *via* apoptosis through mitochondria damage pathway initiated by oxidative stress (156, 197). A slight variation was the proposal suggesting that silica induced both apoptosis and necrosis that depended on the transmembrane potential change of mitochondria. Hyperpolarization induced caspase-3 and 9-mediated apoptosis while depolarization induced no caspase activation during necrosis (198). In addition, using ATP synthesis inhibitors, oligomycin and 2-deoxyglucose, it was observed that decreased ATP level induced NLRP3 activation and necrosis while increased ATP led to apoptosis (199, 200). Therefore, crystal-induced cell death may be also under the control of ATP levels. The extreme redundancy in the types of cell death is difficult to comprehend, likely resulting from the different system setups.

Similar to silica, alum has been reported to induce lysosome rupture thus activating NLRP3 inflammasome (126, 127, 165, 201, 202). Cell death, however, was not determined in the majority of those papers except two reported that NLRP3 and caspase-1 deficiencies did not affect alum-induced macrophage cell death (126, 151). On the other hand, aluminum oxide nanoparticles were reported to depolarize cell membrane and lead to significant cell death in epithelial cells (203). Lima et al. reported that alum-induced macrophage cell death *in vitro* was a direct consequence of

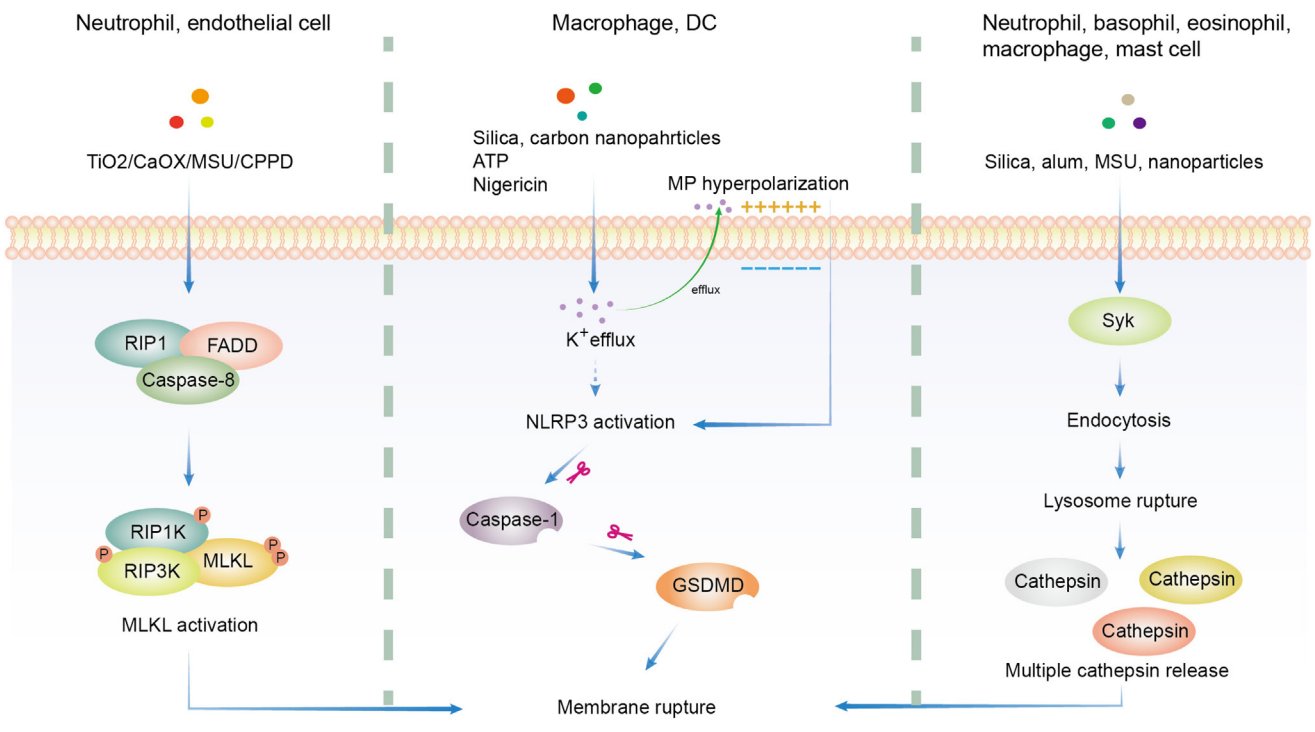

FIGURE 2 | Overview of three major hypotheses of solid particle-induced cell death. In addition to cell death related to reactive oxygen species production, there are three major proposals on solid particle-induced cell death. The first is through receptor-interacting serine/threonine-protein kinase 1/3 (RIPK1/RIPK3)-mixed lineage kinase domain-like (MLKL)-driven necroptosis, which was found in calcium oxalate, monosodium urate (MSU), calcium pyrophosphate dihydrate (CPPD), cystine, TiO_2, and calcium phosphate-treated epithelial cells and neutrophils. The second is through K^+ efflux-activated NACHT, LRR, PYD domains-containing protein 3 (NLRP3)-dependent pyroptosis, which was found in silica, asbestos, carbon nanoparticles-treated macrophages and dendritic cells (DCs). The third is through lysosome rupture-released multiple redundant cathepsins after Syk-dependent phagocytosis, which was found in silica, alum, MSU, and nanoparticle-treated neutrophils, basophils, eosinophils, macrophages, and mast cells. GSDMD, gasdermin D.

lysosomal membrane rupture without involving NLRP3 signaling cascade (166). Although MSU has been used as a model system for NLRP3 inflammation activation, much less is known about its ability to induce cell death although there is one group found that RIPK1-RIPK3-MLKL signaling pathway may be critical for MSU and other crystals-induced neutrophil extracellular DNA release and cell death (7). MSU was found to induce neutrophil PI3K activation, downstream of Syk and Src family kinases. PI3K is a critical element regulating the degranulation of neutrophils, a mechanism contributing to the pathogenesis of gout (204). As direct membrane binding was believed to be important for MSU-induced Syk activation (69) and NLRP3 inflammasome (167), we made a Syk conditional knock out mouse model and found that Syk deficiency indeed reduced MSU-induced cell death (our own observations). The exact mechanism of how MSU activates Syk and Src pathways thus induces cell death remains unclear.

A lot of metal oxide nanoparticles exhibited cytotoxicity (40, 205, 206), as did other common nanoparticles, including CNT, Fullerene (207), dental calculus (208), asbestos (36), carbon black nanoparticles (209), and quantum dots (210). The mechanisms of cytotoxicity, however, can be quite different. Most of them were found to induce ROS production that was associated with mitochondrial dysfunction (155). Unlike other particles, quantum dot treatment increased FAS expression and membrane lipid peroxidation that led to the impairment of mitochondria in human neuroblastoma cells (210). In addition, RIPK1-RIPK3-MLKL axis was proven important in human and murine renal tubular cell death induced by TiO_2 and calcium oxalate (8). Anders's group reported that MSU, calcium oxalate, CPPD, and cystine crystals mediated cell death of kidney epithelial cells (9) that were blocked by necrostatin-1 (inhibitor of necroptosis). This type of cell death was independent of caspase activation, suggesting that NLRP3 inflammasome activation associated with those crystals was not responsible for their cell death (211). As the most abundant innate immune cells, neutrophils phagocytose large amounts of crystals (212). In doing so, they process a special type of cell death by releasing their own DNA to trap those particles, a program called neutrophil extracellular traps (NET), including MSU, Silica, calcium oxalate, calcium phosphate, and asbestos (7). RIPK1-RIPK3-MLKL signaling pathway was found to be critical for this programmed cell death (NETosis) (7, 213). NETosis was also observed in eosinophils and basophils upon particle contact (212).

CONCLUDING REMARKS

Solid particle-mediated cellular responses are an old topic of medicine and becoming more diverse in modern life style. Particulate matters impact us in multiple ways. They represent the latest technologies in vaccine design and cancer therapy. However, the limitations and disadvantages of using these particles and salt crystals in the development of pharmaceuticals, drugs, bio-therapeutics have not been systematically studied. In environmental exposure studies and some bacterial and viral material-based therapeutic regimens, solid particles are seldom pure, with frequent contamination of endotoxins and microbial nucleic acids. These factors must be carefully investigated. At the other end, crystalline arthropathies remain as much as a health threat as they have throughout the time. While the research on this subject has been multifaceted and increasingly intense, particularly with regard to their signaling pathways, we are far from establishing a framework of understanding how these solid structures are perceived by our cells and whether there are a set of critical events governing their cellular activation. As the variations in the types of particles and host cells involved can be extremely diverse, much work is still ahead. Several issues should be considered with higher priority. One is the signaling events in particulate adjuvants that lead to enhanced immune activation. This is critical because these adjuvants are used in population-based vaccination and new varieties are coming into clinical tests. New mechanistic insights will certainly benefit the better designs of vaccines. Another important topic is to develop a systematic approach to study the host responses toward nano- and microparticles. The chemical and geometrical properties of those substances have been studied for decades and their signaling events have been one of the leading topics in immunology for 20 years. Thus far, we are in possession of very few consensuses and are often puzzled by conflicting data. One possible approach is to establish a model system with definable variables, such as the work on LDH by Williams et al. (48). This type of work will gradually lead to more mechanistic insights that enable us to better harness the particles that are in contact with our cells.

AUTHOR CONTRIBUTIONS

YS conceptualized the review and wrote the manuscript except for the inflammasome and the cell death, which were drafted by FS. YS revised the manuscript with assistance from FS.

ACKNOWLEDGMENTS

We thank Ying Xu for the illustrations. This work was supported by the joint Peking-Tsinghua Center for Life Sciences and grants from the National Natural Science Foundation of China General Program (31370878), Key Program (31630023), and Creative Research Groups Program (81621002), National Institutes of Health (R01AI098995), Natural Sciences and Engineering Research Council of Canada (RGPIN-355350/396037), and Canadian Institutes of Health Research (MOP-119295) to YS.

REFERENCES

1. Braakhuis HM, Park MV, Gosens I, De Jong WH, Cassee FR. Physicochemical characteristics of nanomaterials that affect pulmonary inflammation. *Part Fibre Toxicol* (2014) 11:18. doi:10.1186/1743-8977-11-18
2. Kono H, Chen C-J, Ontiveros F, Rock KL. Uric acid promotes an acute inflammatory response to sterile cell death in mice. *J Clin Invest* (2010) 120:1939–49. doi:10.1172/JCI40124
3. Churg A, Wiggs B. Fiber size and number in amphibole asbestos-induced mesothelioma. *Am J Pathol* (1984) 115:437–42.
4. Yano E, Wang Z-M, Wang X-R, Wang M-Z, Lan Y-J. Cancer mortality among workers exposed to amphibole-free chrysotile asbestos. *Am J Epidemiol* (2001) 154:538–43. doi:10.1093/aje/154.6.538
5. Franklin BS, Mangan MS, Latz E. Crystal formation in inflammation. *Annu Rev Immunol* (2016) 34:173–202. doi:10.1146/annurev-immunol-041015-055539

6. Martinon F, Petrilli V, Mayor A, Tardivel A, Tschopp J. Gout-associated uric acid crystals activate the NALP3 inflammasome. *Nature* (2006) 440:237–41. doi:10.1038/nature04516
7. Desai J, Foresto-Neto O, Honarpisheh M, Steiger S, Nakazawa D, Popper B, et al. Particles of different sizes and shapes induce neutrophil necroptosis followed by the release of neutrophil extracellular trap-like chromatin. *Sci Rep* (2017) 7:15003. doi:10.1038/s41598-017-15106-0
8. Honarpisheh M, Foresto-Neto O, Desai J, Steiger S, Gómez LA, Popper B, et al. Phagocytosis of environmental or metabolic crystalline particles induces cytotoxicity by triggering necroptosis across a broad range of particle size and shape. *Sci Rep* (2017) 7:15523. doi:10.1038/s41598-017-15804-9
9. Mulay SR, Desai J, Kumar SV, Eberhard JN, Thomasova D, Romoli S, et al. Cytotoxicity of crystals involves RIPK3-MLKL-mediated necroptosis. *Nat Commun* (2016) 7:10274. doi:10.1038/ncomms10274
10. Castranova V. Signaling pathways controlling the production of inflammatory mediators in response to crystalline silica exposure: role of reactive oxygen/nitrogen species. *Free Radic Biol Med* (2004) 37:916–25. doi:10.1016/j.freeradbiomed.2004.05.032
11. Khan SR. Reactive oxygen species, inflammation and calcium oxalate nephrolithiasis. *Transl Androl Urol* (2014) 3:256–76. doi:10.3978/j.issn.2223-4683.2014.06.04
12. Apostolico Jde S, Lunardelli VA, Coirada FC, Boscardin SB, Rosa DS. Adjuvants: classification, modus operandi, and licensing. *J Immunol Res* (2016) 2016:1459394. doi:10.1155/2016/1459394
13. Rock KL, Hearn A, Chen CJ, Shi Y. Natural endogenous adjuvants. *Springer Semin Immunopathol* (2005) 26:231–46. doi:10.1007/s00281-004-0173-3
14. Flannagan RS, Jaumouille V, Grinstein S. The cell biology of phagocytosis. *Annu Rev Pathol* (2012) 7:61–98. doi:10.1146/annurev-pathol-011811-132445
15. Horie M, Fukui H, Endoh S, Maru J, Miyauchi A, Shichiri M, et al. Comparison of acute oxidative stress on rat lung induced by nano and fine-scale, soluble and insoluble metal oxide particles: NiO and TiO2. *Inhal Toxicol* (2012) 24:391–400. doi:10.3109/08958378.2012.682321
16. Pauluhn J. Pulmonary toxicity and fate of agglomerated 10 and 40 nm aluminum oxyhydroxides following 4-week inhalation exposure of rats: toxic effects are determined by agglomerated, not primary particle size. *Toxicol Sci* (2009) 109:152–67. doi:10.1093/toxsci/kfp046
17. Roursgaard M, Poulsen SS, Poulsen LK, Hammer M, Jensen KA, Utsunomiya S, et al. Time-response relationship of nano and micro particle induced lung inflammation. Quartz as reference compound. *Hum Exp Toxicol* (2010) 29:915–33. doi:10.1177/0960327110363329
18. Wendorf J, Chesko J, Kazzaz J, Ugozzoli M, Vajdy M, O'Hagan D, et al. A comparison of anionic nanoparticles and microparticles as vaccine delivery systems. *Hum Vaccin* (2008) 4:44–9. doi:10.4161/hv.4.1.4886
19. Shanbhag AS, Jacobs JJ, Black J, Galante JO, Glant TT. Macrophage/particle interactions: effect of size, composition and surface area. *J Biomed Mater Res* (1994) 28:81–90. doi:10.1002/jbm.820280111
20. Renwick LC, Brown D, Clouter A, Donaldson K. Increased inflammation and altered macrophage chemotactic responses caused by two ultrafine particle types. *Occup Environ Med* (2004) 61:442–7. doi:10.1136/oem.2003.008227
21. Napierska D, Thomassen LCJ, Rabolli V, Lison D, Gonzalez L, Kirsch-Volders M, et al. Size-dependent cytotoxicity of monodisperse silica nanoparticles in human endothelial cells. *Small* (2009) 5:846–53. doi:10.1002/smll.200800461
22. Wottrich R, Diabate S, Krug HF. Biological effects of ultrafine model particles in human macrophages and epithelial cells in mono- and co-culture. *Int J Hyg Environ Health* (2004) 207:353–61. doi:10.1078/1438-4639-00300
23. Liu W, Wu Y, Wang C, Li HC, Wang T, Liao CY, et al. Impact of silver nanoparticles on human cells: effect of particle size. *Nanotoxicology* (2010) 4:319–30. doi:10.3109/17435390.2010.483745
24. Kusaka T, Nakayama M, Nakamura K, Ishimiya M, Furusawa E, Ogasawara K. Effect of silica particle size on macrophage inflammatory responses. *PLoS One* (2014) 9:e92634. doi:10.1371/journal.pone.0092634
25. Morishige T, Yoshioka Y, Inakura H, Tanabe A, Yao X, Tsunoda S, et al. Cytotoxicity of amorphous silica particles against macrophage-like THP-1 cells depends on particle-size and surface properties. *Pharmazie* (2010) 65:596–9. doi:10.1691/ph.2010.9408
26. Olivier V, Duval J-L, Hindié M, Pouletaut P, Nagel M-D. Comparative particle-induced cytotoxicity toward macrophages and fibroblasts. *Cell Biol Toxicol* (2003) 19:145–59. doi:10.1023/A:1024723326036
27. Braydich-Stolle LK, Schaeublin NM, Murdock RC, Jiang J, Biswas P, Schlager JJ, et al. Crystal structure mediates mode of cell death in TiO2 nanotoxicity. *J Nanopart Res* (2009) 11:1361–74. doi:10.1007/s11051-008-9523-8
28. Donaldson K, Murphy FA, Duffin R, Poland CA. Asbestos, carbon nanotubes and the pleural mesothelium: a review of the hypothesis regarding the role of long fibre retention in the parietal pleura, inflammation and mesothelioma. *Part Fibre Toxicol* (2010) 7:5–5. doi:10.1186/1743-8977-7-5
29. Goodglick LA, Kane AB. Cytotoxicity of long and short crocidolite asbestos fibers in vitro and in vivo. *Cancer Res* (1990) 50:5153–63.
30. Zhao X, Ng S, Heng BC, Guo J, Ma L, Tan TTY, et al. Cytotoxicity of hydroxyapatite nanoparticles is shape and cell dependent. *Arch Toxicol* (2013) 87:1037–52. doi:10.1007/s00204-012-0827-1
31. Palomäki J, Välimäki E, Sund J, Vippola M, Clausen PA, Jensen KA, et al. Long, needle-like carbon nanotubes and asbestos activate the NLRP3 inflammasome through a similar mechanism. *ACS Nano* (2011) 5:6861–70. doi:10.1021/nn200595c
32. Porter DW, Wu N, Hubbs AF, Mercer RR, Funk K, Meng F, et al. Differential mouse pulmonary dose and time course responses to titanium dioxide nanospheres and nanobelts. *Toxicol Sci* (2013) 131:179–93. doi:10.1093/toxsci/kfs261
33. Menas AL, Yanamala N, Farcas MT, Russo M, Friend S, Fournier PM, et al. Fibrillar vs crystalline nanocellulose pulmonary epithelial cell responses: cytotoxicity or inflammation? *Chemosphere* (2017) 171:671–80. doi:10.1016/j.chemosphere.2016.12.105
34. Warheit DB, McHugh TA, Hartsky MA. Differential pulmonary responses in rats inhaling crystalline, colloidal or amorphous silica dusts. *Scand J Work Environ Health* (1995) 21:19–21.
35. Sandberg WJ, Låg M, Holme JA, Friede B, Gualtieri M, Kruszewski M, et al. Comparison of non-crystalline silica nanoparticles in IL-1β release from macrophages. *Part Fibre Toxicol* (2012) 9:32. doi:10.1186/1743-8977-9-32
36. Brunner TJ, Wick P, Manser P, Spohn P, Grass RN, Limbach LK, et al. In vitro cytotoxicity of oxide nanoparticles: comparison to asbestos, silica, and the effect of particle solubility. *Environ Sci Technol* (2006) 40:4374–81. doi:10.1021/es052069i
37. Carter JD, Ghio AJ, Samet JM, Devlin RB. Cytokine production by human airway epithelial cells after exposure to an air pollution particle is metal-dependent. *Toxicol Appl Pharmacol* (1997) 146:180–8. doi:10.1006/taap.1997.8254
38. Cho WS, Duffin R, Howie SE, Scotton CJ, Wallace WA, Macnee W, et al. Progressive severe lung injury by zinc oxide nanoparticles; the role of Zn2+ dissolution inside lysosomes. *Part Fibre Toxicol* (2011) 8:27. doi:10.1186/1743-8977-8-27
39. Cho WS, Duffin R, Thielbeer F, Bradley M, Megson IL, Macnee W, et al. Zeta potential and solubility to toxic ions as mechanisms of lung inflammation caused by metal/metal oxide nanoparticles. *Toxicol Sci* (2012) 126:469–77. doi:10.1093/toxsci/kfs006
40. Fahmy B, Cormier SA. Copper oxide nanoparticles induce oxidative stress and cytotoxicity in airway epithelial cells. *Toxicol In Vitro* (2009) 23:1365–71. doi:10.1016/j.tiv.2009.08.005
41. Gojova A, Guo B, Kota RS, Rutledge JC, Kennedy IM, Barakat AI. Induction of inflammation in vascular endothelial cells by metal oxide nanoparticles: effect of particle composition. *Environ Health Perspect* (2007) 115:403–9. doi:10.1289/ehp.8497
42. Arts JH, Muijser H, Duistermaat E, Junker K, Kuper CF. Five-day inhalation toxicity study of three types of synthetic amorphous silicas in Wistar rats and post-exposure evaluations for up to 3 months. *Food Chem Toxicol* (2007) 45:1856–67. doi:10.1016/j.fct.2007.04.001
43. Choi HS, Ashitate Y, Lee JH, Kim SH, Matsui A, Insin N, et al. Rapid translocation of nanoparticles from the lung airspaces to the body. *Nat Biotechnol* (2010) 28:1300–3. doi:10.1038/nbt.1696
44. Reuzel PG, Bruijntjes JP, Feron VJ, Woutersen RA. Subchronic inhalation toxicity of amorphous silicas and quartz dust in rats. *Food Chem Toxicol* (1991) 29:341–54. doi:10.1016/0278-6915(91)90205-L
45. Morishige T, Yoshioka Y, Inakura H, Tanabe A, Yao X, Narimatsu S, et al. The effect of surface modification of amorphous silica particles on NLRP3 inflammasome mediated IL-1β production, ROS production and endosomal rupture. *Biomaterials* (2010) 31:6833–42. doi:10.1016/j.biomaterials.2010.05.036

46. Drescher D, Orts-Gil G, Laube G, Natte K, Veh RW, Österle W, et al. Toxicity of amorphous silica nanoparticles on eukaryotic cell model is determined by particle agglomeration and serum protein adsorption effects. *Anal Bioanal Chem* (2011) 400:1367. doi:10.1007/s00216-011-4893-7
47. Tomazic-Jezic VJ, Merritt K, Umbreit TH. Significance of the type and the size of biomaterial particles on phagocytosis and tissue distribution. *J Biomed Mater Res* (2001) 55:523–9. doi:10.1002/1097-4636(20010615)55:4<523::AID-JBM1045>3.0.CO;2-G
48. Williams GR, Fierens K, Preston SG, Lunn D, Rysnik O, De Prijck S, et al. Immunity induced by a broad class of inorganic crystalline materials is directly controlled by their chemistry. *J Exp Med* (2014) 211:1019–25. doi:10.1084/jem.20131768
49. Ichida K, Amaya Y, Okamoto K, Nishino T. Mutations associated with functional disorder of xanthine oxidoreductase and hereditary xanthinuria in humans. *Int J Mol Sci* (2012) 13:15475–95. doi:10.3390/ijms131115475
50. Chillarón J, Font-Llitjós M, Fort J, Zorzano A, Goldfarb DS, Nunes V, et al. Pathophysiology and treatment of cystinuria. *Nat Rev Nephrol* (2010) 6:424. doi:10.1038/nrneph.2010.69
51. Bollée G, Harambat J, Bensman A, Knebelmann B, Daudon M, Ceballos-Picot I. Adenine phosphoribosyltransferase deficiency. *Clin J Am Soc Nephrol* (2012) 7:1521–7. doi:10.2215/CJN.02320312
52. Ceballos-Picot I, Daudon M, Harambat J, Bensman A, Knebelmann B, Bollee G. 2,8-Dihydroxyadenine urolithiasis: a not so rare inborn error of purine metabolism. *Nucleosides Nucleotides Nucleic Acids* (2014) 33:241–52. doi:10.1080/15257770.2013.853780
53. Evan AP, Bledsoe SB, Connors BA, Deng L, Liang L, Shao C, et al. Sequential analysis of kidney stone formation in the APRT knockout mouse. *Kidney Int* (2001) 60:910–23. doi:10.1046/j.1523-1755.2001.060003910.x
54. Nasr SH, Sethi S, Cornell LD, Milliner DS, Boelkins M, Broviac J, et al. Crystalline nephropathy due to 2,8-dihydroxyadeninuria: an under-recognized cause of irreversible renal failure. *Nephrol Dial Transplant* (2010) 25:1909–15. doi:10.1093/ndt/gfp711
55. Nuki G, Simkin PA. A concise history of gout and hyperuricemia and their treatment. *Arthritis Res Ther* (2006) 8:S1. doi:10.1186/ar1906
56. Dunn JP, Brooks GW, Mausner J, Rodnan GP, Cobb S. Social class gradient of serum uric acid levels in males. *JAMA* (1963) 185:431–6. doi:10.1001/jama.1963.03060060029012
57. Wilcox WR, Khalaf AA. Nucleation of monosodium urate crystals. *Ann Rheum Dis* (1975) 34:332–9. doi:10.1136/ard.34.4.332
58. Kanevets U, Sharma K, Dresser K, Shi Y. A role of IgM antibodies in monosodium urate crystal formation and associated adjuvanticity. *J Immunol* (2009) 182:1912–8. doi:10.4049/jimmunol.0803777
59. Kam M, Perl-Treves D, Caspi D, Addadi L. Antibodies against crystals. *FASEB J* (1992) 6:2608–13. doi:10.1096/fasebj.6.8.1592211
60. Cherian PV, Schumacher HR Jr. Immunochemical and ultrastructural characterization of serum proteins associated with monosodium urate crystals (MSU) in synovial fluid cells from patients with gout. *Ultrastruct Pathol* (1986) 10:209–19. doi:10.3109/01913128609032219
61. Kozin F, McCarty DJ. Molecular orientation of immunoglobulin G adsorbed to microcrystalline monosodium urate monohydrate. *J Lab Clin Med* (1980) 95:49–58.
62. Barabe F, Gilbert C, Liao N, Bourgoin SG, Naccache PH. Crystal-induced neutrophil activation VI. Involvment of FcgammaRIIIB (CD16) and CD11b in response to inflammatory microcrystals. *FASEB J* (1998) 12:209–20. doi:10.1096/fasebj.12.2.209
63. Desaulniers P, Fernandes M, Gilbert C, Bourgoin SG, Naccache PH. Crystal-induced neutrophil activation. VII. Involvement of Syk in the responses to monosodium urate crystals. *J Leukoc Biol* (2001) 70:659–68. doi:10.1189/jlb.70.4.659
64. Liu-Bryan R, Pritzker K, Firestein GS, Terkeltaub R. TLR2 signaling in chondrocytes drives calcium pyrophosphate dihydrate and monosodium urate crystal-induced nitric oxide generation. *J Immunol* (2005) 174:5016–23. doi:10.4049/jimmunol.174.8.5016
65. Liu-Bryan R, Scott P, Sydlaske A, Rose DM, Terkeltaub R. Innate immunity conferred by toll-like receptors 2 and 4 and myeloid differentiation factor 88 expression is pivotal to monosodium urate monohydrate crystal-induced inflammation. *Arthritis Rheum* (2005) 52:2936–46. doi:10.1002/art.21238
66. Scott P, Ma H, Viriyakosol S, Terkeltaub R, Liu-Bryan R. Engagement of CD14 mediates the inflammatory potential of monosodium urate crystals. *J Immunol* (2006) 177:6370–8. doi:10.4049/jimmunol.177.9.6370
67. Chen CJ, Shi Y, Hearn A, Fitzgerald K, Golenbock D, Reed G, et al. MyD88-dependent IL-1 receptor signaling is essential for gouty inflammation stimulated by monosodium urate crystals. *J Clin Invest* (2006) 116:2262–71. doi:10.1172/JCI28075
68. Neumann K, Castiñeiras-Vilariño M, Höckendorf U, Hannesschläger N, Lemeer S, Kupka D, et al. Clec12a is an inhibitory receptor for uric acid crystals that regulates inflammation in response to cell death. *Immunity* (2014) 40:389–99. doi:10.1016/j.immuni.2013.12.015
69. Ng G, Sharma K, Ward SM, Desrosiers MD, Stephens LA, Schoel WM, et al. Receptor-independent, direct membrane binding leads to cell-surface lipid sorting and Syk kinase activation in dendritic cells. *Immunity* (2008) 29:807–18. doi:10.1016/j.immuni.2008.09.013
70. Swan A, Dularay B, Dieppe P. A comparison of the effects of urate, hydroxyapatite and diamond crystals on polymorphonuclear cells: relationship of mediator release to the surface area and adsorptive capacity of different particles. *J Rheumatol* (1990) 17:1346–52.
71. Mandel NS, Mandel GS, Carroll DJ, Halverson PB. Calcium pyrophosphate crystal deposition. An in vitro study using a gelatin matrix model. *Arthritis Rheum* (1984) 27:789–96. doi:10.1002/art.1780270710
72. Costello JC, Rosenthal AK, Kurup IV, Masuda I, Medhora M, Ryan LM. Parallel regulation of extracellular ATP and inorganic pyrophosphate: roles of growth factors, transduction modulators, and ANK. *Connect Tissue Res* (2011) 52:139–46. doi:10.3109/03008207.2010.491928
73. Ryan LM, McCarty DJ. Understanding inorganic pyrophosphate metabolism: toward prevention of calcium pyrophosphate dihydrate crystal deposition. *Ann Rheum Dis* (1995) 54:939–41. doi:10.1136/ard.54.12.939
74. Schumacher HR. The role of inflammation and crystals in the pain of osteoarthritis. *Semin Arthritis Rheum* (1989) 18:81–5. doi:10.1016/0049-0172(89)90022-X
75. Rosenthal AK, Ryan LM. Calcium pyrophosphate deposition disease. *N Engl J Med* (2016) 374:2575–84. doi:10.1056/NEJMra1511117
76. Ea HK, Uzan B, Rey C, Liote F. Octacalcium phosphate crystals directly stimulate expression of inducible nitric oxide synthase through p38 and JNK mitogen-activated protein kinases in articular chondrocytes. *Arthritis Res Ther* (2005) 7:R915–26. doi:10.1186/ar1763
77. McCarthy G, Westfall P, Masuda I, Christopherson P, Cheung H, Mitchell P. Basic calcium phosphate crystals activate human osteoarthritic synovial fibroblasts and induce matrix metalloproteinase-13 (collagenase-3) in adult porcine articular chondrocytes. *Ann Rheum Dis* (2001) 60:399–406. doi:10.1136/ard.60.4.399
78. Higo T, Duronio V, Tudan C, Burt HM, Jackson JK. Calcium pyrophosphate dihydrate crystal-induced inhibition of neutrophil apoptosis: involvement of Bcl-2 family members. *Inflamm Res* (2010) 59:71–81. doi:10.1007/s00011-009-0073-z
79. Lammert F, Gurusamy K, Ko CW, Miquel J-F, éndez-Sánchez NM, Portincasa P, et al. Gallstones. *Nat Rev Dis Primers* (2016) 2:16024. doi:10.1038/nrdp.2016.24
80. Buhaescu I, Izzedine H. Mevalonate pathway: a review of clinical and therapeutical implications. *Clin Biochem* (2007) 40:575–84. doi:10.1016/j.clinbiochem.2007.03.016
81. Simons K, Ikonen E. How cells handle cholesterol. *Science* (2000) 290:1721–6. doi:10.1126/science.290.5497.1721
82. Moore KJ, Tabas I. Macrophages in the pathogenesis of atherosclerosis. *Cell* (2011) 145:341–55. doi:10.1016/j.cell.2011.04.005
83. Abela GS. Cholesterol crystals piercing the arterial plaque and intima trigger local and systemic inflammation. *J Clin Lipidol* (2010) 4:156–64. doi:10.1016/j.jacl.2010.03.003
84. Abela GS, Aziz K. Cholesterol crystals cause mechanical damage to biological membranes: a proposed mechanism of plaque rupture and erosion leading to arterial thrombosis. *Clin Cardiol* (2005) 28:413–20. doi:10.1002/clc.4960280906
85. Björkegren JLM, Hägg S, Talukdar HA, Foroughi Asl H, Jain RK, Cedergren C, et al. Plasma cholesterol–induced lesion networks activated before regression of early, mature, and advanced atherosclerosis. *PLoS Genet* (2014) 10:e1004201. doi:10.1371/journal.pgen.1004201

86. Duewell P, Kono H, Rayner KJ, Sirois CM, Vladimer G, Bauernfeind FG, et al. NLRP3 inflammasomes are required for atherogenesis and activated by cholesterol crystals. *Nature* (2010) 464:1357–61. doi:10.1038/nature08938
87. Liu L, Gardecki JA, Nadkarni SK, Toussaint JD, Yagi Y, Bouma BE, et al. Imaging the subcellular structure of human coronary atherosclerosis using micro-optical coherence tomography. *Nat Med* (2011) 17:1010–4. doi:10.1038/nm.2409
88. Lim RS, Suhalim JL, Miyazaki-Anzai S, Miyazaki M, Levi M, Potma EO, et al. Identification of cholesterol crystals in plaques of atherosclerotic mice using hyperspectral CARS imaging. *J Lipid Res* (2011) 52:2177–86. doi:10.1194/jlr.M018077
89. Baumer Y, McCurdy S, Weatherby TM, Mehta NN, Halbherr S, Halbherr P, et al. Hyperlipidemia-induced cholesterol crystal production by endothelial cells promotes atherogenesis. *Nat Commun* (2017) 8:1129. doi:10.1038/s41467-017-01186-z
90. Hansson GK, Hermansson A. The immune system in atherosclerosis. *Nat Immunol* (2011) 12:204–12. doi:10.1038/ni.2001
91. Hammerschmidt DE, Greenberg CS, Yamada O, Craddock PR, Jacob HS. Cholesterol and atheroma lipids activate complement and stimulate granulocytes. A possible mechanism for amplification of ischemic injury in atherosclerotic states. *J Lab Clin Med* (1981) 98:68–77.
92. Samstad EO, Niyonzima N, Nymo S, Aune MH, Ryan L, Bakke SS, et al. Cholesterol crystals induce complement-dependent inflammasome activation and cytokine release. *J Immunol* (2014) 192:2837–45. doi:10.4049/jimmunol.1302484
93. Freigang S, Ampenberger F, Weiss A, Kanneganti TD, Iwakura Y, Hersberger M, et al. Fatty acid-induced mitochondrial uncoupling elicits inflammasome-independent IL-1alpha and sterile vascular inflammation in atherosclerosis. *Nat Immunol* (2013) 14:1045–53. doi:10.1038/ni.2704
94. Sjogren U, Mukohyama H, Roth C, Sundqvist G, Lerner UH. Bone-resorbing activity from cholesterol-exposed macrophages due to enhanced expression of interleukin-1alpha. *J Dent Res* (2002) 81:11–6. doi:10.1177/002203450208100104
95. Rajamäki K, Lappalainen J, Öörni K, Välimäki E, Matikainen S, Kovanen PT, et al. Cholesterol crystals activate the NLRP3 inflammasome in human macrophages: a novel link between cholesterol metabolism and inflammation. *PLoS One* (2010) 5:e11765. doi:10.1371/journal.pone.0011765
96. Menu P, Pellegrin M, Aubert J, Bouzourene K, Tardivel A, Mazzolai L, et al. Atherosclerosis in ApoE-deficient mice progresses independently of the NLRP3 inflammasome. *Cell Death Dis* (2011) 2:e137. doi:10.1038/cddis.2011.18
97. Pandey AV, Tekwani BL. Formation of haemozoin/beta-haematin under physiological conditions is not spontaneous. *FEBS Lett* (1996) 393:189–93. doi:10.1016/0014-5793(96)00881-2
98. Davis SP, Amrein M, Gillrie MR, Lee K, Muruve DA, Ho M. *Plasmodium falciparum*-induced CD36 clustering rapidly strengthens cytoadherence via p130CAS-mediated actin cytoskeletal rearrangement. *FASEB J* (2012) 26:1119–30. doi:10.1096/fj.11-196923
99. Gillrie MR, Krishnegowda G, Lee K, Buret AG, Robbins SM, Looareesuwan S, et al. Src-family kinase dependent disruption of endothelial barrier function by *Plasmodium falciparum* merozoite proteins. *Blood* (2007) 110:3426–35. doi:10.1182/blood-2007-04-084582
100. Shio MT, Kassa FA, Bellemare M-J, Olivier M. Innate inflammatory response to the malarial pigment hemozoin. *Microb Infect* (2010) 12:889–99. doi:10.1016/j.micinf.2010.07.001
101. Deroost K, Lays N, Pham T-T, Baci D, Van den Eynde K, Komuta M, et al. Hemozoin induces hepatic inflammation in mice and is differentially associated with liver pathology depending on the *Plasmodium* strain. *PLoS One* (2014) 9:e113519. doi:10.1371/journal.pone.0113519
102. Klonis N, Dilanian R, Hanssen E, Darmanin C, Streltsov V, Deed S, et al. Hematin-hematin self-association states involved in the formation and reactivity of the malaria parasite pigment, hemozoin. *Biochemistry* (2010) 49:6804–11. doi:10.1021/bi100567j
103. Ho M, Webster HK. Immunology of human malaria. A cellular perspective. *Parasite Immunol* (1989) 11:105–16. doi:10.1111/j.1365-3024.1989.tb00652.x
104. Nguyen PH, Day N, Pram TD, Ferguson DJ, White NJ. Intraleucocytic malaria pigment and prognosis in severe malaria. *Trans R Soc Trop Med Hyg* (1995) 89:200–4. doi:10.1016/0035-9203(95)90496-4
105. Pichyangkul S, Saengkrai P, Webster HK. *Plasmodium falciparum* pigment induces monocytes to release high levels of tumor necrosis factor-alpha and interleukin-1 beta. *Am J Trop Med Hyg* (1994) 51:430–5. doi:10.4269/ajtmh.1994.51.430
106. Jaramillo M, Plante I, Ouellet N, Vandal K, Tessier PA, Olivier M. Hemozoin-inducible proinflammatory events in vivo: potential role in malaria infection. *J Immunol* (2004) 172:3101–10. doi:10.4049/jimmunol.172.5.3101
107. Jaramillo M, Gowda DC, Radzioch D, Olivier M. Hemozoin increases IFN-γ-inducible macrophage nitric oxide generation through extracellular signal-regulated kinase- and NF-κB-dependent pathways. *J Immunol* (2003) 171:4243–53. doi:10.4049/jimmunol.171.8.4243
108. Olivier M, Van Den Ham K, Shio MT, Kassa FA, Fougeray S. Malarial pigment hemozoin and the innate inflammatory response. *Front Immunol* (2014) 5:25. doi:10.3389/fimmu.2014.00025
109. Coban C, Ishii KJ, Kawai T, Hemmi H, Sato S, Uematsu S, et al. Toll-like receptor 9 mediates innate immune activation by the malaria pigment hemozoin. *J Exp Med* (2005) 201:19–25. doi:10.1084/jem.20041836
110. Griffith JW, Sun T, McIntosh MT, Bucala R. Pure hemozoin is inflammatory in vivo and activates the NALP3 inflammasome via release of uric acid. *J Immunol* (2009) 183:5208–20. doi:10.4049/jimmunol.0713552
111. Parroche P, Lauw FN, Goutagny N, Latz E, Monks BG, Visintin A, et al. Malaria hemozoin is immunologically inert but radically enhances innate responses by presenting malaria DNA to toll-like receptor 9. *Proc Natl Acad Sci U S A* (2007) 104:1919–24. doi:10.1073/pnas.0608745104
112. Wu X, Gowda NM, Kumar S, Gowda DC. Protein–DNA complex is the exclusive malaria parasite component that activates dendritic cells and triggers innate immune responses. *J Immunol* (2010) 184:4338–48. doi:10.4049/jimmunol.0903824
113. Tiemi Shio M, Eisenbarth SC, Savaria M, Vinet AF, Bellemare M-J, Harder KW, et al. Malarial hemozoin activates the NLRP3 inflammasome through Lyn and Syk kinases. *PLoS Pathog* (2009) 5:e1000559. doi:10.1371/journal.ppat.1000559
114. McKee AS, Munks MW, Marrack P. How do adjuvants work? Important considerations for bew generation adjuvants. *Immunity* (2007) 27:687–90. doi:10.1016/j.immuni.2007.11.003
115. Wen Y, Shi Y. Alum: an old dog with new tricks. *Emerg Microbes Infect* (2016) 5:e25. doi:10.1038/emi.2016.40
116. Glenny AT, Buttle GAH, Muriel FS. Rate of disappearance of diphtheria toxoid injected into rabbits and guinea – pigs: toxoid precipitated with alum. *J Pathol Bacteriol* (1931) 34:267–75. doi:10.1002/path.1700340214
117. Glenny AT, Pope CG, Hilda W, Wallace U. Immunological notes. XVII. The antigenic value of toxoid precipitated by potassium alum. *J Path Bac* (1926) 29:31–40. doi:10.1002/path.1700290106
118. Maschmann E, Küster E, Fischer W. Über die Fähigkeit des Tonerde-Präparates B, Diphtherie-Toxin zu adsorbieren. *Berichte der deutschen chemischen Gesellschaft* (1931) 64:2174–8. doi:10.1002/cber.19310640851
119. Gupta R, Rost BE. Aluminum compounds as vaccine adjuvants. *Vaccine Adjuvants: Preparation Methods and Research Protocols* (2000) 65–89. doi:10.1385/1-59259-083-7:65
120. Murphy K, Weaver C. *Janeway's Immunobiology*. 9th Edition. New York; London: Garland Science (2016).
121. Holt LB. *Developments in Diphtheria Prophylaxis*. London: Heinemann (1950). xvi,181 p.
122. Hutchison S, Benson RA, Gibson VB, Pollock AH, Garside P, Brewer JM. Antigen depot is not required for alum adjuvanticity. *FASEB J* (2012) 26:1272–9. doi:10.1096/fj.11-184556
123. White RG, Coons AH, Connolly JM. Studies on antibody production. III The alum granuloma. *J Exp Med* (1955) 102:73–82.
124. Jordan MB, Mills DM, Kappler J, Marrack P, Cambier JC. Promotion of B cell immune responses via an alum-induced myeloid cell population. *Science* (2004) 304:1808–10. doi:10.1126/science.1089926
125. McKee AS, MacLeod M, White J, Crawford F, Kappler JW, Marrack P. Gr1+IL-4-producing innate cells are induced in response to Th2 stimuli and suppress Th1-dependent antibody responses. *Int Immunol* (2008) 20:659–69. doi:10.1093/intimm/dxn025
126. Eisenbarth SC, Colegio OR, O'Connor W, Sutterwala FS, Flavell RA. Crucial role for the Nalp3 inflammasome in the immunostimulatory properties of aluminium adjuvants. *Nature* (2008) 453:1122. doi:10.1038/nature06939
127. Kool M, Pétrilli V, De Smedt T, Rolaz A, Hammad H, van Nimwegen M, et al. Cutting edge: alum adjuvant stimulates inflammatory dendritic cells through activation of the NALP3 inflammasome. *J Immunol* (2008) 181:3755–9. doi:10.4049/jimmunol.181.6.3755

128. Flach TL, Ng G, Hari A, Desrosiers MD, Zhang P, Ward SM, et al. Alum interaction with dendritic cell membrane lipids is essential for its adjuvanticity. *Nat Med* (2011) 17:479–87. doi:10.1038/nm.2306
129. Franchi L, Nunez G. The Nlrp3 inflammasome is critical for aluminium hydroxide-mediated IL-1beta secretion but dispensable for adjuvant activity. *Eur J Immunol* (2008) 38:2085–9. doi:10.1002/eji.200838549
130. McKee AS, Munks MW, MacLeod MK, Fleenor CJ, Van Rooijen N, Kappler JW, et al. Alum induces innate immune responses through macrophage and mast cell sensors, but these sensors are not required for alum to act as an adjuvant for specific immunity. *J Immunol* (2009) 183:4403–14. doi:10.4049/jimmunol.0900164
131. McKee AS, Burchill MA, Munks MW, Jin L, Kappler JW, Friedman RS, et al. Host DNA released in response to aluminum adjuvant enhances MHC class II-mediated antigen presentation and prolongs CD4 T-cell interactions with dendritic cells. *Proc Natl Acad Sci U S A* (2013) 110:E1122–31. doi:10.1073/pnas.1300392110
132. Thomas M, Keiichi O, Denis B, Claire M, Catherine S, Kouji K, et al. DNA released from dying host cells mediates aluminum adjuvant activity. *Nat Med* (2011) 17:996–1002. doi:10.1038/nm.2403
133. Noges LE, White J, Cambier JC, Kappler JW, Marrack P. Contamination of DNase preparations confounds analysis of the role of DNA in alum adjuvanted vaccines. *J Immunol* (2016) 197:1221–30. doi:10.4049/jimmunol.1501565
134. Shi Y, Evans JE, Rock KL. Molecular identification of a danger signal that alerts the immune system to dying cells. *Nature* (2003) 425:516–21. doi:10.1038/nature01991
135. Wang Y, Ma X, Su C, Peng B, Du J, Jia H, et al. Uric acid enhances the antitumor immunity of dendritic cell-based vaccine. *Sci Rep* (2015) 5:16427. doi:10.1038/srep16427
136. Kool M, Monique AM, Willart M, van Nimwegen I, Bergen P, Pouliot JC, et al. An unexpected role for uric acid as an inducer of T helper 2 cell immunity to inhaled antigens and inflammatory mediator of allergic asthma. *Immunity* (2011) 34:527–40. doi:10.1016/j.immuni.2011.03.015
137. Shi Y, Galusha SA, Rock KL. Cutting edge: elimination of an endogenous adjuvant reduces the activation of CD8 T lymphocytes to transplanted cells and in an autoimmune diabetes model. *J Immunol* (2006) 176:3905–8. doi:10.4049/jimmunol.176.7.3905
138. Kool M, Soullié T, van Nimwegen M, Willart MAM, Muskens F, Jung S, et al. Alum adjuvant boosts adaptive immunity by inducing uric acid and activating inflammatory dendritic cells. *J Exp Med* (2008) 205:869–82. doi:10.1084/jem.20071087
139. Cimica V, Galarza JM. Adjuvant formulations for virus-like particle (VLP) based vaccines. *Clin Immunol* (2017) 183:99–108. doi:10.1016/j.clim.2017.08.004
140. Bachmann MF, Jennings GT. Vaccine delivery: a matter of size, geometry, kinetics and molecular patterns. *Nat Rev Immunol* (2010) 10:787. doi:10.1038/nri2868
141. Mohsen MO, Zha L, Cabral-Miranda G, Bachmann MF. Major findings and recent advances in virus-like particle (VLP)-based vaccines. *Semin Immunol* (2017) 34:123–32. doi:10.1016/j.smim.2017.08.014
142. Link A, Zabel F, Schnetzler Y, Titz A, Brombacher F, Bachmann MF. Innate immunity mediates follicular transport of particulate but not soluble protein antigen. *J Immunol* (2012) 188:3724–33. doi:10.4049/jimmunol.1103312
143. Pavot V, Berthet M, Rességuier J, Legaz S, Handké N, Gilbert SC, et al. Poly(lactic acid) and poly(lactic-co-glycolic acid) particles as versatile carrier platforms for vaccine delivery. *Nanomedicine* (2014) 9:2703–18. doi:10.2217/nnm.14.156
144. Fifis T, Gamvrellis A, Crimeen-Irwin B, Pietersz GA, Li J, Mottram PL, et al. Size-dependent immunogenicity: therapeutic and protective properties of nano-vaccines against tumors. *J Immunol* (2004) 173:3148–54. doi:10.4049/jimmunol.173.5.3148
145. Silva JM, Vandermeulen G, Oliveira VG, Pinto SN, Rodrigues C, Salgado A, et al. Development of functionalized nanoparticles for vaccine delivery to dendritic cells: a mechanistic approach. *Nanomedicine* (2014) 9:2639–56. doi:10.2217/nnm.14.135
146. Slutter B, Soema PC, Ding Z, Verheul R, Hennink W, Jiskoot W. Conjugation of ovalbumin to trimethyl chitosan improves immunogenicity of the antigen. *J Control Release* (2010) 143:207–14. doi:10.1016/j.jconrel.2010.01.007
147. Rice-Ficht AC, Arenas-Gamboa AM, Kahl-McDonagh MM, Ficht TA. Polymeric particles in vaccine delivery. *Curr Opin Microbiol* (2010) 13:106–12. doi:10.1016/j.mib.2009.12.001
148. Thomasin C, Corradin G, Men Y, Merkle HP, Gander B. Tetanus toxoid and synthetic malaria antigen containing poly(lactide)/poly(lactide-co-glycolide) microspheres: importance of polymer degradation and antigen release for immune response. *J Control Release* (1996) 41:131–45. doi:10.1016/0168-3659(96)01363-6
149. Speiser DE, Schwarz K, Baumgaertner P, Manolova V, Devevre E, Sterry W, et al. Memory and effector CD8 T-cell responses after nanoparticle vaccination of melanoma patients. *J Immunother* (2010) 33:848–58. doi:10.1097/CJI.0b013e3181f1d614
150. Franchi L, Munoz-Planillo R, Nunez G. Sensing and reacting to microbes through the inflammasomes. *Nat Immunol* (2012) 13:325–32. doi:10.1038/ni.2231
151. Muñoz-Planillo R, Kuffa P, Martinez-Colon G, Smith BL, Rajendiran TM, Nunez G. K(+) efflux is the common trigger of NLRP3 inflammasome activation by bacterial toxins and particulate matter. *Immunity* (2013) 38:1142–53. doi:10.1016/j.immuni.2013.05.016
152. Schieber M, Chandel NS. ROS function in redox signaling and oxidative stress. *Curr Biol* (2014) 24:R453–62. doi:10.1016/j.cub.2014.03.034
153. Kaminski MM, Roth D, Krammer PH, Gulow K. Mitochondria as oxidative signaling organelles in T-cell activation: physiological role and pathological implications. *Arch Immunol Ther Exp (Warsz)* (2013) 61:367–84. doi:10.1007/s00005-013-0235-0
154. West AP, Shadel GS, Ghosh S. Mitochondria in innate immune responses. *Nat Rev Immunol* (2011) 11:389–402. doi:10.1038/nri2975
155. Manke A, Wang L, Rojanasakul Y. Mechanisms of nanoparticle-induced oxidative stress and toxicity. *Biomed Res Int* (2013) 2013:15. doi:10.1155/2013/942916
156. Thibodeau M, Giardina C, Hubbard AK. Silica-induced caspase activation in mouse alveolar macrophages is dependent upon mitochondrial integrity and aspartic proteolysis. *Toxicol Sci* (2003) 76:91–101. doi:10.1093/toxsci/kfg178
157. Zhou R, Yazdi AS, Menu P, Tschopp J. A role for mitochondria in NLRP3 inflammasome activation. *Nature* (2010) 469:221. doi:10.1038/nature09663
158. Cassel SL, Eisenbarth SC, Iyer SS, Sadler JJ, Colegio OR, Tephly LA, et al. The Nalp3 inflammasome is essential for the development of silicosis. *Proc Natl Acad Sci U S A* (2008) 105:9035–40. doi:10.1073/pnas.0803933105
159. Dostert C, Pétrilli V, Van Bruggen R, Steele C, Mossman BT, Tschopp J. Innate immune activation through Nalp3 inflammasome sensing of asbestos and silica. *Science* (2008) 320:674–7. doi:10.1126/science.1156995
160. Dostert C, Guarda G, Romero JF, Menu P, Gross O, Tardivel A, et al. Malarial hemozoin is a Nalp3 inflammasome activating danger signal. *PLoS One* (2009) 4:e6510. doi:10.1371/journal.pone.0006510
161. Brown DI, Griendling KK. Nox proteins in signal transduction. *Free Radic Biol Med* (2009) 47:1239–53. doi:10.1016/j.freeradbiomed.2009.07.023
162. Meissner F, Molawi K, Zychlinsky A. Superoxide dismutase 1 regulates caspase-1 and endotoxic shock. *Nat Immunol* (2008) 9:866–72. doi:10.1038/ni.1633
163. Meissner F, Seger RA, Moshous D, Fischer A, Reichenbach J, Zychlinsky A. Inflammasome activation in NADPH oxidase defective mononuclear phagocytes from patients with chronic granulomatous disease. *Blood* (2010) 116:1570–3. doi:10.1182/blood-2010-01-264218
164. Brojatsch J, Lima H, Kar AK, Jacobson LS, Muehlbauer SM, Chandran K, et al. A proteolytic cascade controls lysosome rupture and necrotic cell death mediated by lysosome-destabilizing adjuvants. *PLoS One* (2014) 9:e95032. doi:10.1371/journal.pone.0095032
165. Hornung V, Bauernfeind F, Halle A, Samstad EO, Kono H, Rock KL, et al. Silica crystals and aluminum salts activate the NALP3 inflammasome through phagosomal destabilization. *Nat Immunol* (2008) 9:847. doi:10.1038/ni.1631
166. Lima H Jr, Jacobson LS, Goldberg MF, Chandran K, Diaz-Griffero F, Lisanti MP, et al. Role of lysosome rupture in controlling Nlrp3 signaling and necrotic cell death. *Cell Cycle* (2013) 12:1868–78. doi:10.4161/cc.24903
167. Hari A, Zhang Y, Tu Z, Detampel P, Stenner M, Ganguly A, et al. Activation of NLRP3 inflammasome by crystalline structures via cell surface contact. *Sci Rep* (2014) 4:7281. doi:10.1038/srep07281
168. Newman ZL, Leppla SH, Moayeri M. CA-074Me protection against anthrax lethal toxin. *Infect Immun* (2009) 77:4327–36. doi:10.1128/IAI.00730-09
169. Orlowski GM, Colbert JD, Sharma S, Bogyo M, Robertson SA, Rock KL. Multiple cathepsins promote pro-IL-1beta synthesis and NLRP3-mediated IL-1beta activation. *J Immunol* (2015) 195:1685–97. doi:10.4049/jimmunol.1500509

170. Orlowski GM, Sharma S, Colbert JD, Bogyo M, Robertson SA, Kataoka H, et al. Frontline science: multiple cathepsins promote inflammasome-independent, particle-induced cell death during NLRP3-dependent IL-1beta activation. *J Leukoc Biol* (2017) 102:7–17. doi:10.1189/jlb.3HI0316-152R
171. Petrilli V, Papin S, Dostert C, Mayor A, Martinon F, Tschopp J. Activation of the NALP3 inflammasome is triggered by low intracellular potassium concentration. *Cell Death Differ* (2007) 14:1583–9. doi:10.1038/sj.cdd.4402195
172. Lamkanfi M, Mueller JL, Vitari AC, Misaghi S, Fedorova A, Deshayes K, et al. Glyburide inhibits the cryopyrin/Nalp3 inflammasome. *J Cell Biol* (2009) 187:61–70. doi:10.1083/jcb.200903124
173. Bezanilla F. How membrane proteins sense voltage. *Nat Rev Mol Cell Biol* (2008) 9:323–32. doi:10.1038/nrm2376
174. Cala PM. Volume regulation by flounder red blood cells: the role of the membrane potential. *J Exp Zool* (1977) 199:339–44. doi:10.1002/jez.1401990307
175. Daut J, Standen NB, Nelson MT. The role of the membrane potential of endothelial and smooth muscle cells in the regulation of coronary blood flow. *J Cardiovasc Electrophysiol* (1994) 5:154–81. doi:10.1111/j.1540-8167.1994.tb01156.x
176. Sundelacruz S, Levin M, Kaplan DL. Role of membrane potential in the regulation of cell proliferation and differentiation. *Stem Cell Rev* (2009) 5:231–46. doi:10.1007/s12015-009-9080-2
177. Zhou Y, Wong CO, Cho KJ, van der Hoeven D, Liang H, Thakur DP, et al. SIGNAL TRANSDUCTION. Membrane potential modulates plasma membrane phospholipid dynamics and K-Ras signaling. *Science* (2015) 349:873–6. doi:10.1126/science.aaa5619
178. Horng T. Calcium signaling and mitochondrial destabilization in the triggering of the NLRP3 inflammasome. *Trends Immunol* (2014) 35:253–61. doi:10.1016/j.it.2014.02.007
179. Murakami T, Ockinger J, Yu J, Byles V, McColl A, Hofer AM, et al. Critical role for calcium mobilization in activation of the NLRP3 inflammasome. *Proc Natl Acad Sci U S A* (2012) 109:11282–7. doi:10.1073/pnas.1117765109
180. Lee G-S, Subramanian N, Kim AI, Aksentijevich I, Goldbach-Mansky R, Sacks DB, et al. The calcium-sensing receptor regulates the NLRP3 inflammasome through Ca2+ and cAMP. *Nature* (2012) 492:123–7. doi:10.1038/nature11588
181. Katsnelson MA, Rucker LG, Russo HM, Dubyak GR. K+ efflux agonists induce NLRP3 inflammasome activation independently of Ca2+ signaling. *J Immunol* (2015) 194(8):3937–52. doi:10.4049/jimmunol.1402658
182. Yaron JR, Gangaraju S, Rao MY, Kong X, Zhang L, Su F, et al. K(+) regulates Ca(2+) to drive inflammasome signaling: dynamic visualization of ion flux in live cells. *Cell Death Dis* (2015) 6:e1954. doi:10.1038/cddis.2015.277
183. Fröhlich E. The role of surface charge in cellular uptake and cytotoxicity of medical nanoparticles. *Int J Nanomedicine* (2012) 7:5577–91. doi:10.2147/IJN.S36111
184. Morishige T, Yoshioka Y, Inakura H, Tanabe A, Narimatsu S, Yao X, et al. Suppression of nanosilica particle-induced inflammation by surface modification of the particles. *Arch Toxicol* (2012) 86:1297–307. doi:10.1007/s00204-012-0823-5
185. Nel A, Xia T, Mädler L, Li N. Toxic potential of materials at the nanolevel. *Science* (2006) 311:622–7. doi:10.1126/science.1114397
186. Saquib Q, Al-Khedhairy AA, Siddiqui MA, Abou-Tarboush FM, Azam A, Musarrat J. Titanium dioxide nanoparticles induced cytotoxicity, oxidative stress and DNA damage in human amnion epithelial (WISH) cells. *Toxicol In Vitro* (2012) 26:351–61. doi:10.1016/j.tiv.2011.12.011
187. Zhang Z, Shen H-M, Zhang Q-F, Ong C-N. Involvement of oxidative stress in crystalline silica-induced cytotoxicity and genotoxicity in rat alveolar macrophages. *Environ Res* (2000) 82:245–52. doi:10.1006/enrs.1999.4025
188. Gagné F, editor. Chapter 6 – oxidative stress. *Biochemical Ecotoxicology*. Oxford: Academic Press (2014). p. 103–15.
189. Vallyathan V, Robinson V, Reasor M, Stettler L, Bernstein R. Comparative in vitro cytotoxicity of volcanic ashes from Mount St. Helens, El Chichon, and Galunggung. *J Toxicol Environ Health* (1984) 14:641–54. doi:10.1080/15287398409530614
190. Gao N, Keane MJ, Ong T, Wallace WE. Effects of simulated pulmonary surfactant on the cytotoxicity and DNA-damaging activity of respirable quartz and kaolin. *J Toxicol Environ Health A* (2000) 60:153–67. doi:10.1080/009841000156466
191. Lee W, Ahn Y-S, Lee S, Song BM, Hong S, Yoon J-H. Occupational exposure to crystalline silica and gastric cancer: a systematic review and meta-analysis. *Occup Environ Med* (2016) 73(11):794–801. doi:10.1136/oemed-2016-103552
192. McLaughlin JK, Chow WH, Levy LS. Amorphous silica: a review of health effects from inhalation exposure with particular reference to cancer. *J Toxicol Environ Health* (1997) 50:553–66. doi:10.1080/15287399709532054
193. Freire J, Ajona D, de Biurrun G, Agorreta J, Segura V, Guruceaga E, et al. Silica-induced chronic inflammation promotes lung carcinogenesis in the context of an immunosuppressive microenvironment. *Neoplasia* (2013) 15:913–24. doi:10.1593/neo.13310
194. O'Brien A, Scher I, Formal S. Effect of silica on the innate resistance of inbred mice to *Salmonella typhimurium* infection. *Infect Immun* (1979) 25:513–20.
195. Yarahmadi A, Zahmatkesh MM, Ghaffari M, Mohammadi S, Labbafinejad Y, Seyedmehdi SM, et al. Correlation between silica exposure and risk of tuberculosis in Lorestan province of Iran. *Tanaffos* (2013) 12:34–40.
196. Steenland K, Goldsmith DF. Silica exposure and autoimmune diseases. *Am J Ind Med* (1995) 28:603–8. doi:10.1002/ajim.4700280505
197. Sun L, Li Y, Liu X, Jin M, Zhang L, Du Z, et al. Cytotoxicity and mitochondrial damage caused by silica nanoparticles. *Toxicol In Vitro* (2011) 25:1619–29. doi:10.1016/j.tiv.2011.06.012
198. Joshi GN, Knecht DA. Silica phagocytosis causes apoptosis and necrosis by different temporal and molecular pathways in alveolar macrophages. *Apoptosis* (2013) 18:271–85. doi:10.1007/s10495-012-0798-y
199. Eguchi Y, Shimizu S, Tsujimoto Y. Intracellular ATP levels determine cell death fate by apoptosis or necrosis. *Cancer Res* (1997) 57:1835–40.
200. Nomura J, So A, Tamura M, Busso N. Intracellular ATP decrease mediates NLRP3 inflammasome activation upon nigericin and crystal stimulation. *J Immunol* (2015) 195:5718–24. doi:10.4049/jimmunol.1402512
201. Li H, Willingham SB, Ting JP-Y, Re F. Cutting edge: inflammasome activation by alum and alum's adjuvant effect are mediated by NLRP3. *J Immunol* (2008) 181:17–21. doi:10.4049/jimmunol.181.1.17
202. Sharp FA, Ruane D, Claass B, Creagh E, Harris J, Malyala P, et al. Uptake of particulate vaccine adjuvants by dendritic cells activates the NALP3 inflammasome. *Proc Natl Acad Sci U S A* (2009) 106:870–5. doi:10.1073/pnas.0804897106
203. Lin W, Stayton I, Huang Y-W, Zhou X-D, Ma Y. Cytotoxicity and cell membrane depolarization induced by aluminum oxide nanoparticles in human lung epithelial cells A549. *Toxicol Environ Chem* (2008) 90:983–96. doi:10.1080/02772240701802559
204. Popa-Nita O, Rollet-Labelle E, Thibault N, Gilbert C, Bourgoin SG, Naccache PH. Crystal-induced neutrophil activation. IX. Syk-dependent activation of class Ia phosphatidylinositol 3-kinase. *J Leukoc Biol* (2007) 82:763–73. doi:10.1189/jlb.0307174
205. Cao Z, Fang Y, Lu Y, Qian F, Ma Q, He M, et al. Exposure to nickel oxide nanoparticles induces pulmonary inflammation through NLRP3 inflammasome activation in rats. *Int J Nanomedicine* (2016) 11:3331–46. doi:10.2147/IJN.S106912
206. Khan MI, Mohammad A, Patil G, Naqvi SA, Chauhan LK, Ahmad I. Induction of ROS, mitochondrial damage and autophagy in lung epithelial cancer cells by iron oxide nanoparticles. *Biomaterials* (2012) 33:1477–88. doi:10.1016/j.biomaterials.2011.10.080
207. Jia G, Wang H, Yan L, Wang X, Pei R, Yan T, et al. Cytotoxicity of carbon nanomaterials: single-wall nanotube, multi-wall nanotube, and fullerene. *Environ Sci Technol* (2005) 39:1378–83. doi:10.1021/es048729l
208. Montenegro Raudales JL, Yoshimura A, Sm Z, Kaneko T, Ozaki Y, Ukai T, et al. Dental calculus stimulates interleukin-1β secretion by activating NLRP3 inflammasome in human and mouse phagocytes. *PLoS One* (2016) 11:e0162865. doi:10.1371/journal.pone.0162865
209. Reisetter AC, Stebounova LV, Baltrusaitis J, Powers L, Gupta A, Grassian VH, et al. Induction of inflammasome-dependent pyroptosis by carbon black nanoparticles. *J Biol Chem* (2011) 286:21844–52. doi:10.1074/jbc.M111.238519
210. Choi AO, Cho SJ, Desbarats J, Lovrić J, Maysinger D. Quantum dot-induced cell death involves Fas upregulation and lipid peroxidation in human neuroblastoma cells. *J Nanobiotechnology* (2007) 5:1. doi:10.1186/1477-3155-5-1
211. Mulay SR, Kulkarni OP, Rupanagudi KV, Migliorini A, Darisipudi MN, Vilaysane A, et al. Calcium oxalate crystals induce renal inflammation

by NLRP3-mediated IL-1beta secretion. *J Clin Invest* (2013) 123:236–46. doi:10.1172/JCI63679

212. Schorn C, Janko C, Latzko M, Chaurio R, Schett G, Herrmann M. Monosodium urate crystals induce extracellular DNA traps in neutrophils, eosinophils, and basophils but not in mononuclear cells. *Front Immunol* (2012) 3:277. doi:10.3389/fimmu.2012.00277
213. Desai J, Kumar SV, Mulay SR, Konrad L, Romoli S, Schauer C, et al. PMA and crystal-induced neutrophil extracellular trap formation involves RIPK1-RIPK3-MLKL signaling. *Eur J Immunol* (2016) 46:223–9. doi:10.1002/eji.201545605

Conflict of Interest Statement: The authors declare that the research was conducted in the absence of any commercial or financial relationships that could be construed as a potential conflict of interest.

frontiers in Immunology

ORIGINAL RESEARCH
published: 04 September 2018
doi: 10.3389/fimmu.2018.01991

Cellular Clearance and Biological Activity of Calciprotein Particles Depend on Their Maturation State and Crystallinity

Sina Köppert[1†], Andrea Büscher[1†], Anne Babler[1], Ahmed Ghallab[2,3], Eva M. Buhl[4], Eicke Latz[5], Jan G. Hengstler[2], Edward R. Smith[6,7] and Willi Jahnen-Dechent[1]*

[1] Helmholtz-Institute for Biomedical Engineering, RWTH Aachen University Hospital, Aachen, Germany, [2] Leibniz Research Centre for Working Environment and Human Factors, Dortmund, Germany, [3] Department of Forensic Medicine and Toxicology, Faculty of Veterinary Medicine, South Valley University, Qena, Egypt, [4] Electron Microscopy Facility, RWTH Aachen University Hospital, Aachen, Germany, [5] Institute of Innate Immunity, University Hospital Bonn, Bonn, Germany, [6] Department of Nephrology, The Royal Melbourne Hospital, Melbourne, VIC, Australia, [7] Department of Medicine, University of Melbourne, Parkville, VIC, Australia

OPEN ACCESS

Edited by:
Rostyslav Bilyy, Danylo Halytsky Lviv National Medical University, Ukraine

Reviewed by:
Christian Maueröder, VIB-UGent Center for Inflammation Research (IRC), Belgium
Krzysztof Guzik, Jagiellonian University, Poland

***Correspondence:**
Willi Jahnen-Dechent
willi.jahnen@rwth-aachen.de

[†] *These authors have contributed equally to this work*

Specialty section:
This article was submitted to Inflammation, a section of the journal Frontiers in Immunology

Received: *14 May 2018*
Accepted: *13 August 2018*
Published: *04 September 2018*

Citation:
Köppert S, Büscher A, Babler A, Ghallab A, Buhl EM, Latz E, Hengstler JG, Smith ER and Jahnen-Dechent W (2018) Cellular Clearance and Biological Activity of Calciprotein Particles Depend on Their Maturation State and Crystallinity. Front. Immunol. 9:1991. doi: 10.3389/fimmu.2018.01991

Background: The liver-derived plasma protein fetuin-A is a systemic inhibitor of ectopic calcification. Fetuin-A stabilizes saturated mineral solutions by forming colloidal protein-mineral complexes called calciprotein particles (CPP). CPP are initially spherical, amorphous and soft, and are referred to as primary CPP. These particles spontaneously convert into secondary CPP, which are larger, oblongate, more crystalline, and less soluble. CPP mediate excess mineral transport and clearance from circulation.

Methods: We studied by intravital two-photon microscopy the clearance of primary vs. secondary CPP by injecting i.v. synthetic fluorescent CPP in mice. We analyzed CPP organ distribution and identified CPP endocytosing cells by immunofluorescence. Cellular clearance was studied using bone marrow-derived mouse wildtype and scavenger receptor A (SRA)-deficient macrophages, as well as human umbilical cord endothelial cells (HUVEC), monocyte-derived macrophages (hMDM), and human aortic endothelial cells (haEC). We employed mouse wildtype and mutant immortalized macrophages to analyze CPP-induced inflammasome activation and cytokine secretion.

Results: In live mice, only primary CPP were rapidly cleared by liver sinusoidal endothelial cells (LSEC), whereas primary and secondary CPP were cleared by Kupffer cells. Scavenger receptor A (SRA)-deficient bone marrow macrophages endocytosed secondary CPP less well than did wildtype macrophages. In contrast, primary CPP endocytosis did not depend on the presence of SRA, suggesting involvement of an alternative clearance pathway. CPP triggered TLR4 dependent TNFα and IL-1β secretion in cultured macrophages. Calcium content-matched primary CPP caused twice more IL-1β secretion than did secondary CPP, which was associated with increased calcium-dependent inflammasome activation, suggesting that intracellular CPP dissolution and calcium overload may cause this inflammation.

Conclusions: Secondary CPP are endocytosed by macrophages in liver and spleen via SRA. In contrast, our results suggest that primary CPP are cleared by LSEC via

an alternative pathway. CPP induced TLR4-dependent TNFα and inflammasome-dependent IL-1β secretion in macrophages suggesting that inflammation and calcification may be considered consequences of prolonged CPP presence and clearance.

Keywords: calciprotein particle, calcification, inflammation, phosphate, fetuin-A, plasma protein

INTRODUCTION

Patients suffering from chronic kidney disease (CKD), especially patients on dialysis have exceedingly high cardiovascular morbidity and mortality (1). Apart from classical risk factors of cardiovascular disease (CVD) like smoking, hypertension, diabetes and dyslipidemia, elevated serum phosphate, and inflammation have been identified as major risk factors in these patients (2–4). These findings suggest that elevated circulating phosphate triggers CKD-associated CVD, and chronic inflammation and calcification amplify the detrimental effects of high serum phosphate, which cannot be properly regulated for lack of kidney function. Calcium and phosphate are required in millimolar concentrations for metabolism, signaling and hard tissue formation across many branches of the tree of life. In water, millimolar calcium and phosphate however, readily form insoluble salts unless the metastable state is stabilized by complex-forming compounds collectively referred to as mineralization inhibitors or mineral chaperones (5). This fundamental fact has been aptly named Lot's wife's problem (6). Vertebrates with bone made of calcium phosphate have evolved active inhibition mechanisms to prevent unwanted calcium phosphate deposition, calcification, outside the skeleton. The liver derived plasma protein fetuin-A is a systemic inhibitor of ectopic calcification. Fetuin-A deficient mice on a DBA/2 genetic background exhibit extensive extraosseous calcification, especially in brown adipose tissue, skin, heart, lung, and kidney (7, 8). Plasma fetuin-A is associated with and plays a critical role in the stabilization of protein-mineral complexes, named calciprotein particles (CPP) (9, 10). To prevent these calcifications, CPP first form as colloidal nanoparticles, containing fetuin-A, additional plasma proteins, and calcium and phosphate. Particles in this maturation state are called primary CPP. Primary CPP undergo Ostwald ripening with associated structural and compositional rearrangements (11). The resulting crystalloid secondary CPP are ellipsoid-shaped with a crystalline core surrounded by a protein layer (9). The protein layer is complex and shows marked differences in enrichment for certain proteins with particle ripening (12). Nonetheless, fetuin-A, albumin, and the plasma proteins apolipoprotein A1, prothrombin, and complement C3 have been consistently identified across multiple studies (13). Primary CPP reach a hydrodynamic diameter of roughly 50–100 nm, and secondary CPP measure 100–300 nm (11). Secondary CPP are cleared by macrophages via scavenger receptor A and thereby prevent pathological calcium and phosphate deposition. Liver Kupffer cells and marginal zone macrophages in the spleen were shown to be the main cell types involved in the clearance of secondary CPP (14). A mechanism for primary CPP clearance was never reported for lack of stable primary CPP preparations for use in animal and in cell-based studies.

Numerous studies showed that particle-induced inflammation causes cell damage both of the clearing macrophages and surrounding tissue cells alike by starting a vicious cycle of attempted clearance and chronic inflammation. Chronic inflammation is a salient part of e.g., ox-LDL clearance by atherosclerotic lesional macrophages, asbestos-induced inflammation in lung macrophages and indeed macrophage activation caused by a plethora of engineered nanoparticles. Crystalline particles like calcium-phosphate crystals induce an inflammatory response in cells, resulting in expression of TNF-α (15) and necrosis of the cells (16). Conflicting but not necessarily contradictory, data were reported on the inflammatory activity of calcium and phosphate, hydroxyapatite crystals, primary and secondary CPP. A side-by-side comparison in relevant cell types involved in clearance is missing. Multiple pathways have been implicated in the particle-induced secretion of inflammatory cytokines by e.g., clearing macrophages, which can be triggered by activation of the TLR4 (15), protein kinase C-α/activated protein kinase (17), or via the NLRP3 inflammasome (18, 19). Particles smaller than 1 μm and needle-shaped particles most potently induce an inflammatory response (20). The crystal-induced inflammatory response of macrophages can be markedly reduced by serum, which was partly attributed to the presence of fetuin-A in serum (21). Along these lines, fetuin-A containing secondary CPP had less inflammatory potential toward macrophages than had microcrystalline hydroxyapatite with respect to TNFα secretion (22). Thus, the formation of CPP from plasma proteins and calcium phosphate mineral both stabilizes the fluid phase in a metastable state, and dampens the inflammatory potential of mineral crystals, which might otherwise cause crystallopathies. It is however debatable, which form of CPP is more physiologically relevant. Primary CPP spontaneously form in biological fluids supersaturated with mineral ions, but the transformation into secondary CPP under biomimetic laboratory conditions can take many hours to days (23). The instability of primary CPP, which has greatly restricted previous studies, may also portend to spontaneous transformation *ex vivo*, thus at least a proportion of secondary CPP detected in some biological samples may represent a non-physiologically generated artifact. Indeed, we reported finding only copious amounts of secondary CPP in post-mortem ascites of a peritoneal dialysis patient who had died of sclerosing peritonitis (24). Other studies indicate that secondary CPP, while occasionally observed in serum and peritoneal effluent of dialysis patients, are present in much lower amounts than primary CPP

(25). Thus, it remained of critical importance to understand the handling and effects of primary CPP in comparison with their more stable crystalline counterparts.

To this end we studied the clearance trajectories of primary and secondary CPP in live mice and in cultured cells. We report differential clearance of primary CPP and secondary CPP by liver sinusoidal endothelial cells (LSEC) and liver Kupffer cell macrophages, respectively. Furthermore, primary and secondary CPP differentially induced inflammatory responses in cultured macrophages. This finding is important for targeting the correct first responder cells, which may suffer phosphate or CPP-associated inflammatory damage *in vivo*.

MATERIALS AND METHODS

Animal Experimentation

All animal experiments were conducted in agreement with the recommendation of the Federation for Laboratory Animal Science Associations (FELASA), and were approved by the animal welfare committee of the Landesamt für Natur-, Umwelt- und Verbraucherschutz (LANUV, 84-02.04.2013.A113 and 84.02.04.2015.A294). At least three mice each were injected in the clearance experiments and three mice of the genotypes were used to isolate bone marrow-derived macrophages. All mice were maintained in a temperature-controlled room on a 12-h day/night cycle. Food and water were given *ad libitum*.

Protein Purification and CPP Preparation

Bovine fetuin-A (Sigma F2379) was purified by gel-filtration and labeled with Alexa-488 or Alexa-546 NHS ester (Thermo Scientific). Purified fetuin-A was routinely analyzed for LPS activity using the Endosafe ultrasensitive cartridge assay (Charles River). LPS content was <0.1 EU/ml, and did not induce cytokine secretion in macrophages. Labeled fetuin-A monomer was used to prepare primary and secondary CPP (14) or CPP were prepared in medium as described (26). Briefly, fetuin-A based CPP were produced in a solution containing 400 µl 2.5 mg/ml fetuin-A in 140 mM sodium chloride mixed with 100 µl 140 mM sodium chloride and 250 µl 24 mM phosphate buffer (pH 7.4). After thorough mixing, 250 µl of 40 mM calcium chloride solution (pH 7.4) was added. CPP formation proceeded at 37°C with all components pre-warmed. Primary CPP were harvested after 15 min incubation time and secondary CPP after 12 h. The DMEM/FCS-based CPP were prepared in pre-warmed solutions of DMEM containing 10% FCS. Phosphate and calcium were added as stock solutions of sodium phosphate (0.5 M, pH 7.4) and calcium chloride (0.5 M, pH 7.4) to final concentrations of 3.5 mM phosphate and 1.0 mM calcium, respectively. Primary CPP were collected after 1 day of incubation at 37°C and secondary CPP after 7 days. Particles were spun down at 20,000 × g for 20 min and afterwards resuspended in saline for further analysis.

Particle Analysis

Particle size distribution was analyzed using a NanoSight NS 300 particle analyzer (Malvern Instruments) equipped with a 488 nm laser module. Samples were diluted 1:100 in filtered sodium chloride solution (140 mM, passed through a 0.1 µm syringe filter). Depicted results are the average mode of 5 sequences of 30 s recording time each. For transmission electron microscopy, samples were diluted 1:10 in MilliQ water and 1 µl sample was applied onto Formvar-coated nickel grids (Plano, Wetzlar, Germany). The grids were dried at room temperature, and the CPP were visualized without staining. T_{50} assays of fetuin-A containing solutions for CPP preparations were performed as described (27) with minor modifications. Stock solution 1 was NaCl solution: 140 mM NaCl. Stock solution 2 was calcium solution: 40 mM $CaCl_2$+100 mM Hepes+140 mM NaCl pH-adjusted with 10 M NaOH to 7.40 at 37°C. Stock solution 3 was phosphate solution: 19.44 mM Na_2HPO_4+4.56 mM NaH_2PO_4+100 mM Hepes+140 mM NaCl pH-adjusted with 10 M NaOH to 7.40 at 37°C. Before dispensing into 96-well plates, all solutions were prewarmed to 34.5°C. Liquid dispensing was done with a Liquidator96® bench-top pipetting system (Steinbrenner Laborsysteme GmbH) using fresh pipetting tips for every pipetting step. The components were mixed in the following order: (1) NaCl solution, 20 µl/well, (2) fetuin-A/BSA solution (1 mg/ml fetuin-A and 50 g/L BSA in 140 mM NaCl) or DMEM with 10% FCS, 80 µl/well, (3) phosphate solution, 50 µl/well, (4) mix 1 min, and (5) calcium solution, 50 µl/well, mix 1 min. The 96 wells were covered with ThinSeal adhesive sealing film. The assay was performed for 200 cycles with 1.5-s measurements per well and a position delay of 0.1 s in horizontal plate reading mode. Continuous measurements were recorded for hours or days as indicated in the figure legends.

CPP Clearance and Intravital Imaging

Functional intravital imaging of mouse livers and image analysis was performed as described (28) using a customized inverted microscope LSM MP7 (Zeiss, Jena, Germany) with an LD C-Apochromat 40x 1.1 water immersion objective. Briefly, the mice were anesthetized by an intraperitoneal injection of ketamine (100 mg/kg b.w), xylazine (10 mg/kg b.w.), acepromazin (1.7 mg/kg b.w.), and buprenorphine (0.08 mg/kg b.w.). Anesthesia was maintained throughout the observation period using an isoflurane inhaler. Mice were wiped with ethanol and their abdomen was shaved. The abdominal wall was opened with a transverse section of 1 cm length. The liver was carefully extraventralized by gravitational force without touching. The mouse with the liver protruding downward was mounted on a thermostated microscope stage using a large coverslip and pre-warmed Ringer saline. The mice received bolus intravenous injections of Hoechst 33258 and tetramethylrhodamine ethylester to allow visualization of nuclei and liver morphology, respectively (**Table 1**). At time zero, primary or secondary CPP were injected i.v. using a catheter inserted into the tail vein. Mice were injected with an equivalent of 160 µg (protein content) in a maximum volume of 200 µl of either monomeric fetuin-A, primary CPP, or secondary CPP, and intravital two-photon microscopy (2PM) videos were continuously recorded. All intravital imaging experiments were done in at least 3 mice.

TABLE 1 | Fluorescent marker dyes and imaging conditions.

Fluorescent marker dye	Marker for	Dose [mg/kg b.w.]/vehicle	Excitation range [nm]	Source
Hoechst 33258	Nuclei	5 in PBS	720–800	Thermo scientific
Tetramethylrhodamine ethylester (TMRE)	Mitochondrial membrane potential	0.96 in methanol: PBS (1:1)	780–820	Thermo scientific
Alexa-488-labeled fetuin-A	Primary/ Secondary CPP	160 μg (protein) in 0.9% NaCl	740–800	Thermo scientific / Sigma

Organ Preparation and Immunofluorescence

In a separate set of injection experiments mice were anesthesized and injected as above, and sacrificed at times indicated in the figure legends by isofluorane overdosing and organs were collected for histology. Tissues were embedded in Tissue-Tek O.C.T. compound to prepare 5 μm cryosections for subsequent CPP distribution analysis and immunofluorescent staining. Sections were fixed for 5 min with Bouin's fixative, rinsed with 0.1 M Tris pH 8.5, washed with distilled water and blocked with 10% goat serum in PBS. Primary antibodies against F4/80 (ab6640, Abcam) and LYVE-1 (DP3513P, Acris) were used to stain macrophages and liver sinusoidal endothelial cells, respectively. Secondary antibodies were Alexa-488 or Alexa-546 labeled goat anti-rat antibodies (A11006, A11081, Thermo Fisher Scientific). After antibody staining, sections were counterstained with DAPI and mounted in Immu-Mount (Thermo Fisher Scientific). Micrographs were recorded using a Leica DM-IRB 6000 inverted microscope, appropriate illumination and filter sets and a high sensitivity digital Leica black and white camera. Fluorescence micrographs were color-coded and compound fluorescence pictures were composed and enhanced using Adobe Photoshop software. Photos in each figure plate were processed identically.

Cell Culture Experiments

Murine immortalized wildtype and TLR4 knockout macrophages (29) were cultured in RPMI supplemented with 10% fetal calf serum (FCS). Primary bone marrow-derived macrophages were isolated from C57BL/6 wildtype or SRA-deficient mice (14). The cells were differentiated for 10 days using L929-fibroblast conditioned medium. HUVEC were cultured in EGM-2 (Lonza). For endocytosis assays, primary wildtype and SRA-knockout bone marrow-derived macrophages prepared from at least three mice each (14) or human umbilical cord venous endothelial cells HUVEC were seeded in 0.5 ml medium at 500,000 cells/ml in 24-well plates. After overnight culture the cells were incubated for 1 h at 37°C with 100 μg (protein content) in 500 μl medium Alexa488-labeled or Alexa546-labeled fetuin-A monomer. The same amount of labeled fetuin-A was contained in primary or secondary CPP as indicated in the figure legends. Cells were washed twice with PBS, and observed under a microscope, or fixed with 4% paraformaldehyde and fluorescent CPP uptake was measured by flow cytometry. To assess inflammatory cytokine release, immortalized wildtype and TLR4 knockout (ko) macrophages were seeded at 250,000 cells/ml in 24-well plates and kept overnight. For TNFα measurement, cells were starved for 2 h in serum-free RPMI, and then treated with 200 μg/ml (calcium content) primary or secondary CPP, or with 10 ng/ml LPS. After 6 h incubation the culture supernatants were harvested and TNFα levels were measured by ELISA (DY410-05, R&D systems). For IL-1β measurement, cells were primed with 10 ng/ml LPS for 2 h, and subsequently treated with primary or secondary CPP, or with 10 ng/ml LPS for 16 h. Cell culture supernatant was harvested and secreted IL-1β was determined by ELISA (DY401-05, R&D systems).

To test the clearance of primary and secondary CPP in human cells, human monocyte-derived macrophages (hMDM) and primary human aortic endothelial cells (haEC) were also studied. Alexa488-labeled bovine fetuin-A was spiked into 10% FCS/DMEM culture medium to synthesize primary and secondary CPP as described previously (26). Particle synthesis was confirmed by cryoTEM. Monomeric labeled-fetuin-A (1 mg/ml) was also run alongside as a comparator. hMDM were cultured as described (30) with minor modifications. In brief, peripheral blood mononuclear cells were isolated from the buffy coats (diluted 1:1 in PBS containing 2 mM EDTA; PBS-EDTA) of freshly drawn blood of healthy volunteers by Ficoll-paque (GE Healthcare) density centrifugation (350 g for 30 min at 4°C). The mononuclear cell layer was recovered and washed twice in PBS-EDTA and then enriched for monocytes by positive selection with anti-CD14 magnetic beads (Miltenyi Biotec). Macrophages were obtained from these isolates after 7 days of culture in macrophage serum-free medium (Invitrogen, Carlsbad, CA, USA) supplemented with 10% (vol/vol) human serum (Sigma, St. Louis, MS, USA), which was cleared from cryoprecipitates and other particulates/exosomes by centrifugation (18 h at 350,000 × g and 4°C). The medium also contained human macrophage colony-stimulating factor (50 ng/ml; eBioscience, San Diego, CA, USA), penicillin (100 U/ml; Sigma), and streptomycin (0.1 mg/ml; Sigma). Cells were cultured at 37°C and an atmosphere of 5% CO_2. haEC were purchased from Lonza (#CC-2535; Walkersville, USA), cultured in EGM-2 BulletKit (#CC-3162; Lonza) to 70–80% confluence and used at passage 3–7.

For endocytosis assays, cells were seeded in 24-well plates (250,000 cells per well) and rested overnight in fresh culture media prior to experimentation the next day. Cultures were treated in serum-free media supplemented with Alexa488-labeled primary CPP or secondary CPP adjusted to equivalent levels of calcium (100 μg/ml), or monomeric labeled-fetuin-A (1 mg/ml) for 10, 20, 60, or 120 min, after which monolayers were gently washed and fixed with BD Phosflow Fix buffer I (containing 4.2% formaldehyde). Cell-associated fluorescence was measured by flow cytometry using the 488 nm laser for excitation and the FITC filter (527/32) for detection. Non-linear functions were used to fit averaged data for each treatment. In some experiments cells were co-treated with both primary and secondary CPP to investigate competitive uptake. While in others, cells were pre-treated for

30 min with one of several chemical inhibitors at previously defined concentrations as detailed in **Supplementary Table 1** (all from Sigma): cytochalasin D (10 μM), chlorpromazine (10 μg/ml), filipin (2 μg/ml), genestein (200 μM), 5-(N,N-dimethyl)amiloride hydrochloride (10 μM; 5-DMA), MβCD (2 mM), Ly294002 (100 μM), monodansylcadaverine (100 μM; MDC) polyinosinic acid (10 μg/ml) or vehicle (DMSO/media); then washed and switched to media containing AF488-CPP (100 μg/ml) and incubated for 60 min at 37°C; or were pre-treated with blocking antibodies (60 min at 4°C) directed against SRA (AbD Serotec, 10 μg/ml;), TLR2/4/6 (10 μg/ml; Invivogen), CD36 (clone FA6-152; 10 μg/ml; Hycult Biotech), or annexin-2 (20 μg/ml; BD Biosciences) or relevant isotype IgG control (all 10 μg/ml; eBioscience) before incubation with CPP-containing media for 60 min at 37°C.

Statistics

All statistical analyses were carried out using GraphPad Prism version 5.0c and are given as mean values ± standard deviations. One-way ANOVA with Tukey's multiple comparison test was used to test for differences in non-sized matched experimental groups.

RESULTS

Particle Morphology Is Independent of Synthesis Route

We analyzed by electron microscopy the supernatant of a buffered solution supersaturated in calcium and phosphate. The solution also contained purified fetuin-A protein or FCS, which is rich in fetuin-A protein. Both solutions mediate the formation of protein-mineral complexes known as calciprotein particles (CPP). **Figures 1A–D** show primary and secondary CPP formed in the presence of FCS (**Figures 1A,B**) or in the presence of purified fetuin-A protein (**Figures 1C,D**). Primary CPP appeared as spherical particles with a size 50–100 nm in diameter (**Figures 1A,C**). Secondary CPP had overall elliptic shape of up to 100 nm wide and up to 250 nm long. Crystalline spicules were observed in secondary CPP, but not in primary CPP. Nanoparticle tracking analysis measurements shown in **Figures 1E,F** indicated particles with hydrodynamic diameters of 100–125 nm in all preparations, indicating a strong bias of this method toward the shorter particle axis. Importantly, primary and secondary CPP each were morphologically indistinguishable regardless of their route of synthesis. Overall our findings thus confirm numerous studies by our and other laboratories indicating that spherical, poorly crystalline primary CPP spontaneously formed immediately after mixing supersaturated solutions of calcium and phosphate in the presence of purified fetuin-A or in the presence of serum containing fetuin-A; and that the primary CPP spontaneously transformed into elongated secondary CPP of about twice the length. **Figures 1G,H** illustrate that the characteristic Ostwald transformation of primary CPP into secondary CPP occurred irrespective of the mineral supersaturation of the mineral solutions, or the protein content, albeit at widely varying times. We derived computationally from continuous light scatter measurements the crystal transformation time (T_{50}), which indicates the half-maximum transformation of primary into secondary CPP. T_{50} was 2.5 days if CPP formed in DMEM supplemented with 1 mM Ca (total Ca 3.8 mM), 3.5 mM phosphate (total Pi 4.4 mM), and 10% fetal calf serum FCS (**Figure 1G**). T_{50} dropped to 350 min in the presence of 10% FCS (not shown), and further to 75 min in the presence of 1 mg/ml purified fetuin-A (**Figure 1H**), both dissolved in HEPES/NaCl buffer supplemented with 10 mM calcium, 6 mM phosphate at neutral pH. Thus, protein concentration was positively associated with T_{50}, while mineral ion supersaturation was negatively associated with T_{50}. We employed primary and secondary CPP formed with or without fluorescence labeled fetuin-A as indicated in the figure legends, to study their clearance from circulation in live mice, and to study CPP biological activity in cultured macrophages.

Fast Clearance of Primary and Secondary CPP in the Liver

Mice received intravenous bolus injections of 160 μg (fetuin-A content, equals 160 μg calcium content) of fluorescent primary or secondary CPP, an amount which should rapidly be diluted to 10 μg/ml CPP (calcium content) or below in the circulation, a concentration of circulating CPP recently observed in CKD patients (25). We studied CPP liver clearance by intravital 2-photon microscopy. **Figure 2A** shows that primary CPP clearance from sinusoids into liver sinusoidal endothelial cells (LSEC) occurred in <1 min. Since the sinusoidal endothelial cells are typically thin, the CPP associated signal is difficult to see on the stills of **Figure 2A** and can more easily be studied in the videos (**Supplementary Movie 1**). Kupffer cells showed a strong CPP associated fluorescence as early as 2 min after injection. Thereafter, primary CPP in Kupffer cells were rapidly degraded, shown by a fast decline in signal after about 15 min. **Figure 3** illustrates secondary CPP clearance from sinusoids, first into Kupffer cells within 2 min, and only later ∼25 min after injection into LSEC as illustrated by the cartoons above the micrographs. Unlike in primary CPP, no decline in Kupffer cell-associated fluorescence was observed with secondary CPP during the observation period. Kupffer cell-associated fluorescence following secondary CPP clearance was three- to four-fold higher than sinusoidal endothelial cell-associated fluorescence following primary CPP suggesting preferential clearance of crystalloid particles like secondary CPP over soft colloidal particles like primary CPP. **Supplementary Movies 1**, **2** provided in the supplement illustrate complete clearance sequences of primary and secondary CPP in the liver underscoring differential clearance by LSEC and Kupffer cell macrophages, respectively.

Liver Sinusoidal Endothelial Cells Predominantly Clear Primary CPP, Liver Kupffer Cells Predominantly Clear Secondary CPP

In a separate series of experiments we injected mice with a mixture of Alexa546-labeled primary (red) and Alexa488-labeled (green) secondary CPP, harvested organs as indicated in the

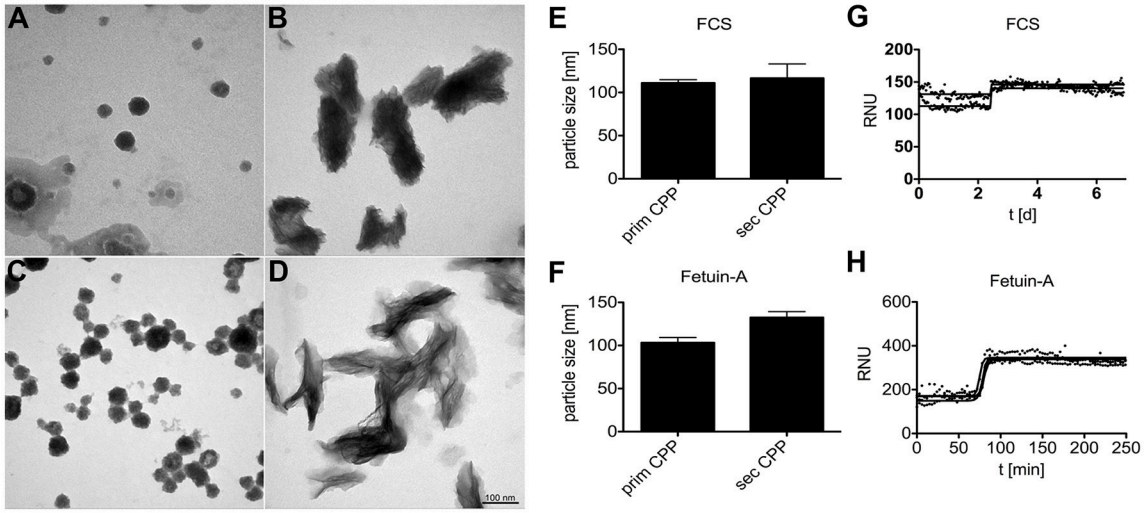

FIGURE 1 | Calciprotein particle CPP formation in protein solutions supersaturated with calcium and phosphate. **(A,B,E,G)** CPP were prepared in DMEM supplemented with 1.0 mM calcium (total Ca 3.8 mM), 3.5 mM phosphate (total Pi 4.4 mM), and 10% fetal calf serum FCS. **(C, D,F,H)** Alternatively, CPP were prepared in HEPES/NaCl buffer supplemented with 10 mM calcium, 6 mM phosphate, and 1.0 mg/ml purified fetuin-A protein. **(A–D)** CPP were harvested by centrifugation and analyzed by electron microscopy or by nanoparticle tracking analysis **(E,F)**. **(A–D)** Depict representative CPP in their primary **(A,C)** and secondary **(B,D)** state. DMEM/FCS-derived and HEPES/fetuin-A-derived primary CPP were similar, but DMEM/FCS-derived secondary CPP appeared denser, yet less crystalline because of higher protein content. Electron microscopy shows that primary and secondary CPP are distinct in shape and size, while nanoparticle tracking analysis **(E,F)** indicated similar particle sizes of around 100–125 nm for all preparations. Continuous nephelometer measurements **(G,H)** indicated a sharp transformation of primary into secondary CPP around 2.5 days and 75 min in the presence of DMEM/FCS and HEPES/fetuin-A protein, respectively.

figure legends, and analyzed CPP distribution in two major clearance organs of the reticulo-endothelial system, liver and spleen. Like in the intravital clearance experiments shown in **Figures 2**, **3**, we observed little overlap in the cell types involved in the clearance of primary CPP (arrows in **Figures 4A,B**) and secondary CPP (arrow heads in **Figures 4A,B**), both in liver (**Figure 4A**), and spleen (**Figure 4B**). Unlike liver and spleen, pancreas, kidney, lung, myocard, and brown adipose fat tissue (BAT) cleared neither primary nor secondary CPP (**Supplementary Figure 3**). We focused on CPP clearance in the liver, because this organ has much higher mass than spleen and will clear most CPP despite similar density of clearing cells (**Figures 4A,B**, **Supplementary Figure 3**). We positively identified the clearing cell types employing immunostaining for the Kupffer cell macrophage marker F4/80 (**Figures 4C,E**). Alternatively, we stained for the liver sinusoidal endothelial cell (LSEC) marker LYVE-1 (**Figures 4D,F**). **Figures 4C,D** illustrate that primary CPP clearance was predominantly mediated by LYVE-1-positive LSEC, implicating for the first time the involvement of a non-myeloid cell type in the clearance of circulating protein-mineral complexes. In contrast, secondary CPP were predominantly cleared by F4/80-positive Kupffer cells (**Figures 4E,F**) corroborating our previous report (14). The finding that primary CPP were cleared by LSEC, while secondary CPP were cleared by liver Kupffer cells is important, because recent research has indicated that early stage protein mineral complexes like primary CPP are likely involved in the pathology of chronic kidney disease-associated calcification, while secondary CPP may indicate prolonged non-physiological ripening of protein-mineral complexes (4).

Scavenger Receptor A-Mediated Endocytosis and Differential Clearance of CPP in Macrophages and Endothelial Cells

Previously we showed that macrophage clearance of secondary CPP was predominantly mediated by scavenger receptor A (SRA) (14). Here we asked if primary CPP clearance likewise required SRA. To this end we treated primary bone marrow macrophages derived from wildtype and scavenger receptor A-deficient mice (SRA ko) for 1 h with fluorescence-labeled fetuin-A monomer, fluorescent primary or secondary CPP, and analyzed endocytosis by flow cytometry. To discriminate fetuin-A and CPP binding from endocytosis we incubated bone marrow-derived macrophages with 100 μg (protein content) in 500 μl medium of fetuin-A monomer, primary and secondary CPP at 4°C to assess binding, or at 37°C to assess endocytosis. Following 1 h of incubation we analyzed cell-associated fluorescence by flow cytometry. Incubation at 4°C yielded much lower cell-associated fluorescence than incubation at 37°C, especially for primary and secondary CPP (**Supplementary Figure 4**). These results indicate that the cells readily endocytosed secondary CPP, and less well also primary CPP. A small amount of fetuin-A monomer was also endocytosed. **Figure 5A** shows that wildtype and SRA ko macrophages endocytosed small amounts of primary CPP equally well. **Figure 5B** shows that the macrophages endocytosed

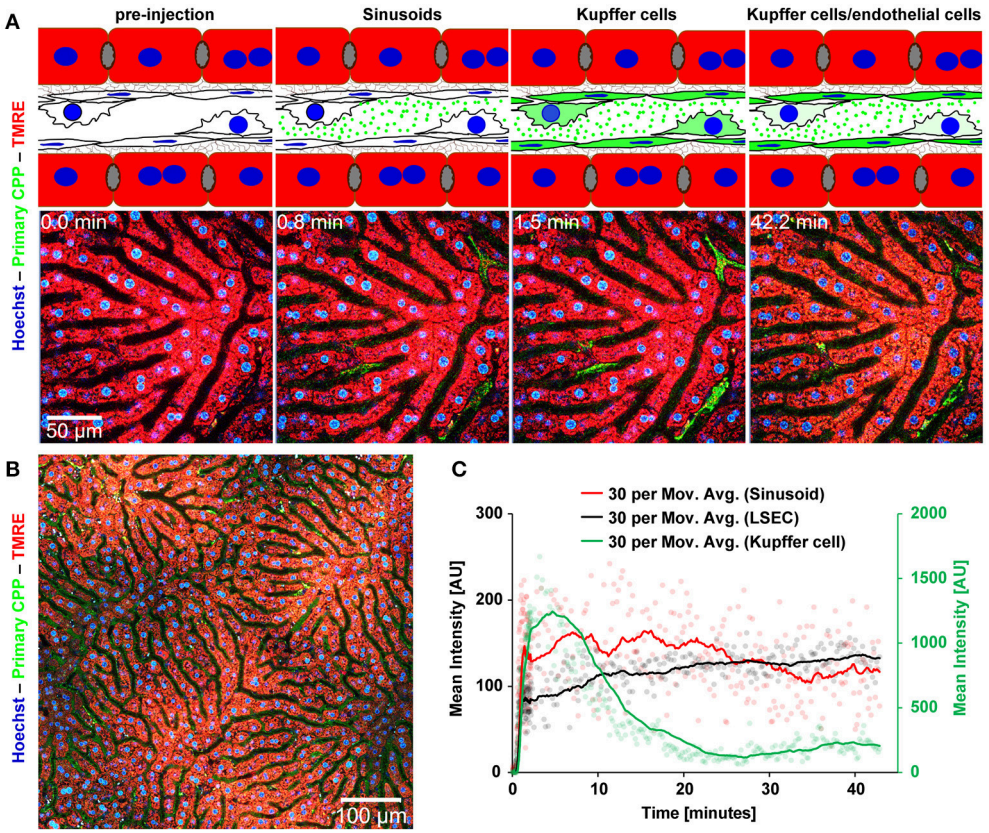

FIGURE 2 | Functional imaging of primary CPP clearance using 2-photon intravital microscopy. Mice received intravenous injections of primary CPP prepared with fluorescent fetuin-A, and the major clearance organ liver was continuously recorded for up to 1 h. Fluorescent intensity was quantified in regions of interest (ROI) and clearance kinetics were calculated. Representative still micrographs with typical views of primary CPP clearing cells are shown. **(A)** Primary CPP clearance from sinusoids into liver sinusoidal endothelial cells (LSEC) occurred within 1 min, and into Kupffer cells within 2 min. Thereafter, primary CPP in Kupffer cells were rapidly degraded, shown by a fast decline of the signal after about 15 min. **(B)** Overview showing a sector of a liver lobule. **(C)** Calculation of mean fluorescence intensity in the sinusoids, LSEC, and Kupffer cells determined by ROI quantification.

five-fold larger amounts of secondary CPP confirming the results shown in **Supplementary Figures 3**, **4**, and mirroring the Kupffer cell discrimination of secondary CPP illustrated in **Figure 3C**. However, SRA-deficient macrophages endocytosed secondary CPP roughly 40% less efficient than did wildtype macrophages corroborating SRA is a major endocytosis receptor for secondary CPP as reported (14), but not for primary CPP. **Figures 5D–G** illustrate the strong discrimination of CPP endocytosis in macrophages, which endocytosed no detectable fetuin-A monomer (**Figure 5D**), small amounts of primary CPP (**Figures 5E,G**, green fluorescence), but large amounts of secondary CPP (**Figures 5F,G** red fluorescence). This strong differential endocytosis of primary vs. secondary CPP was maintained when the macrophages were treated simultaneously with primary and secondary CPP, indicating that the endocytic pathways are separate and non-competitive (**Figure 5G**). Primary vs. secondary CPP discrimination was reversed in HUVEC. Like macrophages, HUVEC endocytosed no detectable fetuin-A monomer (**Figure 5H**), yet unlike macrophages endocytosed large amounts of primary CPP (**Figures 5I,K**, green fluorescence), but small amounts secondary CPP (**Figures 5J,K** red fluorescence). Like in macrophages, HUVEC discrimination of primary vs. secondary CPP was maintained when the cells were treated simultaneously with primary and secondary CPP (**Figure 5K**).

To test the clearance of CPP in primary human cells cultures, human monocyte-derived macrophages (hMDM) and human aortic endothelial cells (haEC) were also studied. **Figures 6A,B** show that hMDM—like mouse macrophages—predominantly cleared secondary CPP, while haEC—like mouse LSEC and HUVEC—predominantly cleared primary CPP. **Figures 6C,D** show that the endocytosis inhibitors cytochalasin D (cyto D), chlorpromazine (CPMZ), and polyinosinic acid (polyI) partially inhibited CPP endocytosis suggesting vesicle-mediated endocytosis of both kinds of CPP, and the involvement of scavenger receptor A (blocked by polyI) exclusively in the endocytosis of secondary CPP, confirming the results shown in **Figure 5** using SRA ko mouse macrophages. Antibody blockade of various receptors confirmed this finding in that anti-SRA antibodies inhibited secondary CPP endocytosis, but not primary CPP endocytosis in hMDM. **Figures 6E,F** show that neither primary nor secondary CPP uptake by hMDM was competitive,

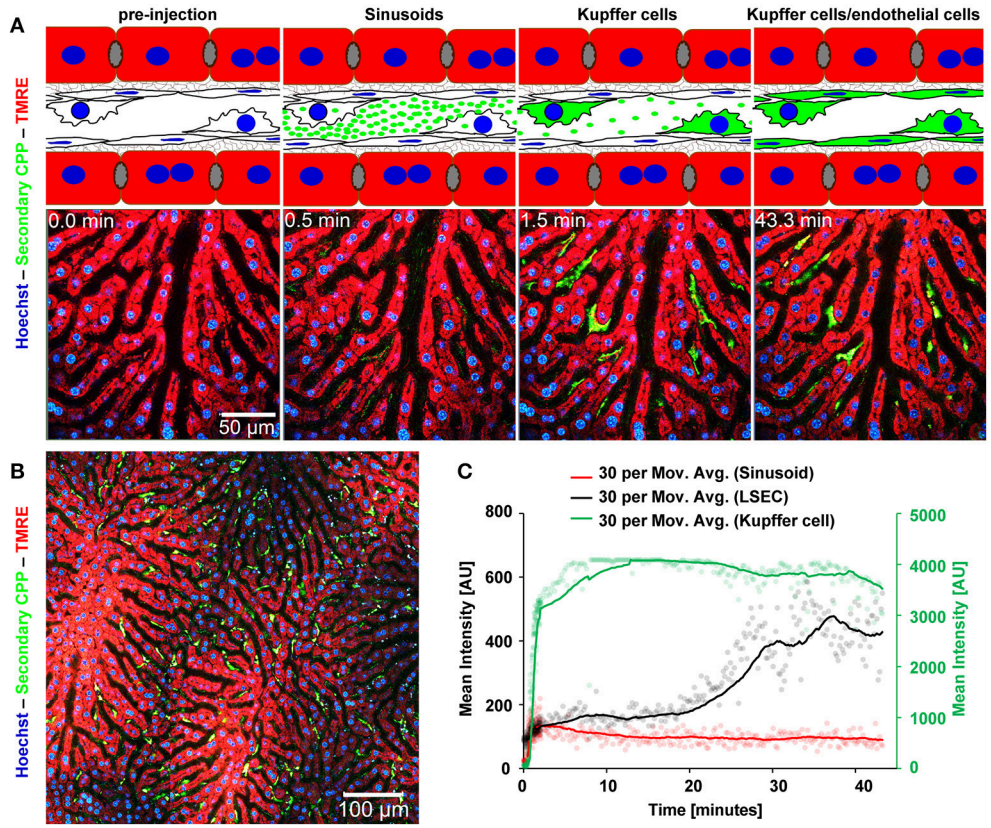

FIGURE 3 | Functional imaging of secondary CPP clearance using 2-photon intravital microscopy. Mice received intravenous injections of secondary CPP prepared with fluorescent fetuin-A, and the major clearance organ liver was continuously recorded for up to 1 h. Fluorescent intensity was quantified in regions of interest (ROI) and clearance kinetics were calculated. Representative still micrographs with typical views of secondary CPP clearing cells are shown. **(A)** Secondary CPP clearance from sinusoids, first into Kupffer cells occurred within 2 min and further into liver sinusoidal endothelial cells (LSEC) within 25 min as illustrated by the cartoons above the micrographs. No decline in Kupffer cell associated fluorescence was determined during the observation period. **(B)** Overview showing a sector of a liver lobule. **(C)** Calculation of mean fluorescence intensity in the sinusoids, LSEC, and Kupffer cells determined by ROI quantification.

again suggesting involvement of distinct cell surface receptors. The fact that both primary and secondary CPP uptake was strongly reduced upon cytoD treatment and partially reduced upon chlorpromazine treatment, albeit more so for primary than secondary CPP, suggested similar endocytic trajectories once the particles had bound their cell surface receptors and endocytosis had begun.

CPP Induced Inflammatory Cytokine Secretion Requires Inflammasome Activation and TLR4-Interaction

Next we asked if calcification media components and CPP endocytosis in particular, triggered an inflammatory response in macrophages and if so, which molecular pathways were involved. We reasoned that the particle nature of CPP might trigger inflammasome activation. To this end we performed speck formation assays using immortalized macrophages expressing the inflammasome adaptor protein *apoptosis-associated speck like protein containing a caspase recruitment domain* fused to *green fluorescent protein* (ASC-GFP). These macrophages are endogenously primed for inflammasome activation (31). We treated the ASC-GFP macrophages with either buffer control, LPS, nigericin, or with calcification media containing elevated calcium or phosphate, or both, as well as with primary or secondary CPP. All calcification media contained identical total calcium as indicated in the figure legends. **Figure 7** shows micrographs of ASC-GFP macrophages with fluorescent specks signifying the recruitment of cytoplasmic ASC into the inflammasome. Of all treatments, nigericin caused the most rapid inflammasome activation, which was accompanied by loss of cellular integrity and cell detachment. In decreasing order of inflammasome activation and deteriorating cell integrity, Ca, Ca + phosphate, primary CPP, secondary CPP, and LPS all caused inflammasome recruitment of ASC and the ensuing cell loss. The late activation by LPS alone was expected, because LPS is known to merely prime macrophages for a "second hit" that will trigger definitive inflammasome activation. The lack of inflammasome activation by elevated phosphate suggests that the phosphate-triggered inflammatory cell activation and ultimately also calcification reported in many studies is either independent of inflammasome activation or is in fact caused

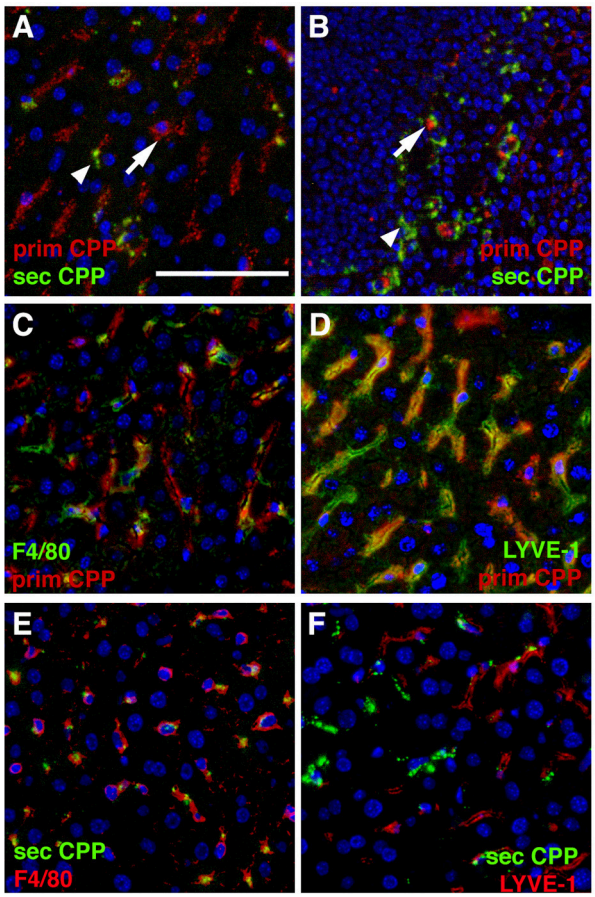

FIGURE 4 | Differential clearance of primary and secondary CPP. Mice were injected with a mixture of fluorescence labeled primary (red) and secondary CPP (green) and the major clearance organs liver **(A,C–F)** and spleen **(B)** were harvested 10 min after injection, sectioned and analyzed for the presence of CPP. Primary CPP (prim CPP, arrows in **A,B**) and secondary CPP (sec CPP, arrow heads in **A,B**) showed distinct non-overlapping distribution in liver **(A)**, and spleen **(B)**. **(C–F)** Co-localization with the macrophage-specific marker F4/80 and the liver sinusoidal endothelial LSEC-specific marker LYVE-1 suggested that primary CPP were predominantly cleared by LYVE-1-positive LSEC, and secondary CPP were predominantly cleared by F4/80-positive liver Kupffer cell macrophages. Scale bar: 25 μm.

by spontaneous calcium phosphate precipitation in the cell culture medium that went unnoticed. **Figure 7** strongly suggests that all Ca-containing preparations triggered inflammasome activation in the order of solubility and thus in the order of availability of ionized Ca to stimulate the macrophages by cellular calcium overload. Nigericin caused immediate influx of cytoplasmic Ca and hence the fastest and strongest cytoplasmic Ca stimulation. Elevated extracellular Ca added to the culture medium alone or in combination with elevated phosphate caused similar intermediate inflammasome activation and cell damage. Primary CPP and secondary CPP caused intermediate to mild inflammasome activation, respectively, accompanied by corresponding reduced cell damage. Collectively, the results presented in **Figure 7** suggest that cytoplasmic calcium is the strongest trigger of speck formation and that calcium phosphates with or without stabilizing protein component will mediate progressively stronger speck formation depending on the solubility of the calcium component. Thus, the addition of calcium and phosphate in established cell culture media will result in varying degrees of cellular calcium overload and biological effects depending on the overall composition, especially the protein content and thus the CPP forming propensity of cell culture media. **Supplementary Figures 1**, **2** corroborate this finding in that the effects of all calcification media were strictly dose-dependent over a range of 5 μg/ml calcium content (**Supplementary Figure 1**), 50 μg/ml (**Supplementary Figure 2**), and 100 μg/ml (**Figure 7**). Our systematic comparison of dose-dependent action of calcification media on real-time ASC inflammasome reporter macrophages underscores that seemingly minor changes in cell-based inflammation and calcification assays will result in different outcomes, which may help explain why individual published studies are almost impossible to compare.

Next we measured inflammatory cytokine secretion following stimulation of wildtype and TLR4-deficient macrophages stimulated with LPS, primary or secondary CPP. Unlike the ASC-GFP reporter macrophages presented in **Figure 7**, **Supplementary Figures 1**, **2**, these macrophages require priming for inflammasome activation and for IL-1β processing. **Figures 8A,C** show as expected LPS-triggered fast release of TNFα, but not of IL-1β a cytokine known to require a "second hit" for inflammasome activation, processing and secretion (32). **Figures 8B,D** show that TLR4-deficient macrophages secreted control levels of both TNFα and IL-1β confirming that TLR4 is the major signaling receptor for LPS. Primary CPP treatment of macrophages caused low level TNFα secretion, yet strong IL-1β secretion confirming that primary CPP triggered inflammasome activation (see **Figure 8**), which is critically required for IL-1β synthesis and secretion. In comparison to primary CPP, secondary CPP caused five-fold increased TNFα secretion indicating preferential stimulation of preformed cytokine secretion. On the other hand, primary CPP caused roughly two-fold higher IL-1β secretion compared to secondary CPP, indicating slower, yet longer lasting macrophage activation. Again these results mirror the inflammasome activation kinetics shown in **Figure 7**. We propose that the softer colloidal primary CPP due to their chemical instability, upon endocytosis and endosomal degradation cause cytoplasmic calcium increase, which triggers a robust and long-lasting inflammatory burst resulting in increased IL-1β secretion. In contrast the more rigid and crystalloid secondary CPP seem to predominantly trigger secretion of preformed TNFα.

DISCUSSION

With recent advances in analytical methods, the existence of calciprotein particles (CPP) that were long proposed on theoretical grounds and had been extensively studied *in vitro* have now been detected and characterized *in vivo*. In chronic kidney disease (CKD), CPP have emerged as potential nanoscale

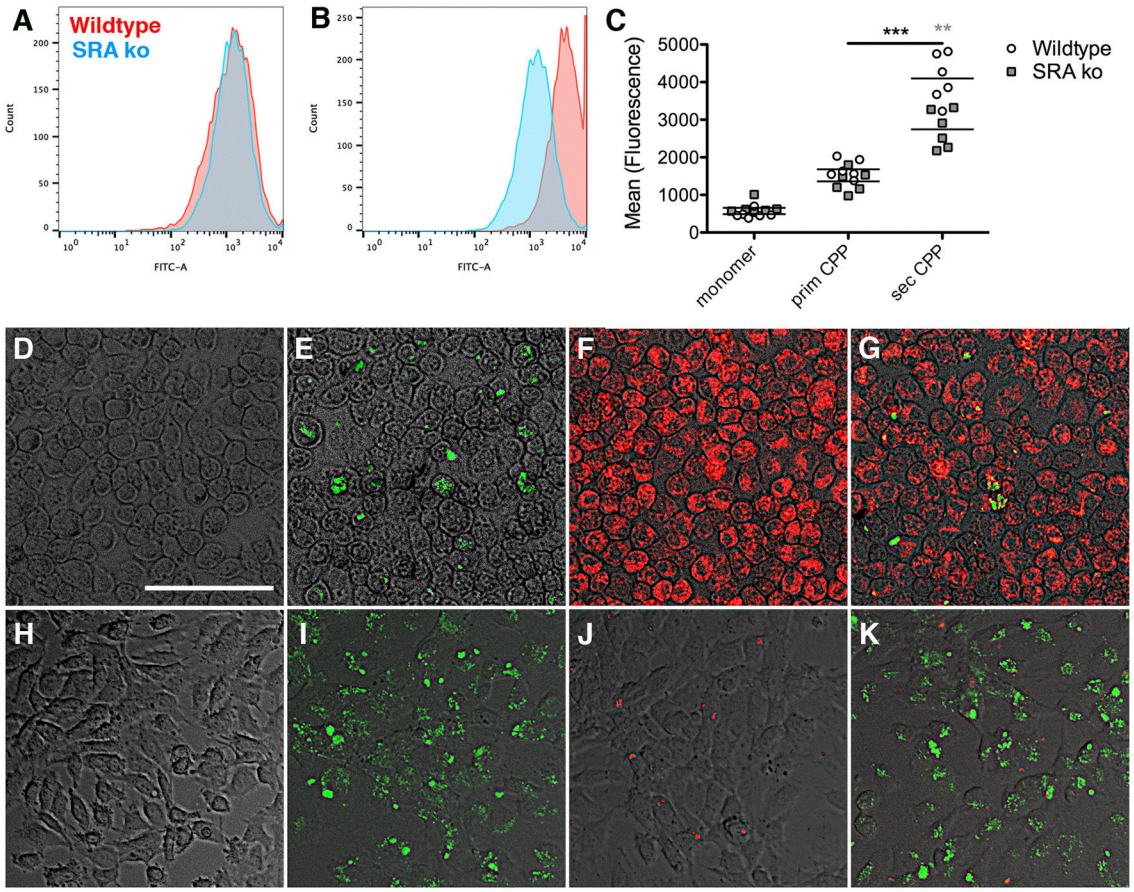

FIGURE 5 | Differential endocytosis of primary and secondary CPP in mouse macrophages and endothelial cells. **(A–C)** Primary bone marrow macrophages derived from wildtype and scavenger receptor A-deficient mice (SRA ko) were treated with fluorescence labeled fetuin-A monomer (not shown) or **(A),** primary or **(B),** secondary CPP for 1 h, and endocytosis was analyzed by flow cytometry. **(C)** Quantitation of endocytosis shows negligible fetuin-A monomer endocytosis, low primary CPP endocytosis but strong secondary CPP endocytosis, which was reduced in SRA-deficient macrophages vs. wildtype. **(D–G)** Fluorescence micrographs of wildtype macrophages and **(H–K),** HUVEC cells treated for 1 h with **(D,H)** labeled fetuin-A monomer **(E,I)** labeled primary CPP (green fluorescence), **(F,J)** secondary CPP (red fluorescence), or **(G,K)** a mixture of primary and secondary CPP. Macrophages endocytosed predominantly secondary CPP **(E–G)**, but HUVEC endocytosed predominantly primary CPP **(I–K),** regardless of whether CPP were incubated individually **(E,F,I,J)** or in combination **(G,K)**. Neither cell type endocytosed detectable amounts of fetuin-A monomer **(D,H)**. Scale bar in **(D)** 75 μm. $^{**}p < 0.01$, $^{***}p < 0.001$.

mediators of phosphate-induced toxicity (4, 12, 33). Similar to the situation in lipoprotein research several decades ago, ongoing research currently unravels CPP metabolism and the relevance of distinct forms of CPP in physiology and disease. We have previously demonstrated rapid blood clearance and contribution to cellular calcification of secondary CPP (14). We reasoned that *in vivo* however, the predominant form of CPP should be primary CPP. Recent work suggests that primary CPP and even earlier forms termed low density CPP—possibly as calciprotein monomers CPM (34)—are associated with CKD in patients who have a much increased risk of calcification (4). Here we demonstrate that primary and secondary CPP are predominantly cleared by endothelial cells and macrophages, respectively. Further the results of our study suggest that CPP-induced inflammation may be associated with cellular calcium overload triggering inflammasome activation and sustained inflammatory cytokine secretion. Thus, phosphate seems to be the driving force of CPP formation (1, 35–38), but calcium overload seems to be causing the inflammation-associated tissue damage and calcification associated with phosphate-induced damage. CPP mobilize excess calcium and phosphate as colloids also containing plasma-derived "mineral chaperone proteins" (5), thus indeed seem to be the "culprit of phosphorous woes" (38), especially if they are continuously formed, yet insufficiently cleared. This scenario is reminiscent of chronic dyslipidemia and the associated high levels of atherogenic lipoprotein complexes, which serve vital carrier function in normal physiology, but turn into disease promoting entities when abundant and modified by e.g., oxidation.

We demonstrated *in vivo* that both LSEC and Kupffer cells clear primary CPP within minutes from the sinusoidal circulation. LSEC play an important role in rapid clearance of primary CPP, in contrast to secondary CPP that are not rapidly taken up by these cells. This confirms the results of

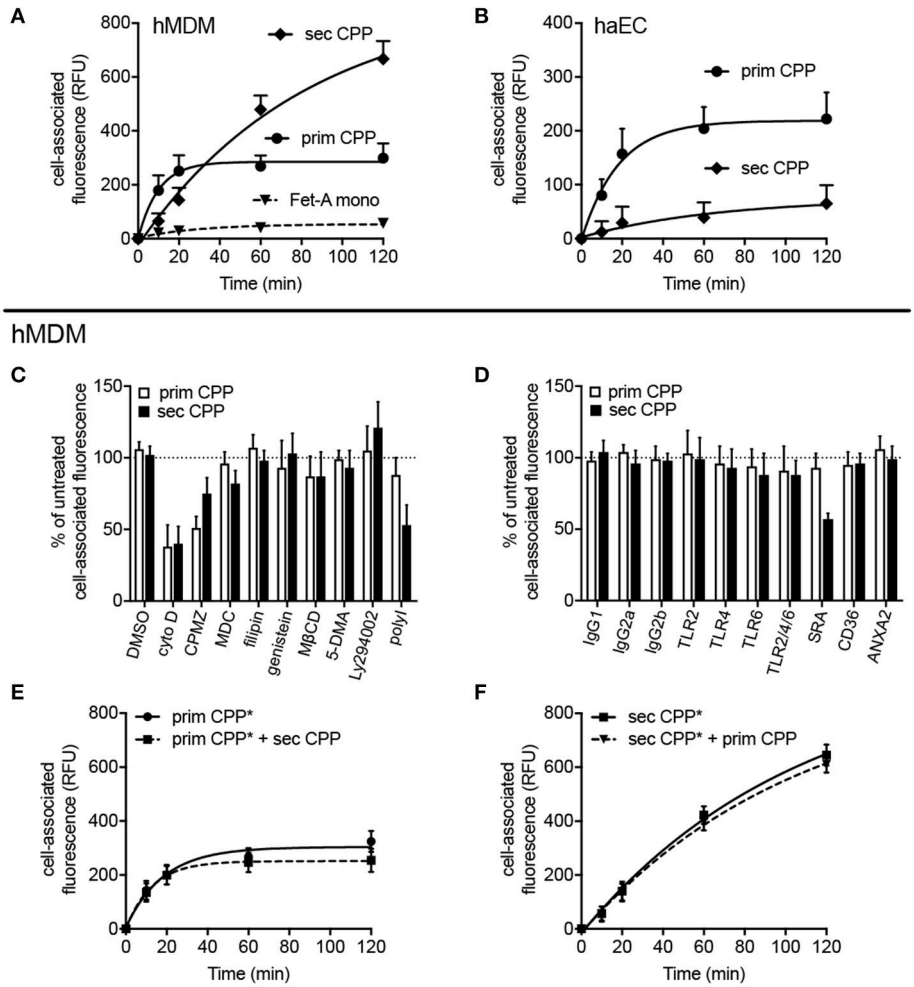

FIGURE 6 | Differential endocytosis of primary and secondary CPP in human monocyte-derived macrophages and aortic endothelial cells. Human monocyte-derived macrophages (hMDM) or human aortic endothelial cells (haEC) were treated with Alexa488-labeled primary or secondary CPP, both 100 μg/mL calcium content, synthesized from FCS/DMEM supplemented with phosphate (final conc. 3.5 mM). Monomeric labeled-fetuin-A was included as a comparator (1 mg/ml). Cell-associated fluorescence was measured by flow cytometry in fixed cells at the stated timepoints. **(A)** Endocyosis observed in hMDM and **(B)** haEC, respectively. **(C,D)** hMDM were pre-treated for 30–60 min with one of several inhibitors (vs. vehicle) or receptor blocking antibodies (vs. isotype control). **(C)** Pre-treatment with cytochalasin **(D)**, an inhibitor of actin polymerization, markedly attenuated uptake of both primary and secondary CPP and (<50% untreated signal; $p < 0.01$) indicating the requirement for active actin-mediated cytoskeletal rearrangement for CPP internalization. Inhibition of protein tyrosine kinase/caveolin-dependent endocytosis (filipin and genestein), lipid-raft synthesis (methyl cyclodextrin-β-cyclodextrin; MβCD), macropinocytosis [5-(N,N-dimethyl)amiloride; 5-DMA], and phosphoinositol-3-kinase-dependent Fcγ receptor-mediated endocytosis (Ly294002) all had no significant effect on CPP uptake. Likewise, pre-treatment with monodansylcadaverine (MDC), an inhibitor of clathrin-mediated endocytosis had no effect on particle uptake. Inhibition of clathrin-dependent endocytosis with chlorpromazine significantly reduced primary CPP internalization (<50%; $p < 0.05$) but not secondary CPP, but may potentially reflect off-target effects due to the non-specificity of the inhibitor. **(D)** Specific immunochemical blockade of TLR2, TLR4, and TLR6, independently of one another, or in combination failed to significantly inhibit uptake of primary or secondary CPP. Neither blockade of CD36, a class B scavenger receptor involved in the uptake of modified LDL particles, or annexin 2, a putative receptor for fetuin-A cellular attachment, had a significant effect on CPP internalization. Consistent with data in the murine macrophage, competitive chemical inhibition of the SR-A with polyinosinic acid (polyI) or immunochemical blockade, markedly decreased endocytosis of secondary CPP (>50%, $p < 0.001$), but not primary CPP. **(E,F)** labeled primary or secondary CPP (CPP*) were added to hMDM with a four-fold excess of unlabeled secondary or primary CPP, respectively to assess whether uptake was competitive. Data are expressed as the mean ±SD, from 6 **(A,B,E,F)** or 4 **(C,D)** independent experiments.

experiments with HUVEC and haEC that likewise preferentially cleared primary over secondary CPP corroborating a role of endothelial cells in the clearance of primary CPP. We speculated that CPP metabolism in healthy subjects is most likely limited to the bone remodeling compartment (6, 39), and to transport epithelia involved in bulk fluid and electrolyte transport like kidney, pancreas, lung, milk glands, placenta, and choroid plexus to name a few. Incidentally these tissues are prone to calcification, especially during inflammatory episodes. We propose that in CKD, the profound disturbance of mineral homeostasis will trigger formation of supraphysiological levels of circulating CPP (4, 25) driving clearing cells into a vicious

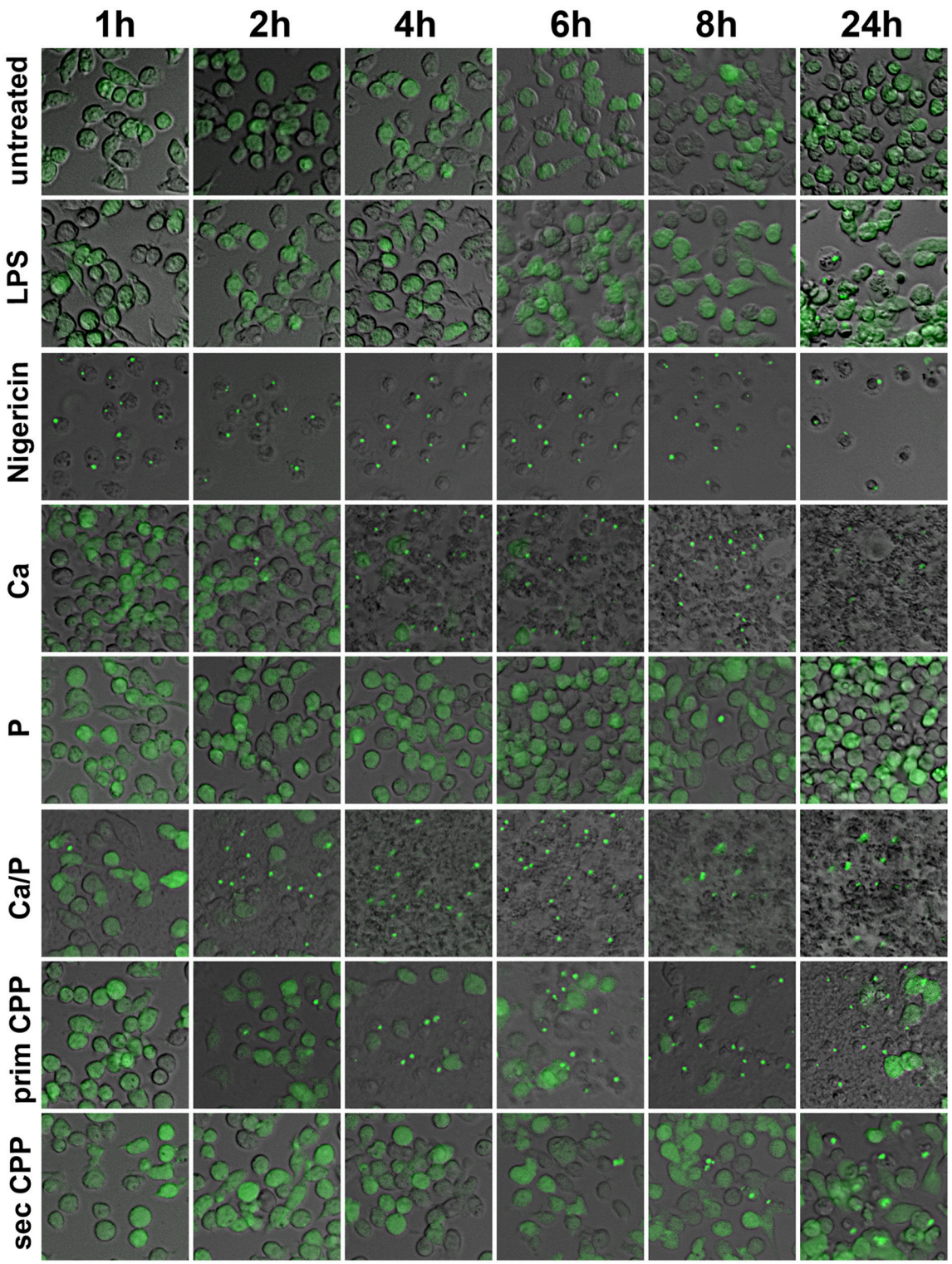

FIGURE 7 | Calcification media induce differential cellular calcium overload and inflammasome activation. Immortalized macrophages expressing the inflammasome adaptor protein labeled *apoptosis-associated speck like protein containing a caspase recruitment domain* ASC fused to *green fluorescent protein,* were exposed to buffer control, LPS, nigericin, or to calcification media with elevated calcium or phosphate, individually and in combination, as well as with primary or secondary CPP. Notably, all calcification media contained an identical total calcium dose of 100 μg, yet differed in the stability of the calcium containing mineral component.

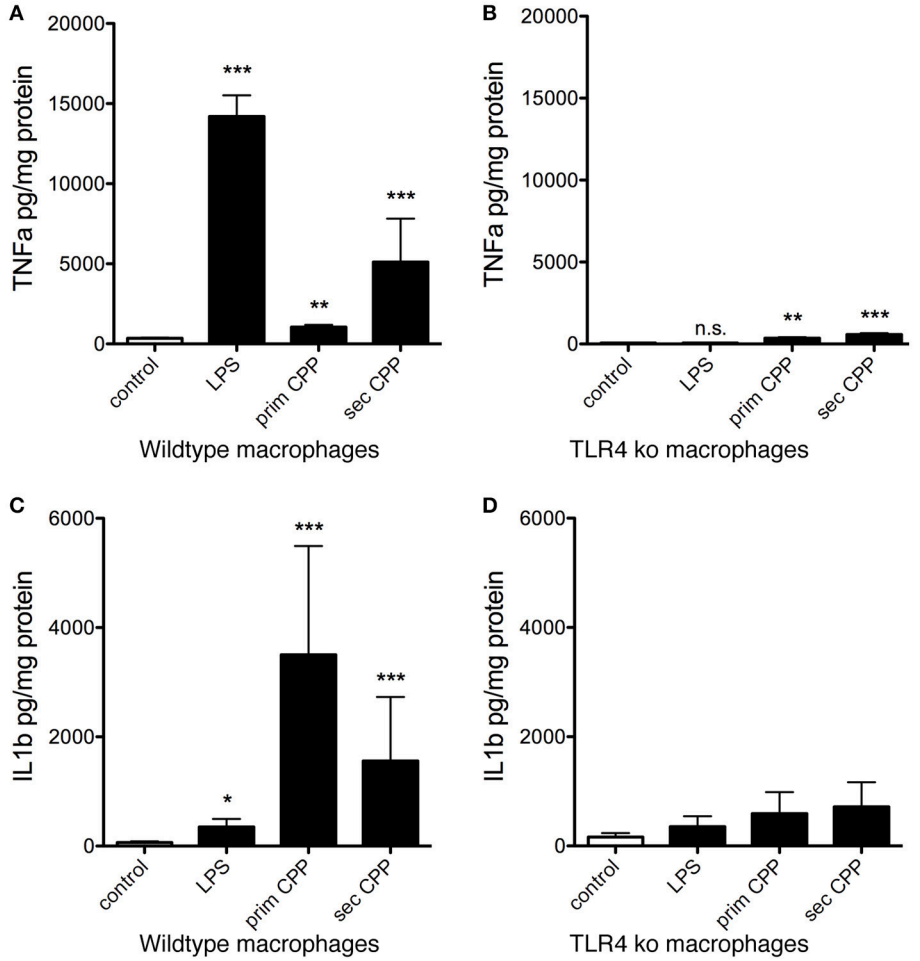

FIGURE 8 | CPP-induced inflammatory cytokine secretion by macrophages is TLR4 dependent. Serum-starved wildtype and TLR4-deficient macrophages (TLR ko) where treated with LPS, primary or secondary CPP. **(A,B)** After 6 h stimulation, inflammatory cytokine TNFα secretion was determined in culture supernatants by ELISA. Secondary CPP caused stronger TNFα secretion than primary CPP. TLR4 ko macrophages showed 10-fold reduced TNFα secretion compared to wildtype macrophages suggesting a major contribution of TLR4 signaling in CPP-triggered TNFα secretion. Nevertheless, CPP-stimulated TLR4 ko still secreted higher amounts of TNFα compared to untreated control (prim CPP $p < 0.01$, sec CPP $p < 0.001$) suggesting a minor contribution to overall TNFα secretion of a TLR4-independent pathway. **(C,D)** After 16 h stimulation, supernatant IL-1β secreted by LPS-primed wildtype macrophages treated with primary CPP was twice as high as treated with secondary CPP. Both values were significantly higher than in wildtype macrophages treated with buffer control or with LPS. TLR4-deficient macrophages show a slight increase in IL-1β processing after the treatment with both types of particles. Overall, inflammatory cytokine secretion was strongly reduced in TLR4 ko. $^{*}p < 0.05$, $^{**}p < 0.01$, $^{***}p < 0.001$.

cycle of CPP clearance and inflammation, a situation further compounded by hallmark pro-inflammatory stimuli associated with dialysis, namely uremic toxins and endotoxin. Thus, endothelial cells should be especially vulnerable to phosphate-associated toxicity in CKD; indeed endothelial dysfunction is possibly one of the earliest manifestations of vascular disease in CKD and other vasculopathies. Strong experimental evidence in fact vindicates phosphate-induced endothelial damage *in vitro* and *in vivo* (40–42). An interventional study reported reduced endothelial damage following dietary phosphate restriction (43), and the use of non-calcium-based phosphate binder use sevelamer has been associated with improvement in endothelial function (FMD) in hyperphosphataemic CKD stage 4 patients (44).

A major finding of this study was that only primary CPP are rapidly cleared by endothelial cells, while primary and secondary CPP are taken up by macrophages. We did not identify an endothelial cell receptor for primary CPP in this work, but positive identification of the clearance trajectory of early CPP forms may allow therapeutic intervention in CPP clearance. Differential clearance could be due to differences in physical properties of primary vs. secondary CPP, the latter being larger and more crystalline triggering phagocytosis on top of receptor mediated endocytosis. Macrophage recognition of crystals and nanoparticles is known to trigger NLPR3 inflammasome activation as described here (45). We hypothesize that distinct surface receptors will bind the respective protein corona of primary and secondary CPP, engaging differentially expressed

clearance receptors in endothelial cells and macrophages. Recent proteomic analyses have revealed that secondary CPP, in particular, show a marked enrichment for the soluble apolipoproteins (e.g., ApoA1) and complement factors that may potentially serve as ligands for particle uptake (12). In addition, primary and secondary CPP may also be discriminated by their size and crystallinity. Both parameters are crucial in macrophage recognition of crystals and nanoparticles, as well as the respective cellular trajectories and signaling pathways engaged (45), and may even drive receptor-independent internalization.

We showed that primary CPP triggered inflammasome speck formation four-fold stronger than secondary CPP. Given their chemical instability and greater solubility under the conditions of endosomal degradation, we suggest that endolysosomal CPP degradation will cause cytoplasmic calcium release, thus triggering inflammasome activation. The relative contributions to NLRP3 activation of increased cytosolic [Ca2+] vs. decreased cytosolic [K+] remain disputed and incompletely defined (46). However, the dose-dependence of CPP action, and control experiments with matched extracellular calcium, which mimicked at high dose the strong NLRP3 inflammasome induction attained with microbial potassium ionophore nigericin, support the notion that CPP stability may determine their inflammatory potential. Cell-specific differential sensitivity may also apply. Bone researchers and tissue engineers routinely employ "osteogenic," mineral-enriched cell culture media to coax mesenchymal precursor cells into an osteoblastic phenotype producing bone-like mineralized matrix. These "professional" mineralizing cells usually form mineralized matrix resembling dystrophic calcification more than mineralized bone, nevertheless without overt signs of inflammation. Calcification researchers on the other hand employ similar or even identical cell culture media to drive cells, e.g., smooth muscle cells, which do not normally mineralize, into pathological calcification. This latter process is usually associated with inflammation. It is presently unclear, what drives this inflammation. Our study suggests that excess mineral uptake and degradation of primary CPP by non-professional mineralizing cells may cause intracellular calcium-triggered inflammasome activation and thus inflammation. Side-by-side comparative studies of professional mineralizing osteoblastic cells and non-professional mineralizing cells including endothelial cells, epithelial cells and smooth muscle cells, which are all known to calcify in CKD, should clarify, if differential sensitivity to cellular calcium load indeed exists. Analyzing gene regulatory networks in these cells should tell if the differential sensitivity is reduced by osteochondrogenic conversion, which is a hallmark of e.g., calcifying smooth muscle cells. We strongly suggest to analyze, apart from cell viability and gene expression, inflammasome activation, a corollary of CPP clearance observed for the first time in this study. Several previous studies have evaluated the effect of calcium phosphate nanoparticles on inflammatory pathways and cell viability. However, relatively few have assessed the effects of biologically native protein-mineral complexes. Of these reports, both FCS and human serum-derived synthetic nanoparticles have been shown to stimulate IL-1β secretion from LPS-primed human monocytes and differentiated macrophage, depending on the length of exposure and on particle size (20, 23, 47). Calcium phosphate or apatite particles present a particularly adsorptive matrix, which may accrue and concentrate biologically active compounds from dilute solutions. Endotoxin even in low amounts is particularly notorious in confounding inflammatory cell assays with nanoparticles (47) and endotoxin contained in uremic plasma could certainly exacerbate the pro-inflammatory capacity of CPP. The plasma protein fetuin-A a major component of CPP, has been described *per se* as an endogenous TLR4 ligand triggering inflammation (48). A recent study on bone marrow lympho-myeloid malfunction in obesity questioned the role of fetuin-A as a physical adapter between TLR4 and dietary saturated fats (49) and earlier studies showed that LPS-free fetuin-A is anti-inflammatory (21) and protects against vascular smooth muscle calcification (50). Commercial fetuin-A preparations are however, impure and usually contain a range of biologically active compounds (51), which may include endotoxin. During this study we routinely tested for the presence of LPS in protein preparations using a high sensitivity endotoxin assay and discarded all preparations containing more than 0.1 EU/ml, a level considered safe for parenteral application in humans. Thus, we detected control level cytokine production and inflammasome activation when cells were treated with fetuin-A protein alone, with a dose identical to the one contained in the respective CPP preparations, effectively ruling out TLR4 binding and pro-inflammatory cell activation by fetuin-A protein under our experimental conditions. Nevertheless, it will be interesting to determine what is the ligand *in vivo* priming TLR4, which is necessary for full induction of the canonical inflammasome. Macrophages studied here were either intrinsically primed for inflammasome induction (**Figure 7**, **Supplementary Figures 1**, **2**) or were LPS-primed for the study of IL-1β secretion. Virtually all particulate inflammasome agonists (silica, urate crystals, cholesterol crystals, alum etc.) only provide the activation signal and require priming by an additional independent stimulus—usually achieved with microbial TLR agonists like LPS *in vitro* (29, 52, 53). Oxidized LDL has been described as one of the few examples of a particle to provide both signals (54), but this was considered controversial due to the ever-present possibility of very low-level endotoxin contamination in reagents (55, 56). Indeed, we recently showed that CPP can bind and effectively concentrate endotoxin from uraemic serum (12) and thus at least in CKD, CPP may combine phosphate, calcium and endotoxin to effectively execute what is well-known as phosphate/inflammation associated endothelial damage ultimately resulting in dramatically increased CVD in CKD patients.

Dietary phosphate reduction and gut phosphate binding is best practice clinical routine in the treatment of CKD patients. Despite these measures CKD patients still have dramatically increased risk of inflammation and vascular calcification. Blood tests performed in several independent laboratories including our laboratories show that cardiovascular risk and calcification propensity are associated with CPP formation (4, 12, 25, 27, 57–61). Clinical CPP monitoring

is not routinely done, because blood testing for calcification propensity is currently not universally available. Monitoring and reducing CPP levels and regulating their cellular uptake in the dialysis-free interval may however, further improve outcome in dialysis patients in addition to phosphate control.

AUTHOR CONTRIBUTIONS

SK, ABü and ES performed experiments, analyzed data, drafted and revised the manuscript. ABa, EL, and JH designed the study, and revised the manuscript. AG performed experiments, analysed data, and revised the manuscript. EB performed experiments. WJ-D designed the study, analyzed data, drafted, and revised the manuscript.

ACKNOWLEDGMENTS

This work was supported by grants awarded to W-JD by the IZKF Aachen of the Medical Faculty or RWTH Aachen, the German Research Foundation (DFG SFB/TRR219-Project C-03), and grants awarded to JH by the German Ministry of Education and Research (BMBF LiSyM 031L0045; 031L0052).

SUPPLEMENTARY MATERIAL

The Supplementary Material for this article can be found online at: https://www.frontiersin.org/articles/10.3389/fimmu.2018.01991/full#supplementary-material

Supplementary Table 1 | Chemical and pharmacological inhibitors used to study CPP endocytosis.

Supplementary Movie 1 | Functional imaging of primary CPP clearance using 2-photon intravital microscopy.

Supplementary Movie 2 | Functional imaging of secondary CPP clearance using 2-photon intravital microscopy.

Supplementary Figure 1 | Calcification media induce differential cellular calcium overload and inflammasome activation. Immortalized macrophages expressing the inflammasome adaptor protein labeled *apoptosis-associated speck like protein containing a caspase recruitment domain* ASC fused to *green fluorescent protein,* were exposed to buffer control, LPS, nigericin, or to calcification media with elevated calcium or phosphate, individually and in combination, as well as with primary or secondary CPP. Notably, all calcification media contained an identical total calcium dose of 5 μg, yet differed in the stability of the calcium containing mineral component. Scale bar 25 μm.

Supplementary Figure 2 | Calcification media induce differential cellular calcium overload and inflammasome activation. Immortalized macrophages expressing the inflammasome adaptor protein labeled *apoptosis-associated speck like protein containing a caspase recruitment domain* ASC fused to *green fluorescent protein,* were exposed to buffer control, LPS, nigericin, or to calcification media with elevated calcium or phosphate, individually and in combination, as well as with primary or secondary CPP. Notably, all calcification media contained an identical total calcium dose of 50 μg, yet differed in the stability of the calcium containing mineral component. Scale bar 25 μm.

Supplementary Figure 3 | Differential clearance of primary and secondary CPP. Mice were injected with fluorescence labeled fetuin-A monomer (red), primary CPP (red), secondary CPP (green), or a mixture of primary (red), and secondary CPP (green) and liver, spleen, pancreas, kidney, lung, heart, and brown adipose fat tissue (BAT) were harvested 10 min after injection, sectioned, and analyzed for the presence of CPP by fluorescence microscopy. Liver and spleen stained positive for primary and secondary CPP, while all other organs stained negative. All organs stained negative for fetuin-A monomer. Considering the relative tissue mass of liver vs. spleen, therefore the liver can be considered the major clearance organ for CPP.

Supplementary Figure 4 | Differential endocytosis of fetuin-A monomer, primary and secondary CPP by bone marrow-derived macrophages. To discriminate fetuin-A and CPP binding from endocytosis we incubated bone marrow-derived macrophages with fetuin-A monomer, primary and secondary CPP at 4°C to assess binding, or at 37°C to assess endocytosis. Following 1 h of incubation we analyzed cell-associated fluorescence by flow cytometry. Incubation at 4°C yielded much lower cell-associated fluorescence than incubation at 37°C, especially for primary and secondary CPP. These results indicate that the cells readily endocytosed secondary CPP, and less well also primary CPP. A small amount of fetuin-A monomer was also endocytosed.

REFERENCES

1. Block G, Klassen P, Lazarus J, Ofsthun N, Lowrie E, Chertow GM. Mineral metabolism, mortality, and morbidity in maintenance hemodialysis. *J Amer Soc Nephrol.* (2004) 15:2208–18. doi: 10.1097/01.ASN.0000133041.27682.A2
2. Massy ZA, Mazière C, Kamel S, Brazier M, Choukroun G, Tribouilloy C, et al. Impact of inflammation and oxidative stress on vascular calcifications in chronic kidney disease. *Pediatr Nephrol.* (2005) 20:380–2. doi: 10.1007/s00467-004-1623-9
3. Dai L, Golembiewska E, Lindholm B, Stenvinkel P. End-stage renal disease, inflammation and cardiovascular outcomes. *Contrib Nephrol.* (2017) 191:32–43. doi: 10.1159/000479254
4. Miura Y, Iwazu Y, Shiizaki K, Akimoto T, Kotani K, Kurabayashi M, et al. Identification and quantification of plasma calciprotein particles with distinct physical properties in patients with chronic kidney disease. *Sci Rep.* 8:1256. doi: 10.1038/s41598-018-19677-4
5. Jahnen-Dechent W, Schäfer C, Ketteler M, McKee MD. Mineral chaperones: a role for fetuin-A and osteopontin in the inhibition and regression of pathologic calcification. *J Mol Med.* (2008) 86:379–89. doi: 10.1007/s00109-007-0294-y
6. Jahnen-Dechent W. Lot's wife's problem revisited: how we prevent pathological calcification. In: Bauerlein E, editor. *Biomineralization,* 2nd Edn. Weinheim: Wiley (2004), 245–267.
7. Schinke T, Amendt C, Trindl A, Pöschke O, Müller-Esterl W, Jahnen-Dechent W. The serum protein alpha2-HS glycoprotein/fetuin inhibits apatite formation *in vitro* and in mineralizing calvaria cells. A possible role in mineralization and calcium homeostasis. *J Biol Chem.* (1996) 271:20789–96. doi: 10.1074/jbc.271.34.20789
8. Schäfer C, Heiss A, Schwarz A, Westenfeld R, Ketteler M, Floege J, et al. The serum protein alpha 2-Heremans-Schmid glycoprotein/fetuin-A is a systemically acting inhibitor of ectopic calcification. *J Clin Invest.* (2003) 112:357–66. doi: 10.1172/JCI17202
9. Heiss A, Duchesne A, Denecke B, Grötzinger J, Yamamoto K, Renné T, et al. Structural basis of calcification inhibition by alpha 2-HS glycoprotein/fetuin-A. Formation of colloidal calciprotein particles. *J Biol Chem.* (2003) 278:13333–41. doi: 10.1074/jbc.M210868200
10. Heiss A, Eckert T, Aretz A, Richtering W, Van Dorp W, Schäfer C, et al. Hierarchical role of fetuin-A and acidic serum proteins in the formation and stabilization of calcium phosphate particles. *J Biol Chem.* (2008) 283:14815–25. doi: 10.1074/jbc.M709938200
11. Wald J, Wiese S, Eckert T, Jahnen-Dechent W, Richtering W, Heiss A. Formation and stability kinetics of calcium phosphate-fetuin-A colloidal particles probed by time-resolved dynamic light scattering. *Soft Matter* (2011) 7:2869–74. doi: 10.1039/c0sm01191f
12. Smith ER, Hewitson TD, Hanssen E, Holt SG. Biochemical transformation of calciprotein particles in uraemia. *Bone* (2018) 110:355–67. doi: 10.1016/j.bone.2018.02.023

13. Wu C-Y, Young L, Young D, Martel J, Young JD. Bions: a family of biomimetic mineralo-organic complexes derived from biological fluids. *PLoS ONE* (2013) 8:e75501. doi: 10.1371/journal.pone.0075501
14. Herrmann M, Schäfer C, Heiss A, Gräber S, Kinkeldey A, Büscher A, et al. Clearance of fetuin-A–containing calciprotein particles is mediated by scavenger receptor-A. *Circ Res.* (2012) 111:575–84. doi: 10.1161/CIRCRESAHA.111.261479
15. Meng ZH, Hudson AP, Schumacher HR, Baker JF, Baker DG. Monosodium urate, hydroxyapatite, and calcium pyrophosphate crystals induce tumor necrosis factor-alpha expression in a mononuclear cell line. *J Rheumatol.* (1997) 24:2385–8.
16. Maurer KH, Schumacher HR. Hydroxyapatite phagocytosis by human polymorphonuclear leucocytes. *Ann Rheum Dis.* (1979) 38:84–8. doi: 10.1136/ard.38.1.84
17. Nadra I, Mason JC, Philippidis P, Florey O, Smythe CDW, McCarthy GM, et al. Proinflammatory activation of macrophages by basic calcium phosphate crystals via protein kinase C and MAP kinase pathways: a vicious cycle of inflammation and arterial calcification? *Circ Res.* (2005) 96:1248–56. doi: 10.1161/01.RES.0000171451.88616.c2
18. Jin C, Frayssinet P, Pelker R, Cwirka D, Hu B, Vignery A, et al. NLRP3 inflammasome plays a critical role in the pathogenesis of hydroxyapatite-associated arthropathy. *Proc Natl Acad Sci USA*. (2011) 108:14867–72. doi: 10.1073/pnas.1111101108
19. Pazár B, Ea H-K, Narayan S, Kolly L, Bagnoud N, Chobaz V, et al. Basic calcium phosphate crystals induce monocyte/macrophage IL-1β secretion through the NLRP3 inflammasome *in vitro*. *J Immunol.* (2011) 186:2495–502. doi: 10.4049/jimmunol.1001284
20. Laquerriere P, Grandjean-Laquerriere A, Jallot E, Balossier G, Frayssinet P, Guenounou M. Importance of hydroxyapatite particles characteristics on cytokines production by human monocytes *in vitro*. *Biomaterials* (2003) 24:2739–47. doi: 10.1016/S0142-9612(03)00089-9
21. Terkeltaub R, Santoro DA, Mandel G, Mandel N. Serum and plasma inhibit neutrophil stimulation by hydroxyapatite crystals. Evidence that serum alpha 2-HS glycoprotein is a potent and specific crystal-bound inhibitor. *Arthrit Rheum.* (1988) 31:1081–9. doi: 10.1002/art.1780310901
22. Smith ER, Hanssen E, McMahon LP, Holt SG. Fetuin-A-containing calciprotein particles reduce mineral stress in the macrophage. *PLoS ONE* (2013) 8:e60904. doi: 10.1371/journal.pone.0060904
23. Peng H-H, Wu C-Y, Young D, Martel J, Young A, Ojcius DM, et al. Physicochemical and biological properties of biomimetic mineralo-protein nanoparticles formed spontaneously in biological fluids. *Small* (2013) 9:2297–307. doi: 10.1002/smll.201202270
24. Olde Loohuis KM, Jahnen-Dechent W, Van Dorp W. The case: milky ascites is not always chylous. *Kidney Int.* (2010) 77:77–8. doi: 10.1038/ki.2009.407
25. Smith ER, Hewitson TD, Cai MMX, Aghagolzadeh P, Bachtler M, Pasch A, et al. A novel fluorescent probe-based flow cytometric assay for mineral-containing nanoparticles in serum. *Sci Rep.* (2017) 7:5686. doi: 10.1038/s41598-017-05474-y
26. Aghagolzadeh P, Bachtler M, Bijarnia R, Jackson C, Smith ER, Odermatt A, et al. Calcification of vascular smooth muscle cells is induced by secondary calciprotein particles and enhanced by tumor necrosis factor-α. *Atherosclerosis* (2016) 251:404–14. doi: 10.1016/j.atherosclerosis.2016.05.044
27. Pasch A, Farese S, Gräber S, Wald J, Richtering W, Floege J, et al. Nanoparticle-based test measures overall propensity for calcification in serum. *J Amer Soc Nephrol.* (2012) 23:1744–52. doi: 10.1681/ASN.2012030240
28. Reif R, Ghallab A, Beattie L, Günther G, Kuepfer L, Kaye PM, et al. *In vivo* imaging of systemic transport and elimination of xenobiotics and endogenous molecules in mice. *Arch Toxicol.* (2017) 91:1335–52. doi: 10.1007/s00204-016-1906-5
29. Hornung V, Bauernfeind F, Halle A, Samstad EO, Kono H, Rock KL, et al. Silica crystals and aluminum salts activate the NALP3 inflammasome through phagosomal destabilization. *Nat Immunol.* (2008) 9:847–56. doi: 10.1038/ni.1631
30. Martinon F, Chen X, Lee A-H, Glimcher LH. TLR activation of the transcription factor XBP1 regulates innate immune responses in macrophages. *Nat Immunol.* (2010) 11:411–8. doi: 10.1038/ni.1857
31. Stutz A, Horvath GL, Monks BG, Latz E. ASC speck formation as a readout for inflammasome activation. In: De Nardo CM, Latz E editors. *The Inflammasome: Methods and Protocols.* Totowa, NJ: Humana Press (2013). p. 91–101.
32. Medzhitov R, Shevach EM, Trinchieri G, Mellor AL, Munn DH, Gordon S, et al. Highlights of 10 years of immunology. *Nat Rev Immunol.* (2011) 11:693–702. doi: 10.1038/nri3063
33. Chen W, Anokhina V, Dieudonne G, Abramowitz MK, Kashyap R, Yan C, et al. Patients with advanced chronic kidney disease and vascular calcification have a large hydrodynamic radius of secondary calciprotein particles. *Nephrol Dial Transplant.* (2018) 99:2434–9. doi: 10.1093/ndt/gfy117
34. Heiss A, Pipich V, Jahnen-Dechent W, Schwahn D. Fetuin-A is a mineral carrier protein: small angle neutron scattering provides new insight on Fetuin-A controlled calcification inhibition. *Biophys J.* (2010) 99:3986–95. doi: 10.1016/j.bpj.2010.10.030
35. Block G, Raggi P, Bellasi A, Kooienga L, Spiegel D. Mortality effect of coronary calcification and phosphate binder choice in incident hemodialysis patients. *Kidney Int.* (2007) 71:438–41. doi: 10.1038/sj.ki.5002059
36. Block GA, Wheeler DC, Persky MS, Kestenbaum B, Ketteler M, Spiegel DM, et al. Effects of phosphate binders in moderate CKD. *J Amer Soc Nephrol.* (2012) 23:1407–15. doi: 10.1681/ASN.2012030223
37. Kuro-o M. Klotho, phosphate and FGF-23 in ageing and disturbed mineral metabolism. *Nature Rev Nephrol.* (2013) 9:650–60. doi: 10.1038/nrneph.2013.111
38. Kuro-o M. Calciprotein particle (CPP): a true culprit of phosphorus woes? *Nefrologia* (2014) 34:1–4. doi: 10.3265/Nefrologia.pre2013
39. Brylka L, Jahnen-Dechent W. The role of Fetuin-A in physiological and pathological mineralization. *Calcified Tiss Int.* (2013) 93:355–64. doi: 10.1007/s00223-012-9690-6
40. Di Marco GS, Hausberg M, Hillebrand U, Rustemeyer P, Wittkowski W, Lang D, et al. Increased inorganic phosphate induces human endothelial cell apoptosis *in vitro*. *Am J Physiol Renal Physiol.* (2008) 294:F1381–7. doi: 10.1152/ajprenal.00003.2008
41. Di Marco GS, Konig M, Stock C, Wiesinger A, Hillebrand U, Reiermann S, et al. High phosphate directly affects endothelial function by downregulating annexin II. *Kidney Int.* (2013) 83:213–22. doi: 10.1038/ki.2012.300
42. Stevens KK, Denby L, Patel RK, Mark PB, Kettlewell S, Smith GL, et al. Deleterious effects of phosphate on vascular and endothelial function via disruption to the nitric oxide pathway. *Nephrol Dial Transplant.* (2017) 32:1617–27. doi: 10.1093/ndt/gfw25
43. Van TV, Watari E, Taketani Y, Kitamura T, Shiota A, Tanaka T, et al. Dietary phosphate restriction ameliorates endothelial dysfunction in adenine-induced kidney disease rats. *J Clin Biochem Nutr.* (2012) 51:27–32. doi: 10.3164/jcbn.11-96
44. Yilmaz MI, Sonmez A, Saglam M, Yaman H, Kilic S, Eyileten T, et al. Comparison of calcium acetate and sevelamer on vascular function and fibroblast growth factor 23 in CKD patients: a randomized clinical trial. *Am J Kidney Dis.* (2012) 59:177–85. doi: 10.1053/j.ajkd.2011.11.007
45. Nakayama M. Macrophage recognition of crystals and nanoparticles. *Front Immunol.* (2018) 9:103. doi: 10.3389/fimmu.2018.00103
46. Katsnelson MA, Rucker LG, Russo HM, Dubyak GR. K+ efflux agonists induce NLRP3 inflammasome activation independently of Ca2+ signaling. *J Immunol.* (2015) 194:3937–52. doi: 10.4049/jimmunol.1402658
47. Pele L, Haas CT, Hewitt R, Faria N, Brown A, Powell J. Artefactual nanoparticle activation of the inflammasome platform: *in vitro* evidence with a nano-formed calcium phosphate. *Nanomedicine* (2015) 10:1379–90. doi: 10.2217/nnm.14.58
48. Pal D, Dasgupta S, Kundu R, Maitra S, Das G, Mukhopadhyay S, et al. Fetuin-A acts as an endogenous ligand of TLR4 to promote lipid-induced insulin resistance. *Nat Med.* (2012) 18:1279–85. doi: 10.1038/nm.2851
49. Liu A, Chen M, Kumar R, Stefanovic-Racic M, O'Doherty RM, Ding Y, et al. Bone marrow lympho-myeloid malfunction in obesity requires precursor cell-autonomous TLR4. *Nat Commun* (2018) 9:708. doi: 10.1038/s41467-018-03145-8
50. Reynolds JL, Skepper JN, McNair R, Kasama T, Gupta K, Weissberg PL, et al. Multifunctional roles for serum protein fetuin-a in inhibition of human vascular smooth muscle cell calcification. *J Amer Soc Nephrol.* (2005) 16:2920–30. doi: 10.1681/ASN.2004100895
51. Nie Z. Fetuin: its enigmatic property of growth promotion. *Amer J Physiol.* (1992) 263:C551–62. doi: 10.1152/ajpcell.1992.263.3.C551

52. Martinon F, Pétrilli V, Mayor A, Tardivel A, Tschopp J. Gout-associated uric acid crystals activate the NALP3 inflammasome. *Nature* (2006) 440:237–41. doi: 10.1038/nature04516
53. Duewell P, Kono H, Rayner KJ, Sirois CM, Vladimer G, Bauernfeind FG, et al. NLRP3 inflammasomes are required for atherogenesis and activated by cholesterol crystals. *Nature* (2010) 464:1357–61. doi: 10.1038/nature 08938
54. Stewart CR, Stuart LM, Wilkinson K, Van Gils JM, Deng J, Halle A, et al. CD36 ligands promote sterile inflammation through assembly of a Toll-like receptor 4 and 6 heterodimer. *Nature Immunol.* (2009) 11:155–61. doi: 10.1038/ni.1836
55. Erridge C, Webb DJ, Spickett CM. Toll-like receptor 4 signalling is neither sufficient nor required for oxidised phospholipid mediated induction of interleukin-8 expression. *Atherosclerosis* (2007) 193:77–85. doi: 10.1016/j.atherosclerosis.2006.08.032
56. Erridge C. Endogenous ligands of TLR2 and TLR4: agonists or assistants? *J Leukoc Biol.* (2010) 87:989–99. doi: 10.1189/jlb.1209775
57. Smith ER, Cai MM, McMahon LP, Pedagogos E, Toussaint ND, Brumby C, et al. Serum fetuin-A concentration and fetuin-A-containing calciprotein particles in patients with chronic inflammatory disease and renal failure. *Nephrology* (2013) 18:215–21. doi: 10.1111/nep.12021
58. Smith ER, Ford ML, Tomlinson LA, Bodenham E, McMahon LP, Farese S, et al. Serum calcification propensity predicts all-cause mortality in predialysis CKD. *J Amer Soc Nephrol.* (2014) 25:339–48. doi: 10.1681/ASN.2013060635
59. Keyzer CA, De Borst MH, Van Den Berg E, Jahnen-Dechent W, Arampatzis S, Farese S, et al. Calcification propensity and survival among renal transplant recipients. *J Amer Soc Nephrol.* (2016) 27:239–48. doi: 10.1681/ASN.2014070670
60. Lorenz G, Steubl D, Kemmner S, Pasch A, Koch-Sembdner W, Pham D, et al. Worsening calcification propensity precedes all-cause and cardiovascular mortality in haemodialyzed patients. *Sci Rep.* (2017) 7:13368. doi: 10.1038/s41598-017-12859-6
61. Pasch A, Block GA, Bachtler M, Smith ER, Jahnen-Dechent W, Arampatzis S, et al. Blood calcification propensity, cardiovascular events, and survival in patients receiving hemodialysis in the EVOLVE trial. *Clin J Amer Soc Nephrol.* (2017) 12:315–22. doi: 10.2215/CJN.04720416

Conflict of Interest Statement: The authors declare that the research was conducted in the absence of any commercial or financial relationships that could be construed as a potential conflict of interest.

frontiers in Immunology

ORIGINAL RESEARCH
published: 29 May 2018
doi: 10.3389/fimmu.2018.01163

Cholesterol Crystal-Mediated Inflammation Is Driven by Plasma Membrane Destabilization

*Fei Shu[1,2], Jiahuan Chen[2], Xiaojie Ma[3], Yunzhou Fan[3], Li Yu[2], Wencheng Zheng[2], Matthias W. Amrein[4,5], Tie Xia[2] and Yan Shi[2,6]**

[1] Peking University-Tsinghua University-National Institute of Biological Sciences Joint Graduate Program, School of Life Sciences, Peking University, Beijing, China, [2] Department of Basic Medical Sciences, Center for Life Sciences, Institute for Immunology, Beijing Key Lab for Immunological Research on Chronic Diseases, Tsinghua University, Beijing, China, [3] Department of Chemical Biology, School of Pharmaceutical Sciences, Peking University, Beijing, China, [4] Department of Cell Biology, Snyder Institute, University of Calgary, Calgary, AB, Canada, [5] Department of Anatomy, Snyder Institute, University of Calgary, Calgary, AB, Canada, [6] Department of Microbiology, Immunology and Infectious Diseases, Snyder Institute, University of Calgary, Calgary, AB, Canada

Atherosclerosis is driven by an inflammatory milieu in the walls of artery vessels. Initiated early in life, it progresses to plaque formation and form cell accumulation. A culprit in this cascade is the deposition of cholesterol crystals (CC). The involvement of smaller crystals in the early stage of atherosclerotic changes may be critical to the long-term pathological development. How these small crystals initiate the pro-inflammatory events is under study. We report here an unexpected mechanism that microscopic CC interact with cellular membrane in a phagocytosis-independent manner. The binding of these crystals extracts cholesterol from the cell surface. This process causes a sudden catastrophic rupture of plasma membrane and necrosis of the bound cells independent of any known cell death-inducing pathways, releasing inflammatory agents associated with the necrotic cell death. Our results, therefore, reveal a biophysical aspect of CC in potentially mediating the inflammatory progress in atherosclerosis.

Keywords: cholesterol crystals, cell death, inflammation, membrane rupture, signal free

OPEN ACCESS

Edited by:
Liwu Li,
Virginia Tech, United States

Reviewed by:
Hongkuan Fan,
Medical University of South Carolina, United States
Vijay Rathinam,
University of Connecticut Health Center, United States

****Correspondence:***
Yan Shi
yanshi@biomed.tsinghua.edu.cn

Specialty section:
This article was submitted to Molecular Innate Immunity, a section of the journal Frontiers in Immunology

Received: *05 February 2018*
Accepted: *09 May 2018*
Published: *29 May 2018*

Citation:
Shu F, Chen J, Ma X, Fan Y, Yu L, Zheng W, Amrein MW, Xia T and Shi Y (2018) Cholesterol Crystal-Mediated Inflammation Is Driven by Plasma Membrane Destabilization. Front. Immunol. 9:1163. doi: 10.3389/fimmu.2018.01163

INTRODUCTION

The accumulation of cholesterol crystals (CC) in atherosclerotic lesions reflects the imbalance of cholesterol homeostasis. LDL transports esterified cholesterol from the liver to artery walls *via* LDL receptor. The esterified cholesterol is then deposited in the subintima and becomes readily accessible to macrophages and muscle cells. Ester hydrolases in these cells convert the esterified cholesterol into its free form, leading to the crystal formation (1). This is countered by the reverse transport mediated by HDL (2). At late stages of development, large amounts of clinical data suggest that the volume expansion associated with cholesterol solidification creates a rupture force exerted on the fibrous cap of the plaques (3, 4). Thromboembolism may thus result.

The accumulation of CC starts early in young animals. Due to their minuscule sizes and limitations of standard microscopy techniques, direct visualization has not been easy. With refinements of preparation protocols (5, 6) and development of label-free Raman scattering imaging technology (7), the presence of the small crystals became detectable. Those improved detections strongly suggest their involvement in much of the initial atherosclerotic development. In fact, cholesterol-lowering treatment used early is protective but is ineffective in the later stages (8). Mechanistically, the presence of CC in the early pathogenesis is considered to be a significant contributor to local inflammation (9).

It has been suggested that NLRP3 inflammasome was critically involved in the plaque formation (5, 10). However, other reports failed to recapture this association (11, 12). On the other hand, several groups have found that IL-1α (12) and the complement system (13) are activated by CC. Therefore, how CC-mediated inflammation contributes to the early vascular damage is still not well understood. One suspected but ill-defined aspect of CC-mediated cytotoxicity is their ability to damage the plasma membrane (14).

In studying phagocytosis of particulate structures, we made a surprising finding that unlike phagocytosis of most solid structures, the adhesion force between macrophages and CC does not rely on Syk kinase, a common signaling intermediate in phagocytosis. The attachment strength between CC and plasma membrane is a function of the cholesterol in the latter. Furthermore, the binding of CC causes the transfer of membrane cholesterol to the crystal, leading to necrosis in macrophages. This physical damage-induced cell death is pro-inflammatory yet independent of common cell death induction pathways, including NLRP3 inflammasome, mixed lineage kinase domain-like kinase (MLKL) (15), gasdermin D (GSDMD) (16), Caspase 1/8, Ca^{2+} signaling (17), and calpain-mediated cellular damage (18). In fact, this membrane destabilization can be recaptured by giant plasma-membrane vesicle (GPMV) upon CC contact, further confirming its biophysical nature independent of intracellular signaling cascades. Our results, therefore, suggest a potential biophysical interaction between the CC and the plasma membrane, leading to an inflammatory milieu via sudden collapse of the latter as a consequence of cholesterol extraction.

MATERIALS AND METHODS

Mice

Mice, all C57BL/6, were housed at Laboratory Animal Research Center of Tsinghua University. The wild type and *Il1r1*$^{-/-}$, *Apoe*$^{-/-}$, *Casp1*$^{-/-}$, *Nfkb1*$^{-/-}$mice were from Jackson Laboratory. *Casp11*$^{-/-}$, *Casp11*^{tg} were gifts from Dr. V. M. Dixit (Genetech, Inc.). *Nlrp3*$^{-/-}$ was a gift from Dr. Z. F. Jiang (Peking University). *Lyz2cre* was a gift from Dr. L. Wu (Tsinghua University). *Ripk3*$^{-/-}$*Casp8*$^{-/-}$ was a gift from Dr. X. Lin (Tsinghua University). *GFP* transgenic was a gift from Dr. H. Qi (Tsinghua University). *Syk*$^{fl/fl}$ was generated by a commercial vender (Biocytogen). The gene-deficient mice were genotyped with the following primers: for *Casp1* were GAGACATATAAGGGAGAAGGG and ATGGCACACCACA GATATCGG and TGCTAAAGCGCATGCTCCAGACTG; for *Casp11* were TGAAATGCATGTACTGAGAGCAAGG and CAATTGACTTGGGGATTCTGG and GTCAGAGATGAAAG ACTTTGCTGC; for *Nlrp3* were GCTATTCGGCTATGACT GGG and ACTTTCTCGGCAGGAGCAAG and TTGCCA CTGCTTATGTCCC and GCACACACACCTCCCTAACA; for *Nfκb* were GCAAACCTGGGAATACTTCATGTGACTAAG and ATAGGCAAGGTCAGAATGCACCAGAAGTCC and AAATG TGTCAGTTTCATAGCCTGAAGAACG; for *Il1r* were CTCGT GCTTTACGGTATCGC and GGTGCAACTTCATAGAGAGA TGA and TTCTGTGCATGCTGGAAAAC. All experiments performed were approved by the animal research committee of Tsinghua University.

Cells

BMDM was produced as previously described (19). iBMDM (immortalized) cell line was a gift from Dr. X. Lin (Tsinghua University). $CD4^+$ T cell was isolated with mouse $CD4^+$ T cell isolation kit from Stemcell (19852A). 3T3 cell line was a gift from Dr. H. Qi (Tsinghua University). Mouse endothelial cells were isolated as described elsewhere (20). MDCK, RAW264.7, THP-1 cell line were from ATCC. BMDC and I.P. Mac was produced following the protocols in Current protocols in Immunology (2011). DC1940 cell line was a gift from Dr. L. Wu (Tsinghua University).

Reagents

All reagents were purchased from Sigma-Aldrich unless otherwise indicated. Annexin V-FITC/PI Apoptosis Detection Kit was purchased from 4A Biotech (FXP018). LDH Cytotoxicity Assay Kit and propidium iodide were purchased from Beyotime (C0016, C1002 and ST512). DNA transfection reagent was purchased from Neofect (TF20121201). LPS transfer reagent was purchased from Promega (Fugene E231A). APC-Ly-6G ab was purchased from Sungene Biotech (M100L7-11A). FITC-Ly-6B.2 ab was purchased from GeneTex (GTX43417). Pronase was from Roche (18572720). CSFE and mouse TNFα were purchased from BioLegend (79898, 575202). Cycloheximide was purchased from Santa Cruz (sc-3508B). TRIzol reagent was purchased from Thermo (Ambion 15596018). Reverse transcribe kit and DNase I were purchased from TaKaRa (RR047A, 2212). RT-PCR super mix was purchased from Transgen biotech (AQ401). z-VAD-FMK, z-IETD-FMK, and z-LEHD-FMK were purchased from R&D system (FMK001, FMK007, and FMK008). Calpeptin was purchased from Enzo Life Sciences (BML-PI101). Cholesteryl BODIPY was purchased from Avanti Polar Lipid (810255P). Mouse IL-1β ELISA kit was purchased from eBioscience (88-7013). Membrane filter 0.22 μm SSWP was purchased from Millipore (SSWP02500). [1,2-^{3}H(N)]-cholesterol was purchased from PerkinElmer (NET139250UC). Sulfo-NHS-LC-Biotin was purchased from APExBIO (A8003). Streptavidin was purchased from NEB (N7021S). MLKL and GSDMD shRNA were purchased from Sigma-Aldrich TRC shRNA libraries and TRC IDs are TRCN0000360818 (MLKL), TRCN0000219620 (GSDMD1), TRCN0000198776 (GSDMD2). SHC002 (non-target shRNA) was used as negative control.

Crystals

MSU was made as previously described (21). Cholesterol crystal was made by cholesterol re-precipitation followed by ultra-sonication. Briefly, cholesterol powder was dissolved in warm acetone and then cooled down to precipitate cholesterol. The precipitated solids were washed with ddH_2O three times, then dried off. PBS was added into the cholesterol crystal to reach a concentration for 25 mg/ml. The suspension was then treated with needle ultra-sonication to break large crystals into smaller ones (power: 30%, time: 60 min) to reach an average size around 1 μm. The sonication time was reduced to harvest larger crystal (10–20 μm: 5 min, 5–10 μm: 10 min, 2–5 μm: 30 min).

Neutrophil Infiltration Assay

Supernatants from crystal-treated BMDM were collected by centrifugation followed with filtration through a 0.22-μm pore

membrane. Crystals in saline or the supernatants were injected i.p. The peritoneal lavage fluid was collected 16 h after the injection. Briefly, mice were euthanized and its peritoneum was exposed. The peritoneum was lavaged with 10 ml ice-cold PBS containing 5 mM EDTA. Cells were stained with APC-Ly6G and FITC- Ly6B.2 following manufacturer's instructions. Total cells number was counted with a hemocytometer then the samples were read with C6 Flow Cytometer. FACS data were analyzed with FlowJo V10.

LDH Release Assay

Cell culture medium was replaced with Opti-MEM 2 h before stimulus treatment. Supernatants from the treated cells were collected and centrifuged (10,000 *g* 5 min) to remove solid particles. 20 µl each of lactate, INT, and diaphorase were combined to produce the reaction mixture. 120 µl of the supernatant from each sample was transferred to a new 96-well plate and mixed with 60 µl reaction mixture for 30 min at RT. Serum-free medium was used as the 0% control and lysate of the untreated cell was used as the 100% maximal release. Samples' absorbance was read at 490 nm. LDH release from treated cells was determined based on a standard curve.

Cell Death

Cells were collected after the indicated treatments and resuspended with Annexin V binding buffer which contains suggested concentration of Annexin V-FITC. 15 min later, supernatant was discarded by centrifugation. The cells were resuspended in the binding buffer with PI. Samples were read with C6 flow cytometer immediately. FACS data were analyzed with FlowJo V10.

For PI staining assay, cells were harvested and washed with PBS twice. CSFE were diluted in PBS and mix with cell suspension with a final concentration of 10 nM CFSE and 10^7 cells/ml and then incubated for 15 min at RT. An equal volume of culture medium was added into the cells and wait for 5 min. Cells were washed and resuspended with culture media and plated in 24-well plates. After the treatment, supernatants were removed and PI (500 nM in PBS) was added into the well followed by a 2-min incubation. Fluorescent images were captured at 488 and 561 nm with fluorescent microscope. CFSE and PI-positive cell numbers were analyzed with CellProfiler 2.1.1 and project module MOD. cpproj. The proportion of PI-positive cells in total CSFE-positive cells was regarded as the cell death ratio.

Atherosclerosis Model

Apoe$^{-/-}$ mice were crossed with *Casp1*$^{-/-}$, *Casp11*$^{-/-}$, *Nlrp3*$^{-/-}$, *Il1r1*$^{-/-}$, and *Nfkb1*$^{-/-}$. Mice were fed with high-fat diet (21% fat, 0.15% cholesterol, MD12015, Medicience, Ltd.) or the control diet starting 3 weeks of age for 12 weeks. Each group has almost equal male and female mice. Mice were then sacrificed and the aorta was isolated. Heart perfusion was performed to prevent clotting. The connective tissue and fat around the aorta were removed with tweezers under dissecting microscope carefully. 3% (w/v) of Oil Red O in 2-protanol was used as the stock staining solution (22). Oil Red O working solution was diluted from the stock with ddH_2O at 6:4 ratio. Stained samples were rinsed with 70% 2-propanal quickly then moved to Oil Red O working solution and stain for 30 min on a slow shaker. The samples were rinsed again in 70% 2-propanal for 10 s and returned to ddH_2O. The aortas were opened en face by tweezers and ophthalmic scissors with acupuncture needles fixing the aorta. The aortas were imaged with microscope and the area of red plaques was determined with microscope (Olympus) image program which based on the pixel size.

shRNA Knock Down Assay

Plasmids including shRNA and the package construct (Δ8.9 and VSVG) were purified from transformed *E. coli* with EndoFree Plasmid Midi Kit (CWBIO, CW2105S). 293FT cells were cultured in a 25 cm^2 flask with 60–80% confluency. Culture media were replaced 2 h before DNA transfer. 2 µg shRNA plasmid, 1 µg Δ8.9, and 1 µg VSVG were mixed in 50 µl of OptiMem medium. 4 µl DNA transfection reagent was added to the mixture OptiMem medium and incubated at RT for 20 min. The mixture was added into 293FT medium carefully. 6 h later, the media were replaced with DMEM containing 20% serum. Virus-containing supernatants were harvested 60 h after the DNA transfection and then centrifuged at 1,000 *g* for 10 min to discard the debris. iBMDM cells were cultured in 24-well plates with 20–30% of the area covered by cells. Polybrene (final concentration 8 µg/ml) was mixed with the virus-containing supernatant and the mixture was transferred into the cell culture. The plates were centrifuged at 500 *g* at 30°C for 90 min and then exchanged into regular culture medium. 48 h after the virus infection, 2 µg/ml puromycin was added to the medium. Puromycin-resistant cells were harvested several days later and their RNA was extracted with TRIzol Reagent following manufacturer's instructions. RNA concentration was determined by Nanodrop 2000 (Thermo). 1 µg RNA was reverse transcribed to cDNA immediately with a reverse transcription kit (Takara, RR047A). Gene expression was determined by real time PCR.

RT-PCR

All procedures were performed per manufacturer's instructions of the SYBR Green qPCR SuperMix (Transgen Biotch, AQ101). Primers for mouse MLKL were AATTGTACTCTGGGAAATTGCCA and TCTCCAAGATTCCGTCCACAG. Primers for mouse GSDMD were TACTGCCTTCTGAACAGGAA and GTCACCACAA ACAGGTCATC. β-actin expression was used as internal control and primer sequences were TTGCTGACAGGATGCAGAAG and ACATCTGCTGGAAGGTGGAC.

LPS Intracellular Delivery

For LPS delivery, cells were cultured on 24-well plate, and the media were replaced with 300 µl Opti-MEM. LPS (2 µg/ml final) and transfect reagent Fugene (0.25% v/v final) were mixed in 50 µl Opti-MEM and incubated at RT for 15 min before being slowly added into the cell culture.

Atomic Force Microscopy

All crystals were glued to cantilever (Arrow TL- 1, Nanoworld) with epoxy (21) at least 12 h before use. All attraction forces between cell and crystal were measured with JPK CellHesion (JPK) (23). Briefly, the measurement was carried in the relative

force feedback contact/tapping mode (IP gain: 50 Hz; IG gain: 0.001 Hz; correct baseline: 1; relative set point: 0.5 nN; *z* length: 50 μm; extend delay: 0 s; constant height). Data were analyzed with JPK Data Processing. Maximum binding forces were calculated and plotted. Each dot presents a single measurement.

Attraction forces between crystal and lipid monolayer were measured with JPK NanoWizard II (JPK). All set up was the same as the JPK CellHesion except *z* length was 10 μm. AFM scanning mode was used to confirm domain formation.

Cholesterol Transfer Assay

10 μg of BODIPY-cholesterol in DMSO (20 mg/ml) was mixed with 2 mg of MβCD in PBS (100 mg/ml). Bath sonication at 37°C was used to solubilize the cholesterol. BODIPY-cholesterol and MβCD mix solution was added to cells in serum-free culture medium (10% v/v) and incubated at 37°C for 20 min. Cells were washed with PBS three times and replaced with fresh culture medium. They were imaged with fluorescent microscope to confirm the labeling efficiency. The cells were returned to culture to allow cells to settle on the bottom. 200 μg/ml CC, MSU, or Silica crystals were added to the cells and incubated for different durations, and eventually lysed with 1% NP40. The lysates were centrifuged at 500 *g* for 5 min. The supernatants were discarded and the residual crystals were washed with 1% NP40 two more times. The washed crystals were resuspended with ddH_2O and the fluorescence associated with the crystals was analyzed with C6 flow cytometer or fluorescent microscope.

Cells were labbeled with NHS-LC-biotin (Thermo, 21327) first following manufacturer's instruction. Then Labeling cell surface with [1,2-^{3}H(N)]-cholesterol followed the same procedure described above except cholesterol-[^{3}H] was diluted in cholesterol and MβCD mixture (1:100 molar ratio in PBS). Cholesterol-[^{3}H] labeled cells were treated with crystals for 24 h and then lysed with 10% NP40 for 1 min. Cell lysates and crystals were centrifuged at 500 *g* for 5 min. The crystals were washed with 1% NP40 then resuspended with PBS. The crystals in the suspension were mixed with streptavidin conjugated agarose beads (Thermo, 20347) for 15 min to remove cell membrane debris. Collect the crystal with spin column (Thermo, 69725) then mix the crystals with ULTIMA GOLD (PerkinElmer, 6013327) and read with the liquid scintillation counter.

GPMV Membrane Integrity Assay

BMDM of *GFP*^{tg} mice was cultured as previously described (24). The cells were washed with ice-cold PBS (pH 8.0) three times and cell numbers were counted. They were resuspended at a concentration of 3×10^7 cells/ml in PBS (pH 8.0). 1 mg of Sulfo-NHS-LC-Biotin was added into the suspension for 1 ml of the preparation and then incubated at RT for 30 min. Biotin was quenched by washing the cell with PBS + 100 mM glycine three times. The cells were plated in the 6-well plate with 3×10^6 cells per well and the GPMV was produced following a published protocol (25): The GPMV-containing supernatant was collected and moved to a round glass slide which had been coated with Streptavidin for 2 h at 37°C. 2 h later, the supernatant was discarded and GPMV attached to the glass slide was washed with GPMV buffer twice. GPMV attachment was confirmed by microscope. A cantilever which had been glued with a crystal on the top was first moved to settle on the GPMV using the relative force feedback contact/tapping mode (IP gain: 50 Hz; IG gain: 0.001 Hz; correct baseline: 1; relative set point: 1 nN; *z* length: 5 μm; extended delay: 10,000 s; retract delay: 0 s; constant height). The fluorescence of GFP inside GPMV was imaged every 20 or 30 s for 2 h. The image data were analyzed in ImageJ. Briefly, mean fluorescence intensity of GPMV was measured and the value of Intensity $_{GPMV}$/Intensity $_{Background}$ was calculated. This I_G/I_B was normalized to its initial value to eliminate fluorescent intensity difference between individual GPMV. In order to digitalize the fluorescence change of GPMV, we subtracted I_G/I_B value of any given point by the same I_G/I_B of the same vesicle after 5 min. The maximal differential from each GPMV was used to plot Max MFI reduction (K_{5min} = normalized $I_G/I_{B\ 5min\ before}$ − normalized $I_G/I_{B\ after}$).

Lipid Bilayer Preparation

Lipid bilayers were prepared according to a published protocol (26). Briefly, DOPC, sphingomyelin, and cholesterol were mixed and dissolved in chloroform solution with 1 mg total lipid/50 μl at the indicated ratios. Chloroform was dried off in vacuum for 2 h. The remaining lipids were resuspended with 100 μl PBS. 10 μl of the lipid suspension was added to 150 μl of supported lipid bilayer buffer (SLB, 150 mM NaCl, 10 mM HEPES, pH 7.4) and sonicated in a bath sonicator to yield small unilamellar vesicles. A clean mica surface was obtained by peeling off the outer layer with adhesive tape. The lipid mixture was placed on the mica and $CaCl_2$ (final concentration 3 mM) was added to the mixture. The preparation was incubated at 37°C for 2 min then at 65°C for 15 min. The bilayer was washed with 65°C SLB 15 times then cooled slowly.

Statistics

All plot graphs show means with SEM. Statistical analysis for each independent experiment was performed with an unpaired, Student's *t*-test. A *p* value of less than 0.05 was considered significant. *<0.05; **<0.01; ***<0.001; N.S., not significant. All experiments were repeated at least three times independently except **Figures 2E,F** where pooled data from several experiments were used.

RESULTS

We first studied the activation parameters of macrophages stimulated by CC. **Figure 1A** shows i.p. injection of CC induced the infiltration of neutrophils after 16 h, similar to silica crystals (24). To understand the factors promoting such an *in vivo* response, macrophages were treated with CC and the culture supernatants were similarly injected i.p. **Figure 1B** shows that the supernatants from both silica and CC-treated cells also induced this inflammatory response. As cytokine production and necrosis can both release pro-inflammatory agents (27), IL-1β, IL-1α, IL-6, and TNFα production and cell death were analyzed. IL-1β was readily detected in the supernatant of BMDM/CC coculture, suggesting that NLRP3 inflammasome was activated as reported previously (**Figure 1C**) (5). CC also induced other pro-inflammatory agents (Figure S1A in Supplementary Material) indicating a broad

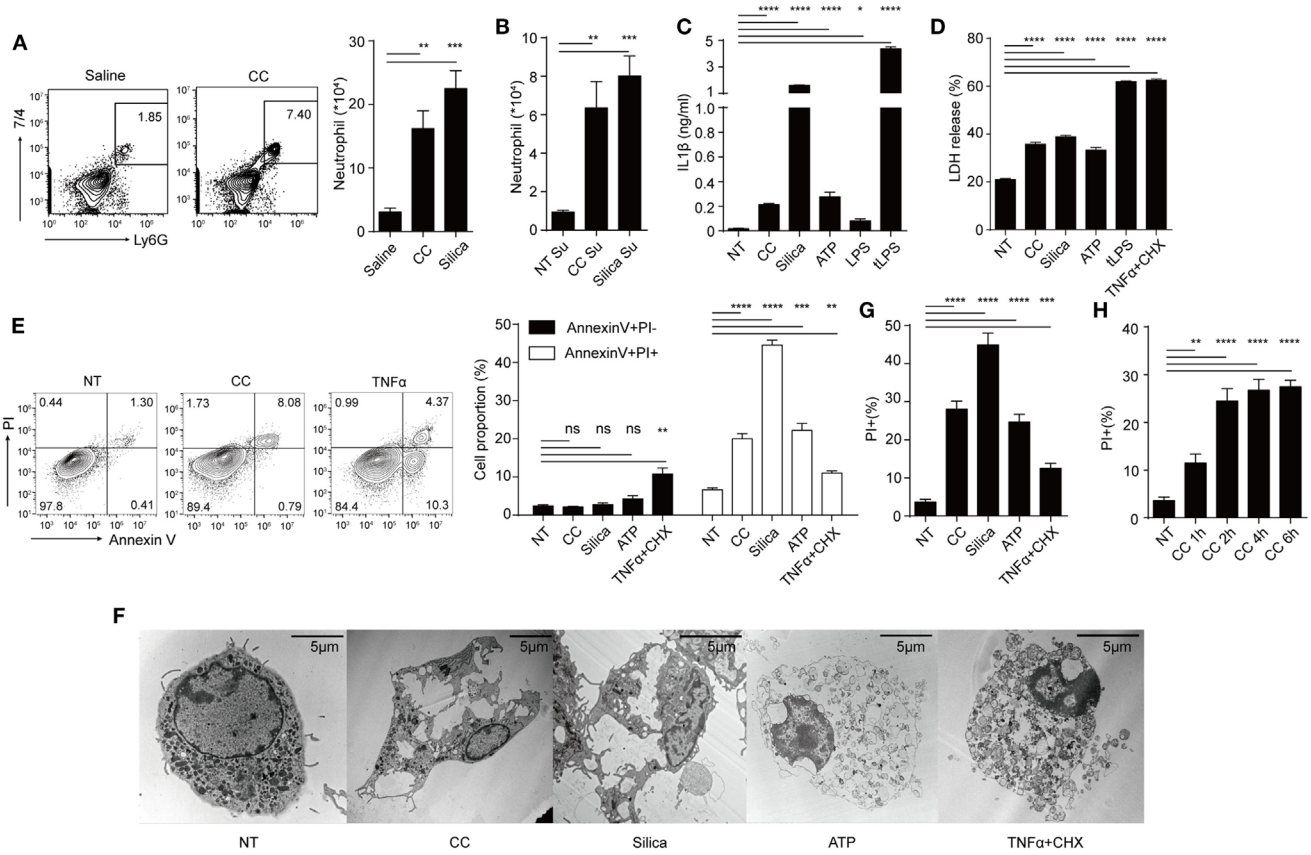

FIGURE 1 | Cholesterol crystals (CC) induce both NLRP3 inflammasome activation and a rapid necrotic cell death in the phagocytic cells. **(A)** C57BL/6 mice were i.p. injected with 500 μg of Silica or CC in 1 ml saline and rested for 16 h. Intraperitoneal cells were harvested and stained with Ly6G-APC and 7/4-FITC. The right panel is the bar graph of FACS plots on the left. $n = 4$ (n indicates the number of repeats of each group), $N = 3$ (N indicates the number of biological repeats of the experiment). Two-tailed Student's t analysis results for all figures are indicated as follows: $p < 0.001$: ***; $p < 0.01$: **; $p < 0.05$: *; p at 0.05 or larger was considered non-significant: ns. **(B)** Supernatants of treated BMDM (CC: 1 mg/ml, Silica:500 μg/ml for 8 h) in 12-well plates (about 4×10^5 cells) were collected and injected i.p. 16 h later intraperitoneal cells were harvested and stained as in **(A)**. $n = 4$. $N = 3$. **(C)** BMDM were primed with Pam3csk4 (100 ng/ml) for 12 h and then treated with indicated stimulus for 12 h (CC:500 μg/ml, Silica: 100 μg/ml, ATP:5 mM, LPS: 2 μg/ml, tLPS: LPS was packed into liposome with final concentration 2 μg/ml as described in the Section Materials and Methods). IL-1β concentration was determined by ELISA. $n = 6$. $N = 3$. **(D)** BMDM were primed then treated as in **(C)** for 12 h and the cell death was determined by LDH assay. TNFα + CHX:100 ng/ml TNFα plus 50 μg/ml Cycloheximide. $n = 4$. $N = 3$. **(E)** BMDM were primed then treated as in **(D)** except treatment duration (CC: 2 h, Silica: 1 h, ATP: 2 h, TNFα + CHX: 6 h) then were collected and stained with Annexin V-FITC and PI. The right panel is the bar graphs of FACS plots on the left. $n = 4$. $N = 4$. **(F)** TEM picture of BMDM primed then treated as in **(E)**. **(G)** BMDM were primed then treated as in **(E)** except stained with PI. This is to indicate that using PI + staining alone faithfully recaptures nearly cell death events as in **(E)**. $n = 6$. $N = 3$. **(H)** BMDM were primed then treated with CC (500 μg/ml) for different durations then stained with PI. PI + percentages are shown. $n = 6$. $N = 3$.

spectrum of inflammatory response to this crystal. Simultaneously, CC triggered substantial cell death, as determined by LDH release and Annexin V PI staining (**Figures 1D,E**). In contrast to TNFα, CC-treated cells displayed typical necrotic plasma-membrane rupture (**Figure 1F**) and did not show an intermediate stage of Annexin V^+ PI^- that is associated with apoptosis (**Figure 1E**). Therefore, CC-mediated cell death was nearly captured in full by PI-positive staining alone (**Figures 1E,G**). This cell death was detectable within 1 h (**Figure 1H**), again suggesting an apoptosis-independent cell death programing. Considering the high spontaneous LDH release (NT in **Figure 1D**) and LDH release requires larger pore on cell membrane, which may miss the initial loss of membrane integrity, than Pi staining. We decided to use Pi staining assay as the main readout for cell death. As atherosclerosis progresses, macrophages, DCs, smooth muscle cells, and T cells are found inside the lesion intima (1). We tested CC cytotoxicity on those cells (Figures S1B,C in Supplementary Material). $CD4^+$ T cells, fibroblast (3T3), and endothelial cells (MuEC and MDCK) showed little necrotic cell death in CC treatment while DCs and macrophages exhibited Annexin V^+ PI^+ staining. We also tested cytotoxicity mediated by CC of different sizes. Figure S1D in Supplementary Material shows that cell death was more prominent with CC less than 5 μm. Therefore, CC can induce both NLRP3 inflammasome activation and a rapid necrotic cell death in the phagocytic cells.

As Caspase 1/11 activation leads to pyroptosis, a form of cell death resulting from plasma-membrane permeability change (16, 28), the role of NLRP3 inflammasome in CC-mediated cell death was analyzed. Primed, gene-deficient BMDM were treated with CC, silica, ATP and liposome-delivered LPS (confirmation of

gene deletion is shown in Figure S2A in Supplementary Material). NLRP3-deficient BMDM failed to produce IL-1β as expected (**Figure 2A**). NFκb and Caspase 1 were both critically involved in IL-1β production, which are known to regulate the priming and the production phases of IL-1β, respectively (29) (**Figure 2A**). Interestingly, Caspase1 deficiency did not impact CC-mediated cell death. The killing efficiency was not altered in *Casp1&11*$^{-/-}$ or the Caspase 11 transgene version of *Casp1&11*$^{-/-}$ BMDM (**Figure 2B**) (30). LDH released to the medium confirmed the result in Pi staining assay (Figure S2D in Supplementary Material). In line with this finding, *Nlrp3*$^{-/-}$ macrophages showed a degree of necrotic cell death similar to WT cells (**Figure 2B**). As well-known activators of NLRP3 inflammasome, it seems to be surprising that ATP and silica-induced cell death does not rely on NLRP3 inflammasome, However, there have been reports suggesting that ATP, $Al(OH)_3$, Silica, CPPD, LLOMe-induced

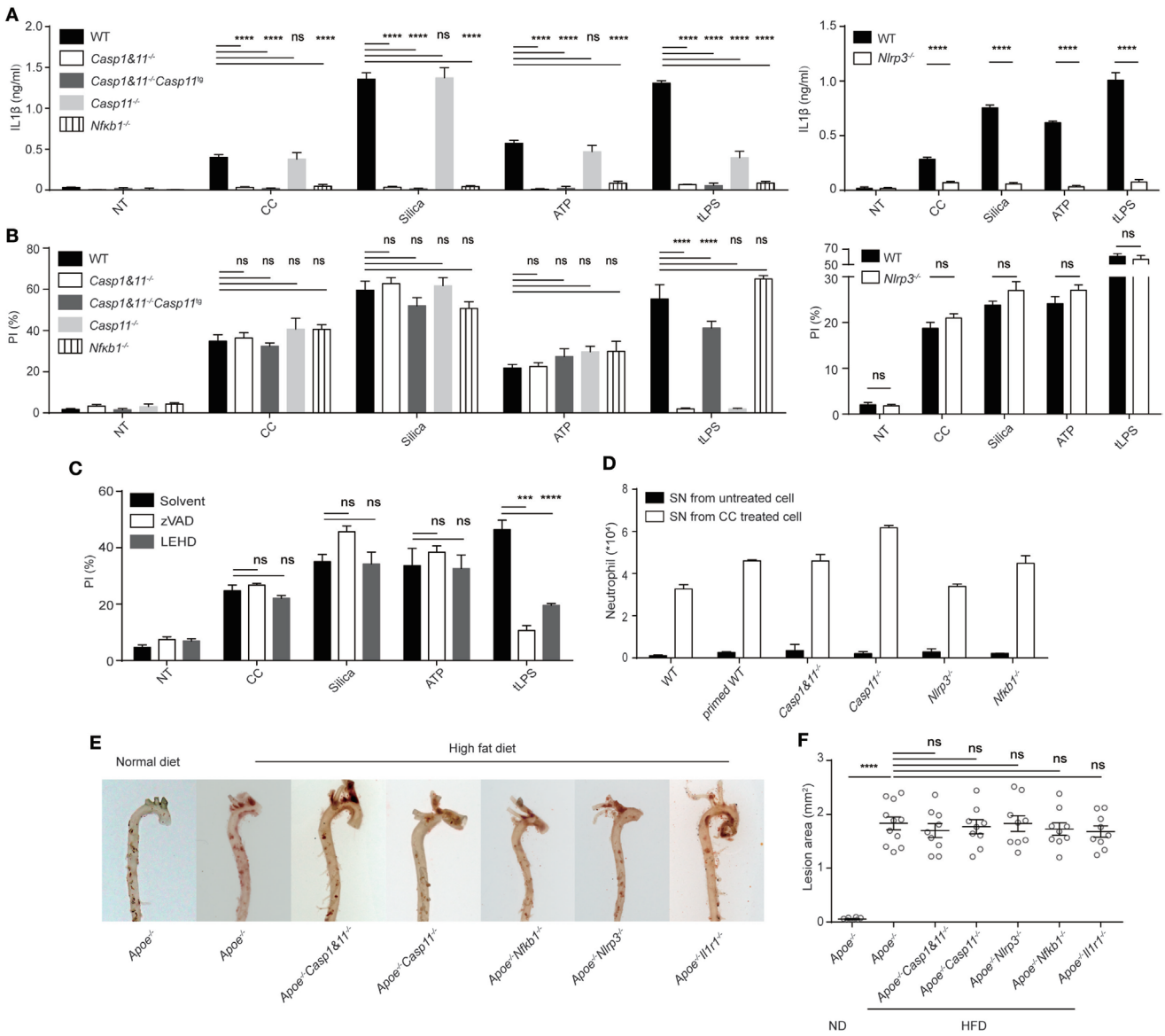

FIGURE 2 | Cholesterol crystals (CC)-mediated cell death and its pro-inflammatory property is unrelated to NLRP3 inflammasome. **(A)** BMDM with indicated genotypes were primed with Pam3csk4 then treated with indicated stimuli for 6 h as in **Figure 1C**. IL-1β was determined by ELISA. $n = 4$. $N = 4$. **(B)** BMDM were primed and then treated as in **Figure 1C** except treatment duration (CC: 2 h, Silica: 1 h, ATP: 2 h, tLPS: 6 h). Cell death was determined by PI staining. $n = 6$. $N = 5$. **(C)** BMDM were primed then pretreated with Caspase inhibitor (z-VAD-FMK: 10 μM, z-LEHD-FMK: 2 μM) 0.5 h before the stimulus treatments as in **(B)**. Cell death was determined as in **(B)**. $n = 6$. $N = 5$. **(D)** BMDM from WT or gene-deficient mice were cultured. Supernatants were collected and injected identical to **Figure 1B**. 16 h later, intraperitoneal cells were harvested and stained as in **Figure 1B**. $n = 3$. $N = 3$. **(E)** Inflammasome component-deficient mice were crossed to *Apoe*$^{-/-}$. Homozygous mice were fed with high-fat diet for 12 weeks and then the aorta from these mice were stained with Oil Red O. **(F)** The aortas in E were opened *en face* (Figure S2 in Supplementary Material) and imaged with microscope. The area of red plaques was determined with Olympus microscope image program based on pixel size.

macrophage cell death proceeded unimpeded under *Nlrp3* or *Casp1* deficient background (31–34). This is likely that those triggers may mediate some form of membrane damage or cellular stress independent of NLPR3/Caspase 1 pathway. Pan caspase inhibitor zVAD and Caspase 9 inhibitor LEHD again did not alter the rate of cell death (**Figure 2C**). Therefore, CC-mediated cell death is different from pyroptosis, and is unrelated to the roles of Caspase 1 and NLRP3 in IL-1β production.

As CC promote a pro-inflammatory milieu in **Figures 1A,B**, we compared necrotic death-associated inflammation to that mediated by simultaneous IL-1β production. While the CC-treated BMDM released stimulatory factors in supernatants that promoted peritoneal neutrophil recruitment, this effect was minimally altered in *Casp1&11*$^{-/-}$, *Nlrp3*$^{-/-}$, or *Nfkb1*$^{-/-}$ BMDM (**Figure 2D**), suggesting that the inflammatory IL-1β production was not the sole factor promoting inflammatory responses in our setting, at least in the light of the necrotic death-mediated releases of intracellular contents. *Apoe*$^{-/-}$ (a component of LDL transport system) mice have increased cholesterol levels and heightened plaque formation when fed with a high-fat diet (35). In these mice, deficiencies in Caspase1 and 11, NLRP3, IL-1 receptor, and NFκb did not alter the arteriosclerotic plaque formation (**Figures 2E,F**; Figure S2B in Supplementary Material). This result disagrees with a previous report that NLRP3 activation was involved in atherosclerosis development (5), instead in line with later reports suggesting the lack of influence by this inflammasome complex (11, 12). While these discrepancies could be results of experimental settings, our data suggest the possibility that necrotic cell death may function as a pro-inflammatory signaling in atherosclerotic progression independent of the NLRP3 inflammasome activation. Furthermore, we tested which kind of cytosolic contents is inflammatory. CC-treated cell supernatant was treated with DNAase, pronase (Figure S2C in Supplementary Material). The result shows that both proteolytic and DNA digestions reduced neutrophil infiltration, suggesting that necrotic releases of nucleic acids and proteins are indeed inflammatory (36, 37).

We wondered if CC-mediated cell death was regulated by any known cell death pathways independent of Caspase 1&11 and NLRP3 (38). In recent years, two membrane-targeting, pyroptosis-inducing mechanisms have been proposed. MLKL, a component of necroptosome, mediates necroptosis typically involving a death receptor (i.e., TNFR1), RIPK1 and RIPK3. MLKL is phosphorylated by RIPK3 and mediates the plasma-membrane disruption. This pathway is particularly active in the absence of Caspase activation (39, 40). Caspases 1 and 11 on the other hand process GSDMD, promoting its N-terminal fragment to translocate to the plasma membrane to form a pore-like structure, leading to pyroptosis (16). We tested the involvement of MLKL and GSDMD by gene knockdown. MLKL knockdown macrophages (**Figure 3A**) showed cell death similar to the control-treated cells, a result collaborated by the lack of cell death inhibition by necrostatin-1 (data not shown), an inhibitor of RIPK1. In comparison, TNFα + ZVAD-induced cell death was reduced (**Figure 3A**) (41). GSDMD knockdown also failed to reduce CC-induced, although blocked tLPS-induced cell death (**Figure 3B**). We tested potential involvement of TNFR1-Caspase 8 axis as it is known to regulate apoptosis and alternative Caspase 1 activation (42). *Rip3*$^{-/-}$*Casp8*$^{-/-}$ did not show any change of CC-mediated cell death (**Figure 3C**). The uptake of solid structures induces Ca^{2+} signaling; Ca^{2+} influx can lead to mitochondria ROS production that triggers executioner caspases. In addition, massive Ca^{2+} increase can activate the calpain system that results in endo-reticulum structural damage (17, 43). **Figures 3D,E** show that while IL-1β production was sensitive to 2APB (IP3 receptor blocker) and Thapsigargin (Sarco/endoplasmic reticulum Ca^{2+} ATPase inhibitor), neither treatment resulted in reduced cell death. A general calpain inhibitor, calpeptin (44), and high extracellular K^+ also failed to inhibit the cell death (**Figure 3F**; Figure S2E in Supplementary Material). Therefore, our results suggest that CC appeared to mediate a necrotic cell death without involving the common pathways such as apoptosis, pyroptosis, ROS production, and calpain-based self-internal digestion.

To study the nature of CC-mediated cell death, atomic force microscopy (45) -based single cell force spectroscopy (SCFS) was used to measure its binding affinity to the cellular membrane (23). Similar to silica crystal, CC induced a substantial binding force to macrophage cell surface and the affinity increased over time under a set contact force of 0.5 nN (data not shown). A typical Fc receptor-mediated phagocytosis of a solid particle is a complex process that requires an early phase cortical cytoskeleton remodeling regulated by GTPases such as CDC42, Rac1, and Rho (46) followed by signaling chains involving src family kinase, Syk as well as PI3Ks (46). Upon a particle binding, local actomyosin system generates the initial membrane contour that fully engages the solid target. This creates the initial binding affinity. Simultaneously, src family kinases phosphorylate ITAM motifs contained in phagocytic receptor complexes, which attracts Syk to the membrane. Syk then activates PI3K/PLC and other downstream signals for a full spectrum phagocytic activation (46). From a biophysical angle, the second stage, critically dependent on Syk, is characterized by irreversible strong binding forces (21, 23). In addition, Syk signaling also contributes to the restriction of receptor lateral diffusion, optimizing the signaling feedback loop during phagocytosis (47). The CC contact force was sensitive to actin polymerization inhibitor cytochalasin B, similar to Silica (**Figure 3G**). To our surprise, this force was completely intact in the presence of Syk inhibitor piceatannol (**Figure 3G**). In contrast to cytochalasin B, piceatannol had minimal impact on CC-mediated cell death (**Figure 3H**).

In our lab, solid particle phagocytosis (including MSU, basic calcium phosphate, calcium pyrophosphate dihydrate, allopurinol, silica, prefabricated latex beads, and several preparations of alum salt) has always shown a complete dependence on Syk, exhibiting a strong binding force as determined by AFM (data not shown). CC has been the only exception. This result suggested that strong affinity measured by SCFS was not mediated by typical phagocytosis signaling. Considering the off target/unintended effects of inhibitors and the lethality of the full Syk deficiency (vascular development defects) (48), we generated a conditional inducible deletion strain (**Figure 3I**). In brief, a Frt-framed box was inserted in between exons 2 and 3, which contained an

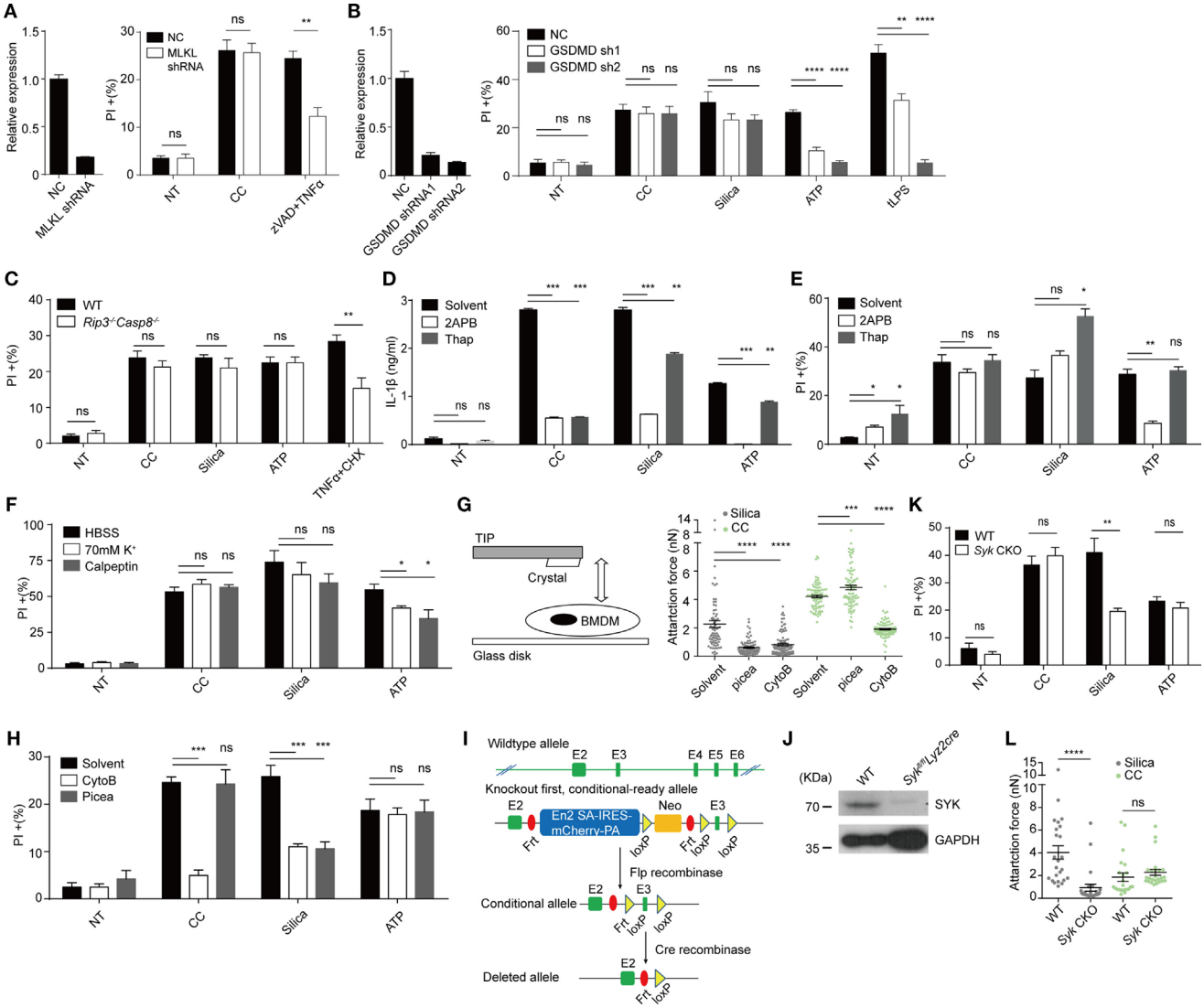

FIGURE 3 | Cholesterol crystals (CC)-mediated cell death is unrelated to mixed lineage kinase domain-like kinase (MLKL), gasdermin D (GSDMD), CASP8, Ca^{2+} influx, K^+ efflux and SYK. **(A)** Left: MLKL was knocked down in iBMDM by shRNA. Gene expression was determined by Q-PCR. Right: iBMDM were treated with CC for 2 h or zVAD (10 μM) plus TNFα (50 ng/ml) and CHX (50 μg/ml) for 12 h and then the cell death was determined with PI staining. $n = 6$. $N = 5$. **(B)** Left: GSDMD was knocked down in iBMDM by shRNA as in **(A)**. Right: iBMDM were primed then treated identical to **Figure 1C** except for the treatment duration (CC: 2 h, Silica: 1 h, ATP: 2 h, tLPS: 6 h). Cell death was determined with PI staining. $n = 6$. $N = 4$. **(C)** BMDM with Caspase 8 deficiency were treated and stained as in **Figure 1G**. $n = 6$. $N = 3$. **(D)** BMDM were primed then pretreated with 50 μM 2APB or 1 μM Thapsigargin for 0.5 h before stimulus treatment as in **Figure 1C**. 6 h later, IL1β production was determined by ELISA. $n = 4$. $N = 3$. **(E)** Identical to **(D)** except for the treatment duration (CC: 2 h, Silica: 1 h, ATP: 2 h). Cell death was determined with PI staining. $n = 5$. $N = 6$. **(F)** BMDM were primed and the media were exchanged into HBSS, 70 mM K^+ HBSS, or HBSS containing 100 μM Calpeptin 15 min before stimulus treatment as in **Figure 1C** except for the treatment duration (CC: 2 h, Silica: 1 h, ATP: 2 h). Cell death was determined with PI staining. $n = 6$. $N = 5$. **(G)** The left panel shows the schematic of how attraction force between crystals and cells was measured by AFM. Right panel: BMDM were primed and pretreated with piceatannol (50 μM) or Cytochalasin B (1 μg/ml) for 20 min. The attraction force after 5 s contact time was measured by AFM. $N = 3$. **(H)** BMDM were pretreated as in **(G)** before being treated with stimuli as in **Figure 1C** except for the treatment duration (CC: 2 h, Silica: 1 h, ATP: 2 h). Cell death was determined by PI staining. $n = 6$. $N = 3$. **(I)** The design of Syk CKO. **(J)** Syk expression in *Syk* CKO BMDM was examined by western blot. $N = 3$. **(K)** *Syk* CKO and WT BMDM were primed and treated with stimuli as in **Figure 1C** except for the treatment duration (CC: 2 h, Silica: 1 h, ATP: 2 h). Cell death was determined by PI staining. $n = 6$. $N = 7$. **(L)** The attraction forces after 5 s contact time between *Syk* CKO BMDM and crystals were measured by AFM. $N = 3$.

En2-SA-IRES-mCherry-PA fragment and a neomycin cassette, with a loxP site in between. The exon 3 was additionally framed by a loxP pair. The original design led to a Syk-null genotype. A crossing to a full body Frt converted the original deficient strain into a conditional knockout allele. A further crossing to *Lyz2cre* deleted exon 3 to produce a strain with a restricted myeloid Syk deficiency. In comparison with the systemic deletion, these mice show no visible abnormality yet macrophages in this strain were largely devoid of Syk (**Figure 3J**). The cell death mediated by CC was unaffected by the Syk deletion, in sharp contrast to

silica crystals (**Figure 3K**). The SCFS using Syk-deficient macrophages confirmed that the absence of Syk did not impact the binding, while the affinity of silica crystal to the macrophage was significantly reduced (**Figure 3L**). Therefore, the strong binding of CC to the plasma membrane does not rely on Syk-dependent phagocytosis.

Our previous work on MSU crystal revealed that in the receptor-independent phagocytosis, MSU crystals preferentially engage membrane cholesterol. This binding sorts cell-surface lipids, particularly lipid rafts, and a spontaneous Syk activation (21). We wondered if cell membrane cholesterol was similarly involved in the CC binding. Upon depletion of membrane cholesterol by MβCD, the CC-mediated binding was significantly reduced (**Figure 4A**). We created a synthetic bilayer membrane with base DOPC, or in mixture with sphingomyelin/cholesterol (21). The quality of the membrane on a mica surface was confirmed with the scanning mode AFM (**Figure 4B**) which revealed well-defined lipid domains (49). The contact of cholesterol-containing bilayer generated higher binding force than DOPC alone (**Figure 4C**). Similar to other crystal growth, CC can expand in the presence of free cholesterol in the environment (50). We wondered if cell-surface cholesterol content was disturbed upon CC contact. BMDM were loaded with Bodipy-cholesterol and incubated with label-free CC. Interestingly, CC became Bodipy-positive after the co-incubation (**Figure 4D**). To verify that this transfer was contact-dependent, the cells and CC were separated in a transwell setup, and no Bodipy transfer was detected (Figures S3A,B in Supplementary Material). A detailed time course comparison showed that over time the labeled cholesterol from BMDM was gradually transferred to a percentage of CC, while this transfer was minimal for MSU and silica crystals (**Figures 4E,F**). MFI of CC as a whole was also higher than MSU and silica controls (Figure S3C in Supplementary Material). To exclude the possibility that this transfer was a result of Bodipy-cholesterol falling off the cell membrane, as Bodipy may change cholesterol hydrophobic property, tritium (^{3}H)-replaced cholesterol was used to label BMDM and the cells were incubated with silica and CC. The crystals were then harvested and read with a scintillation counter. **Figure 4G** shows that CC preferentially attracted cholesterol while the radioactivity on silica was much less. These results demonstrate that CC can attract cell-surface cholesterol for their own growth, reminiscent of typical crystal growth that absorbs its precursor from the environment.

The scenario presented above implicates a possibility that depletion of membrane cholesterol mediates necrotic membrane rupture. To capture this event, we treated cells with MβCD. This treatment led to a necrotic cell death in contrast with the apoptosis induced by TNFα (**Figure 4H**). A CC was delivered by SCFS to be in contact with a GFP-expressing BMDM, and the setup was monitored by a microscope over time. Initially, the GFP signal remained steady under CC contact. However, the signal was suddenly lost. The cell in contact exhibited an "explosive" perfusion of GFP label (**Figure 4I**; Movie S1 in Supplementary Material). To confirm that such a death event was independent of cellular signaling, we generated GPMV, a "ghost" bubble exocytosed by phagocytes treated with PFA (25). GFP-expressing BMDM were pre-labeled with biotin, and the cells were treated with PFA to obtain GPMV. These GPMV were attached to glass surface coated with streptavidin for anchoring against free motion. CC glued to AFM cantilever was used to contact with these vesicles and the fluorescence intensity was again recorded by time-lapse videos (**Figure 4I**; Movie S2 in Supplementary Material). In comparison with silica crystals and latex beads, CC-contacted GPMV also displayed a higher frequency of "explosive" sudden loss of label, suggesting a catastrophic membrane rupture event (**Figure 4J**; Movies S2–S5 in Supplementary Material). In comparison, while GFP signal might wane with latex beads and silica, the loss was not significantly over the spontaneous loss in the untreated GPMV (**Figure 4J**). The frequency of this occurrence under CC contact was statistically higher than silica and latex bead control (**Figure 4K**). Therefore, CC-mediated depletion of the membrane cholesterol is associated with a high probability of sudden rupture of vesicles in both live cells and GPMV, suggesting a signaling-independent, biophysical assault to the plasma membrane that result in a quick induction of necrotic cell death.

DISCUSSION

Besides apoptosis (Type I, caspase dependent) and autosis (Type II, ion channel dependent), cell death characterized by the rupture of plasma membrane (Type III) was believed to be a passive event, occurring in pathological states such as hypoxia (27, 51). The rapid release of cytosolic content was believed to dump intracellular "DAMPs" to the environment, causing inflammation. This notion of passive death has taken a dramatic turn in recent years. It has been found that under inhibition of caspase cascade, a typical apoptotic signal (such as TNFR ligation) can drive a different type of cell death, akin to necrosis (52). Mechanistically, TNFR1 signaling activates RIPK1 which subsequently activates RIPK3. RIPK3 phosphorylates MLKL, promoting the latter's translocation to the plasma membrane (53). The helical structure of MLKL switches into a new conformation which forms uncontrolled cation channels on the membrane (54). This type of cell death differs from conventional necrosis in its sensitivity to RIPK1 inhibition (by necrostatin-1). Feng's group found that Caspase1 activation by inflammasomes or direct LPS binding to Caspase 4/5/11 leads to GSDMD cleavage, sending its N-terminal fragment to be buried into the plasma membrane, creating a similar pore-forming structure (16). This type of cell death is termed pyroptosis due to the involvement of caspase activities. As these seminal findings delineate the precise mechanism of cell death upon membrane permeability changes, whether necrotic cell death can take place independent of these two pathways is not known. Except for physical damage associated with detergent treatment, ice crystal formation during freezing, and membrane piercing by sharp objects such as crystals, a physiological/pathologic situation whereby membrane rupture-mediated cell death is no longer a major concern to the mainstream immunologists. In this report, we propose that membrane lipid disruption, in this case, cholesterol depletion may be sufficient to induce membrane rupture "biophysically." This finding, in turn, raises the possibility that small CC formed in the initiation stage of

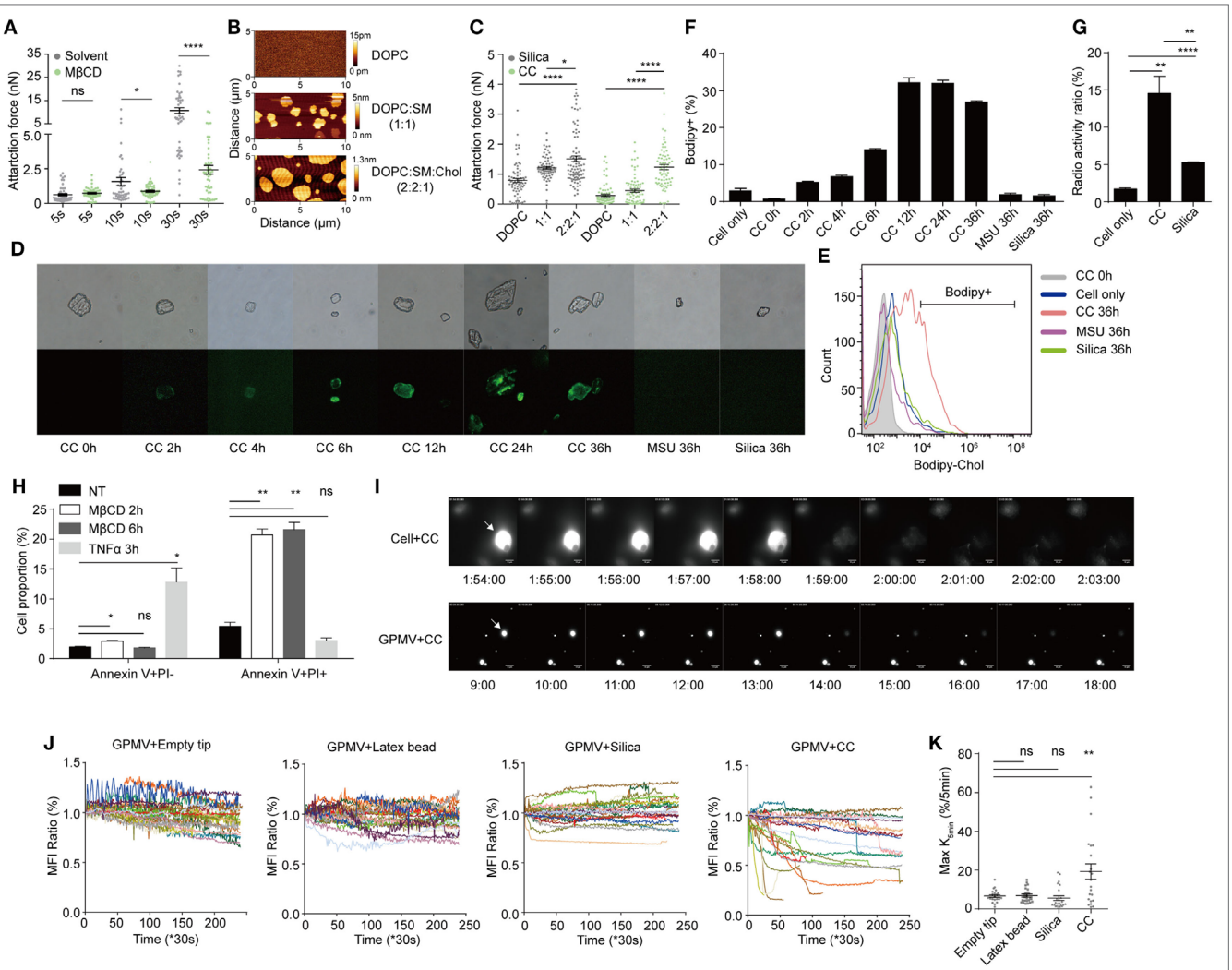

FIGURE 4 | Cholesterol crystals (CC) extract cholesterol from membrane thus induce signaling free membrane rupture. **(A)** BMDM membrane cholesterol was depleted by MβCD (4 mg/ml) incubation in serum-free medium for 0.5 h. The attraction force between CC and cells after different contact times was measured by AFM. $N = 3$. **(B)** Lipid bilayers with or without cholesterol/SM were produced. The surface of the bilayer was scanned by JPK NanoWizard. The shade of color indicates the height of the surface. **(C)** The attraction forces between crystal and lipid bilayers were measured by AFM with a contact time of 30 s. $N = 3$. **(D)** BMDM were labeled with Bodipy-cholesterol delivered by MβCD and treated with CC (100 μg/ml), MSU (100 μg/ml), or silica (80 μg/ml). After different lengths of incubation at 37°C, cells were lysed and the fluorescence on collected crystals were observed with fluorescence microscope. **(E)** The collected crystals in **(D)** were analyzed with FACS. **(F)** The bar graphs of Bodipy-positive crystals in **(E)**. $n = 3$. $N = 6$. **(G)** BMDM was labeled with cholesterol-[H^3] and treated with CC (100 μg/ml), silica (100 μg/ml). 24 h later, cells were lysed and the radioactivity of the collected crystals was detected. $n = 4$. $N = 3$. **(H)** BMDM were treated with MβCD (8 mg/ml) for 2 or 6 h or with TNFα plus CHX for 3 h. Cells were collected and stained with Annexin V and PI. Samples were analyzed by FACS. $n = 4$. $N = 4$. **(I)** Upper: A GFP-expressing BMDM was contacted by a CC constantly. GFP fluorescence of the cell was imaged every 20 s with a 488-nm laser in FITC channel. The pictures show the cell fluorescence around the moment of "explosion." Numbers below the pictures indicate the time since crystal contact. Lower: a GFP-containing giant plasma-membrane vesicle (GPMV) was contacted by a CC constantly. The rest was identical to the upper panel. The white arrow indicates the crystal-contacted cell or GPMV. **(J)** Mean fluorescence intensity of GPMV and background was measured with ImageJ. Fold change (compared with initial value) curve of $MFI_{GPMV}/MFI_{Background}$ during CC and other crystal contact was calculated. Each curve represents a crystal-contacted vesicle. **(K)** Maximum reduction of normalized $MFI_{GPMV}/MFI_{Background}$ within 5 min during the contact was manually identified and plotted.

atherosclerosis may induce pro-inflammatory reactions simply *via* membrane destabilization in the absence of any known death pathway signaling.

The role of CC in atherosclerotic development is widely recognized (55). However, exactly how the smaller amounts of CC contribute to the initiation of the early pathology is a subject of study. While there is no doubt that CC can mediate NLRP3 activation that leads to IL-1β production (5), whether this pathway contributes to the disease development, however, is still debated (11). In our setting, the IL-1β production by phagocytes is irrelevant to the neutrophil infiltration, suggesting it is a relatively minor player. Our early paper provides a likely explanation (56). In an experimental gout model, the IL-1β produced by phagocytes signals through IL-1R on the parenchymal cells,

opening a systematic feedback loop of IL-1β production (56). In other words, in the absence of involvement of non-hematopoietic cells, NLRP3 inflammasome activation by macrophages alone is insufficient for systemic inflammation. It is possible that for the formation of small CC in the artery walls, the signaling is not strong enough to reach a sustained inflammation, which may account for the lack of involvement of NLRP3 in atherosclerosis.

Previously, we proposed that in the absence of any receptor function, the ligation of plasma membrane lipids was sufficient to trigger lipid domain sorting and Syk-dependent phagocytic signaling (21). As the binding of CC to the plasma membrane exerts a force in the range of phagocytic events, it was unexpected that Syk was not required for such a strong force. The exact nature of this high binding affinity is unknown, although the exceedingly high binding force revealed in our AFM analysis of CC interaction with cholesterol-containing lipid domain may offer some clue. The extraction of cholesterol from the membrane may mimic the precursor condensation onto the crystalline surface in the typical growth of organic crystals (57), which may be translated into a force exerted on the plasma membrane. This notion, however, requires vigorous experimental verification, as alternative explanation may exist. Several recent papers took on the issue of solid particle-induced necrotic cell death, particularly with regard to neutrophil extracellular trap (NET) formation. It was found that nano particles, such as those of 10 nm diameter, triggered significant release of chromatin DNA that trapped those solid structures. Apparently, this NETosis may rely on cellular necrotic factors such as MLKL and RIPK1 (58), and may also require ROS production from NADPH oxidase complex (59). The question remains how those particles initiate their contact with the plasma membrane which can be regarded as the initial step for downstream cellular consequences (60). One proposal suggests that particle surface hydrophobicity may be critical for the membrane interactions. Simple decoration via surface PEGylation reduced the NETosis and DNA release, suggesting a loss of the ability of these particles to interact with phagocytes (60). Therefore, it is likely that a surface interaction, such as hydrophobicity-based attachment may be critical for CC to engage the membrane and contributes in some way to the cell death seen in our setting. CC-based cholesterol extraction then further weakens the plasma membrane. Whether hydrophobicity of particles plays a part in our system is, therefore, worthy of further analysis.

We do not understand why cholesterol depletion mediates the rapid "explosive" necrosis. The literature suggests the lipid homeostasis is critical for the plasma-membrane integrity and impacts various forms of programmed cell death (61). On the other hand, lipid disturbance can in general alter plasma-membrane permeability. In one proposal, with the increased amount of cholesterol, membrane orders increase, which prevents the pore formation particularly when the membrane is in an oxidative environment (62). Another possibility is that cholesterol in the membrane has a strong tendency to reduce the activities of several classes of ion channels, including inward-rectifying, voltage-gated and Ca^{2+} sensitive K^+ channels, as well as voltage-gated Na^+ and Ca^{2+} channels (63). The reduction of the cholesterol in the membrane may thus disrupt several ion and osmotic gradients that lead to membrane collapse. These, however, remain to be speculations until more refined experimental analyses. The implication of cholesterol depletion as a regulator for cardiovascular necrosis is at the moment difficult to prove experimentally, as such as "physical" depletion cannot be studied with a genetic model. Nevertheless, our work strongly suggests that clinical interventions via targeting IL-1β may be of limited value; the cholesterol control at the very early stage of atherosclerotic changes should be a more viable method for the prevention of cardiovascular diseases.

ETHICS STATEMENT

All mouse experiment protocols were approved by the animal research committee of Tsinghua University.

AUTHOR CONTRIBUTIONS

FS performed all the experiments unless noted below. JC provided assistance in the atherosclerosis experiments. XM and YF provided help in cell culture, ELISA, and western blotting analyses. LY helped in cell death work. WZ helped in mouse husbandry. MA and TX provided technical support in AFM and lipid bilayer preparation. YS conceptualized the project, designed experiments, and wrote the manuscript.

ACKNOWLEDGMENTS

The authors thank Drs. V. M. Dixit, Z. Jiang, L. Wu, X. Lin, H. Qi, and K. Rock for their generous gifts. The authors thank L. Mu, Z. Tu, N. Kang, H. Rong, Y. Zhang, and D. Song for technical help. The authors thank L. Cui and Y. Hu for preparing EM sample and technical assistance. The authors thank B. Li for help in radioactive labeling. This work was supported by the joint Peking-Tsinghua Center for Life Sciences and grants from the National Natural Science Foundation of China General Program (31370878), Key Program (31630023), and Creative Research Groups Program (81621002), the National Institutes of Health (R01AI098995), Natural Sciences and Engineering Research Council of Canada (RGPIN-355350/396037), and Canadian Institutes of Health Research (MOP-119295) to YS.

SUPPLEMENTARY MATERIAL

The Supplementary Material for this article can be found online at https://www.frontiersin.org/articles/10.3389/fimmu.2018.01163/full#supplementary-material.

MOVIE S1 | CELL + CC: *GFP*^{tg} BMDM were cultured on a glass slide. An AFM tip with cholesterol crystal was moved to touch the cell under constant height. GFP fluorescence of the cell was imaged every 20 s with a 488-nm laser in FITC channel. The time segment around the "explosion" was shown.

MOVIE S2 | Giant plasma-membrane vesicle (GPMV) + CC: GFP-containing GPMV were harvested and "glued" to the bottom of glass disk with biotin and streptavidin. The rest was identical to Movie S1 in Supplementary Material except that the recording interval was 30 s.

MOVIE S3 | Giant plasma-membrane vesicle + Empty tip: all procedures were identical to Movie S2 in Supplementary Material except AFM tip was replaced with an empty tip and all the recording frames were shown.

MOVIE S4 | Giant plasma-membrane vesicle + Latex bead: all procedures were identical to Movie S3 in Supplementary Material except AFM tip was functionalized with a latex bead.

MOVIE S5 | Giant plasma-membrane vesicle + Silica: all procedures were identical to Movie S3 in Supplementary Material except AFM tip was functionalized with a silica crystal.

REFERENCES

1. Moore KJ, Tabas I. Macrophages in the pathogenesis of atherosclerosis. *Cell* (2011) 145(3):341–55. doi:10.1016/j.cell.2011.04.005
2. Simons K, Ikonen E. How cells handle cholesterol. *Science* (2000) 290(5497):1721–6. doi:10.1126/science.290.5497.1721
3. Abela GS. Cholesterol crystals piercing the arterial plaque and intima trigger local and systemic inflammation. *J Clin Lipidol* (2010) 4(3):156–64. doi:10.1016/j.jacl.2010.03.003
4. Abela GS, Aziz K. Cholesterol crystals cause mechanical damage to biological membranes: a proposed mechanism of plaque rupture and erosion leading to arterial thrombosis. *Clin Cardiol* (2005) 28(9):413–20. doi:10.1002/clc.4960280906
5. Duewell P, Kono H, Rayner KJ, Sirois CM, Vladimer G, Bauernfeind FG, et al. NLRP3 inflammasomes are required for atherogenesis and activated by cholesterol crystals. *Nature* (2010) 464(7293):1357–61. doi:10.1038/nature08938
6. Liu L, Gardecki JA, Nadkarni SK, Toussaint JD, Yagi Y, Bouma BE, et al. Imaging the subcellular structure of human coronary atherosclerosis using micro-optical coherence tomography. *Nat Med* (2011) 17(8):1010–4. doi:10.1038/nm.2409
7. Lim RS, Suhalim JL, Miyazaki-Anzai S, Miyazaki M, Levi M, Potma EO, et al. Identification of cholesterol crystals in plaques of atherosclerotic mice using hyperspectral CARS imaging. *J Lipid Res* (2011) 52(12):2177–86. doi:10.1194/jlr.M018077
8. Björkegren JL, Hägg S, Talukdar HA, Foroughi Asl H, Jain RK, Cedergren C, et al. Plasma cholesterol-induced lesion networks activated before regression of early, mature, and advanced atherosclerosis. *PLoS Genet* (2014) 10(2):e1004201. doi:10.1371/journal.pgen.1004201
9. Hansson GK, Hermansson A. The immune system in atherosclerosis. *Nat Immunol* (2011) 12(3):204–12. doi:10.1038/ni.2001
10. Rajamäki K, Lappalainen J, Oörni K, Välimäki E, Matikainen S, Kovanen PT, et al. Cholesterol crystals activate the NLRP3 inflammasome in human macrophages: a novel link between cholesterol metabolism and inflammation. *PLoS One* (2010) 5(7):e11765. doi:10.1371/journal.pone.0011765
11. Menu P, Pellegrin M, Aubert JF, Bouzourene K, Tardivel A, Mazzolai L, et al. Atherosclerosis in ApoE-deficient mice progresses independently of the NLRP3 inflammasome. *Cell Death Dis* (2011) 2(3):e137. doi:10.1038/cddis.2011.18
12. Freigang S, Ampenberger F, Weiss A, Kanneganti TD, Iwakura Y, Hersberger M, et al. Fatty acid-induced mitochondrial uncoupling elicits inflammasome-independent IL-1alpha and sterile vascular inflammation in atherosclerosis. *Nat Immunol* (2013) 14(10):1045–53. doi:10.1038/ni.2704
13. Samstad EO, Niyonzima N, Nymo S, Aune MH, Ryan L, Bakke SS, et al. Cholesterol crystals induce complement-dependent inflammasome activation and cytokine release. *J Immunol* (2014) 192(6):2837–45. doi:10.4049/jimmunol.1302484
14. Tabas I. Consequences of cellular cholesterol accumulation: basic concepts and physiological implications. *J Clin Invest* (2002) 110(7):905–11. doi:10.1172/JCI0216452
15. Mulay SR, Desai J, Kumar SV, Eberhard JN, Thomasova D, Romoli S, et al. Cytotoxicity of crystals involves RIPK3-MLKL-mediated necroptosis. *Nat Commun* (2016) 7:10274. doi:10.1038/ncomms10274
16. Shi J, Zhao Y, Wang K, Shi X, Wang Y, Huang H, et al. Cleavage of GSDMD by inflammatory caspases determines pyroptotic cell death. *Nature* (2015) 526(7575):660–5. doi:10.1038/nature15514
17. Zhivotovsky B, Orrenius S. Calcium and cell death mechanisms: a perspective from the cell death community. *Cell Calcium* (2011) 50(3):211–21. doi:10.1016/j.ceca.2011.03.003
18. Liu X, Van Vleet T, Schnellmann RG. The role of calpain in oncotic cell death. *Annu Rev Pharmacol Toxicol* (2004) 44:349–70. doi:10.1146/annurev.pharmtox.44.101802.121804
19. Desrosiers MD, Cembrola KM, Fakir MJ, Stephens LA, Jama FM, Shameli A, et al. Adenosine deamination sustains dendritic cell activation in inflammation. *J Immunol* (2007) 179(3):1884–92. doi:10.4049/jimmunol.179.3.1884
20. Kobayashi M, Inoue K, Warabi E, Minami T, Kodama T. A simple method of isolating mouse aortic endothelial cells. *J Atheroscler Thromb* (2005) 12(3):138–42. doi:10.5551/jat.12.138
21. Ng G, Sharma K, Ward SM, Desrosiers MD, Stephens LA, Schoel WM, et al. Receptor-independent, direct membrane binding leads to cell-surface lipid sorting and Syk kinase activation in dendritic cells. *Immunity* (2008) 29(5):807–18. doi:10.1016/j.immuni.2008.09.013
22. Beattie JH, Duthie SJ, Kwun IS, Ha TY, Gordon MJ. Rapid quantification of aortic lesions in apoE(-/-) mice. *J Vasc Res* (2009) 46(4):347–52. doi:10.1159/000189795
23. Flach TL, Ng G, Hari A, Desrosiers MD, Zhang P, Ward SM, et al. Alum interaction with dendritic cell membrane lipids is essential for its adjuvanticity. *Nat Med* (2011) 17(4):479–87. doi:10.1038/nm.2306
24. Hari A, Zhang Y, Tu Z, Detampel P, Stenner M, Ganguly A, et al. Activation of NLRP3 inflammasome by crystalline structures via cell surface contact. *Sci Rep* (2014) 4:7281. doi:10.1038/srep07281
25. Sezgin E, Kaiser HJ, Baumgart T, Schwille P, Simons K, Levental I. Elucidating membrane structure and protein behavior using giant plasma membrane vesicles. *Nat Protoc* (2012) 7(6):1042–51. doi:10.1038/nprot.2012.059
26. Unsay JD, Cosentino K, Garcia-Saez AJ. Atomic force microscopy imaging and force spectroscopy of supported lipid bilayers. *J Vis Exp* (2015) 101:e52867. doi:10.3791/52867
27. Golstein P, Kroemer G. Cell death by necrosis: towards a molecular definition. *Trends Biochem Sci* (2007) 32(1):37–43. doi:10.1016/j.tibs.2006.11.001
28. Hagar JA, Powell DA, Aachoui Y, Ernst RK, Miao EA. Cytoplasmic LPS activates caspase-11: implications in TLR4-independent endotoxic shock. *Science* (2013) 341(6151):1250–3. doi:10.1126/science.1240988
29. Franchi L, Eigenbrod T, Muñoz-Planillo R, Nuñez G. The inflammasome: a caspase-1-activation platform that regulates immune responses and disease pathogenesis. *Nat Immunol* (2009) 10(3):241–7. doi:10.1038/ni.1703
30. Kayagaki N, Warming S, Lamkanfi M, Vande Walle L, Louie S, Dong J, et al. Non-canonical inflammasome activation targets caspase-11. *Nature* (2011) 479(7371):117–21. doi:10.1038/nature10558
31. Muñoz-Planillo R, Kuffa P, Martínez-Colón G, Smith BL, Rajendiran TM, Núñez G. K+ efflux is the common trigger of NLRP3 inflammasome activation by bacterial toxins and particulate matter. *Immunity* (2013) 38(6):1142–53. doi:10.1016/j.immuni.2013.05.016
32. Cassel SL, Eisenbarth SC, Iyer SS, Sadler JJ, Colegio OR, Tephly LA, et al. The Nalp3 inflammasome is essential for the development of silicosis. *Proc Natl Acad Sci U S A* (2008) 105(26):9035–40. doi:10.1073/pnas.0803933105
33. Eisenbarth SC, Colegio OR, O'Connor W, Sutterwala FS, Flavell RA. Crucial role for the Nalp3 inflammasome in the immunostimulatory properties of aluminium adjuvants. *Nature* (2008) 453(7198):1122–6. doi:10.1038/nature06939
34. Mariathasan S, Weiss DS, Newton K, McBride J, O'Rourke K, Roose-Girma M, et al. Cryopyrin activates the inflammasome in response to toxins and ATP. *Nature* (2006) 440(7081):228–32. doi:10.1038/nature04515
35. Zhang SH, Reddick RL, Piedrahita JA, Maeda N. Spontaneous hypercholesterolemia and arterial lesions in mice lacking apolipoprotein E. *Science* (1992) 258(5081):468–71. doi:10.1126/science.1411543
36. Rock KL, Kono H. The inflammatory response to cell death. *Annu Rev Pathol* (2008) 3:99–126. doi:10.1146/annurev.pathmechdis.3.121806.151456
37. Marichal T, Ohata K, Bedoret D, Mesnil C, Sabatel C, Kobiyama K, et al. DNA released from dying host cells mediates aluminum adjuvant activity. *Nat Med* (2011) 17(8):996–1002. doi:10.1038/nm.2403
38. Galluzzi L, Vitale I, Abrams JM, Alnemri ES, Baehrecke EH, Blagosklonny MV, et al. Molecular definitions of cell death subroutines: recommendations of the nomenclature committee on cell death 2012. *Cell Death Differ* (2012) 19(1):107–20. doi:10.1038/cdd.2011.96

39. Han J, Zhong C-Q, Zhang D-W. Programmed necrosis: backup to and competitor with apoptosis in the immune system. *Nat Immunol* (2011) 12(12):1143–9. doi:10.1038/ni.2159
40. Wu J, Huang Z, Ren J, Zhang Z, He P, Li Y, et al. Mlkl knockout mice demonstrate the indispensable role of Mlkl in necroptosis. *Cell Res* (2013) 23(8):994–1006. doi:10.1038/cr.2013.91
41. Ofengeim D, Yuan JY. Regulation of RIP1 kinase signalling at the crossroads of inflammation and cell death. *Nat Rev Mol Cell Biol* (2013) 14(11):727–36. doi:10.1038/nrm3683
42. Philip NH, Dillon CP, Snyder AG, Fitzgerald P, Wynosky-Dolfi MA, Zwack EE, et al. Caspase-8 mediates caspase-1 processing and innate immune defense in response to bacterial blockade of NF-κB and MAPK signaling. *Proc Natl Acad Sci U S A* (2014) 111(20):7385–90. doi:10.1073/pnas.1403252111
43. Zhong Z, Zhai Y, Liang S, Mori Y, Han R, Sutterwala FS, et al. TRPM2 links oxidative stress to NLRP3 inflammasome activation. *Nat Commun* (2013) 4:1611. doi:10.1038/ncomms2608
44. Chen J, Ganguly A, Mucsi AD, Meng J, Yan J, Detampel P, et al. Strong adhesion by regulatory T cells induces dendritic cell cytoskeletal polarization and contact-dependent lethargy. *J Exp Med* (2017) 214(2):327–38. doi:10.1084/jem.20160620
45. Rensen S, Doevendans P, Van Eys G. Regulation and characteristics of vascular smooth muscle cell phenotypic diversity. *Neth Heart J* (2007) 15(3):100–8. doi:10.1007/BF03085963
46. Flannagan RS, Jaumouillé V, Grinstein S. The cell biology of phagocytosis. *Annu Rev Pathol* (2012) 7(1):61–98. doi:10.1146/annurev-pathol-011811-132445
47. Jaumouillé V, Farkash Y, Jaqaman K, Das R, Lowell CA, Grinstein S. Actin cytoskeleton reorganization by syk regulates fcγ receptor responsiveness by increasing its lateral mobility and clustering. *Dev Cell* (2014) 29(5):534–46. doi:10.1016/j.devcel.2014.04.031
48. Sebzda E, Hibbard C, Sweeney S, Abtahian F, Bezman N, Clemens G, et al. Syk and Slp-76 mutant mice reveal a cell-autonomous hematopoietic cell contribution to vascular development. *Dev Cell* (2006) 11(3):349–61. doi:10.1016/j.devcel.2006.07.007
49. Connell SD, Heath G, Olmsted PD, Kisil A. Critical point fluctuations in supported lipid membranes. *Faraday Discuss* (2013) 161:91–111; discussion 113–50. doi:10.1039/C2FD20119D
50. Kellner-Weibel G, Yancey PG, Jerome WG, Walser T, Mason RP, Phillips MC, et al. Crystallization of free cholesterol in model macrophage foam cells. *Arterioscler Thromb Vasc Biol* (1999) 19(8):1891–8. doi:10.1161/01.ATV.19.8.1891
51. Zong WX, Thompson CB. Necrotic death as a cell fate. *Genes Dev* (2006) 20(1):1–15. doi:10.1101/gad.1376506
52. Degterev A, Huang Z, Boyce M, Li Y, Jagtap P, Mizushima N, et al. Chemical inhibitor of nonapoptotic cell death with therapeutic potential for ischemic brain injury. *Nat Chem Biol* (2005) 1(2):112–9. doi:10.1038/nchembio711
53. Sun L, Wang H, Wang Z, He S, Chen S, Liao D, et al. Mixed lineage kinase domain-like protein mediates necrosis signaling downstream of RIP3 kinase. *Cell* (2012) 148(1–2):213–27. doi:10.1016/j.cell.2011.11.031
54. Xia B, Fang S, Chen X, Hu H, Chen P, Wang H, et al. MLKL forms cation channels. *Cell Res* (2016) 26(5):517–28. doi:10.1038/cr.2016.26
55. Grebe A, Latz E. Cholesterol crystals and inflammation. *Curr Rheumatol Rep* (2013) 15(3):313. doi:10.1007/s11926-012-0313-z
56. Chen CJ, Shi Y, Hearn A, Fitzgerald K, Golenbock D, Reed G, et al. MyD88-dependent IL-1 receptor signaling is essential for gouty inflammation stimulated by monosodium urate crystals. *J Clin Invest* (2006) 116(8):2262–71. doi:10.1172/JCI28075
57. Jiang Y, Kellermeier M, Gebaue D, Lu Z, Rosenberg R, Moise A, et al. Growth of organic crystals via attachment and transformation of nanoscopic precursors. *Nat Commun* (2017) 8:15933. doi:10.1038/ncomms15933
58. Desai J, Foresto-Neto O, Honarpisheh M, Steiger S, Nakazawa D, Popper B, et al. Particles of different sizes and shapes induce neutrophil necroptosis followed by the release of neutrophil extracellular trap-like chromatin. *Sci Rep* (2017) 7(1):15003. doi:10.1038/s41598-017-15106-0
59. Biermann MH, Podolska MJ, Knopf J, Reinwald C, Weidner D, Maueröder C, et al. Oxidative burst-dependent NETosis is implicated in the resolution of necrosis-associated sterile inflammation. *Front Immunol* (2016) 7:557. doi:10.3389/fimmu.2016.00557
60. Muñoz LE, Bilyy R, Biermann MH, Kienhöfer D, Maueröder C, Hahn J, et al. Nanoparticles size-dependently initiate self-limiting NETosis-driven inflammation. *Proc Natl Acad Sci U S A* (2016) 113(40):E5856–65. doi:10.1073/pnas.1602230113
61. Agmon E, Stockwell BR. Lipid homeostasis and regulated cell death. *Curr Opin Chem Biol* (2017) 39:83–9. doi:10.1016/j.cbpa.2017.06.002
62. Van der Paal J, Neyts EC, Verlackt CCW, Bogaerts A. Effect of lipid peroxidation on membrane permeability of cancer and normal cells subjected to oxidative stress. *Chem Sci* (2016) 7(1):489–98. doi:10.1039/c5sc02311d
63. Levitan I, Fang Y, Rosenhouse-Dantsker A, Romanenko V. Cholesterol and ion channels. *Subcell Biochem* (2010) 51:509–49. doi:10.1007/978-90-481-8622-8_19

Conflict of Interest Statement: The authors declare that the research was conducted in the absence of any commercial or financial relationships that could be construed as a potential conflict of interest.

frontiers in Immunology

ORIGINAL RESEARCH
published: 14 August 2018
doi: 10.3389/fimmu.2018.01866

Autophagy Protects From Uremic Vascular Media Calcification

Bianca Frauscher[1], Alexander H. Kirsch[1], Corinna Schabhüttl[1], Kerstin Schweighofer[1], Máté Kétszeri[1], Marion Pollheimer[2], Duska Dragun[3,4], Katrin Schröder[5], Alexander R. Rosenkranz[1], Kathrin Eller[1] and Philipp Eller[6]*

[1] Clinical Division of Nephrology, Department of Internal Medicine, Medical University of Graz, Graz, Austria, [2] Institute of Pathology, Medical University of Graz, Graz, Austria, [3] Clinic for Nephrology and Critical Care Medicine, Charité - Universitätsmedizin Berlin, Freie Universitat Berlin, Humboldt-Universitat zu Berlin, Berlin, Germany, [4] Institute of Health (BIH), Berlin, Germany, [5] Institute for Cardiovascular Physiology, Goethe-University, Frankfurt, Germany, [6] Intensive Care Unit, Department of Internal Medicine, Medical University of Graz, Graz, Austria

Chronic kidney disease and diabetes mellitus are associated with extensive media calcification, which leads to increased cardiovascular morbidity and mortality. Here, we investigated the role of autophagy in the pathogenesis of uremic vascular media calcification. DBA/2 mice were fed with high-phosphate diet (HPD) in order to cause vascular calcification. DBA/2 mice on standard chow diet were used as control. In parallel, autophagy and its response to rapamycin, 3-methyladenine (3-MA), and bafilomycin were studied in an *in vitro* model using mouse vascular smooth muscle cells (MOVAS). DBA/2 mice on HPD developed severe vascular media calcification, which is mirrored *in vitro* by culturing MOVAS under calcifying conditions. Both, *in vitro* and *in vivo*, autophagy significantly increased in MOVAS under calcifying conditions and in aortas of HPD mice, respectively. Histologically, autophagy was located to the aortic *Tunica media*, but also vascular endothelial cells, and was found to continuously increase during HPD treatment. 3-MA as well as bafilomycin blocked autophagy in MOVAS and increased calcification. *Vice versa*, rapamycin treatment further increased autophagy and resulted in a significant decrease of vascular calcification *in vitro* and *in vivo*. Rapamycin reduced *Runx2* transcription levels in aortas and MOVAS to control levels, whereas it increased α-smooth muscle actin and *Sm22α* transcription in MOVAS to control levels. Furthermore, rapamycin-treated HPD mice survived significantly longer compared to HPD controls. These findings indicate that autophagy is an endogenous response of vascular smooth muscle cells (VSMC) to protect from calcification in uremia. Induction of autophagy by rapamycin protects cells and mice from uremic media calcification possibly by inhibiting osteogenic transdifferentiation of VSMC.

Keywords: vascular smooth muscle cells, rapamycin, hydroxyapatite crystals, inflammation, phosphate, chronic kidney disease

OPEN ACCESS

Edited by:
Hans-Joachim Anders, Ludwig-Maximilians-Universität München, Germany

Reviewed by:
Willi Jahnen-Dechent, RWTH Aachen Universität, Germany
Stephen Zewinger, Universitätsklinikum des Saarlandes, Germany
Alessandra Ghigo, Università degli Studi di Torino, Italy

***Correspondence:**
Kathrin Eller
kathrin.eller@medunigraz.at

Specialty section:
This article was submitted to Inflammation, a section of the journal Frontiers in Immunology

Received: *20 April 2018*
Accepted: *27 July 2018*
Published: *14 August 2018*

Citation:
Frauscher B, Kirsch AH, Schabhüttl C, Schweighofer K, Kétszeri M, Pollheimer M, Dragun D, Schröder K, Rosenkranz AR, Eller K and Eller P (2018) Autophagy Protects From Uremic Vascular Media Calcification. Front. Immunol. 9:1866. doi: 10.3389/fimmu.2018.01866

INTRODUCTION

Chronic kidney disease (CKD) and especially end stage renal disease (ESRD) are associated with an extensive increase in cardiovascular mortality and morbidity (1). Cardiovascular disease is the single greatest cause of mortality in CKD/ESRD, and it is to a large extent driven by abnormal mineral metabolism leading to extensive arterial calcifications, a reduced vascular compliance,

left ventricular hypertrophy, and sudden cardiac death (2). Contrary to non-uremic patients where arterial calcification typically affects intimal atherosclerotic plaques, patients with CKD predominantly develop calcification of the tunica media (3, 4). It is currently believed that increase in serum phosphate levels is the driving force leading to vascular media calcification (5). High-phosphate levels in combination with other mediators, which are dysregulated in uremia, induce vascular smooth muscle cells (VSMC) to transdifferentiate from a contractile to proliferative, osteoblastic, and/or inflammatory phenotypes (6, 7). Interestingly, the adverse effects of high serum phosphate and/or phosphate overload in human health do not seem to be limited to advanced stages of CKD, as it has been found in earlier stages of CKD and also in the general population (8–10).

Different murine models of CKD mimicking media calcification exist (11). Recently, we established a new murine model with acute renal failure due to phosphate nephropathy which can be induced in DBA/2 mice subjected to high-phosphate diet (HPD) (12–14). DBA/2 mice have an alternative splice variant of the *Abcc6* gene resulting in an increased susceptibility to develop tissue calcification (15). Within 5–14 days mice develop calcification within the *Tunica media* of the aorta, which is more pronounced in the abdominal part of the aorta mimicking the situation in ESRD patients (14). Whereas inflammation is of crucial importance in the development of renal calcification (13), vascular media calcification does not seem to be dependent on immune cells (14).

The three different types of autophagy, namely microautophagy, chaperone-mediated autophagy, and macroautophagy, have all been extensively reviewed in the past (16, 17). We focused in our studies on macroautophagy, which will be referred to as autophagy hereafter. Autophagy is a highly conserved cellular process responsible for removal or recycling of long-lived proteins and organelles. It is essential for cell survival, differentiation, and development, and the cellular response to stress (18). A widely used marker of autophagy is microtubule-associated protein light chain 3 (LC3). It exists as cytosolic LC3-I and converts to LC3-II, which mainly inserts into isolation membranes and autophagosomes. The amount of LC3-II closely correlates with the number of autophagosomes (19). The p62 protein, also called sequestosome 1, is a ubiquitin-binding scaffold protein, which is degraded by autophagy (20). Thereby low levels of p62 protein represent states of augmented autophagy.

Since autophagy takes place in every eukaryotic cell, it plays an important role in all organ systems and has been implicated in an expanding list of disease processes (16). Growing evidence suggests that autophagy also plays a role in vascular pathophysiology including uremic media calcification (21). Dai and coworkers provided *in vitro* evidence that high-phosphate levels induced radical oxygen species (ROS) production results in increased autophagy in VSMC. This process protected cells from calcification thereby providing an endogenous protective mechanism counteracting phosphate-induced vascular calcification (22). So far, data on pharmacologic augmentation of autophagy to improve uremic vascular media calcification *in vivo* are scarce. Recently, Peng and coworkers showed that autophagy plays a role in the calcification process of the aorta, but they were using a non-CKD calcification model (23).

We now aimed to characterize autophagy and its role in uremic media calcification induced by high-phosphate levels *in vivo* and *in vitro*. Furthermore, we influenced autophagy pharmacologically and studied the effects on uremic media calcification.

MATERIALS AND METHODS

In Vivo Studies

Female 8-week-old dilute brown non-agouti 2 (DBA/2NCrl) mice were obtained from Charles River (Sulzfeld, Germany) and housed in a virus/antibody-free environment in the laboratory animal facility of the Medical University of Graz. These mice are susceptible to ectopic renal calcification and media calcification when exposed to increased oral phosphate loads (15).

To induce media calcification, they were placed on HPD (Altromin, Germany) containing 20.2 g/kg of phosphorus, 9.4 g/kg of calcium, 0.7 g/kg of magnesium, and 500 IU/kg of vitamin D3. The standard chow contained 7.0 g/kg of phosphorous, 10.0 g/kg of calcium, 2.2 g/kg of magnesium, and 1,000 IU/kg of vitamin D3. The mice were then followed for 5 and 12 days. For the interventional studies a rapamycin (LC Labs, Woburn, MA, USA) stock solution was prepared by dissolving rapamycin in 100% ethanol, which was then dissolved in sterile saline for intraperitoneal injection at a dose of 0.5 mg/kg body wt. Daily intraperitoneal rapamycin or vehicle administration was started either on 3 days prior or 5 days after starting HPD.

All animal experiments were approved by the Committee of the Ethics of Animal Experiments of the Austrian Ministry (BMWFW-66.010/0061-WF/V/3b/2016). All experiments were conducted under strict adherence of the law of Austria.

In Vitro Studies

Mouse vascular smooth muscle cells (MOVAS) were bought from the American Type Culture Collection (ATTC, Manassas, VA, USA). Cells were cultured in high glucose Dulbecco's Modified Eagle's Medium (ATTC) supplemented with 10% FCS (Gibco, Life Technology, Vienna, Austria) and an antibiotic mixture of 1% penicillin/streptomycin (Gibco) at 37°C in a humidified, 5% CO_2 atmosphere. Cells were seeded in six-well plates at a density of 1.0×10^4 cells/cm^2. At confluence, the medium was supplemented with either 1.25 mM β-glycerophosphate (βGP) (Sigma Aldrich, St. Louis, MO, USA) and 25 μg/mL ascorbic acid (AA) (Sigma Aldrich) or with 2.5 mM βGP and 50 μg/mL AA for 7, 14, and 21 days to induce calcification (24).

To induce or inhibit autophagy, cells were exposed to 10 μM rapamycin (LC labs), to 5 mM 3-methyladenine (3-MA) (Sigma Aldrich) or to 20 nM bafilomycin A1 (Sigma Aldrich). The medium including rapamycin, 3-MA, or bafilomycin was changed every other day.

To measure the autophagic flux on day 21, cells were exposed to 50 nM bafilomycin A1 for 3 h before harvesting.

Reverse Transcription Real-Time Polymerase Chain Reaction

Murine tissue and cells were stored at −80°C and the AllPrep®DNA/RNA/Protein Mini Kit (Qiagen, Venlo, Netherlands) was used to

isolate RNA, strictly following the manufacturer's instructions. Complementary DNA transcripts from RNA was synthesized by using Superscript III Transcription Kit (Invitrogen, Carlsbad, CA, USA) and random primers (Invitrogen) for reverse transcription of 100 ng total RNA. Real-time PCR was performed in duplicates on a CFX96 Real-Time System (BioRad, Hercules, CA, USA).

For quantification of respective genes, TaqMan gene expression assays (Applied Biosystems, Foster City, DA, USA) for *Trp53in* (Mm00458142_g1), *Igfbp3* (Mm01187817_m1), *Hmox1* (Mm00516005-m1), *Adrb2* (Mm02524224_s1), *Atg16l1* (Mm00513085_m1), *Il-1beta* (Mm00434228_m1), *Tnf-alpha* (Mm00443258_m1), *Tbx21* (Mm00450960_m1), *Il-6* (Mm00446190_m1), *Foxp3* (Mm00475162_m1), and *Sm22*-α (Mm00441661_g1) were used. SYBR Green Mastermix (BioRad) was used for the detection of *Hprt* and *Runx2* with the following primers: *Hprt* forward 5′GCT TCC TCC TCA GAC CGC TTT TTG C 3′ and reverse 5′ATC GCT AAT CAC GAC GCT GGG ACT G 3′. *Runx2* forward 5′TCC TAT CTG AGC CAG ATG ACA TCC 3′ and reverse 5′CCG GTC TCC CCC GGG TAC C 3′. *Hprt* gene served as the housekeeping reference. Results were calculated with the 2ΔΔCT method.

Western Blot Analysis

Protein was isolated by sonicating murine tissue as well as cells in a homogenization buffer (0.25 mol/L sucrose, 10 mmol/L HEPES, pH 7.5, and 1 mmol/L EDTA, pH 8.0) containing HALTTM Protease Inhibitor Cocktail, EDTA-free (Thermo Fisher Scientific, Rockford, IL, USA) and quantified with PierceTM BCA Protein Assay Kit (Thermo Fisher Scientific) according to the manufactures' instruction. Aliquots of total protein were separated using 12% sodium dodecyl sulfate polyacrylamide gel electrophoresis for 1.5–2 h at 100 V. Subsequently, proteins were transferred to polyvinylidene fluoride membranes (Merck Millipore, Burlington, MA, USA) for 90 min 150 mA. Membranes were blocked in 5% nonfat dry milk/TBST for 3 h at room temperature and subsequently incubated with primary antibodies against GAPDH (Cell Signalling, Cambridge, UK), p62 (Abcam, Cambridge, UK), and LC3 (Novus Biologicals, Littleton, CO, USA) overnight at 4°C, followed by the appropriate HRP-conjugated secondary antibody (Cell Signalling) for 1 h at room temperature. Protein signals were visualized using PierceTM ECL Western Blotting Substrate (Thermo Fisher Scientific) and a ChemiDoc System (BioRad). Densitometric analyses were performed using Image Lab software (BioRad).

Biochemical Analyses and *In Vitro* Detection of Calcification

Calcium content of the aortas and the kidneys was determined using the Calcium Detection Assay Kit (Abcam) following the manufacturer's instructions and normalized to tissue weight. To quantify the calcium levels in MOVAS, cells were decalcified with HCl and the calcium content in supernatants was determined using the Calcium Detection Assay Kit (Abcam) according to the manufacturer's instruction. Total protein was quantified using the PierceTM BCA Protein Assay Kit (Thermo Scientific) following the manufacturer's instructions. The calcium content was normalized to the protein content.

Blood urea nitrogen (BUN) levels were measured using a colorimetric detection kit (Thermo Fisher Scientific) following the manufacturer's instructions.

Calcium deposition was evaluated by staining the cells with Alizarin Red (Sigma Aldrich). Cells were washed with PBS, fixed in 4% paraformaldehyde for 15 min, stained with 2% Alizarin Red for 10 min at room temperature, and rinsed with distilled water. The stained cells were extracted with 10% cetylpyridium chloride (Sigma Aldrich) for 10 min. The OD was measured at 570 nm.

Histological Evaluation

Aortas of DBA/2 mice were isolated and conserved for paraffin embedding. The extent of media calcification was determined histologically using Alizarin Red S staining. Alizarin Red staining was performed by incubating rehydrated paraffin sections in 2% Alizarin Red S solution (Sigma Aldrich) followed by rinsing in acetone and acetone xylene.

Light chain 3 was stained on paraffin sections using the three-layer immunoperoxidase staining protocol. Briefly, deparaffinized tissue sections were treated with standardized heat-mediated antigen retrieval in an automated de-cloaking chamber (Aptum, Southampton, UK), quenched in 0.3% H_2O_2 in methanol, blocked with biotin/avidin blocking kit (Vector Laboratories Inc., Burlingame, CA, USA), and stained with rabbit-derived primary antibody for LC3 (Novus Biologicals). A biotin-conjugated goat anti-rabbit IgG (Jackson ImmunoResearch Laboratories, West Grove, PA, USA) was used as a secondary antibody.

For performing nitro blue tetrazolium (NBT) staining, paraffin embedded sections were deparaffinized, washed in HBSS and incubated with NBT (1.6 mg/mL) in HBSS at 37°C for 20 min. Photographs were taken using a 20× objective.

Formalin-fixed renal tissue was embedded in paraffin and cut in 4 µm sections. The sections were stained with periodic acid Schiff's.

Immunofluorescence

MOVAS were grown on glass chamber slides and fixed in 4% paraformaldehyde for 20 min. After permeabilization with 100% ice-cold methanol, the cells were rinsed with PBS and washing buffer (0.1% BSA/PBS) and incubated for 45 min with blocking buffer. Then the slides were incubated for 1 h with the primary antibody rabbit-anti-α-smooth muscle actin (SMA) (Sigma Aldrich). The slides were extensively washed and incubated with FITC conjugated secondary antibody for 1 h at room temperature. Slides were mounted in ProLong Gold anti-fade with DAPI (Thermo Fisher Scientific) for imaging. Evaluation was performed on an LSM510 META (Zeiss, Oberkochen, Germany).

Statistical Analyses

All statistical analyses were performed using GraphPad Prism 6.0 (GraphPad Software, La Jolla, CA, USA) and results are shown as mean ± SEM. Testing for normality was done using the Kolmogorov–Smirnov test with Dallal–Wilkinson–Lillifors correction. When comparing two groups, according to the distribution nonparametric Mann–Whitney *U* test or unpaired Student's *t*-test was used. When comparing three or more groups, ANOVA or Kruskal–Wallis test was performed with subsequent Dunn's test with adjustment for multiple comparisons. The survival

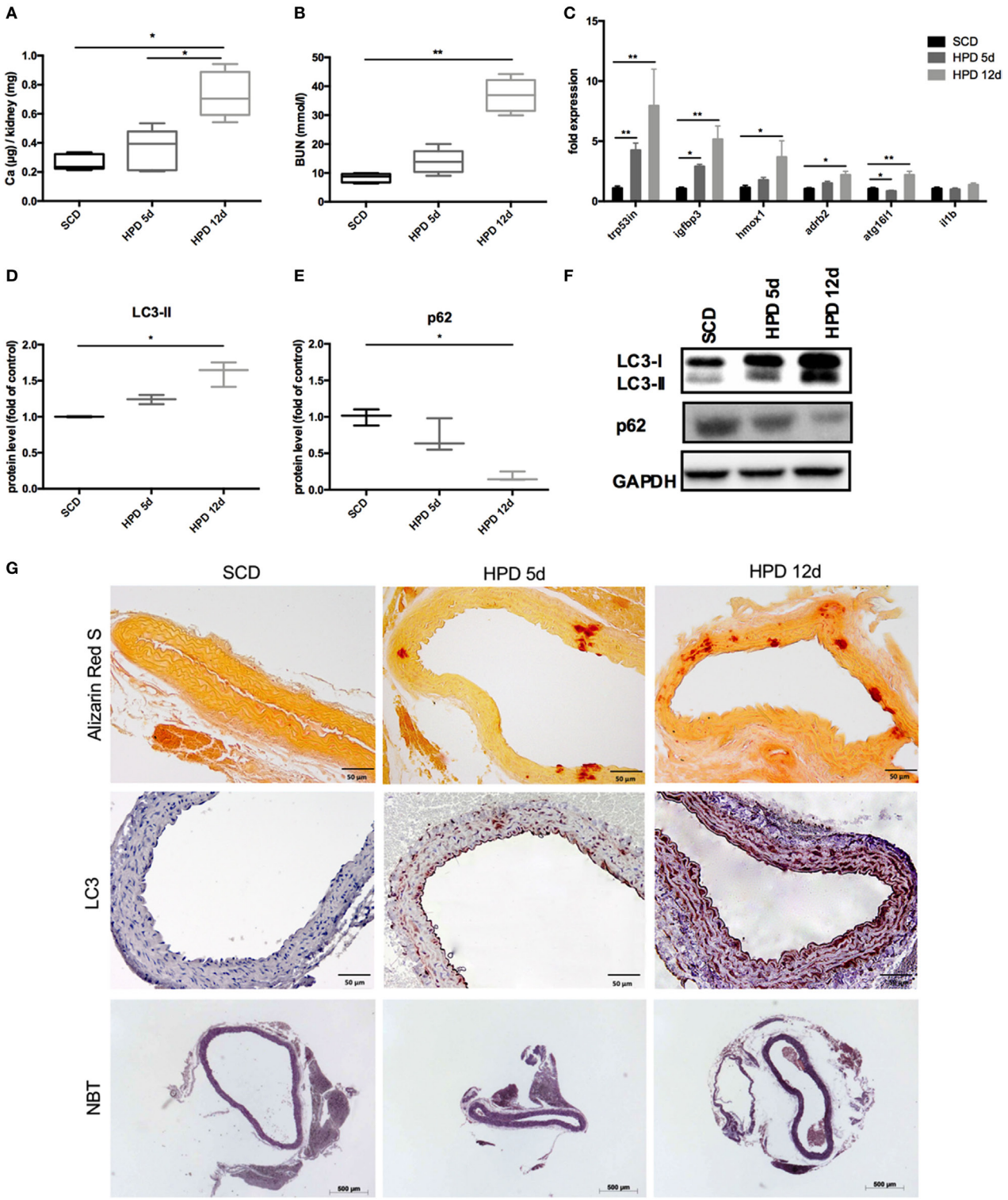

FIGURE 1 | Autophagy is increased in uremic media calcification. DBA/2 mice were fed with high-phosphate diet (HPD; gray bars) or standard chow diet (SCD; black bars) for 5 or 12 days, respectively (SCD: $n = 11$; HPD 5d: $n = 6$, HPD 12d $n = 4$). **(A)** Calcium content in kidneys was measured quantitatively. **(B)** Blood urea nitrogen (BUN) levels were evaluated. **(C)** qPCR analysis of respective autophagy related genes and *Il-1beta* was performed from aortas. Western Blot analysis for **(D)** light chain 3 (LC3) and **(E)** p62 levels was performed. Three independent experiments have been performed. **(F)** A representative western blot is provided. **(G)** Aortas of SCD- and HPD-fed mice were stained with Alizarin Red, with an antibody detecting LC3 or nitro blue tetrazolium (NBT). Representative pictures from aorta sections are shown. All data are presented as mean ± SEM. $^{*}p < 0.05$, $^{**}p < 0.01$.

comparison of rapamycin and vehicle-treated mice were plotted using the Kaplan–Meier method and log-rank (Mantel-Cox) test. A two-sided $p < 0.05$ was considered statistically significant.

RESULTS

Induction of Autophagy in Aortic VSMC in an *In Vivo* Model of Uremic Media Calcification

DBA/2 mice develop uremic media calcification when treated with HPD (13, 14). This was confirmed in our mice by measuring the calcium content in the kidney quantitatively (**Figure 1A**) and by evaluating BUN levels (**Figure 1B**) 5 and 12 days after starting HPD as compared to standard chow diet (SCD)-treated mice. By performing gene chip arrays, we previously detected autophagy pathway-associated genes to be regulated in DBA/2 mice that were subjected to HPD (14). We already showed an increase of *Trp53* and *Igfbp3* mRNA in aortas of HPD mice after 5 and 14 days (14). Therefore, we further evaluated DBA/2 mice for calcification and induction of autophagy in the aorta. We confirmed the increase in the autophagy-associated genes *Trp53in* and *Igfbp3* in aortas of 5 days HPD-treated mice as compared to SCD-treated

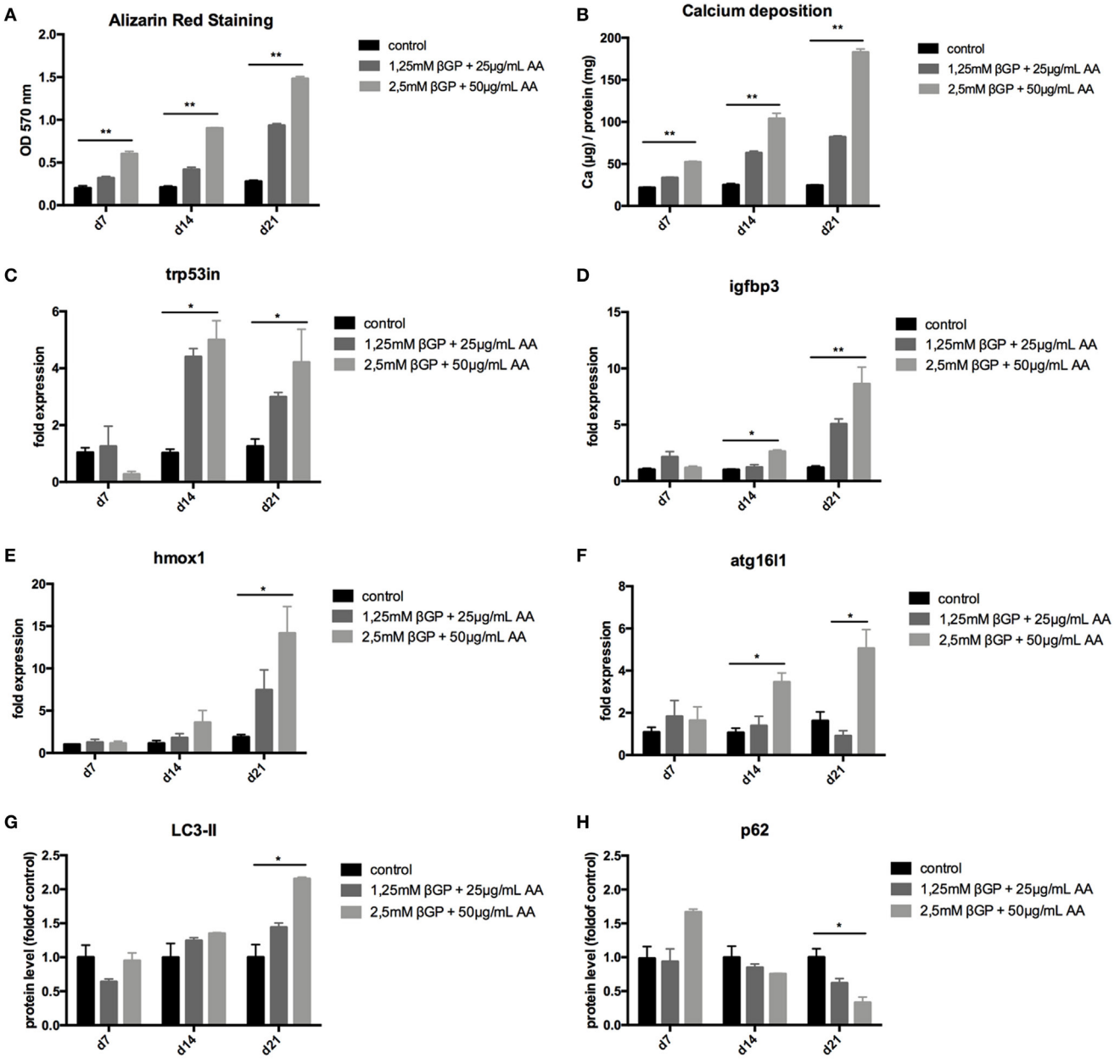

FIGURE 2 | Continued

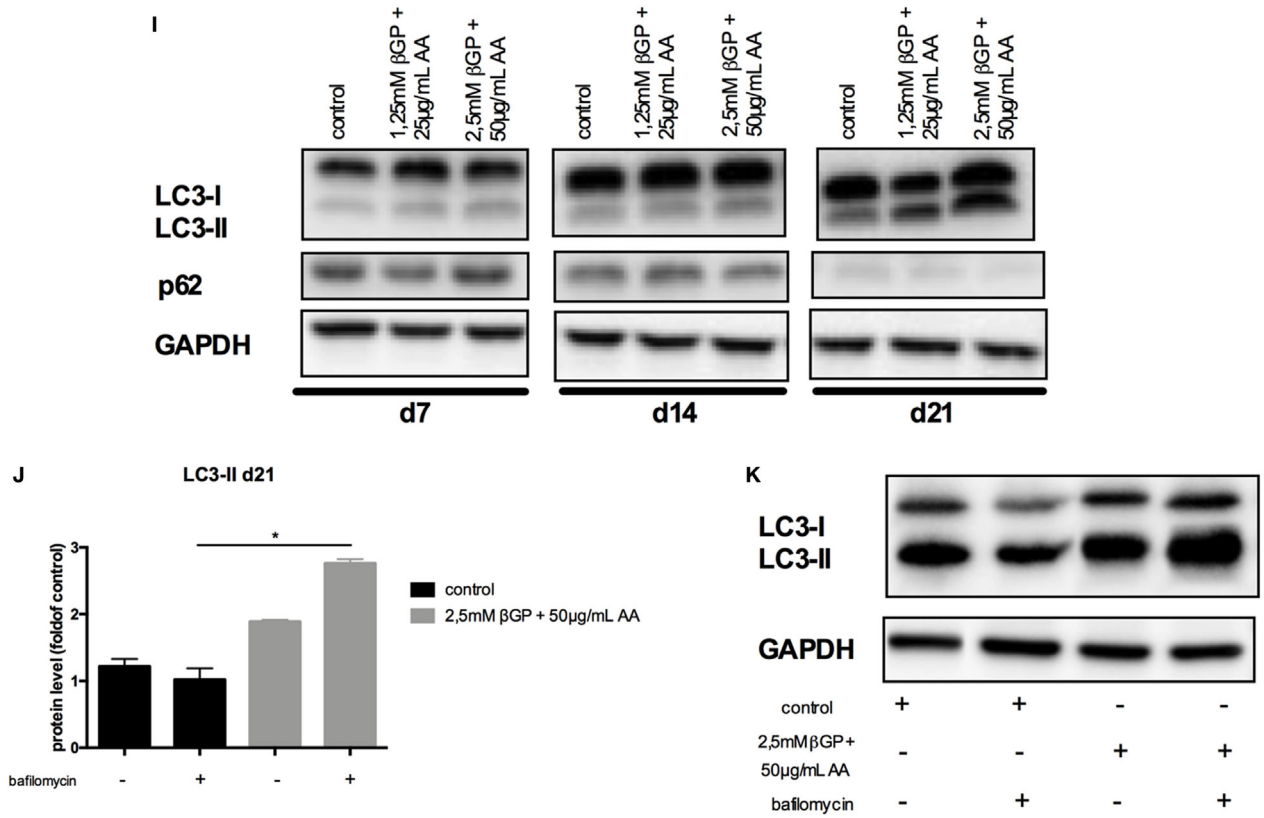

FIGURE 2 | Calcification induces autophagy in MOVAS. MOVAS were cultured in the absence (black bars) or the presence (gray bars) of two different calcifying conditions for 7, 14, or 21 days ($n = 4$ per time point and group). **(A)** Calcium deposition in cells was analyzed by Alizarin staining and photometric quantification. **(B)** The cellular calcium content was evaluated quantitatively. **(C–F)** qPCR analysis for respective autophagy-associated genes was performed. Western Blot analysis for detection of **(G)** light chain 3 (LC3) and **(H)** p62 levels was performed. Three independent experiments were performed. **(I)** A representative western blot is shown. **(J,K)** After 21 days of culture, the autophagic flux was evaluated in MOVAS after short-term bafilomycin treatment ($n = 3$). **(K)** A representative LC3 Western blot is shown. All data are presented as mean ± SEM. $^{*}p < 0.05$, $^{**}p < 0.01$.

controls, which was even more pronounced after 12 days of HPD treatment (**Figure 1C**). Also other autophagy-associated genes such as *Hmox1*, *Adrb2*, and *Atg16l1* showed a comparable pattern of regulation (**Figure 1C**). Of note, *IL-1beta* mRNA expression in aortas was not regulated at indicated time points (**Figure 1C**). Protein markers of autophagy, namely LC3-II and p62, were regulated accordingly to gene expression data implicating activation of autophagy in the aorta of HPD-treated mice (**Figures 1D–F**). By performing Alizarin Red S staining calcification of the aorta was located to the *Tunica media* and correlated with the length of HPD treatment (**Figure 1G**). In parallel, autophagy as detected by LC3-II immunohistochemistry was found to increase in vascular smooth cells of the *Tunica media* as well as in the vascular endothelial cell layer (**Figure 1G**). Furthermore, we performed NBT staining to detect ROS production in aortic specimen. An increased staining pattern in the *Tunica media* was detected in 12 days treated HPD mice as compared to SCD mice (**Figure 1G**).

Induction of Autophagy in Mouse Vascular Smooth Muscle Cells (MOVAS) Under Calcifying Conditions

To mimic vascular calcification in smooth muscle cells *in vitro*, cells were subjected to calcifying conditions by supplementing the medium with two different concentrations of AA and β-glycerolphosphate for up to 21 days. These conditions resulted in increased calcification of MOVAS both over time and with increasing phosphate and AA supplementation as shown by quantification of Alizarin Red S stains (**Figure 2A**) and of the cellular calcium content (**Figure 2B**). Starting from day 14, autophagy-associated genes *Trp53in*, *Igfbp3*, *Hmox1*, and *Atg16l1* were increased in MOVAS treated with phosphate supplementation, reaching significance in the high-phosphate supplementation group (**Figures 2C–F**). The protein marker of autophagy, LC3-II, significantly increased in MOVAS treated for 21 days with high-phosphate supplementation (**Figures 2G,I**). In line, p62 decreased under the

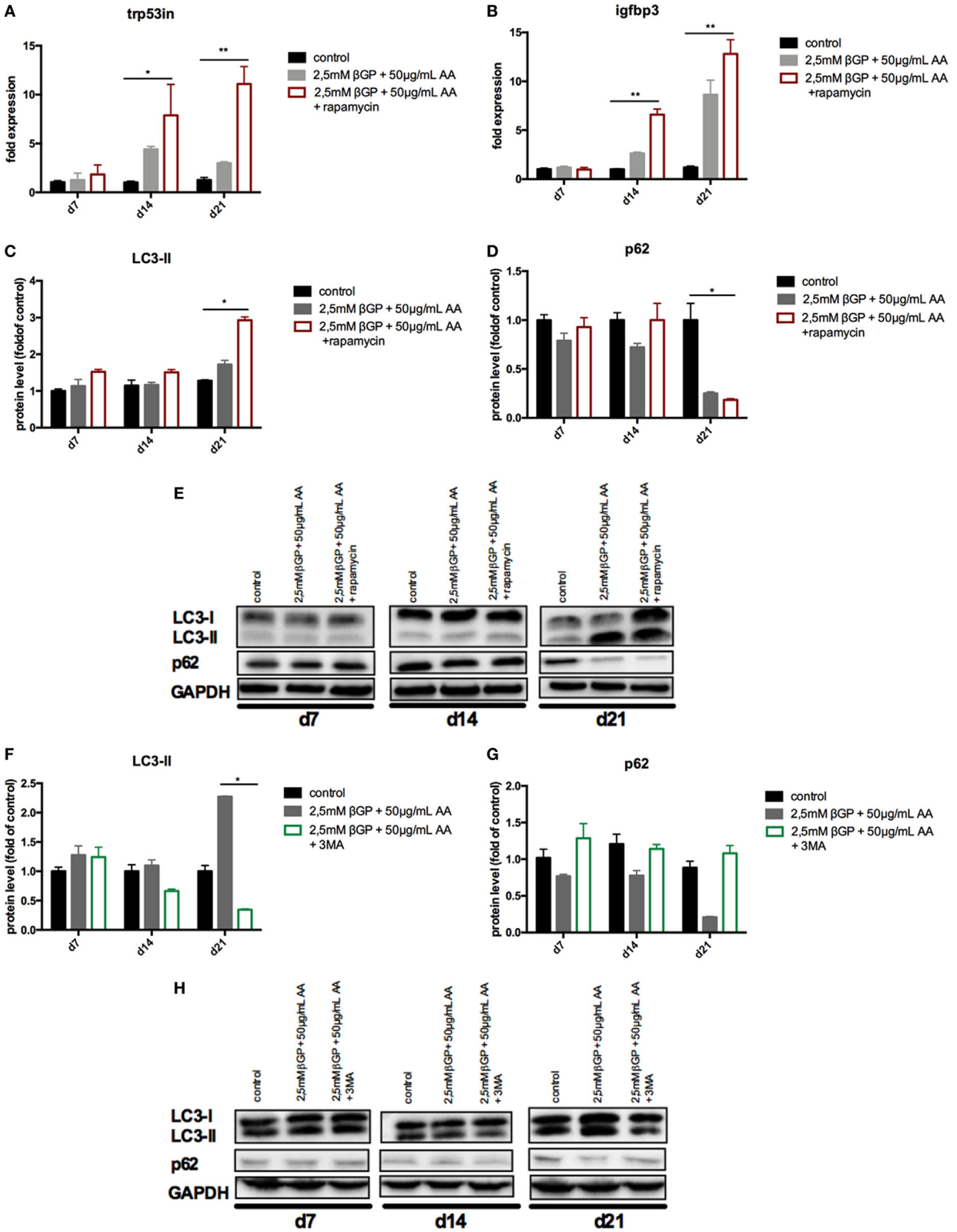

FIGURE 3 | Autophagy is influenced in MOVAS by rapamycin and 3-methyladenine (3-MA). MOVAS were cultured in the presence (gray bars) or absence of calcifying conditions (black bars) and additionally exposed to 10 µM rapamycin (red bars) or to 5 mM 3-MA (green bars) for 7, 14, or 21 days. qPCR analysis [**(A,B)**; $n = 4$] from cells as well as Western Blot analysis [**(C–H)**; $n = 3$] were performed. Representative western blots for each treatment are shown **(E,H)**. All data are presented as mean ± SEM. $^{*}p < 0.05$, $^{**}p < 0.01$.

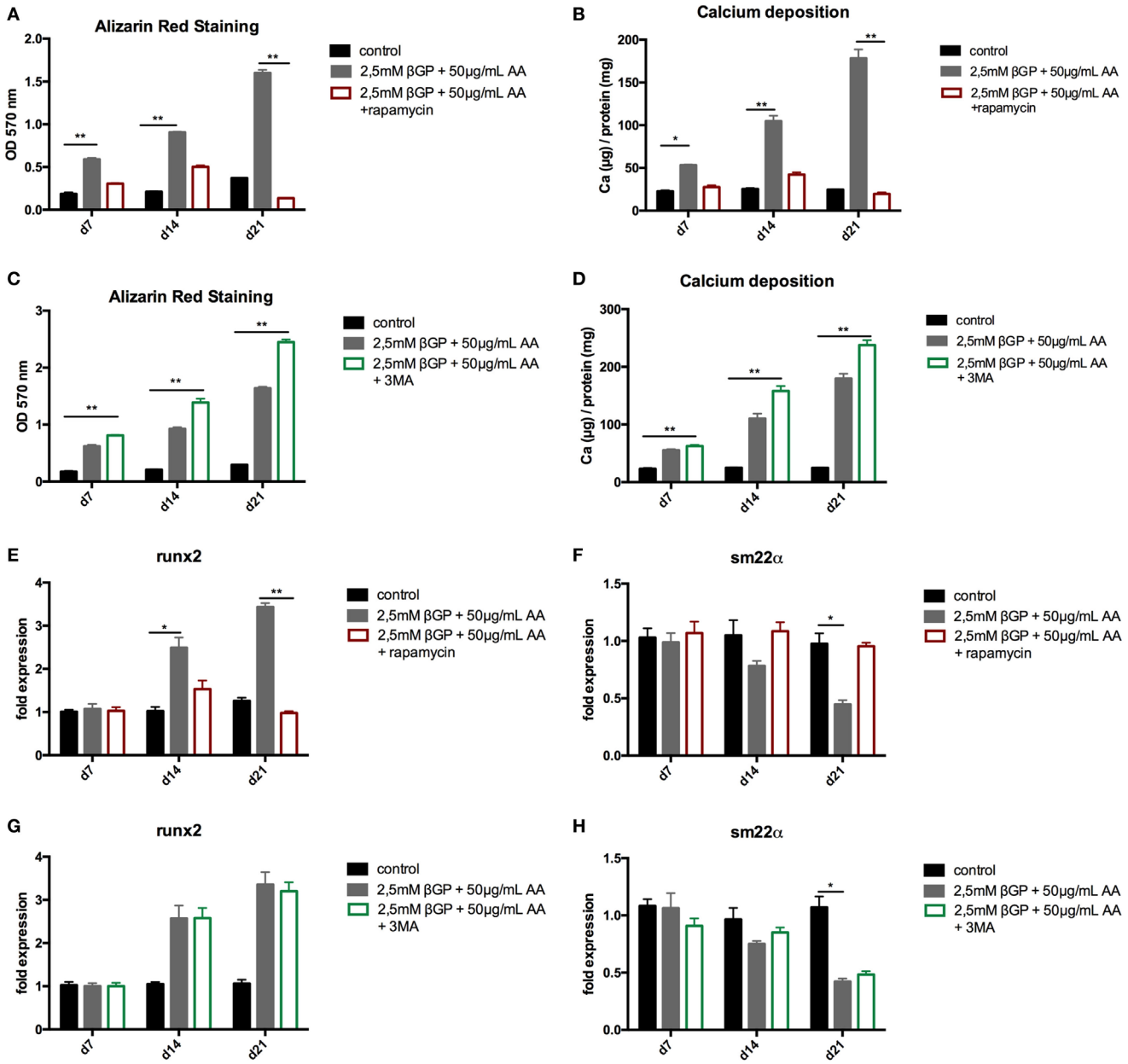

FIGURE 4 | Induction and blockade of autophagy influences calcification of MOVAS. MOVAS were cultured in the presence (gray bars) or absence of calcifying conditions (black bars) and additionally exposed to 10 µM rapamycin (red bars) or to 5 mM 3-methyladenine (3-MA) (green bars) for 7, 14, or 21 days. Quantification of Alizarin Red S ($n = 4$) staining of cells treated either with rapamycin **(A)** or 3-MA **(C)** was done. Cells treated with rapamycin **(B)** or 3-MA **(D)** were analyzed for their calcium content. qPCR analysis [**(E–H)**; $n = 4$] from cells were performed. All data are presented as mean ± SEM. $^{*}p < 0.05$, $^{**}p < 0.01$.

same conditions (**Figures 2H,I**). To evaluate the autophagic flux in our cells, MOVAS were treated with calcifying and non-calcifying conditions. After 21 days, they were subjected to bafilomycin for 3 h and subsequently analyzed for their LC3-II content. LC3-II was increased in MOVAS treated with bafilomycin as compared to respective controls proving that the calcifying medium increased autophagy in MOVAS (**Figures 2J,K**).

Induction of Autophagy by Rapamycin-Treatment Decreased Calcification in MOVAS

To influence autophagy in MOVAS, cells subjected to calcifying conditions (50 µg/mL AA and 2.5 mM β-glycerolphosphate) were treated with 10 µM rapamycin or 3-MA in order to increase or block autophagy, respectively. Rapamycin treatment nearly

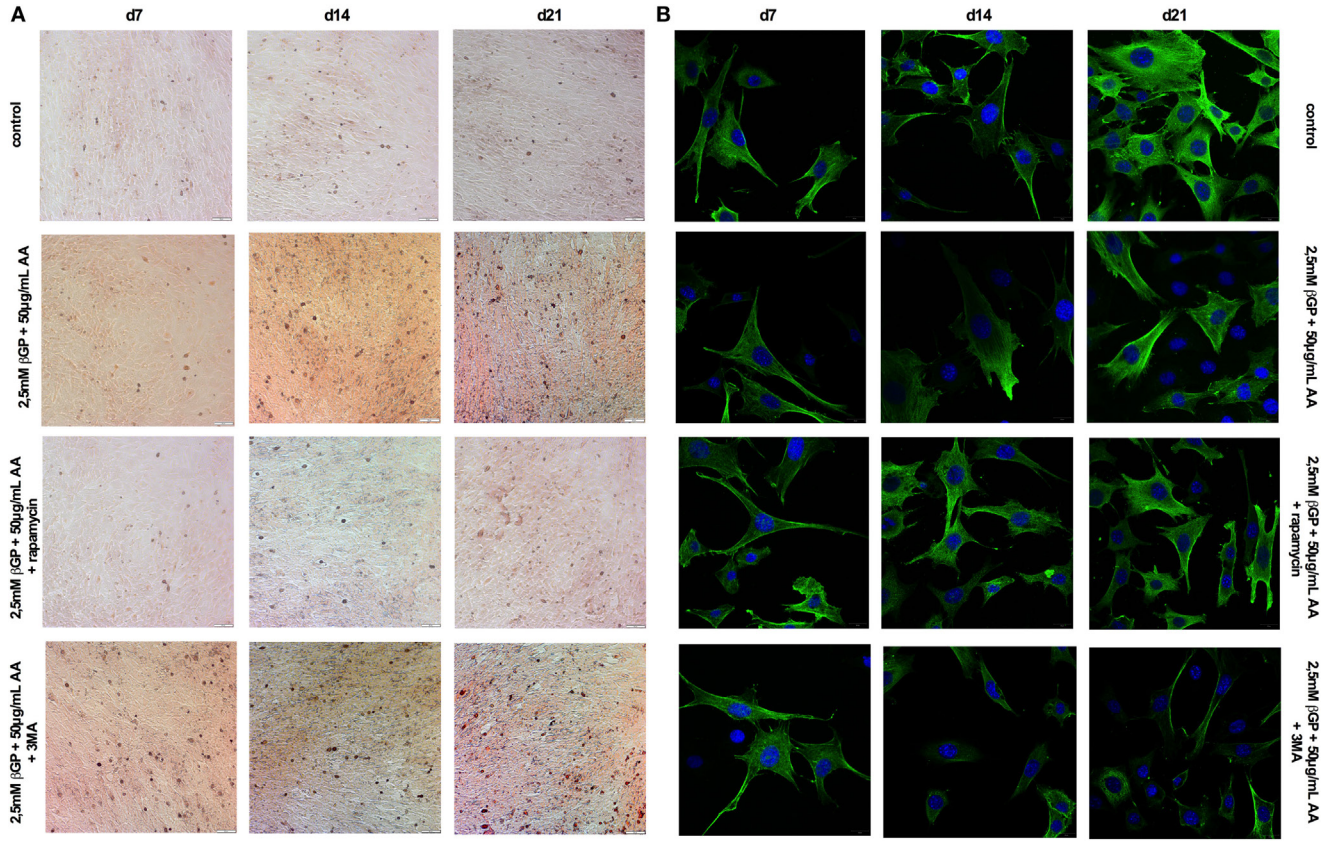

FIGURE 5 | Induction and blockade of autophagy influences calcification and α-smooth muscle actin (SMA) expression of MOVAS. MOVAS were cultured in the presence or absence of calcifying conditions and additionally exposed to 10 µM rapamycin or to 5 mM 3-methyladenine (3-MA) for 7, 14, or 21 days. Representative pictures from **(A)** Alizarin Red S and **(B)** α-SMA stained cells are shown.

doubled the mRNA expression of the autophagy-associated genes *Trp53in* and *Igfbp3* after 14 and 21 days (**Figures 3A,B**). LC3-II protein was 1.5-fold increased in MOVAS under calcifying conditions as compared to control cells. Adding rapamycin to the calcifying medium resulted in a threefold increase in LC3-II protein on day 21 (**Figures 3C,E**). The level of p62 protein expression were comparable between MOVAS under calcifying conditions with or without rapamycin (**Figures 3D,E**). Nevertheless, a significant reduction of p62 protein in MOVAS was only detected under calcifying conditions with rapamycin as compared to MOVAS treated with control medium after 21 days of culture (**Figures 3D,E**). Even though rapamycin only moderately induced autophagy in MOVAS, calcification as measured by Alizarin stain was decreased by rapamycin already after 7 days of treatment. Significance was reached after 21 days of treatment (**Figures 4A** and **5A**). This was confirmed by measuring the calcium content quantitatively in the cells (**Figure 4B**). *Runx2* mRNA expression, as a marker of osteoblastic VSMC differentiation, increased in MOVAS under calcifying conditions after 14 and 21 days (**Figure 4E**). This increase was blunted by rapamycin treatment (**Figure 4E**). *Sm22*α transcription as a marker for adult VSMCs was decreased in MOVAS under calcifying conditions after 21 days, which was abolished when cells were additionally treated with rapamycin (**Figure 4F**). Also α-SMA stainings as a marker for cellular contractility was found to be decreased in MOVAS after 14 and 21 days of calcifying conditions, which was blunted by rapamycin treatment (**Figure 5B**).

Next, MOVAS under calcifying conditions were treated with 3-MA, which blocks autophagy. After 21 days of treatment 3-MA reversed LC3-II and p62 protein levels to MOVAS incubated with standard medium (**Figures 3F–H**). Calcification of MOVAS increased by 3-MA treatment after 14 and 21 days (**Figures 4C,D**). 3-MA treatment did not differentially regulate *Runx2* and *Sm22*α transcription as compared to MOVAS under calcifying conditions (**Figures 4G,H**). α-SMA protein expression was further decreased in MOVAS treated with 3-MA after 14 and 21 days as compared to MOVAS under calcifying conditions (**Figure 5B**). Of note, we saw a similar regulation pattern when using an alternative autophagy blocker, namely bafilomycin (Figure S1 in Supplementary Material).

As control MOVAS incubated with standard medium were treated with either rapamycin, 3-MA, or bafilomycin, but no differences in the level of autophagy-associated genes and proteins was detected as compared to MOVAS incubated with standard medium (Figure S2 in Supplementary Material).

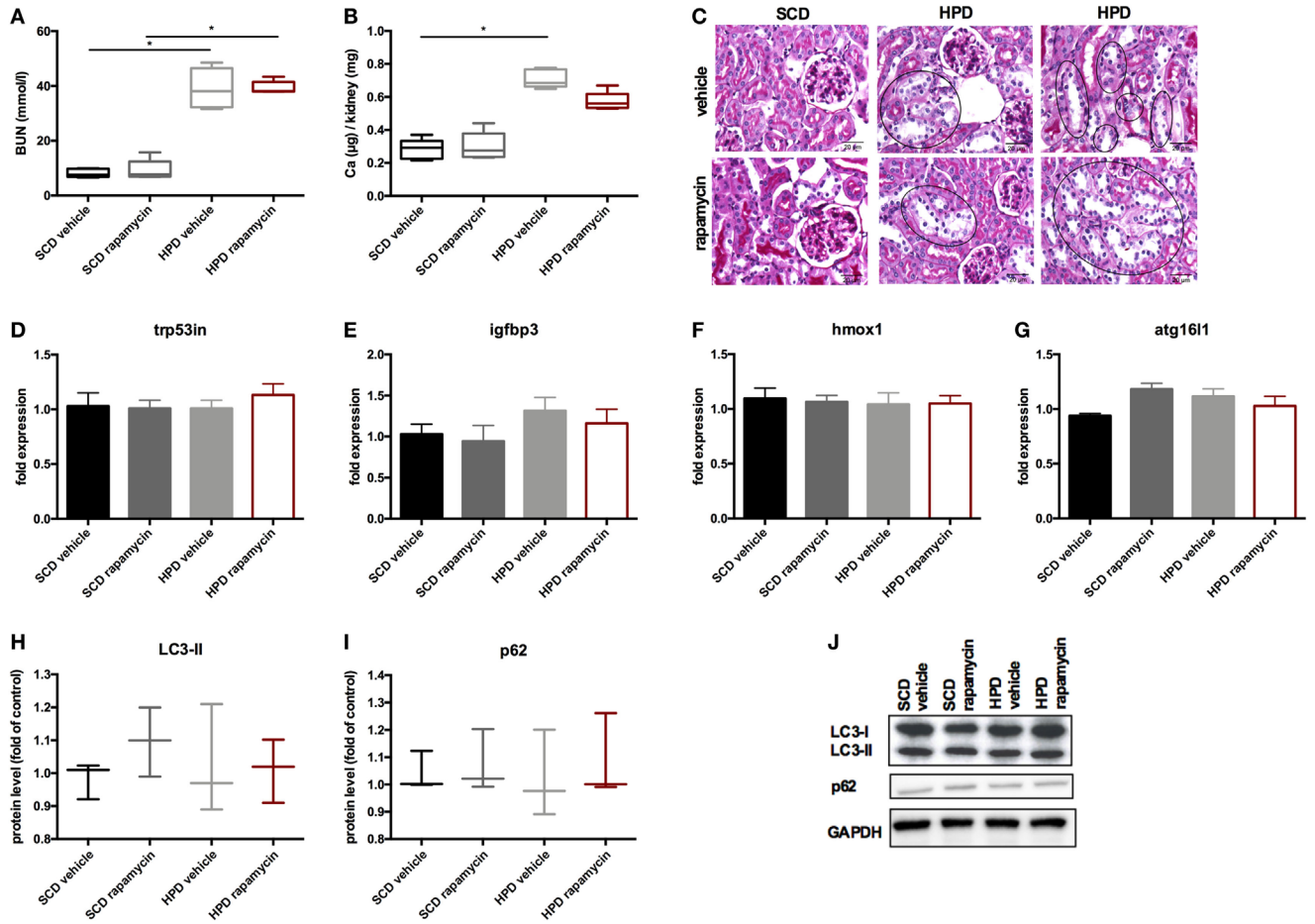

FIGURE 6 | Rapamycin does not influence the renal phenotype. DBA/2 mice were fed with high-phosphate diet (HPD) or standard chow diet (SCD) for 12 days and were additionally treated with rapamycin or vehicle starting from day −3 (SCD + vehicle: black bar, SCD + Rapa: gray bar; HPD + vehicle: light gray bar; HPD + Rapa: red bar). **(A)** Serum-blood urea nitrogen (BUN) levels and **(B)** calcium content of the kidneys was evaluated in mice 12 days after starting HPD ($n = 5$). **(C)** Representative pictures of periodic acid Schiff's stained kidney sections are provided. Areas of early necrotic tubular epithelial cells are marked by black circles. **(D–G)** qPCR analysis ($n = 5$ per group) for expression of respective autophagy-associated genes was performed from kidney tissue. **(H)** Light chain 3 (LC3) and **(I)** p62 levels were evaluated by Western Blot analysis ($n = 3$). A representative Western blot is shown **(J)**.

Rapamycin-Treatment Improves Uremic Media Calcification and Survival *In Vivo*

To increase autophagy *in vivo*, DBA/2 mice were treated with 0.5 mg/kg body weight of rapamycin or vehicle once daily starting 3 days before starting HPD. Controls were treated either with rapamycin or vehicle and were fed with SCD. First, mice were evaluated for the renal phenotype. DBA/2 mice fed with HPD displayed significantly increased BUN levels, which were not altered by rapamycin-treatment (**Figure 6A**). Also calcifications in the kidney did not significantly differ between HPD-fed mice treated with vehicle or rapamycin (**Figure 6B**). Kidney histology also remained unchanged in HPD mice treated either with vehicle or rapamycin (**Figure 6C**). HPD mice showed unaltered glomeruli, but signs of acute tubular injury mainly in the distal tubules. Distal tubular cells displayed vacuolization and loss of nuclear staining as markers for beginning cell necrosis (**Figure 6C**). Autophagy in the kidneys was not influenced by HPD or rapamycin treatment as shown by qPCR of autophagy-associated genes (**Figures 6D–G**) as well as LC3-II and p62 evaluations (**Figures 6H–J**).

Next, the vascular phenotype in aortas was evaluated. Autophagy was increased in HPD mice and rapamycin-treatment even augmented this increase as shown in autophagy-associated gene expression (**Figure 7A**) as well as increase in LC3-II and decrease in p62 protein levels (**Figures 7C–E**). Aortic calcification as shown by calcium contents in the aorta was significantly reduced in rapamycin-treated as compared to vehicle HPD mice (**Figure 7F**). Rapamycin-treatment blunted the increase of pro-inflammatory cytokine mRNA expression such as *Tnf-alpha* and *Il-6* in aortas of HPD mice (**Figure 7B**). In line, *tbx21* mRNA expression, which transcribes the master gene regulator of TH1 cells Tbet, was decreased by rapamycin-treatment in aortas of HPD-fed mice (**Figure 7B**). The master gene regulator of regulatory T cells *foxp3* was significantly increased in aortas of rapamycin-treated HPD mice (**Figure 7B**). Aortas of HPD mice showed a significant increase in the transcription of *Runx2*, which was reduced to the level found in aortas of SCD mice when HPD mice were treated with rapamycin (**Figure 7G**). Previously, we provided evidence that DBA/2 mice on HPD die because of

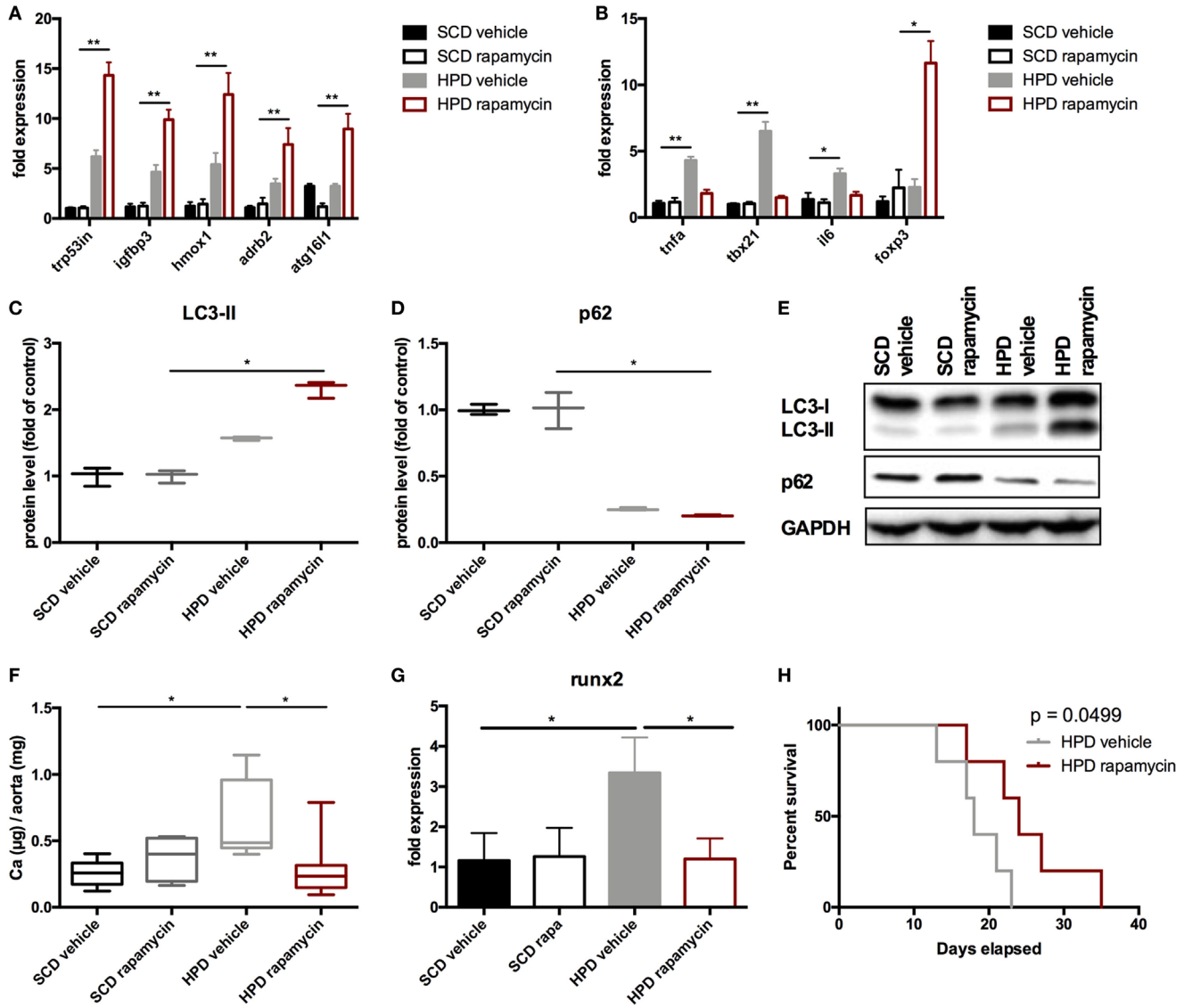

FIGURE 7 | Rapamycin ameliorates uremic media calcification. DBA/2 mice were fed with high-phosphate diet (HPD) or standard chow diet (SCD) for 12 days and were additionally treated with rapamycin or vehicle starting from day −3 (SCD + vehicle: black bar, SCD + Rapa: gray bar; HPD + vehicle: light gray bar; HPD + Rapa: red bar). qPCR analysis ($n = 5$ per group) for expression of **(A)** respective autophagy and **(B)** inflammatory genes was performed from aortic tissue. **(C)** Light chain 3 (LC3) and **(D)** p62 levels were evaluated by Western Blot analysis ($n = 3$). A representative Western blot is shown **(E)**. **(F)** The total calcium content of aortas was analyzed (SCD: $n = 5$; HPD: $n = 9$). **(G)** qPCR analysis ($n = 5$ per group) for expression of Runx2 in aortas was performed. **(H)** A Kaplan–Meier-plot of mice subjected to HPD and treated with either Rapamycin (red line) or vehicle (gray line) is provided ($n = 14$ per group). All data are presented as mean ± SEM. $^{*}p < 0.05$, $^{**}p < 0.01$.

bradycardia and sudden cardiac death due to extensive cardiovascular calcification (13). Thus, we evaluated whether rapamycin-treatment improves survival in HPD-fed mice. HPD-mice treated with rapamycin survived significantly longer when treated with rapamycin (**Figure 7H**).

Rapamycin-Treatment Delays Progression of Established Uremic Media Calcification

To test whether rapamycin has the capacity to improve uremic media calcification when started with established vascular calcification, rapamycin-treatment was started on day 5 of HPD treatment and followed until day 12. Here, rapamycin-treatment did not significantly influence LC3-II and p62 protein expression in aortas of HPD-fed mice (**Figures 8A–C**). Nevertheless, calcification of aortas was still significantly decreased in rapamycin- as compared to vehicle-treated HPD-fed mice (**Figure 8D**).

DISCUSSION

Here, we provide compelling evidence that uremic media calcification increases autophagy in VSMC *in vitro* and *in vivo*. Since pharmacologically enhancing autophagy resulted in improved

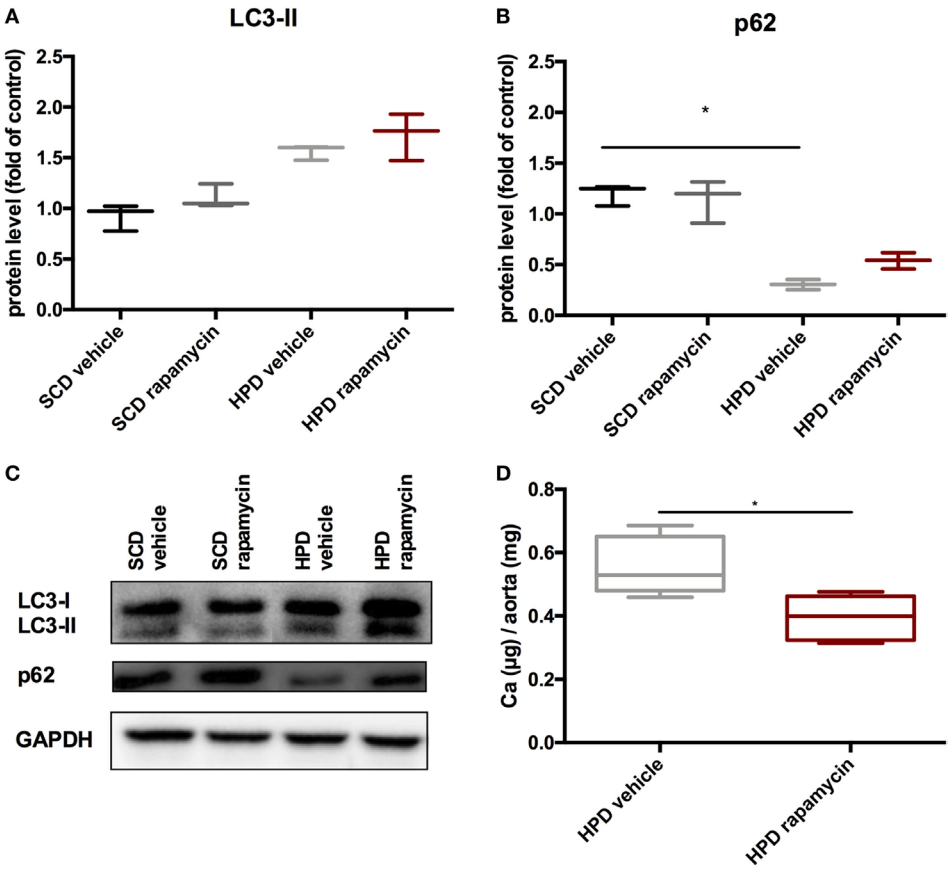

FIGURE 8 | Rapamycin improves uremic media calcification in mice with established vascular calcification. DBA/2 mice were fed with high-phosphate diet (HPD) or standard chow diet (SCD) for 12 days and were additionally treated with Rapamycin or vehicle starting from day 5 (SCD + vehicle: black bar, SCD + Rapa: gray bar; HPD + vehicle: light gray bar; HPD + Rapa: red bar). Western Blot analysis ($n = 3$) for detection of **(A)** light chain 3 (LC3) and **(B)** p62 levels were performed. **(C)** A representative Western blot is shown. **(D)** Total calcium content of aortas was evaluated ($n = 5$ per group). All data are presented as mean ± SEM. *$p < 0.05$.

uremic media calcification and survival, autophagy provides an endogenous protective response.

There exist increasing data that autophagy is a protective response of the body to counteract atherosclerosis, but those models mainly used Apo E knockout mice thereby reflecting human atherosclerosis rather than uremic media calcification (21). The data on autophagy in uremic media calcification, which critically differs from atherosclerosis in terms of histological features and pathomechanisms (25), are scarce. Dai and coworkers provided compelling *in vitro* evidence that stimulation of VSMC by high-phosphate conditions increases autophagy in cells and protects from calcification (22). We on the one hand confirmed their *in vitro* findings and on the other hand extended their findings to the *in vivo* situation. We used an acute model of uremia induced by HPD, which is accompanied by vascular media calcification (14). Here, calcification of the *Tunica media* was paralleled by an increase of autophagy in VSMC. When increasing autophagy by using rapamycin in our high-phosphate fed DBA/2 mice, we were not only able to significantly decrease calcification of aortas but also to extend the life span of mice. In our hands, rapamycin was also able to decrease calcification of the aortas when started with already established vascular calcification. Importantly, the protective effects of rapamycin were not attributable to an improved kidney function since neither renal function nor calcification was altered by rapamycin treatment. So far, we can only speculate about the different susceptibility to protection of calcification by autophagy induction in aortas versus kidney. Probably the calcification process in the kidney is overwhelming in our model thereby resulting in necrosis rather than autophagy.

A major limitation of our *in vivo* studies is the fact that the systemic anti-inflammatory effects of rapamycin may contribute to the improved outcome of rapamycin-treated mice. Rapamycin is a well-known inducer of regulatory T cells *in vivo* and *in vitro* (26, 27). In line, *Foxp3* transcription was significantly increased in aortic samples of rapamycin-treated mice while macrophage and Th1 cell marker transcription were suppressed. Still, the role of inflammation in the development of uremic media calcification is heavily discussed (14, 25, 28). Our group recently proved evidence that infiltration of immune cells in our model of acute uremic media calcification is rather a secondary phenomenon induced by calcification (14). Future *in vivo* experiments using autophagy inducers, which are more specific and do not influence the immune system such as TAT-Beclin (29), are clearly needed

to show the impact of autophagy on calcification of the aorta and survival of mice.

The classical way to induce autophagy in cells is *via* nutrient/amino acid deprivation as seen in fasting (21), which is also a plausible inducer in our model since food intake and body weight drop significantly on HPD (data not shown). Furthermore, the production of ROS induces autophagy. This activation pathway has been attributed to phosphate-induced autophagy in VSMC in the past (22) and we also found *in vivo* signs of increased ROS production in aortas induced by HPD, which were shown by NBT stains. Still, further experiments are needed to delineate the role of ROS in our *in vivo* setting. Recent evidence suggests that activation of the inflammasome increases autophagy as well. Obviously, there exists a two-way regulation since autophagy also leads to removal of intracellular DAMPs, inflammasome components, or cytokines resulting in decreased inflammasome activation (30). The autophagy related gene *Atg16l1* has been linked to the inflammasome in the past since depletion of this gene resulted in an enhanced endotoxin-induced IL-1beta production (31). We found *Atg16l1* mRNA transcripts to be significantly increased in aortic samples of HPD fed mice, but we did not detect changes in *IL-1beta* transcription levels in aortic samples of high-phosphate treated mice. Thus, this pathway might not be critically involved in the calcification process of the aorta. Most of the autophagy activation pathways have been proven to be mTOR-dependent, but also independent pathways have been described (21).

It is generally believed that autophagy releases amino acids and fatty acids to produce energy for survival. However, if cellular damage becomes irreparable, cells can destroy themselves completely by autophagy (32). So far, it has been proposed that autophagy inhibits the formation of matrix vesicle release in VSMC, which is crucial for the calcification process of the cells (22). Nevertheless, whether this process also holds true in the *in vivo* situation needs further exploration. Contrary to Dai et al. (22), we detected *Runx2* mRNA transcription—as a marker of osteogenic transdifferentiation of VSMC (33)—to be significantly increased under calcifying conditions *in vivo* and *in vitro*. Interestingly, rapamycin-treatment blunted the *Runx2* mRNA increase both in MOVAS and in the aorta of HPD-fed mice. In line with our hypothesis that autophagy inhibits osteogenic transdifferentiation of VSMCs, α-SMA protein expression and *SM22*α transcription were found to be increased in rapamycin-treated MOVAS, whereas 3-MA-treated MOVAS showed decreased expression of both markers. Reduction of both α-SMA and SM22α has been attributed to osteogenic transdifferentiation of VSMCs (34, 35).

In summary, autophagy is an endogenous protective response of VSMC during uremia to prevent calcification possibly by inhibiting osteogenic transdifferentiation of VSMCs. Increasing autophagy may be an attractive strategy to improve vascular calcification in the CKD population.

ETHICS STATEMENT

All animal experiments were approved by the Committee of the Ethics of Animal Experiments of the Austrian Ministry (BMWFW-66.010/0061-WF/V/3b/2016). All experiments were conducted under strict adherence of the law of Austria.

AUTHOR CONTRIBUTIONS

BF—performed experiments, analyzed data, and drafted the manuscript. AK, DD, and PE—designed study and revised manuscript. CS, KeS, and MK—performed experiments and revised manuscript. MP and KaS—performed experiments, analyzed data, and revised manuscript. AR—revised manuscript. KE—designed study, analyzed data, and drafted the manuscript.

FUNDING

This work was supported by the Austrian Science Funds (FWF) to PE (P27537-B26) and the PhD programs MOLMED and MOLIN (W1241) of the Medical University of Graz, which are supported by the Austrian Science Funds (FWF).

SUPPLEMENTARY MATERIAL

The Supplementary Material for this article can be found online at https://www.frontiersin.org/articles/10.3389/fimmu.2018.01866/full#supplementary-material.

FIGURE S1 | Autophagy and calcification is influenced in MOVAS by bafilomycin. MOVAS were cultured in the presence (gray bars) or absence of calcifying conditions (black bars) and additionally exposed to 20 nM bafilomycin (dashed green bars) for 7, 14, or 21 days ($n = 4$ per group). Quantification of **(A)** Alizarin Red S staining of cells and **(B)** calcium deposition in MOVAS was done. **(C,D)** qPCR as well as **(E–G)** Western Blot analysis from MOVAS were performed. Representative western blots are shown **(G)**. All data are presented as mean ± SEM. $^{*}p < 0.05$, $^{**}p < 0.01$.

FIGURE S2 | Calcification and autophagy remained unaltered in MOVAS under non-calcifying conditions by rapamycin, 3-methyladenine (3-MA), and bafilomycin. MOVAS were cultured in the absence of calcifying conditions (black bars) and additionally exposed to 10 μM rapamycin (red bars) or to 5 mM 3-MA (green bars) or to 20 nM bafilomycin (dashed green bars) for 7, 14, or 21 days ($n = 4$ per group). Quantification of **(A)** Alizarin Red S staining of cells and **(B)** calcium deposition in MOVAS was done. **(C–F)** qPCR as well as **(G–L)** Western Blot analysis from MOVAS were performed. Representative western blots are shown **(I,L)**. All data are presented as mean ± SEM.

REFERENCES

1. Go AS, Chertow GM, Fan DJ, McCulloch CE, Hsu CY. Chronic kidney disease and the risks of death, cardiovascular events, and hospitalization. *N Engl J Med* (2004) 351:1296–305. doi:10.1056/NEJMoa041031
2. London GM. Cardiovascular calcifications in uremic patients: clinical impact on cardiovascular function. *J Am Soc Nephrol* (2003) 14:S305–9. doi:10.1097/01.ASN.0000081664.65772.EB
3. Vervloet M, Cozzolino M. Vascular calcification in chronic kidney disease: different bricks in the wall? *Kidney Int* (2017) 91:808–17. doi:10.1016/j.kint.2016.09.024
4. London GM, Guerin AP, Marchais SJ, Metivier F, Pannier B, Adda H. Arterial media calcification in end-stage renal disease: impact on all-cause and cardiovascular mortality. *Nephrol Dial Transplant* (2003) 18:1731–40. doi:10.1093/ndt/gfg414
5. Cannata-Andía JB, Martin KJ. The challenge of controlling phosphorus in chronic kidney disease. *Nephrol Dial Transplant* (2016) 31:541–7. doi:10.1093/ndt/gfv055

6. Paloian NJ, Giachelli CM. A current understanding of vascular calcification in CKD. *Am J Physiol Renal Physiol* (2014) 307:F891–900. doi:10.1152/ajprenal.00163.2014
7. Schlieper G, Schurgers L, Brandenburg V, Reutelingsperger C, Floege J. Vascular calcification in chronic kidney disease: an update. *Nephrol Dial Transplant* (2016) 31:31–9. doi:10.1093/ndt/gfv111
8. Foley RN, Collins AJ, Herzog CA, Ishani A, Kalra PA. Serum phosphorus levels associate with coronary atherosclerosis in young adults. *J Am Soc Nephrol* (2009) 20:397–404. doi:10.1681/ASN.2008020141
9. Foley RN. Phosphate levels and cardiovascular disease in the general population. *Clin J Am Soc Nephrol* (2009) 4:1136–9. doi:10.2215/CJN.01660309
10. Adeney KL, Siscovick DS, Ix JH, Seliger SL, Shlipak MG, Jenny NS, et al. Association of serum phosphate with vascular and valvular calcification in moderate CKD. *J Am Soc Nephrol* (2009) 20:381–7. doi:10.1681/ASN.2008040349
11. Shobeiri N, Adams MA, Holden RM. Vascular calcification in animal models of CKD: a review. *Am J Nephrol* (2010) 31:471–81. doi:10.1159/000299794
12. Eller P, Eller K, Kirsch AH, Patsch JJ, Wolf AM, Tagwerker A, et al. A murine model of phosphate nephropathy. *Am J Pathol* (2011) 178:1999–2006. doi:10.1016/j.ajpath.2011.01.024
13. Kirsch AH, Smaczny N, Riegelbauer V, Sedej S, Hofmeister A, Stojakovic T, et al. Regulatory T cells improve nephrocalcinosis but not dystrophic cardiac calcinosis in DBA/2 mice. *Am J Pathol* (2013) 183:382–90. doi:10.1016/j.ajpath.2013.04.012
14. Kirsch AH, Kirsch A, Artinger K, Schabhüttl C, Goessler W, Klymiuk I, et al. Heterogeneous susceptibility for uraemic media calcification and concomitant inflammation within the arterial tree. *Nephrol Dial Transplant* (2015) 30:1995–2005. doi:10.1093/ndt/gfv265
15. Meng H, Vera I, Che N, Wang X, Wang SS, Ingram-Drake L, et al. Identification of Abcc6 as the major causal gene for dystrophic cardiac calcification in mice through integrative genomics. *Proc Natl Acad Sci U S A* (2007) 104:4530–5. doi:10.1073/pnas.0607620104
16. Choi AMK, Ryter SW, Levine B. Autophagy in human health and disease. *N Engl J Med* (2013) 368:1845–6. doi:10.1056/NEJMc1303158
17. Devenish RJ. Autophagy and the evasion of host defense: a new variation on the theme for Burkholderia cepacia? *Autophagy* (2011) 7:1269–70. doi:10.4161/auto.7.11.17941
18. Feng Y, He D, Yao Z, Klionsky DJ. The machinery of macroautophagy. *Cell Res* (2014) 24:24–41. doi:10.1038/cr.2013.168
19. Kabeya Y, Mizushima N, Ueno T, Yamamoto A, Kirisako T, Noda T, et al. LC3, a mammalian homologue of yeast Apg8p, is localized in autophagosome membranes after processing. *EMBO J* (2000) 19:5720–8. doi:10.1093/emboj/19.21.5720
20. Komatsu M, Waguri S, Koike M, Sou Y-S, Ueno T, Hara T, et al. Homeostatic levels of p62 control cytoplasmic inclusion body formation in autophagy-deficient mice. *Cell* (2007) 131:1149–63. doi:10.1016/j.cell.2007.10.035
21. Nussenzweig SC, Verma S, Finkel T. The role of autophagy in vascular biology. *Circ Res* (2015) 116:480–8. doi:10.1161/CIRCRESAHA.116.303805
22. Dai X-Y, Zhao M-M, Cai Y, Guan Q-C, Zhao Y, Guan Y, et al. Phosphate-induced autophagy counteracts vascular calcification by reducing matrix vesicle release. *Kidney Int* (2013) 83:1042–51. doi:10.1038/ki.2012.482
23. Peng Y-Q, Xiong D, Lin X, Cui R-R, Xu F, Zhong J-Y, et al. Oestrogen inhibits arterial calcification by promoting autophagy. *Sci Rep* (2017) 7:3549. doi:10.1038/s41598-017-03801-x
24. Mackenzie NCW, Zhu D, Longley L, Patterson CS, Kommareddy S, MacRae VE. MOVAS-1 cell line: a new in vitro model of vascular calcification. *Int J Mol Med* (2011) 27:663–8. doi:10.3892/ijmm.2011.631
25. Amann K. Media calcification and intima calcification are distinct entities in chronic kidney disease. *Clin J Am Soc Nephrol* (2008) 3:1599–605. doi:10.2215/CJN.02120508
26. Battaglia M, Stabilini A, Draghici E, Gregori S, Mocchetti C, Bonifacio E, et al. Rapamycin and interleukin-10 treatment induces T regulatory type 1 cells that mediate antigen-specific transplantation tolerance. *Diabetes* (2006) 55:40–9. doi:10.2337/diabetes.55.01.06.db05-0613
27. Battaglia M, Stabilini A, Roncarolo M-G. Rapamycin selectively expands CD4+CD25+FoxP3+ regulatory T cells. *Blood* (2005) 105:4743–8. doi:10.1182/blood-2004-10-3932
28. Yamada S, Tokumoto M, Tatsumoto N, Taniguchi M, Noguchi H, Nakano T, et al. Phosphate overload directly induces systemic inflammation and malnutrition as well as vascular calcification in uremia. *Am J Physiol Renal Physiol* (2014) 306:F1418–28. doi:10.1152/ajprenal.00633.2013
29. Shoji-Kawata S, Sumpter R, Leveno M, Campbell GR, Zou Z, Kinch L, et al. Identification of a candidate therapeutic autophagy-inducing peptide. *Nature* (2013) 494:201–6. doi:10.1038/nature11866
30. Sun Q, Fan J, Billiar TR, Scott MJ. Inflammasome and autophagy regulation – a two-way street. *Mol Med* (2017) 23:188–95. doi:10.2119/molmed.2017.00077
31. Saitoh T, Fujita N, Jang MH, Uematsu S, Yang B-G, Satoh T, et al. Loss of the autophagy protein Atg16L1 enhances endotoxin-induced IL-1beta production. *Nature* (2008) 456:264–8. doi:10.1038/nature07383
32. Das G, Shravage BV, Baehrecke EH. Regulation and function of autophagy during cell survival and cell death. *Cold Spring Harb Perspect Biol* (2012) 4(6):a008813. doi:10.1101/cshperspect.a008813
33. Nakahara T, Sato H, Shimizu T, Tanaka T, Matsui H, Kawai-Kowase K, et al. Fibroblast growth factor-2 induces osteogenic differentiation through a Runx2 activation in vascular smooth muscle cells. *Biochem Biophys Res Commun* (2010) 394:243–8. doi:10.1016/j.bbrc.2009.11.038
34. Montes de Oca A, Madueño JA, Martinez-Moreno JM, Guerrero F, Muñoz-Castañeda J, Rodriguez-Ortiz ME, et al. High-phosphate-induced calcification is related to SM22α promoter methylation in vascular smooth muscle cells. *J Bone Miner Res* (2010) 25:1996–2005. doi:10.1002/jbmr.93
35. Satomi-Kobayashi S, Kinugasa M, Kobayashi R, Hatakeyama K, Kurogane Y, Ishida T, et al. Osteoblast-like differentiation of cultured human coronary artery smooth muscle cells by bone morphogenetic protein endothelial cell precursor-derived regulator (BMPER). *J Biol Chem* (2012) 287:30336–45. doi:10.1074/jbc.M111.329110

Conflict of Interest Statement: The authors declare that the research was conducted in the absence of any commercial or financial relationships that could be construed as a potential conflict of interest.

frontiers in Immunology

ORIGINAL RESEARCH
published: 08 August 2018
doi: 10.3389/fimmu.2018.01850

Neutrophil Depletion Exacerbates Pregnancy Complications, Including Placental Damage, Induced by Silica Nanoparticles in Mice

Kazuma Higashisaka[1,2†], Akitoshi Nakashima[3†], Yuki Iwahara[1†], Aiko Aoki[3], Masahiro Nakayama[4], Itaru Yanagihara[4], Ying Lin[1], Kazuya Nagano[1], Shin-ichi Tsunoda[5,6,7], Shigeru Saito[3], Yasuo Yoshioka[1,8,9*] and Yasuo Tsutsumi[1,7*]*

[1] Laboratory of Toxicology and Safety Science, Graduate School of Pharmaceutical Sciences, Osaka University, Suita, Japan, [2] Department of Legal Medicine, Osaka University Graduate School of Medicine, Suita, Japan, [3] Department of Obstetrics and Gynecology, University of Toyama, Toyama, Japan, [4] Department of Developmental Medicine, Research Institute, Osaka Women's and Children's Hospital, Izumi, Japan, [5] The Faculty of Pharmaceutical Sciences, Kobe Gakuin University, Kobe, Japan, [6] Laboratory of Biopharmaceutical Research, National Institutes of Biomedical Innovation, Health and Nutrition, Ibaraki, Japan, [7] The Center for Advanced Medical Engineering and Informatics, Osaka University, Suita, Japan, [8] Vaccine Creation Project, BIKEN Innovative Vaccine Research Alliance Laboratories, Research Institute for Microbial Diseases, Osaka University, Suita, Japan, [9] BIKEN Center for Innovative Vaccine Research and Development, The Research Foundation for Microbial Diseases of Osaka University, Suita, Japan

Recent advances in nanotechnology have led to the development of nanoparticles with innovative functions in various fields. However, the biological effects of nanoparticles—particularly those on the fetus—need to be investigated in detail, because several previous studies have shown that various nanoparticles induce pregnancy complications in mice. In this regard, our previous findings in mice suggested that the increase in peripheral neutrophil count induced by treatment with silica nanoparticles with a diameter of 70 nm (nSP70) may play a role in the associated pregnancy complications. Therefore, here, we sought to define the role of neutrophils in nSP70-induced pregnancy complications. The peripheral neutrophil count in pregnant BALB/c mice at 24 h after treatment with nSP70 was significantly higher than in saline-treated mice. In addition, maternal body weight, uterine weight, and the number of fetuses in nSP70-treated mice pretreated with anti-antibodies, which deplete neutrophils, were significantly lower than those in nSP70-treated mice pretreated with phosphate-buffered saline or isotype-matched control antibodies. Histology revealed that neutrophil depletion increased nSP70-induced placental damage from the decidua through the spongiotrophoblast layer and narrowed spiral arteries in the placentae. In addition, depletion of neutrophils augmented nSP70-induced cytotoxicity to fetal vessels, which were covered with endothelium. The rate of apoptotic cell death was significantly higher in the placentae of anti-nSP70-treated mice than in those from mice pretreated with isotype-matched control antibodies. Therefore, impairment of placental vessels and apoptotic cell death due to nSP70 exposure is exacerbated in the placentae of nSP70-treated mice pretreated with anti-antibodies. Depletion of neutrophils worsens nSP70-induced pregnancy complications in mice; this exacerbation was due to enhanced impairment of placental vessels and increased apoptotic cell death in maternal placentae. Our results provide basic information regarding the mechanism underlying silica-nanoparticle-induced pregnancy complications.

Keywords: apoptosis, nanotoxicology, placenta, placental vessels, pregnancy complications

OPEN ACCESS

Edited by:
Shrikant R. Mulay, Ludwig-Maximilians-Universität München, Germany

Reviewed by:
Zhengwei Ma, Augusta University, United States
Suchita Nadkarni, Queen Mary University of London, United Kingdom

***Correspondence:**
Kazuma Higashisaka higashisaka@phs.osaka-u.ac.jp;
Yasuo Yoshioka y-yoshioka@biken.osaka-u.ac.jp;
Yasuo Tsutsumi ytsutsumi@phs.osaka-u.ac.jp

†These authors have contributed equally to this work.

Specialty section:
This article was submitted to Inflammation, a section of the journal Frontiers in Immunology

Received: *25 April 2018*
Accepted: *26 July 2018*
Published: *08 August 2018*

Citation:
Higashisaka K, Nakashima A, Iwahara Y, Aoki A, Nakayama M, Yanagihara I, Lin Y, Nagano K, Tsunoda S-i, Saito S, Yoshioka Y and Tsutsumi Y (2018) Neutrophil Depletion Exacerbates Pregnancy Complications, Including Placental Damage, Induced by Silica Nanoparticles in Mice. Front. Immunol. 9:1850. doi: 10.3389/fimmu.2018.01850

INTRODUCTION

Compared with conventional materials, nanoparticles offer unique physicochemical properties and innovative functions. Consequently, research into nanoparticles and their development and commercialization in various industrial fields, such as food, cosmetics, and medicine, is rapidly progressing (1–3). However, one bottleneck in the development of nanoparticles is that their size-associated novel functions have the potential to exert unknown biological effects at unexpected sites in the body. Therefore, the expanding use of nanoparticles has increased the urgency of collecting relevant safety information. In particular, the reproductive toxicity of chemical substances is a public health concern. Because infants typically are more sensitive to environmental toxins than adults (4), infants and fetuses may experience unexpected effects even when they are exposed to amounts that are nontoxic to adults. Several recent studies have reported on the reproductive toxicity of nanoparticles (5–7). For example, we previously demonstrated that intravenous treatment with silica nanoparticles 70 nm in diameter (nSP70) induced greater intrauterine growth restriction and placental damage in mice than did silica particles larger than 100 nm (5). We speculated that nSP70-induced pregnancy complications were due to placental damage, which did not occur in the mice treated with larger particles (5). However, details of the mechanism underlying this effect are minimally understood.

To address this insufficiency, we focused on the roles of neutrophils, which are the most abundant leukocytes in humans and important factors in placental dysfunction and direct damage to developing embryos (8, 9). For example, increased neutrophils counts promoted endothelial dysfunction after placental ischemia (10), and endothelial cell damage subsequent to neutrophil activation may contribute to preeclampsia and intrauterine growth restriction (11, 12). Moreover, neutrophils are associated with vascular dysfunction in preeclamptic women, and activated neutrophils may induce increased production of myeloperoxidase in the placental and endothelial cells of these patients (13, 14). In fact, we previously showed that intravenous treatment with nSP70 increased peripheral neutrophil counts in nonpregnant mice (15). Therefore, we consider that neutrophils might be components of the mechanism by which nSP70 induce pregnancy complications.

Here, we evaluated the role of neutrophils in nSP70-associated pregnancy complications in mice. Our results demonstrate that neutrophils may protect against pregnancy complications—especially the nSP70-triggered breakdown of pregnancy maintenance. Our results provide important information regarding the mechanism underlying nSP70-induced pregnancy complications.

Abbreviations: FSC, forward-scattered light; HE, hematoxylin and eosin; IL, interleukin; NET, neutrophil extracellular trap; nSP70, silica nanoparticles with a diameter of 70 nm; PBS, phosphate-buffered saline; SSC, side-scattered light; TUNEL, TdT-mediated dUTP nick-end labeling; VEGF, vascular endothelial growth factor.

MATERIALS AND METHODS

Animals

Pregnant BALB/c mice [age, 8–10 weeks; gestational day (GD) 13–14] were purchased from Nippon SLC (Shizuoka, Japan). The mice were housed in a ventilated animal room maintained at 20 ± 2°C with a12:12-h light:dark cycle and given unrestricted access to water and forage (FR-2, Funabashi Farm, Chiba, Japan). Dams were weighed daily.

Silica Nanoparticles

Silica nanoparticles were purchased from Micromod Partikeltechnologie (Rostock–Warnemünde, Germany). Before use, the particles were sonicated for 5 min and vortexed for 1 min. Preparations of silica nanoparticles were checked for contamination with lipopolysaccharide by using an LAL Endotoxin Assay Kit (GenScript, Piscataway, NJ, USA).

Injection of Silica Nanoparticles

Pregnant BALB/c mice were injected intravenously with nSP70 (0.8 mg/mouse) on GD 16 and then euthanized under anesthesia on GD 17. Blood samples collected at 24 h after treatment and before euthanasia were centrifuged at 3,000 *g* for 15 min to obtain plasma. Uteri, fetuses, and placentae were weighed, and the placentae were prepared for histological examination.

In Vivo Neutrophil Depletion

Neutrophil depletion was achieved by intraperitoneal injection of anti-Ly-6G antibodies (clone 1A8; BioLegend, San Diego, CA, USA), isotype-matched control antibodies (clone RTK2758; BioLegend), or phosphate-buffered saline (PBS) into pregnant BALB/c mice ($n = 5$ or 6 per group) at 24 h before nSP70 injection (that is, on GD 15).

Flow Cytometry

Red blood cells in collected blood samples were lysed with ammonium chloride. All staining procedures were performed in PBS containing 2% fetal calf serum. To minimize nonspecific binding, we preincubated single-cell suspensions with anti-CD16/CD32 antibodies (clone 93; eBioscience, San Diego, CA, USA). Cells were labeled with combinations of phycoerythrin-conjugated Gr-1 antibodies (clone RB6-8C5; eBioscience), allophycocyanin-conjugated CD11b antibodies (clone M1/70; BD Pharmingen, San Diego, CA, USA), fluorescein-isothiocyanate-conjugated F4/80 antibodies (clone CI:A3-1; AbD Serotec, Oxford, UK), and phycoerythrin-Cy7-conjugated CD11c antibodies (clone HL3; BD Pharmingen). The cells were resuspended in staining buffer containing 7-amino-actinomycin D (BD Pharmingen), and the stained cells were analyzed for surface phenotype by means of a FACS Canto flow cytometer (BD Biosciences, Franklin Lakes, NJ, USA). The cells were gated according to side-scattered light (SSC) area and forward-scattered light (FSC) area and then according to SSC height/SSC width, FSC height/FSC width, and 7-amino-actinomycin D staining to eliminate doublet cells and dead cells (parent population). The proportion of neutrophils (that is, $CD11b^+$ $Gr\text{-}1^+$ $F4/80^-$) was calculated as a percentage of the parent population.

Histology

At 24 h after the administration of nSP70, placentae were removed from mice and placed in fixative solution (10% neutral buffered formalin, Nacalai Tesque, Kyoto, Japan). Paraffin-embedded sections were prepared and stained by the Applied Medical Research Laboratory (Osaka, Japan).

Immunohistochemistry

At 24 h after the administration of nSP70, the placentae of mice were removed and placed in fixative solution (10% neutral buffered formalin). Sections (thickness, 5 μm) were deparaffinized in xylene, rehydrated in a graded series of alcohol, and boiled in citrate buffer at 121°C for 15 min in an autoclave for antigen retrieval. Endogenous peroxidase activity was quenched by incubating in 3% hydrogen peroxide in methanol for 15 min, and the sections were then incubated in 5% normal goat serum to block nonspecific binding. After extensive washes with PBS, the sections were reacted with anti-CD31 (clone ab124432; Abcam, Cambridge, MA, USA) as a primary antibody and the detection was performed according to the manufacturer's instructions provided with the Vectastain kit (Vector Laboratories, Burlingame, CA, USA).

Measurement of the Areas of Fetal and Maternal Vessels

To precisely differentiate fetal vessels from maternal vessels in the labyrinth layer of placentae, we performed CD31 staining; fetal vessels and sporadic nucleated erythrocytes are CD31-positive, whereas maternal vessels are CD31-negative (16) (Figure S1 in Supplementary Material). Three random areas were selected per placenta, and the proportions of fetal and maternal vessel areas to total area were calculated by using ImageJ software (National Institutes of Health, Bethesda, MD, USA). At least five placentas in each group were evaluated.

Evaluation of Apoptosis in Placentae

Transferase-mediated dUTP nick-end labeling (TUNEL) staining (catalog no. G7130, DeadEnd Colorimetric TUNEL System, Promega, Fitchburg, WI, USA) was used to detect apoptotic cells. Placental tissue sections were prepared according to the manufacturer's instructions (Vectastain Kit, Vector Laboratories). After being washed, sections were counterstained with Mayer's hematoxylin, washed in water, and successively immersed in graded ethanol solutions and xylene before being cover slipped. In control sections, control nonimmune mouse IgG (Vector Laboratories) was used as the primary antibody. TUNEL-positive nuclei (apoptotic nuclei) in the placenta were counted, and the apoptotic index of each section was calculated as the number of nuclei that stained TUNEL-positive as a percentage of the total number of nuclei found within the section.

Statistical Analyses

Statistical analyses were performed by using Ekuseru–Toukei 2012 software (Social Survey Research Information Co., Ltd., Tokyo, Japan). Results shown in **Figures 1**–**3** are expressed as means ± SEM, and Bonferroni's method was used to compare differences. Data in the remaining figures are expressed as means ± SD, and Kruskal–Wallis and Mann–Whitney methods were used to compare differences. *P*-values lower than 0.05 were considered statistically significant.

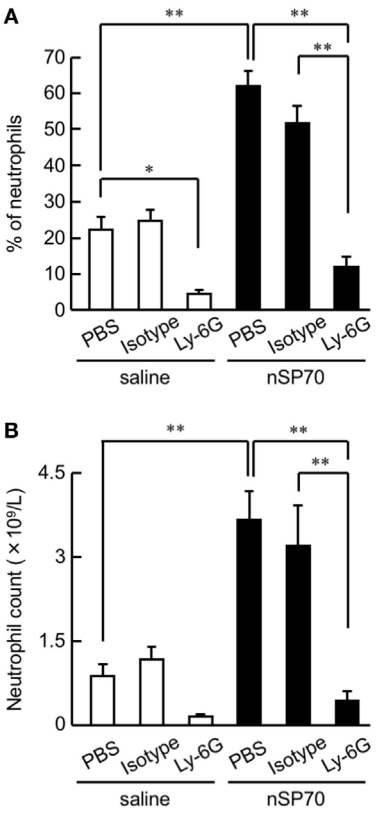

FIGURE 1 | Effects of treatment with silica nanoparticles on neutrophil levels in pregnant mice. Pregnant BALB/c mice were intravenously injected with silica nanoparticles with a diameter of 70 nm (0.8 mg/mouse) or saline on gestational day 16. **(A)** The proportion (%) of neutrophils in the peripheral blood of each mouse was determined by flow cytometry at 24 h after treatment. **(B)** The neutrophil count in the peripheral blood of each mouse was calculated by multiplying the neutrophil proportion by the total white blood cell count. Data are presented as means ± SEM; $n = 5$ or 6; $^{*}P < 0.05$ and $^{**}P < 0.01$.

RESULTS

Induction of Neutrophilia in nSP70-Treated Pregnant Mice

To assess the proportion of neutrophils after treatment with nSP70, pregnant BALB/c mice were intravenously treated with nSP70 (0.8 mg/mouse) on GD 16; lipopolysaccharide contamination in the nSP70 solution was below the limit of detection (<0.01 EU/mL). At 24 h after treatment, the proportion of neutrophils was significantly higher in mice treated with nSP70 than in saline-treated mice, suggesting that nSP70 might also induce neutrophilia in pregnant mice (**Figure 1A**). To reduce the neutrophil count, we then intraperitoneally injected pregnant BALB/c mice on GD 15 with anti-Ly-6G antibodies (or PBS or isotype-matched

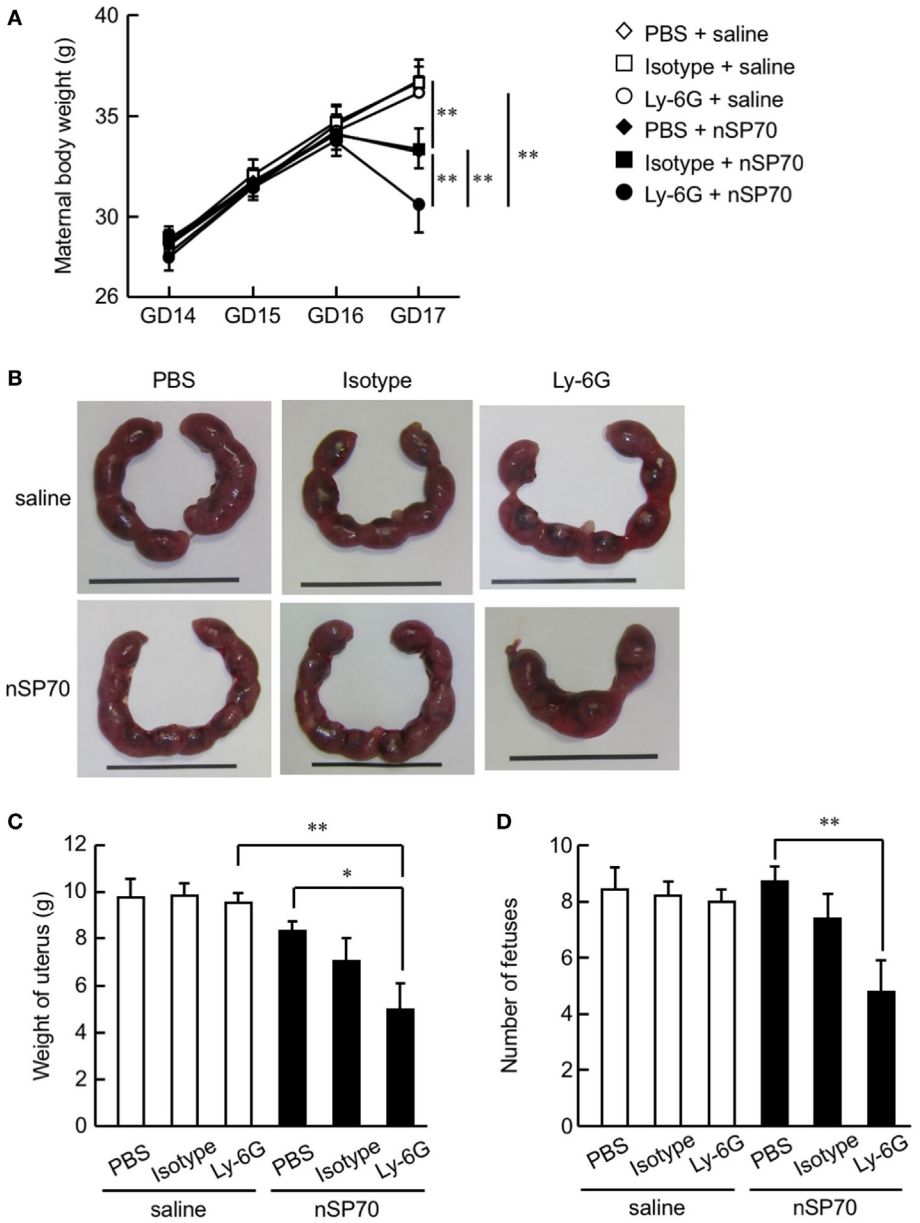

FIGURE 2 | Depletion of neutrophils exacerbates the decrease in maternal body weight in silica nanoparticles with a diameter of 70 nm (nSP70)-treated mice. Pregnant BALB/c mice were intraperitoneally treated with anti-Ly-6G antibodies or isotype control antibodies (150 μg/mouse) on gestational day 15; 24 h later, they received nSP70 (0.8 mg/mouse) or saline by intravenous injection. **(A)** Maternal body weights were assessed daily. **(B)** Representative uteri from mice. On gestation day 17, **(C)** the excised uteri were weighed and **(D)** the fetuses excised from each uterus were counted. Data are presented as means ± SEM; $n = 9$ or 10; $^{*}P < 0.05$ and $^{**}P < 0.01$.

antibodies, as controls); 24 h later, we injected them with nSP70 (0.8 mg/mouse). In nSP70-treated mice, the proportion of neutrophils was significantly lower in those pretreated with anti-Ly-6G antibodies than with PBS or isotype-matched control antibodies (**Figure 1A**). By multiplying the proportion of neutrophils by the total white blood cell count, we showed that pretreatment with anti-Ly-6G antibodies significantly curtailed the nSP70-induced increase in neutrophil count, thus supporting the results of the flow cytometric analysis (**Figure 1B**). Furthermore, we tested for the presence of different neutrophil subsets on the basis of CD16/CD62L expression. During acute inflammation, three neutrophil subsets are found in the blood: $CD16^{bright}/CD62L^{dim}$ cells that are capable of suppressing T-cell proliferation (activated); $CD16^{dim}/CD62L^{bright}$ cells with a banded nuclear morphology (immature); and phenotypically normal $CD16^{bright}/CD62L^{bright}$ neutrophils (mature) (17–19). We found that the mature neutrophil population was greater in nSP70-injected mice pretreated with PBS than in saline-injected mice pretreated with PBS, but there was

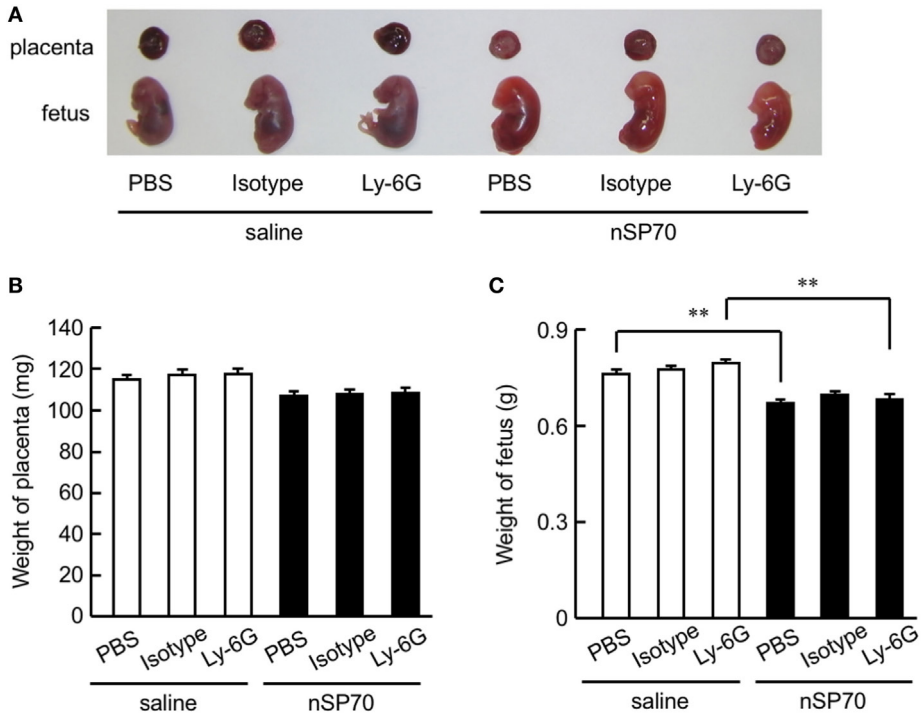

FIGURE 3 | Effects of neutrophil depletion on pregnancy complications in silica nanoparticles with a diameter of 70 nm (nSP70)-treated mice. Pregnant BALB/c mice were treated intraperitoneally with anti-Ly-6G or isotype-matched control antibodies (150 μg/mouse) on gestational day (GD) 15; 24 h later, mice received either nSP70 or saline by intravenous injection. The uteri were excised on GD 17. **(A)** Representative placentae and fetuses. **(B)** Placental weight and **(C)** fetal weight were assessed. Data are presented as means ± SEM; $n = 9$ or 10; $^{**}P < 0.01$.

no significant difference in the activated neutrophil population between these two groups (Figure S2 in Supplementary Material). This result suggests that nSP70 triggers an increase in neutrophil maturation only. In an analysis of the influence of nSP70 on other blood cell types, granulocyte counts were significantly increased in nSP70-treated mice compared with controls, and pretreatment with anti-Ly-6G antibodies significantly dampened the nSP70-induced granulocyte increase, consistent with the results of flow cytometry (Figure S3A in Supplementary Material). In contrast, the numbers of total leukocytes (Figure S3B in Supplementary Material), monocytes (Figure S3C in Supplementary Material), lymphocytes (Figure S3D in Supplementary Material), platelets (Figure S3E in Supplementary Material), and erythrocytes (Figure S3F in Supplementary Material) did not differ between nSP70-treated and control mice, regardless of anti-Ly-6G treatment. These findings suggest that the increased neutrophil count in nSP70-treated mice reflected an increase in the number of granulocytes after nSP70 injection. Moreover, the percentage of $CD4^+$ T-cells in the peripheral blood was significantly lower in nSP70-injected mice pretreated with PBS than in saline-injected mice pretreated with PBS (Figure S4A in Supplementary Material), although the percentage of $CD4^+$ $FOXP3^+$ regulatory T-cells did not differ between nSP70-treated mice pretreated with PBS and saline-treated mice pretreated with PBS (Figure S4B in Supplementary Material). These results suggest that the proportion of T-cells decreases as the proportion of neutrophils increases in the peripheral blood of mice treated with nSP70.

Neutrophil Depletion Exacerbates Pregnancy Complications in nSP70-Treated Mice

To evaluate the association between nSP70-induced pregnancy complications and the increased number of neutrophils after treatment with nSP70, we evaluated maternal body weight and placental weight after neutrophil depletion. Maternal body weight on GD 17 was lower in nSP70-treated mice than in saline-treated mice, as previously reported (**Figure 2A**) (5). Furthermore, body weight was significantly lower in nSP70-treated dams pretreated with anti-Ly-6G antibodies than in nSP70-treated mice pretreated with PBS or isotype-matched control antibodies (**Figure 2A**). Uteri were harvested at GD 17 (**Figure 2B**), and fetuses were counted. As seen with maternal body weight, pretreatment with anti-Ly-6G antibodies exacerbated the decrease in uterine weight in nSP70-treated mice compared with that after PBS (**Figure 2C**). Similarly, anti-Ly-6G–nSP70-treated mice had significantly fewer fetuses than PBS–nSP70-treated dams (**Figure 2D**). These results suggest that neutrophil depletion exacerbated nSP70-induced pregnancy complications.

We then weighed the harvested placentae and fetuses (**Figure 3A**). Whereas mice that had received nSP70 had smaller fetuses than those that had received saline (5), neither placental weight (**Figure 3B**) nor number of fetuses (**Figure 3C**) differed between nSP70-injected mice pretreated with anti-Ly-6G antibodies and those given PBS or isotype-matched control antibodies.

Next, to assess the viability of pups born to nSP70-treated mice after neutrophil depletion, pregnant BALB/c mice were intraperitoneally injected with anti-Ly-6G or isotype control-matched antibodies 24 h before intravenous injection of nSP70 (0.8 mg/mouse). Whereas the number of neonates did not differ between nSP70-treated mice pretreated with PBS or saline (Figure S5A in Supplementary Material), nSP70-treated mice pretreated with anti-Ly-6G antibodies tended to birth fewer live pups than those pretreated with PBS or isotype-matched control antibodies. In comparison, the body weight (Figure S5B in Supplementary Material) and length (Figure S5C in Supplementary Material) of neonates did not differ between treatment groups. These results suggest that neutrophils played a protective role in pregnancy in nSP70-treated mice—particularly in the maintenance of pregnancy.

Neutrophil Depletion Leads to Placental Dysfunction in nSP70-Treated Mice

Normal placental development is required for embryonic growth, and placental dysfunction has been associated with miscarriage and fetal growth restriction (20, 21). Therefore, we considered that neutrophil depletion in nSP70-treated mice might alter placental function. To assess the relationship between neutrophil depletion and placental dysfunction, we histologically evaluated placental pathology by staining with hematoxylin and eosin (HE) (**Figure 4A**). The placentae of mice treated with nSP70 in the absence of neutrophil depletion showed tissue damage in the spongiotrophoblast layer, which segregates the maternal vasculature from the fetal vasculature in the placenta. In addition, blood flow was poor overall, and scant blood was present in the vessels around the decidua and chorionic plate. We obtained these same results in our previous study (5). In contrast, the placentae of nSP70-treated mice pretreated with anti-Ly-6G antibodies showed pronounced tissue damage from the decidua through the spongiotrophoblast layer, which now also contained areas of necrosis (**Figure 4B**). Furthermore, the placentae of nSP70-treated mice pretreated with anti-Ly-6G antibodies showed marginal congestion (**Figure 4C**) and bleeding in the decidua (**Figure 4D**). Comparison of the placentae of nSP70-treated mice with and without anti-Ly-6G antibody pretreatment revealed a slight decline in neutrophil abundance in the placentae of nSP70-treated mice pretreated with anti-Ly-6G antibody (Figure S6 in Supplementary Material). These results suggest that the

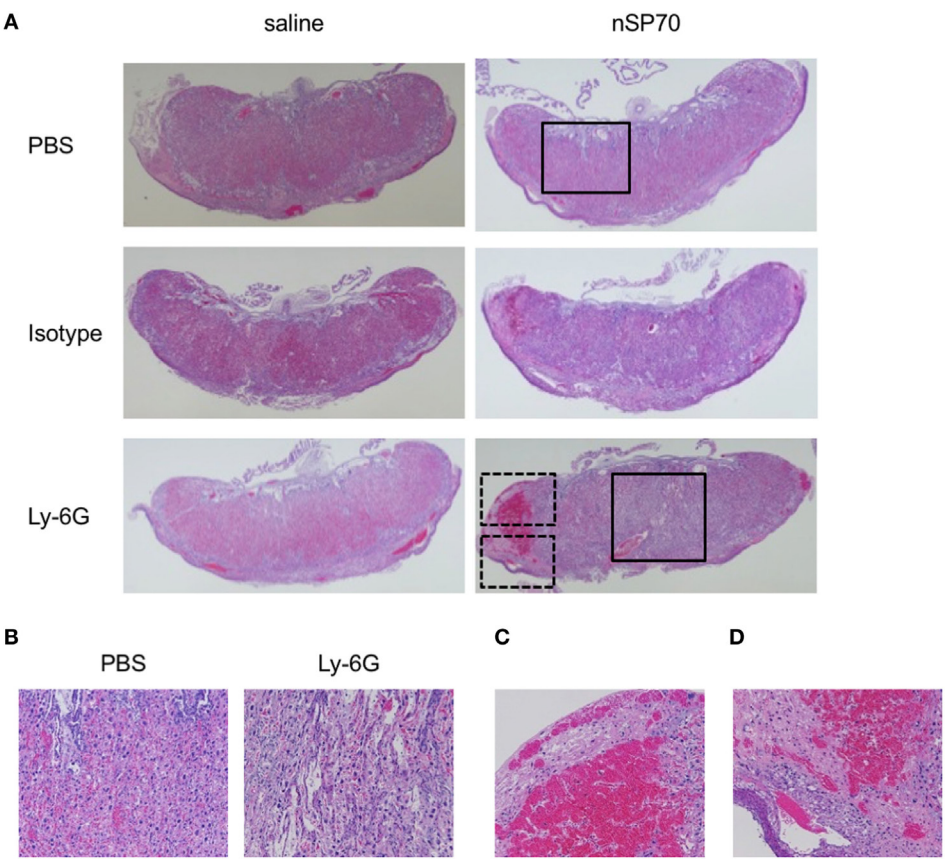

FIGURE 4 | Structural abnormalities of placenta. Pregnant BALB/c mice were intraperitoneally injected with anti-Ly-6G or isotype-matched control antibodies (150 μg/mouse) on gestational day (GD) 15; 24 h later, mice received silica nanoparticles with a diameter of 70 nm (0.8 mg/mouse) or saline by intravenous injection. The placentae were excised on GD 17. **(A)** Placental sections were stained with hematoxylin and eosin and examined histologically. **(B)** Magnified images of the areas within the solid boxes in panel **(A)**. Magnified images of the areas within the **(C)** top and **(D)** bottom dashed boxes in panel **(A)**.

exacerbation of pregnancy complications induced by peripheral neutrophil depletion is related to the decline in neutrophil abundance in the placental tissue.

Because narrowing of placental vessels impairs placental formation (22), we histologically evaluated the area of spiral arteries, maternal vessels, and fetal vessels in the placentae. The spiral arteries, which delivery maternal blood to the labyrinth layer in the placenta (23, 24), were narrower in the placentae of anti-Ly-6G–nSP70-treated mice than in mice pretreated with isotype-matched control antibodies (**Figures 5A,B**). In addition, the placental structure in mice is hemochorial, and fetal, but not maternal, vessels are lined with endothelium (16). We, therefore, performed CD31

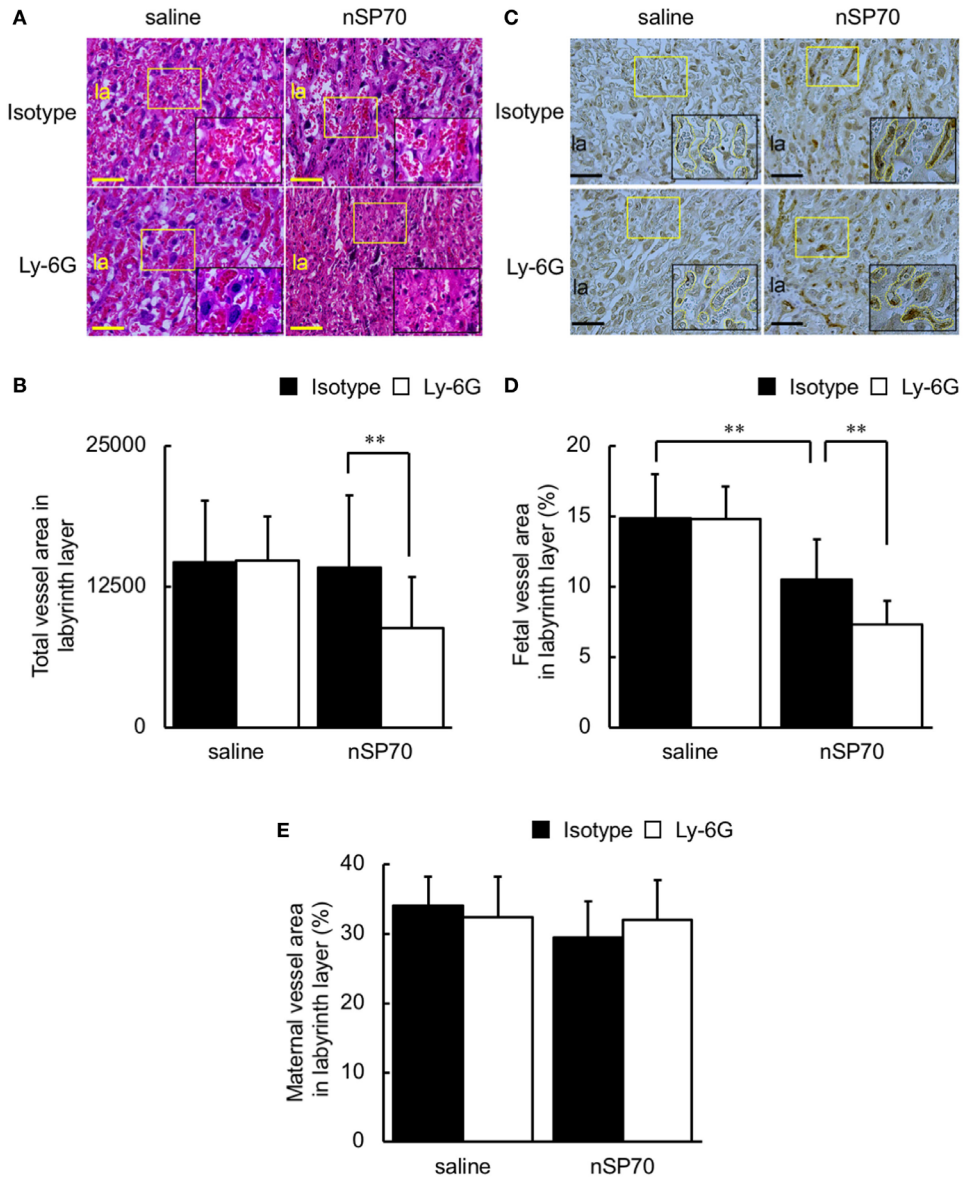

FIGURE 5 | Neutrophil depletion decreases vessel area in the placentae of silica nanoparticles with a diameter of 70 nm (nSP70)-treated mice. Pregnant BALB/c mice were treated intraperitoneally with anti-Ly-6G or isotype-matched control antibodies (150 μg/mouse) on gestational day (GD) 15; 24 h later, mice were injected intravenously with nSP70 (0.8 mg/mouse) or saline. Placentae were excised on GD 17. **(A)** Placental sections were stained with hematoxylin and eosin and examined histologically. The area in the yellow rectangle was enlarged and is shown at lower right. **(B)** Several random areas were selected per placenta, and total vessel areas in the labyrinth layer were calculated. Data are presented as means ± SD; $n = 34–62$. **(C)** Placental sections were stained with CD31. The area in the yellow rectangle was enlarged and is shown at lower right. Fetal vessels are traced with yellow lines in the enlarged insets. Three regions per placenta were randomly selected, and the proportions of **(D)** fetal and **(E)** maternal vessel area to total area were calculated. Data are presented as means ± SD; $n = 12–16$; $^{**}P < 0.01$. Scale bar: 100 μm. Abbreviation: la: labyrinth layer.

staining to differentiate fetal vessels, the inner surfaces of which are covered with CD31-positive endothelium, from maternal vessels, which are CD31-negative. Scattered placental vessels were lined with CD31-positive cells in the absence of nSP70 treatment. In contrast, nSP70 treatment led to the presence of dense CD31-positive, narrow fetal vessels in the placentae (**Figure 5C**), and fetal vessel area was significantly smaller in the placentae of mice treated with nSP70 in the absence of anti-Ly-6G antibodies than in mice treated with saline (**Figure 5D**). In addition, anti-Ly-6G antibodies augmented the narrowing of fetal vessels in the placentae of nSP70-treated mice, but anti-Ly-6G–saline-treatment did not confer any effects on the fetal vessels (**Figure 5D**). Furthermore, neither nSP70 nor anti-Ly-6G antibodies impaired the maternal vessels in the labyrinth layer (**Figure 5E**). Taken together, these findings suggest that nSP70 impaired spiral arteries and fetal vessels, which were coated with endothelium appropriately, and these effects were augmented by neutrophil depletion.

Staining by using terminal TUNEL showed that apoptotic cells were more numerous in both the spongiotrophoblast layer (**Figures 6A,B**) and labyrinth layer (**Figure 6C**) of anti-Ly-6G–nSP70-treated mice than in mice treated with isotype-matched control antibodies followed by nSP70. In addition, the percentage of TUNEL-stained nuclei was significantly higher within the spongiotrophoblast layer (**Figure 6D**) and labyrinth layer (**Figure 6E**) of anti-Ly-6G–nSP70-treated mice than in those from nSP70-treated mice pretreated with isotype-matched control antibodies. These findings suggest that neutrophil depletion increased nSP70-induced placental damage, with the induction of apoptosis and a potential reduction of the number of fetuses.

DISCUSSION

Several epidemiological studies have demonstrated the association between maternal exposure to fine particles during pregnancy and adverse pregnancy outcomes, such as low birth weight, preterm birth, and fetal death (25, 26). For example, a cohort study in Ohio reported that women exposed to higher than the standard exposure level of $PM_{2.5}$ (airborne fine particulate matter measuring <2.5 μm in diameter) over the course of pregnancy were at 19% increased risk for preterm birth (27). Although these reports support the adverse effects of maternal exposure to particulate air pollution on birth outcome, the mechanisms for these effects have remained unclear. Moreover, several studies have shown that some nanoparticles can induce pregnancy complications in mice, but the details of the mechanism are not completely understood.

From this viewpoint, here we sought to assess nanoparticle-induced reproductive toxicity in mice and to elucidate its mechanism. We found that the maternal body weights of nSP70-treated mice were decreased and that their placentae demonstrated tissue destruction in the spongiotrophoblast layer on GD 17, unlike those of saline-treated mice, as previously reported (5). In addition, neutrophil depletion exacerbated nSP70-induced pregnancy complications and placental damage (**Figures 2** and **4**), suggesting that neutrophils help to suppress pregnancy complications. Furthermore, our studies have demonstrated that, compared with controls, mice that received nSP70 had about 20% lower uterine weights and significantly higher fetal resorption rates. In contrast, although we confirmed the nSP70-induced decrease in maternal body weight, it was less pronounced than that seen previously, and fetal resorption rates here were lower than in those in our previous study. We consider that this difference might reflect the difference in the number of nSP70 injections between the two studies.

In this regard, our previous study evaluated the effects of silica nanoparticles on fetuses after two injections (5), whereas here we assessed the effects after a single injection of silica nanoparticles. In the previous study, we administered silica nanoparticles to pregnant mice twice without neutrophil depletion and evaluated the subsequent pregnancy complications. The maternal body weights of these twice-injected mice were lower than those of nSP70-treated mice with neutrophil depletion. However, almost all of the fetuses of the dams that received two injections died *in utero* (data not shown), and we surmised that it might be difficult to assess the effects of neutrophils on fetuses or placenta by using our previous procedure. We, therefore, elected to use a single injection of silica nanoparticles in the current study, and this difference in methodology might have caused the differences between the previous and present data.

It is important to note the differences in timing of the experimental treatments in the current study. Previously, we investigated the time course of the change in the proportion of neutrophils after treatment with nSP70 in nonpregnant mice. Although the proportion in mice treated with nSP70 was significantly higher than that in saline-treated mice at 24 h, the proportions of neutrophils at both 2 and 72 h after nSP70 treatment were significantly lower than those in saline-treated mice at the same time points (15). We detected nSP70 in the livers of mice within 2 h of injection (28); therefore, prompt recruitment of neutrophils to the liver might have resulted in the transient decrease in the observed proportion of neutrophils in the peripheral blood 2 h after administration of nSP70. During the neutrophil's lifespan of a few days, essential processes involved in restoring homeostasis after nSP70-induced neutrophilia may have resulted in the decrease in the proportion of neutrophils observed 72 h after nSP70 injection. Here, our treatments occurred relatively late in gestation, whereas some reports have studied similar effects earlier in pregnancy in the mouse. Girardi et al. (29) demonstrated that complement C5a-mediated recruitment of neutrophils in the placenta at day 8 of pregnancy is critical to pregnancy loss and the development of fetal damage. Nadkarni et al. (30) showed that, at a time of active placental development in the mouse, neutrophil-induced T-cells might be essential for normal placentation, including placental vascular development, and for fetal growth. Thus, there is a need to assess the effects of neutrophil depletion and nSP70 treatment not only in late pregnancy but also in early pregnancy.

Recent reports indicate that neutrophils may contribute to the clearance of nanoparticles. For example, using flow cytometry, Stephen et al. demonstrated that nanoparticles in both the peripheral blood and spleen were taken up at dramatically higher rates by granulocytes than by monocytes and that neutrophil depletion increased the numbers of particles in the blood (31). In addition, as shown in several recent studies (including our own), transportation of nanoparticles through the blood–placenta

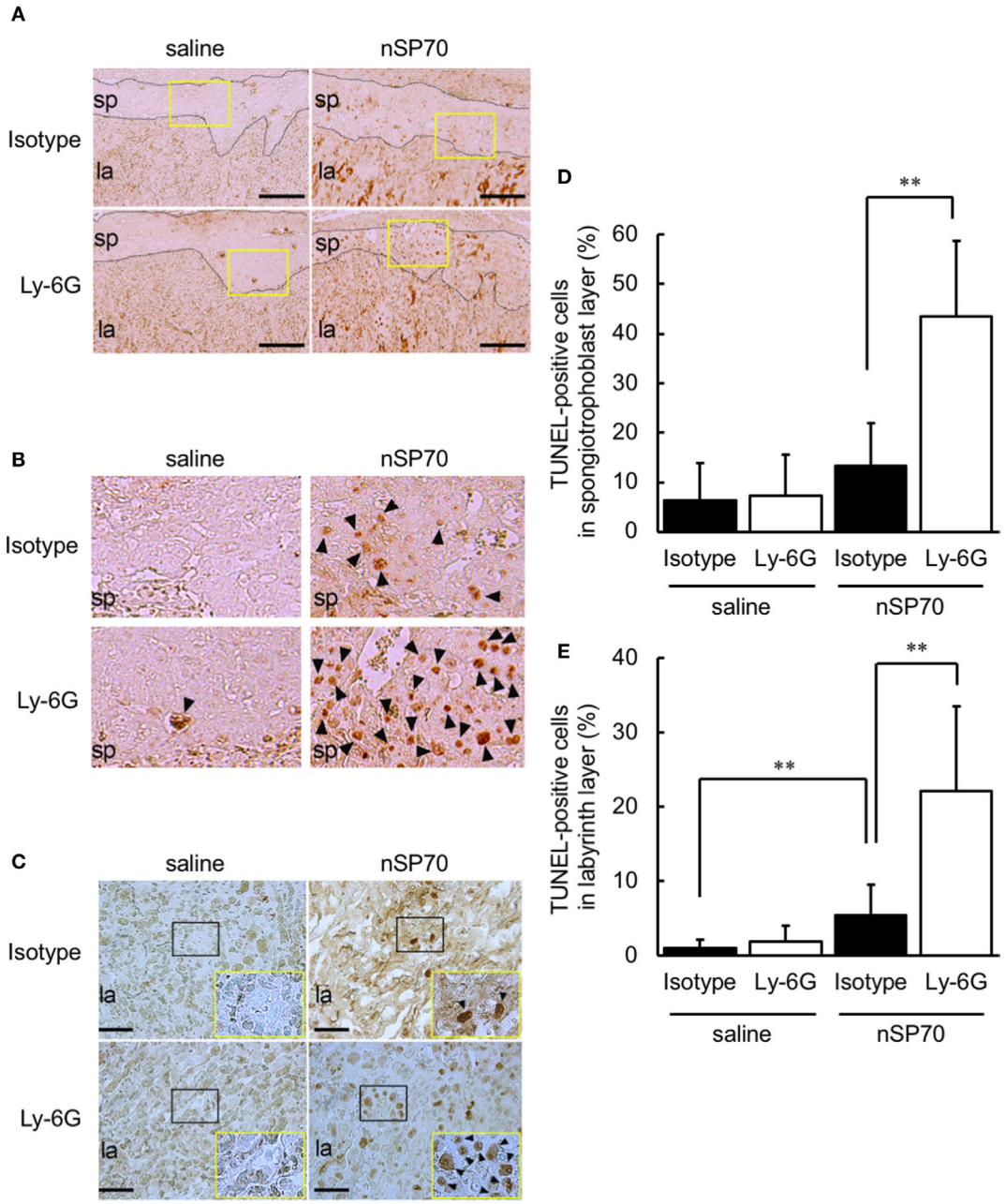

FIGURE 6 | Treatment with silica nanoparticles with a diameter of 70 nm (nSP70) after neutrophil depletion increases the number of apoptotic cells in the placenta. Pregnant BALB/c mice were treated intraperitoneally with anti-Ly-6G or isotype-matched control antibodies (150 μg/mouse) on gestational day (GD) 15; 24 h later, mice were injected intravenously with nSP70 (0.8 mg/mouse) or saline. Placentae were excised on GD 17. Placental sections were stained with transferase-mediated dUTP nick-end labeling (TUNEL) to reveal apoptotic cells in the spongiotrophoblast and labyrinth layers. **(A)** The black dotted lines separate the spongiotrophoblast layer from the labyrinth layer. Scale bar: 200 μm. **(B)** The regions within the yellow rectangles in **(A)** are enlarged. **(C)** In the labyrinth layers, the regions within the black rectangles are enlarged and are shown at lower right. Scale bar: 100 μm. TUNEL-positive nuclei in the **(D)** spongiotrophoblast layer and **(E)** labyrinth layer of placentae was counted; the apoptotic index for each section was calculated as the number of TUNEL-positive nuclei divided by the total number of nuclei within the evaluated section and converted to a percentage. Data are presented as means ± SD; $n = 8–16$; $^{**}P < 0.01$. Arrowheads: TUNEL-positive cells. Abbreviations: la: labyrinth layer, sp: spongiotrophoblast layer.

barrier is one of the causes of the induction of pregnancy complications by nanoparticles (32, 33). These combined results prompted our hypothesis that depletion of neutrophils, which take up nanoparticles, might increase the content of silica nanoparticles in the blood. Consequently, the distribution of silica nanoparticles to the placenta would increase as well, perhaps resulting in nSP70-induced structural abnormalities of the placenta. In this regard, the activated neutrophil population

($CD16^{bright}/CD62L^{dim}$) tended to be lower in nSP70-injected mice pretreated with anti-Ly-6G antibodies than in nSP70-injected mice pretreated with PBS or isotype-matched control antibodies (Figure S2 in Supplementary Material). Neutrophil activation may stimulate particle clearance; therefore, we consider that these results support our hypothesis that a decrease in the activated neutrophil population may lead to an increase in the translocation of silica nanoparticles from blood to placenta. Moreover, together with our histopathologic findings (**Figure 4**), the slight decline in neutrophil abundance in the placentae of nSP70-treated mice pretreated with anti-Ly-6G antibody (Figure S6 in Supplementary Material) suggests that the exacerbation of pregnancy complications by peripheral neutrophil depletion is related to a reduction in neutrophil abundance in the placental tissue and thus diminution of the protective effects on circulatory and placental tissues. Furthermore, to confirm our hypothesis, we sought to assess the silicon content of the placentae of mice after treatment with nSP70 with or without prior depletion of neutrophils. However, under both conditions the placental silicon concentration was below the limit of detection by inductively coupled plasma–atomic emission spectrometry (data not shown). Therefore, additional studies are needed to assess the changes in silica nanoparticle content in the placentae and blood of mice in which neutrophil counts are normal or depleted.

Here, HE staining and immunohistochemistry analysis revealed that, when neutrophil counts were diminished, nSP70 induced placental damage (**Figure 4A**), impaired placental vessels (**Figure 5B**), and increased the number of apoptotic cells in the placentae (**Figure 6**) compared with those under normal neutrophil counts. Normal placental development requires the coordinated production of vascular endothelial growth factor (VEGF) and its receptor, fms-like tyrosine kinase-1 (34), and neutrophil-derived VEGF-A induces the angiogenic activity of CXC chemokines (35), However, the production level of VEGF did not differ between the placentae of nSP70-treated mice pretreated with anti-Ly-6G antibodies and those of mice pretreated with isotype-matched control antibodies (data not shown). From this perspective, we propose that, once neutrophil depletion has increased the concentration of silica nanoparticles in the blood, the translocation of silica nanoparticles from blood to placenta increases. Thus, the cytotoxicity of nSP70 on placentae, including the vascular endothelium of spiral arteries and fetal vessels, might be exacerbated. However, the precise mechanism underlying nSP70-induced pregnancy complications remains to be clarified.

Preeclampsia and fetal growth restriction is known as complications associated with pregnancy, and involvement with autophagy has been reported as one of the causes (36). Autophagy is essential for vascular remodeling during the first stage of placentation (37), and impaired autophagy during preeclampsia increases the exposure of trophoblasts to oxidative and inflammatory stress (38). In addition, autophagy might suppress the activation of endotoxin-induced inflammasomes and may moderate the production of inflammatory cytokines, including interleukin (IL) 1β and IL-18 (36, 39). Inflammation in pregnant mice is thought to be an important factor in nanoparticle-induced pregnancy complications. Therefore, we considered that neutrophil depletion might disrupt autophagy, resulting in the activation of inflammasomes. Ultimately, neutrophil depletion may worsen the placental cellular damage induced by nSP70.

We demonstrated here that neutrophil depletion exacerbated pregnancy complications in nSP70-treated mice (**Figures 2** and **3**) and increased the placental damage induced by nSP70 (**Figure 4**). Although neutrophils are considered typical immunocompetent cells that promote inflammatory responses, it has recently been reported that neutrophils might directly contribute to the suppression of inflammation (40, 41). For example, neutrophil extracellular traps (NETs), resulting from excessive accumulations of neutrophils, reportedly induce the degradation of inflammatory mediators, including cytokines and chemokines, which are released by activated neutrophils; in this way they may terminate inflammatory responses (42). We previously reported that the concentrations of double-stranded DNA—a major component of NETs—in nSP70-treated mice were significantly higher than those in control mice (15). Therefore, we surmise that the neutrophil depletion that exacerbates pregnancy complications in nSP70-treated mice is connected with the protective roles of these cells, such as their contribution to the formation of NETs.

ETHICS STATEMENT

All of the experiments involving mice were performed in accordance with the animal welfare guidelines of Osaka University and the National Institutes of Biomedical Innovation, Health, and Nutrition of Japan.

AUTHOR CONTRIBUTIONS

KH, YI, and YY designed the study. KH, AN, YI, AA, IY, and YL performed the experiments and analyzed data. KH, AN, and YY wrote the manuscript. AN, MN, IY, KN, ST, and SS provided technical support and conceptual advice. YT supervised all of the projects. All authors discussed the results and commented on the manuscript.

ACKNOWLEDGMENTS

We thank Ms. Kaori Murayama, Ms. Risako Nagahashi, and Ms. Nobuyo Hashino for their laboratory support.

FUNDING

This study was supported by Grants-in-Aid for Scientific Research from the Japan Society for the Promotion of Science (no. 16K01437 to KH, no. 25136712 to YY, no. 26242055 to YT, and no. 15K12540 to YT); by a Health Labor Sciences Research Grant from the Ministry of Health, Labor, and Welfare of Japan (no. H25-kagaku-ippan-005 to YT and no. H28-syokuhin-wakate-014 to KH); and by The Takeda Science Foundation (to KH).

SUPPLEMENTARY MATERIAL

The Supplementary Material for this article can be found online at https://www.frontiersin.org/articles/10.3389/fimmu.2018.01850/full#supplementary-material.

REFERENCES

1. Cheng Z, Al Zaki A, Hui JZ, Muzykantov VR, Tsourkas A. Multifunctional nanoparticles: cost versus benefit of adding targeting and imaging capabilities. *Science* (2012) 338(6109):903–10. doi:10.1126/science.1226338
2. Raj S, Jose S, Sumod US, Sabitha M. Nanotechnology in cosmetics: opportunities and challenges. *J Pharm Bioallied Sci* (2012) 4(3):186–93. doi:10.4103/0975-7406.99016
3. Wang H, Du LJ, Song ZM, Chen XX. Progress in the characterization and safety evaluation of engineered inorganic nanomaterials in food. *Nanomedicine (Lond)* (2013) 8(12):2007–25. doi:10.2217/nnm.13.176
4. Wigle DT, Arbuckle TE, Turner MC, Berube A, Yang Q, Liu S, et al. Epidemiologic evidence of relationships between reproductive and child health outcomes and environmental chemical contaminants. *J Toxicol Environ Health B Crit Rev* (2008) 11(5–6):373–517. doi:10.1080/10937400801921320
5. Yamashita K, Yoshioka Y, Higashisaka K, Mimura K, Morishita Y, Nozaki M, et al. Silica and titanium dioxide nanoparticles cause pregnancy complications in mice. *Nat Nanotechnol* (2011) 6(5):321–8. doi:10.1038/nnano.2011.41
6. Shirasuna K, Usui F, Karasawa T, Kimura H, Kawashima A, Mizukami H, et al. Nanosilica-induced placental inflammation and pregnancy complications: different roles of the inflammasome components NLRP3 and ASC. *Nanotoxicology* (2015) 9(5):554–67. doi:10.3109/17435390.2014.956156
7. Zhang XF, Park JH, Choi YJ, Kang MH, Gurunathan S, Kim JH. Silver nanoparticles cause complications in pregnant mice. *Int J Nanomedicine* (2015) 10:7057–71. doi:10.2147/IJN.S95694
8. Girardi G, Yarilin D, Thurman JM, Holers VM, Salmon JE. Complement activation induces dysregulation of angiogenic factors and causes fetal rejection and growth restriction. *J Exp Med* (2006) 203(9):2165–75. doi:10.1084/jem.20061022
9. Giaglis S, Stoikou M, Grimolizzi F, Subramanian BY, van Breda SV, Hoesli I, et al. Neutrophil migration into the placenta: good, bad or deadly? *Cell Adh Migr* (2016) 10(1–2):208–25. doi:10.1080/19336918.2016.1148866
10. Regal JF, Lillegard KE, Bauer AJ, Elmquist BJ, Loeks-Johnson AC, Gilbert JS. Neutrophil depletion attenuates placental ischemia-induced hypertension in the rat. *PLoS One* (2015) 10(7):e0132063. doi:10.1371/journal.pone.0132063
11. Gupta AK, Hasler P, Holzgreve W, Hahn S. Neutrophil NETs: a novel contributor to preeclampsia-associated placental hypoxia? *Semin Immunopathol* (2007) 29(2):163–7. doi:10.1007/s00281-007-0073-4
12. Laresgoiti-Servitje E. A leading role for the immune system in the pathophysiology of preeclampsia. *J Leukoc Biol* (2013) 94(2):247–57. doi:10.1189/jlb.1112603
13. Cadden KA, Walsh SW. Neutrophils, but not lymphocytes or monocytes, infiltrate maternal systemic vasculature in women with preeclampsia. *Hypertens Pregnancy* (2008) 27(4):396–405. doi:10.1080/10641950801958067
14. Gandley RE, Rohland J, Zhou Y, Shibata E, Harger GF, Rajakumar A, et al. Increased myeloperoxidase in the placenta and circulation of women with preeclampsia. *Hypertension* (2008) 52(2):387–93. doi:10.1161/HYPERTENSIONAHA.107.107532
15. Higashisaka K, Kunieda A, Iwahara Y, Tanaka K, Nagano K, Mukai Y, et al. Neutrophilia due to silica nanoparticles induces release of double-stranded DNA. *J Nanomed Nanotechnol* (2014) 5:236. doi:10.4172/2157-7439.1000236
16. Miner JJ, Cao B, Govero J, Smith AM, Fernandez E, Cabrera OH, et al. Zika virus infection during pregnancy in mice causes placental damage and fetal demise. *Cell* (2016) 165(5):1081–91. doi:10.1016/j.cell.2016.05.008
17. Eruslanov EB, Lyadova IV, Kondratieva TK, Majorov KB, Scheglov IV, Orlova MO, et al. Neutrophil responses to *Mycobacterium tuberculosis* infection in genetically susceptible and resistant mice. *Infect Immun* (2005) 73(3):1744–53. doi:10.1128/IAI.73.3.1744-1753.2005
18. Pillay J, Kamp VM, van Hoffen E, Visser T, Tak T, Lammers JW, et al. A subset of neutrophils in human systemic inflammation inhibits T cell responses through Mac-1. *J Clin Invest* (2012) 122(1):327–36. doi:10.1172/JCI57990
19. Tak T, Wijten P, Heeres M, Pickkers P, Scholten A, Heck AJR, et al. Human CD62L(dim) neutrophils identified as a separate subset by proteome profiling and in vivo pulse-chase labeling. *Blood* (2017) 129(26):3476–85. doi:10.1182/blood-2016-07-727669
20. Gasperowicz M, Otto F. The notch signalling pathway in the development of the mouse placenta. *Placenta* (2008) 29(8):651–9. doi:10.1016/j.placenta.2008.06.004
21. Kibschull M, Gellhaus A, Winterhager E. Analogous and unique functions of connexins in mouse and human placental development. *Placenta* (2008) 29(10):848–54. doi:10.1016/j.placenta.2008.07.013
22. Boeldt DS, Bird IM. Vascular adaptation in pregnancy and endothelial dysfunction in preeclampsia. *J Endocrinol* (2017) 232(1):R27–44. doi:10.1530/JOE-16-0340
23. Simmons DG, Fortier AL, Cross JC. Diverse subtypes and developmental origins of trophoblast giant cells in the mouse placenta. *Dev Biol* (2007) 304(2):567–78. doi:10.1016/j.ydbio.2007.01.009
24. Whitley GS, Cartwright JE. Cellular and molecular regulation of spiral artery remodelling: lessons from the cardiovascular field. *Placenta* (2010) 31(6):465–74. doi:10.1016/j.placenta.2010.03.002
25. Proietti E, Roosli M, Frey U, Latzin P. Air pollution during pregnancy and neonatal outcome: a review. *J Aerosol Med Pulm Drug Deliv* (2013) 26(1):9–23. doi:10.1089/jamp.2011.0932
26. Lamichhane DK, Leem JH, Lee JY, Kim HC. A meta-analysis of exposure to particulate matter and adverse birth outcomes. *Environ Health Toxicol* (2015) 30:e2015011. doi:10.5620/eht.e2015011
27. DeFranco E, Moravec W, Xu F, Hall E, Hossain M, Haynes EN, et al. Exposure to airborne particulate matter during pregnancy is associated with preterm birth: a population-based cohort study. *Environ Health* (2016) 15:6. doi:10.1186/s12940-016-0094-3
28. Yoshida T, Yoshioka Y, Morishita Y, Aoyama M, Tochigi S, Hirai T, et al. Protein corona changes mediated by surface modification of amorphous silica nanoparticles suppress acute toxicity and activation of intrinsic coagulation cascade in mice. *Nanotechnology* (2015) 26(24):245101. doi:10.1088/0957-4484/26/24/245101
29. Girardi G, Berman J, Redecha P, Spruce L, Thurman JM, Kraus D, et al. Complement C5a receptors and neutrophils mediate fetal injury in the antiphospholipid syndrome. *J Clin Invest* (2003) 112(11):1644–54. doi:10.1172/JCI200318817
30. Nadkarni S, Smith J, Sferruzzi-Perri AN, Ledwozyw A, Kishore M, Haas R, et al. Neutrophils induce proangiogenic T cells with a regulatory phenotype in pregnancy. *Proc Natl Acad Sci U S A* (2016) 113(52):E8415–24. doi:10.1073/pnas.1611944114
31. Jones SW, Roberts RA, Robbins GR, Perry JL, Kai MP, Chen K, et al. Nanoparticle clearance is governed by Th1/Th2 immunity and strain background. *J Clin Invest* (2013) 123(7):3061–73. doi:10.1172/JCI66895
32. Shi H, Magaye R, Castranova V, Zhao J. Titanium dioxide nanoparticles: a review of current toxicological data. *Part Fibre Toxicol* (2013) 10:15. doi:10.1186/1743-8977-10-15
33. Liu Y, Li H, Xiao K. Distribution and biological effects of nanoparticles in the reproductive system. *Curr Drug Metab* (2016) 17(5):478–96. doi:10.2174/1389200217666160105111436
34. Lam C, Lim KH, Karumanchi SA. Circulating angiogenic factors in the pathogenesis and prediction of preeclampsia. *Hypertension* (2005) 46(5):1077–85. doi:10.1161/01.HYP.0000187899.34379.b0
35. Scapini P, Morini M, Tecchio C, Minghelli S, Di Carlo E, Tanghetti E, et al. CXCL1/macrophage inflammatory protein-2-induced angiogenesis in vivo is mediated by neutrophil-derived vascular endothelial growth factor-A. *J Immunol* (2004) 172(8):5034–40. doi:10.4049/jimmunol.172.8.5034
36. Nakashima A, Aoki A, Kusabiraki T, Cheng SB, Sharma S, Saito S. Autophagy regulation in preeclampsia: pros and cons. *J Reprod Immunol* (2017) 123:17–23. doi:10.1016/j.jri.2017.08.006
37. Nakashima A, Yamanaka-Tatematsu M, Fujita N, Koizumi K, Shima T, Yoshida T, et al. Impaired autophagy by soluble endoglin, under physiological hypoxia in early pregnant period, is involved in poor placentation in preeclampsia. *Autophagy* (2013) 9(3):303–16. doi:10.4161/auto.22927
38. Zhang Y, Hu X, Gao G, Wang Y, Chen P, Ye Y. Autophagy protects against oxidized low density lipoprotein-mediated inflammation associated with preeclampsia. *Placenta* (2016) 48:136–43. doi:10.1016/j.placenta.2016.09.015
39. Saitoh T, Fujita N, Jang MH, Uematsu S, Yang BG, Satoh T, et al. Loss of the autophagy protein Atg16L1 enhances endotoxin-induced IL-1beta production. *Nature* (2008) 456(7219):264–8. doi:10.1038/nature07383

40. Mantovani A, Cassatella MA, Costantini C, Jaillon S. Neutrophils in the activation and regulation of innate and adaptive immunity. *Nat Rev Immunol* (2011) 11(8):519–31. doi:10.1038/nri3024
41. He YM, Li X, Perego M, Nefedova Y, Kossenkov AV, Jensen EA, et al. Transitory presence of myeloid-derived suppressor cells in neonates is critical for control of inflammation. *Nat Med* (2018) 24(2):224–31. doi:10.1038/nm.4467
42. Schauer C, Janko C, Munoz LE, Zhao Y, Kienhofer D, Frey B, et al. Aggregated neutrophil extracellular traps limit inflammation by degrading cytokines and chemokines. *Nat Med* (2014) 20(5):511–7. doi:10.1038/nm.3547

Conflict of Interest Statement: YY is employed by the Research Foundation for Microbial Diseases of Osaka University. All other authors declare no competing financial interests.

frontiers in Immunology

ORIGINAL RESEARCH
published: 02 October 2018
doi: 10.3389/fimmu.2018.02266

Inert Coats of Magnetic Nanoparticles Prevent Formation of Occlusive Intravascular Co-aggregates With Neutrophil Extracellular Traps

Rostyslav Bilyy[1], Harald Unterweger[2], Bianca Weigel[2], Tetiana Dumych[1], Solomiya Paryzhak[1], Volodymyr Vovk[1], Ziyu Liao[2,3], Christoph Alexiou[2], Martin Herrmann[4†] and Christina Janko[2*†]*

[1] Danylo Halytsky Lviv National Medical University, Lviv, Ukraine, [2] Section of Experimental Oncology and Nanomedicine (SEON), Department of Otorhinolaryngology, Head and Neck Surgery, Else Kröner-Fresenius-Stiftung Professorship, Universitätsklinikum Erlangen, Erlangen, Germany, [3] Master Programme in Advanced Materials and Processes, Technische Fakultät, Friedrich-Alexander-Universität Erlangen-Nürnberg, Erlangen, Germany, [4] Department of Internal Medicine 3 - Rheumatology and Immunology, Friedrich-Alexander-Universität Erlangen-Nürnberg and Universitätsklinikum Erlangen, Erlangen, Germany

OPEN ACCESS

Edited by:
Uday Kishore,
Brunel University London,
United Kingdom

Reviewed by:
Angelo A. Manfredi,
Università Vita-Salute San Raffaele,
Italy
Yi Zhao,
West China Hospital of Sichuan University, China
Gudrun Stenbeck,
Brunel University London,
United Kingdom

***Correspondence:**
Martin Herrmann
martin.herrmann@uk-erlangen.de
Christina Janko
christina.janko@uk-erlangen.de

[†]These authors share senior authorship

Specialty section:
This article was submitted to Molecular Innate Immunity, a section of the journal Frontiers in Immunology

Received: 02 June 2018
Accepted: 11 September 2018
Published: 02 October 2018

Citation:
Bilyy R, Unterweger H, Weigel B, Dumych T, Paryzhak S, Vovk V, Liao Z, Alexiou C, Herrmann M and Janko C (2018) Inert Coats of Magnetic Nanoparticles Prevent Formation of Occlusive Intravascular Co-aggregates With Neutrophil Extracellular Traps. Front. Immunol. 9:2266. doi: 10.3389/fimmu.2018.02266

If foreign particles enter the human body, the immune system offers several mechanisms of response. Neutrophils forming the first line of the immune defense either remove pathogens by phagocytosis, inactivate them by degranulation or release of reactive oxygen species or immobilize them by the release of chromatin decorated with the granular proteins from cytoplasm as neutrophil extracellular traps (NETs). Besides viable microbes like fungi, bacteria or viruses, also several sterile inorganic particles including nanoparticles reportedly activate NET formation. The physicochemical nanoparticle characteristics fostering NET formation are still elusive. Here we show that agglomerations of non-stabilized superparamagnetic iron oxide nanoparticles (SPIONs) induce NET formation by isolated human neutrophils, in whole blood experiments under static and dynamic conditions as well as *in vivo*. Stabilization of nanoparticles with biocompatible layers of either human serum albumin or dextran reduced agglomeration and NET formation by neutrophils. Importantly, this passivation of the SPIONs prevented vascular occlusions *in vivo* even when magnetically accumulated. We conclude that higher order structures formed during nanoparticle agglomeration primarily trigger NET formation and the formation of SPION-aggregated NET-co-aggregates, whereas colloid-disperse nanoparticles behave inert and are alternatively cleared by phagocytosis.

Keywords: neutrophil extracellular traps (NETs), superparamagnetic iron oxide nanoparticles (SPIONs), biocompatibility, vascular occlusion, clearance, nanoparticle aggregation

INTRODUCTION

Nanoparticles have attracted increasing attention for biomedical applications. Especially superparamagnetic iron oxide nanoparticles (SPIONs) can be used as contrast agent in magnetic resonance imaging (MRI), as drug transporter for magnetic drug targeting (MDT) or as magnetizer for cells in magnetic tissue engineering. To ensure a safe use in biomedicine, the interaction

of SPIONs with components of the human blood system must be warranted. For host defense and biocompatibility, neutrophils play a major role. They are the most frequent leukocyte type in human blood, representing more than 65% of all white blood cells. In inflammatory conditions, neutrophils are the first type of leukocyte that migrates toward the site of insult where they produce inflammatory mediators and chemoattractants. To eliminate foreign pathogens, neutrophils have a broad range of antimicrobial functions (1). For instance, activated neutrophils can phagocytose, release antimicrobial granules, and produce reactive oxygen species (ROS) during a process referred to as oxidative burst. Neutrophils catch and immobilize pathogens by the release of neutrophil extracellular traps (NETs), composed of extracellular decondensed DNA, covered with nuclear histones and granular antimicrobial proteins, preventing the spread of pathogens and initiating their inactivation (2).

The neutrophils' defense mechanisms reportedly occur not only for viable pathogens, but also for sterile nanoparticles (3). Interestingly, amongst others, size dependent effects decide by which mechanism particles are cleared from the body. For nanodiamonds it has been shown that very small nanoparticles (10–40 nm) induce fast damage of plasma membranes and instability of the lysosomal compartment, leading to the immediate formation of NETs, whereas larger particles (100–1,000 nm) behaved rather inertly (3). Fungal hyphae and yeasts are cleared via NETosis and phagocytosis, respectively (4).

For SPIONs, data on the size dependency of the neutrophil response are lacking. This is true for *in vitro* experiments as well as for *in vivo* experiments mimicking the intended clinical use. Thus, for application of SPIONs as drug transporters for magnetic drug targeting, the interactions of SPIONs have to be analyzed in the presence of a magnetic field. Here we show that in the absence of an appropriate coating nanoparticles tend to form irreversible agglomerates, prone to cause NET formation, vascular occlusion and thrombotic events. Coating the SPIONs with dextran or albumin prevented agglomeration, NET formation and vascular occlusions. We conclude that coating of SPIONs is required for safe biomedical applications, especially if the particles are applied intravascularly.

MATERIALS AND METHODS

Synthesis of Superparamagnetic Iron Oxide Nanoparticles (SPIONs) and Coating

Lauric acid-coated iron oxide nanoparticles were synthesized using a co-precipitation method as described by Tietze et al. (5). In brief, Fe(II) and Fe(III) salts were dissolved in water, then NH_3 solution 25% was added under stirring. SPIONs were coated with lauric acid (LA) *in situ* or afterwards after washing, respectively.

For coating with LA afterwards, the precipitate was washed with 1.3% ammonium hydroxide solution, and then LA (dissolved in acetone) was added and the whole dispersion was heated to 90°C for 4 min under stirring. The resulting LA-coated SPIONs ($SPION^{LA1}$) were washed 10 times with 1.3% ammonium hydroxide solution.

For *in situ* coating with LA, after precipitation of the particles by NH_3 and heating to 90°C, 1.25 g LA solution (dissolved in acetone) was added, cooled down and dialyzed ($SPION^{LA2}$) (6). $SPION^{LA2}$ were further stabilized with human serum albumin according to Zaloga et al. ($SPION^{LA-HSA}$) (6). Briefly, AlbIX solution (10% w/V, Albumedix, Nottingham, England) was dialyzed (MWCO 8 kDa, Spectra/Por® 6) against 4.5 l of ultrapure water (4 water changes, 5 h). Tangential ultrafiltration (MWCO 30 kDa) was used to concentrate the solution to the original volume. Subsequently, 10 ml of the respective albumin solution were stirred with 200 rpm at room temperature and $SPION^{LA2}$ was added dropwise through a 0.8 µm syringe filter to receive a total iron concentration of 2.5 mg/ml. After 10 min stirring, excess albumin was removed by tangential ultrafiltration (7).

Dextran-coated SPIONs ($SPION^{DEX}$) were synthesized according to Unterweger et al. with slight modifications (8). In brief, $FeCl_3$ and $FeCl_2$ (molar ratio $Fe^{3+}/Fe^{2+} = 2$) were added to an aqueous solution containing 8.8% (w/w) dextran. Addition of ammonia to the ice cold solution led to the precipitation of the particles. The suspension was heated to 75°C for 45 min and afterwards cooled to room temperature. Particles were purified by dialysis and ultrafiltration. The dextran shell was cross-linked with epichlorohydrin under basic conditions to increase particle stability. Finally, particles were purified by dialysis and ultrafiltration. All nanoparticle solutions were sterile filtered using syringe filters and the total iron content was determined employing microwave plasma atomic emission spectroscopy. Nanoparticles were previously characterized physicochemically; basic features are summarized in **Table 1**.

Preparation of Human Material

All analyses of human material were performed in full agreement with institutional guidelines and with the approval of the Ethical Committee of the University Hospital Erlangen (permission number 257_14B). Platelet-rich plasma was generated by centrifuging lithium-heparin anticoagulated venous whole blood from normal healthy volunteers at 200 g for 10 min. Polymorphonuclear cells (PMN) were obtained by density gradient centrifugation using Lymphflot (Bio-Rad Medical Diagnostics GmbH, Dreieich, Germany) as described elsewhere (9). In brief, whole blood was diluted with phosphate buffered saline (PBS) and pipetted carefully onto Lymphflot solution and centrifuged for 20 min at 850 g without brake (acceleration 1, deceleration 0). Then, the plasma and peripheral blood mononuclear cells (PBMC) layer were discarded. The PMN-rich

TABLE 1 | Physicochemical characterization of SPIONs.

SPION name	Stock conc. (mg/ml)	Size by dynamic light scattering (DLS) (nm)	Zeta potential (mV)
$SPION^{LA1}$	4.41	127.9	−30.7
$SPION^{LA2}$	11.96	55.8	−25.1
$SPION^{LA-HSA}$	5.16	58.9	−11.9
$SPION^{DEX}$	5.74	31.0	−1.7

layer on top of the erythrocytes was collected and erythrocytes were removed by hypotonic lysis. Cell viability and cell count were determined by MUSE cell analyzer (Merck-Millipore, Billerica, MA, USA).

Animal Experiments

Studies involving animals, including housing and care, euthanasia, and experimental protocols were conducted in accordance with the local animal ethical committee in the animal house of Danylo Halytsky Lviv National Medical University, permission number 5/23.02/17, under the supervision of a certified veterinary doctor. Ten white laboratory rabbits, 4-month old males were used for this investigation. Rabbits were housed in individual cages in a temperature/humidity/light-controlled environment, with both food and drinking water available *ad libitum*. Specifically, a rabbit was injected with sedative, afterwards fixed and 500 μg of SPION nanoparticles were injected into the central artery of the ear. Injection site was 2–3 cm from the base of the ear. Central artery goes in the middle of the era, then providing left and right marginal veins. A neodymium magnet (5 cm in diameter) was placed just below one of the marginal veins (more external), while the other vein was gently pressed at the base of the air, to limit the blood flow and direct all the blood flow to the vein with the placed magnet. The ear was immobilized on the magnet for at least 20 min after SPION injection; then the vessels were examined for clottings. If needed, the animal was sacrificed and ear tissues were fixed in 4% paraformaldehyde (PFA), then embedded and processed for hematoxylin and eosin (HE) staining and immune histochemistry using previously described techniques (10).

Sterility and Endotoxin Content of SPIONs

For sterility testing, nanoparticles were diluted in H_2O to receive concentrations of 250, 50, and 10 μg/ml. H_2O and saliva (diluted 1/5 and 1/25) served as negative and positive controls, respectively. 100 μl of test sample were plated onto the agar plates in duplicates, and incubated at 37°C for 72 h. After 72 h, petri dishes were analyzed for growing colonies and documented by photography. Endotoxin-content of the nanoparticles was analyzed by EndoZyme endotoxin test (Hyglos, Bernried, Germany) according to the manufacturer's instructions. Nanoparticles were tested in concentrations of 25 and 50 μg/ml in endotoxin-free water. Endotoxin spiked samples served as controls. To 100 μl of standards and samples, reaction mixture (consisting of enzyme, substrate, assay buffer) was added and the reaction was monitored for 90 min at 37°C in a Microplate Reader Filter Max F5 (Molecular Devices; Biberach an der Riss, Germany; excitation 360 nm/emission 465 nm). The endotoxin amount [EU/ml] of the samples was calculated according to the standard curve parameters. Assay was accepted when spiking recovery of the samples was between 50 and 200%.

Incubation of SPIONs With PMN or Whole Blood

Nanoparticles were taken up in plasma or PBS in a concentration of 400 μg/ml and pre-incubated for 10 min. PMN were taken up in PBS or plasma in a density of 4×10^6/ml. Fifty microliters nanoparticles and 50 μl PMN were pipetted together in small FACS tubes, resulting in a final nanoparticle concentration of 200 μg/ml and a PMN density of 2×10^6/ml and incubated for 3 h at 37°. Analogous, PMN were taken up in RPMI medium containing 10% FBS and incubated with nanoparticles. NET formation was stimulated with 100 ng/ml Phorbol myristate acetate (PMA, Sigma Aldrich, St Louis, MO, USA). After incubation, cells were fixed with 100 μl 1% PFA in PBS.

One hundred microliters whole blood were incubated with 200 μg/ml nanoparticles for 3 h at 37°C in small FACS tubes. After 3 h, erythrocytes were lysed by formic acid (pH 2.7) and pH was reconstituted by a solution containing sodium carbonate, sodium chloride and sodium sulfate (pH 11.2). Cells were washed with PBS, centrifuged and supernatant was discarded. The pellet was taken up in 100 μl 1% PFA in PBS. Cells were analyzed in flow cytometry or fluorescence microscopy.

Incubation of PMN or Whole Blood With SPIONs in Presence of Magnet

Seven hundred and fifty microliters PMN (1×10^6/ml) or 500 μl whole blood were filled into Eppendorf tubes. Magnets (diameter 0.5 cm) were glued to the vials using adhesive tape. Forty micrograms per milliliters SPIONs were added and shaken in horizontal position for 3 h at 37°C. NET formation was stimulated with 100 ng/ml PMA. After 3 h, the magnets were removed, the tubes were inverted several times and nanoparticle agglomerates were harvested. Smears from PMN were prepared on glass slides, stained with Sytox Green Nucleic Acid Stain (Therma Fisher Scientific, Waltham, MA, USA) washed, embedded with mounting medium and analyzed in fluorescence microscopy. Whole blood agglomerates were filtered with 70 μm cell strainers, washed repeatedly with PBS and embedded in Tissue Tek at −20°C for preparation of cryosections.

Flow Cytometry

PMN integrity was analyzed in flow cytometry using a Gallios cytofluorometer™ (Beckman Coulter, Fullerton, CA, USA). Viable PMN were identified and gated by forward scatter (FSC) and side scatter (SSC) properties. Data were analyzed employing Kaluza™ software Version 1.2 (Beckman Coulter, Fullerton, CA, USA) and processed in Microsoft Excel.

Fluorescence Microscopy

Cells were transferred to 96 well plates and centrifuged at 500 g for 5 min to sediment cells and NETs. Then, NETs were visualized by a Zeiss AxioObserver.Z1 fluorescence microscope (Carl Zeiss AG, Oberkochen, Germany). Pictures were processed with ZEN pro 2012 software (Carl Zeiss AG) and Adobe Photoshop.

Immune Histochemistry

Ten micrometers cryosections (embedded in Tissue Tek) were prepared and stored at −20°C until use. Then, sections were fixed with aceton-methanol (1:1) for 90 s. Cryosections were dried at room temperature for 5 min and blocked with 10% FBS in PBS for 1 h at room temperature. Cells on slides were permeabilized with 0.1% Triton X-100 in H_2O for

10 min at room temperature. Primary antibody for neutrophil elastase (NE) (Abcam, United Kingdom, ab21595) 1:200 or for citrullated histone H3 (citH3) (Abcam, ab5103) 1:200 were added in 10% FBS in PBS overnight at 4°C. Slides were washed three times with PBS and incubated for 1.5 h at room temperature in the dark with secondary anti-rabbit IgG antibody conjugated with Cy5 (Jackson ImmunoReseach, Suffolk, United Kingdom, 11-175-144) 1:400 in H_2O. Slides were washed with PBS three times and incubated with Sytox Green (2.5 μM) for 15 min at room temperature. Slides were washed with H_2O three times and slides were embedded with DAKO fluorescent mounting medium (Dako, Hamburg, Germany). Samples without primary antibodies served as controls. Slides were analyzed in fluorescence microscopy.

RESULTS

Nanoparticles for application into the blood stream must fulfill several requirements. They have to be free of microbial or endotoxin contaminations, have to be stable as colloids and must not cause adverse (immune) reactions in the presence of blood cells and plasma components. Neutrophils are the most abundant cells in human blood and form the first line immune defense against invaders, like microbial, fungal or nanoparticular origin. In this study we investigated if SPIONs cause activation of neutrophils with concomitant NET formation in the presence and absence of magnetic fields. For that, SPIONs with different coatings, hydrodynamic sizes and physicochemical properties were applied, as summarized in **Table 1**. All used SPION systems were free of bacterial contaminations and endotoxin content was below 0.5 EU/mg (data not shown).

In vitro Formation of SPION-Aggregated NET-Co-aggregates in Plasma, PBS, or Medium Containing 10% Serum

Two hundred micrograms per milliliters SPIONs were suspended in plasma, PBS or medium containing 10% serum and incubated for 10 min. We observed that the SPIONs exhibited different colloidal stabilities, with $SPION^{LA1}$ and $SPION^{LA2}$ forming clusters after incubation in the presence of PBS **(Figure 1A)**; incubation with plasma or medium containing 10% serum did not induce clusters due to the formation of stabilizing protein coronae (**Figures 1B**, **2A**) (11, 12).

After 3 h of incubation with PMN in PBS we found extracellular DNA in those samples in which nanoparticle aggregates had been observed **(Figure 1C)**. PMA as canonical stimulator for NET formation also induced extracellular DNA in the presence of PBS. In plasma or serum-containing medium no NET formation was observed for SPIONs; NETs were induced by PMA, however, they were considerably smaller (**Figures 1D**, **2B**). So far, it seems that formation of NETs in the presence of SPIONs depends either on the size of the nanoparticle agglomerates or on the medium (PBS, plasma or serum-containing medium). Analysing PMN with viable morphology by means of forward and side scatter we detected aggregated NETs (aggNETs) for $SPION^{LA1}$ and $SPION^{LA2}$ in PBS, but not for the other nanoparticles **(Figure 1E)**. In the presence of plasma or medium containing 10% serum, no aggNETs were detected after incubation with SPIONs (**Figures 1F**, **2C**).

In vitro Formation of SPION-Aggregated NET-Co-aggregates in Media Containing 10% Serum in the Presence of a Magnetic Field

To analyze *in vitro* NET formation in media containing 10% serum PMN were incubated with 40 μg/ml SPIONs on an orbital shaker to prevent passive sedimentation of the nanoparticles. Then the samples were subjected or not to magnetic fields for 3 h under constant shaking at 37°C. In these conditions $SPION^{LA1}$, $SPION^{LA2}$, and $SPION^{LA-HSA}$ accumulated close to the magnets. The $SPION^{LA-HSA}$ conglomerates were instable and could easily be resuspended by shaking; those of $SPION^{LA1}$ and $SPION^{LA2}$ formed tight and stable aggregates that could not be resuspended by shaking. In the absence of magnets no agglomerations were detected **(Figure 3A)**.

Centrifuged samples were stained for NETs. Fluorescence microscopy revealed fibers of extracellular/extranuclear DNA for $SPION^{LA1}$ and $SPION^{LA2}$ incubated in the presence of a magnetic field. These looked similar to NETs induced by PMA **(Figure 3C)**, LPS, MSU crystals, and zymosan (not shown); in the absence of a magnetic field no extracellular DNA fibers were detected **(Figure 3B)**. Brightfield microscopy showed dark nanoparticles entrapped in the NETs **(Figure 3C)**. Fluorescence microscopy of a $SPION^{LA1}$–induced aggNET-co-aggregate revealed DNA fibers around the nanoparticle agglomerate **(Figure 3D).**

Ex vivo Formation of SPION-Aggregated NET-Co-aggregates in Whole Blood in the Presence of a Magnetic Field

Next we incubated whole blood with 40 μg/ml SPIONs in the absence or presence of a magnetic field. The samples were incubated on an orbital shaker. After 3 h we observed brown agglomerates sticking to the tube walls close to the magnets for $SPION^{LA1}$ and $SPION^{LA2}$, which were easily visible by the naked eye. For $SPION^{DEX}$ and $SPION^{LA-HSA}$ no visible agglomerates were detected **(Figure 4A)**. To analyze the agglomerates in more detail, we isolated the large structures employing a 70 μM mesh **(Figure 4B)**. In the absence of a magnetic field, no large agglomerates were formed; we only detected small brown structures for $SPION^{LA1}$ and $SPION^{LA2}$. PMA induced NETs appeared whitish since they did not contain dark brown nanoparticles. Cryosections of the agglomerates were stained for neutrophil elastase (NE), citrullinated histone H3 (citH3), and extracellular DNA. In the presence of $SPION^{LA1}$ and $SPION^{LA2}$ large structures developed, which contained iron oxide nanoparticle aggregates arranged in large rows (dark structures in bright field). Around the nanoparticle rows several bound viable PMN were detected by nuclear Sytox fluorescence and brightfield imaging. The aggregated nanoparticle structures were stained positive for NE, citH3, and extracellular DNA, although the green signal of the latter was partially quenched

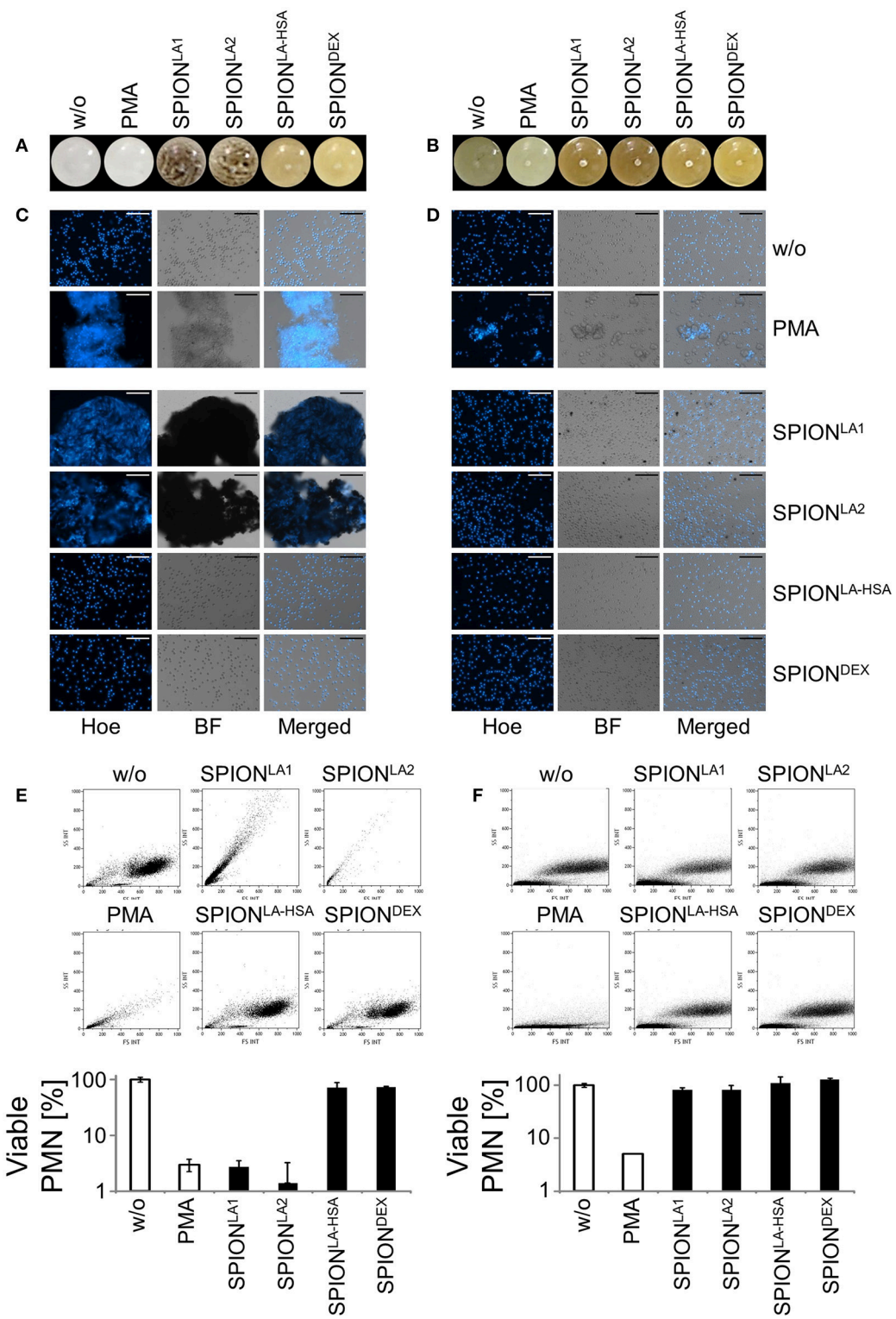

FIGURE 1 | Non-stabilized SPIONs induce NET formation in protein-free buffer but not in plasma. In PBS non-stabilized SPIONs (200 μg/ml) form agglomerates **(A)**, whereas in plasma the particles are stabilized by protein coronae **(B)**. PMN were incubated with 200 μg/ml nanoparticles for 3 h in PBS **(C)** or plasma **(D)**. Then, samples were stained with Hoechst, and prepared for fluorescence microscopy. PMA treated and untreated cells served as positive and negative control, respectively. Scale bars refer to 100 μm **(C,D)**. Measurement of neutrophils by flow cytometry and evaluation of viable PMN count based on forward and side scatter properties in PBS **(E)** or plasma **(F)**. Experiment was performed in triplicates of at least two independent donors; representative data of one donor (mean values with standard deviations) are shown **(E,F)**.

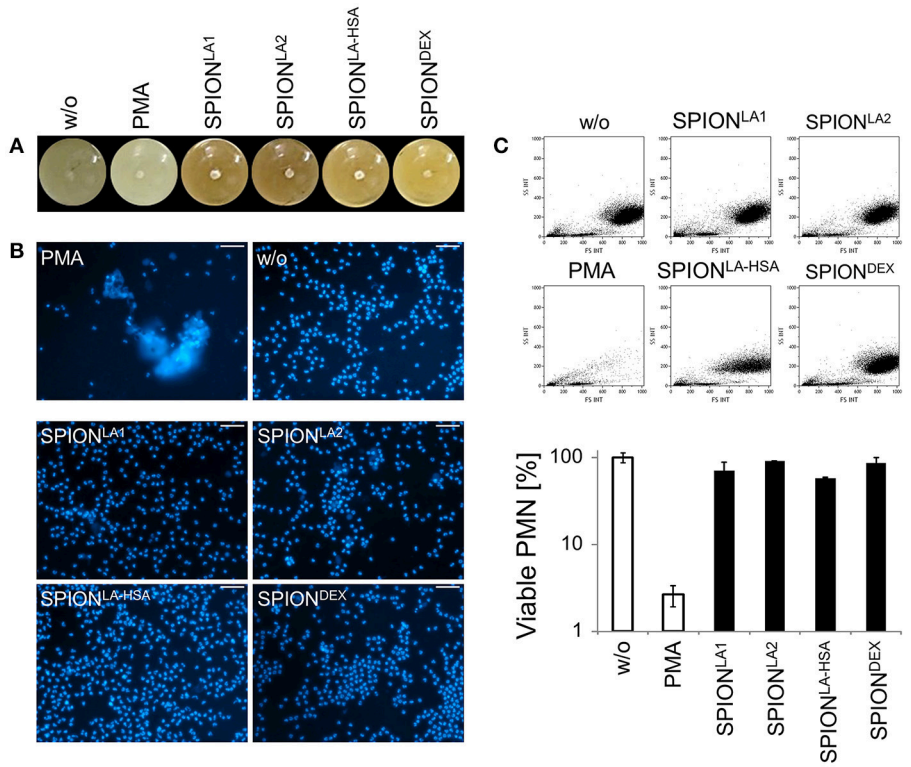

FIGURE 2 | Serum reduced NET formation of isolated PMN. In serum-containing medium (R10) all SPIONs (200 μg/ml) are colloidally stable **(A)**. Isolated PMN were incubated with 200 μg/ml nanoparticles for 3 h in R10. Then, cells were stained with Hoechst, and prepared for fluorescence microscopy. PMA treated and untreated cells served as positive and negative control, respectively. Scale bars refer to 50 μm **(B)**. Measurement of neutrophils by flow cytometry and evaluation of viable PMN count based on forward and side scatter properties. Experiment was performed in triplicates of at least two independent donors; representative data of one donor (mean values with standard deviations) are shown **(C)**.

by the brownish particles. We conclude that magnet-induced primary nanoparticle agglomerates activate NET formation and build larger secondary structures glued together by aggNETs **(Figures 4C,D)**.

In vivo Formation of SPION-Aggregated NET-Co-aggregates

To test whether SPION-aggNET-co-aggregates also form *in vivo* we injected SPION^{LA1} nanoparticles into the central arterial vessel of rabbit ears and subjected the distal vessel to an external magnetic field. After 20 min black agglomerations inside branches of the marginal veins of the ear were visible **(Figure 5A)**. The intravascular agglomerates remained visible for at least 3 days after injection, when the animals were sacrificed and the ear tissue subjected to analyses by histology. Serial sections through the black agglomerates and staining with HE revealed two vascular clots with one containing a dense package of SPION^{LA1} (**Figure 5B**; clot 1). Staining with PI (red) and anti-dDNA IgM (green) showed that the agglomeration contained extracellular DNA **(Figure 5C)**. Clot 2 was positive for myeloperoxidase and DNA, but did not contain any SPION^{LA1} **(Figure 5D)**. Importantly, clot 2 was not in direct proximity to the nanoparticles, thus, neutrophils might have been activated by massive cell stress due to the downstream vessel occlusion. Alternative coating of the SPIONs with HSA or dextran (SPION^{LA-HSA} and SPION^{DEX}) prevented vascular occlusions even in the presence of a magnetic field (data not shown).

DISCUSSION

Uncoated SPIONs tend to agglomerate due to magnetic attraction, high surface energy and van der Waals forces (13). In our study, SPION^{LA1} and SPION^{LA2} formed nanoparticle agglomerates in blood *in vitro* and *in vivo*, when brought into magnetic fields (**Figures 4**, **5**). These instable agglomerates activated NET formation and were glued together by the extracellular chromatin. NET formation stabilized the agglomerates, leading to the formation of firm SPION-aggNETs-co-aggregates that may even occlude vessels. Thus, appropriate coating of SPIONs (SPION^{LA-HSA} or SPION^{DEX}) prevents the formation of occlusive aggregates, increases the safety of the SPIONs and allows their therapeutic use.

Nanoparticles injected in the blood are known to be opsonized by serum proteins including complement compounds, immunoglobulins, fibronectin, and apolipoproteins (14). This

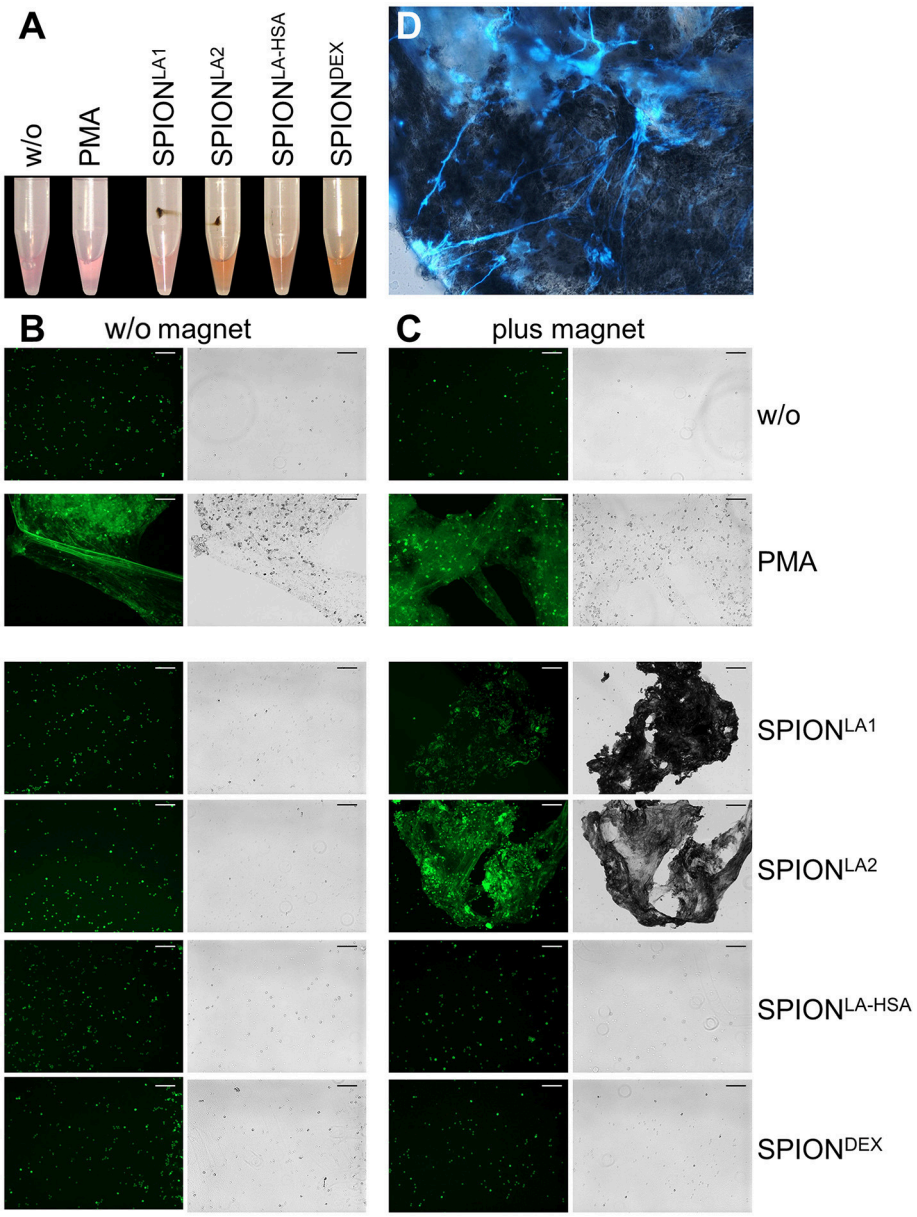

FIGURE 3 | Magnetic fields increase NET formation of isolated PMN in serum-containing media. Isolated PMN were incubated with 40 μg/ml SPIONs in R10 media under constant shaking at 37°C in the absence or presence of magnetic fields. After 3 h, magnets were removed and the tube walls rinsed with medium **(A)**. The harvested cells were stained with Sytox Green and prepared for fluorescence microcopy. Scale bars refer to 100 μm **(B,C)**. Smear of the SPION^{LA1}- induced aggNET-co-aggregate was stained with Hoechst 33342 **(D)**.

protein corona increases biocompatibility of the nanoparticles and raises their colloidal stability (15–17). We showed that in the presence of pure plasma, plasma containing cell culture medium or whole blood nanoparticle agglomeration was prevented (**Figures 1D**, **2**), whereas in PBS agglomeration occurred in non-sufficiently coated SPIONs (**Figure 1A**). After injection of nanoparticles into the blood stream, opsonisation with plasma proteins results in uptake by cells of the reticuloendothelial system (18). Thus, the majority of the nanoparticles are quickly removed by Kupffer cells of the liver and spleen (19). To circumvent fast clearance of therapeutic nanoparticles from the blood stream, coating with e.g. polyethylene glycol (PEG) is used to mask particles and to increase circulation times (20). For application of SPIONs as drug transporter in magnetic drug targeting, intraarterial injection in the tumor supplying vessels can reduce early clearance (5, 21).

Besides macrophages and monocytes, also neutrophils are involved in the phagocytic removal of pathogens. The decision if neutrophils detoxify pathogens by phagocytosis or NET formation has been shown to depend on the pathogen size

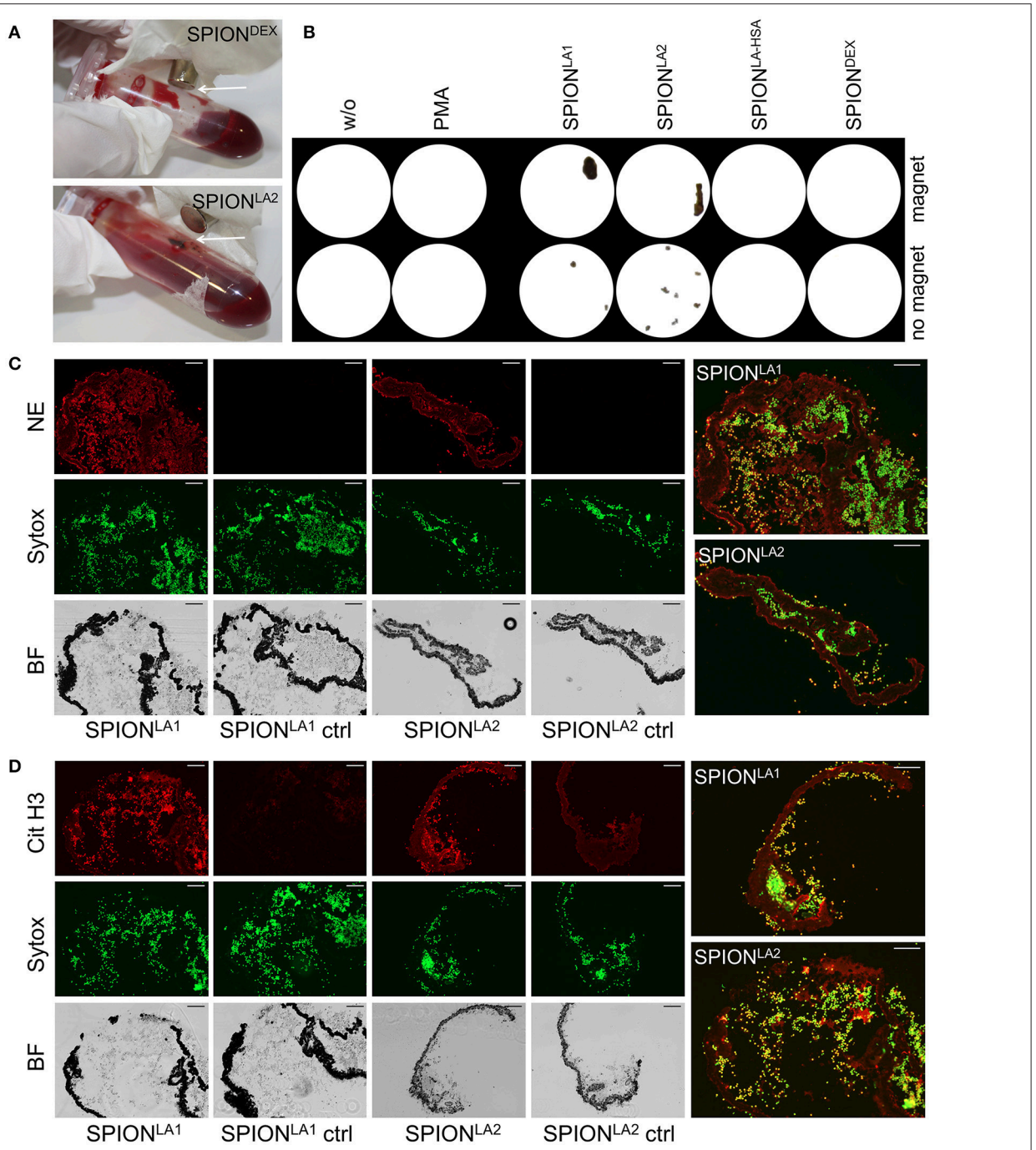

FIGURE 4 | NETosis in whole blood in absence/presence of magnet. Whole blood was incubated with 40 μg/ml SPIONs under constant shaking at 37°C in the absence or presence of magnetic fields **(A)**. After 3 h, agglomerates were harvested on 70 μm mesh cell strainers and prepared for sectioning **(B).** Cryosections (10 μm) of agglomerates were stained for neutrophil elastase (NE) **(C)** or citrinulated histone H3 (cit H3) **(D)** and analyzed in fluorescence microscopy. Scale bars refer to 100 μm. Large images represent overlays of the green and red fluorescences for SPION^{LA1} and SPION^{LA2} **(C,D)**.

amongst others (22). Here, neutrophil elastase plays a crucial role. Yeast particles for example are quickly phagocytosed, with fusion of NE-containing granules to the phagosome. When neutrophils meet a pathogen that is too big to be taken up into phagosomes, NE is slowly released into the cytosol, translocates into the nucleus and promotes chromatin decondensation (4). We observed in our experiments that NET formation depends on the agglomeration of nanoparticles. Agglomeration of insufficiently coated SPIONs was caused in the absence of stabilizing proteins (**Figures 1**, **2**) or due to active enrichment under a magnetic

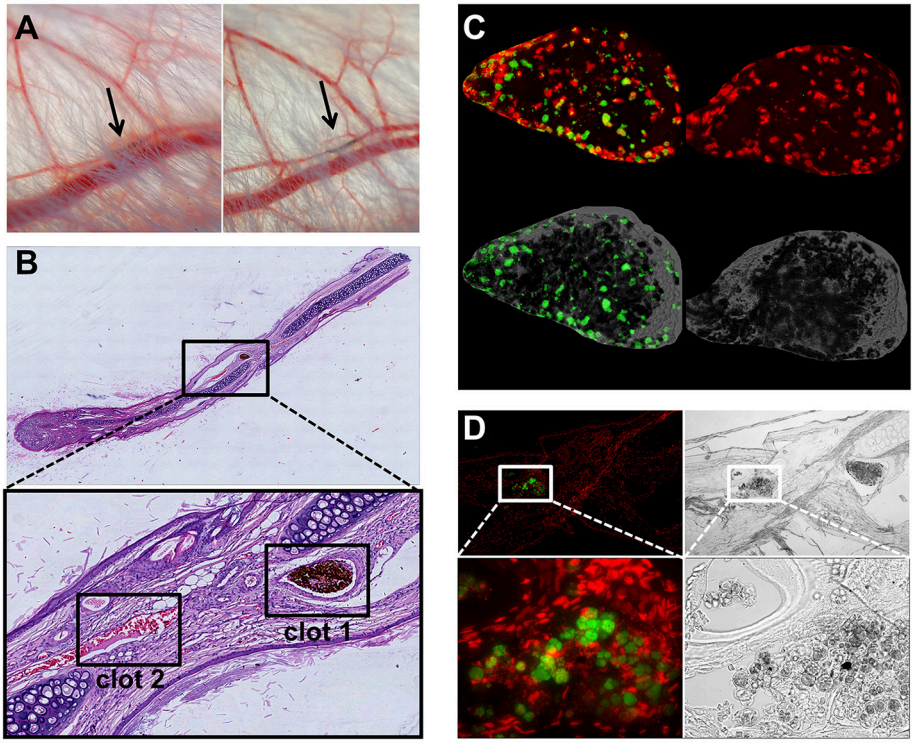

FIGURE 5 | Magnetic fields induce SPION^{LA1}-aggNET-co-aggregates *in vivo*. Magnetic field induces aggregation of SPION^{LA1} and aggNET in the vessel of rabbit ears, as early as 20 min after injection (left) and up to 3 days after injection (right) **(A)**. The area imaged was positioned on top of permanent neodymium magnet immediately after injection. HE staining of section from rabbit ear (Clot 1, SPION^{LA1}-aggNET-co-aggregates area with initiated clot formation; Clot 2, canonical clot formed) **(B)**. Clot 1 stained for externalized DNA (green) by anti-DNA IgM antibody, and DNA (red) by PI **(C)**; Clot 2 contained Myeloperoxidase (green) and DNA (red) **(D)**.

field (**Figures 3–5**). Thus, size of the nanoparticle clusters, local nanoparticle concentration or the surface structure might play a role for the subsequent formation of NETs. In line with this, it has been shown that the topology of biomaterial implants is crucial to prevent neutrophil activation as well as acute and chronic inflammation (23). Cross-linked alginate implants attract more neutrophils than alginate injected as solution (24).

Our findings indicate that the 3D architecture of nanoparticles and their agglomerates can regulate neutrophils' responses and effector mechanisms. We showed that with magnetically induced agglomeration of nanoparticles, the formation of firm aggNET-SPION-co-aggregates is induced in a selective manner (**Figure 3**). This also happens in the circulation *in vivo*. These firm aggregates can form non-canonical thrombi that are able to occlude vessels (**Figure 5**). This is comparable to the aggNET-mediated microvascular thrombosis in sepsis (25, 26). The action of the plasma proteins, aggNETs and of NET-associated proteins (NE, histones) further increases size and stability of the thrombi. Indeed, NE can cleave and inactivate tissue factor pathway inhibitor, leading to increased pro-coagulant activity, with concomitant platelet activation and accelerated thrombus formation (27–29). In addition, aggNET-borne histones in turn activate platelets (30). The mutual activation of aggNETs and the canonical coagulation pathway further promotes coagulation and may form tight vascular occlusions, often in the capillary bed.

Besides the coagulation system, interactions of NETs with the complement system have additionally become apparent. Activated complement proteins can induce NET formation, and NETs *vice versa* can serve as a platform for complement activation (31). Previously, iron oxide-based contrast agents showed their potential to trigger hypersensitivity reactions or complement activation (32, 33). For SPION^{DEX} dedicated for magnetic resonance imaging we previously proofed the absence of complement activation *in vitro* and complement-activation related pseudoallergy (CARPA) *in vivo,* probably due to tight coverage of the iron surface by complete cross-linking of the dextran shell (8, 34), indicating the importance of proper coatings for biocompatibility. For SPIONs dedicated for magnetic drug targeting (SPION^{LA-HSA}) we previously showed that an artificial albumin protein corona can colloidally stabilize iron oxide nanoparticles and increase their biocompatibility (11, 35, 36).

Here we report that SPION^{LA1} and SPION^{LA2} did not agglomerate and did not induce NETosis in plasma or serum containing cell culture media in the absence of a magnetic field. However, as soon as a magnetic field was applied, a topological structure evolved which favors NET formation and thrombogenicity. Both drawbacks were clearly prevented

in preparations of $SPION^{LA-HSA}$ and $SPION^{DEX}$ which were coated with human serum albumin or dextran.

AUTHOR CONTRIBUTIONS

RB developed experimental setup for animal experiments and performed animal microphotography. RB, TD, and SP performed experiments with rabbits. VV and BW processed, stained, and analyzed tissues and cells in microscopy, HU synthesized and characterized SPIONs. ZL and CJ performed flow cytometry, CA, RB, MH, and CJ planned the experiments and wrote the manuscript.

FUNDING

This work was carried out with financial support from the Bavarian State Ministry for the Environment and Consumer Protection, FUMIN Bridge Funding appropriations, the Manfred Roth Stiftung, Fürth, and the Emerging Fields Initiative (EFI) of the University of Erlangen-Nürnberg (BIG-THERA).

ACKNOWLEDGMENTS

We thank Eveline Schreiber and Julia Band for their excellent technical support.

REFERENCES

1. Bardoel BW, Kenny EF, Sollberger G, Zychlinsky A. The balancing act of neutrophils. *Cell Host Microbe* (2014) 15:526–36. doi: 10.1016/j.chom.2014.04.011
2. Brinkmann V, Reichard U, Goosmann C, Fauler B, Uhlemann Y, Weiss DS, et al. Neutrophil extracellular traps kill bacteria. *Science* (2004) 303:1532–5. doi: 10.1126/science.1092385
3. Munoz LE, Bilyy R, Biermann MH, Kienhofer D, Maueroder C, Hahn J, et al. Nanoparticles size-dependently initiate self-limiting NETosis-driven inflammation. *Proc Natl Acad Sci USA*. (2016) 113:E5856–65. doi: 10.1073/pnas.1602230113
4. Branzk N, Lubojemska A, Hardison SE, Wang Q, Gutierrez MG, Brown GD, et al. Neutrophils sense microbe size and selectively release neutrophil extracellular traps in response to large pathogens. *Nat Immunol.* (2014) 15:1017–25. doi: 10.1038/ni.2987
5. Tietze R, Lyer S, Durr S, Struffert T, Engelhorn T, Schwarz M, et al. Efficient drug-delivery using magnetic nanoparticles–biodistribution and therapeutic effects in tumor bearing rabbits. *Nanomedicine* (2013) 9:961–71. doi: 10.1016/j.nano.2013.05.001
6. Zaloga J, Pottler M, Leitinger G, Friedrich RP, Almer G, Lyer S, et al. Pharmaceutical formulation of HSA hybrid coated iron oxide nanoparticles for magnetic drug targeting. *Eur J Pharm Biopharm.* (2016) 101:152–62. doi: 10.1016/j.ejpb.2016.01.017
7. Zaloga J, Stapf M, Nowak J, Pottler M, Friedrich RP, Tietze R, et al. Tangential flow ultrafiltration allows purification and concentration of lauric acid-/albumin-coated particles for improved magnetic treatment. *Int J Mol Sci.* (2015) 16:19291–307. doi: 10.3390/ijms160819291
8. Unterweger H, Janko C, Schwarz M, Dezsi L, Urbanics R, Matuszak J, et al. Non-immunogenic dextran-coated superparamagnetic iron oxide nanoparticles: a biocompatible, size-tunable contrast agent for magnetic resonance imaging. *Int J Nanomedicine* (2017) 12:5223–38. doi: 10.2147/IJN.S138108
9. Nilsson C, Aboud S, Karlen K, Hejdeman B, Urassa W, Biberfeld G. Optimal blood mononuclear cell isolation procedures for gamma interferon enzyme-linked immunospot testing of healthy Swedish and Tanzanian subjects. *Clin Vaccine Immunol.* (2008) 15:585–9. doi: 10.1128/CVI.00161-07
10. Bilyy R, Fedorov V, Vovk V, Leppkes M, Dumych T, Chopyak V, et al. Neutrophil extracellular traps form a barrier between necrotic and viable areas in acute abdominal inflammation. *Front Immunol.* (2016) 7:424. doi: 10.3389/fimmu.2016.00424
11. Janko C, Zaloga J, Pöttler M, Dürr S, Eberbeck D, Tietze R, et al. Strategies to optimize the biocompatibility of iron oxide nanoparticles – "SPIONs safe by design". *J Magn Magn Mater.* (2017) 431:281–4. doi: 10.1016/j.jmmm.2016.09.034
12. Lundqvist M, Augustsson C, Lilja M, Lundkvist K, Dahlback B, Linse S, et al. The nanoparticle protein corona formed in human blood or human blood fractions. *PLoS ONE* (2017) 12:e0175871. doi: 10.1371/journal.pone.0175871
13. Ali A, Zafar H, Zia M, Ul Haq I, Phull AR, Ali JS, et al. Synthesis, characterization, applications, and challenges of iron oxide nanoparticles. *Nanotechnol Sci Appl.* (2016) 9:49–67. doi: 10.2147/NSA.S99986
14. Vonarbourg A, Passirani C, Saulnier P, Benoit JP. Parameters influencing the stealthiness of colloidal drug delivery systems. *Biomaterials* (2006) 27:4356–73. doi: 10.1016/j.biomaterials.2006.03.039
15. Nguyen VH, Lee BJ. Protein corona: a new approach for nanomedicine design. *Int J Nanomedicine* (2017) 12:3137–51. doi: 10.2147/IJN.S129300
16. Gebauer JS, Malissek M, Simon S, Knauer SK, Maskos M, Stauber RH, et al. Impact of the nanoparticle-protein corona on colloidal stability and protein structure. *Langmuir* (2012) 28:9673–9. doi: 10.1021/la301104a
17. Monopoli MP, Pitek AS, Lynch I, Dawson KA. Formation and characterization of the nanoparticle-protein corona. *Methods Mol Biol.* (2013) 1025:137–55. doi: 10.1007/978-1-62703-462-3_11
18. Owens DE III, Peppas NA. Opsonization, biodistribution, and pharmacokinetics of polymeric nanoparticles. *Int J Pharm.* (2006) 307:93–102. doi: 10.1016/j.ijpharm.2005.10.010
19. Sadauskas E, Wallin H, Stoltenberg M, Vogel U, Doering P, Larsen A, et al. Kupffer cells are central in the removal of nanoparticles from the organism. *Part Fibre Toxicol.* (2007) 4:10. doi: 10.1186/1743-8977-4-10
20. Suk JS, Xu Q, Kim N, Hanes J, Ensign LM. PEGylation as a strategy for improving nanoparticle-based drug and gene delivery. *Adv Drug Deliv Rev.* (2016) 99(Pt A):28–51. doi: 10.1016/j.addr.2015.09.012
21. Alexiou C, Arnold W, Klein RJ, Parak FG, Hulin P, Bergemann C, et al. Locoregional cancer treatment with magnetic drug targeting. *Cancer Res.* (2000) 60:6641–8.
22. Warnatsch A, Tsourouktsoglou TD, Branzk N, Wang Q, Reincke S, Herbst S, et al. Reactive oxygen species localization programs inflammation to clear microbes of different size. *Immunity* (2017) 46:421–32. doi: 10.1016/j.immuni.2017.02.013
23. Selders GS, Fetz AE, Radic MZ, Bowlin GL. An overview of the role of neutrophils in innate immunity, inflammation and host-biomaterial integration. *Regen Biomater.* (2017) 4:55–68. doi: 10.1093/rb/rbw041
24. Jhunjhunwala S, Aresta-DaSilva S, Tang K, Alvarez D, Webber MJ, Tang BC, et al. Neutrophil responses to sterile implant materials. *PLoS ONE* (2015) 10:e0137550. doi: 10.1371/journal.pone.0137550
25. Kimball AS, Obi AT, Diaz JA, Henke PK. The emerging role of NETs in venous thrombosis and immunothrombosis. *Front Immunol.* (2016) 7:236. doi: 10.3389/fimmu.2016.00236
26. Jimenez-Alcazar M, Rangaswamy C, Panda R, Bitterling J, Simsek YJ, Long AT, et al. Host DNases prevent vascular occlusion by neutrophil extracellular traps. *Science* (2017) 358:1202–6. doi: 10.1126/science.aam8897
27. Clark SR, Ma AC, Tavener SA, McDonald B, Goodarzi Z, Kelly MM, et al. Platelet TLR4 activates neutrophil extracellular traps to ensnare bacteria in septic blood. *Nat Med.* (2007) 13:463–9. doi: 10.1038/nm1565
28. Massberg S, Grahl L, von Bruehl ML, Manukyan D, Pfeiler S, Goosmann C, et al. Reciprocal coupling of coagulation and innate immunity via neutrophil serine proteases. *Nat Med.* (2010) 16:887–96. doi: 10.1038/nm.2184
29. von Bruhl ML, Stark K, Steinhart A, Chandraratne S, Konrad I, Lorenz M, et al. Monocytes, neutrophils, and platelets cooperate to initiate and

propagate venous thrombosis in mice *in vivo*. *J Exp Med.* (2012) 209:819–35. doi: 10.1084/jem.20112322
30. Martinod K, Wagner DD. Thrombosis: tangled up in NETs. *Blood* (2014) 123:2768–76. doi: 10.1182/blood-2013-10-463646
31. de Bont CM, Boelens WC, Pruijn GJM. NETosis, complement, and coagulation: a triangular relationship. *Cell Mol Immunol*. (2018). doi: 10.1038/s41423-018-0024-0. [Epub ahead of print].
32. Banda NK, Mehta G, Chao Y, Wang G, Inturi S, Fossati-Jimack L, et al. Mechanisms of complement activation by dextran-coated superparamagnetic iron oxide (SPIO) nanoworms in mouse versus human serum. *Part Fibre Toxicol.* (2014) 11:64. doi: 10.1186/s12989-014-0064-2
33. Szebeni J, Fishbane S, Hedenus M, Howaldt S, Locatelli F, Patni S, et al. Hypersensitivity to intravenous iron: classification, terminology, mechanisms and management. *Br J Pharmacol.* (2015) 172:5025–36. doi: 10.1111/bph.13268
34. Unterweger H, Dezsi L, Matuszak J, Janko C, Poettler M, Jordan J, et al. Dextran-coated superparamagnetic iron oxide nanoparticles for magnetic resonance imaging: evaluation of size-dependent imaging properties, storage stability and safety. *Int J Nanomedicine* (2018) 13:1899–915. doi: 10.2147/IJN.S156528
35. Friedrich RP, Janko C, Poettler M, Tripal P, Zaloga J, Cicha I, et al. Flow cytometry for intracellular SPION quantification: specificity and sensitivity in comparison with spectroscopic methods. *Int J Nanomedicine* (2015) 10:4185–201. doi: 10.2147/IJN.S82714
36. Zaloga J, Janko C, Nowak J, Matuszak J, Knaup S, Eberbeck D, et al. Development of a lauric acid/albumin hybrid iron oxide nanoparticle system with improved biocompatibility. *Int J Nanomedicine* (2014) 9:4847–66. doi: 10.2147/IJN.S68539

Conflict of Interest Statement: The authors declare that the research was conducted in the absence of any commercial or financial relationships that could be construed as a potential conflict of interest.

The reviewer GS and handling Editor declared their shared affiliation.

frontiers in Immunology

MINI REVIEW
published: 06 July 2018
doi: 10.3389/fimmu.2018.01559

Neutrophil Extracellular Traps Formation and Aggregation Orchestrate Induction and Resolution of Sterile Crystal-Mediated Inflammation

Yanhong Li[1†], Xue Cao[1†], Yi Liu[1], Yi Zhao[1,2] and Martin Herrmann[2]*

[1] Department of Rheumatology and Immunology, West China Hospital, Sichuan University, Chengdu, China, [2] Department of Internal Medicine 3, Rheumatology and Immunology, Friedrich-Alexander-University Erlangen-Nürnberg (FAU), Erlangen, Germany

OPEN ACCESS

Edited by:
Philippe Saas, INSERM U1098 Interactions Hôte-Greffon-Tumeur & Ingénierie Cellulaire et Génique, France

Reviewed by:
Francesca Oliviero, Università degli Studi di Padova, Italy
Angelo A. Manfredi, Università Vita-Salute San Raffaele, Italy

***Correspondence:**
Yi Zhao
zhao.y1977@163.com

[†]Co-first author.

Specialty section:
This article was submitted to Inflammation, a section of the journal Frontiers in Immunology

Received: *30 March 2018*
Accepted: *25 June 2018*
Published: *06 July 2018*

Citation:
Li Y, Cao X, Liu Y, Zhao Y and Herrmann M (2018) Neutrophil Extracellular Traps Formation and Aggregation Orchestrate Induction and Resolution of Sterile Crystal-Mediated Inflammation. Front. Immunol. 9:1559. doi: 10.3389/fimmu.2018.01559

The formation of neutrophil extracellular traps (NETs) to immobilize pathogens represents a novel antimicrobial strategy of the immune system. The microcrystals related to human diseases are classified into endogenous microcrystals, including monosodium urate (MSU), calcium pyrophosphate dihydrate, calcium carbonate, calcium phosphate, calcium oxalate, cholesterol, and exogenous material like crystals from silica. Although microcrystals possess distinct compositions and shapes, they have a common characteristic: they stimulate neutrophils to release NETs. In low and high densities, neutrophils form NETs and aggregated NETs (aggNETs) that reportedly orchestrate the initiation and resolution of sterile crystal-mediated inflammation, respectively. Here, we summarize the different roles of NETs and aggNETs stimulated by the crystals mentioned above in related inflammatory reactions. The NETosis-derived products may represent a potential therapeutic target in crystal-mediated diseases.

Keywords: sterile crystal, inflammation, neutrophil, neutrophil extracellular traps, aggregated neutrophil extracellular traps

INTRODUCTION

Neutrophils are the most abundant circulated leukocytes in blood and represent the first line of innate immune system to defense against the injury or infection, including bacteria, fungi, and protozoa. In addition to their classical functions like phagocytosis and degranulation, neutrophils are endowed with a novel antimicrobial strategy. They are able to entrap and kill pathogens by extruding their nucleohistone network into the extracellular space, known as neutrophil extracellular traps (NETs) (1). NETs formation can be induced by various kinds of stimuli, such as specific microbes, sterile inflammatory mediators like lipopolysaccharides (LPS), phorbol-12-myristate-13-acetate (PMA), IL-8, ionomycin (2) or cytokines (3), immune complexes, activated platelets (4), particulate matter, and microcrystals (5). Under certain circumstances NETs formation is accompanied by a unique cell death program referred to as NETosis. The latter is distinct from apoptosis and necrosis (1, 6). During NETosis, the chromatin decondenses, the membranes of nucleus and granules disintegrate to generate chromatin blended with nuclear and granular proteins and enzymes. Following the rupture of the cellular membrane, chromatin is decorated with a plethora of internal molecules, including histones, neutrophil elastase (NE), myeloperoxidase (MPO), proteinase-3 (PR3), lactoferrin, cathepsin G,

matrix metalloprotease 9, peptidoglycan-recognition proteins, high mobility group protein B1, pentraxin, LL-37, and the bactericidal/permeability-increasing protein (1, 6). These contents are then expelled into the extracellular environment (1, 7–10). However, several aspects of NETs formation still remain elusive. In some forms of NETs formation the production of reactive oxygen species (ROS) by NADPH oxidase or mitochondria emerged to play an integral role; ROS helps to translocate the granular proteins MPO and NE into the nucleus (6, 7). Meanwhile, a number of molecules have been identified contributing to NETs formation, including peptidyl arginine deiminase 4 (PADI4), TGF-β-activated kinase 1, intracellular Ca^{2+}, and RAF/MEK/ERK (11). Due to the complicated structure and cytotoxic enzymes, NETs have been implicated in orchestrating the local immune response *via* eliminating pathogens, releasing pro-inflammatory mediators, and damaging tissue directly (12–18). In the pathogenesis of autoimmune inflammatory diseases, such as vasculitis, RA, and SLE they may serve as source of neoantigens that trigger the production of autoantibodies. A number of studies have suggested that NETs are involve in trapping microcrystals when the human body is exposed to crystals from monosodium urate (MSU), calcium pyrophosphate dihydrate (CPP), cholesterol, calcium carbonate ($CaCO_3$), calcium phosphate (CaP), calcium oxalate (CaOx), or silica under conditions of sterile inflammation (19). The latent role of NETs in crystal-induced inflammation is either to induce local necroinflammation or to perform a state of alleviating inflammation, just like acute or chronic gout, respectively (20). Herein, we review the current state of knowledge regarding NETs formation and aggregation in sterile inflammation induced by different sizes and shapes of microcrystals.

MONOSODIUM URATE CRYSTALS

Crystals of MSU monohydrate ($NaC_5H_3N_4O_3.H_2O$) are macroscopically needle-shaped (21, 22). Their deposition in joints and soft tissues can cause an acute, inflammatory joint disease, usually referred to as gouty arthritis (23). In joints, MSU crystals induce the secretion of cytokines and chemokines by phagocytes, including interleukin (IL)-1β, tumor necrosis factor (TNF), IL-6, and IL-8 (24). These inflammatory mediators are crucial to amplify inflammation by the recruitment into the joint synovial fluid of further neutrophils and monocytes (24). MSU crystals are supposed to activate neutrophils to release cytokines and induce infiltration of further neutrophils to form NETs (25, 26) leading to acute, extremely painful, and tissue-damaging inflammation in joints.

The NET release from neutrophils induced by MSU crystals is a complex yet highly coordinated sequence of events. To facilitate this, a lot of signaling pathways have been evolved. It was reported that NADPH oxidase-mediated ROS production is required for NETs formation evoked by MSU crystals (19, 27). Neutrophils from patients with chronic granulomatous disease (CGD) or NADPH oxidase-deficient mice displayed weak NETs formation in response to MSU (19, 27). *In vitro*, neutrophils treated with various anti-oxidants, lack ROS production and NETs formation in response to MSU crystals (19, 27). Furthermore, NETs formation induced by soluble uric acid is mediated by NF-κB activation is independent of ROS production (28). Unexpectedly, there is report that MSU crystals induce NETosis in an NADPH oxidase-independent fashion distinct from PMA-induced NETosis (29). Also, autophagy, necroptosis, RIPK1-RIPK3-MLKL signaling, and endosomal acidification have emerged as key regulators of MSU crystal-induced NETs formation (20, 30). The stress-related protein REDD1 which expressed in neutrophils is regulated in development and DNA damage responses. At the attack phase of familial Mediterranean fever (FMF), upregulated REDD1 promote autophagy and augment NETs formation (31). Consistently, during remission phases of FMF, the transcription of REDD1 is impaired and resistant to autophagy-mediated NETs release (31). Specifically, blocking phosphatidylinositol 3-kinase signaling or phagolysosome fusion prevents MSU crystal-induced NETs formation (26, 30). Result from RIPK3 knockout murine demonstrated that neutrophils deficient in RIPK3 are unable to release NETs in response to MSU crystal *in vitro* or *in vivo* (26). By contrast, other studies showed that PMA stimulates NETs release independent of RIPK 3 and MLKL signaling (32). Studies have described substantial effects of the purinergic receptors, P2Y and P2Y6 on MSU crystal-induced NETs formation (33). MRS2578, an inhibitor of P2Y6, reportedly restrained neutrophil migration and production of ROS as shown by live cell imaging. This suggests that purinergic receptors are involved in NETs formation (33). Interestingly, SK&F96365 inhibited MSU crystal-induced NETs formation by affecting a store-operated calcium entry channel (33). Neutrophils and phagocytes internalize small urate micro-aggregates (UMA; <1μm in size) in the circulation and thus suppress MSU crystals formation (34). Gradually, mass of urate micro-aggregates exceeds the phagocytic ability of neutrophils leading to MSU crystals formation. Consequently, neutrophils are frustrated in phagocytosis and generate NETs (34, 35).

The NETs formation in response to MSU crystals is a complex process modulated by a plethora of factors, including inflammatory cytokines. In a MSU crystal-induced arthritis model has been shown that IL-1 inhibition is effective to control MSU-mediated inflammation (36). Neutrophil exhibit an enhanced NETs release in response to synovial fluid from gout patients, partially hindered by the IL-1β antagonist anakinra (30) and IL-1β accelerates NETs formation triggered by MSU crystals (37).

Interestingly, IL-1β alone does not stimulate NETs release (37) and positive feedback loops are crucial for NETs formation. In joints NETs release dangerous neutrophilic cargoes like histones and granule proteins like myeloperoxidase (MPO) and NE (1) further amplifying MSU crystal-induced inflammation. In addition, NE cleaves pro-IL-1β into its bioactive IL-1β and IL-1β is a crucial cytokine of the inflammatory response in gout. It recruits neutrophils to joints and enhances NETs formation triggered by MSU crystals (37–39). Apart from that, DAMPs released from NETs, such as DNA-activating Toll-like receptors or NLRP3 inflammasomes can augment inflammatory responses (40). MSU crystals induce NETosis through neutrophils in patients with gout. NETosis is further enhanced by impaired NETs degradation result from low DNase-1 activity in synovial fluids, in conjunction with enriched actin that is resistant to DNase degradation (29, 40). The aberrant accumulation of aggregated NETs (aggNETs) is associated with NETs clearance deficiency and formation of

extended NETs-crystal aggregates (40). In high neutrophil densities, NETs will agglomerate and form aggNETs (19).

It has been shown that aggNETs degrade pro-inflammatory chemokines and cytokines and suppress crystal-induced inflammation (19) *in vitro* and *in vivo*. Animal studies suggest an important anti-inflammatory role of aggNETs in the regulation of cytokines like TNF-α, IL-1β and IL-6, and chemokines, such as chemokine ligand CCL2 and monocyte chemoattractant protein-1 (19). Collectively, these findings suggest that aggNETs promote the resolution of acute gouty arthritis (19). Despite its important role in the resolution of inflammation, little is known about the regulation of aggNETs formation. It has been reported that MSU crystals induced aggNETs formation depends on the production of ROS (19). *In vitro*, neutrophils of patients with CGD co-cultured with MSU crystals show reduced formation of aggNETs (19). *In vivo*, NADPH oxidase-deficient mice reduced the formation of aggNETs, when stimulated with MSU, both in an air pouch model, and in MSU crystal-induced paw inflammation (19). Accordingly, the authors also reported that ATP, lactoferrin (19), IL-1β (37) and the P2Y6 receptor antagonist MRS2578 (33) enhance and inhibit MSU crystal-induced aggNETs formation, respectively (**Figure 1**).

CALCIUM PYROPHOSPHATE DIHYDRATE CRYSTALS

Calcium pyrophosphate dihydrate (CCP) crystals display a rhomboid or elongated shape, and are generally shorter than 10 μm in length (41). They tend to deposit in joints and causes pseudogout, characterized by periodic acute joint flares (42). CPP crystals directly interact with and activate macrophages to release IL-1β, which attract more neutrophils to the inflamed joints (43–46). Neutrophils phagocytosis of CPP crystals resulted in the release of NETs composed of extracellular DNA colocalizing with citrullinated histone H4 and myeloperoxidase (MPO) (47). CPP crystals elicited NETs faster and more efficiently than PMA (47). Going along with nuclear DNA morphological changes, neutrophils execute an NADPH oxidase-independent process of NETs release (47). The activity of the ERK/MEK signaling pathway, heat shock protein 90, and PI3K are essential for NETs formation triggered by CPP crystals (47). An intact cytoskeleton is required for CPP crystal-promoted NETs extrusion (47) and the release of IL-1β, IL-8, TNF-α, and GM-CSF from macrophages and neutrophils are important driving forces that promote NETs formation (47). In turn, NETs release ROS, MPO, DNA, IL-1β, and IL-8, and thus further activate inflammation, which can damage the joints (47).

CHOLESTEROL CRYSTALS

Cholesterol is a lipid of endogenous or environmental origin. When the temperature in plasma is under 37°C, circulating cholesterol will form monohydrate cholesterol crystals which foster the formation of atherosclerotic plaques (48). In addition to the crystallization of cholesterol in the circulation the release of IL-1β may activate the IL-1receptors (IL-1R) on the surface of neutrophils to further enhance the migration of neutrophils into the site of atherosclerotic lesions (49–53). The first observation that cholesterol crystals trigger NETs formation reported that translocation of ROS, NE, and PR3 into the nucleus are required for cholesterol crystals to induce NETs release (54). Interestingly, inhibiting peptidyl arginine deiminase enzymes did not affect NETs formation triggered by cholesterol crystals (54), whereas

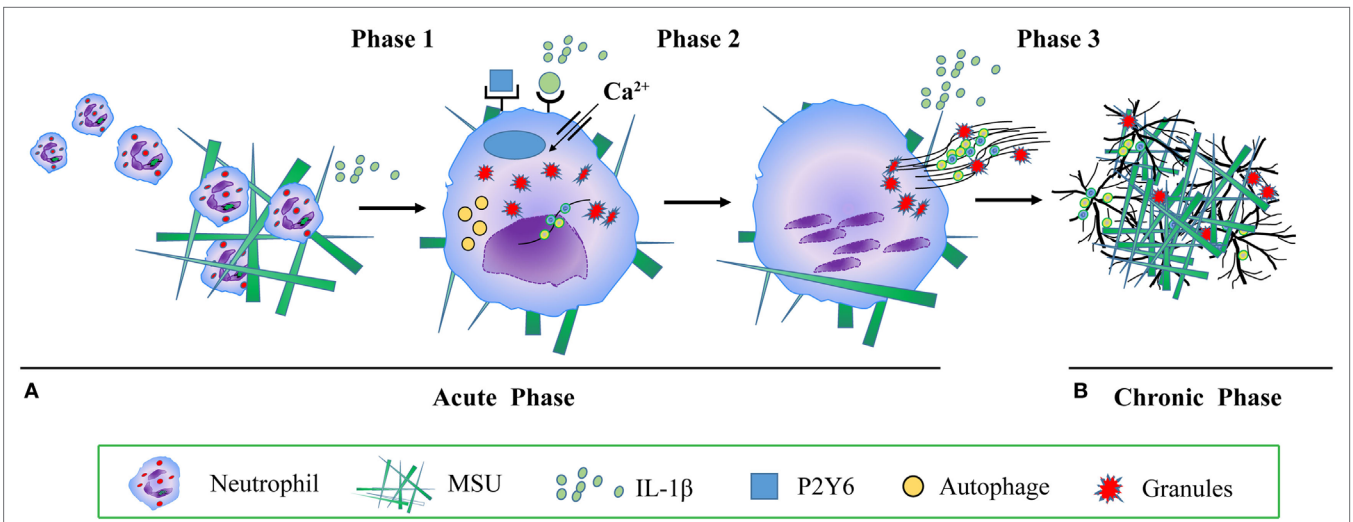

FIGURE 1 | The molecular mechanism of monosodium urate (MSU) crystals induced neutrophil extracellular traps (NETs) and aggregated NETs (aggNETs) formation. **(A)** Acute gouty attack: phase 1 MSU crystals induce mononuclear phagocytes to secrete cytokines and chemokines, including interleukin (IL)-1β, tumor necrosis factor, IL-6, and IL-8. IL-1β recruits further neutrophils into the synovial joint; phase 2 neutrophils take up MSU crystals, a process activating reactive oxygen species, autophagy, RIPK1-RIPK3-MLKL signaling, P2Y6 receptor, endosomal acidification, calcium entry channel, IL-1β, and inducing NETs formation. NETs release dangerous neutrophils' cargo, such as histones, MPO, NE, cytokine, DAMPs, chemokines, leading to acute, painful, and tissue-damaging inflammation; **(B)** chronic tophaceous gout: phase 3 under conditions of high neutrophil densities, aggNETs are formed, degrade pro-inflammatory chemokines and cytokines, and suppress crystal-induced inflammation. Abbreviations: MPO, myeloperoxidase; NE, neutrophil elastase; DAMPs, danger associated molecular patterns.

NE and PR3-deficient mice do not form NETs in an atherosclerosis model and exhibited a reduced plaque size relative to controls (54). NETs augment the transcription of pro-inflammatory cytokines. In co-cultures with cholesterol crystals, NETs can enhance the cytokines released from macrophage *via* the IL-1/IL-17 loop (54). NETs and cholesterol crystals can also activate Th17 cells to sustain a chronic sterile inflammation (54). Overall, NETs release modulated the inflammation in atherosclerotic plaques.

CALCIUM CARBONATE CRYSTALS

Calcium carbonate—a white and tasteless microcrystalline powder—is generally less than 1 μm in diameter (54) and possess different shapes encompassing layered, rhombohedral, irregular, needlelike, spherulitic, or cubelike shape according to various polymorphic crystalline phases (55). As the component of pancreatic juice, calcium carbonate crystals can induce NETs and aggregate NETs formation (56, 57). Ductal occlusion is a main cause in the pathogenesis of pancreatitis; however, the mechanism of action remains elusive. Samples of histological tissue sections and pancreatic juice from patients with pancreatitis show aggNETs, as a specific occluding agent that agglomerate in the pancreatic ducts (58). Further studies confirmed that bicarbonate ions and calcium carbonate crystals can both induce aggNETs formation in the ductal tree during pancreatitis *via* a PADI4-dependent signaling pathway (58, 59).

SILICA CRYSTALS

Silica crystals, also termed crystalline silica or silicon dioxide (SiO_2), are usually harmless and non-toxic crystals; however, inhalation of silica can cause pulmonary inflammation (58). Prolonged exposure to silica crystals, especially for coal-miners and smokers, confers a great risk to develop pneumoconiosis silicosis, a chronic, progressive, irreversible, and incurable disease characterized by pulmonary fibrosis. Therefore, the understanding of the mechanisms of silica-induced pulmonary fibrosis is indispensably. After the interaction with silica, alveolar macrophages and endothelial cells (60) ingest silica, activate the NALP3 inflammasome (61), produce ROS and lead to phagolysosomal damage (60). Then massive chemokines and pro-inflammatory cytokines like IL-1β and TNF-α are generated, neutrophils are recruited to lung tissue and assist in the clearance of the silica crystals (60). In addition to phagocytic clearance, neutrophils undergo NETosis (60, 62–64) is an important factor in the establishment of the lung disease (65).

At onset of the diseases, NETs are scarce and release numerous pro-inflammatory cytokines and cytotoxic contents which promote the acute inflammation (20). Along with the disease progression, aggNETs are formed and showed an anti-inflammatory effect on the local microenvironment by eliminating pro-inflammatory mediators, trapping silica coated with proteases and sequester them in silicotic nodules, which resemble gouty tophi (20). The persistence of silicotic nodules is prone to sustain inflammation and may cause silicosis or even lung cancer (60).

FURTHER CRYSTALLINE MATERIALS

There is evidence that CaP and CaOx may trigger RIPK1-RIPK3-MLKL-dependent neutrophil necroptosis and promote NETs or aggNETs formation *in vitro* and *in vivo* (20). When exposed to CaP, IL-1β derived from macrophages activates NETs formation which in turn induces the secretion of TNF-α by macrophages (66). Further studies on NETs in CaP or CaOx related to diseases like nephrolithiasis are needed.

CONCLUSION

Sterile crystal-mediated diseases, such as gout, pseudogout, atherosclerosis, and silicosis are highly prevalent worldwide. As summarized here, NETs are often involved in the progression of these kinds of diseases where they play detrimental and also beneficial roles. The activation of the NALP3 inflammasome, production of ROS, and the pro-inflammatory cytokines IL-1β, TNF-α are critical for NETosis in crystal-induced inflammation. NETs and aggNETs govern acute and chronic phase of sterile inflammation, respectively. Finally, targeting NETosis and NETs-derived products may provide new therapeutic approaches for crystal-mediated diseases.

AUTHOR CONTRIBUTIONS

YL and XC contributed equally to this article. YL, XC, and YZ wrote the first draft of this article. YL, XC, and YZ designed the figures. YL and MH critically revised the manuscript for important intellectual content. All authors approved the final version.

FUNDING

The present work was supported by the National Natural Science Foundation of China (81771742) to YZ and the National Key Research and Development Program of China (Project No. 2016YFC0906201) to YL.

REFERENCES

1. Brinkmann V, Reichard U, Goosmann C, Fauler B, Uhlemann Y, Weiss DS, et al. Neutrophil extracellular traps kill bacteria. *Science* (2004) 303(5663):1532–5. doi:10.1126/science.1092385
2. Parker H, Dragunow M, Hampton MB, Kettle AJ, Winterbourn CC. Requirements for NADPH oxidase and myeloperoxidase in neutrophil extracellular trap formation differ depending on the stimulus. *J Leukoc Biol* (2012) 92(4):841–9. doi:10.1189/jlb.1211601
3. Keshari RS, Jyoti A, Dubey M, Kothari N, Kohli M, Bogra J, et al. Cytokines induced neutrophil extracellular traps formation: implication for the inflammatory disease condition. *PLoS One* (2012) 7(10):e48111. doi:10.1371/journal.pone.0048111
4. Carestia A, Kaufman T, Schattner M. Platelets: new bricks in the building of neutrophil extracellular traps. *Front Immunol* (2016) 7:271. doi:10.3389/fimmu.2016.00271
5. Sørensen OE, Borregaard N. Neutrophil extracellular traps – the dark side of neutrophils. *J Clin Invest* (2016) 126(5):1612. doi:10.1172/JCI84538

6. Steinberg BE, Grinstein S. Unconventional roles of the NADPH oxidase: signaling, ion homeostasis, and cell death. *Sci STKE* (2007) 2007(379):e11. doi: 10.1126/stke.3792007pe11
7. Fuchs TA, Abed U, Goosmann C, Hurwitz R, Schulze I, Wahn V, et al. Novel cell death program leads to neutrophil extracellular traps. *J Cell Biol* (2007) 176(2):231. doi:10.1083/jcb.200606027
8. Kolaczkowska E, Kubes P. Neutrophil recruitment and function in health and inflammation. *Nat Rev Immunol* (2013) 13(3):159. doi:10.1038/nri3399
9. Jaillon S, Peri G, Delneste Y, Frémaux I, Doni A, Moalli F, et al. The humoral pattern recognition receptor PTX3 is stored in neutrophil granules and localizes in extracellular traps. *J Exp Med* (2007) 204(4):793–804. doi:10.1084/jem.20061301
10. Kessenbrock K, Krumbholz M, Schönermarck U, Back W, Gross WL, Werb Z, et al. Netting neutrophils in autoimmune small-vessel vasculitis. *Nat Med* (2009) 15(6):623. doi:10.1038/nm.1959
11. Metzler KD, Goosmann C, Lubojemska A, Zychlinsky A, Papayannopoulos V. A myeloperoxidase-containing complex regulates neutrophil elastase release and actin dynamics during NETosis. *Cell Rep* (2014) 8(3):883–96. doi:10.1016/j.celrep.2014.06.044
12. Wang Y, Li M, Stadler S, Correll S, Li P, Wang D, et al. Histone hypercitrullination mediates chromatin decondensation and neutrophil extracellular trap formation. *J Cell Biol* (2009) 184(2):205. doi:10.1083/jcb.200806072
13. Leshner M, Wang S, Lewis C, Zheng H, Chen XA, Santy L, et al. PAD4 mediated histone hypercitrullination induces heterochromatin decondensation and chromatin unfolding to form neutrophil extracellular trap-like structures. *Front Immunol* (2012) 3(2–3):307. doi:10.3389/fimmu.2012.00307
14. Hakkim A, Fuchs TA, Martinez NE, Hess S, Prinz H, Zychlinsky A, et al. Activation of the Raf-MEK-ERK pathway is required for neutrophil extracellular trap formation. *Nat Chem Biol* (2011) 7(2):75. doi:10.1038/nchembio.496
15. Keshari RS, Verma A, Barthwal MK, Dikshit M. Reactive oxygen species-induced activation of ERK and p38 MAPK mediates PMA-induced NETs release from human neutrophils. *J Cell Biochem* (2013) 114(3):532–40. doi:10.1002/jcb.24391
16. Alemán OR, Mora N, Cortes-Vieyra R, Uribe-Querol E, Rosales C. Transforming growth factor-β-activated kinase 1 is required for human FcγRIIIb-induced neutrophil extracellular trap formation. *Front Immunol* (2016) 7:277. doi:10.3389/fimmu.2016.00277
17. Demaurex N, Monod A, Lew DP, Krause KH. Characterization of receptor-mediated and store-regulated Ca2+ influx in human neutrophils. *Biochem J* (1994) 297(Pt 3):595. doi:10.1042/bj2970595
18. Behnen M, Leschczyk C, Möller S, Batel T, Klinger M, Solbach W, et al. Immobilized immune complexes induce neutrophil extracellular trap release by human neutrophil granulocytes via FcγRIIIB and Mac-1. *J Immunol* (2014) 193(4):1954–65. doi:10.4049/jimmunol.1400478
19. Schauer C, Janko C, Munoz LE, Zhao Y, Kienhöfer D, Frey B, et al. Aggregated neutrophil extracellular traps limit inflammation by degrading cytokines and chemokines. *Nat Med* (2014) 20(5):511. doi:10.1038/nm.3547
20. Desai J, Foresto-Neto O, Honarpisheh M, Steiger S, Nakazawa D, Popper B, et al. Particles of different sizes and shapes induce neutrophil necroptosis followed by the release of neutrophil extracellular trap-like chromatin. *Sci Rep* (2017) 7(1):15003. doi:10.1038/s41598-017-15106-0
21. Mandel NS, Mandel GS. Monosodium urate monohydrate, the gout culprit. *J Am Chem Soc* (1976) 98(8):2319–23. doi:10.1021/ja00424a054
22. Perrin CM, Dobish MA, Keuren EV, Swift JA. Monosodium urate monohydrate crystallization. *CrystEngComm* (2011) 13(4):1111–7. doi:10.1039/c0ce00737d
23. Kuo CF, Grainge MJ, Zhang W, Doherty M. Global epidemiology of gout: prevalence, incidence and risk factors. *Nat Rev Rheumatol* (2015) 11(11):649. doi:10.1038/nrrheum.2015.91
24. Martin WJ, Harper JL. Innate inflammation and resolution in acute gout. *Immunol Cell Biol* (2010) 88(1):15–9. doi:10.1038/icb.2009.89
25. Hahn J, Knopf J, Maueröder C, Kienhöfer D, Leppkes M, Herrmann M. Neutrophils and neutrophil extracellular traps orchestrate initiation and resolution of inflammation. *Clin Exp Rheumatol* (2016) 34(4 Suppl 98):6.
26. Desai J, Kumar SV, Mulay SR, Konrad L, Romoli S, Schauer C, et al. PMA and crystal-induced neutrophil extracellular trap formation involves RIPK1-RIPK3-MLKL signaling. *Eur J Immunol* (2016) 46(1):223–9. doi:10.1002/eji.201545605
27. Schorn C, Janko C, Krenn V, Zhao Y, Munoz LE, Schett G, et al. Bonding the foe – NETting neutrophils immobilize the pro-inflammatory monosodium urate crystals. *Front Immunol* (2012) 3:376. doi:10.3389/fimmu.2012.00376
28. Arai Y, Nishinaka Y, Arai T, Morita M, Mizugishi K, Adachi S, et al. Uric acid induces NADPH oxidase-independent neutrophil extracellular trap formation. *Biochem Biophys Res Commun* (2014) 443(2):556. doi:10.1016/j.bbrc.2013.12.007
29. Chatfield SM, Grebe K, Whitehead LW, Rogers KL, Nebl T, Murphy JM, et al. Monosodium urate crystals generate nuclease-resistant neutrophil extracellular traps via a distinct molecular pathway. *J Immunol* (2018) 200(5):1802–1816. doi:10.4049/jimmunol.1701382
30. Mitroulis I, Kambas K, Chrysanthopoulou A, Skendros P, Apostolidou E, Kourtzelis I, et al. Neutrophil extracellular trap formation is associated with IL-1β and autophagy-related signaling in gout. *PLoS One* (2011) 6(12):e29318. doi:10.1371/journal.pone.0029318
31. Skendros P, Chrysanthopoulou A, Rousset F, Kambas K, Arampatzioglou A, Mitsios A, et al. REDD1 links stress with IL-1β-mediated familial Mediterranean fever attack through autophagy-driven neutrophil extracellular traps. *J Allergy Clin Immunol* (2017) 140(5):1378–87. doi:10.1016/j.jaci.2017.02.021
32. Amini P, Stojkov D, Wang X, Wicki S, Kaufmann T, Wong WW, et al. NET formation can occur independently of RIPK3 and MLKL signaling. *Eur J Immunol* (2016) 46(1):178–84. doi:10.1002/eji.201545615
33. Sil P, Hayes CP, Reaves BJ, Breen P, Quinn S, Sokolove J, et al. P2Y6 receptor antagonist MRS2578 inhibits neutrophil activation and aggregated neutrophil extracellular trap formation induced by gout-associated monosodium urate crystals. *J Immunol* (2017) 198(1):428–42. doi:10.4049/jimmunol.1600766
34. Pieterse E, Jeremic I, Czegley C, Weidner D, Biermann MH, Veissi S, et al. Blood-borne phagocytes internalize urate microaggregates and prevent intravascular NETosis by urate crystals. *Sci Rep* (2016) 6:38229. doi:10.1038/srep38229
35. Manfredi AA, Ramirez GA, Rovere-Querini P, Maugeri N. The neutrophil's choice: phagocytose vs make neutrophil extracellular traps. *Front Immunol* (2018) 9:288. doi:10.3389/fimmu.2018.00288
36. Torres R, Macdonald L, Croll SD, Reinhardt J, Dore A, Stevens S, et al. Hyperalgesia, synovitis and multiple biomarkers of inflammation are suppressed by interleukin 1 inhibition in a novel animal model of gouty arthritis. *Ann Rheum Dis* (2009) 68(10):1602–8. doi:10.1136/ard.2009.109355
37. Sil P, Wicklum H, Surell C, Rada B. Macrophage-derived IL-1β enhances monosodium urate crystal-triggered NET formation. *Inflamm Res* (2017) 66(3):227–37. doi:10.1007/s00011-016-1008-0
38. Schett G, Dayer JM, Manger B. Interleukin-1 function and role in rheumatic disease. *Nat Rev Rheumatol* (2016) 12(1):14–24. doi:10.1038/nrrheum.2016.166
39. Amaral FA, Costa VV, Tavares LD, Sachs D, Coelho FM, Fagundes CT, et al. NLRP3 inflammasome-mediated neutrophil recruitment and hypernociception depend on leukotriene B(4) in a murine model of gout. *Arthritis Rheum* (2012) 64(2):474. doi:10.1002/art.33355
40. Franklin BS, Mangan MS, Latz E. Crystal formation in inflammation. *Annu Rev Immunol* (2016) 34(1):173. doi:10.1146/annurev-immunol-041015-055539
41. Burt HM, Jackson JK, Rowell J. Calcium pyrophosphate and monosodium urate crystal interactions with neutrophils: effect of crystal size and lipoprotein binding to crystals. *J Rheumatol* (1989) 16(6):809–17.
42. Liubryan R, Lioté F. Monosodium urate and calcium pyrophosphate dihydrate (CPPD) crystals, inflammation, and cellular signaling. *Joint Bone Spine* (2005) 72(4):295–302. doi:10.1016/j.jbspin.2004.12.010
43. Martinon F, Pétrilli V, Mayor A, Tardivel A, Tschopp J. Gout-associated uric acid crystals activate the NALP3 inflammasome. *Nature* (2006) 440(7081):237–41. doi:10.1038/nature04516
44. Pétrilli V, Martinon F. The inflammasome, autoinflammatory diseases, and gout. *Joint Bone Spine* (2007) 74(6):571–6. doi:10.1016/j.jbspin.2007.04.004
45. Martinon F, Glimcher LH. Gout: new insights into an old disease. *J Clin Invest* (2006) 116(8):2073–5. doi:10.1172/JCI29404
46. Oliveira SHP, Canetti C, Ribeiro RA, Cunha FQ. Neutrophil migration induced by IL-1β depends upon LTB4 released by macrophages and upon TNF-α and IL-1β released by mast cells. *Inflammation* (2008) 31(1):36–46. doi:10.1007/s10753-007-9047-x
47. Pang L, Hayes CP, Buac K, Yoo DG, Rada B. Pseudogout-associated inflammatory calcium pyrophosphate dihydrate microcrystals induce formation of neutrophil extracellular traps. *J Immunol* (2013) 190(12):6488. doi:10.4049/jimmunol.1203215
48. Small DM. George lyman duff memorial lecture. Progression and regression of atherosclerotic lesions. Insights from lipid physical biochemistry. *Arteriosclerosis* (1988) 8(2):103–29. doi:10.1161/01.ATV.8.2.103

49. Lessner SM, Prado HL, Waller EK, Galis ZS. Atherosclerotic lesions grow through recruitment and proliferation of circulating monocytes in a murine model. *Am J Pathol* (2002) 160(6):2145–55. doi:10.1016/S0002-9440(10)61163-7
50. Swirski FK, Pittet MJ, Kircher MF, Aikawa E, Jaffer FA, Libby P, et al. Monocyte accumulation in mouse atherogenesis is progressive and proportional to extent of disease. *Proc Natl Acad Sci U S A* (2006) 103(27):10340–5. doi:10.1073/pnas.0604260103
51. Landsman L, Bar-On L, Zernecke A, Kim KW, Krauthgamer R, Shagdarsuren E, et al. CX3CR1 is required for monocyte homeostasis and atherogenesis by promoting cell survival. *Blood* (2009) 113(4):963. doi:10.1182/blood-2008-07-170787
52. Duewell P, Kono H, Rayner KJ, Sirois CM, Vladimer G, Bauernfeind FG, et al. NLRP3 inflammasomes are required for atherogenesis and activated by cholesterol crystals. *Nature* (2010) 464(7293):1357–61. doi:10.1038/nature08938
53. Grebe A, Latz E. Cholesterol crystals and inflammation. *Curr Rheumatol Rep* (2013) 15(3):313. doi:10.1007/s11926-012-0313-z
54. Warnatsch A, Ioannou M, Wang Q, Papayannopoulos V. Inflammation. Neutrophil extracellular traps license macrophages for cytokine production in atherosclerosis. *Science* (2015) 349(6245):316–20. doi:10.1126/science.aaa8064
55. Cizer Ö, Rodriguez-Navarro C, Ruiz-Agudo E, Elsen J, Gemert DV, Balen KV. Phase and morphology evolution of calcium carbonate precipitated by carbonation of hydrated lime. *J Sci Mater* (2012) 47(16):6151–65. doi:10.1007/s10853-012-6535-7
56. Tong H, Ma W, Wang L, Wan P, Hu J, Cao L. Control over the crystal phase, shape, size and aggregation of calcium carbonate via a L-aspartic acid inducing process. *Biomaterials* (2004) 25(17):3923. doi:10.1016/j.biomaterials.2003.10.038
57. Beck R, Andreassen JP. Influence of crystallization conditions on crystal morphology and size of CaCO3 and their effect on pressure filtration. *Aiche J* (2011) 58(1):107–21. doi:10.1002/aic.12566
58. Leppkes M, Maueröder C, Hirth S, Nowecki S, Günther C, Billmeier U, et al. Externalized decondensed neutrophil chromatin occludes pancreatic ducts and drives pancreatitis. *Nat Commun* (2016) 7:10973. doi:10.1038/ncomms10973
59. Bilyy R, Fedorov V, Vovk V, Leppkes M, Dumych T, Chopyak V, et al. Neutrophil extracellular traps form a Barrier between necrotic and viable areas in acute abdominal inflammation. *Front Immunol* (2016) 7(5):424. doi:10.3389/fimmu.2016.00424
60. Hornung V, Bauernfeind F, Halle A, Samstad EO, Kono H, Rock KL, et al. Silica crystals and aluminum salts mediate NALP-3 inflammasome activation via phagosomal destabilization. *Nat Immunol* (2008) 9(8):847. doi:10.1038/ni.1631
61. Hari A, Zhang Y, Tu Z, Detampel P, Stenner M, Ganguly A, et al. Activation of NLRP3 inflammasome by crystalline structures via cell surface contact. *Sci Rep* (2014) 4(7281):7281. doi:10.1038/srep07281
62. Lo Re S, Dumoutier L, Couillin I, Van Vyve C, Yakoub Y, Uwambayinema F, et al. IL-17A-producing gammadelta T and Th17 lymphocytes mediate lung inflammation but not fibrosis in experimental silicosis. *J Immunol* (2010) 184(11):6367–77. doi:10.4049/jimmunol.0900459
63. Borges VM, Lopes MF, Falcão H, Leite-Júnior JH, Rocco PR, Davidson WF, et al. Apoptosis underlies immunopathogenic mechanisms in acute silicosis. *Am J Respir Cell Mol Biol* (2002) 27(1):78. doi:10.1165/ajrcmb.27.1.4717
64. Zhai R, Ge X, Li H, Tang Z, Liao R, Kleinjans J. Differences in cellular and inflammatory cytokine profiles in the bronchoalveolar lavage fluid in bagassosis and silicosis. *Am J Ind Med* (2004) 46(4):338–44. doi:10.1002/ajim.20051
65. Brinkmann V, Goosmann C, Kuhn LI, Zychlinsky A. Automatic quantification of in vitro NET formation. *Front Immunol* (2012) 3:413. doi:10.3389/fimmu.2012.00413
66. Peng HH, Liu YJ, Ojcius DM, Lee CM, Chen RH, Huang PR, et al. Mineral particles stimulate innate immunity through neutrophil extracellular traps containing HMGB1. *Sci Rep* (2017) 7(1):16628. doi:10.1038/s41598-017-16778-4

Conflict of Interest Statement: The authors declare that the research was conducted in the absence of any commercial or financial relationships that could be construed as a potential conflict of interest.

frontiers in Immunology

MINI REVIEW
published: 20 August 2018
doi: 10.3389/fimmu.2018.01883

The Role of Inhibitory Receptors in Monosodium Urate Crystal-Induced Inflammation

Maria J. Fernandes and Paul H. Naccache*

Department of Microbiology-Infectious Diseases and Immunology, Faculty of Medicine, Laval University, CHU de Québec Research Center, Québec, QC, Canada

Inhibitory receptors are key regulators of immune responses. Aberrant inhibitory receptor function can either lead to an exacerbated or defective immune response. Several regulatory mechanisms involved in the inflammatory reaction induced by monosodium urate crystals (MSU) during acute gout have been identified. One of these mechanisms involves inhibitory receptors. The engagement of the inhibitory receptors Clec12A and SIRL-1 has opposing effects on the responses of neutrophils to MSU. We review the general concepts of inhibitory receptor biology and apply them to understand and compare the modulation of MSU-induced inflammation by Clec12A and SIRL-1. We also discuss gaps in our knowledge of the contribution of inhibitory receptors to the pathogenesis of gout and propose future avenues of research.

Keywords: monosodium urate crystals, inflammation, gout, inhibitory receptors, neutrophils

OPEN ACCESS

Edited by:
Hans-Joachim Anders, Ludwig-Maximilians-Universität München, Germany

Reviewed by:
Stefanie Steiger, Klinikum der Universität München, Germany
Arian Dominic John Laurence, Newcastle University, United Kingdom

****Correspondence:***
Maria J. Fernandes
maria.fernandes@crchul.ulaval.ca

Specialty section:
This article was submitted to Inflammation, a section of the journal Frontiers in Immunology

Received: *04 May 2018*
Accepted: *30 July 2018*
Published: *20 August 2018*

Citation:
Fernandes MJ and Naccache PH (2018) The Role of Inhibitory Receptors in Monosodium Urate Crystal-Induced Inflammation. Front. Immunol. 9:1883. doi: 10.3389/fimmu.2018.01883

INTRODUCTION

Crystal-induced arthropathies are a group of disorders that are triggered by crystal deposits in articular and periarticular tissues (1). Monosodium urate crystals (MSU) cause one the most common inflammatory arthritis known as gout (2). Although significant advancements have been made in our understanding of the pathogenesis of this very painful and usually self-limiting arthritis, the role of immune inhibitory receptors in gout is only starting to emerge.

Inhibitory receptors play key roles in regulating almost every aspect of an immune response mainly by blocking activating pathways (3–5). The integration of activating and inhibitory signals by leukocytes determines the nature of an immune response. Among the vast repertoire of inhibitory receptors expressed by neutrophils, CLEC12A and SIRL-1 modulate MSU-induced inflammation. The ligation of these two receptors has opposing effects on certain neutrophil effector functions induced by MSU offering novel insights into alternative mechanisms through which inflammation in gout can be regulated (**Figure 1**). Herein, we provide a brief overview of the immunopathogenesis of gout and an overview of the biology of inhibitory receptors, their role in MSU-induced inflammation, as well as their therapeutic potential and suggestions for future research.

MSU-INDUCED INFLAMMATION

Monosodium urate crystals are a crystallized form of uric acid, a product of purine metabolism (6). Uric acid is ubiquitous and only becomes inflammatory when it crystallizes to form MSU. Since MSU form in individuals with serum levels of uric acid that are chronically above the saturation point, the first line of treatment of gout is the pharmacological reduction of uric acid (7).

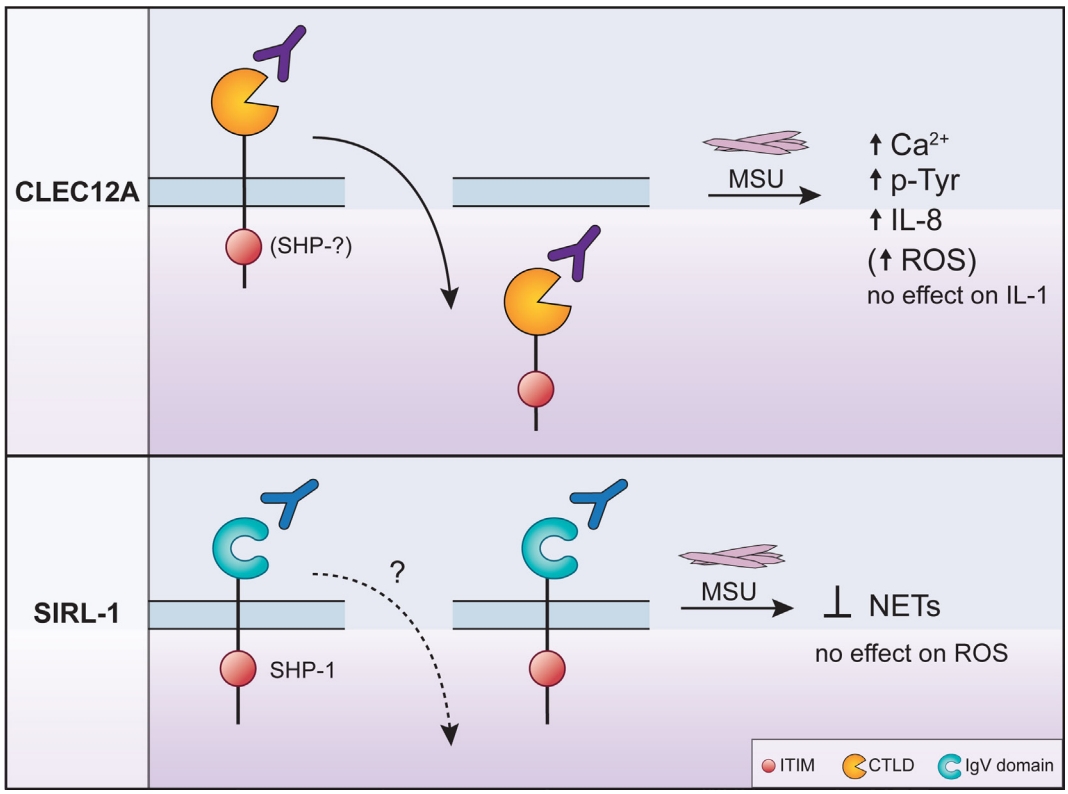

FIGURE 1 | The regulation of monosodium urate crystal (MSU)-induced neutrophil activation by CLEC12A and SIRL-1 after engagement with specific antibodies. The engagement of CLEC12A on the surface of human neutrophils with a specific antibody (50C1) induces its internalization (*solid arrow pointing downwards*) resulting in the enhancement of the signaling events and effector functions shown in the figure. The phosphatases that interact with the immunoreceptor tyrosine-based inhibitory motif (ITIM) of CLEC12A in primary cells remain unknown (*top panel*). By contrast, the ligation of SIRL with the anti-SIRL-1 antibody inhibits neutrophil extracellular trap (NET) formation. In primary cells, the ITIM of SIRL-1 interacts with SHP-1. The MSU-induced responses that are not regulated by either receptor are also shown and underscore the specificity of inhibitory receptor function. The anti-SIRL-1 antibody has therapeutic potential since it inhibits NET formation.

Monosodium urate crystals are a potent pro-inflammatory stimulus for professional phagocytes, the main drivers of acute gouty arthritis (8, 9). When these crystals accumulate in the joint, they activate resident mononuclear phagocytes to release several inflammatory mediators including IL-1β. The key role of IL-1β plays is underscored by the ability of IL-1 inhibitors to diminish the symptoms of an acute gout attack (10). IL-1β induces the expression of adhesion molecules by endothelial cells and the production of chemokines that promote a massive influx of neutrophils into the joint (11, 12). The recruited neutrophils very effectively drive the inflammatory reaction by secreting S100A9 proteins and pro-inflammatory cytokines including the potent chemoattractant for neutrophils IL-8 (13). Neutrophils also release reactive oxygen species (ROS) and degradative enzymes that cause joint destruction. The pivotal role of the neutrophil in gout is supported by a significant decrease in MSU-induced inflammation in dogs depleted of neutrophils (14, 15). Monocytes are also recruited to the affected joint and contribute to gout by producing pro-inflammatory cytokines such as IL-1 and IL-6.

Monosodium urate crystals activate a unique subset of signaling pathways in the neutrophil [reviewed in Ref. (13)]. These include the Src-family kinases (e.g., Lyn), PKC, PI-3K, Tec, and Syk. Syk is required for the MSU-induced increase in intracellular calcium levels, the production of superoxide and potentially the activation of MAP kinases. The MSU-induced synthesis of cytokines and degranulation depends on the activation of PI-3K.

One intriguing feature of acute gouty arthritis is its spontaneous resolution, typically within 7–10 days (16). Neutrophils not only secrete pro-inflammatory mediators when activated by MSU but also release neutrophil extracellular traps (NETs) (17–19). These extracellular web-like structures composed of decondensed DNA and neutrophil granule enzymes contribute to the resolution of inflammation by densely clustering MSU within them forming structures known as aggregated NETs or tophi (18, 19). Aggregated NETs form when neutrophils are present at high density which is typical of a gout attack (20). NETs also degrade pro-inflammatory cytokines and chemokines that become trapped in these structures dampening the inflammatory reaction. Additional mechanisms that terminate acute gout include the coating of MSU with lipoproteins, the production of TGFβ, IL-10, and the clearance of apoptotic neutrophils (21). IL-37, a cytokine produced by monocytes and dendritic cells, downregulates the MSU-induced production of cytokines and dampens neutrophil recruitment in mouse models of gout (22).

Negative regulatory mechanisms not only dampen a gout attack but also influence its initiation by modulating the threshold of activation of leukocytes. These negative regulatory pathways are downstream effectors of inhibitory receptors expressed on the surface of the cell. Each leukocyte expresses a diverse repertoire of inhibitory receptors (4). The challenge to understanding the role of these receptors in gout is to identify those that regulate the mechanisms underlying MSU-induced inflammation.

HOW DO INHIBITORY RECEPTORS WORK? GENERAL CONCEPTS

Inhibitory receptors are essential for the maintenance of immune homeostasis as well as the termination of an immune response by blocking signaling pathways that lead to cellular activation (23). Aberrant inhibitory receptor function could either cause anergy or an excessive immune response.

Inhibitory receptors are composed of a variable number of extracellular ligand-binding domains, a transmembrane domain and a cytoplasmic tail that contains at least one immunoreceptor tyrosine-based inhibitory motif (ITIM) (3). The extracellular ligand-binding domains of inhibitory receptors come in two flavors, those that have the structure of the immunoglobulin superfamily (IgSF) domain and those with a C-type lectin-like domain (CTLD) (24).

Once engaged by a ligand, inhibitory receptors signal through their ITIM(s) (23) that is composed of six amino acids, (I/V/L/S) xYxx(L/V) ("x" denotes any amino acid, "Y" is tyrosine). Briefly, engagement of inhibitory receptors induces their clustering and the phosphorylation of the tyrosine residue of their ITIM(s) by a Src kinase that serves as a ligand for the subsequent recruitment of cytoplasmic phosphatases such as SHP-1, SHP-2, and SHIP to the plasma membrane. These phosphatases dephosphorylate signaling proteins involved in activating pathways. Inhibitory receptors can also negatively regulate cellular activation by binding adaptor proteins such as the negative regulator of the Src family, Csk (c-Src tyrosine kinase), Dok adaptor proteins (Downstream of Kinase), or Cbl (Casitas B-lineage lymphoma). These events likely occur in specialized membrane domains such as lipid rafts as has been described in lymphocytes (25).

Inhibitory receptors regulate many aspects of leukocyte development and function (3). Some of the functions they regulate in phagocytes include phagocytosis, the production of ROS and cytokines (4, 5). Although there is some degree of redundancy in their function, these receptors also differentially affect leukocyte function as illustrated by SIRL and CLEC12A in MSU-induced inflammation (discussed below). A loss of function of an inhibitory receptor can thus dysregulate multiple leukocyte functions and cause inflammatory diseases.

THE ROLE OF INHIBITORY RECEPTORS IN MSU-INDUCED INFLAMMATION

To understand the role of inhibitory receptors in an inflammatory response, the modulation of their expression and their clustering, the phosphorylation of their ITIM motif(s), and the recruitment of protein partners are studied *in vitro*. Although these experimental approaches only offer us a snapshot of the involvement of these inhibitory receptors in the continuum of the cellular and chemical events of an inflammatory response, they provide insight into how these receptors work. Experiments in knock-out mice complement *in vitro* studies by revealing the outcome of the integration of activating and inhibitory signals in a specific inhibitory receptor-deficient background.

Studies in neutrophils identified two inhibitory receptors associated with MSU-induced inflammation, namely, MICL (the myeloid inhibitory C-type lectin-like receptor, CLEC12A, DCAL-2, CLL-1, and CD371) and the IgSF receptor known as SIRL-1 (the signal inhibitory receptor on leukocytes-1). The ligation of these receptors regulates MSU-induced activation of neutrophils in different ways underscoring the ability of inhibitory receptors to differentially regulate leukocyte function.

CLEC12A

CLEC12A belongs to the C-type lectin superfamily of proteins. It harbors an extracellular CTLD linked to its transmembrane domain by a neck domain and one ITIM motif (VTYADL) in its cytoplasmic tail (26–28). CTLDs bind a diverse array of glycan ligands of endogenous or microbial origin (29–33) in a calcium-dependent manner or *via* alternative mechanisms. They can also bind non-glycan ligands (e.g., proteins and lipids). CLEC12A is devoid of the known amino acid required for glycan and calcium binding in its CTLD, rendering the identification of its natural ligands a challenge. Murine CLEC12A binds various mouse tissues, the identity of which remains to be determined (34, 35). Regarding the neck domain, it allows the oligomerization of CLRs increasing their affinity for their ligand (36, 37). It remains unknown whether human CLEC12A oligomerizes in primary cells under resting and/or stimulated conditions. Human CLEC12A is predominantly a myeloid receptor but is also expressed in some lymphocyte populations (e.g., B cells) (26–28, 38, 39). As for the underlying molecular mechanisms through which CLEC12A regulates leukocyte functions, its ITIM binds SHP-1 and SHP-2 in RAW cells (**Table 1**) (26). This observation requires confirmation in human primary cells.

It is now widely accepted that one of the key roles of CLEC12A is to negatively regulate myeloid cell function and that it is associated with several inflammatory diseases (40–44). The function of CLEC12A is regulated by changes in its expression (26–28). TLR ligands (e.g., LPS and pam2csk4), for instance, downregulate CLEC12A expression in human monocytes. In a human skin abrasion model of inflammation, the expression of CLEC12A is also reduced (45). The effect of the downregulation of CLEC12A expression was studied in several cell types (**Table 1**). In monocyte-derived dendritic cells, the internalization of CLEC12A induced by its ligation with a specific antibody suppressed TLR-induced cytokine production such as IL-12 (27). By contrast, the expression of CCR7 was enhanced (27). Together, these observations indicate that CLEC12A expression is downregulated in response to various inflammatory stimuli that signal through different receptors resulting in the modulation of leukocyte activation.

Several lines of evidence indicate that CLEC12A negatively regulates myeloid cell function in MSU-induced inflammation.

TABLE 1 | Overview of the molecular mechanisms that govern CLEC12A and SIRL-1 function in different cell types.

CLEC12A								**SIRL-1**			
Antibody	None	50C1	None	hDCAL-2	hDCAL-2	hDCAL-2	5D3	None	Anti-SIRL-1	Anti-SIRL-1	Anti-SIRL-1
Cell type	RAW	Human neutrophil	Clec12A KO neutrophils	iDC	iDC	iDC	MDDC	Human monocyte	RBL-2H3 (and 293 cells)	RBL-2H3	Human neutrophil
Stimulus	Pervan.	MSU	MSU	None	LPS/zymosan	CD40L-Fc	CCL2	Pervan.	Pervan.	Anti-TNP IgE	MSU (or ops. bacteria)
Receptor internalization		Yes		Yes	Yes	Yes	Yes				
Co-IP	SHP-1 and SHP-2							SHP-1	SHP-1 (SHP-2 in 293 cells)		
Signaling		↑ [Intracellular calcium], global tyrosine phospho	↑ Phospho. $p40^{phox}$	↑ Tyrosine phospho pp38 and ppERK					ITIM phospho		
Functions enhanced		IL-8 release	ROS	CCR7 expression and production of TNFα, IL-6, IL-10, and MIP-3β	CCR7, DC-LAMP, expression	CCR7, DC-LAMP, CD83, CD86, IL-12, IL-6, IL-10, and TNFα expression; co-cultured T cell production of IFN-γ					
Functions diminished or inhibited					IL-12 (and TNFα for LPS)		Migration toward CCL2			Degranulation	NET release
Functions not affected		IL-1 production	IL-1 production		IL-6 and IL-10 production						ROS (or intra-cellular killing)

The studies were chosen according to the insight they provide on the molecular mechanisms governing CLEC12A and SIRL-1 function. The information in this table does not cover all the published findings on these receptors. Additional references can be found in the text. The signaling events downstream of both receptors and their effect on cell function depend on the cellular context and type of stimulus.
iDC, immature dendritic cells; MDDC, monocyte-derived dendritic cells; Pervan., pervanadate; phospho, phosphorylation; ops, opsonized; NET, neutrophil extracellular trap; ITIM, immunoreceptor tyrosine-based inhibitory motif; ROS, reactive oxygen species; MSU, monosodium urate crystals.

The stimulation of neutrophils with MSU crystals downregulates the cell-surface expression of CLEC12A (40). CLEC12A is not shed, but is internalized and degraded. When the cell-surface expression of CLEC12A is downregulated with a specific antibody, an enhancement in the MSU-induced increase of the concentration of intracellular free calcium, the tyrosine phosphorylation of proteins, and the release of IL-8 is observed. Similar observations were made in a neutrophil-like cell line in which CLEC12A expression was silenced (40). Similar to other inhibitory receptors, CLEC12A exhibits selectivity in its suppressive properties. Although it dampens the release of IL-8 induced by MSU, it does not regulate the MSU-induced secretion of IL-1 by human neutrophils. Our observations *in vitro* were corroborated *in vivo* in a knock-out mouse model of CLEC12A (41). MSU-induced inflammation in these mice was characterized by a significant increase in the recruitment of leukocytes to the site of inflammation. Of pertinence to gout, is the production of significantly higher amounts of ROS by CLEC12A deficient, mouse leukocytes partly due to the phosphorylation of the $p40^{phox}$, a subunit of NADPH oxidase (41). It remains to be determined whether CLEC12A modulates the production of ROS in human neutrophils. Together, the above observations identify a regulatory role for CLEC12A in various leukocyte effector functions relevant to the immunopathogenesis of gout.

SIRL-1

SIRL-1 is an IgSF receptor that is expressed on myeloid cells including neutrophils, eosinophils, monocytes, and dendritic cells (46). SIRL harbors one extracellular IgV domains and two ITIMs (VtYaeL and HeYaaL) in its cytoplasmic portion that recruit SHP-1 and SHP-2 indicative of a negative regulatory function for this receptor [**Table 1**; (46)].

SIRL-1 negatively regulates innate immune responses toward various stimuli. As is the case with CLEC12A, the cell-surface expression of SIRL-1 diminishes when certain stimuli activate monocytes and neutrophils (47, 48). The decrease in expression may enhance cell activation since monocytes with a low expression of SIRL-1 produce more TNFα in response to Curdlan than $SIRL^{high}$ monocytes. While a decrease in SIRL-1 expression enhances cell activation, its ligation with a specific antibody (anti-SIRL) has the opposite effect. In the RBL-2H3 cell *in vitro* model of FcεRI activation, for instance, ligation of SIRL-1 with anti-SIRL antibody inhibited IgE-induced degranulation [**Table 1**; (46)]. Likewise, in human neutrophils, SIRL-1 ligation suppresses NET formation induced by opsonized *S. aureus* but not the production of ROS, thereby underscoring a certain degree of functional selectivity (49).

SIRL-1 also inhibits neutrophil activation in response to MSU. The ligation of SIRL-1 with anti-SIRL suppresses MSU-induced formation of NETs (49). This inhibitory effect on the release of NETs seems specific for stimuli that signal through Fc receptors since MSU-induced NET formation is Fcγ receptor-dependent and SIRL does not downregulate the formation of NETs by neutrophils stimulated with non-opsonized *S. aureus* or LPS (49, 50). It is noteworthy that SIRL-1 does not dampen extracellular ROS production in response to MSU which is consistent with the fact that MSU-induced formation of NETs is ROS independent. Together, these observations indicate that SIRL suppresses MSU-induced NET release in a ROS-independent but FcR-dependent manner.

WHAT INDUCES THE ENGAGEMENT OF INHIBITORY RECEPTORS IN THE CONTEXT OF MSU-INDUCED INFLAMMATION?

The evidence that CLEC12A and SIRL-1 modulate MSU-induced neutrophil activation was obtained from experiments performed with naked crystals. MSU thus trigger activating signaling pathways by directly interacting with components of the cell surface. Since MSU are composed of a rugged, crystalline surface that is negatively charged, it is difficult to envisage how such a surface can exhibit the same level of specificity as a conventional "hand in the glove" receptor–ligand interaction. One receptor through which MSU activates signaling in human neutrophils is the Fc receptor FcγRIIIb (50). Since there are no antibodies on naked crystals, MSU seem to act as an opportunistic ligand for Fc receptors. It stands to reason that the same applies to the other receptors with which MSU have been shown to interact including CLEC12A, CD11b, CD14, TLR2, and TLR4 (6, 13, 41, 50). It is likely that MSU induces the clustering of these receptors to induce their activation, possibly in signaling hubs located in specialized membrane domains as reported for other inhibitory receptors causing cellular activation (25). An elegant study provided evidence that MSU interacts with components of cellular membranes, particularly cholesterol, supporting this notion (51). These electrostatic interactions induce changes in the composition and distribution of lipid-rich domains of the plasma membrane and most likely cause the clustering of receptors on the cell surface resulting in cell activation. Immune receptors signal through these membrane domains (25).

WHAT CAN WE LEARN ABOUT THE MODULATION OF MSU-INDUCED NEUTROPHIL ACTIVATION BY CLEC12A AND SIRL-1?

CLEC12A and SIRL-1 elegantly illustrate the ability of inhibitory receptors to have distinct effects on leukocyte activation. Whereas the ligation of SIRL-1 with a specific antibody leads to the downregulation of cellular effector functions, the antibody-induced ligation and internalization of CLEC12A enhances cellular activation. This implies that the downregulation of the cell-surface expression of CLEC12A releases its inhibitory effect and consequently lowers the threshold of activation of neutrophils toward MSU. These observations suggest that CLEC12A may be constitutively phosphorylated in resting cells to increase the threshold of activation. The phosphorylation status of the ITIM of CLEC12A remains, however, to be determined in resting and stimulated cells. With regards to SIRL-1, it is most likely constitutively phosphorylated since it associates with SHP-1 in resting monocytes. This notion is supported by the inhibition

of the MSU-induced formation of NETs after the ligation of SIRL-1. Since the anti-SIRL-1 antibody inhibits MSU-induced formation of NET, it is an agonistic antibody. By contrast, the anti-CLEC12A antibody does not seem to have agonistic effects since it enhances cell activation by binding CLEC12A. Although the role of CLE12A and SIRL-1 in gout remains to be fully characterized, these two receptors may regulate neutrophil activation in a temporal manner since NET formation is a later response to MSU than the mobilization of calcium.

WHERE SHOULD WE GO FROM HERE?

To develop a more complete picture of the immunopathogenesis of gout, the constellation of inhibitory receptors that regulate myeloid cell responses toward MSU needs to be identified. Moreover, it is essential to identify the ligands for these receptors to better understand their functional and temporal role during homeostasis and inflammation as well as their mode of action. Pyz et al. (34) reported that CLEC12A binds endogenous ligands whose identity remains to be determined. *In vivo* studies will also be informative. With regards to CLEC12A, for instance, it may also contribute to the resolution of inflammation in gout since the arthritis phenotype in CLEC12A knock-out mice persists for a significantly longer period of time than in wild-type mice (42).

ARE INHIBITORY RECEPTORS A CLINICALLY RELEVANT, THERAPEUTIC TARGET FOR GOUT?

The dampening of MSU-induced neutrophil activation by the SIRL-1 antibody supports the notion that targeting myeloid inhibitory receptors is a promising and new therapeutic option for the treatment of gout. Inhibitory receptors could also be targeted with compounds that preserve their expression once the mechanisms underlying their internalization and degradation are characterized. Targeting inhibitory receptors that regulate the threshold activation of neutrophils during the early stages of a gout attack would be beneficial since there is a therapeutic window of opportunity prior to the peak of a gout attack during which patients feel a slight pain. Colchicine is one such drug that effectively reduces inflammation if administered during the early phase of an acute gout attack. A mechanism through which colchicine may dampen a gout attack is by preserving the cell-surface expression of CLEC12A on neutrophils (40).

It is difficult to predict whether targeting endogenous inhibitory pathways will cause less adverse effects than currently used drugs. Considering the limited choice of anti-inflammatory drugs to treat gout due, in part, to contraindications in many cases, it is timely to consider developing additional drugs to treat gout attacks (52). A recent drug developed to treat gout, anti-IL-1 is efficacious but further cost/benefit and safety studies are required prior to widely using it to treat this arthropathy (10).

It is an exciting time for inhibitory receptor research since we have better tools to study their biology and a clearer picture of how they work facilitating the investigation of their function and role in disease. At least two other inhibitory pathways in lymphocytes are targeted for the treatment of rheumatoid arthritis and cancer (53) providing a proof of concept of the therapeutic value of targeting inhibitory receptors to treat disease. Considering that gout is one of the few types of arthritis whose causative agent is known, defining the role of inhibitory pathways in this disease will serve as a paradigm for understanding the pathogenesis of other types of arthritis and identifying novel therapeutic targets.

AUTHOR CONTRIBUTIONS

MF and PHN contributed equally to the writing of the manuscript.

FUNDING

This work was funded by operating funds awarded to MG by the Canadian Institutes of Health Research (CIHR) (grant no. MOP_142408) and an Investigator award from the Arthritis Society (grant no. INS-12-028).

REFERENCES

1. Ramonda R, Oliviero F, Galozzi P, Frallonardo P, Lorenzin M, Ortolan A, et al. Molecular mechanisms of pain in crystal-induced arthritis. *Best Pract Res Clin Rheumatol* (2015) 29:98–110. doi:10.1016/j.berh.2015.04.025
2. Ragab G, Elshahaly M, Bardin T. Gout: an old disease in new perspective – a review. *J Adv Res* (2017) 8:495–511. doi:10.1016/j.jare.2017.04.008
3. Munitz A. Inhibitory receptors on myeloid cells: new targets for therapy? *Pharmacol Ther* (2010) 125:128–37. doi:10.1016/j.pharmthera.2009.10.007
4. Steevels TA, Meyaard L. Immune inhibitory receptors: essential regulators of phagocyte function. *Eur J Immunol* (2011) 41:575–87. doi:10.1002/eji.201041179
5. Favier B. Regulation of neutrophil functions through inhibitory receptors: an emerging paradigm in health and disease. *Immunol Rev* (2016) 273:140–55. doi:10.1111/imr.12457
6. Busso N, So A. Mechanisms of inflammation in gout. *Arthritis Res Ther* (2010) 12:206. doi:10.1186/ar2952
7. Harrold L. New developments in gout. *Curr Opin Rheumatol* (2013) 25:304–9. doi:10.1097/BOR.0b013e32835fd5e5
8. Malawista SE, de Boisfleury AC, Naccache PH. Inflammatory gout: observations over a half-century. *FASEB J* (2011) 25:4073–8. doi:10.1096/fj.11-1201ufm
9. Martin WJ, Walton M, Harper J. Resident macrophages initiating and driving inflammation in a monosodium urate monohydrate crystal-induced murine peritoneal model of acute gout. *Arthritis Rheum* (2009) 60:281–9. doi:10.1002/art.24185
10. So A, Dumusc A, Nasi S. The role of IL-1 in gout: from bench to bedside. *Rheumatology (Oxford)* (2018) 57:i12–9. doi:10.1093/rheumatology/kex449
11. Martinon F, Petrilli V, Mayor A, Tardivel A, Tschopp J. Gout-associated uric acid crystals activate the NALP3 inflammasome. *Nature* (2006) 440:237–41. doi:10.1038/nature04516
12. Cronstein BN, Sunkureddi P. Mechanistic aspects of inflammation and clinical management of inflammation in acute gouty arthritis. *J Clin Rheumatol* (2013) 19:19–29. doi:10.1097/RHU.0b013e31827d8790
13. Popa-Nita O, Naccache PH. Crystal-induced neutrophil activation. *Immunol Cell Biol* (2010) 88:32–40. doi:10.1038/icb.2009.98
14. Phelps P, McCarty DJ Jr. Crystal-induced inflammation in canine joints. II. Importance of polymorphonuclear leukocytes. *J Exp Med* (1966) 124:115–26. doi:10.1084/jem.124.1.115
15. Chang YH, Garalla EJ. Suppression of urate crystal-induced canine joint inflammation by heterologous anti-polymorphonuclear leukocyte serum. *Arthritis Rheum* (1968) 11:145–50. doi:10.1002/art.1780110204

16. Abhishek A, Roddy E, Doherty M. Gout – a guide for the general and acute physicians. *Clin Med* (2017) 17:54–9. doi:10.7861/clinmedicine.17-1-54
17. Mitroulis I, Kambas K, Chrysanthopoulou A, Skendros P, Apostolidou E, Kourtzelis I, et al. Neutrophil extracellular trap formation is associated with IL-1beta and autophagy-related signaling in gout. *PLoS One* (2011) 6:e29318. doi:10.1371/journal.pone.0029318
18. Schorn C, Janko C, Latzko M, Chaurio R, Schett G, Herrmann M. Monosodium urate crystals induce extracellular DNA traps in neutrophils, eosinophils, and basophils but not in mononuclear cells. *Front Immunol* (2012) 3:277. doi:10.3389/fimmu.2012.00277
19. Chatfield SM, Grebe K, Whitehead LW, Rogers KL, Nebl T, Murphy JM, et al. Monosodium urate crystals generate nuclease-resistant neutrophil extracellular traps via a distinct molecular pathway. *J Immunol* (2018) 200:1802–16. doi:10.4049/jimmunol.1701382
20. Schett G, Schauer C, Hoffmann M, Herrmann M. Why does the gout attack stop? A roadmap for the immune pathogenesis of gout. *RMD Open* (2015) 1:e000046. doi:10.1136/rmdopen-2015-000046
21. Steiger S, Harper JL. Mechanisms of spontaneous resolution of acute gouty inflammation. *Curr Rheumatol Rep* (2014) 16:392. doi:10.1007/s11926-013-0392-5
22. Liu L, Xue Y, Zhu Y, Xuan D, Yang X, Liang M, et al. Interleukin 37 limits monosodium urate crystal-induced innate immune responses in human and murine models of gout. *Arthritis Res Ther* (2016) 18:268. doi:10.1186/s13075-016-1167-y
23. Daeron M, Jaeger S, Du Pasquier L, Vivier E. Immunoreceptor tyrosine-based inhibition motifs: a quest in the past and future. *Immunol Rev* (2008) 224:11–43. doi:10.1111/j.1600-065X.2008.00666.x
24. Long EO. Regulation of immune responses through inhibitory receptors. *Annu Rev Immunol* (1999) 17:875–904. doi:10.1146/annurev.immunol.17.1.875
25. Varshney P, Yadav V, Saini N. Lipid rafts in immune signalling: current progress and future perspective. *Immunology* (2016) 149:13–24. doi:10.1111/imm.12617
26. Marshall AS, Willment JA, Lin HH, Williams DL, Gordon S, Brown GD. Identification and characterization of a novel human myeloid inhibitory C-type lectin-like receptor (MICL) that is predominantly expressed on granulocytes and monocytes. *J Biol Chem* (2004) 279:14792–802. doi:10.1074/jbc.M313127200
27. Chen CH, Floyd H, Olson NE, Magaletti D, Li C, Draves K, et al. Dendritic-cell-associated C-type lectin 2 (DCAL-2) alters dendritic-cell maturation and cytokine production. *Blood* (2006) 107:1459–67. doi:10.1182/blood-2005-08-3264
28. Lahoud MH, Proietto AI, Ahmet F, Kitsoulis S, Eidsmo L, Wu L, et al. The C-type lectin Clec12A present on mouse and human dendritic cells can serve as a target for antigen delivery and enhancement of antibody responses. *J Immunol* (2009) 182:7587–94. doi:10.4049/jimmunol.0900464
29. Drickamer K, Fadden AJ. Genomic analysis of C-type lectins. *Biochem Soc Symp* (2002) 69:59–72. doi:10.1042/bss0690059
30. Weis WI, Taylor ME, Drickamer K. The C-type lectin superfamily in the immune system. *Immunol Rev* (1998) 163:19–34. doi:10.1111/j.1600-065X.1998.tb01185.x
31. McGreal EP, Martinez-Pomares L, Gordon S. Divergent roles for C-type lectins expressed by cells of the innate immune system. *Mol Immunol* (2004) 41:1109–21. doi:10.1016/j.molimm.2004.06.013
32. Pyz E, Marshall AS, Gordon S, Brown GD. C-type lectin-like receptors on myeloid cells. *Ann Med* (2006) 38:242–51. doi:10.1080/07853890600608985
33. Drickamer K. C-type lectin-like domains. *Curr Opin Struct Biol* (1999) 9:585–90. doi:10.1016/S0959-440X(99)00009-3
34. Pyz E, Huysamen C, Marshall ASJ, Gordon S, Taylor PR, Brown GD. Characterisation of murine MICL (CLEC12A) and evidence for an endogenous ligand. *Eur J Immunol* (2008) 38:1157–63. doi:10.1002/eji.200738057
35. Sagar D, Singh NP, Ginwala R, Huang X, Philip R, Nagarkatti M, et al. Antibody blockade of CLEC12A delays EAE onset and attenuates disease severity by impairing myeloid cell CNS infiltration and restoring positive immunity. *Sci Rep* (2017) 7:2707. doi:10.1038/s41598-017-03027-x
36. McQueen KL, Parham P. Variable receptors controlling activation and inhibition of NK cells. *Curr Opin Immunol* (2002) 14:615–21. doi:10.1016/S0952-7915(02)00380-1
37. Feinberg H, Guo Y, Mitchell DA, Drickamer K, Weis WI. Extended neck regions stabilize tetramers of the receptors DC-SIGN and DC-SIGNR. *J Biol Chem* (2005) 280:1327–35. doi:10.1074/jbc.M409925200
38. Bill M, B van Kooten Niekerk P, S Woll P, Laine Herborg L, Stidsholt Roug A, Hokland P, et al. Mapping the CLEC12A expression on myeloid progenitors in normal bone marrow; implications for understanding CLEC12A-related cancer stem cell biology. *J Cell Mol Med* (2018) 22:2311–8. doi:10.1111/jcmm.13519
39. Kasahara S, Clark EA. Dendritic cell-associated lectin 2 (DCAL2) defines a distinct CD8alpha- dendritic cell subset. *J Leukoc Biol* (2012) 91:437–48. doi:10.1189/jlb.0711384
40. Gagne V, Marois L, Levesque JM, Galarneau H, Lahoud MH, Caminschi I, et al. Modulation of monosodium urate crystal-induced responses in neutrophils by the myeloid inhibitory C-type lectin-like receptor: potential therapeutic implications. *Arthritis Res Ther* (2013) 15:R73. doi:10.1186/ar4250
41. Neumann K, Castineiras-Vilarino M, Hockendorf U, Hannesschlager N, Lemeer S, Kupka D, et al. Clec12a is an inhibitory receptor for uric acid crystals that regulates inflammation in response to cell death. *Immunity* (2014) 40:389–99. doi:10.1016/j.immuni.2013.12.015
42. Redelinghuys P, Whitehead L, Augello A, Drummond RA, Levesque JM, Vautier S, et al. MICL controls inflammation in rheumatoid arthritis. *Ann Rheum Dis* (2016) 75:1386–91. doi:10.1136/annrheumdis-2014-206644
43. Michou L, Cornelis F, Levesque JM, Bombardieri S, Balsa A, Westhovens R, et al. A genetic association study of the CLEC12A gene in rheumatoid arthritis. *Joint Bone Spine* (2012) 79:451–6. doi:10.1016/j.jbspin.2011.12.012
44. Begun J, Lassen KG, Jijon HB, Baxt LA, Goel G, Heath RJ, et al. Integrated genomics of Crohn's disease risk variant identifies a role for CLEC12A in antibacterial autophagy. *Cell Rep* (2015) 11:1905–18. doi:10.1016/j.celrep.2015.05.045
45. Marshall AS, Willment JA, Pyz E, Dennehy KM, Reid DM, Dri P, et al. Human MICL (CLEC12A) is differentially glycosylated and is down-regulated following cellular activation. *Eur J Immunol* (2006) 36:2159–69. doi:10.1002/eji.200535628
46. Steevels TA, Lebbink RJ, Westerlaken GH, Coffer PJ, Meyaard L. Signal inhibitory receptor on leukocytes-1 is a novel functional inhibitory immune receptor expressed on human phagocytes. *J Immunol* (2010) 184:4741–8. doi:10.4049/jimmunol.0902039
47. Van Avondt K, Fritsch-Stork R, Derksen RHWM, Meyaard L. Ligation of signal inhibitory receptor on leukocytes-1 suppresses the release of neutrophil extracellular traps in systemic lupus erythematosus. *PLoS ONE* (2013) 8(10):e78459. doi:10.1371/journal.pone.0078459
48. Steevels TA, van Avondt K, Westerlaken GH, Stalpers F, Walk J, Bont L, et al. Signal inhibitory receptor on leukocytes-1 (SIRL-1) negatively regulates the oxidative burst in human phagocytes. *Eur J Immunol* (2013) 43:1297–308. doi:10.1002/eji.201242916
49. Van Avondt K, van der Linden M, Naccache PH, Egan DA, Meyaard L. Signal inhibitory receptor on leukocytes-1 limits the formation of neutrophil extracellular traps, but preserves intracellular bacterial killing. *J Immunol* (2016) 196:3686–94. doi:10.4049/jimmunol.1501650
50. Barabe F, Gilbert C, Liao N, Bourgoin SG, Naccache PH. Crystal-induced neutrophil activation VI. Involvment of FcgammaRIIIB (CD16) and CD11b in response to inflammatory microcrystals. *FASEB J* (1998) 12:209–20. doi:10.1096/fasebj.12.2.209
51. Ng G, Sharma K, Ward SM, Desrosiers MD, Stephens LA, Schoel WM, et al. Receptor-independent, direct membrane binding leads to cell-surface lipid sorting and Syk kinase activation in dendritic cells. *Immunity* (2008) 29:807–18. doi:10.1016/j.immuni.2008.09.013
52. Vargas-Santos AB, Neogi T. Management of gout and hyperuricemia in CKD. *Am J Kidney Dis* (2017) 70:422–39. doi:10.1053/j.ajkd.2017.01.055
53. Buchbinder EI, Desai A. CTLA-4 and PD-1 pathways: similarities, differences, and implications of their inhibition. *Am J Clin Oncol* (2016) 39:98–106. doi:10.1097/COC.0000000000000239

Conflict of Interest Statement: The authors declare that the research was conducted in the absence of any commercial or financial relationships that could be construed as a potential conflict of interest.

frontiers in Immunology

ORIGINAL RESEARCH
published: 22 January 2018
doi: 10.3389/fimmu.2017.02000

Volcanic Ash Activates the NLRP3 Inflammasome in Murine and Human Macrophages

David E. Damby[1,2], Claire J. Horwell[3], Peter J. Baxter[4], Ulrich Kueppers[1], Max Schnurr[5], Donald B. Dingwell[1] and Peter Duewell[5]**

[1] Department of Earth and Environmental Sciences, Ludwig-Maximilians-Universität (LMU) München, Munich, Germany, [2] Volcano Science Center, United States Geological Survey, Menlo Park, CA, Unites States, [3] Department of Earth Sciences, Institute of Hazard, Risk and Resilience, Durham University, Durham, United Kingdom, [4] Institute of Public Health, University of Cambridge, Cambridge, United Kingdom, [5] Division of Clinical Pharmacology, Medizinische Klinik und Poliklinik IV, Klinikum der Universität München, Munich, Germany

Volcanic ash is a heterogeneous mineral dust that is typically composed of a mixture of amorphous (glass) and crystalline (mineral) fragments. It commonly contains an abundance of the crystalline silica (SiO_2) polymorph cristobalite. Inhalation of crystalline silica can induce inflammation by stimulating the NLRP3 inflammasome, a cytosolic receptor complex that plays a critical role in driving inflammatory immune responses. Ingested material results in the assembly of NLRP3, ASC, and caspase-1 with subsequent secretion of the interleukin-1 family cytokine IL-1β. Previous toxicology work suggests that cristobalite-bearing volcanic ash is minimally reactive, calling into question the reactivity of volcanically derived crystalline silica, in general. In this study, we target the NLRP3 inflammasome as a crystalline silica responsive element to clarify volcanic cristobalite reactivity. We expose immortalized bone marrow-derived macrophages of genetically engineered mice and primary human peripheral blood mononuclear cells (PBMCs) to ash from the Soufrière Hills volcano as well as representative, pure-phase samples of its primary componentry (volcanic glass, feldspar, cristobalite) and measure NLRP3 inflammasome activation. We demonstrate that respirable Soufrière Hills volcanic ash induces the activation of caspase-1 with subsequent release of mature IL-1β in a NLRP3 inflammasome-dependent manner. Macrophages deficient in NLRP3 inflammasome components are incapable of secreting IL-1β in response to volcanic ash ingestion. Cellular uptake induces lysosomal destabilization involving cysteine proteases. Furthermore, the response involves activation of mitochondrial stress pathways leading to the generation of reactive oxygen species. Considering ash componentry, cristobalite is the most reactive pure-phase with other components inducing only low-level IL-1β secretion. Inflammasome activation mediated by inhaled ash and its potential relevance in chronic pulmonary disease was further evidenced in PBMC using the NLRP3 small-molecule inhibitor CP-456,773 (CRID3, MCC950). Our data indicate the functional activation of the NLRP3 inflammasome by volcanic ash in murine and human macrophages *in vitro*. Cristobalite is identified as the apparent driver, thereby contesting previous assertions that chemical and structural imperfections may be sufficient to abrogate the reactivity of volcanically derived cristobalite. This

OPEN ACCESS

Edited by:
Rostyslav Bilyy, Danylo Halytsky Lviv National Medical University, Ukraine

Reviewed by:
Luis Enrique Munoz, University of Erlangen-Nuremberg, Germany
Seth Lucian Masters, Walter and Eliza Hall Institute of Medical Research, Australia

***Correspondence:**
David E. Damby
ddamby@usgs.gov;
Peter Duewell
peter.duewell@med.uni-muenchen.de

Specialty section:
This article was submitted to Inflammation, a section of the journal Frontiers in Immunology

Received: *17 October 2017*
Accepted: *22 December 2017*
Published: *22 January 2018*

Citation:
Damby DE, Horwell CJ, Baxter PJ, Kueppers U, Schnurr M, Dingwell DB and Duewell P (2018) Volcanic Ash Activates the NLRP3 Inflammasome in Murine and Human Macrophages. Front. Immunol. 8:2000. doi: 10.3389/fimmu.2017.02000

is a novel mechanism for the stimulation of a pro-inflammatory response by volcanic particulate and provides new insight regarding chronic exposure to environmentally occurring particles.

Keywords: inflammasome, NLRP3, reactive oxygen species, lysosomal damage, volcanic ash, cristobalite, silica, mineral dust

INTRODUCTION

Explosive volcanic eruptions generate vast plumes of ash. Their fall-out can affect extensive populated areas beyond the immediate vicinity of a volcano. Ash is defined as the portion of the erupted ejecta less than 2 mm in diameter, and it is a heterogeneous mixture of glassy fragments, containing variable amounts of crystals and older rock from the volcanic edifice (lithics). Since the 1980 eruption of Mount St. Helens, USA, when ash impacted more than a million inhabitants in the Pacific Northwest, it has been known that a substantial fraction of the ejecta is of micron, or even sub-micron, size and, therefore, potentially capable of being a human respiratory health hazard (1).

An exacerbation of airway problems, such as asthma and chronic bronchitis, due to the heightened levels of fine particles in the ambient air suspended from the ash deposits, was an expected finding at Mount St. Helens (2). The presence of a significant amount of respirable crystalline silica, mainly as cristobalite, however, was wholly unforeseen and has led to repeated toxicological testing of the ash to help establish the implications of ash exposure for human health [see review in reference (3)]. In particular, there was concern regarding the risks of developing silicosis in the general population and outdoor workers due to the established consequences of crystalline silica exposure, mainly as quartz, in industrial settings (4). The eruptions of the Soufrière Hills volcano on Montserrat, West Indies, starting in 1995 and lasting over 15 years, led to similar intensive study of the volcanic cristobalite hazard (3, 5). Ongoing work has constrained the presence of cristobalite in ash to eruptions that involve lava domes or incorporate pre-existing, altered flow-units (5, 6). This is because cristobalite forms by secondary mineralization or hydrothermal alteration in these environments and, therefore, is not present in primary magmatic ejecta. These discoveries have defined the environmental side of the hazard; however, the capacity of volcanic cristobalite to incite disease remains enigmatic (7, 8).

Previously, we have observed no systematic difference in reactivity when comparing ash containing crystalline silica, predominantly as cristobalite, and ash containing negligible amounts of crystalline silica (9, 10). Experimentally, cristobalite-bearing volcanic ash has incited granuloma formation *in vivo* (1, 11), but it is consistently less inflammatory and fibrogenic than would be expected for a crystalline silica-bearing dust (3, 12). However, we have recently reported on the propensity of volcanic ash to initiate an inflammatory immune response *in vitro* in macrophages (10). Crystalline silica in other mixed-mineral dusts is known to be variably reactive (13), whereby its pathogenicity may be altered by inherent structural and chemical defects along with effects imparted by other constituents in a mixed-phase dust; indeed, structural and chemical defects of volcanic cristobalite (which contains up to 3 wt.% aluminum) together with its presence in a heterogeneous dust have all been previously implicated in its reduced potency (8, 14, 15). The conflicting results to date have hindered efforts to provide health risk assessments (16), which consider all available evidence from *in vitro* and *in vivo* toxicological tests. A mechanistic understanding of the hazard posed by volcanic ash is needed to resolve the existing conundrum and provide appropriate public health advice during future volcanic eruptions.

Inflammation plays a pivotal role in crystal-driven disease progression and can be observed in patients with particle-induced lung diseases (17). Although the exact mechanisms of how pathogenic particles drive inflammation is not completely understood, it has been shown that danger-associated molecular patterns, such as endogenous uric acid (gout) or cholesterol (atherosclerosis) as well as exogenous particles like asbestos (asbestosis) or crystalline silica (silicosis), share features of crystalline particles that activate the NLRP3 inflammasome (also known as CIAS1, NALP3, or cryopyrin) (18–20). The NLRP3 inflammasome belongs to the Nod-like receptor pyrin-containing family of cytosolic receptors and, together with the adapter molecule apoptosis-associated speck-like protein containing a CARD domain (ASC), it forms a multi-protein platform that recruits and activates caspase-1. Caspase-1 belongs to the inflammatory caspases and leads to the processing and secretion of the pro-inflammatory cytokines interleukin-1 beta (IL-1β) and IL-18 into their active forms (21). While the exact upstream mechanism of NLRP3 activation remains unclear and is part of ongoing studies, the current understanding of NLRP3 inflammasome assembly mainly consists of a two-hit mechanism. NLRP3, as well as the pro-form of IL-1β, is not constitutively expressed and needs transcriptional priming. The first step in activation can be achieved by the germ line-encoded TLRs that usually sense microbial cell wall components or viral DNA and RNA molecules. The NLRP3 inflammasome senses crystalline danger signals that can occur during autoinflammatory diseases, such as gout or atherosclerosis, and environmental diseases, such as silicosis or asbestosis (18, 20, 22). IL-1 cytokines are potent mediators of innate immunity in response to crystalline silica exposure (23, 24) and have been implicated in the pathophysiology of human and experimental diseases (25, 26).

Here, we report on the propensity of volcanic cristobalite to activate the NLRP3 inflammasome, in the wake of a series of inconclusive toxicological investigations of ash from recent major eruptions. The NLRP3 inflammasome has emerged as a central mechanism in mediating cellular responses to various endo- and exogenous signals and particles related to environmental

and life-style diseases. Given the established hazard posed by respirable crystalline silica in occupational settings, the capacity of volcanic ash to stimulate IL-1β release by macrophages *in vitro* (10), and the observation that instigation of chronic disease by crystalline silica is NLRP3-dependent (27, 28), we have chosen to test the ability of cristobalite-bearing volcanic ash to promote inflammation by activating the inflammasome pathway.

MATERIALS AND METHODS

Volcanic Ash Sample and Major Component Control Particles

Ash sample MRA5/6/99 is a respirable sample isolated from fresh ash that fell at Soufrière Hills volcano, Montserrat, on 5 June 1999. The ash was generated during a dome-collapse event, a particular style of eruption known to produce fine-grained, cristobalite-rich ash (5, 29). The respirable fraction was isolated using the Minisplit classification system at 16,000 rpm (British Rema, Sheffield, UK), which segregates particles within a vortex. The bulk tephra (sieved to 1 mm) was first separated to give a sub-10 μm fraction, and this fraction was further separated to give the sub-4 μm fraction. Sample MRA5/6/99 has been used extensively in ash characterization and toxicity studies; the ash is characterized in detail by Horwell et al. (29) and the crystallographic properties of the cristobalite it contains by Damby et al. (14). The sample comprises ~15 wt.% crystalline silica as cristobalite, with the other major constituents being volcanic glass (amorphous silica) and plagioclase feldspar; additional minor phases identified were hornblende, orthopyroxene, titanomagnetite, and oxides (10, 29).

Pure-phase mineral samples of the primary components were analyzed alongside MRA5/6/99 to constrain their reactivity in the NLRP3 inflammasome model. Cristobalite was synthesized by heating ultra-high purity quartz glass (Heraeus HOMOSIL® 101, Hanau, Germany) for 12 h in a platinum crucible at 1,600°C in air. As a representative feldspar, we sourced labradorite (feldspar), an intermediate member of the plagioclase series, from the Bavarian State Collection for Mineralogy (Munich, Germany). Anhydrous andesite glass was produced from high temperature (1,450°C) melting of a sub-sample of Soufrière Hills pumice (described below) in a Nabertherm HI 04/17 furnace (Lilienthal, Germany) in air for 12 h. The sample was then stirred under similar conditions in a second furnace to ensure a homogenous melt and rapidly quenched to produce glass. A cristobalite-free pumice sample from the 12 July 2003 eruption of Soufrière Hills volcano was included as the mineralogy is similar to MRA5/6/99, and it thus serves as a natural material control for the minor phases identified above [see reference (30)]. All componentry samples were ground dry in a mortar and pestle prior to use.

Sample Characterization

The particle size distributions of the samples were measured using a Coulter LS 230 Analyzer (Beckman Coulter Inc., CA, USA). Data were collected using the following refractive indices: 1.63 for Soufrière Hills ash, as optimized in Horwell (31), 1.49 for crystalline silica, 1.56 for feldspar, and 1.53 for synthetic andesitic glass (32). Data are the average of three 60-s runs and are analyzed according to the Mie scattering theory. The surface area of sample MRA5/6/99 is 3.6 m^2/g as measured by the BET method of nitrogen adsorption (33).

Imaging of the volcanic ash sample was carried out on a Hitachi SU-70 FE-SEM (Hitachi, Ltd., Tokyo, Japan) in the GJ Russell Microscopy Facility, Department of Physics, Durham University. Images were collected at an operating voltage of 6.0 kV and a working distance of 14 mm. Sample mineralogy was confirmed by powder X-ray diffraction on a Bruker AXS D8 ADVANCE (Bruker Corp., MA, USA) with DAVINCI design in 2θ reflection mode using Cu radiation and a Ni filter in the Department of Chemistry, Durham University.

Cell Lines and Reagents

Wild-type and knock-out bone marrow-derived immortalized mouse macrophage cell lines (iMΦ) were generated with a recombinant retrovirus, carrying v-myc and v-raf(mil) oncogenes, as previously described by Hornung et al. (22). Cells were cultured in DMEM supplemented with L-glutamine, 10% FCS (all Gibco, Darmstadt, Germany) and ciprofloxacin (Sigma, Taufkirchen, Germany). Freshly isolated human peripheral blood mononuclear cells (PBMCs) from randomly selected donors were obtained using density gradient centrifugation with subsequent red blood cell lysis. Cells were kept and stimulated in RPMI supplemented with L-glutamine, 10% FCS (all Gibco, Darmstadt, Germany) and ciprofloxacin (Sigma, Taufkirchen, Germany). iMΦ were seeded at a density of 1×10^5 cells/96 well and PBMC at a density of 1×10^6 cells/96 well and primed with 200 ng/ml (iMΦ) or 100 pg/ml (PBMC) lipopolysaccharide (LPS, InvivoGen, Toulouse, France) for 2 h. For inhibitor studies, latrunculin A (Lat A), CA-074-ME, (2R,4R)-4-aminopyrrolidine-2,4-dicarboxylic acid (APDC), and CP-456,773 (CRID3, MCC950) were used at 20 μM and applied 1 h prior to stimulation. Cells were then stimulated with ash and componentry samples as indicated or with 5 mM adenosine triphosphate (ATP), 200 ng/ml polydeoxyadenylic acid • polythymidylic acid (dAdT), 10 μM nigericin (all Sigma Aldrich, Taufkirchen, Germany), or 1 mM H-Leu-Leu-OMe Hydrochloride (Santa Cruz, Heidelberg, Germany). After 6 h, IL-1α, IL-1β, IL-6, and TNFα cytokine levels in supernatants were measured by ELISA (all BD Biosciences, Heidelberg, Germany) or for supernatants and cell lysates with western blot analysis.

Western Blot

Immortalized macrophages and human PBMC were seeded and stimulated, as described above, but in serum-free media. Supernatants were removed and processed for protein precipitation. Briefly, equivalent amounts of methanol and 20 vol.% chloroform were added to supernatants, vortexed, and centrifuged at 12k rcf for 5 min. The top aqueous layer was discarded and methanol was added to remove remaining chloroform from precipitated whole-protein pellets. Samples were centrifuged at 12k rcf for 5 min, supernatants were carefully removed and the protein pellets were air-dried. Precipitates were resolubilized in Lämmli buffer and heated at 95°C for 5 min. Samples were separated using SDS-PAGE and blotted for protein detection.

Membranes were blocked with 3% BSA and incubated with goat anti-mouse caspase-1 p20 (Santa Cruz, Heidelberg, Germany), goat anti-mouse IL-1β, or goat anti-human IL-1β (all R&D Systems, Wiesbaden-Nordenstadt, Germany) pAb overnight. HRP-coupled donkey anti-goat IgG secondary antibodies were incubated for 2 h. HRP-coupled β-actin IgG mAb served as loading control.

Light Microscopy

iMΦ were treated with 500 µg/ml volcanic ash for 6 h. Particle-treated cells were imaged by light microscopy using a Zeiss Axiovert 200 M microscope (Zeiss, Oberkochen, Germany). Cell images were acquired using a 20× objective.

Confocal Laser Reflection and Immune Fluorescence Imaging

iMΦ were seeded in glass-bottom dishes (Thermo Scientific, Darmstadt, Germany) at a density of 1×10^5 cells/ml in complete DMEM and allowed to adhere. Cells were incubated with the quenching dye conjugate DQ-Ovalbumin (DQ-OVA) in the presence or absence of MRA5/6/99 for 4 h. Cells were washed and counterstained with the membrane dye Alexa Fluor® 647-conjugated cholera toxin B subunit (Ctx B) and the nucleic acid stain Hoechst 33342 (Invitrogen, Karlsruhe, Germany). Combined reflection and immune fluorescence data were acquired using a Leica TCS SP5 AOBS confocal laser scanning microscope with 63× magnification (Wetzlar, Germany).

Statistical Analysis

All results are expressed as mean ± SD. Comparisons and significance between two groups was assessed by Student's *t*-test. The level of significance is assigned to $p \leq 0.05$.

RESULTS

Processing of Volcanic Ash by Macrophages

Macrophages are a first line of defense against inhaled particles and are responsible for coordinating an inflammatory immune response. Therefore, they are key targets for *in vitro* assessment of the hazard posed by atmospheric particles. Diverse crystalline material has been reported to activate the NLRP3 inflammasome *via* phagosomal destabilization with lysosomal content leaking into the cytosol. Consequently, this leads to activation of a plethora of endoproteases and oxidative stress molecules by a not yet completely understood mechanism (22, 34). However, particle size is known to be important for entering the endosomal compartment, as reported for silica crystals with an average size of 1–2 µm (22). Volcanic ash comprises a wide range of particle sizes depending on the fragmentation efficiency of the eruption (35), but can contain a substantial respirable component (31). To represent pulmonary exposures, we used an isolated respirable ash sample, obtained through fractioning and sieving methods previously described (29), that derived from a dome-collapse event at Soufrière Hills volcano (MRA5/6/99) and synthetic particles of its corresponding componentry (**Figure 1A**). The ash sample

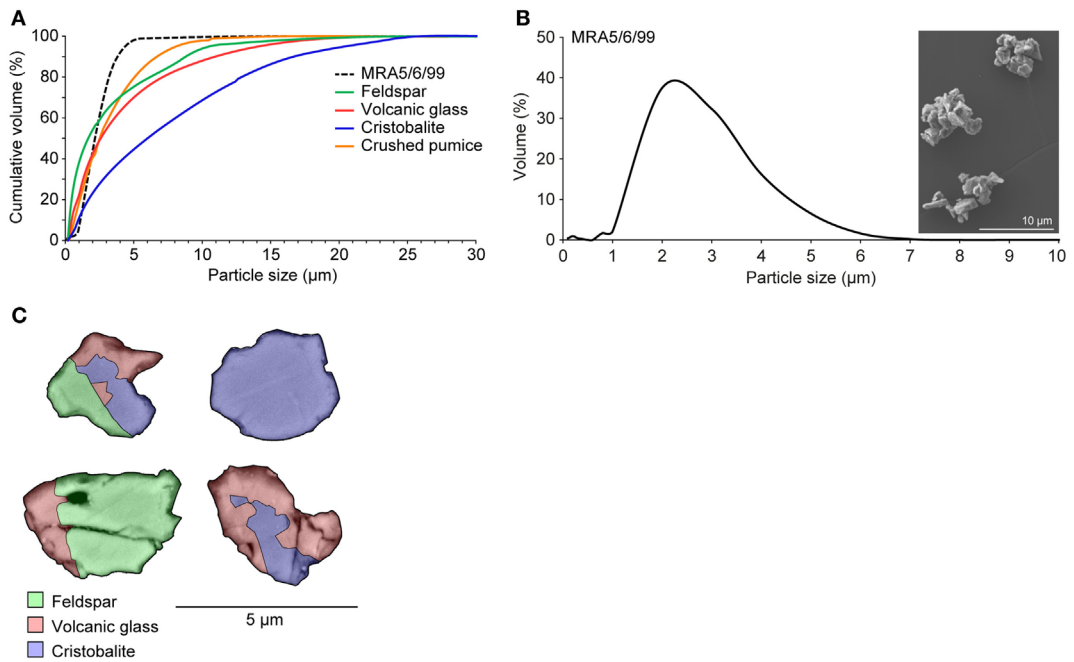

FIGURE 1 | Characteristics of isolated volcanic ash and pure-phase componentry. **(A)** Cumulative particle size distributions of volcanic ash sample MRA5/6/99 and componentry samples. **(B)** Particle size distribution and SEM image of volcanic ash sample MRA5/6/99 (×4.00k magnification). All particle size data are the average of three runs. **(C)** False-color backscatter SEM image of ash in cross section (×10k magnification) evidencing the heterogeneous distribution of predominant phases: cristobalite, feldspar, and volcanic glass. Electron dispersive X-ray spectroscopy was employed for mineral identification. Images were collected at 8.0 kV and a 14.5 mm working distance.

is particularly fine-grained: scanning electron microscopy and particle sizing data of the isolated sample show that the particles are <5 μm, with a mode of 2 μm (**Figure 1B**). Backscatter SEM imaging reveals a heterogeneous distribution of volcanic glass, feldspar, and cristobalite as the predominant phases (**Figure 1C**). The ash sample has been previously reported to be successfully internalized by differentiated THP-1 cells, the human monocytic cell line (10).

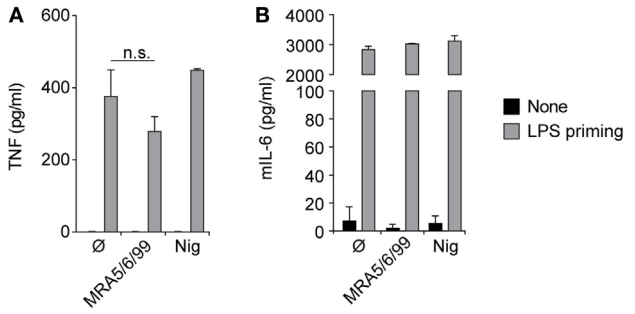

FIGURE 2 | Volcanic ash does not induce a primary inflammatory response. Lipopolysaccharide (LPS)-primed and unprimed wild-type murine macrophages were stimulated with volcanic ash sample MRA5/6/99 or nigericin and **(A)** TNFα and **(B)** IL-6 from supernatants were examined by ELISA. Representative data from two independent experiments are shown.

Volcanic Ash Induces Inflammation and Leads to IL-1β Secretion

The inhalation and deposition of particulate pollutants, such as diesel exhaust, asbestos, or silica, in the small airways is known to induce inflammatory responses leading to sustained inflammation, lung fibrosis, and cancer (22, 25). The abundance of cristobalite in ash from Soufrière Hills volcano, as well as in ash from a large number of other dome-forming volcanoes [see (7) and references therein], and the potential for ash to induce the secretion of inflammatory cytokines prompted us to test the inflammatory response to ash particles further. Accordingly, we treated mouse macrophages with ash sample MRA5/6/99 and determined levels of TNFα, IL-6 and IL-1β in culture supernatants (**Figures 2** and **3A**). As expected, cells responded normally to the microbial TLR4 agonist LPS with high levels of TNFα and IL-6; however, no relevant cytokine secretion was detectable after exposure to volcanic ash without prior LPS stimulation (**Figures 2** and **3A**). Compared to other pro-inflammatory cytokines, pro-IL-1β lacks a signaling peptide sequence to exit the cell *via* golgi translocation. IL-1β is not constitutively expressed and requires transcriptional upregulation in response to a canonical NF-κB pathway or microbial stimuli, such as LPS, sensed by TLR receptors. As IL-1β itself is predominantly activated in a NLRP3/caspase-1-dependent manner, we investigated the involvement of the NLRP3 inflammasome in the response to volcanic ash.

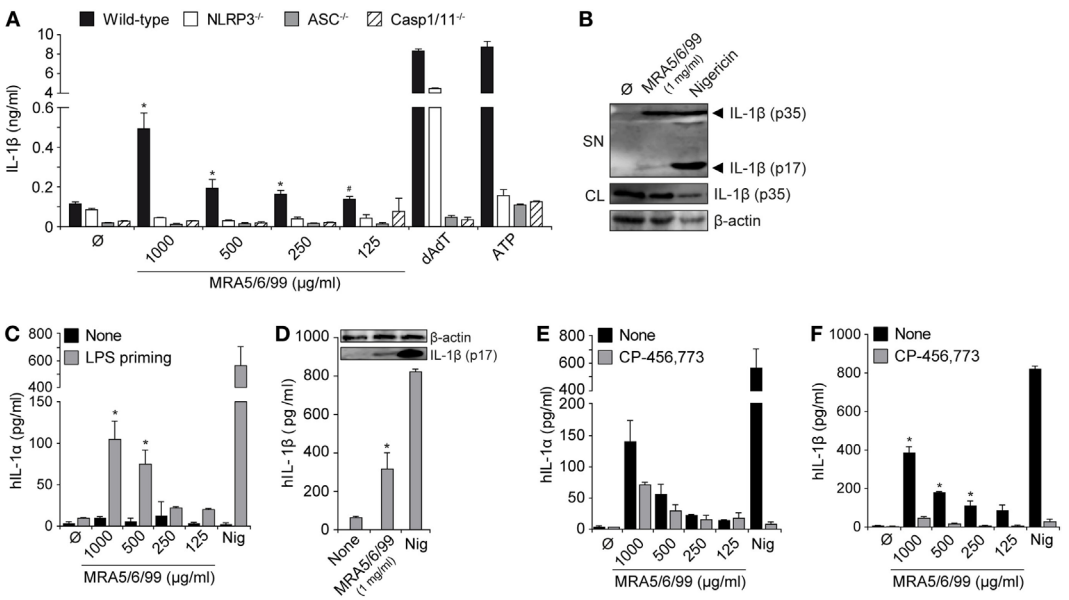

FIGURE 3 | Volcanic ash-induced IL-1β production is NLRP3 inflammasome dependent. Lipopolysaccharide (LPS)-primed macrophages from wild-type or knock-out mice (NLRP3$^{-/-}$, ASC$^{-/-}$, and Casp-1/11$^{-/-}$) were stimulated with MRA5/6/99 at indicated concentrations. **(A)** IL-1β from supernatants (SN) was measured with ELISA. **(B)** Mature IL-1β (p17) inSN and pro-IL-1β (p35) from cell lysates (CL) of cells stimulated with 1 mg/ml MRA5/6/99 was assessed by western blot. β-actin IgG mAb served as loading control. **(C,D)** Primary human peripheral blood mononuclear cells (PBMC) were either LPS-primed or left untreated and subsequently stimulated with MRA5/6/99. **(C)** IL-1α and **(D)** IL-1β levels in SN were determined by ELISA. Insertion **(D)** shows the western blot of bioactive IL-1β (p17) detected from SN. **(E,F)** IL-1α and IL-1β in SN of ash-treated human PBMC in the presence or absence of the NLRP3 inhibitor CP-456,773, assessed by ELISA. Positive controls are poly(dAdT), as a NLRP3-independent inducer, and adenosine triphosphate (ATP) or nigericin, as NLRP3-dependent inducers of IL-1β. Representative data from two independent experiments performed as triplicates are shown. **(A)** $^{*}p \leq 0.05$, compared to NLRP3$^{-/-}$, ASC$^{-/-}$, Caspase-1$^{-/-}$; $^{\#}p \leq 0.05$, compared to NLRP3$^{-/-}$ and ASC$^{-/-}$; **(C,D)** $^{*}p \leq 0.05$, compared to none (Ø); **(E,F)** $^{*}p \leq 0.05$, compared to inhibitor (CP-456,773).

Volcanic Ash-Induced IL-1β Secretion Involves the NLRP3 Inflammasome and Caspase-1 Activation

Activation of the NLRP3 inflammasome results in assembly with the adaptor protein apoptosis-associated speck-like protein containing a CARD (ASC) and subsequent activation of caspase-1, with the release of active IL-1β. We stimulated immortalized wild-type macrophages or cells with deficiencies in the inflammasome signaling components NLRP3, ASC, or Caspase-1/11 with LPS (TLR4 ligand) and subsequently incubated the cells with volcanic ash sample MRA5/6/99 (**Figure 3A**). Only LPS-primed macrophages responded with high amounts of IL-1β, pointing toward the involvement of the NLRP3 inflammasome. Analysis of supernatants revealed a strong and dose-dependent secretion of IL-1β from wild-type macrophages whereas cells with defects in NLRP3 signaling ($NLRP3^{-/-}$, $ASC^{-/-}$, and $Caspase\text{-}1/11^{-/-}$) components failed to secrete IL-1β in response to volcanic ash exposure (**Figure 3A**). As control served the double-stranded DNA mimic dAdT that signals NLRP3 independently *via* the DNA sensor absent in melanoma 2 (AIM2), still requiring the adapter molecule ASC as well as caspase-1 for the processing of IL-1β (36). ATP signaling *via* the ligand-gated cation channel P2×7 served as the NLRP3-dependent positive control. To further confirm proteolytic cleavage of IL-1β into its active form (p17 subunit), we performed a western blot analysis of whole cell lysates and the corresponding supernatants. As expected, volcanic ash was able to induce activation of mature IL-1β, however, in a moderate way compared to the positive control nigericin, a highly potent pore-forming toxin (**Figure 3B**).

We further analyzed the ash-induced release of IL-1 family cytokines (IL-1α and IL-1β) from freshly isolated primary human PBMCs (**Figures 3C–E**). The closely related homolog IL-1α is, in contrast to IL-1β, biologically active, although little is known about its activation and secretion. IL-1α represents a key alarmin from dying cells and plays a pivotal role in acute particle-induced lung inflammation (37). Here, we show that volcanic ash samples alone are not capable of inducing IL-1 secretion in the absence of LPS priming. In contrast, LPS-activated PBMCs secreted high amounts of IL-1α and IL-1β in a dose-dependent manner (**Figure 3C**). Secretion of bioactive IL-1β again was assessed by western blot showing the cleaved p17 fragment in supernatants of ash- or nigericin-treated samples (**Figure 3D**). Finally, the contribution of the NLRP3 inflammasome was confirmed using the specific NLRP3 inflammasome inhibitor CP-456,773 (CRID3, MCC950) that has been described earlier (38). The data show that CP-456,773 potently inhibited the release of IL-1β and, to a lesser extent, IL-1α (**Figures 3E,F**). Despite the well-described functions of IL-1β, IL-1α exists in two different forms, surface-bound pro-IL-1α and a mature secreted form. The fact that IL-1α can, on one hand, signal independently of inflammasome activation but, on the other hand, requires caspase-1 and mature IL-1β for secretion suggests the involvement of other inflammatory pathways, which are yet to be exactly investigated (39).

Cristobalite Is the Apparent Driver of IL-1β Secretion by Volcanic Ash

Volcanic ash is a heterogeneous dust, the componentry of which can vary substantially amongst eruptions and even within the same eruption. Therefore, identifying the phase(s) responsible for the observed reactivity is critical for hazard assessment in the event of an eruption, where ash componentry analysis is a first priority in rapid-response efforts (9, 40). Despite the fact that all of the mineral phases present in volcanic ash are not biosoluble on the timescale of our experiments, or on the expected timescale of phagocytosis *in vivo*, physiologically relevant cations (K^+, Na^+, Ca^{2+}) could be leached from the glass component *via* intra-cellular processing of particles in a matter of hours to days (41) by lysosomal fluid, a buffered, acidic (pH 5.5) solution largely comprising citric acid (42). This may augment the intra- and extra-cellular cation budget, an established condition implicated in inflammasome assembly and activation (43, 44). As neither the compositionally equivalent glass sample nor pumice, which is predominantly composed of glass, were comparably reactive, we discount particle alteration and glass leaching as primary controls on NLRP3 and subsequent caspase-1 activation by volcanic ash. This conclusion is substantiated by minimal (and equivalent) extraction of K^+ and Na^+ in leaching experiments conducted in dilute citric acid, the primary organic ligand in lysosomal fluid, and at a relevant pH (41). Therefore, we do not expect any significant alteration to the bulk phase assemblage throughout the experimental exposures, and contend that single-phase exposures are appropriate to probe the reactivity of the mixed-phase volcanic ash.

Of the componentry samples, the silica compound cristobalite triggered the strongest dose-dependent release of IL-1β (**Figure 4A**), suggesting it is the predominant driver behind production of IL-1β by volcanic ash. This aligns with the established propensity of cristobalite to induce production of IL-1β through activation of the NLRP3 inflammasome (45). We note, however, that intermediate levels of IL-1β were detected as well as the active caspase-1 subunit p20 in response to treatment of LPS-primed macrophages by all componentry samples (**Figures 4B,C**), thereby strengthening the evidence of NLRP3 involvement.

Volcanic Ash Acts through Translocation Into the Cytosol *via* Lysosomal Disruption and Reactive Oxygen Species (ROS) Production

To demonstrate that volcanic ash was internalized by macrophages, we incubated immortalized macrophages with the isolated ash sample for 4 h and imaged untreated and particle-treated cells by light microscopy (**Figure 5A**). The material was taken up by the cells, resulting in massive clustering of particles within the cell, and the intensity of optical refraction (darker cells) illustrates the capacity of the macrophages in particle clearance. This aligns with other recent observations of successful phagocytosis of volcanic ash by macrophages with little associated decrease in cell viability (10, 46). We next combined confocal laser reflection and fluorescence imaging to further consider cellular uptake of

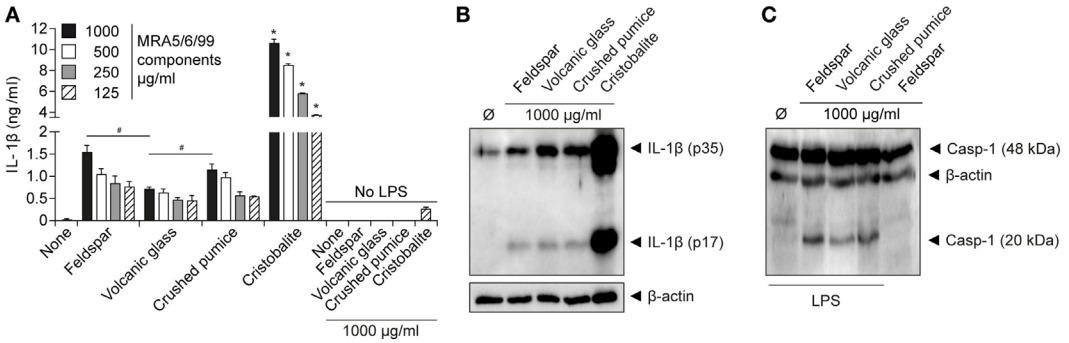

FIGURE 4 | Cristobalite is the main component for volcanic ash-induced IL-1β release. Lipopolysaccharide (LPS)-primed and unprimed wild-type murine macrophages were stimulated with the major ash components (feldspar, volcanic glass, and cristobalite) and natural crushed pumice sample at indicated concentrations. **(A)** IL-1β from supernatants (SN) was examined by ELISA and **(B)** assessment of mature IL-1β (p17) from SN of LPS-primed macrophages by western blot. **(C)** Activated caspase-1 (p20 subunit) in supernatant detected by western blot analysis. Representative data from two independent experiments performed as triplicates are shown. $^{*}p \leq 0.05$, compared to other components; $^{\#}p \leq 0.05$.

volcanic ash. We co-incubated the cells with the quenching dye DQ-OVA that, upon proteolytic processing, allowed us to monitor the endo-lysosomal compartment of living cells. As expected, DQ-OVA showed a distinct vesicular distribution in the absence of ash. In contrast, ash-treated cells showed enlarged vesicles with enhanced particle uptake (**Figure 5B**). Furthermore, ash and DQ-OVA translocated to the cytosol and showed partial co-localization. Faint fluorescence across the entire cytosol is evident of spreading and advanced dilution of the DQ quenching dye.

To test if endosomal uptake was necessary for ash-induced cytokine production, we incubated cells with the endocytosis inhibitor Lat A prior to ash exposure of the cells and measured IL-1β secretion (**Figure 5C**). Lat A completely inhibited ash-induced IL-1β release, whereas it had no influence on cytokine secretion mediated by the pore-forming toxin nigericin, strengthening the role of lysosomal uptake in response to volcanic ash. The data further reveal that lysosomal uptake seems to be the main uptake mechanism leading to lysosomal rupture with subsequent IL-1β release. In terms of lysosomal destabilization, enzymes become proteolytically active and are released into cytosol for inflammasome activation. Cathepsins are protein-degrading enzymes that become cleaved upon lysosomal maturation and are released as active forms into the cytosol. The cathepsin family comprises multiple proteins involved in IL-1β processing with cathepsin B being a well-described player involved in NLRP3 activation (22, 47). To test the contribution of cathepsins in volcanic ash-induced NLRP3 activation, we pre-incubated wild-type macrophages with the cathepsin B inhibitor CA-074-Me prior to ash exposure and measured IL-1β secretion (**Figure 5D**). Inhibition of cathepsin B completely inhibited IL-1β secretion, compared to partial effects observed with the lysosomotropic agent L-leucyl-L-leucine methyl ester (Leu-Leu-OMe). With respect to particulate and non-particulate structures, the data further show that, in terms of NLRP3-dependent IL-1β processing, redundant roles of cathepsin family members might play a role, as previously described (48).

Particulate substances or fibers are likely candidates for the initiation of ROS (19). While ROS are an important feature of maintaining immune homeostasis, excessive production results in inflammation and carcinogenesis as postulated for inhaled asbestos fibers, with mechanisms such as "frustrated" phagocytosis being discussed (19, 49, 50). It has been shown that, in most scenarios, ROS are associate stimulators of particle-induced NLRP3 inflammasome activation. We show here that ROS production is involved in ash-induced IL-1β release, using the small-molecule ROS scavenger (2R,4R)-4-aminopyrrolidine-2,4-dicarboxylic acid (APDC), which completely abrogated IL-1β secretion (**Figure 5E**). Previous work has shown that volcanic ash has the capacity to generate large amounts of ROS, largely due to the presence of non-crystalline-silica minerals (33, 51); however, the primary non-crystalline-silica components of volcanic ash have no history of inducing an inflammatory response (11, 52). In the present study, we observed low but dose-dependent production of IL-1β by the major constituents but, critically, the crushed pumice sample, which contains a similar assemblage of "non-crystalline-silica minerals," was minimally reactive. Therefore, while auxiliary mineral-based ROS generation may be partially implicated in the observed volcanic ash reactivity, volcanic cristobalite is the likely candidate for NLRP3-mediated IL-1β production by volcanic ash.

DISCUSSION

There is mounting evidence that, while not overtly toxic, volcanic ash exposure can result in general insult with the potential for chronic toxicity by inciting a low, but significant, pro-inflammatory response and resulting in delayed inflammation *in vivo* (10, 11). In this study, we identify a prominent role for ash-induced inflammation, and provide the first mechanism-specific response of macrophages to volcanic ash, whereby phagosomal uptake results in significant secretion of mature IL-1β. This secretion is caspase-1 and ASC dependent, identifying the involvement of an inflammasome-mediated pathway. Critically, silencing of the murine NLRP3 gene as well as inhibition of human NLRP3 completely abolished ash-induced IL-1β secretion. We show that endocytosis and cathepsins are involved in the induction

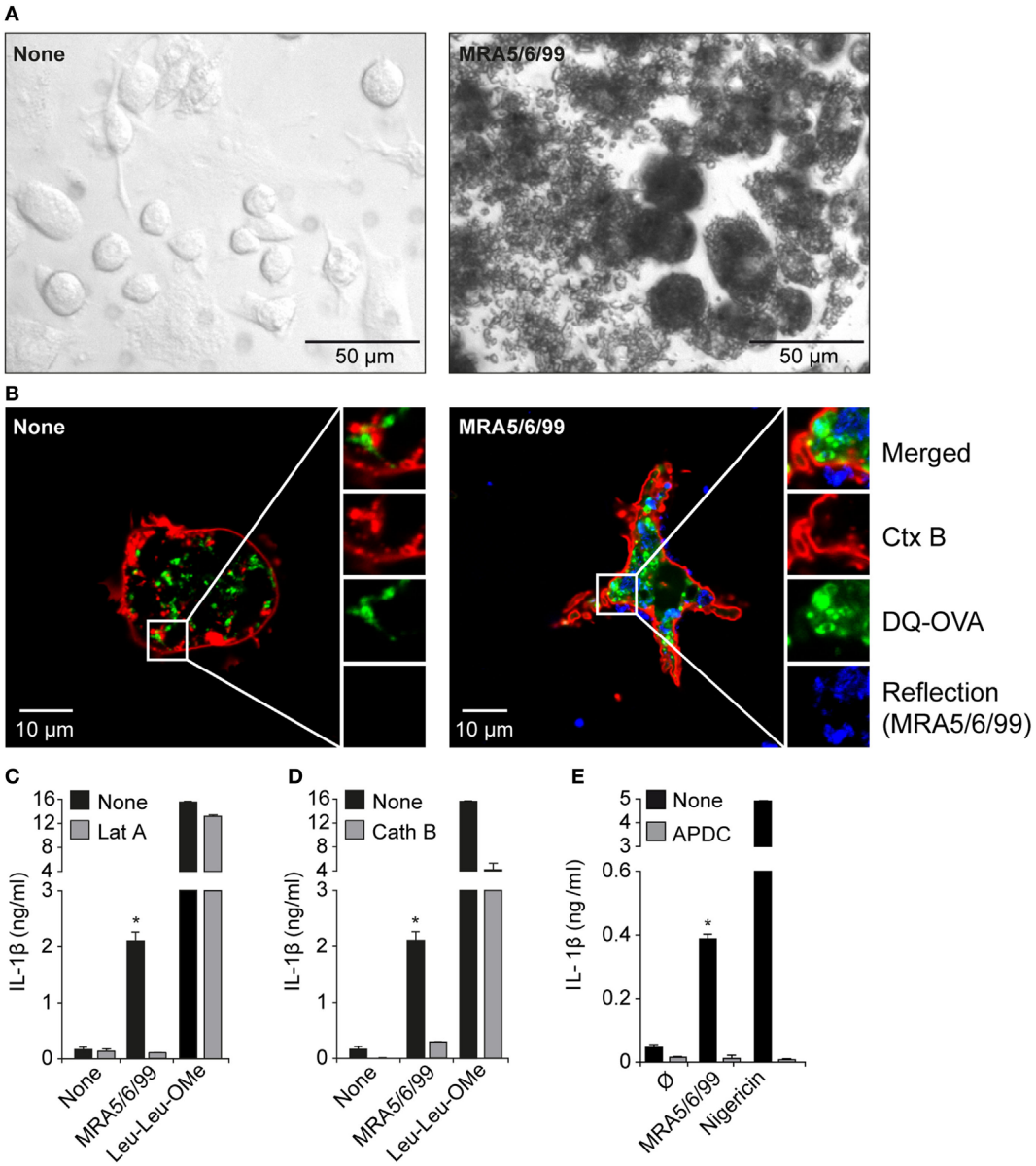

FIGURE 5 | Internalization of volcanic ash by macrophages induces lysosomal damage and reactive oxygen species (ROS). **(A)** Light microscopy (20× magnification) and **(B)** laser scanning microscopy images (63× magnification) of untreated wild-type murine macrophages and macrophages treated with volcanic ash sample MRA5/6/99 for 4 h and stained with Ctx B (red) and DQ-Ovalbumin (DQ-OVA) (green). **(C–E)** LPS-primed immortalized macrophages were stimulated with 1 mg/ml MRA5/6/99 in the presence or absence of the endocytosis inhibitor latrunculin A (Lat A) **(C)**, the cathepsin B inhibitor CA-074-Me **(D)**, or the ROS scavenger (2R,4R)-4-aminopyrrolidine-2,4-dicarboxylic acid (APDC) **(E)**. Secretion of IL-1β in supernatants was measured by ELISA. Leu-Leu-OMe and nigericin served as lysosomotropic positive control and NLRP3-dependent inflammasome activator, respectively. Representative data from two independent experiments are shown. *$p \leq 0.05$, compared to inhibitors (Lat A, Cath B, APDC).

of IL-1β secretion, which indicates that lysosomal maturation, with subsequent rupture and loss of lysosomal contents into the cytosol, is one major mechanism of volcanic ash-induced inflammation *in vitro*. The NLRP3 inflammasome as an ash-responsive element appears to be predominantly mediated by the crystalline silica phase (cristobalite), although other phases induced a low-level response. The componentry of volcanic ash is variable and intrinsically linked to eruption history, and, by isolating the reactivity of cristobalite, these data provide a new avenue for considering the propensity for volcanic ash to incite inflammation in order to better constrain the respiratory hazard posed during future eruptions.

The exact mechanism of how crystalline structures act on inflammasome activation remains elusive. Among others, including ROS involvement, discussed are scavenger receptors such as the macrophage receptor with collagenous structure

(MARCO), CD36, or CD204, with MARCO identified as the dominant contributor in the C57BL/6 mouse model (53). However, the contribution of these receptors upon silica crystal uptake with subsequent IL-1β maturation remains controversial, since alveolar macrophages derived from MARCO-null mice show increased IL-1β cytokine release (54). Although scavenger receptor binding or membrane binding of crystalline particles without internalization may also be sufficient for silica-induced IL-1β production (55), lysosomal crystal uptake and procession is required for a potent inflammatory response. It is well accepted that the activation of the NLRP3 inflammasome pathway requires two steps: an initial, for example, NF-κB-mediated, priming step and a second stimulus for NLRP3 assembly with subsequent caspase-1 cleavage. Although we could clearly show that volcanic ash is capable of inducing NLRP3 activation *in vitro*, a link to the initial priming step is still missing. One explanation is provided by the fact that ROS seem to act upstream of NLRP3 activation, involving the NF-κB pathway upon phagocytosis (56, 57), although ROS are capable of performing both activation and inactivation of NF-κB pathways. However, volcanic ash exposure rarely occurs in isolation, for example, there will be concomitant exposure with anthropogenic pollution in populated regions (58), and other phases may initiate signaling. Another priming mechanism was described by Monick et al. (46), involving the ability of ash particles to promote bacterial infection by altered pathogen killing. This, in turn, would lead to an increased microbial burden with enhanced NF-κB signaling (Step 1) *via* pattern recognition receptors and result in a vicious circle.

Chronic inflammation resulting from particle-induced inflammasome activation, for example, in silicosis or asbestosis, is thought to derive from the inability of cells to destroy the ingested material, leading to successive rounds of apoptosis and re-ingestion of the crystalline material (4). Volcanic ash (including MRA5/6/99), however, has proven to be minimally apoptotic and necrotic to macrophages (10, 46), which suggests successful clearance of ash from the lungs. The combination of effective clearance and inflammasome activation may explain previous results from instillation experiments, such as those discussed above by Lee and Richards (11), who observed granuloma in the lymph nodes followed by considerably delayed lung inflammation, but no fibrosis. Prompt transport of ash to the lymphatic system would preclude an immediate and robust response *in situ*, yet inflammasome-initiated signaling may result in the delayed inflammation observed relative to pure crystalline silica. Despite this, in the most comprehensive clinical study to date, no hilar node enlargement was observed in chest X-rays of 37 children on Montserrat who had been exposed to volcanic ash from the Soufrière Hills volcano for 10 years (59). Clinical manifestations of exposure, therefore, are presently unknown.

The disparity in response between pure-phase cristobalite and volcanic ash is attributable, in part, to the heterogeneous nature of both the bulk ash (which is ~15 wt.% cristobalite) and the ash particles themselves (with individual particles often being comprised of various mineral components as seen in **Figure 1C**). However, the extent of this disparity, as also observed in previous work (10, 12), suggests that the reactivity of volcanic cristobalite itself is suppressed. Crystalline silica reactivity may be contingent on fracturing the surfaces of crystals in equilibrium (60). The high-energy nature of ash generation, through both explosive eruptions and dome-collapse events, ensures that volcanic cristobalite surfaces will be readily and commonly fractured. Nanoscale chemical and structural investigations of surface-exposed cristobalite crystals reveal no evidence for occlusion (8), and the presence of a reactive cristobalite surface has been implicated in the binding of similar proteins by cristobalite-rich volcanic ash and a crystalline silica standard (61). Therefore, intrinsic modifications may act to suppress volcanic cristobalite reactivity beyond the aforementioned diminished surface area-dose, as previously postulated (8, 14). In particular, all volcanic cristobalite is chemically impure, containing up to 3 wt.% aluminum (7, 8); incorporation of structural aluminum at an equivalent dopant concentration has been shown to suppress cristobalite reactivity (15), and may affect the presence of certain surface moieties (i.e., silanols) deemed critical for crystalline silica reactivity (62). Critically, however, volcanic cristobalite appears to be sufficiently reactive to have initiated a response here.

Significant advances in our understanding of the hazard posed by volcanic ash have been made in recent years; however, a serious concern regarding the crystalline silica polymorph cristobalite, the only toxic mineral phase appreciably present in volcanic ash, has persisted. The observations presented herein confirm adherence to the "variable entity" description of crystalline silica, as defined for quartz by Donaldson and Borm (13) and considered for volcanic cristobalite by Horwell et al. (8), whereby the reactive-silica burden for volcanic cristobalite is insufficient to initiate the more immediate and robust response observed with pure crystalline silica. As discussed, previously reported chemical and structural modifications have been hypothesized to alter the pathogenicity of volcanic cristobalite relative to a pure-phase standard (8). We show here, for the first time, that these modifications are insufficient to abrogate reactivity completely. With the potential for volcanic eruptions to impact millions of people, and with so few epidemiological studies having been conducted, mechanistic insight into the potential for ash to cause disease is of immediate public health value. Identification of an established pathway involved in other particle-induced diseases and through which volcanic ash can induce a chronic inflammatory response offers a foundation on which to provide health risk assessments during future volcanic crises.

ETHICS STATEMENT

This study was carried out in accordance with the Ethics Committee of the Ludwig-Maximilians-University of Munich (24.02.2006GP/cp).

AUTHOR CONTRIBUTIONS

DED designed the study, performed the particle synthesis and characterization, and drafted the manuscript. PD designed the study, carried out the immunoassays, and drafted the manuscript. CH, PB, UK, MS, and DBD helped conceive the study. All authors read and approved the final manuscript and are accountable for all aspects of the work.

ACKNOWLEDGMENTS

The immortalized macrophage cell lines were a kind gift from Prof. Eicke Latz, Institute of Innate Immunity, University of Bonn, Germany. Thanks to Kai Uwe-Hess, Department of Earth and Environmental Sciences, Ludwig-Maximilians-Universität (LMU) München, Munich, Germany, for providing the sample of synthetic cristobalite. We are indebted to MC Leewis for providing an internal USGS review. Any use of trade, product, or firm names is for descriptive purposes only and does not imply endorsement by the U.S. Government.

FUNDING

This work has been funded by the ERC Advanced Grant—Explosive Volcanism in the Earth System: Experimental Insights (EVOKES, no. 247076) to DBD, as well as by the DFG as part of the CRC 1123 (B7) to PD and MS; the International Doctoral Program i-Target: Immunotargeting of Cancer funded by the Elite Network of Bavaria to MS. UK acknowledges support by the Marie Curie Initial Training Network "VERTIGO," funded through the European Seventh Framework Programme (FP7 2007–2013) under Grant Agreement number 607905.

REFERENCES

1. Green FHY, Vallyathan V, Mentnech MS, Tucker JH, Merchant JA, Kiessling P, et al. Is volcanic ash a pneumoconiosis risk? *Nature* (1981) 293:216–7. doi:10.1038/293216a0
2. Bernstein RS, Baxter PJ, Falk H, Ing R, Foster L, Frost F. Immediate public health concerns and actions in volcanic eruptions: lessons from the Mount St. Helens eruptions, May 18–October 18, 1980. *Am J Public Health* (1986) 76:25–37. doi:10.2105/AJPH.76.Suppl.25
3. Horwell CJ, Baxter PJ. The respiratory health hazards of volcanic ash: a review for volcanic risk mitigation. *Bull Volcanol* (2006) 69:1–24. doi:10.1007/s00445-006-0052-y
4. Mossman BT, Churg A. Mechanisms in the pathogenesis of asbestosis and silicosis. *Am J Respir Crit Care Med* (1998) 157:1666–80. doi:10.1164/ajrccm.157.5.9707141
5. Baxter PJ, Bonadonna C, Dupree R, Hards VL, Kohn SC, Murphy MD, et al. Cristobalite in volcanic ash of the Soufriere Hills Volcano, Montserrat, British West Indies. *Science* (1999) 283:1142–5. doi:10.1126/science.283.5405.1142
6. Horwell CJ, Williamson BJ, Llewellin EW, Damby DE, Le Blond JS. The nature and formation of cristobalite at the Soufrière Hills volcano, Montserrat: implications for the petrology and stability of silicic lava domes. *Bull Volcanol* (2013) 75:696. doi:10.1007/s00445-013-0696-3
7. Damby DE. *From Dome to Disease: The Respiratory Toxicity of Volcanic Cristobalite [Durham theses]*. Durham, UK: Durham University e-theses (2012). p. 1–258.
8. Horwell CJ, Williamson BJ, Donaldson K, Le Blond JS, Damby DE, Bowen L. The structure of volcanic cristobalite in relation to its toxicity; relevance for the variable crystalline silica hazard. *Part Fibre Toxicol* (2012) 9:44. doi:10.1186/1743-8977-9-44
9. Horwell CJ, Baxter PJ, Hillman SE, Calkins JA, Damby DE, Delmelle P, et al. Physicochemical and toxicological profiling of ash from the 2010 and 2011 eruptions of Eyjafjallajökull and Grímsvötn volcanoes, Iceland using a rapid respiratory hazard assessment protocol. *Environ Res* (2013) 127:63–73. doi:10.1016/j.envres.2013.08.011
10. Damby DE, Murphy FA, Horwell CJ, Raftis J, Donaldson K. The in vitro respiratory toxicity of cristobalite-bearing volcanic ash. *Environ Res* (2016) 145:74–84. doi:10.1016/j.envres.2015.11.020
11. Lee SH, Richards RJ. Montserrat volcanic ash induces lymph node granuloma and delayed lung inflammation. *Toxicology* (2004) 195(2–3):155–65. doi:10.1016/j.tox.2003.09.013
12. Wilson MR, Stone V, Cullen RT, Searl A, Maynard RL, Donaldson K. In vitro toxicology of respirable Montserrat volcanic ash. *Occup Environ Med* (2000) 57(11):727–33. doi:10.1136/oem.57.11.727
13. Donaldson K, Borm PJA. The quartz hazard: a variable entity. *Ann Occup Hyg* (1998) 42(5):287–94. doi:10.1016/S0003-4878(98)00044-1
14. Damby DE, Llewellin EW, Horwell CJ, Williamson BJ, Najorka J, Cressey G, et al. The alpha-beta phase transition in volcanic cristobalite. *J Appl Crystallogr* (2014) 47(Pt 4):1205–15. doi:10.1107/S160057671401070X
15. Nattrass C, Horwell CJ, Damby DE, Brown D, Stone V. The effect of aluminium and sodium impurities on the in vitro toxicity and pro-inflammatory potential of cristobalite. *Environ Res* (2017) 159:164–75. doi:10.1016/j.envres.2017.07.054
16. Hincks TK, Aspinall WP, Baxter A, Sparks RSJ, Woo G. Long term exposure to respirable volcanic ash on Montserrat: a time series simulation. *Bull Volcanol* (2006) 68:266–84. doi:10.1007/s00445-005-0006-9
17. Kamp DW, Weitzman SA. The molecular basis of asbestos induced lung injury. *Thorax* (1999) 54:638–52. doi:10.1136/thx.54.7.638
18. Martinon F, Petrilli V, Mayor A, Tardivel A, Tschopp J. Gout-associated uric acid crystals activate the NALP3 inflammasome. *Nature* (2006) 440(7081):237–41. doi:10.1038/nature04516
19. Dostert C, Petrilli V, Van Bruggen R, Steele C, Mossman BT, Tschopp J. Innate immune activation through Nalp3 inflammasome sensing of asbestos and silica. *Science* (2008) 320:674–7. doi:10.1126/science.1156995
20. Duewell P, Kono H, Rayner KJ, Sirois CM, Vladimer G, Bauernfeind FG, et al. NLRP3 inflammasomes are required for atherogenesis and activated by cholesterol crystals. *Nature* (2010) 464(7293):1357–61. doi:10.1038/nature08938
21. Martinon F, Burns K, Tschopp J. The inflammasome: a molecular platform triggering activation of inflammatory caspases and processing of proIL-beta. *Mol Cell* (2002) 10:417–26. doi:10.1016/S1097-2765(02)00599-3
22. Hornung V, Bauernfeind F, Halle A, Samstad EO, Kono H, Rock KL, et al. Silica crystals and aluminum salts activate the NALP3 inflammasome through phagosomal destabilization. *Nat Immunol* (2008) 9:847–56. doi:10.1038/ni.1631
23. Driscoll KE, Maurer JK. Cytokine and growth factor release by alveolar macrophages: potential biomarkers of pulmonary toxicity. *Toxicol Pathol* (1991) 19:398–405. doi:10.1177/0192623391019004-108
24. Davis GS, Pfeiffer LM, Hemenway DR. Persistent overexpression of interleukin-1beta and tumor necrosis factor-alpha in murine silicosis. *J Environ Pathol Toxicol Oncol* (1998) 17:99–114.
25. Rimal B, Greenberg AK, Rom WN. Basic pathogenetic mechanisms in silicosis: current understanding. *Curr Opin Pulm Med* (2005) 11:169–73. doi:10.1097/01.mcp.0000152998.11335.24
26. Huaux F. New developments in the understanding of immunology in silicosis. *Curr Opin Allergy Clin Immunol* (2007) 7:168–73. doi:10.1097/ACI.0b013e32802bf8a5
27. Mossman BT, Glenn RE. Bioreactivity of the crystalline silica polymorphs, quartz and cristobalite, and implications for occupational exposure limits (OELs). *Crit Rev Toxicol* (2013) 43(8):632–60. doi:10.3109/10408444.2013.818617
28. Cassel SL, Eisenbarth SC, Iyer SS, Sadler JJ, Colegio OR, Tephly LA, et al. The Nalp3 inflammasome is essential for the development of silicosis. *Proc Natl Acad Sci U S A* (2008) 105(26):9035–40. doi:10.1073/pnas.0803933105
29. Horwell CJ, Sparks RSJ, Brewer TS, Llewellin EW, Williamson BJ. The characterisation of respirable volcanic ash from the Soufriere Hills Volcano, Montserrat, with implications for health hazard. *Bull Volcanol* (2003) 65:346–62. doi:10.1007/s00445-002-0266-6
30. Horwell CJ, Hillman SE, Cole PD, Loughlin SC, Llewellin EW, Damby DE, et al. Controls on variations in cristobalite abundance in ash generated by the Soufrière hills volcano, Montserrat in the period 1997–2010. *Geol Soc Lond Mem* (2014) 39:399–406. doi:10.1144/M39.21
31. Horwell CJ. Grain size analysis of volcanic ash for the rapid assessment of respiratory health hazard. *J Environ Monit* (2007) 9(10):1107–15. doi:10.1039/b710583p
32. Kerr PF. *Optical Mineralogy*. New York: McGraw-Hill College (1977).

33. Horwell CJ, Fenoglio I, Ragnarsdottir KV, Sparks RSJ, Fubini B. Surface reactivity of volcanic ash from the eruption of Soufrière Hills volcano, Montserrat, West Indies with implications for health hazards. *Environ Res* (2003) 93(2):202–15. doi:10.1016/S0013-9351(03)00044-6
34. Zhou R, Tardivel A, Thorens B, Choi I, Tschopp J. Thioredoxin-interacting protein links oxidative stress to inflammasome activation. *Nat Immunol* (2010) 11:136–40. doi:10.1038/ni.1831
35. Kueppers U, Scheu B, Spieler O, Dingwell DB. Fragmentation efficiency of explosive volcanic eruptions: a study of experimentally generated pyroclasts. *J Volcanol Geotherm Res* (2006) 153(1–2):125–35. doi:10.1016/j.jvolgeores.2005.08.006
36. Hornung V, Ablasser A, Charrel-Dennis M, Bauernfeind F, Horvath G, Caffrey DR, et al. AIM2 recognizes cytosolic dsDNA and forms a caspase-1-activating inflammasome with ASC. *Nature* (2009) 458:514–8. doi:10.1038/nature07725
37. Rabolli V, Badissi AA, Devosse R, Uwambayinema F, Yakoub Y, Palmai-Pallag M, et al. The alarmin IL-1α is a master cytokine in acute lung inflammation induced by silica micro- and nanoparticles. *Part Fibre Toxicol* (2014) 11:69. doi:10.1186/s12989-014-0069-x
38. Primiano MJ, Lefker BA, Bowman MR, Bree AG, Hubeau C, Bonin PD, et al. Efficacy and pharmacology of the NLRP3 inflammasome inhibitor CP-456,773 (CRID3) in murine models of dermal and pulmonary inflammation. *J Immunol* (2016) 197(6):2421–33. doi:10.4049/jimmunol.1600035
39. Gross O, Yazdi AS, Thomas CJ, Masin M, Heinz LX, Guarda G, et al. Inflammasome activators induce interleukin-1α secretion via distinct pathways with differential requirement for the protease function of caspase-1. *Immunity* (2012) 36(3):388–400. doi:10.1016/j.immuni.2012.01.018
40. Damby DE, Horwell CJ, Baxter PJ, Delmelle P, Donaldson K, Dunster C, et al. The respiratory health hazard of tephra from the 2010 Centennial eruption of Merapi with implications for occupational mining of deposits. *J Volcanol Geotherm Res* (2013) 261:376–87. doi:10.1016/j.jvolgeores.2012.09.001
41. Fiantis D, Nelson M, Shamshuddin J, Goh TB, Van Ranst E. Leaching experiments in recent tephra deposits from Talang volcano (West Sumatra), Indonesia. *Geoderma* (2010) 156(3–4):161–72. doi:10.1016/j.geoderma.2010.02.013
42. Stebounova LV, Guio E, Grassian VH. Silver nanoparticles in simulated biological media: a study of aggregation, sedimentation, and dissolution. *J Nanopart Res* (2010) 13:233–44. doi:10.1007/s11051-010-0022-3
43. Muñoz-Planillo R, Kuffa P, Martínez-Colón G, Smith BL, Rajendiran TM, Núñez G. K+ efflux is the common trigger of NLRP3 inflammasome activation by bacterial toxins and particulate matter. *Immunity* (2013) 38(6):1142–53. doi:10.1016/j.immuni.2013.05.016
44. Schorn C, Frey B, Lauber K, Janko C, Strysio M, Keppeler H, et al. Sodium overload and water influx activate the NALP3 inflammasome. *J Biol Chem* (2011) 286:35–41. doi:10.1074/jbc.M110.139048
45. Sayan M, Mossman BT. The NLRP3 inflammasome in pathogenic particle and fibre-associated lung inflammation and diseases. *Part Fibre Toxicol* (2016) 13(51):1–15. doi:10.1186/s12989-016-0162-4
46. Monick MM, Baltrusaitis J, Powers LS, Borcherding JA, Caraballo JC, Mudunkotuwa I, et al. Effects of Eyjafjallajökull volcanic ash on innate immune system responses and bacterial growth in vitro. *Environ Health Perspect* (2013) 121(6):691–8. doi:10.1289/ehp.1206004
47. Hoegen T, Tremel N, Klein M, Angele B, Wagner H, Kirschning C, et al. The NLRP3 inflammasome contributes to brain injury in pneumococcal meningitis and is activated through ATP-dependent lysosomal cathepsin B release. *J Immunol* (2011) 187(10):5440–51. doi:10.4049/jimmunol.1100790
48. Orlowski GM, Colbert JD, Sharma S, Bogyo M, Robertson SA, Rock KL. Multiple cathepsins promote pro-IL-1β synthesis and NLRP3-mediated IL-1β activation. *J Immunol* (2015) 195(4):1685–97. doi:10.4049/jimmunol.1500509
49. Hansen K, Mossman BT. Generation of superoxide from alveolar macrophages exposed to asbestiform and nonfibrous particles. *Cancer Res* (1987) 47(6):1681–6.
50. Shukla A, Gulumian M, Hei TK, Kamp D, Rahman Q, Mossman BT. Multiple roles of oxidants in the pathogenesis of asbestos-induced diseases. *Free Radic Biol Med* (2003) 34(9):1117–29. doi:10.1016/S0891-5849(03)00060-1
51. Horwell CJ, Fenoglio I, Fubini B. Iron-induced hydroxyl radical generation from basalitic volcanic ash. *Earth Planet Sci Lett* (2007) 261:662–9. doi:10.1016/j.epsl.2007.07.032
52. Housley DG, Bérubé KA, Jones TP, Anderson S, Pooley FD, Richards RJ. Pulmonary epithelial response in the rat lung to instilled Montserrat respirable dusts and their major mineral components. *Occup Environ Med* (2002) 59:466–72. doi:10.1136/oem.59.7.466
53. Hamilton RF Jr, Thakur SA, Holian A. Silica binding and toxicity in alveolar macrophages. *Free Radic Biol Med* (2008) 44(7):1246–58. doi:10.1016/j.freeradbiomed.2007.12.027
54. Biswas R, Hamilton RF Jr, Holian A. Role of lysosomes in silica-induced inflammasome activation and inflammation in absence of MARCO. *J Immunol Res* (2014) 2014:304180. doi:10.1155/2014/304180
55. Hari A, Zhang Y, Tu Z, Detampel P, Stenner M, Ganguly A, et al. Activation of NLRP3 inflammasome by crystalline structures via cell surface contact. *Sci Rep* (2014) 4(7281):1–8. doi:10.1038/srep07281
56. Bauernfeind FG, Horvath G, Stutz A, Alnemri ES, MacDonald K, Speert D, et al. Cutting edge: NF-κB activating pattern recognition and cytokine receptors license NLRP3 inflammasome activation by regulating NLRP3 expression. *J Immunol* (2009) 183(2):787–91. doi:10.4049/jimmunol.0901363
57. Gloire G, Legrand-Poels S, Piette J. NF-κB activation by reactive oxygen species: fifteen years later. *Biochem Pharmacol* (2006) 72(11):1493–505. doi:10.1016/j.bcp.2006.04.011
58. Tomašek I, Horwell CJ, Damby DE, Barošová H, Geers C, Petri-Fink A, et al. Combined exposure of diesel exhaust particles and respirable Soufrière Hills volcanic ash causes a (pro-)inflammatory response in an in vitro multicellular epithelial tissue barrier model. *Part Fibre Toxicol* (2016) 13(1):67. doi:10.1186/s12989-016-0178-9
59. Baxter PJ, Searl AS, Cowie HA, Jarvis D, Horwell CJ. Evaluating the respiratory health risks of volcanic ash at the eruption of the Soufrière Hills Volcano, Montserrat, 1995 to 2010. *Geol Soc Lond Mem* (2014) 39:407–25. doi:10.1144/M39.22
60. Turci F, Pavan C, Leinardi R, Tomatis M, Pastero L, Garry D, et al. Revisiting the paradigm of silica pathogenicity with synthetic quartz crystals: the role of crystallinity and surface disorder. *Part Fibre Toxicol* (2015) 13(32):1–12. doi:10.1186/s12989-016-0136-6
61. Jones T, BéruBé K. The bioreactivity of the sub-10 μm component of volcanic ash: Soufrière Hills volcano, Montserrat. *J Hazard Mater* (2011) 194:128–34. doi:10.1016/j.jhazmat.2011.07.092
62. Pavan C, Fubini B. Unveiling the variability of "quartz hazard" in light of recent toxicological findings. *Chem Res Toxicol* (2017) 30:469–85. doi:10.1021/acs.chemrestox.6b00409

Conflict of Interest Statement: The authors declare no conflict of interest. The funding bodies had no input into the design of the study, collection, analysis and interpretation of data, or writing of the manuscript.

frontiers in Immunology

ORIGINAL RESEARCH
published: 29 March 2018
doi: 10.3389/fimmu.2018.00619

Anti-Transforming Growth Factor β IgG Elicits a Dual Effect on Calcium Oxalate Crystallization and Progressive Nephrocalcinosis-Related Chronic Kidney Disease

Stefanie Steiger[1]†, Julia Felicitas Grill[1†], Qiuyue Ma[1†], Tobias Bäuerle[2], Jutta Jordan[2], Michaela Smolle[3], Claudia Böhland[4], Maciej Lech[1] and Hans-Joachim Anders[1]**

[1] Division of Nephrology, Medizinische Klinik und Poliklinik IV, Klinikum der Universität München, Munich, Germany, [2] Preclinical Imaging Platform Erlangen, Institute of Radiology, Friedrich-Alexander-Universität Erlangen-Nürnberg, Erlangen, Germany, [3] Ludwig-Maximilians Universität München, Biomedizinisches Centrum, Munich, Germany, [4] Department of Radiation Oncology, Ludwig-Maximilians Universität München, Munich, Germany

OPEN ACCESS

Edited by:
Philippe Saas,
INSERM UMR1098 Interactions Hôte-Greffon-Tumeur & Ingénierie Cellulaire et Génique, France

Reviewed by:
Joseph Isaac Shapiro,
Marshall University, United States
Yufeng Huang,
University of Utah, United States

***Correspondence:**
Stefanie Steiger
stefanie.steiger@med.uni-muenchen.de;
Hans-Joachim Anders
hans-joachim.anders@med.uni-muenchen.de

†These authors have contributed equally to this work.

Specialty section:
This article was submitted to Inflammation, a section of the journal Frontiers in Immunology

Received: 24 January 2018
Accepted: 12 March 2018
Published: 29 March 2018

Citation:
Steiger S, Grill JF, Ma Q, Bäuerle T, Jordan J, Smolle M, Böhland C, Lech M and Anders H-J (2018) Anti-Transforming Growth Factor β IgG Elicits a Dual Effect on Calcium Oxalate Crystallization and Progressive Nephrocalcinosis-Related Chronic Kidney Disease. Front. Immunol. 9:619. doi: 10.3389/fimmu.2018.00619

Crystallopathies are a heterogeneous group of diseases caused by intrinsic or environmental microparticles or crystals, promoting tissue inflammation and scarring. Certain proteins interfere with crystal formation and growth, e.g., with intrarenal calcium oxalate (CaOx) crystal formation, a common cause of kidney stone disease or nephrocalcinosis-related chronic kidney disease (CKD). We hypothesized that immunoglobulins can modulate CaOx microcrystal formation and crystal growth and that therefore, biological IgG-based drugs designed to specifically target disease modifying proteins would elicit a dual effect on the outcome of CaOx-related crystallopathies. Indeed, both the anti-transforming growth factor (TGF)β IgG and control IgG1 antibody impaired CaOx crystallization *in vitro*, and decreased intrarenal CaOx crystal deposition and subsequent CKD in mice on an oxalate-rich diet compared to oxalate-fed control mice. However, the TGFβ-specific IgG antibody showed nephroprotective effects beyond those of control IgG1 and substantially reduced interstitial fibrosis as indicated by magnetic resonance imaging, silver and α-smooth muscle actin staining, RT-qPCR, and flow cytometry for pro-fibrotic macrophages. Suppressing interstitial fibrosis slowed the decline of glomerular filtration rate (GFR) compared to treatment with control IgG1 [slope of $m = -8.9$ vs. $m = -14.5$ µl/min/100 g body weight (BW)/day, $\Delta = 38.3\%$], an increased GFR at the end of the study (120.4 vs. 42.6 µl/min/100 g BW, $\Delta = 64.6\%$), and prolonged end stage renal disease (ESRD)-free renal survival by 10 days ($\Delta = 38.5\%$). Delayed onset of anti-TGFβ IgG from day 7 was no longer effective. Our results suggest that biological drugs can elicit dual therapeutic effects on intrinsic crystallopathies, such as anti-TGFβ IgG antibody treatment inhibits CaOx crystallization as well as interstitial fibrosis in nephrocalcinosis-related CKD.

Keywords: calcium oxalate, crystallization, transforming growth factor β, fibrosis, nephrocalcinosis, chronic kidney disease

INTRODUCTION

Crystal deposition is relatively common in the kidneys and is often associated with inflammation, tubular injury, and interstitial fibrosis (1). Crystals of calcium oxalate (CaOx) are commonly found in kidney stone disease (1) accounting for approximately 80% of all types of kidney stones and can cause chronic kidney disease (CKD) (2). Unlike symptomatic urolithiasis, intrarenal nephrocalcinosis is often asymptomatic, but can lead to significant kidney injury and renal failure (3–5). The mechanism of CaOx crystal formation involves a combination of processes including urine supersaturation of stone-forming salts, such as calcium and oxalate, urinary pH, and lack of crystallization inhibitors in the urine (6, 7). These crystallization inhibitors like nephrocalcin, osteopontin (8), Tamm–Horsfall glycoprotein (9), and uropontin (10) have been identified in the urine of healthy individuals but they are decreased in kidney stone formers. Interactions between CaOx crystals and the tubular compartment evoking an inflammatory response associated with the release of pro-inflammatory mediators, cell death, and leukocyte infiltration, which further contributes to tubular atrophy and interstitial fibrosis, leading to progressive nephrocalcinosis (11). We first speculated that proteins potentially suitable for therapy in humans could have a similar protective effect on CaOx crystallization, e.g., immunoglobulin (IgG).

Therapies to prevent renal failure from CaOx crystal-induced nephropathy and/or nephrocalcinosis have been directed principally at lowering serum and urine oxalate, the use of an oxalate-reduced diet and calcium supplementation in patients with enteric hyperoxaluria, as well as anti-inflammatory therapies (12). CKD progression in nephrocalcinosis is associated with profound interstitial fibrosis (13), a histopathological feature of kidney atrophy thought to contribute to CKD progression (14). Transforming growth factor (TGF)β is a critical mediator of organ fibrosis and has been repeatedly validated as a molecular target in disease (15). However, in renal fibrosis only few studies assessed glomerular filtration rate (GFR), a clinically relevant marker of renal excretory function, as an endpoint in studies with interventions modeling renal fibrogenesis.

We hypothesized that anti-TGFβ IgG may not only inhibit interstitial fibrosis but also influence the crystallization of CaOx inside the kidney, which both should synergize to prevent nephrocalcinosis-related GFR decline, i.e., CKD progression. To address this concept, we employed a mouse model of progressive CaOx crystal-driven CKD (13) with preemptive or delayed anti-TGFβ IgG treatment (16, 17).

MATERIALS AND METHODS

Animal Studies

Eight-week old male C57BL/6N mice were obtained from Charles River Laboratories (Sulzfeld, Germany). Mice were housed in groups of five in filter-top cages and had access to food and water *ad libitum*. Cages, nest lets, food, and water were sterilized by autoclaving before use. Oxalate-rich diet was prepared by adding 50 µmol/g sodium oxalate to a calcium-free standard diet (Ssniff, Soest, Germany) as previously described (13, 18). Mice were split into four groups ($n = 5$ mice per group): the first group received a control diet without sodium oxalate (control), the second group was injected intraperitoneally (i.p.) with the murine control IgG1 monoclonal antibody (isotype-matched control 13C4 antibody), the third group with the murine IgG1 monoclonal anti-TGFβ antibody that neutralizes all three TGFβ isoforms (1D11, both antibodies kindly provided by Genzyme Corporation, Sanofi, Framingham, MA, USA) 1 day after starting the oxalate-rich diet every alternate day [1.5 mg/kg body weight (BW), total of seven injections] (16, 19), and the fourth group received an oxalate-rich diet only (oxalate only). Serum and urine samples were collected as well as GFR measured from all experimental and control groups on day 0 and before sacrifice by cervical dislocation on day 7 or 14. Urine samples were acidified immediately after collection for oxalic acid estimations. Kidneys were harvested after sacrifice. One kidney was used for flow cytometry analysis and the other was divided into two equal parts. One part was kept in RNA later solution at −80°C for RNA isolation and the second part was kept in 4% formalin to be embedded in paraffin for histology analysis.

For delayed IgG1 or anti-TGFβ antibody treatment, all mice were put on a control diet ($n = 5$) or an oxalate-rich diet ($n = 5$) and two groups of mice received additionally either the control IgG1 antibody (i.p., 1.5 mg/kg BW, $n = 5$) or the anti-TGFβ antibody (i.p., 1.5 mg/kg BW, $n = 5$) four times starting from day 7 every alternate day until sacrifice on day 14 (Figure S1 in Supplementary Material).

Assessment of Kidney Injury

Kidney sections of 2 µm were stained with Pizzolato to visualize CaOx crystal deposition, which was quantified (% area) using ImageJ software as described previously (20). Periodic acid-Schiff (PAS) reagent was used to assess kidney injury, which was scored by assessing the percentage of atrophic tubules. CD3+ T cells and F4/80+ macrophages (both Serotec, Kidlington, UK) were identified by immunostaining. Fibrotic areas were identified by immunostaining for silver and α-smooth muscle actin (α-SMA) (Dako GmbH, Hamburg, Germany). Quantification of immunostaining (% area) was done using ImageJ software. An observer blinded to the experimental condition performed all assessments. Serum blood urea nitrogen (BUN) (DiaSys, Holzheim, Germany), serum and urine oxalic acid (oxalate) (Libios, Pontcharra-sur-Turdine, France), and urine calcium (Sigma-Aldrich, Taufkirchen, Germany) were measured using commercially available kits as per manufacturer's protocol.

Transcutaneous GFR Assessment and Calculation

Glomerular filtration rate measurements were performed in conscious mice on day 0, 7, and 14 ($n = 5$ per group). Briefly, mice were anesthetized with isoflurane to mount a miniaturized imager device built from two light-emitting diodes, a photodiode, and a battery (MediBeacon™ Inc., Mannheim, Germany) onto the shaved neck of the animals (21). The background signal of the skin was recorded for 5 min. Then, mice received a single injection of FITC-sinistrin (i.v., 150 mg/kg BW) (MediBeacon™

Inc., Mannheim, Germany). Each mouse was kept in a single cage and the signal was recorded for 90 min. Data were analyzed using the imaging device MPD Studio software (MediBeacon™ Inc., Mannheim, Germany). GFR (μl/min/100 g BW) was calculated from the decrease of fluorescence intensity of FITC-sinistrin over time using the three-compartment model with linear correction (injection, plasma, and interstitial compartment, $t1/2$ of FITC-sinistrin), BW of mouse, and an empirical conversion factor as per manufacturer's protocol (21, 22). The slope of daily GFR loss (m) was determined with the linear equation using Microsoft Excel

$$\mathrm{GFR}\left[\mu\mathrm{L/min/100\,g\ BW}\right]=\frac{14{,}616.8\ [\mu\mathrm{L\ per\ 100\,g\ BW}]}{t\frac{1}{2}(\mathrm{FITC-sinistrin})\ [\mathrm{minute}]}.$$

CaOx Crystal Formation *In Vitro*

The formation of CaOx crystals *in vitro* has previously been described in more detail (7). Briefly, 50 μl of a $Na_2C_2O_4$ solution (oxalate, 0.1 mM, pH 7.3) was mixed with 50 μl $CaCl_2$ solution (0.1 mM, pH 7.3) in a 96-well plate at room temperature (RT) for 5 min (CaOx only). To investigate the effect of the IgG1 or anti-TGFβ antibody on CaOx crystal formation, $Na_2C_2O_4$ solution was pre-incubated with or without the IgG1 or anti-TGFβ antibody (0.2 μg/ml) or an IgG F(ab′)2 fragment antibody (0.2 μg/ml) for 1 h at RT prior to addition of $CaCl_2$ buffer (CaOx + IgG1). Different forms of CaOx crystals [CaOx monohydrate (COM) and CaOx dihydrate (COD)] were visualized under a Leica microscopy and quantified using flow cytometry (BD FACSCalibur, Becton Dickinson, NJ, USA).

RNA Preparation and Real-Time Quantitative PCR

The RNA extraction kit from Qiagen (Düsseldorf, Germany) was used to isolate total RNA from kidneys ($n = 5$ per group) following the manufacturer's instructions. RNA quality was assessed using agarose gels before being transcribed into cDNA using reverse transcriptase (Superscript II) (Invitrogen, Carlsbad, CA, USA). Real-time RT-PCR was performed using SYBRGreen PCR master mix and analyzed with a Light Cycler 480 (Roche, Mannheim, Germany). All gene expression values were normalized using 18s rRNA as a housekeeping gene. All primers used for amplification were purchased from Metabion (Martinsried, Germany) and are listed in **Table 1**.

TABLE 1 | Murine primer sequences.

Target	Primer sequences
KIM-1	Forward 5′-TCAGCTCGGGAATGCACAA-3′ Reverse 5′-TGGTTGCCTTCCGTGTCTCT-3′
TIMP-2	Forward 5′-CAGACGTAGTGATCAGAGCCAAA-3′ Reverse 5′-ACTCGATGTCTTTGTCAGGTCC-3′
IL-6	Forward 5′-TGATGCACTTGCAGAAAACA-3′ Reverse 5′-ACCAGAGGAAATTTTCAATAGGC-3′
TNFα	Forward 5′-CCACCACGCTCTTCTGTCTAC-3′ Reverse 5′-AGGGTCTGGGCCATAGAACT-3′
ACOX1	Forward 5′-CTTGGATGGTAGTCCGGAGA-3′ Reverse 5′-TGGCTTCGAGTGAGGAAGTT-3′
PGC1α	Forward 5′-AGTCCCATACACAACCGCAG-3′ Reverse 5′-CCCTTGGGGTCATTTGGTGA-3′
PPARα	Forward 5′-TGCAAACTTGGACTTGAACG-3′ Reverse 5′-GATCAGCATCCCGTCTTTGT-3′
TGFβ1	Forward 5′-CAACCCAGGTCCTTCCTAAA-3′ Reverse 5′-GGAGAGCCCTGGATACCAAC-3′
TGFβR1	Forward 5′-GCTCCTCATCGTGTTGGTG-3′ Reverse 5′-CAGTGACTGAGACAAAGCAAAGA-3′
TGFβ2	Forward 5′-CCGCATCTCCTGCTAATGTTG-3′ Reverse 5′-AATAGGCGGCATCCAAAGC-3′
TGFβR2	Forward 5′-GCTGCATATCGTCCTGTGG-3′ Reverse 5′-TCACATCGCAAAACTTGCAC-3′
Collagen1α1	Forward 5′-ACATGTTCAGCTTTGTGGACC-3′ Reverse 5′-TAGGCCATTGTGTATGCAGC-3′
Fibronectin-1	Forward 5′-GGAGTGGCACTGTCAACCTC-3′ Reverse 5′-ACTGGATGGGGTGGGAAT-3′
iNOS	Forward 5′-GAGACAGGGAAGTCTGAAGCAC-3′ Reverse 5′-CCAGCAGTAGTTGCTCCTCTTC-3′
18s RNA	Forward 5′-GCAATTATTCCCCATGAACG-3′ Reverse 5′-AGGGCCTCACTAAACCATCC-3′

Flow Cytometry Analysis

Kidneys were harvested from mice and then digested in digestion buffer (collagenase/DNase1 solution) for 40 min at 37°C. Digested tissue was passed through a 70 μm filter and washed with cold PBS. For isolating leukocytes, a Nycodenz solution (Axis-Shield, Oslo, Norway) was used to separate CaOx crystals and tissue from renal immune cells. Single cell suspensions were then washed with wash buffer (0.1% BSA, 0.01% sodium azide in PBS) and FcR blocked with anti-mouse CD16/32 (2.4G2) for 5 min. After blocking, cells were stained with the surface antibodies PE/Cy5 anti-mouse CD45 (BioLegend, Fell, Germany), V450 anti-mouse CD11b (BioLegend, Fell, Germany), APC anti-mouse F4/80 (BioRad, München, Germany), FITC anti-mouse CD206 (BD Biosciences, Germany), and PE anti-mouse Cx3CR1 (BD Biosciences, Heidelberg, Germany) for 30 min at 4°C in the dark. Following incubation, cells were washed, centrifuged, and GolgiPlug added for 15 min to avoid release of intracellular cytokines. Cells were then washed, resuspended in cell fixation/permeabilization buffer for an additional 15 min and washed in perm wash buffer. Intracellular antibody for PE/Cy7 anti-mouse TGFβ1 was added to the cell suspension for 40 min at 4°C. After incubation, cells were washed with PBS and reconstituted in 1 ml fresh wash buffer. Flow cytometry analysis was performed using the BD FACSCanto II (Becton Dickinson, NJ, USA) and data analyzed with the software FlowJo 8.7 (Tree Star Inc., Ashland, OR, USA). For determining the absolute number of cells/microlitre, Invitrogen AccuCheck counting beads (Thermo Fisher Scientific, PCB100, Langenselbold, Germany) were used and the absolute cell counts calculated according to manufacturer's instruction.

Magnetic Resonance Imaging (MRI)

Kidneys from IgG1- and anti-TGFβ-treated mice with nephrocalcinosis on day 14 ($n = 4$ each group) were harvested and processed in 1.5% agarose gel, and placed in a whole body coil for mice (Bruker BioSpin, Ettlingen, Germany) of a dedicated

small animal ultra-high-field magnetic resonance tomograph scanner (ClinScan 7 T, Bruker BioSpin, Ettlingen, Germany). Standard sequences for morphology and mapping of T1 and T2 relaxation times (Siemens, Erlangen, Germany) were performed on kidneys in sagittal orientation. By mapping of relaxation times, specific magnetic properties of tissues are quantified. An increase of T1 relaxation time is associated with fibrosis, while prolonged T2 relaxation times are found in inflammation (13). For post-processing of images, three regions of interest were placed in the cortex, outer and inner medulla, respectively, to determine T1 and T2 relaxation times (Osirix, Bernex, Switzerland, open-source software).

Microscale Thermophoresis

MST was used to characterize binding affinity between IgG1 and soluble sodium oxalate. Soluble oxalate at various concentrations (1 nM–5 mM) and IgG1 (250 nM) were incubated for 1 h at RT. Measurements were performed with the Monolith NT.LabelFree MST device using standard capillaries (NanoTemper Technologies, Munich, Germany). Buffer only, soluble sodium oxalate or IgG1 only were used as controls. Measurements were performed at 25°C in 67 mM $NaPO_4$ buffer, 150 mM NaCl, and 0.05% Tween 20 at pH 7.4. The infrared laser power was between 20 and 40%, and 40–70% LED power was used. A laser on time of 30 s and a laser off time of 5 s were used. Data from the binding assays were analyzed using Nanotemper analysis.

Statistical Analysis

Statistical analysis was carried out using Student's *t*-test, two-way ANOVA with Bonferroni's correction, or one-way ANOVA with Tukey's comparison and performed using GraphPad Prism5.0 Software. Data are presented as mean ± SEM. Significance was considered to be attained at a value of $p < 0.05$, ns indicates not significant.

RESULTS

IgG1 Influences CaOx Crystal Formation Without Binding to Soluble Oxalate *In Vitro*

Calcium oxalate can crystallize in three different hydrate forms: COM, COD, and CaOx trihydrate crystals (7). Among these, COM crystals are the most common form of CaOx crystals present in urinary calculi in humans compared to COD crystals (23, 24). To investigate whether a monoclonal anti-TGFβ IgG antibody can directly influence CaOx crystal formation, we pre-incubated $Na_2C_2O_4$ (sodium oxalate) with the anti-TGFβ IgG or the control IgG1 antibody followed by addition of $CaCl_2$ (calcium chloride) to form CaOx crystals *in vitro*. Light microscopy revealed that COM crystals were predominantly formed whereas in the presence of anti-TGFβ or IgG1 the number of CaOx crystals decreased compared to CaOx only ($Na_2C_2O_4$ + $CaCl_2$ only) (**Figure 1A**). Using flow cytometry analysis, we identified small and big COM crystals as well as COD crystals depending on their size (side scatter vs. forward scatter), which in numbers significantly decreased upon pre-incubation with the anti-TGFβ or IgG1 antibody compared to CaOx crystals only (**Figure 1B**). Pre-incubated of sodium oxalate with only an IgG F(ab′)2 fragment prior to addition of calcium chloride revealed that the number of small and big COM crystals as well as COD crystals significantly decreased compared to CaOx alone (**Figure 1B**, white bars). However, no difference in the CaOx crystal formation was observed between pre-incubation with the anti-TGFβ or IgG1 antibody and the IgG F(ab′)2 fragment (**Figure 1B**). To rule out the possibility that IgG1 could interfere with soluble oxalate, we used microscale thermophoresis, a sensitive method that enables the quantitative analysis of molecular interactions in solution based on the movement of molecules along temperature gradients (25–27). Incubation of soluble oxalate with IgG1 revealed that soluble oxalate did not bind to IgG1 (data not shown). These findings indicate that IgG antibodies and even only the IgG F(ab′)2 fragment can directly affect CaOx crystal formation *in vitro*.

IgG1 Antibody Treatment Ameliorates Renal Outcome in Chronic Oxalate Nephropathy *In Vivo*

To investigate whether the effect of anti-TGFβ IgG antibody treatment on CaOx crystal formation also applies *in vivo*, we used a previously characterized mouse model of CaOx crystal-induced nephropathy (13). Feeding mice a high-oxalate diet resulted in the deposition of CaOx crystals in the cortex, as well as the outer and inner medulla compared to mice receiving the control diet, as illustrated by the % area of CaOx crystal deposition in **Figure 2A** (red bars). Early administration of hyperoxaluric mice with the anti-TGFβ (oxalate + anti-TGFβ) or control IgG1 antibody (oxalate + IgG1) significantly reduced intrarenal CaOx crystal deposits compared to untreated mice with nephrocalcinosis (oxalate only) after 14 days (**Figure 2A**). Serum as well as urinary oxalate levels significantly increased following oxalate feeding, whereas antibody treatment significantly reduced oxaluria in mice with nephrocalcinosis (Figure S1 in Supplementary Material). Urinary calcium levels rather declined upon feeding a calcium-depleted diet without being affected by antibody treatment (Figure S1 in Supplementary Material). Water intake was 0.2 ml/g BW in the control group ($n = 5$ per cage) and 0.29 ml/g BW in the oxalate only group ($n = 5$ per cage) on day 14 (data not shown).

Preemptive anti-TGFβ and IgG1 antibody treatment improved renal function, as indicated by decreased serum BUN levels (**Figure 2B**) compared to animals receiving a high-oxalate diet only after 14 days. This data was in line with progressive tubular atrophy and dilation in mice with nephrocalcinosis (oxalate only), which significantly decreased following preemptive administration of the antibodies, as indicated by PAS staining (**Figure 2C**) and intrarenal mRNA expression levels of the kidney injury marker-1 and tissue inhibitor of metalloproteinase-2 (**Figure 2D**). We did not observe any differences in the above measured parameters between the oxalate only and the antibody-treated groups on day 7 (data not shown). The data indicate that anti-TGFβ IgG prevents mice from CaOx crystal-induced nephropathy by influencing CaOx crystal formation.

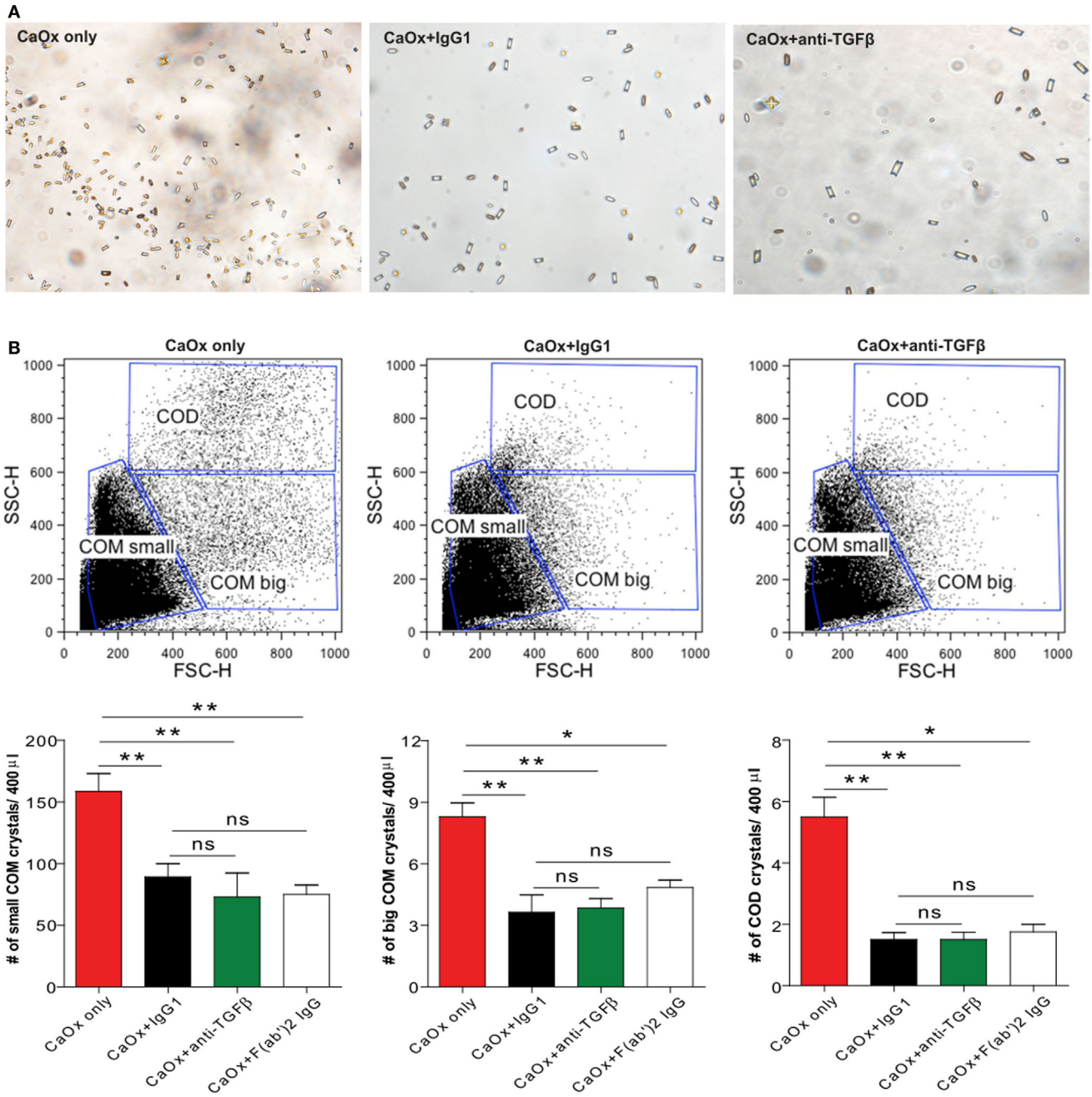

FIGURE 1 | IgG1 affects calcium oxalate (CaOx) crystal formation *in vitro*. $Na_2C_2O_4$ (oxalate) solution was pre-incubated with or without the control IgG1 (CaOx + IgG1) or anti-transforming growth factor (TGF)β IgG antibody (CaOx + anti-TGFβ) or an IgG F(ab′)2 fragment antibody [CaOx + F(ab′)2 IgG] for 1 h at room temperature and then $CaCl_2$ solution added. After 5 min, CaOx monohydrate (COM) and CaOx dihydrate (COD) crystals were formed and visualized under the light microscope **(A)**. Quantification of COM and COD crystals by size (forward scatter vs. sideward scatter) using flow cytometry analysis **(B)**. Data are mean ± SEM ($n = 5$). $^*p < 0.05$, $^{**}p < 0.01$ are considered significant.

The Dual Effect of Anti-TGFβ IgG Attenuates CaOx Crystal-Related Tissue Inflammation

Given the potential of CaOx crystals to induce tubular atrophy, we next looked at the effect of anti-TGFβ IgG antibody therapy on the inflammatory response. As shown in **Figure 3A**, expression profiling of the inflammatory mediators interleukin 6 and tumor necrosis factor α showed a significant increase in the mRNA levels in mice with nephrocalcinosis (oxalate only) compared to the control group on day 14 (**Figure 3A**). This inflammatory response was significantly reduced in IgG1 antibody-treated mice and even further in mice treated with anti-TGFβ IgG (**Figure 3A**).

Nephrocalcinosis-related progressive CKD is associated with increasing infiltration of immune cells, e.g., macrophages into the renal interstitial compartment (13, 28). Using immunostaining of kidney sections, we observed that anti-TGFβ and IgG1 antibody treatment reduced the number of intrarenal CD3+ T cells and F4/80+ macrophages compared to mice with nephrocalcinosis (**Figure 3B**).

In a recent study, alterations in the energy metabolism including fatty acid oxidation have been observed in kidneys from human subjects with CKD and in mouse models of kidney fibrosis (29). They also found that high levels of TGFβ during renal fibrosis play an important role in inhibiting fatty acid oxidation and thereby aggravating disease progression (29). We, therefore, examined the effect of anti-TGFβ treatment on the fatty acid metabolism. Intrarenal mRNA expression profiling revealed that peroxisome proliferator-activated receptor gamma coactivator 1 alpha, peroxisome proliferator-activated receptor alpha, and peroxisomal acyl-coenzyme A oxidase 1 were reduced in mice with nephrocalcinosis (oxalate only, red bars) (**Figure 3C**). Interestingly, anti-TGFβ treatment restored the renal energy metabolism compared to the oxalate only group (**Figure 3C**). We confirmed that neutralizing TGFβ *in vivo* inhibited TGFβ signaling as indicated by decreased intrarenal mRNA expression of TGFβ1 and TGFβ2 as well as the receptors TGFβR1 and TGFβR2 (**Figure 3D**). Together, the data indicate that anti-TGFβ IgG treatment prevents mice from CaOx crystal-induced inflammation but increased fatty acid oxidation.

The Dual Effect of Anti-TGFβ IgG Reduces the Number of Pro-Inflammatory Macrophages

Different macrophage phenotypes are associated with either the resolution of inflammation and tissue regeneration or persistent injury and progression to tissue atrophy, whereby their heterogeneity is determined by the microenvironment (30–32). We, therefore, carried out flow cytometry analysis to understand the diversity of phenotypes among the infiltrating macrophages.

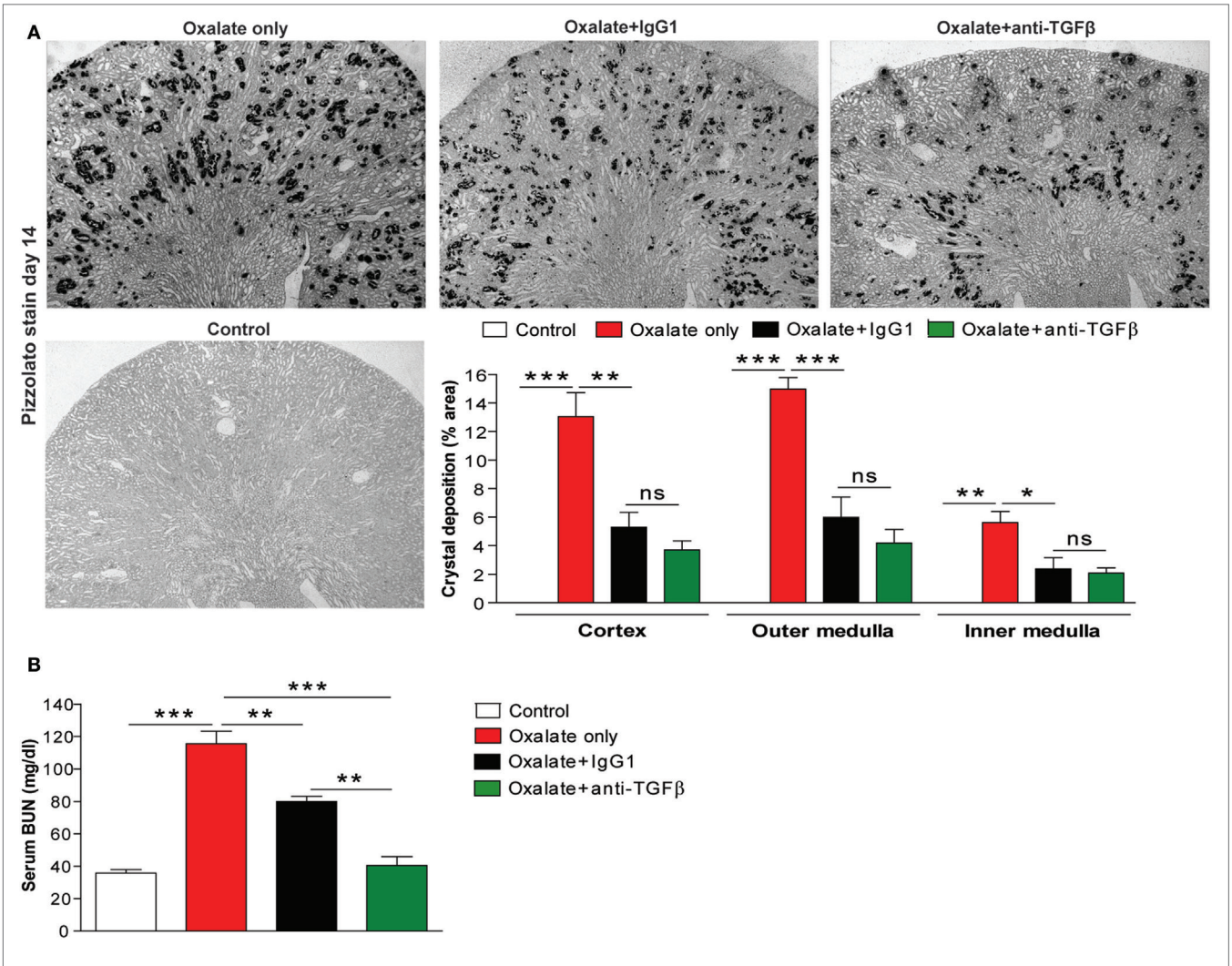

FIGURE 2 | Continued

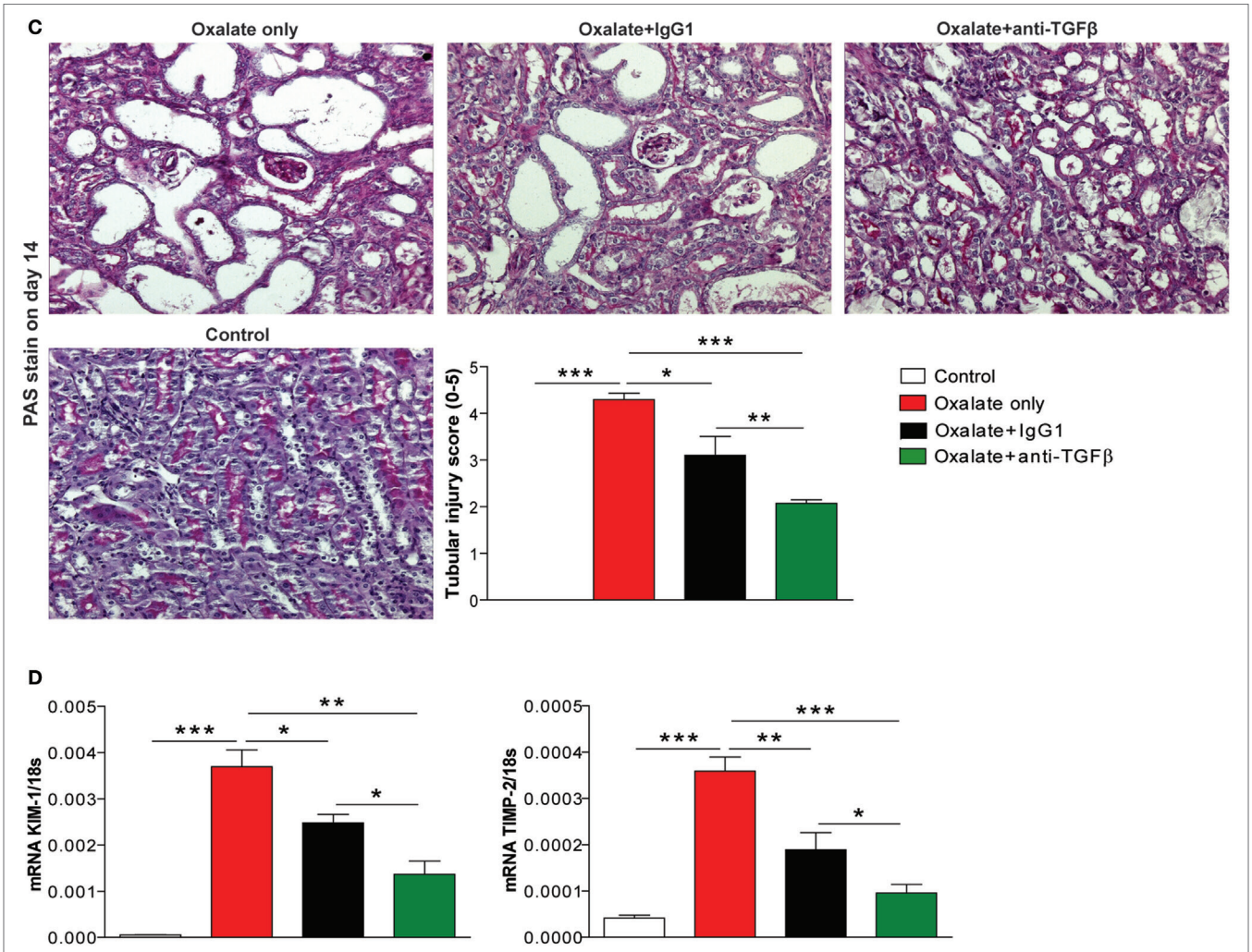

FIGURE 2 | IgG antibody treatment improves renal outcome in CaOx crystal-induced injury *in vivo*. **(A)** Mice were either fed an oxalate-rich diet for 14 days (oxalate only) or were additionally injected with an IgG1 (oxalate + IgG1) or anti-transforming growth factor (TGF)β IgG antibody (oxalate + anti-TGFβ) or fed a control diet (control) (total 7 i.p. injections). **(A)** Quantification of CaOx crystal deposition (% area) in cortex, outer and inner medulla of Pizzolato stained kidney sections from the four groups on day 14. **(B)** Renal functional parameter serum blood urea nitrogen (BUN) levels on day 14. **(C)** Periodic acid-Schiff (PAS) staining illustrating tubular injury (original magnification 20×) and quantification of the tubular injury score. **(D)** Intrarenal mRNA expression of the kidney injury marker (KIM)-1 and tissue inhibitor of metalloproteinase (TIMP)-2. Data are mean ± SEM from five mice per group out of two independent experiments. ns, not significant. $^{*}p < 0.05$, $^{**}p < 0.01$, $^{***}p < 0.001$ are considered significant.

We noted that nephrocalcinosis is associated with increased numbers of CD45+ leukocytes in IgG1-treated mice compared to the control group (**Figures 4A,B**). However, anti-TGFβ IgG treatment significantly reduced the number of CD45+ leukocytes in mice with nephrocalcinosis (**Figure 4B**). The infiltrating macrophages were identified as CD45+ F4/80+ CD11b+ (**Figure 4B**). Phenotype analysis of macrophages revealed that these were pro-inflammatory (M1-like) macrophages (CD45+ F4/80+ CD11b+ CX3CR1+ CD206−) and M2-like macrophages (CD45+ F4/80+ CD11b+ CX3CR1+ CD206+) (**Figure 4A**) (30). Upon anti-TGFβ antibody treatment, the number of renal pro-inflammatory macrophages was significantly reduced compared to IgG1-treated or untreated mice with nephrocalcinosis (**Figure 4C**), which was consistent with less intrarenal mRNA expression of inducible nitric oxide synthase (iNOS), a mediator of inflammatory responses (**Figure 4D**). This indicates that anti-TGFβ treatment reduces the number of pro-inflammatory (M1-like) macrophages during nephrocalcinosis.

The Dual Effect of Anti-TGFβ IgG Suppresses Nephrocalcinosis-Related Interstitial Fibrosis

Progressive nephrocalcinosis is associated with diffuse interstitial fibrosis, a process widely thought to contribute to CKD worsening (13, 33). We next investigated the impact of anti-TGFβ antibody treatment on interstitial fibrosis during chronic CaOx crystal-induced nephropathy. Immunohistochemistry staining

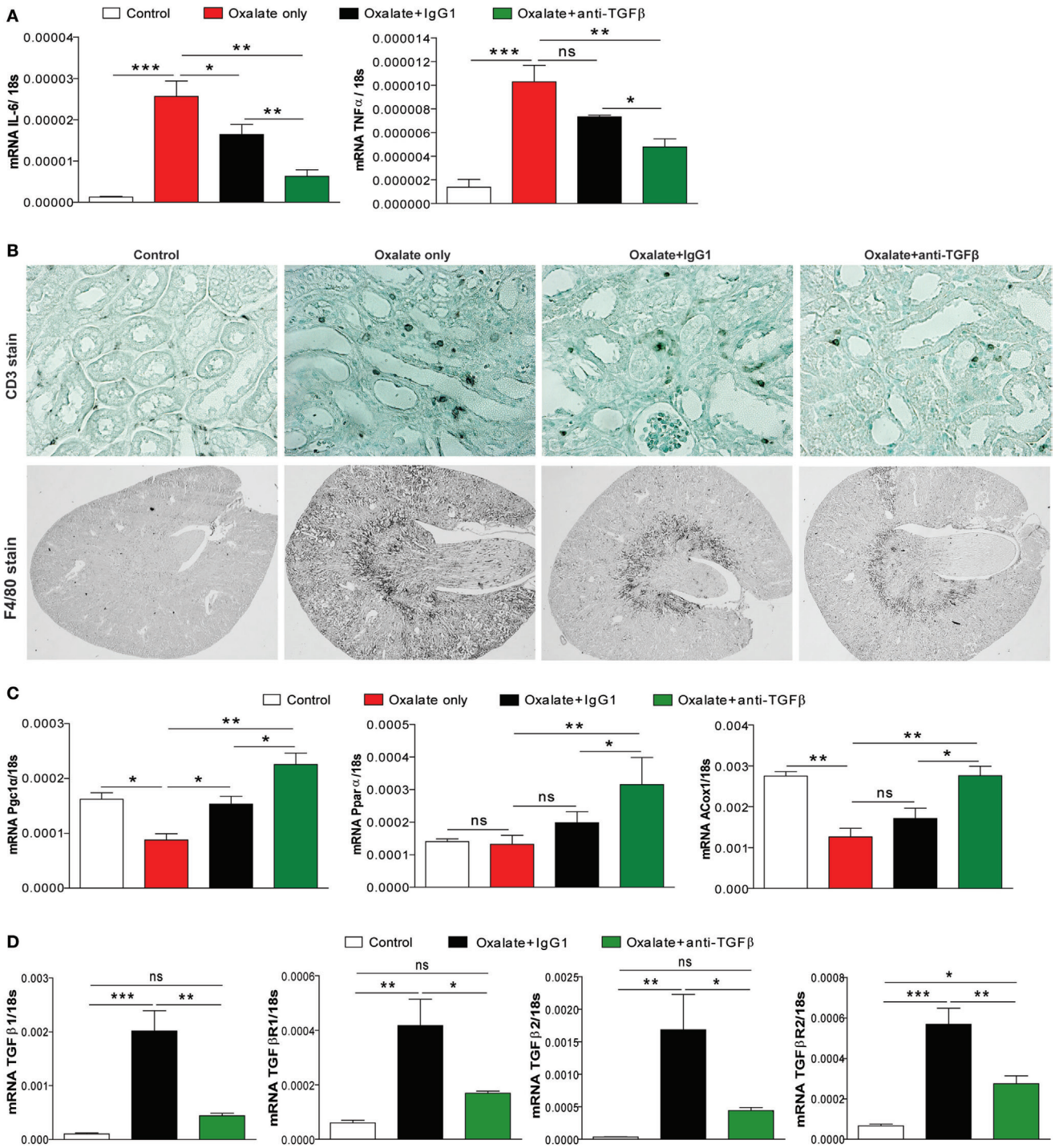

FIGURE 3 | Anti-transforming growth factor (TGF)β IgG treatment ameliorates renal inflammation in chronic oxalate nephropathy. C57BL/6N mice were either fed an oxalate-rich diet for 14 days (oxalate only) or were additionally injected with an IgG1 (oxalate + IgG1) or anti-TGFβ antibody (oxalate + anti-TGFβ) or fed a control diet (control) (total 7 i.p. injections). **(A)** Intrarenal mRNA expression of the inflammatory cytokines interleukin (IL)-6 and tumor necrosis factor (TNF)α. **(B)** Immunostaining illustrating infiltrating CD3+ T cells and F4/80+ macrophages on kidney sections. **(C,D)** Intrarenal mRNA of the fatty acid enzymes peroxisome proliferator-activated receptor gamma coactivator 1 alpha (PGC1α), peroxisome proliferator-activated receptor alpha (PPARα), and peroxisomal acyl-coenzyme A oxidase 1 (ACOX1) **(C)**, and of the TGFβ signaling-related genes TGFβ1 and TGFβ2 as well as the receptors TGFβR1 and TGFβR2 **(D)** was performed on kidney RNA isolates. Data are mean ± SEM from five mice per group out of two independent experiments. ns, not significant. $^{*}p < 0.05$, $^{**}p < 0.01$, $^{***}p < 0.001$ are considered significant.

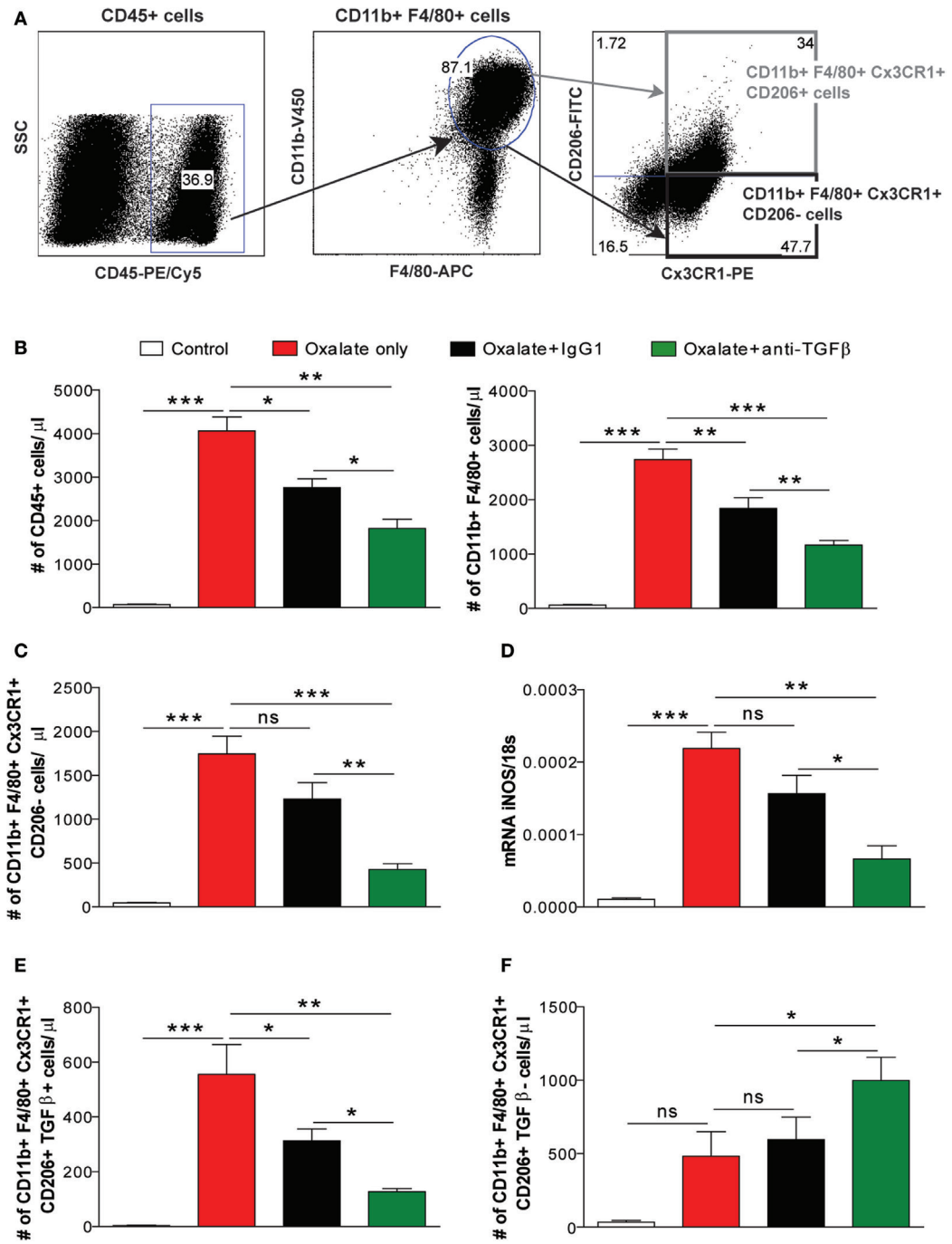

FIGURE 4 | Treatment with the anti-transforming growth factor (TGF)β IgG antibody decreases nephrocalcinosis-related macrophage infiltrates. C57BL/6N mice were either fed a control diet, a high-oxalate diet only or combined with IgG1 or anti-TGFβ antibody treatment for 14 days. **(A,B)** Flow cytometric analysis of infiltrating CD45+ leukocytes and gating strategy of CD45+ F4/80+ CD11b+ macrophages in kidneys with absolute numbers. **(C)** Renal infiltrating macrophages identified as pro-inflammatory (M1-like) (CD45+ F4/80+ CD11b+ CX3CR1+ CD206–) macrophages with absolute cell numbers. **(D)** mRNA expression of inducible nitric oxide synthase (iNOS) was performed on kidney RNA isolates. **(E,F)** Absolute cell numbers of pro-fibrotic (M2a-like) macrophages (CD45+ F4/80+ CD11b+ CX3CR1+ CD206+ TGFβ+) **(E)** and anti-inflammatory (M2c-like) macrophages (CD45+ F4/80+ CD11b+ CX3CR1+ CD206+ TGFβ–) **(F)** in the kidneys. Data are mean ± SEM from six to seven mice per group out of two independent experiments. ns, not significant. $^{*}p < 0.05$, $^{**}p < 0.01$, $^{***}p < 0.001$ are considered significant.

of kidney sections for silver and αSMA revealed an increase of fibrotic lesions in mice with nephrocalcinosis as demonstrated by % area (**Figures 5A,B**). Following anti-TGFβ or IgG1 antibody treatment, however, we observed significantly less fibrosis (**Figures 5A,B**), which was in line with decreased intrarenal mRNA expression levels of the fibrosis marker collagen-1α1 and

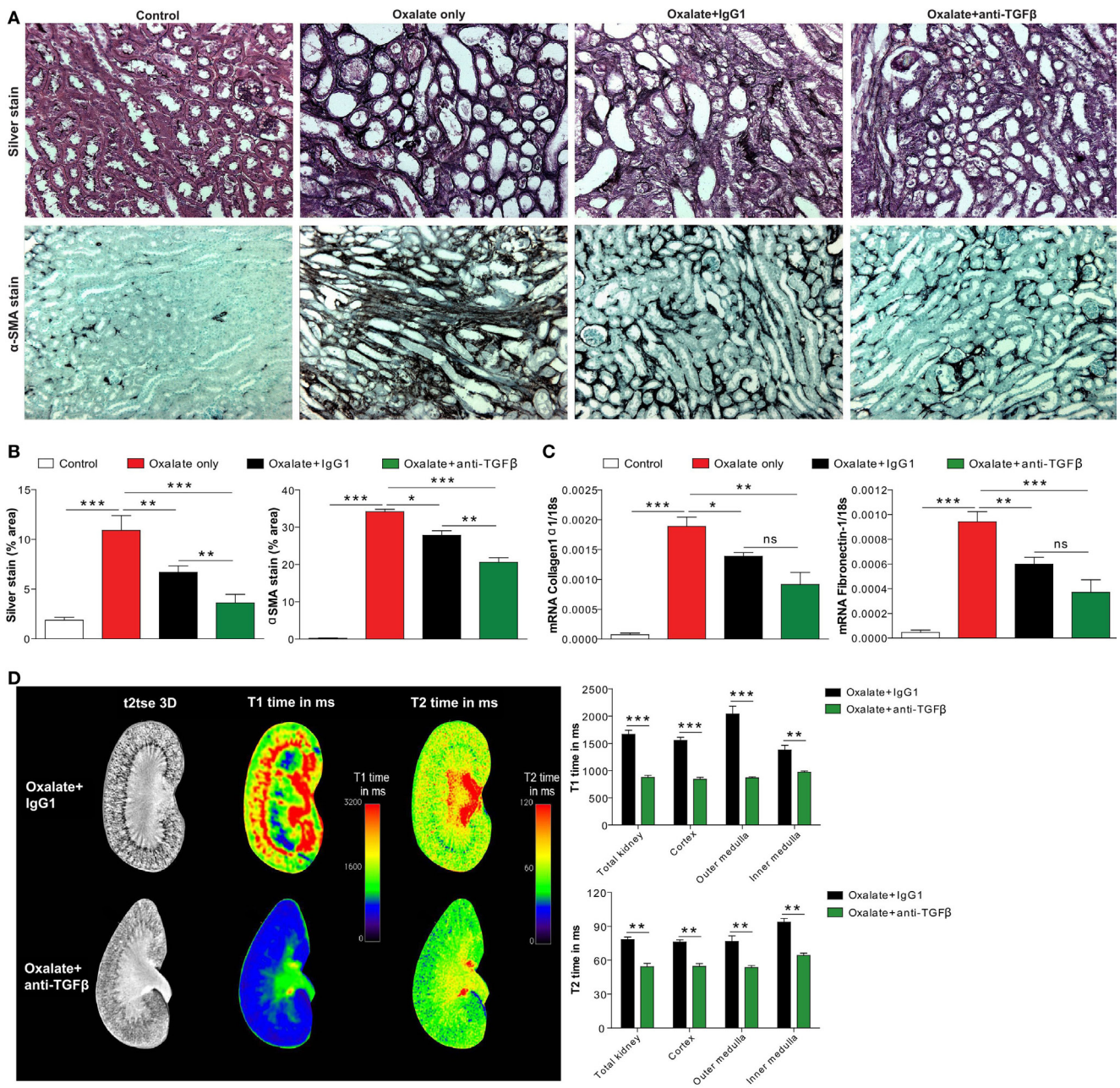

FIGURE 5 | Neutralizing transforming growth factor (TGF)β inhibits nephrocalcinosis-related fibrosis. C57BL/6N mice were fed a high-oxalate diet only or in combination with preemptive IgG1 or anti-TGFβ antibody treatment for 14 days. **(A,B)** Immunohistochemistry images **(A)** and quantification of silver and alpha smooth muscle actin (αSMA) staining **(B)** was performed on kidney sections. **(C)** mRNA expression of collagen1α1 and fibronectin-1 was performed on kidney RNA isolates. **(D)** Magnetic resonance imaging of kidneys of IgG1 or anti-TGFβ antibody-treated mice with nephrocalcinosis. Representative images and quantification of T1 and T2 relaxation interval time showed significant differences in inflammation and fibrosis between the two groups. Data are mean ± SEM from five mice in each group. ns, not significant. *$p < 0.05$, **$p < 0.01$, ***$p < 0.001$ are considered significant.

fibronectin-1 in the anti-TGFβ antibody treatment compared to the oxalate only group (**Figure 5C**). Further flow cytometry analysis showed that the number of pro-fibrotic (M2a-like) macrophages (CD45+ F4/80+ CD11b+ CX3CR1+ CD206+ TGFβ+) (34) significantly decreased (**Figure 4E**), whereas the number of anti-inflammatory (M2c-like) macrophages (CD45+ F4/80+ CD11b+ CX3CR1+ CD206+ TGFβ−) increased (**Figure 4F**) upon anti-TGFβ treatment in mice with nephrocalcinosis. In addition, we performed MRI of kidneys from mice with nephrocalcinosis. Compared to mice given the IgG1 antibody, animals receiving the anti-TGFβ antibody displayed a significant decrease in T1 and T2 time interval in the MRI analysis, suggesting less

renal inflammation and fibrosis following TGFβ neutralization in mice with nephrocalcinosis (**Figure 5D**). Together, inhibiting fibrosis attenuates nephrocalcinosis-related CKD in association with a shift from pro-inflammatory (M1-like) and pro-fibrotic (M2a-like) macrophages toward an anti-inflammatory (M2c-like) macrophage phenotype.

Preemptive but Not Delayed-Onset Inhibition of TGFβ-Mediated Interstitial Fibrosis Prevents Progressive GFR Decline

To study the impact of less interstitial fibrosis on progressive GFR decline, we repetitively measured GFR in mice on oxalate diet (day 0 and 14) or control diet (day 14). The GFR measurement process relies on a percutaneous acquisition of the clearance kinetics of a fluorescent signal emitted by the fluorescent tracer FITC-sinistrin upon bolus injection, a diagnostic tool in rodents (13, 35) and humans (36). We used a three-compartment kinetic model with linear correction to determine the GFR in mice. This model covers the injection process, the plasma volume, and the interstitial compartment allowing further refinement by correcting for shifts observed occasionally during measurements (37). After injecting FITC-sinistrin into a mouse that was fed a control diet (control) for 14 days, the fluorescent signal quickly increased at the beginning and descends down to the initial baseline level as it gets filtered by the kidneys after approximately 90 min. An example is illustrated in **Figure 6A**. The fluorescent signal of FITC-sinistrin was automatically recorded and the half-life ($t1/2$) determined (curve fitting 40% after peak signal, green dotted line) for calculating the GFR (21). Feeding mice an oxalate-rich diet resulted in an impaired renal clearance of FITC-sinistrin as indicated by the higher fluorescence intensity after 90 min (**Figure 6B**) compared to the FITC-sinistrin signal from a healthy mouse (**Figure 6A**). However, preemptive anti-TGFβ IgG therapy resulted in a decrease in the fluorescence intensity of FITC-sinistrin of mice with nephrocalcinosis after 90 min (**Figure 6D**) compared to an IgG1-treated mouse with nephrocalcinosis (**Figure 6C**).

Next, we calculated the three effect sizes: (1) the slope of daily GFR decline, (2) the GFR at the end of the study, and (3) the end stage renal disease (ESRD)-free renal survival. As illustrated in **Figure 6E**, the daily GFR loss was calculated using the linear equation (solid lines) between baseline (day 0) and day 14 indicating the slope (m) of the linear lines. Using this linear equation, we extended these lines (dotted lines) up to when they reached the GFR cut off of 15 µl/min/100 g BW, which we defined as ESRD (gray range). We found that the slope of daily GFR loss was $m = -15.6$ in mice with nephrocalcinosis (oxalate only, table and red line) compared to IgG1 treatment ($m = -14.5$) (**Figure 6E**, table and black line). However, preemptive TGFβ inhibition decreased the slope by $\Delta = 38.3\%$ ($m = -8.9$) (**Figure 6E**, table and green line). At the end of the study on day 14, we observed a significant difference in the GFR in the IgG1-treated mice with an increase from 19.9 to 42.6 µl/min/100 g BW ($\Delta = 53.2\%$, $p = 0.04$) compared to oxalate-fed mice only (**Figure 6E**, table). This beneficial effect on the GFR on day 14 was further improved by treating mice with the anti-TGFβ IgG antibody (42.6–120.4 µl/min/100 g BW) ($\Delta = 64.6\%$, $p = 0.0007$) compared to IgG1-treated mice with nephrocalcinosis (**Figure 6E**, table). Assuming a linear GFR decline in the future, IgG1 treatment extended the ESRD-free renal survival compared to untreated mice with nephrocalcinosis by 2 days ($\Delta = 12.5\%$, black dotted line). Anti-TGFβ IgG therapy on the other hand prolonged the ESRD-free renal survival time even up to 10 days ($\Delta = 38.5\%$, green dotted line) compared to IgG1-treated mice.

In a clinical setting, anti-fibrotic treatments might be mainly considered upon detecting renal fibrosis in a diagnostic kidney biopsy but the window-of-opportunity for targeting renal fibrosis in CKD is unknown. Therefore, we explored the capacity of a delayed anti-TGFβ IgG treatment to improve GFR in mice with nephrocalcinosis by initiating anti-TGFβ or control IgG1 therapy from day 7, a time point when some tubular atrophy had already established (Figure S2 in Supplementary Material). Assessing the renal excretory function, we observed no protective effect of TGFβ inhibition with any of the aforementioned parameters (Figure S2 in Supplementary Material). Together, the data show that preemptive inhibition of TGFβ-driven interstitial fibrosis significantly preserves GFR decline and increased the ESRD-free renal survival of mice with progressive nephrocalcinosis-related CKD. However, delayed onset of TGFβ inhibition does no longer attenuate renal function decline or expand the ESRD-free renal survival.

DISCUSSION

We hypothesized that anti-TGFβ IgG antibody treatment may not only inhibit interstitial fibrosis but also influence the crystallization of CaOx inside the kidney, which both should synergize to prevent nephrocalcinosis-related GFR decline. We now show that the anti-TGFβ IgG antibody has a dual role by influencing the crystallization process of CaOx crystals and inhibiting interstitial fibrosis in a mouse model of progressive CaOx crystal-induced nephropathy.

In kidney stone disease or nephrocalcinosis, interactions between urinary constituents and CaOx crystals may influence one or more critical processes in the stone pathogenesis, including crystal nucleation, aggregation, growth, and adhesion of crystals and/or aggregates to the epithelial cell surface in the kidney (38). The mechanism of CaOx crystallization involves a combination of processes, including urine supersaturation of stone-forming salts, such as calcium and oxalate, urinary pH (6, 7, 39). A variety of urinary constituents have been identified as possible inhibitors of CaOx crystallization, growth, and cell membrane adhesion, in particular macromolecules (40–42), proteins (9, 10, 43–45), and phospholipids (46). Unlike healthy individuals, patients with CaOx nephrolithiasis or nephrocalcinosis show decreased urinary CaOx crystallization inhibitors. CaOx crystals can be coated with alternating electron-dense and light fibrils, or covered with a more amorphous granular material indicating binding of proteins to CaOx crystals (8, 47). Using a proteomics approach, Fong-ngern et al. identified a large number of apical proteins on distal renal tubular epithelial cells that can bind to COM crystals (48). To our knowledge, we report for the first time that an anti-TGFβ IgG and the control IgG1 antibody can influence CaOx

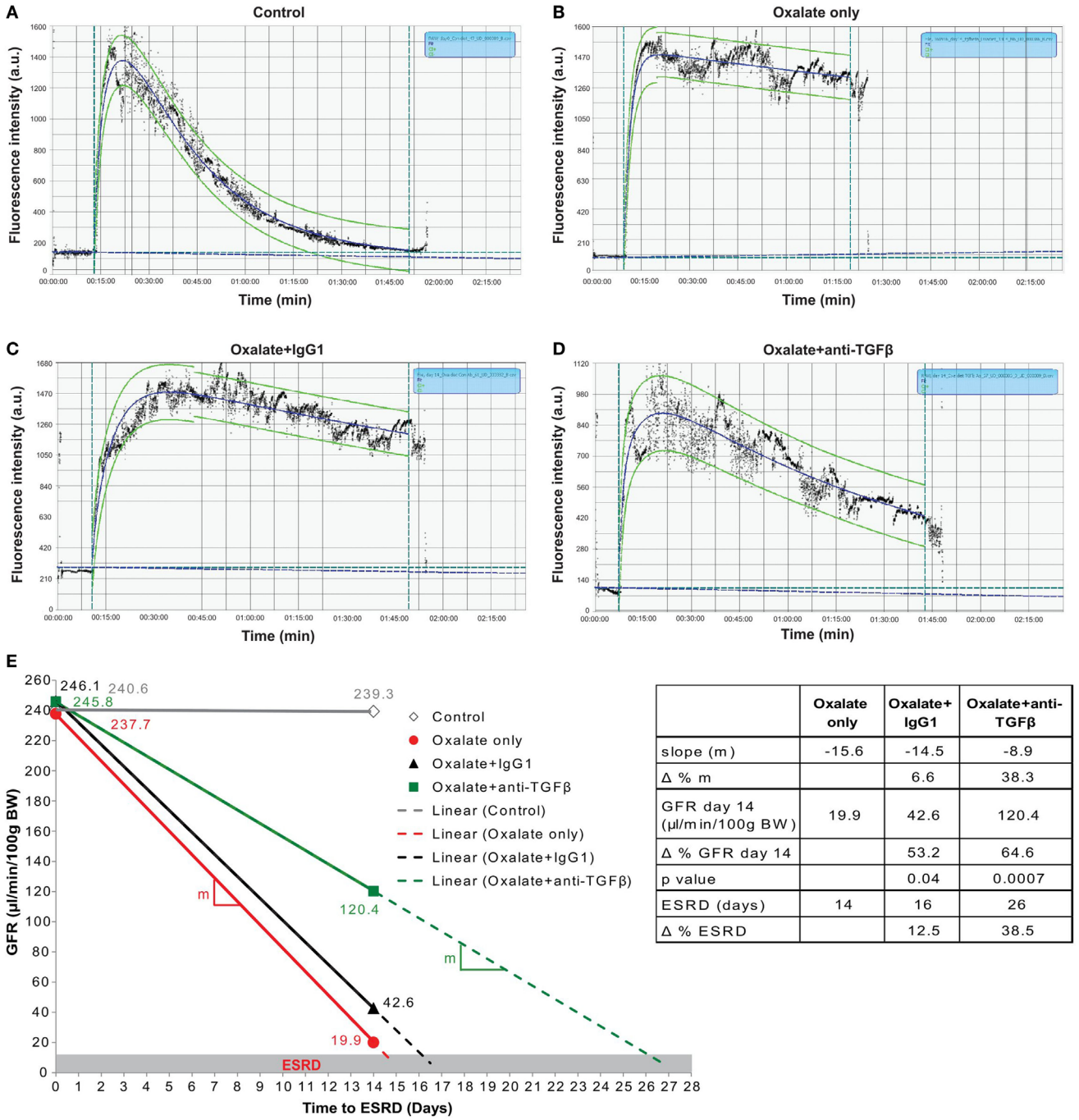

	Oxalate only	Oxalate+ IgG1	Oxalate+anti-TGFβ
slope (m)	-15.6	-14.5	-8.9
Δ % m		6.6	38.3
GFR day 14 (µl/min/100g BW)	19.9	42.6	120.4
Δ % GFR day 14		53.2	64.6
p value		0.04	0.0007
ESRD (days)	14	16	26
Δ % ESRD		12.5	38.5

FIGURE 6 | Preemptive transforming growth factor (TGF)β neutralization attenuates progressive glomerular filtration rate (GFR) decline. C57BL/6N mice were either fed a control diet (control), a high-oxalate diet (oxalate only) or an oxalate-rich diet combined with preemptive IgG1 or anti-TGFβ antibody treatment (oxalate + IgG1 and oxalate + anti-TGFβ) for up to 14 days. **(A–D)** Representative images of FITC-sinistrin fluorescence intensity curves using the three-compartment model with linear correction from a healthy mouse (control) **(A)**, a mouse with nephrocalcinosis **(B)**, an IgG1-treated mouse **(C)**, or anti-TGFβ antibody-treated mouse **(D)** with nephrocalcinosis. **(E)** GFR decline of all four groups from day 0 to 14 illustrated by the effect sizes: linear equation with slope (*m*, colored lines), GFR on day 14, and time to end stage renal disease (ESRD) (dotted lines and table). Δ represents difference expressed in percent (%). Data are mean ± SEM from five to seven mice per group and representative of one out of two independent experiments.

crystal formation *in vitro* as well as *in vivo* using a mouse model of progressive CaOx crystal-induced nephropathy. We also found that the IgG F(ab′)2 fragment can influence CaOx crystallization *in vitro*. On the other hand, blocking TNFR signaling with Etanercept, a fusion protein consisting of an extracellular TNR receptor 2 and an Fc domain of the human IgG1, has been shown

to reduce renal CaOx crystal deposition and prevent progressive nephrocalcinosis in mice (49). Thus, the exact mechanism of CaOx crystallization counteracting with IgG1 or the two main fragments is currently unknown and will need further investigation. So far, therapeutic approaches in humans primarily focus on reducing the risk of recurrent CaOx crystal formation (50) *via*, e.g., dietary restriction of oxalate-rich products (51), or reducing calcium and increasing citrate (52, 53).

Injury to every segment of the nephron can ultimately lead to loss of the entire nephron (54, 55). Toxic, inflammatory, or ischemic injury damages tubular cells leading to cell death, microvascular rarefaction, and fibroblast activation (56). Excessive myofibroblast accumulation of extracellular matrix in the interstitial and vascular compartment are accompanied by a significant decline in GFR and impaired epithelial regeneration (56). A variety of preclinical strategies to inhibit or even reverse interstitial fibrosis have been shown to be effective in rodents. For example, Kramann et al. demonstrated in two kidney fibrosis models that inhibiting the hedgehog pathway transcriptional effector GLI2 reduced renal fibrosis by limiting myofibroblast proliferation (57). Our finding confirms that administration of an anti-TGFβ IgG antibody can effectively prevent interstitial fibrosis in progressive CKD (16, 19, 58, 59). However, we did not observe a preservation of renal function upon delayed anti-TGFβ IgG antibody treatment. In addition, overexpression of latent TGFβ1 was shown to decrease both SMAD2/3 activation (transcription factors of canonical TGFβ1 signaling) and the number of myofibroblasts (60), which is in line with findings that SMAD3 knockout mice are protected from renal fibrosis (61, 62). Recent data also highlight a role for non-canonical TGFβ1 signaling *via* the transcription factor p53, a regulator of pro-fibrotic gene expression and cell cycle control in tubular epithelial cells (63–65), and for the complement factor C5 as therapeutic targets for fibrosis-related CKD (66). Strategies and efficacy of pharmacological therapies to reduce CKD progression are of upmost need (67). A dual-specific antibody approach for TGFβ neutralization successfully attenuated fibrosis in a mouse model of UUO (68). On the other hand, blocking TGFβ and Wnt-activated β-catenin crosstalk in proximal tubules enhances progressive CKD (69), suggesting that TβRII activity and the lack of proximal tubules stability may exacerbate fibrosis (70). Other than determining serum BUN and creatinine levels as well as other excretory markers of renal function, these animal studies did not assess GFR as primary endpoint. In our preclinical study, we used the transcutaneous GFR system based on the fluorescent tracer FITC-sinistrin, which is a precise method for repeated measurements in conscious and unrestricted mice to calculate the GFR (21, 22, 35, 37). Fresolimumab, a TGFβ neutralizing antibody did not elicit any positive effect on the GFR in a randomized control trial including 416 patients with diabetic kidney disease (71). Moreover, the anti-fibrotic agent pirfenidone was reported to consistently attenuate the GFR decline in mice and humans (72, 73).

In summary, anti-TGFβ IgG antibody treatment inhibits both CaOx crystallization and interstitial fibrosis in a model of CaOx crystal-induced nephropathy. Blocking TGFβ significantly improved the GFR decline by 38.3%, increased the GFR at the end of the study by 64.6%, and prolonged the time to ESRD by 38.5% compared to IgG1 control treatment. However, this nephroprotective effect got lost upon delayed onset of TGFβ blockade. We conclude that anti-TGFβ IgG antibody treatment elicits a dual effect on CaOx crystallization and interstitial fibrosis, which represents a novel therapeutic approach to delay progressive nephrocalcinosis-related CKD.

ETHICS STATEMENT

All animal experiments were performed in accordance with the European protection law of animal welfare and were approval by the local government authorities Regierung von Oberbayern (reference number: 55.2-1-54-2532-189-2015).

AUTHOR CONTRIBUTIONS

SS and H-JA designed the study; SS, JG, QM, JJ, MS, and CB performed the experiments; SS, JG, QM, TB, JJ, MS, and ML analyzed and interpreted the data; SS and H-JA wrote the manuscript. All authors reviewed the manuscript.

ACKNOWLEDGMENTS

We thank Jana Mandelbaum and Dan Draganovici for expert technical support, as well as Patrick Finn and Steve Ledbetter from Genzyme Corporation, a Sanofi Company, for providing the antibodies for treatment. This work is presented in the thesis project of J.F. Grill to the Medical Faculty of the Klinikum der Universität München, Munich, Germany.

FUNDING

This work was supported by grants from the Deutsche Forschungsgemeinschaft to SS (STE2437/2-1) and to H-JA (AN372/16-2, 20-1, 23-1, 24-1).

SUPPLEMENTARY MATERIAL

The Supplementary Material for this article can be found online at https://www.frontiersin.org/articles/10.3389/fimmu.2018.00619/full#supplementary-material.

FIGURE S1 | Anti-TGFβ IgG treatment decreases oxaluria but has no effect on calcinuria. C57BL/6N mice were either fed a control diet (control), a high-oxalate diet (oxalate only) or an oxalate-rich diet combined with preemptive IgG1 or anti-TGFβ antibody treatment (oxalate + IgG1 and oxalate + anti-TGFβ) for up to 14 days. Serum and urine oxalate levels **(A)** and urine calcium levels **(B)** on day 14. Data are mean ± SEM from five mice per group. ns, not significant. $^{*}p < 0.05$, $^{**}p < 0.01$, $^{***}p < 0.001$ are considered significant.

FIGURE S2 | Delayed anti-TGFβ IgG treatment does not improve renal function in chronic oxalate nephropathy. **(A)** Flow diagram of experimental design: C57BL/6N mice were fed an oxalate-rich diet combined with delayed IgG1 or anti-TGFβ treatment (total of 4 i.p. injections) (oxalate + IgG1 or oxalate + anti-TGFβ) compared to control diet (control) for 14 days. **(B–D)** Renal function was assessed by determining the serum blood urea nitrogen (BUN) levels **(B)**, tubular injury by periodic acid-Schiff (PAS) staining **(C)**, and measuring the glomerular filtration rate (GFR) **(D)** on day 14. Data are mean ± SEM from five mice per group. ns, not significant. $^{*}p < 0.05$, $^{**}p < 0.01$, $^{***}p < 0.001$ are considered significant.

REFERENCES

1. Khan SR. Crystal-induced inflammation of the kidneys: results from human studies, animal models, and tissue-culture studies. *Clin Exp Nephrol* (2004) 8:75–88. doi:10.1007/s10157-004-0292-0
2. Evan AP. Physiopathology and etiology of stone formation in the kidney and the urinary tract. *Pediatr Nephrol* (2010) 25:831–41. doi:10.1007/s00467-009-1116-y
3. Pearle MS, Calhoun EA, Curhan GC; Urologic Diseases of America P. Urologic diseases in America project: urolithiasis. *J Urol* (2005) 173:848–57. doi:10.1097/01.ju.0000152082.14384.d7
4. Evan AP, Lingeman JE, Worcester EM, Bledsoe SB, Sommer AJ, Williams JC Jr, et al. Renal histopathology and crystal deposits in patients with small bowel resection and calcium oxalate stone disease. *Kidney Int* (2010) 78:310–7. doi:10.1038/ki.2010.131
5. Rule AD, Krambeck AE, Lieske JC. Chronic kidney disease in kidney stone formers. *Clin J Am Soc Nephrol* (2011) 6:2069–75. doi:10.2215/CJN.10651110
6. Shen Y, Li S, Xie A, Xu W, Qiu L, Yao H, et al. Controlled growth of calcium oxalate crystal in bicontinuous microemulsions containing amino acids. *Colloids Surf B Biointerfaces* (2007) 58:298–304. doi:10.1016/j.colsurfb.2007.04.004
7. Thongboonkerd V, Semangoen T, Chutipongtanate S. Factors determining types and morphologies of calcium oxalate crystals: molar concentrations, buffering, pH, stirring and temperature. *Clin Chim Acta* (2006) 367:120–31. doi:10.1016/j.cca.2005.11.033
8. McKee MD, Nanci A, Khan SR. Ultrastructural immunodetection of osteopontin and osteocalcin as major matrix components of renal calculi. *J Bone Miner Res* (1995) 10:1913–29. doi:10.1002/jbmr.5650101211
9. Hess B, Nakagawa Y, Coe FL. Inhibition of calcium oxalate monohydrate crystal aggregation by urine proteins. *Am J Physiol* (1989) 257:F99–106.
10. Shiraga H, Min W, VanDusen WJ, Clayman MD, Miner D, Terrell CH, et al. Inhibition of calcium oxalate crystal growth in vitro by uropontin: another member of the aspartic acid-rich protein superfamily. *Proc Natl Acad Sci U S A* (1992) 89:426–30. doi:10.1073/pnas.89.1.426
11. Mulay SR, Anders HJ. Crystal nephropathies: mechanisms of crystal-induced kidney injury. *Nat Rev Nephrol* (2017) 13:226–40. doi:10.1038/nrneph.2017.10
12. Cochat P, Rumsby G. Primary hyperoxaluria. *N Engl J Med* (2013) 369:649–58. doi:10.1056/NEJMra1301564
13. Mulay SR, Eberhard JN, Pfann V, Marschner JA, Darisipudi MN, Daniel C, et al. Oxalate-induced chronic kidney disease with its uremic and cardiovascular complications in C57BL/6 mice. *Am J Physiol Renal Physiol* (2016) 310:F785–95. doi:10.1152/ajprenal.00488.2015
14. Duffield JS. Cellular and molecular mechanisms in kidney fibrosis. *J Clin Invest* (2014) 124:2299–306. doi:10.1172/JCI72267
15. Hawinkels LJ, Ten Dijke P. Exploring anti-TGF-beta therapies in cancer and fibrosis. *Growth Factors* (2011) 29:140–52. doi:10.3109/08977194.2011.595411
16. Liang X, Schnaper HW, Matsusaka T, Pastan I, Ledbetter S, Hayashida T. Anti-TGF-beta antibody, 1D11, ameliorates glomerular fibrosis in mouse models after the onset of proteinuria. *PLoS One* (2016) 11:e0155534. doi:10.1371/journal.pone.0155534
17. Grafe I, Yang T, Alexander S, Homan EP, Lietman C, Jiang MM, et al. Excessive transforming growth factor-beta signaling is a common mechanism in osteogenesis imperfecta. *Nat Med* (2014) 20:670–5. doi:10.1038/nm.3544
18. Ma Q, Steiger S, Anders HJ. Sodium glucose transporter-2 inhibition has no renoprotective effects on non-diabetic chronic kidney disease. *Physiol Rep* (2017) 5(7):e13228. doi:10.14814/phy2.13228
19. Lavoie P, Robitaille G, Agharazii M, Ledbetter S, Lebel M, Lariviere R. Neutralization of transforming growth factor-beta attenuates hypertension and prevents renal injury in uremic rats. *J Hypertens* (2005) 23:1895–903. doi:10.1097/01.hjh.0000182521.44440.c5
20. Mulay SR, Kulkarni OP, Rupanagudi KV, Migliorini A, Darisipudi MN, Vilaysane A, et al. Calcium oxalate crystals induce renal inflammation by NLRP3-mediated IL-1beta secretion. *J Clin Invest* (2013) 123:236–46. doi:10.1172/JCI63679
21. Schreiber A, Shulhevich Y, Geraci S, Hesser J, Stsepankou D, Neudecker S, et al. Transcutaneous measurement of renal function in conscious mice. *Am J Physiol Renal Physiol* (2012) 303:F783–8. doi:10.1152/ajprenal.00279.2012
22. Friedemann J, Heinrich R, Shulhevich Y, Raedle M, William-Olsson L, Pill J, et al. Improved kinetic model for the transcutaneous measurement of glomerular filtration rate in experimental animals. *Kidney Int* (2016) 90:1377–85. doi:10.1016/j.kint.2016.07.024
23. Durrbaum D, Rodgers AL, Sturrock ED. A study of crystal matrix extract and urinary prothrombin fragment 1 from a stone-prone and stone-free population. *Urol Res* (2001) 29:83–8. doi:10.1007/s002400000163
24. Mandel NS, Mandel GS, Hasegawa AT. The effect of some urinary stone inhibitors on membrane interaction potentials of stone crystals. *J Urol* (1987) 138:557–62. doi:10.1016/S0022-5347(17)43258-7
25. Zillner K, Jerabek-Willemsen M, Duhr S, Braun D, Langst G, Baaske P. Microscale thermophoresis as a sensitive method to quantify protein: nucleic acid interactions in solution. *Methods Mol Biol* (2012) 815:241–52. doi:10.1007/978-1-61779-424-7_18
26. Zhang W, Duhr S, Baaske P, Laue E. Microscale thermophoresis for the assessment of nuclear protein-binding affinities. *Methods Mol Biol* (2014) 1094:269–76. doi:10.1007/978-1-62703-706-8_21
27. Seidel SA, Dijkman PM, Lea WA, van den Bogaart G, Jerabek-Willemsen M, Lazic A, et al. Microscale thermophoresis quantifies biomolecular interactions under previously challenging conditions. *Methods* (2013) 59:301–15. doi:10.1016/j.ymeth.2012.12.005
28. Knauf F, Asplin JR, Granja I, Schmidt IM, Moeckel GW, David RJ, et al. NALP3-mediated inflammation is a principal cause of progressive renal failure in oxalate nephropathy. *Kidney Int* (2013) 84:895–901. doi:10.1038/ki.2013.207
29. Kang HM, Ahn SH, Choi P, Ko YA, Han SH, Chinga F, et al. Defective fatty acid oxidation in renal tubular epithelial cells has a key role in kidney fibrosis development. *Nat Med* (2015) 21:37–46. doi:10.1038/nm.3762
30. Anders HJ, Ryu M. Renal microenvironments and macrophage phenotypes determine progression or resolution of renal inflammation and fibrosis. *Kidney Int* (2011) 80:915–25. doi:10.1038/ki.2011.217
31. Lech M, Gröbmayr R, Ryu M, Lorenz G, Hartter I, Mulay SR, et al. Macrophage phenotype controls long-term AKI outcomes – kidney regeneration versus atrophy. *J Am Soc Nephrol* (2014) 25:292–304. doi:10.1681/ASN.2013020152
32. Lech M, Anders HJ. Macrophages and fibrosis: how resident and infiltrating mononuclear phagocytes orchestrate all phases of tissue injury and repair. *Biochim Biophys Acta* (2013) 1832:989–97. doi:10.1016/j.bbadis.2012.12.001
33. Tampe D, Zeisberg M. Potential approaches to reverse or repair renal fibrosis. *Nat Rev Nephrol* (2014) 10:226–37. doi:10.1038/nrneph.2014.14
34. Kim MG, Kim SC, Ko YS, Lee HY, Jo SK, Cho W. The role of M2 macrophages in the progression of chronic kidney disease following acute kidney injury. *PLoS One* (2015) 10:e0143961. doi:10.1371/journal.pone.0143961
35. Schock-Kusch D, Geraci S, Ermeling E, Shulhevich Y, Sticht C, Hesser J, et al. Reliability of transcutaneous measurement of renal function in various strains of conscious mice. *PLoS One* (2013) 8:e71519. doi:10.1371/journal.pone.0071519
36. Zitta S, Schrabmair W, Reibnegger G, Meinitzer A, Wagner D, Estelberger W, et al. Glomerular filtration rate (GFR) determination via individual kinetics of the inulin-like polyfructosan sinistrin versus creatinine-based population-derived regression formulae. *BMC Nephrol* (2013) 14:159. doi:10.1186/1471-2369-14-159
37. Shmarlouski A, Shulhevich Y, Geraci S, Friedemann J, Gretz N, Neudecker S, et al. Automatic artifact removal from GFR measurements. *Biomed Signal Process Control* (2014) 14:30–41. doi:10.1016/j.bspc.2014.06.010
38. Ratkalkar VN, Kleinman JG. Mechanisms of stone formation. *Clin Rev Bone Miner Metab* (2011) 9:187–97. doi:10.1007/s12018-011-9104-8
39. Manissorn J, Fong-Ngern K, Peerapen P, Thongboonkerd V. Systematic evaluation for effects of urine pH on calcium oxalate crystallization, crystal-cell adhesion and internalization into renal tubular cells. *Sci Rep* (2017) 7:1798. doi:10.1038/s41598-017-01953-4
40. Rimer JD, Kolbach-Mandel AM, Ward MD, Wesson JA. The role of macromolecules in the formation of kidney stones. *Urolithiasis* (2017) 45:57–74. doi:10.1007/s00240-016-0948-8
41. Conte A, Roca P, Genestar C, Grases F. Uric acid and its relationship with glycosaminoglycans in normal and stone-former subjects. *Nephron* (1989) 52:162–5. doi:10.1159/000185621
42. Atmani F, Khan SR. Role of urinary bikunin in the inhibition of calcium oxalate crystallization. *J Am Soc Nephrol* (1999) 10(Suppl 14):S385–8.

43. Hess B. The role of Tamm-Horsfall glycoprotein and nephrocalcin in calcium oxalate monohydrate crystallization processes. *Scanning Microsc* (1991) 5:689–95; discussion 96.
44. Chen WC, Lin HS, Chen HY, Shih CH, Li CW. Effects of Tamm-Horsfall protein and albumin on calcium oxalate crystallization and importance of sialic acids. *Mol Urol* (2001) 5:1–5. doi:10.1089/109153601750124186
45. Tsujihata M, Miyake O, Yoshimura K, Kakimoto KI, Takahara S, Okuyama A. Fibronectin as a potent inhibitor of calcium oxalate urolithiasis. *J Urol* (2000) 164:1718–23. doi:10.1097/00005392-200011000-00090
46. Bigelow MW, Wiessner JH, Kleinman JG, Mandel NS. Surface exposure of phosphatidylserine increases calcium oxalate crystal attachment to IMCD cells. *Am J Physiol* (1997) 272:F55–62.
47. Wesson JA, Worcester EM, Wiessner JH, Mandel NS, Kleinman JG. Control of calcium oxalate crystal structure and cell adherence by urinary macromolecules. *Kidney Int* (1998) 53:952–7. doi:10.1111/j.1523-1755.1998.00839.x
48. Fong-Ngern K, Peerapen P, Sinchaikul S, Chen ST, Thongboonkerd V. Large-scale identification of calcium oxalate monohydrate crystal-binding proteins on apical membrane of distal renal tubular epithelial cells. *J Proteome Res* (2011) 10:4463–77. doi:10.1021/pr2006878
49. Mulay SR, Eberhard JN, Desai J, Marschner JA, Kumar SV, Weidenbusch M, et al. Hyperoxaluria requires TNF receptors to initiate crystal adhesion and kidney stone disease. *J Am Soc Nephrol* (2017) 28:761–8. doi:10.1681/ASN.2016040486
50. Fink HA, Wilt TJ, Eidman KE, Garimella PS, MacDonald R, Rutks IR, et al. Medical management to prevent recurrent nephrolithiasis in adults: a systematic review for an American College of Physicians Clinical Guideline. *Ann Intern Med* (2013) 158:535–43. doi:10.7326/0003-4819-158-7-201304020-00005
51. Tiselius HG. Should we modify the principles of risk evaluation and recurrence preventive treatment of patients with calcium oxalate stone disease in view of the etiologic importance of calcium phosphate? *Urolithiasis* (2015) 43(Suppl 1):47–57. doi:10.1007/s00240-014-0698-4
52. Tiselius HG. Epidemiology and medical management of stone disease. *BJU Int* (2003) 91:758–67. doi:10.1046/j.1464-410X.2003.04208.x
53. Straub M, Strohmaier WL, Berg W, Beck B, Hoppe B, Laube N, et al. Diagnosis and metaphylaxis of stone disease. Consensus concept of the National Working Committee on stone disease for the upcoming German urolithiasis guideline. *World J Urol* (2005) 23:309–23. doi:10.1007/s00345-005-0029-z
54. Schnaper HW. Remnant nephron physiology and the progression of chronic kidney disease. *Pediatr Nephrol* (2014) 29:193–202. doi:10.1007/s00467-013-2494-8
55. Romagnani P, Remuzzi G, Glassock R, Levin A, Jager KJ, Tonelli M, et al. Chronic kidney disease. *Nat Rev Dis Primers* (2017) 3:17088. doi:10.1038/nrdp.2017.88
56. Zeisberg M, Neilson EG. Mechanisms of tubulointerstitial fibrosis. *J Am Soc Nephrol* (2010) 21:1819–34. doi:10.1681/ASN.2010080793
57. Kramann R, Fleig SV, Schneider RK, Fabian SL, DiRocco DP, Maarouf O, et al. Pharmacological GLI2 inhibition prevents myofibroblast cell-cycle progression and reduces kidney fibrosis. *J Clin Invest* (2015) 125:2935–51. doi:10.1172/JCI74929
58. Benigni A, Zoja C, Campana M, Corna D, Sangalli F, Rottoli D, et al. Beneficial effect of TGFbeta antagonism in treating diabetic nephropathy depends on when treatment is started. *Nephron Exp Nephrol* (2006) 104:e158–68. doi:10.1159/000094967
59. Miyajima A, Chen J, Lawrence C, Ledbetter S, Soslow RA, Stern J, et al. Antibody to transforming growth factor-beta ameliorates tubular apoptosis in unilateral ureteral obstruction. *Kidney Int* (2000) 58:2301–13. doi:10.1046/j.1523-1755.2000.00414.x
60. Huang Y, Border WA, Noble NA. Perspectives on blockade of TGFbeta overexpression. *Kidney Int* (2006) 69:1713–4. doi:10.1038/sj.ki.5000260
61. Inazaki K, Kanamaru Y, Kojima Y, Sueyoshi N, Okumura K, Kaneko K, et al. Smad3 deficiency attenuates renal fibrosis, inflammation, and apoptosis after unilateral ureteral obstruction. *Kidney Int* (2004) 66:597–604. doi:10.1111/j.1523-1755.2004.00779.x
62. Sato M, Muragaki Y, Saika S, Roberts AB, Ooshima A. Targeted disruption of TGF-beta1/Smad3 signaling protects against renal tubulointerstitial fibrosis induced by unilateral ureteral obstruction. *J Clin Invest* (2003) 112:1486–94. doi:10.1172/JCI200319270
63. Higgins SP, Tang Y, Higgins CE, Mian B, Zhang W, Czekay RP, et al. TGF-beta1/p53 signaling in renal fibrogenesis. *Cell Signal* (2017) 43:1–10. doi:10.1016/j.cellsig.2017.11.005
64. Venkatachalam MA, Weinberg JM, Kriz W, Bidani AK. Failed tubule recovery, AKI-CKD transition, and kidney disease progression. *J Am Soc Nephrol* (2015) 26:1765–76. doi:10.1681/ASN.2015010006
65. Yang L, Besschetnova TY, Brooks CR, Shah JV, Bonventre JV. Epithelial cell cycle arrest in G2/M mediates kidney fibrosis after injury. *Nat Med* (2010) 16:535–43. doi:10.1038/nm.2144
66. Boor P, Konieczny A, Villa L, Schult AL, Bücher E, Rong S, et al. Complement C5 mediates experimental tubulointerstitial fibrosis. *J Am Soc Nephrol* (2007) 18:1508–15. doi:10.1681/ASN.2006121343
67. Pollock C, Zuk A, Anders HJ, Ganji MR, Johnson DW, Kasiske B, et al. The establishment and validation of novel therapeutic targets to retard progression of chronic kidney disease. *Kidney Int Suppl* (2017) 7:8. doi:10.1016/j.kisu.2017.07.008
68. McGaraughty S, Davis-Taber RA, Zhu CZ, Cole TB, Nikkel AL, Chhaya M, et al. Targeting Anti-TGF-beta therapy to fibrotic kidneys with a dual specificity antibody approach. *J Am Soc Nephrol* (2017) 28:3616–26. doi:10.1681/ASN.2017010013
69. Nlandu-Khodo S, Neelisetty S, Phillips M, Manolopoulou M, Bhave G, May L, et al. Blocking TGF-beta and beta-catenin epithelial crosstalk exacerbates CKD. *J Am Soc Nephrol* (2017) 28:3490–503. doi:10.1681/ASN.2016121351
70. Basile DP, Mehrotra P. Surprising enhancement of fibrosis by tubule-specific deletion of the TGF-beta receptor: a new twist on an old paradigm. *J Am Soc Nephrol* (2017) 28:3427–9. doi:10.1681/ASN.2017080947
71. Voelker J, Berg PH, Sheetz M, Duffin K, Shen T, Moser B, et al. Anti-TGF-beta1 antibody therapy in patients with diabetic nephropathy. *J Am Soc Nephrol* (2017) 28:953–62. doi:10.1681/ASN.2015111230
72. Park HS, Bao L, Kim YJ, Cho IH, Lee CH, Hyun BH, et al. Pirfenidone suppressed the development of glomerulosclerosis in the FGS/Kist mouse. *J Korean Med Sci* (2003) 18:527–33. doi:10.3346/jkms.2003.18.4.527
73. Cho ME, Smith DC, Branton MH, Penzak SR, Kopp JB. Pirfenidone slows renal function decline in patients with focal segmental glomerulosclerosis. *Clin J Am Soc Nephrol* (2007) 2:906–13. doi:10.2215/CJN.01050207

Conflict of Interest Statement: The authors declare that the research was conducted in the absence of any commercial or financial relationships that could be construed as a potential conflict of interest.

frontiers in Immunology

ORIGINAL RESEARCH
published: 22 August 2018
doi: 10.3389/fimmu.2018.01863

Calcium Oxalate Differentiates Human Monocytes Into Inflammatory M1 Macrophages

Paul R. Dominguez-Gutierrez[1], Sergei Kusmartsev[1], Benjamin K. Canales[1] and Saeed R. Khan[1,2]*

[1] Department of Urology, University of Florida, Gainesville, FL, United States, [2] Department of Pathology, Immunology and Laboratory Medicine, College of Medicine, University of Florida, Gainesville, FL, United States

Purpose: A number of hyperoxaluric states have been associated with calcium oxalate (CaOx) deposits in the kidneys. In animal models of stone disease, these crystals interact with circulating monocytes that have migrated into the kidney as part of innate immunity. Similarly, macrophages surround CaOx crystals in kidneys of patients excreting high levels of oxalate. We investigate the effect of this exposure and subsequent human immunological response *in vitro.*

Materials and methods: Primary human monocytes were collected from healthy donors and exposed to CaOx, potassium oxalate, and zinc oxalate (ZnOx). Cytokine production was measured with a multiplex ELISA. Quantitative reverse transcription-polymerase chain reaction was done to validate the mRNA profile expression. M1 macrophage phenotype was confirmed with immunofluorescence microscopy.

Results: Both primary monocytes and THP-1 cells, a human monocytic cell line, respond strongly to CaOx crystals in a dose-dependent manner producing TNF-α, IL-1β, IL-8, and IL-10 transcripts. Exposure to CaOx followed by 1 h with LPS had an additive effect for cytokine production compared to LPS alone, however, LPS followed by CaOx led to significant decrease in cytokine production. Supernatants taken from monocytes were previously exposed to CaOx crystals enhance M2 macrophage crystal phagocytosis. CaOx, but not potassium or ZnOx, promotes monocyte differentiation into inflammatory M1-like macrophages.

Conclusion: In our *in vitro* experiment, human monocytes were activated by CaOx and produced inflammatory cytokines. Monocytes recognized CaOx crystals through a specific mechanism that can enhance or decrease the innate immune response to LPS. CaOx promoted M1 macrophage development. These results suggest that monocytes have an important role promoting CaOx-induced inflammation.

Keywords: kidney stones, calcium oxalate, monocytes, macrophages, inflammatory cytokines, nephrolithiasis

Abbreviations: CaOx, calcium oxalate; CCL2 (MCP-1), chemokine (C-C motif) ligand 2 (monocyte chemoattractant protein-1); CCL22 (MDC), chemokine (C-C motif) ligand 22 (macrophage-derived chemokine); IL-1b, interleukin 1 beta; IL-1Ra, interleukin 1 receptor antagonist; IL-6, interleukin 6; IL-8, interleukin 8; IL-10, interleukin 10; IFNα2a, interferon alpha 2a; IFNβ, interferon beta; IFNγ, interferon gamma; K_2Ox, potassium oxalate; LPS, lipopolysaccharides; qRT-PCR, quantitative real-time PCR; TLR-4, toll-like receptor 4; TNFa, tumor necrosis factor-alpha; ZnOx, zinc oxalate.

OPEN ACCESS

Edited by:
Hans-Joachim Anders, Ludwig-Maximilians-Universität München, Germany

Reviewed by:
Takahiro Yasui, Nagoya City University, Japan
Yolande Richard, Institut National de la Santé et de la Recherche Médicale (INSERM), France

****Correspondence:***
Paul R. Dominguez-Gutierrez
paul.dominguez@urology.ufl.edu

Specialty section:
This article was submitted to Inflammation, a section of the journal Frontiers in Immunology

Received: *30 April 2018*
Accepted: *27 July 2018*
Published: *22 August 2018*

Citation:
Dominguez-Gutierrez PR, Kusmartsev S, Canales BK and Khan SR (2018) Calcium Oxalate Differentiates Human Monocytes Into Inflammatory M1 Macrophages. Front. Immunol. 9:1863. doi: 10.3389/fimmu.2018.01863

INTRODUCTION

A variety of crystals can form and accumulate within the kidney. These deposits can eventually lead to nephrolithiasis, a painful condition that is increasingly prevalent and costly around the world (1, 2). Calcium oxalate (CaOx) crystals are the major constituent of the most common kidney stones which start as deposits or plugs within the inner medullary collecting ducts or on subepithelial deposits of calcium phosphate on the renal papillae of patients with, among other abnormalities, high urinary oxalate levels or hyperoxaluria (3–7), which is most common in patients with primary hyperoxaluria. In rodents, hyperoxaluria leads to rapid crystallization of CaOx within the renal proximal tubular lumen (8, 9). Although most CaOx crystals move with the filtrate through the nephron, some crystals remain attached to tubular epithelial cells and appear to migrate into the renal interstitium. Over time, these crystals become surrounded, engulfed, and eventually cleared by tissue macrophages with minimal visible inflammatory changes. Similarly, Taguchi et al. recently demonstrated by renal papillary tip tissue biopsy that human CaOx stone formers have high amounts of tissue inflammatory markers but minimal visible inflammatory changes, suggesting that low-grade renal immune responses do occur in CaOx stone formers (10).

Tissue macrophages play important and complex roles in homeostasis, regulating immunity, inflammation, and angiogenesis while scavenging apoptotic cells (11). We have demonstrated *in vitro* that human macrophages are capable of engulfing, phagocytizing, and gradually disintegrating CaOx crystals and human stones fragments (12). These activated macrophages release an array of cytokines and chemokines intended to attract circulating monocytes to the site of tissue inflammation. Monocytes and macrophages have been implicated in CaOx stone disease in both humans and rodent models (13–16). Hyperoxaluric C57BL/6J mice expressed M-CSF and CCL2 which could potentially recruit monocytes (14); hyperoxaluric C57BL/6J mice that received M1 macrophage transfusions displayed increased CaOx production of IL-6 and TNFα compared to those that received M2 macrophage transfusions (15). In addition, M-CSF-deficient mice had significantly higher CaOx deposition in the kidneys than those of the wild-type mice (16). Furthermore, Okada et al. reported an overall increase in CD68 (+) macrophages in 60 patients who underwent radical nephrectomy for renal cancer who were then retrospectively classified as stone formers (13). Furthermore, Williams et al. demonstrated that monocytes isolated from the peripheral blood of CaOx stone formers ($n = 12$) displayed significantly lower mitochondrial maximal respiration, reserve capacity, and bioenergetic health index compared to healthy donors (17). To further our understanding of these immune responses, we exposed primary human monocytes and a monocyte cell line (THP-1 cells) to soluble oxalate, CaOx crystals, and a variety of other minerals and controls to determine response, time-dependent effects, and inflammatory cytokine and chemokine production.

MATERIALS AND METHODS

Reagents and Culture Media

Ultrapure 99.999% CaOx (Alfa Aesar), potassium oxalate (K_2Ox), zinc oxalate (ZnOx), and 200 nm or smaller hydroxyapatite (HA) crystals were purchased from Sigma-Aldrich. 500–1,000 ng/ml LPS from *S. enterica* serotype Minnesota Re595 (LPS Se, TLR4 ligand, Ultrapure grade, Sigma-Aldrich) was used as a positive control for innate immune stimulation (18–21). *In vitro* experiments were conducted using RPMI 1640 medium supplemented with 10% fetal bovine serum, 20 mM HEPES, 20 mM sodium pyruvate, and 100 U/ml penicillin–streptomycin (Hyclone Laboratories, Logan, Utah).

Cell Culture

Human monocytic cell line THP-1 cells were obtained from the American Type Culture Collection (ATCC, Manassas, VA, USA). For analysis of THP-1 monocyte response to crystals *in vitro*, log phase cells were seeded at 1×10^6 cells/ml in a 24-well plate.

Preparation of Primary Human Monocytes

Following institutional review board approval, human buffy coat samples without demographic data were obtained from LifeSouth Community Blood Center (Gainesville, FL, USA). Peripheral blood mononuclear cells (PBMCs) were separated by Lymphoprep (Accu-Prep, 1.077 g/ml, Oslo, Norway) gradient density centrifugation per manufacturer's recommendations. PBMCs were washed twice with 10 ml of PBS, and red blood cells were lysed using ACK lysing buffer (BioWhittaker, Walkersville, MD, USA). Monocytes were purified from PBMC using the MACS method (Miltenyi Biotec, Bergisch Gladbach, Germany) per manufacturer's instructions. Briefly, cells were incubated with beads conjugated with anti-CD14 and positively selected using LS columns (Miltenyi Biotec). 95% of recovered cells expressed monocyte marker CD14.

Preparation of Primary Human Macrophages

Cytokine-Induced Differentiation

Monocytes were differentiated into macrophages over 6 days by seeding in 24-well culture plate (1×10^6 cell/ml) in complete RPMI 1640 culture medium and treating with 20 ng/ml of either recombinant human M-CSF or recombinant human GM-CSF at day 0 and day 3.

CaOx-Induced Differentiation

Monocytes were seeded in 24-well culture plate (1×10^6 cell/ml) in complete RPMI 1640 culture medium and exposed to 0.05 mM (64.0 μg/ml) or 2.5 mM (320 μg/ml) CaOx.

Phagocytosis Assay Using Qdot525 Labeled CaOx

Primary human monocytes were stimulated with 2.5 mM CaOx, HA, or PBS as a control for 18 h. Supernatants were collected and centrifuged to pellet any mineral, cells, and debris. Clean supernatant was frozen at −80°C. Autologous monocytes were differentiated into M2 macrophages as described above. At day 6, media was removed and a solution of half fresh media and half supernatants from the monocyte treatments was added. After 8 h, 1.56 mM (200 mg/ml) Qdot 525-labeled CaOx was added. After 1 h, macrophages were washed three times with PBS to remove any extracellular CaOx. CaOx was labeled with

Qdot 525 amino quantum dots (Qdot525, Applied Biosystems) following a modified manufacturer's protocol. 100 µl of Qdot525 was mixed with 1.0 ml of borate buffer and 0.5 ml of 2.50 mM (320 µg/ml) CaOx in 10 nM borate buffer. At 4°C, 10 µl of 10 mg/ml 1-Ethyl-3-(3-dimethylaminopropyl) carbodiimide (Thermo Scientific, Waltham, MA, USA) was added to the above and incubated for 1 min. Following incubation, Qdot525-CaOx was washed three times with PBS, pelleted, and resuspended in 1 ml of fresh media. At 20× magnification, EVOS FL Cell Imaging System (Applied Biosystems) evaluated intercellular uptake of CaOx crystals. Macrophages positive for Qdot 525-labled CaOx were visually determined using photoshop. $N = 3$ for each treatment group.

Immunofluorescence and HEMA 3 Staining of Macrophages

Macrophages were fixed with 4% paraformaldehyde and 1% glutaraldehyde for 10 min. Followed by rinsing and blocking with 2% BSA, macrophages were stained with primary antibodies for M1 markers CD68 (Abcam ab955) and CD86 (Abcam, ab53004) and M2 markers CD163 (Abcam, ab87099), CD206 (Abcam, ab8918), and phosphorylated STAT6 (Abcam, ab28829). Secondary antibody staining was done with Alexa Fluor 488, goat anti-mouse IgG (Abcam, ab150113) and Cy5, and goat anti-rabbit IgG (Abcam, ab6563). PROTOCOL Hema 3 staining systems (Fisher Scientific) were used to stain macrophage morphology according to the manufacturer's protocol.

Quantitative Real-Time PCR (qPCR)

Total cellular RNA was isolated from monocytes using Direct-zol RNA MiniPrep (Zymo Research) according to the manufacturer's instructions. RNA concentration was measured with a Take3 plate on a Synergy H1 plate reader (BioTek). cDNA for each RNA sample was synthesized in 20 µl reactions using the High-Capacity cDNA Reverse Transcription Kit (Applied Biosystems) following the manufacturer's protocol. qPCR analysis was performed using a 7900HT Fast Real-Time PCR System (Applied Biosystems). cDNA-specific TaqMan Gene expression assays for human TNFα (assay ID: Hs01113624_g1), IL-1β (assay ID: Hs01555410_m1), IL-6 (assay ID: Hs00985639_m1), IL-8 (assay ID: Hs00174103_m1), and CCL2 (assay ID: Hs00234140_m1) from Applied Biosystems were used in the study. A Eukaryote 18s rRNA (assay ID: 4319413E) was used as an endogenous control. Relative expression of mRNA was determined by the $\Delta\Delta C_T$ method where the cycle threshold (C_T) values were determined for the mRNA expression relative to untreated controls.

Multiplex Cytokine ELISA Assay

Cell-free cell culture supernatant samples were stored at −20°C until analyzed. The system used was a multiplex ELISA assay manufactured by Meso Scale Discovery (MSD, Gaithersburg, MD, USA) containing 10 individual ELISAs per well. Supernatants were tested with a U-PLEX Proinflammatory Panel1 Human Kit [a multiplex 96-well ELISA plate based assay that contained primary antibodies to IL-12, IL-10, TNFα, IL-6, IL22, interleukin 1 receptor antagonist (IL-1Ra), interferon alpha 2a (IFNα2a), interferon beta (IFNβ), interferon gamma (IFNγ), and IL-1β] per manufacturer's recommendations. Briefly, the MSD plex assays were run as follows. Calibration curves were prepared in the supplied assay diluent for human serum, with a range of 40,000–1.2 pg/ml, depending on the cytokine. Arrays were preincubated with 25 µl per well of assay diluent for 30 min. After the pre-incubation, 25 µl sample or calibrator was added in duplicate to the appropriate wells. The array was then incubated at room temperature for 2 h with primary antibody. The array was washed with PBS plus 0.05% Tween 20, and 25 µl detection antibody reagent was added. After 2 h of incubation at room temperature with secondary antibody, the array was washed, and the detection buffer was added. Results were read with a QuickPlex SQ 120. Sample cytokine concentrations were determined using MSD Discovery Workbench 4.0 software.

Data Analysis

Analyses were performed using JMP Pro version 10 (SAS, Cary, NC, USA). Dunnett's with Control and Tukey-Kramer Honest Significant Difference test was used to evaluate significance. *P* value less than 0.05 was considered significant.

RESULTS

CaOx Stimulates the Production of Inflammatory Cytokines in THP-1 Cells

Human monocytic THP-1 cells were exposed to 100, 10, and 1× dose taper of CaOx (**Figure 1**, blue bars), K_2Ox (**Figure 1**, gray bars), or HA (**Figure 1**, orange bars) over a period of 8 h. When exposed to CaOx crystals, THP-1 cells upregulated the expression ($p < 0.05$) of TNFα, IL-1β, IL-8, IL-10, IL-23, and CCL2 (monocyte chemotactic protein-1/MCP-1) in a time and dose-dependent manner (**Figure 1**, blue bars). However, THP-1 cells did not display a dose-dependent response to soluble K_2Ox and showed a rather moderate time-dependent response (**Figure 1**, gray bars). HA failed to stimulate a significant immune response (**Figure 1**, orange bars).

Primary Human Monocytes Respond to CaOx but Not HA

Primary human monocytes were treated with CaOx (**Figure 2**, blue bars) and assayed for expression changes. TNFα, IL-1β, IL-6, IL-8, and CCL2 increased significantly ($p < 0.05$) in monocytes treated with CaOx; however, HA (**Figure 2**, orange bars) had no significant effect. LPS (gray bars) and PBS (UTx, red bars) were used as positive and negative controls, respectively (**Figure 2**).

CaOx Alters Monocytes' Response to LPS Exposure

Primary human monocytes exposed to LPS followed 1 h later by CaOx (**Figure 3**, gray bars) displayed a significant decrease ($p < 0.05$) of TNFα, IL-1β, IL-8, and CCL2 (**Figures 3A,B,D,E**) compared to LPS alone (**Figure 3**, red bars) and CaOx followed by LPS exposure (**Figure 3**, orange bars). Also, CaOx followed by LPS (orange) exposure displayed significantly higher levels of

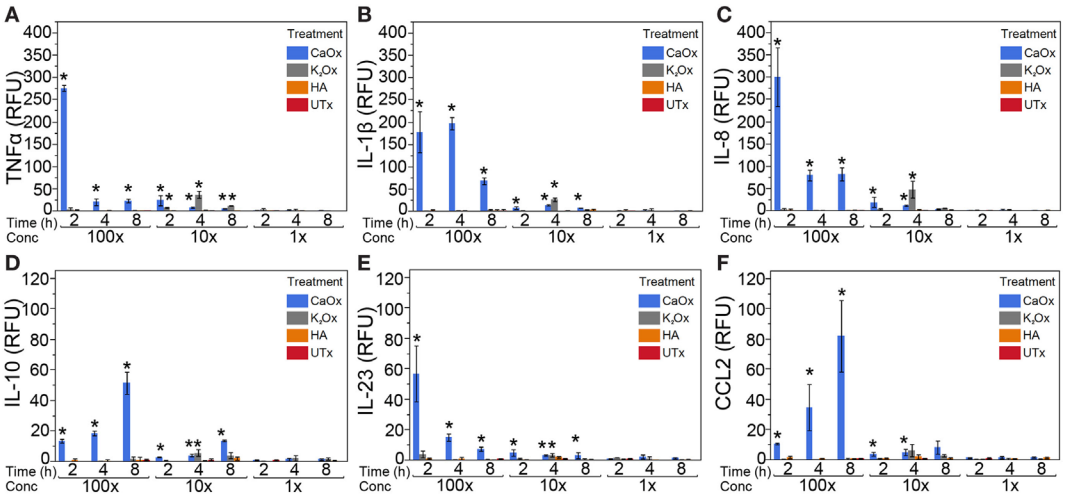

FIGURE 1 | Calcium oxalate (CaOx) induces a dose- and time-dependent expression of inflammatory cytokines in the human monocytic THP-1 cell line. THP-1 cells were treated with molar 100× (7.81 mM, 1,000 μg/ml), 10× (0.78 mM, 100.0 μg/ml), and 1× (0.078 mM, 10.0 μg/ml) CaOx (blue); 100× (6.84 mM, 1,138 μg/ml), 10× (0.68 mM, 113.8 μg/ml), and 1× (0.068 mM, 11.4 μg/ml) potassium oxalate (gray, K_2Ox); 100× (1.99 mM, 1,000 μg/ml), 10× (0.20 mM, 100.0 μg/ml), and 1× (0.020 mM, 10.0 μg/ml l) hydroxyapatite (orange, HA); or untreated controls (red, UTx). Following treatment, cells were incubated for 2, 4, or 8 h. Total RNA was purified from respective cell pellets and analyzed by quantitative real-time PCR for relative fold expression of TNFα **(A)**, IL-1β **(B)**, IL-8 **(C)**, IL-10 **(D)**, IL-23 **(E)**, and CCL2 **(F)**. mRNA expression was normalized with 18s RNA respectively. All results are expressed as relative fold change units (RFU) ± SD from four independent experiments. *$p < 0.05$ compared to UTx.

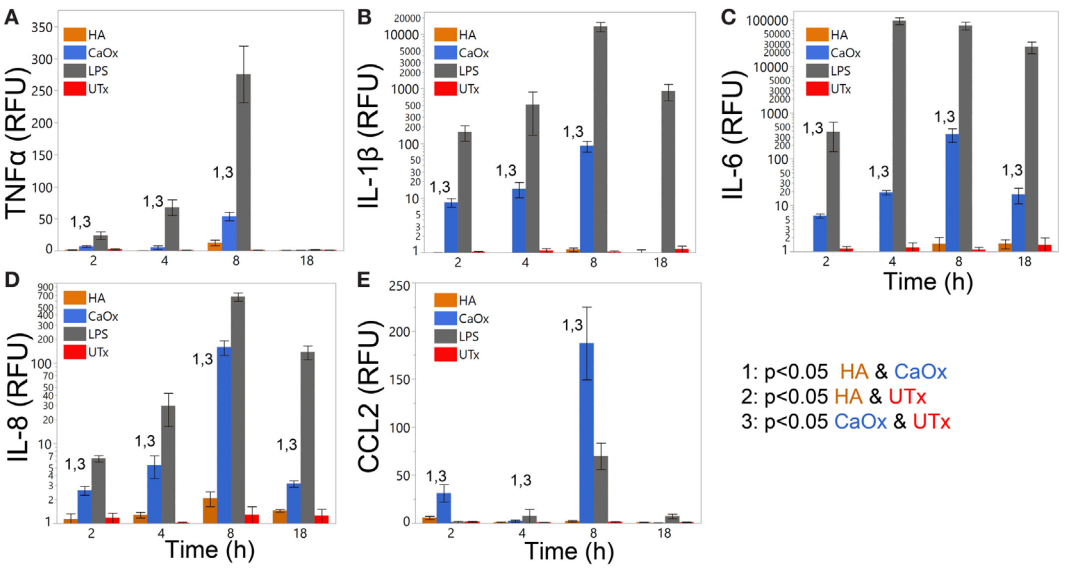

FIGURE 2 | Calcium oxalate (CaOx) but not hydroxyapatite (HA) stimulates proinflammatory cytokine expression in primary human monocytes in a time-dependent manner. Primary human monocytes cells were treated with 1.95 mM (250 μg/ml) CaOx (blue), 0.40 mM (200 μg/ml) HA (orange), 1 μg/ml LPS (gray, positive control), and UTx (red, untreated) and incubated for 2, 4, 8, or 18 h. Total RNA was purified from respective cell pellets and analyzed by quantitative real-time PCR for relative fold expression of TNFα **(A)**, IL-1β **(B)**, IL-6 **(C)**, IL-8 **(D)**, and CCL2 **(E)**. mRNA expression was normalized with 18s RNA respectively. All results are expressed as relative fold change units (RFU) ± SD from four independent experiments. *$p < 0.05$ compared to UTx.

expression for these cytokines and chemokines ($p < 0.05$) than LPS alone (**Figures 3A,B,D,E** red bars). IL-6 appears to be primarily driven by LPS; however, CaOx followed by LPS exposure appears to have a delayed IL-6 response compared to the other LPS exposures (**Figure 3C**).

Monocytes Exposed to CaOx Enhanced M2 Macrophage Uptake of CaOx Crystals

Primary human monocytes were exposed to CaOx, HA, or untreated (UTx) for 24 h. Matched donor primary monocytes were differentiated into M2 macrophages with M-CSF. The

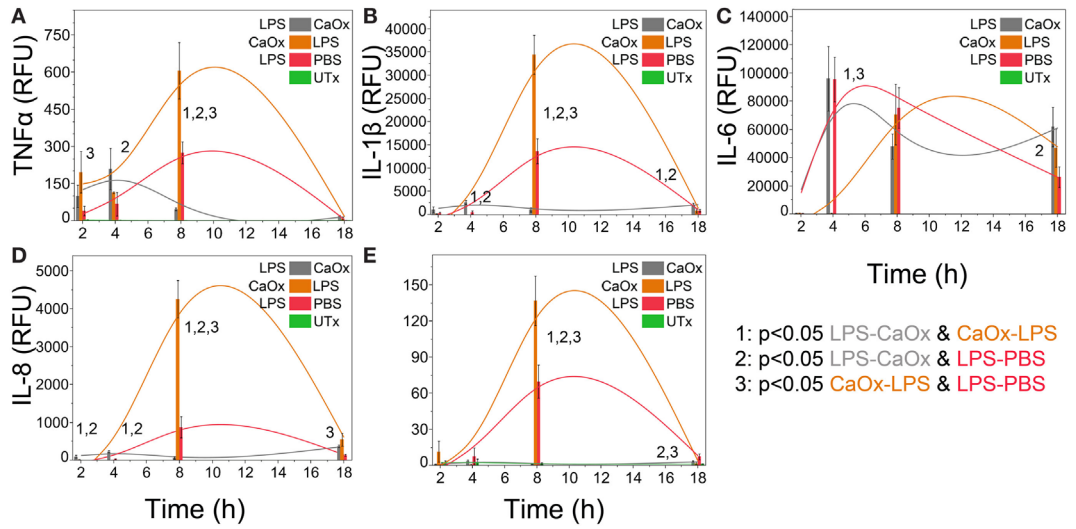

FIGURE 3 | Calcium oxalate (CaOx) upregulates or downregulates inflammatory cytokine expression in monocytes response to LPS depending on order of exposure. Primary human monocytes cells were incubated for 1 h with 500 ng/ml LPS, 1.95 mM (250 μg/ml) CaOx, or PBS. After incubation, monocytes were exposed to 1.95 mM CaOx (gray), 500 ng/ml LPS (orange), or 500 ng/ml LPS (red), respectively and incubated for 2, 4, 8, or 18 h. Untreated samples (UTx, green) only received PBS for both incubations. Total RNA was purified from respective cell pellets and analyzed by quantitative real-time PCR for relative fold expression of TNFα **(A)**, IL-1β **(B)**, IL-6 **(C)**, IL-8 **(D)**, and CCL2 **(E)**. mRNA expression was normalized with 18s RNA respectively. All results are expressed as relative fold change units (RFU) ± SD from four independent experiments. Tukey-Kramer Honest significant difference test was used to determine significance for multiple comparisons.

culture supernatants were transferred to matched donors of primary human M2 macrophages 2 h prior to CaOx exposure (**Figure 4**). Within 1 h of exposure, macrophages (79.0 ± 2.30%) pretreated with supernatant from CaOx-treated monocytes displayed significantly greater uptake than macrophages pretreated with supernatant from HA-treated (17.6 ± 3.50%, $p < 0.0001$) or UTx (9.70 ± 2.31%, $p < 0.0001$) monocytes (**Figure 4**).

Macrophage Differentiation Is Specific to CaOx and Not to K_2Ox or ZnOx

Primary human monocytes were exposed to CaOx over a period of 6 days. At day 3 of CaOx exposure, monocytes stained with HEMA 3 displayed macrophage-like morphology similar to GM-CSF-treated monocytes (**Figure 5A**). To validate CaOx specificity, primary monocytes were exposed to CaOx, K_2Ox, or ZnOx over a period of 6 days (**Figure 5B**). ZnOx did not induce differentiation of primary monocytes; however, some monocytes displayed macrophage-like morphology when exposed to K_2Ox (**Figure 5B**). K_2Ox and UTx displayed a minimal number of macrophages. M-CSF- and GM-CSF-induced macrophages were positive controls and formed M2 and M1 macrophages, respectively.

CaOx Induces Inflammatory M1-Like Macrophage Differentiation and Cytokine/Chemokine Production

Primary human monocytes were again exposed to CaOx over a period of 6 days. M-CSF- and GM-CSF-induced macrophages were positive controls and form M2 and M1 macrophages respectively. CaOx differentiated macrophages and GM-CSF-induced (M1) macrophages were CD86 and CD68 double positive compared to M-CSF induced (M2) macrophages that were double negative (**Figure 6A**). Macrophages were also double stained for CD163 and CD68 or CD206 (mannose receptor) and phosphorylated (p)STAT6. Both CaOx induced and GM-CSF-induced macrophages were negative for CD163, CD206, and pSTAT6; however, M-CSF induced macrophages where positive for all three markers (**Figure 6B**; Figure S1 in Supplementary Material).

CaOx-Induced Macrophages Produce M1-Like Macrophage Cytokine and Chemokine Profiles

M1 marker IL-12 was significantly higher for both CaOx ($p = 0.0051$) and GM-CSF ($p < 0.0001$) induced macrophages compared to M-CSF induction after LPS treatment; M2 marker IL-10 was significantly lower for both CaOx ($p < 0.0001$) and GM-CSF ($p < 0.0001$) induction compared to M-CSF induction (**Figures 7A,B**). After LPS exposure, TNFα ($p = 0.0002$, $p < 0.0001$) and CCL22 ($p < 0.0001$, $p < 0.0001$) were significantly higher in CaOx and GM-CSF-induced macrophages, but significantly lower for IL-6 ($p < 0.0001$, $p < 0.0001$), IFNα2a ($p = 0.0003$, $p = 0.0027$), and IFNβ ($p < 0.0001$, $p < 0.0001$) compared to M-CSF induced macrophages (**Figures 7C,E–H**). For the PBS control, CCL22 ($p = 0.0007$, $p < 0.0001$) and IL-1Ra ($p < 0.0001$, $p < 0.0001$) were significantly higher in CaOx and GM-CSF-induced macrophages (**Figures 7D,E**). INFγ ($p < 0.0001$) was significantly higher in LPS-stimulated GM-CSF-induced macrophages (**Figure 7I**). IL-1β ($p = 0.0055$) significantly lower in LPS-stimulated CaOx-induced macrophages (**Figure 7J**).

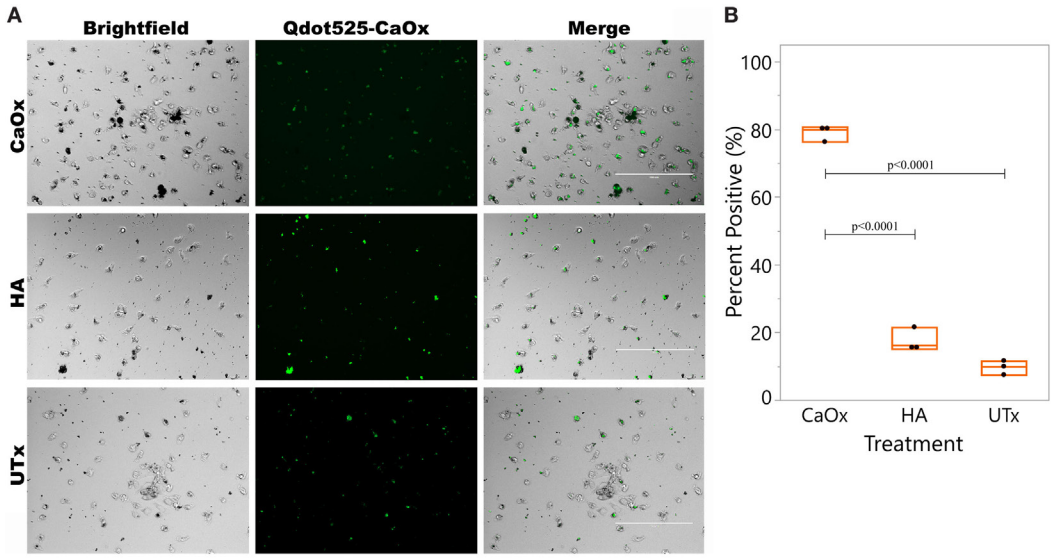

FIGURE 4 | CaOx stimulated monocytes to enhance M2 macrophage uptake of CaOx. **(A)** Primary monocytes were treated with M-CSF for 6 days to differentiate into M2 macrophages. Donor matched monocytes were exposed to 2.50 mM calcium oxalate (CaOx), hydroxyapatite (HA), or untreated (UTx, PBS) and incubated for 24 h. Supernatants from monocytes was transferred to the M2 macrophages and incubated for 2 h. After 2 h, macrophages were exposed to 1.56 mM Qdot525 labeled CaOx and uptake was imaged after 1 h with an Evos FL Auto microscope GFP light cube. **(B)** 79.0 ± 2.30% of macrophages exposed to CaOx supernatant had phagocytosed Qdot525 labeled CaOx compared to 17.6 ± 3.50% of macrophages exposed to HA supernatant ($p < 0.0001$) and 9.70 ± 2.31% of UTx ($p < 0.0001$). Images are representative of $n = 3$ at 20× magnification.

DISCUSSION

Since this study attempts to model crystal and immune cell interactions *in vitro*, a critical appraisal of our methodology is important. First, in order to standardize the exposure of oxalate between the different mineral types, molarity was used. Because CaOx (CaC_2O_4) and K_2Ox ($K_2C_2O_4$) differ in molecular weight, 1,000 μg/ml of CaOx contains a greater number of oxalate molecules than 1,000 μg/ml of K_2Ox. Therefore, to achieve 7.81 mM oxalate using CaOx and K_2Ox, more K_2Ox (1,438 μg/ml) is needed than CaOx (1,000 μg/ml). Second, to control for calcium molecules, molarity (mols of calcium per unit volume) was used. For example, 1 mM HA ($HCa_5O_{13}P_3$) has five times the number of calcium atoms than 1 mM CaOx (CaC_2O_4). Thus, the variations in concentration between experiment and controls are an attempt to control for mineral concentration, so mM and mg/ml values are used when possible.

The biological levels of oxalate vary according to the biological fluid. Serum oxalate in normal individuals range from 0.2 to 10 μmol/l and in renal failure is as high as 89 μmol/liter (5, 22–24). For children with primary hyperoxaluria type 1, serum levels have been reported to be 125.7 μmol/l (25). In the saliva of 41 healthy males and 40 females, oxalate was reported to range from 0.10 ± 0.09 and 0.18 ± 0.17 μM, respectively (26). Oxalate in tartar was reported to be 3.3 ± 1.2 mmol/kg tartar (26). In urine, normal individuals excrete 0.222–0.444 mmol (20–40 mg) of oxalate daily; however, for individuals with primary hyperoxaluria, urinary oxalate excretion is 1.5–3.0 mmols (135–270 mg) per day (27). To establish the optimal response of monocytes to oxalate, we tested a range from as high as 7.81 mM (1,000 μg/ml) to 0.50 mM (64.0 μg/ml) CaOx.

In our *in vitro* model, CaOx crystals stimulate a significant, finely regulated, dose- and time-dependent release of TNFα, IL-1β, IL-6, IL-8, and CCL2 (**Figures 1** and **2**) from both human monocytes and THP-1 cells, similar to the innate immune response seen after LPS or peptidoglycan exposure (18, 28, 29). Consistent with Williams et al. results (17), we also demonstrate IL-6 expression in primary human monocytes (**Figure 2C**, blue bars). THP-1 cells expressed IL-23 and IL-10; however, primary human monocytes did not express IL-23 and IL-10. THP-1 cells are a human monocytic cell line derived from a 1-year-old male with acute monocytic leukemia (30). Though they are similar to primary monocytes, their response can differ. Sintiprungrat et al. reported IFNα expression by U937 human monocytic cells when exposed to CaOx (31). However, THP-1 cells and primary human monocytes did not express IFNα, IFNβ, and IFNγ that could be detected by qPCR (data not shown). Exposing THP-1 cells to K_2Ox did not cause a response (**Figure 1**, gray bars), but over time, K_2Ox precipitated to form CaOx (**Figure 5B**), which was likely responsible for the small THP-1 response noted using 10× concentration (**Figure 1**, gray bars). HA caused no response in THP1 cells (**Figures 1** and **2**, orange bars). Similarly, neither K_2Ox nor ZnOx drove macrophage differentiation compared to CaOx (**Figure 5**); it appears that human monocytes recognize CaOx crystals, but not oxalate or hydroxyapatite.

With the exception of IL-6, the cytokines TNFα and IL-1β, and the chemokines IL-8 and CCL2 have dramatically different responses depending on if the primary human monocytes first

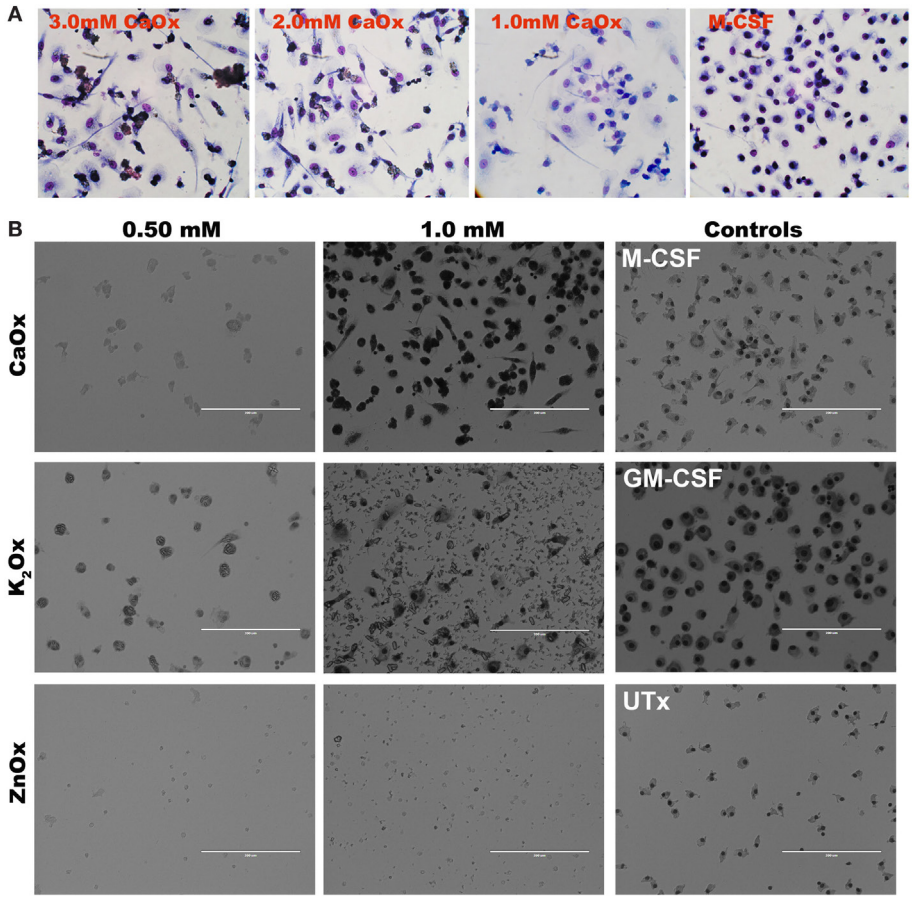

FIGURE 5 | Calcium oxalate (CaOx) induces macrophage-like morphology in 3 days. **(A)** Primary monocytes were exposed to 1.0, 2.0, or 3.0 mM CaOx, or 20 ng/ml M-CSF for 3 days. After day 3, cells were stained with HEMA 3 kit for macrophage morphology. **(B)**. Primary human monocytes were exposed to 0.50 or 1.00 mM of CaOx, potassium oxalate (K_2Ox), or zinc oxalate (ZnOx) and incubated for 6 days. Images are representative of $n = 3$ at 20× magnification.

encountered CaOx or LPS. Monocytes exposed to CaOx followed by LPS (CaOx-LPS, **Figure 3**, orange bars) displayed a greater response than that of LPS alone (**Figure 3**, red bars), suggesting that oxidative stress caused by CaOx enhances toll-like receptor 4 activation in monocytes (32, 33). However, the reverse leads to an unpredicted response: monocytes exposed to LPS followed by CaOx (LPS-CaOx, **Figure 3**, gray bars) display decreased expression of cytokines and chemokines compared to CaOx followed by LPS (**Figure 3**, orange bars) or LPS alone (**Figure 3**, red bars). This type of response resembles LPS tolerance, where low doses of LPS exposure attenuate subsequent responses to higher doses of LPS (18, 28, 29). Li et al. reported that the calcium sensing receptor (CaSR) recognized CaOx in HK-2 cells and promoted crystal adhesion in rat kidneys (34). Kelly et al. reported that the CaSR inhibited LPS activation of NFκB and TNFα secretion in mouse peritoneal macrophages when they were pre-exposed to calcium (35). However, we observed the decreased effect in reverse where the monocytes were pre-exposed to the LPS followed by CaOx (LPS-CaOx). When we exposed primary human monocytes to HA followed by LPS, cytokine and chemokine expression were not affected (data not shown). This may be due to the CaSR only recognizing calcium ions. CaOx and HA are highly insoluble with solubility product constants (Ksp) of 2.7×10^{-9} and 1×10^{-34} respectively. CaOx may act as a type of "binary switch," triggering two different intra-cellular pathways with the same signal. This phenomenon has been reported when monocytes were exposed to monosodium urate (MSU) crystals alone (inflammatory pathways through NALP3) or MSU crystals in the presence of dead cells (sterile inflammatory pathway *via* Clec12a) (36). This unique response may have an important role in the gut. The gut is under a constant burden of LPS and periodic burden of CaOx. Foods such as spinach contain 400–900 mg of oxalate; for example, 100 g of New Zealand spinach is reported to have 736 mg of soluble oxalate and 220 mg of CaOx (37–39). Most of the oxalate absorbed is excreted in the urine, but 10% or less is secreted back into the intestine (40). The LPS-CaOx response would simulate what happens when an individual consumes a food such as spinach where the gut is in constant exposure to LPS and other bacterial ligands and only periodically exposed to high amounts of oxalate. The LPS-CaOx response would be evolutionarily beneficial. The inflammatory response from CaOx or CaOx-LPS would be detrimental and potentially lead to

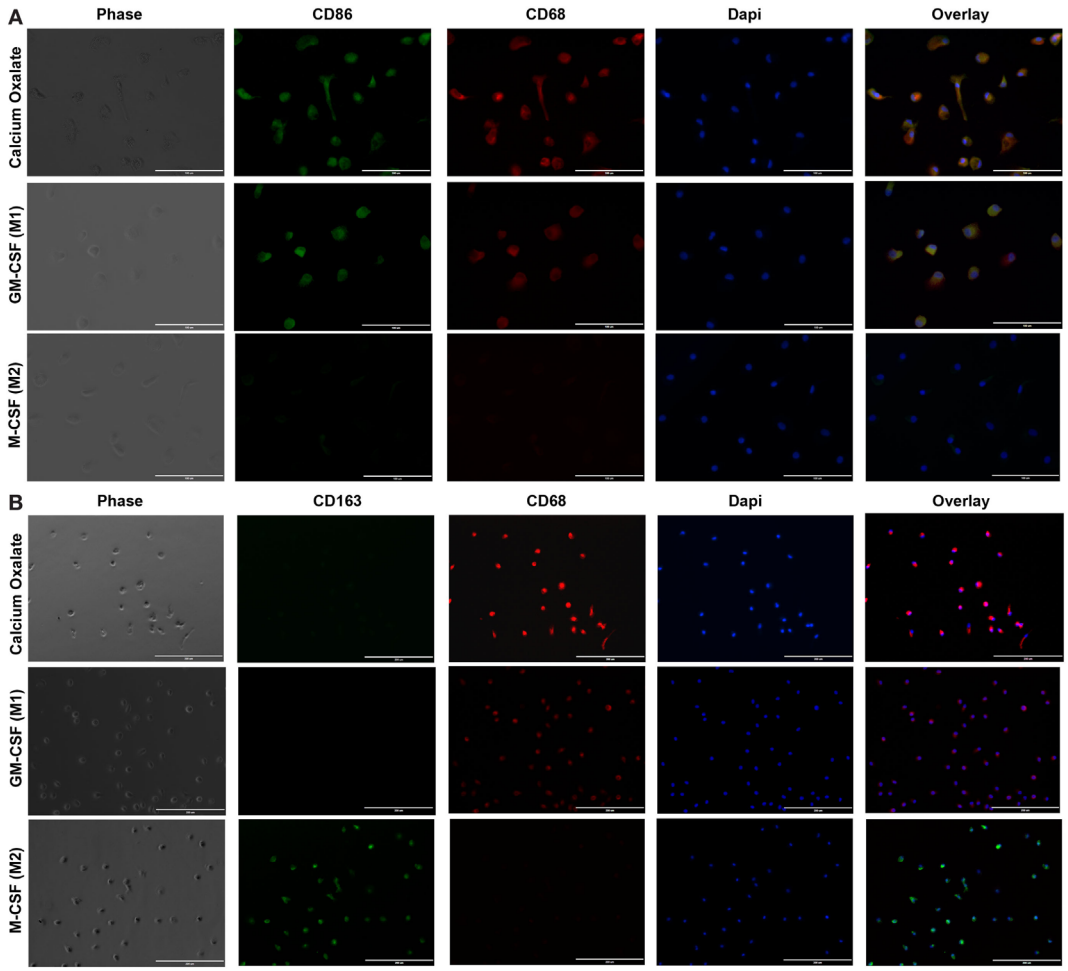

FIGURE 6 | Calcium oxalate (CaOx) induces monocytes to differentiate into inflammatory (M1) macrophages. Primary monocytes were exposed to 1.95 mM CaOx, 20 ng/ml M-CSF (M2 control), or GM-CSF (M1 control) and incubated for 6 days. **(A)** After day 6, cells were fixed and stained with rabbit anti-CD86 (green) and mouse anti-CD68 (red) (40×, bar, 100 μm) or **(B)** double stained with rabbit anti-CD163 (green) and mouse anti-CD68 (red) (20×, bar, 200 μm). Nuclei were counterstained by 4,6-diamidino-2-phenylindole (DAPI, blue). N = 3.

inflammatory bowel disease. It is interesting to note that CaOx stone disease is highly associated with IBD (41–43).

In our experiment, monocytes respond to CaOx by producing inflammatory cytokines, such as tumor necrosis factor-alpha, IL-1β, and IL-6, and chemokines, such as CCL2. These signals activate and recruit circulating monocytes and tissue macrophages to promote CaOx clearance (12). Consistent with our previous work, the supernatant from monocytes previously exposed to CaOx crystals enhanced M2 macrophage phagocytosis of CaOx (**Figure 4**) (12). CaOx alone causes the monocytes to undergo differentiation into macrophages (**Figures 5** and **6**). Since neither K_2Ox nor ZnOx was able to drive differentiation, monocytes likely utilize a receptor that preferentially recognizes the CaOx crystals.

Calcium oxalate and GM-CSF (positive control) macrophages were positive for M1 macrophage markers CD68 and CD86 and negative for M2 markers CD163, CD206, and pSTAT6 (**Figure 6A**; Figure S1 in Supplementary Material). CaOx and GM-CSF produce proinflammatory cytokines IL-12 (M1 signature marker) and TNFα when stimulated with LPS (**Figures 7A,C**). CCL22, regardless of LPS treatment, appears to be an M1 marker and is highly elevated by both GM-CSF and CaOx exposure (**Figure 7E**). The CaOx and GM-CSF-induced macrophages were negative for CD163 (M2 marker) unlike the M-CSF induced macrophages (**Figure 6B**). After LPS stimulation, IL-6, IFNα2a, and IFNβ were significantly higher in the M-CSF induced macrophages than in the CaOx and GM-CSF-induced macrophages (**Figures 7F–H**). IL-1Ra is an antagonist of IL-1α and IL-1β and protects the host from endotoxin-induced injury (44, 45). We have previously shown that IL-1Ra was secreted by M2 macrophages in response to CaOx and human CaOx kidney stones (12). CaOx, GM-CSF, and M-CSF macrophage phenotypes responded to LPS stimulation by producing IL-1Ra; however, IL-1ra was significantly elevated in the unstimulated CaOx and GM-CSF-induced macrophages compared to M-CSF-induced macrophages (**Figure 7D**). IFNγ appears to be specific to LPS-stimulated GM-CSF-induced macrophages (**Figure 7I**). Overall, these results indicate that CaOx-induced macrophages display an M1 macrophage phenotype.

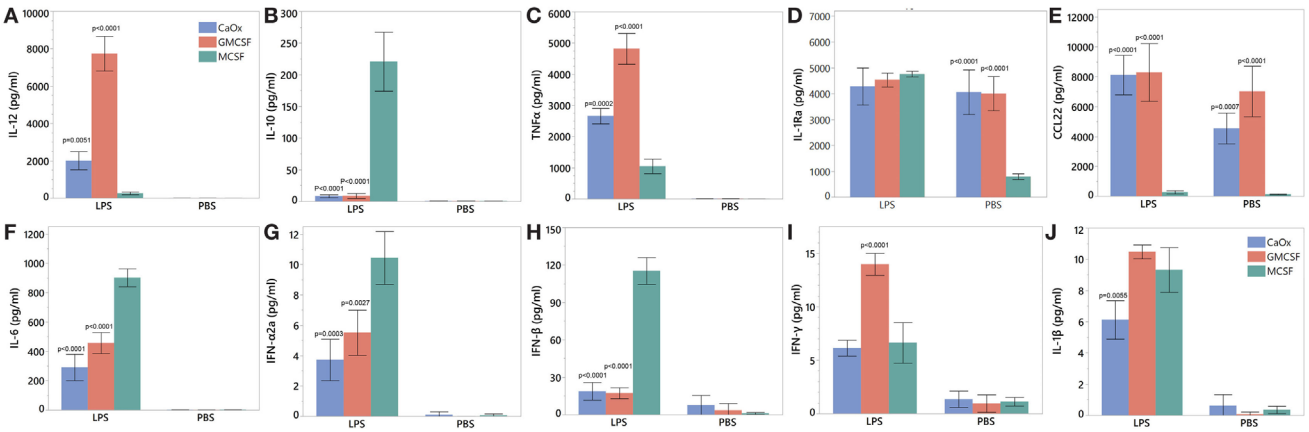

FIGURE 7 | Cytokine profile of calcium oxalate (CaOx)-induced inflammatory (M1) macrophages after stimulation with LPS. Primary monocytes were exposed to 1.95 mM CaOx, 20 ng/ml M-CSF (M2 control), or GM-CSF (M1 control) and incubated for 6 days. At day 6, macrophages were exposed to 1 μg/ml LPS or PBS (control) and incubated for 24 h. Supernatant was collected at 24 h and for IL-12 **(A)**, IL-10 **(B)**, TNFα **(C)**, IL-6 **(D)**, IL22 **(E)**, interleukin 1 receptor antagonist **(F)**, interferon alpha 2a **(G)**, interferon beta **(H)**, interferon gamma **(I)**, and IL-1β **(J)** protein analysis using Meso Scale Discovery U-Plex (10 multiplex) ELISA. All results are expressed as pg/ml ± SD from four independent experiments. *$p < 0.05$ compared to M-CSF.

CONCLUSION

Human monocytes and human monocyte cell lines respond in a specific manner to the CaOx crystal, eliciting a local, tissue inflammatory response that drives M1 macrophage differentiation. This response was not seen after exposure to hydroxyapatite crystals or various oxalate controls. The unique and opposite response of monocytes to LPS-CaOx and CaOx-LPS appears to indicate the existence of CaOx receptor with a binary switch function, similar to what has been described for MSU receptors. Prolong exposure to CaOx induces monocytes to differentiate into M1 macrophages. Further investigation into the signaling mechanism is needed.

HUMAN AND ANIMAL RIGHTS

Following institutional review board approval, human buffy coat samples were purchased from LifeSouth Community Blood Centers. Buffy coats were received de-identified without any donor information. No animals were used for this study.

CONSENT FORM

Following institutional review board approval, this study did not require a consent form, since no human donors were recruited for this study.

AUTHOR CONTRIBUTIONS

PD-G: project development, data collection, data analysis, manuscript writing, and manuscript editing. SK: project development and manuscript editing. BC: project development and manuscript editing. SRK: project development and manuscript editing.

FUNDING

PD-G is a recipient of the 2016–2018 Urology Care Foundation Research Scholar Award. NIDDK T32DK094789 supported PD-G and this research.

SUPPLEMENTARY MATERIAL

The Supplementary Material for this article can be found online at https://www.frontiersin.org/articles/10.3389/fimmu.2018.01863/full#supplementary-material.

FIGURE S1 | Calcium oxalate (CaOx) induced macrophages lack M2 macrophage markers phosphorylated STAT6 and CD206. CaOx- and GM-CSG-induced macrophages were negative for M2 macrophage markers pSTAT6 and CD206. M-CSF macrophages were positive for both pSTAT6 and CD206. Cells were fixed and stained with rabbit anti-pSTAT6 (green) and mouse anti-CD206 (red) (40×, bar, 100 μm). Nuclei were counterstained by 4,6-diamidino-2-phenylindole (DAPI, blue). $N = 3$.

REFERENCES

1. Fink HA, Wilt TJ, Eidman KE, Garimella PS, MacDonald R, Rutks IR, et al. Medical management to prevent recurrent nephrolithiasis in adults: a systematic review for an American College of Physicians Clinical Guideline. *Ann Intern Med* (2013) 158:535–43. doi:10.7326/0003-4819-158-7-201304020-00005
2. Litwin MS, Saigal CS, editors. Economic impact of urologic disease. *Urologic Diseases in America*. (Chap. 14), US Department of Health and Human Services, Public Health Service, National Institutes of Health, National Institute of Diabetes and Digestive and Kidney Diseases. Washington, DC: US Government Printing Office (2012). NIH Publication No. 12-7865. p. 463–96.
3. Danpure CJ, Rumsby G. Molecular aetiology of primary hyperoxaluria and its implications for clinical management. *Expert Rev Mol Med* (2004) 6:1–16. doi:10.1017/S1462399404007203
4. Cochat P, Rumsby G. Primary hyperoxaluria. *N Engl J Med* (2013) 369:649–58. doi:10.1056/NEJMra1301564
5. Hoppe B, Beck BB, Milliner DS. The primary hyperoxalurias. *Kidney Int* (2009) 75:1264–71. doi:10.1038/ki.2009.32
6. Hoppe B, Kemper MJ, Bökenkamp A, Langman CB. Plasma calcium-oxalate saturation in children with renal insufficiency and in children with primary hyperoxaluria. *Kidney Int* (1998) 54:921–5. doi:10.1046/j.1523-1755.1998.00066.x

7. Evan AP, Lingeman JE, Worcester EM, Bledsoe SB, Sommer AJ, Williams JC, et al. Renal histopathology and crystal deposits in patients with small bowel resection and calcium oxalate stone disease. *Kidney Int* (2010) 78:310–7. doi:10.1038/ki.2010.131
8. Khan SR, Finlayson B, Hackett RL. Experimental calcium oxalate nephrolithiasis in the rat. Role of the renal papilla. *Am J Pathol* (1982) 107:59–69.
9. Gokhale JA, Glenton PA, Khan SR. Characterization of Tamm-Horsfall protein in a rat nephrolithiasis model. *J Urol* (2001) 166:1492–7. doi:10.1016/S0022-5347(05)65818-1
10. Taguchi K, Hamamoto S, Okada A, Unno R, Kamisawa H, Naiki T, et al. Genome-wide gene expression profiling of Randall's plaques in calcium oxalate stone formers. *J Am Soc Nephrol* (2017) 28:333–47. doi:10.1681/ASN.2015111271
11. Wynn TA, Chawla A, Pollard JW. Macrophage biology in development, homeostasis and disease. *Nature* (2013) 496:445–55. doi:10.1038/nature12034
12. Kusmartsev S, Dominguez-Gutierrez PR, Canales BK, Bird VG, Vieweg J, Khan SR. Calcium oxalate stone fragment and crystal phagocytosis by human macrophages. *J Urol* (2016) 195:1143–51. doi:10.1016/j.juro.2015.11.048
13. Okada A, Hamamoto S, Taguchi K, Unno R, Sugino T, Ando R, et al. Kidney stone formers have more renal parenchymal crystals than non-stone formers, particularly in the papilla region. *BMC Urol* (2018) 18:19. doi:10.1186/s12894-018-0331-x
14. Okada A, Yasui T, Fujii Y, Niimi K, Hamamoto S, Hirose M, et al. Renal macrophage migration and crystal phagocytosis via inflammatory-related gene expression during kidney stone formation and elimination in mice: detection by association analysis of stone-related gene expression and microstructural observation. *J Bone Miner Res* (2010) 25:2701–11. doi:10.1002/jbmr.158
15. Taguchi K, Okada A, Hamamoto S, Unno R, Moritoki Y, Ando R, et al. M1/M2-macrophage phenotypes regulate renal calcium oxalate crystal development. *Sci Rep* (2016) 6:35167. doi:10.1038/srep35167
16. Taguchi K, Okada A, Kitamura H, Yasui T, Naiki T, Hamamoto S, et al. Colony-stimulating factor-1 signaling suppresses renal crystal formation. *J Am Soc Nephrol* (2014) 25:1680–97. doi:10.1681/ASN.2013060675
17. Williams J, Holmes RP, Assimos DG, Mitchell T. Monocyte mitochondrial function in calcium oxalate stone formers. *Urology* (2016) 93:.e1–6. doi:10.1016/j.urology.2016.03.004
18. Nahid MA, Satoh M, Chan EKL. Mechanistic role of microRNA-146a in endotoxin-induced differential cross-regulation of TLR signaling. *J Immunol* (2011) 186:1723–34. doi:10.4049/jimmunol.1002311
19. Nahid MA, Satoh M, Chan EK. MicroRNA in TLR signaling and endotoxin tolerance. *Cell Mol Immunol* (2011) 8:388–403. doi:10.1038/cmi.2011.26
20. Pauley KM, Satoh M, Pauley BA, Dominguez-Gutierrez PR, Wallet SM, Holliday LS, et al. Formation of GW/P bodies as marker for microRNA-mediated regulation of innate immune signaling in THP-1 cells. *Immunol Cell Biol* (2010) 88:205–12. doi:10.1038/icb.2009.84
21. Taganov KD, Boldin MP, Chang K-J, Baltimore D. NF-kappaB-dependent induction of microRNA miR-146, an inhibitor targeted to signaling proteins of innate immune responses. *Proc Natl Acad Sci U S A* (2006) 103:12481–6. doi:10.1073/pnas.0605298103
22. Worcester EM, Nakagawa Y, Bushinsky DA, Coe FL. Evidence that serum calcium oxalate supersaturation is a consequence of oxalate retention in patients with chronic renal failure. *J Clin Invest* (1986) 77:1888–96. doi:10.1172/JCI112516
23. Hoppe B, Leumann E. Diagnostic and therapeutic strategies in hyperoxaluria: a plea for early intervention. *Nephrol Dial Transplant* (2004) 19:39–42. doi:10.1093/ndt/gfg507
24. Hönow R, Simon A, Hesse A. Interference-free sample preparation for the determination of plasma oxalate analyzed by HPLC-ER: preliminary results from calcium oxalate stone-formers and non-stone-formers. *Clin Chim Acta* (2002) 318:19–24. doi:10.1016/S0009-8981(01)00729-X
25. Hoppe B, Kemper MJ, Bökenkamp A, Portale AA, Cohn RA, Langman CB. Plasma calcium oxalate supersaturation in children with primary hyperoxaluria and end-stage renal failure. *Kidney Int* (1999) 56:268–74. doi:10.1046/j.1523-1755.1999.00546.x
26. Wahl R, Kallee E. Oxalic acid in saliva, teeth and tooth tartar. *Clin Chem Lab Med* (1994) 32:821–5. doi:10.1515/cclm.1994.32.11.821
27. Coe FL, Parks JH, Asplin JR. The pathogenesis and treatment of kidney stones. *N Engl J Med* (1992) 327:1141–52. doi:10.1056/NEJM199210153271607
28. Ceribelli A, Yao B, Dominguez-Gutierrez PR, Nahid MA, Satoh M, Chan EKL. MicroRNAs in systemic rheumatic diseases. *Arthritis Res Ther* (2011) 13:229. doi:10.1186/ar3377
29. Nahid MA, Yao B, Dominguez-Gutierrez PR, Kesavalu L, Satoh M, Chan EKL. Regulation of TLR2-mediated tolerance and cross-tolerance through IRAK4 modulation by miR-132 and miR-212. *J Immunol* (2013) 190:1250–63. doi:10.4049/jimmunol.1103060
30. Tsuchiya S, Yamabe M, Yamaguchi Y, Kobayashi Y, Konno T, Tada K. Establishment and characterization of a human acute monocytic leukemia cell line (THP-1). *Int J Cancer* (1980) 26:171–6. doi:10.1002/ijc.2910260208
31. Sintiprungrat K, Singhto N, Thongboonkerd V. Characterization of calcium oxalate crystal-induced changes in the secretome of U937 human monocytes. *Mol Biosyst* (2016) 12:879–89. doi:10.1039/c5mb00728c
32. Tawadros PS, Powers KA, Ailenberg M, Birch SE, Marshall JC, Szaszi K, et al. Oxidative stress increases surface toll-like receptor 4 expression in murine macrophages via ceramide generation. *Shock* (2015) 44:157–65. doi:10.1097/SHK.0000000000000392
33. Powers KA, Szászi K, Khadaroo RG, Tawadros PS, Marshall JC, Kapus A, et al. Oxidative stress generated by hemorrhagic shock recruits toll-like receptor 4 to the plasma membrane in macrophages. *J Exp Med* (2006) 203:1951–61. doi:10.1084/jem.20060943
34. Li X, Ma J, Shi W, Su Y, Fu X, Yang Y, et al. Calcium oxalate induces renal injury through calcium-sensing receptor. *Oxid Med Cell Longev* (2016) 2016:5203801. doi:10.1155/2016/5203801
35. Kelly JC, Lungchukiet P, Macleod RJ. Extracellular calcium-sensing receptor inhibition of intestinal EpithelialTNF signaling requires CaSR-mediated Wnt5a/Ror2 interaction. *Front Physiol* (2011) 2:17. doi:10.3389/fphys.2011.00017
36. Neumann K, Castiñeiras-Vilariño M, Höckendorf U, Hannesschläger N, Lemeer S, Kupka D, et al. Clec12a is an inhibitory receptor for uric acid crystals that regulates inflammation in response to cell death. *Immunity* (2014) 40:389–99. doi:10.1016/j.immuni.2013.12.015
37. Brogren M, Savage GP. Bioavailability of soluble oxalate from spinach eaten with and without milk products. *Asia Pac J Clin Nutr* (2003) 12:219–24.
38. Massey LK. Food oxalate: factors affecting measurement, biological variation, and bioavailability. *J Am Diet Assoc* (2007) 107:1191–4; quiz 1195. doi:10.1016/j.jada.2007.04.007
39. Holmes RP, Assimos DG. The impact of dietary oxalate on kidney stone formation. *Urol Res* (2004) 32:311–6. doi:10.1007/s00240-004-0437-3
40. Holmes RP, Knight J, Assimos DG. Lowering urinary oxalate excretion to decrease calcium oxalate stone disease. *Urolithiasis* (2016) 44:27–32. doi:10.1007/s00240-015-0839-4
41. Fagagnini S, Heinrich H, Rossel J-B, Biedermann L, Frei P, Zeitz J, et al. Risk factors for gallstones and kidney stones in a cohort of patients with inflammatory bowel diseases. *PLoS One* (2017) 12:e0185193. doi:10.1371/journal.pone.0185193
42. Cury DB, Moss AC, Schor N. Nephrolithiasis in patients with inflammatory bowel disease in the community. *Int J Nephrol Renovasc Dis* (2013) 6:139–42. doi:10.2147/IJNRD.S45466
43. da Silva Gaspar SR, Mendonça T, Oliveira P, Oliveira T, Dias J, Lopes T. Urolithiasis and Crohn's disease. *Urol Ann* (2016) 8:297–304. doi:10.4103/0974-7796.184879
44. Arend WP, Malyak M, Guthridge CJ, Gabay C. Interleukin-1 receptor antagonist: role in biology. *Annu Rev Immunol* (1998) 16:27–55. doi:10.1146/annurev.immunol.16.1.27
45. Arend WP. The balance between IL-1 and IL-1Ra in disease. *Cytokine Growth Factor Rev* (2002) 13:323–40. doi:10.1016/S1359-6101(02)00020-5

Conflict of Interest Statement: The authors declare that the research was conducted in the absence of any commercial or financial relationships that could be construed as a potential conflict of interest.

frontiers in Immunology

ORIGINAL RESEARCH
published: 25 September 2018
doi: 10.3389/fimmu.2018.02173

The Long Pentraxin PTX3 Is an Endogenous Inhibitor of Hyperoxaluria-Related Nephrocalcinosis and Chronic Kidney Disease

Julian A. Marschner[1†], Shrikant R. Mulay[1†], Stefanie Steiger[1], Lidia Anguiano[1], Zhibo Zhao[1], Peter Boor[2], Khosrow Rahimi[3], Antonio Inforzato[4,5], Cecilia Garlanda[4,5], Alberto Mantovani[4,5] and Hans-Joachim Anders[1]*

[1] Nephrologisches Zentrum, Medizinische Klinik und Poliklinik IV, Klinikum der Universität München, Munich, Germany, [2] Department of Nephrology, Institute of Pathology, RWTH University of Aachen, Aachen, Germany, [3] DWI-Leibniz Institute for Interactive Materials, Aachen, Germany, [4] Department of Inflammation and Immunology, Humanitas Clinical and Research Center, Rozzano, Italy, [5] Department of Biomedical Sciences, Humanitas University, Pieve Emanuele, Italy

The long pentraxin 3 (PTX3) exerts a variety of regulatory functions in acute and chronic tissue inflammation. In particular, PTX3 acts as an opsonin for a variety of pathogens and endogenous particles. We hypothesized that PTX3 would exhibit opsonin-like functions toward calcium oxalate crystals, too, and inhibit crystal growth. This process is fundamental in kidney stone disease as well as in hyperoxaluria-related nephrocalcinosis, the paradigmatic cause of chronic kidney disease (CKD) in children with primary hyperoxaluria type I due to genetic defects in oxalate metabolism. Direct effects of PTX3 on calcium oxalate crystals were investigated *in chemico* by adding recombinant PTX3 to supersaturated calcium and oxalate solutions. PTX3, but not isomolar concentrations of albumin, dose-dependently inhibited crystal growth. *In vivo*, the PTX3 protein was undetectable in tubular epithelial cells and urine of wild-type mice under physiological conditions. However, its levels increased within 3 weeks of feeding an oxalate-rich diet, an exposure inducing hyperoxaluria-related nephrocalcinosis and CKD in selected mouse strains (male and female C57BL/6N and male Balb/c mice) but not in others (male and female 129SV and CD-1, male and female Balb/c mice). Genetic ablation of *ptx3* in nephrocalcinosis un-susceptible B6;129 mice was sufficient to raise the oxalate nephropathy phenotype observed in susceptible strains. We conclude that PTX3 is an endogenous inhibitor of calcium oxalate crystal growth. This mechanism limits hyperoxaluria-related nephrocalcinosis, e.g., in primary or secondary hyperoxaluria, and potentially also in the more prevalent kidney stone disease.

Keywords: kidney stone, colic, hyperoxaluria, crystals, nephrolithiasis, urolithiasis, PTX3

OPEN ACCESS

Edited by:
Uday Kishore, Brunel University London, United Kingdom

Reviewed by:
Robert Braidwood Sim, University of Oxford, United Kingdom
Lubka T. Roumenina, INSERM U1138 Centre de Recherche des Cordeliers, France

***Correspondence:**
Hans-Joachim Anders
hjanders@med.uni-muenchen.de

[†]These authors have contributed equally to this work

Specialty section:
This article was submitted to Molecular Innate Immunity, a section of the journal Frontiers in Immunology

Received: *30 April 2018*
Accepted: *03 September 2018*
Published: *25 September 2018*

Citation:
Marschner JA, Mulay SR, Steiger S, Anguiano L, Zhao Z, Boor P, Rahimi K, Inforzato A, Garlanda C, Mantovani A and Anders H-J (2018) The Long Pentraxin PTX3 Is an Endogenous Inhibitor of Hyperoxaluria-Related Nephrocalcinosis and Chronic Kidney Disease. Front. Immunol. 9:2173. doi: 10.3389/fimmu.2018.02173

INTRODUCTION

Pentraxins are immunoregulatory acute phase proteins induced upon disruption of homeostasis (1). The short pentraxins, C-reactive protein and serum amyloid P are synthesized in hepatocytes in response to IL-6. C-reactive protein and serum amyloid P act as opsonins binding to a number of microorganisms, dead cells, and other particles to facilitate complement–mediated killing or phagocytosis (2). As opposed to the short pentraxins, the long pentraxin PTX3 is locally produced and released at sides of infection and inflammation by several immune and non-immune cells, including neutrophils, macrophages, myeloid dendritic, endothelial and epithelial cells in response to inflammatory cytokines (i.e., IL-1β and TNF-α) and Toll-like receptor agonists (3, 4). Importantly, expression of PTX3 has been documented in the murine uroepithelium during uropathogenic *E. coli* (UPEC) infections, where it enhances phagocytosis of UPEC by innate immune cells (5). Indeed, amongst the numerous immunoregulatory functions of this pentraxin, recognition of extracellular particles (i.e., microbial moieties) and promotion of their phagocytosis by macrophages, neutrophils and dendritic cells are fundamental opsonic activities (6–10).

Some extracellular particles are of crystalline nature and account for a broad spectrum of acute and chronic diseases (11). Numerous studies show that the cellular arm of the immune system handles crystalline and non-crystalline extracellular particles in a similar way, however little is known regarding the role of humoral immune elements in the recognition and control of crystalline particles (12–14). Here we focus on the interaction of PTX3 with calcium oxalate (CaOx) crystals. CaOx stones account for the vast majority of calculi in kidney stone disease, i.e., nephro- and urolithiasis, affecting around 12% of men and 5% of women during their lifetime (15). In addition, intrarenal CaOx crystal retention causes nephrocalcinosis, a state that is usually asymptomatic but can lead to progressive nephron loss and chronic kidney disease (CKD), especially in rare genetic forms of hyperoxaluria (15, 16). The traditional pathogenic concept of nephrolithiasis and nephrocalcinosis is based on urine supersaturation of minerals or on the lack of sufficient crystallization inhibitors (17–19). Intratubular microcrystals adhere to the luminal membrane of tubular epithelial cells via a group of adhesion molecules (20–28). Adherent microcrystals grow by apposition of minerals and ultimately form crystal plugs obstructing tubules followed by nephron atrophy, interstitial inflammation and fibrosis with loss of renal excretory function, i.e., CKD (16, 29, 30).

Serum proteins, such as albumin as well as plasma fractions containing alpha-globulins and beta-globulins inhibit CaOx crystal aggregation via a variety of mechanisms (31, 32). We recently observed that also the humoral immune effector and opsonin immunoglobulin G inhibits CaOx crystal growth *in vitro* (33). Because of their high molecular weight neither albumin nor IgG pass the filtration barrier and are therefore not constituents of the glomerular ultrafiltrate or urine in healthy individuals and stone formers. We therefore hypothesized that an opsonin, such as PTX3, which is likely expressed by tubular epithelial cells (i.e., beyond the renal filtration barrier) and, therefore, directly released into the urine (5), may act as an endogenous inhibitor of CaOx crystal aggregation inside renal tubules. Thereby PTX3 might limit nephrocalcinosis during hyperoxaluria, a hypothesis that is supported by the evidence presented and discussed in this study.

RESULTS

Recombinant Human PTX3 Inhibits Supersaturation-Induced CaOx Crystal Aggregation

To test our hypothesis, we first added increasing doses of recombinant human PTX3 or equimolar concentrations of bovine serum albumin (BSA) to a supersaturated solution of sodium oxalate and calcium chloride. The crystal preparation was optimized to produce calcium oxalate monohydrate crystals, since this species is mostly found in human oxalate kidney stones (34, 35). Calcium oxalate monohydrate crystal formation was confirmed by phase contrast microscopy and the crystal size was assessed by digital morphometry 24 h later. PTX3, but not bovine serum albumin, dose-dependently reduced crystal size statistically significantly from a concentration of 100 nM or higher (**Figures 1A,B**). The effect of rhPTX3 on calcium oxalate crystal size distribution and, for comparison, that of equimolar concentrations of BSA were confirmed by flow cytometry based on intensity of the forward scatter signal from CaOx monohydrate crystals (**Figures 1C,D**). Noteworthy, the reported inhibitory effects of human albumin on kidney stone formation rely on a different mechanism, which favors generation of di- and trihydrate forms of calcium oxalate crystals (36). Both types of crystals adhere poorly to the luminal membrane of tubular epithelial cells and are flushed out more easily (25). Hence we conclude that the long pentraxin PTX3 inhibits aggregation and growth of CaOx monohydrate crystals *in vitro* at nanomolar concentrations in a dose-dependent manner.

Hyperoxaluria-Induced Nephrocalcinosis Is Associated With Tubular PTX3 Secretion

The human PTX3 is a 381 amino acid glycoprotein with a predicted molecular weight of 40.165 Da. However, the recombinant protein runs in SDS-PAGE gels at an apparent MW of ∼45 kDa, due to N-linked glycosylation at Asn220 (37, 38). The functional PTX3 molecule is an homo-oligomer that comprises eight identical protomer subunits (i.e., octamer) with a total MW of ∼340 kDa (39, 40), which would most likely prevent circulating PTX3 from passing the glomerular filtration barrier and reaching the urine (40). PTX3 is expressed by the murine uroepithelium during UPEC infections, and has been described in the bladder of patients with urinary tract infections (UTIs) (5), however expression of this pentraxin in the human uroepithelium has not been documented yet. Therefore, before assessing the role of PTX3 on CaOx crystal growth *in vivo*, we first examined whether renal epithelial cells express PTX3 and excrete it into the urine. The human protein atlas (41, 42) reports no baseline expression of PTX3 mRNA in four human renal epithelial cell lines (HEK293, NTERA-2, PC-3, RPTEC-TERT1, data available at https://www.proteinatlas.org/

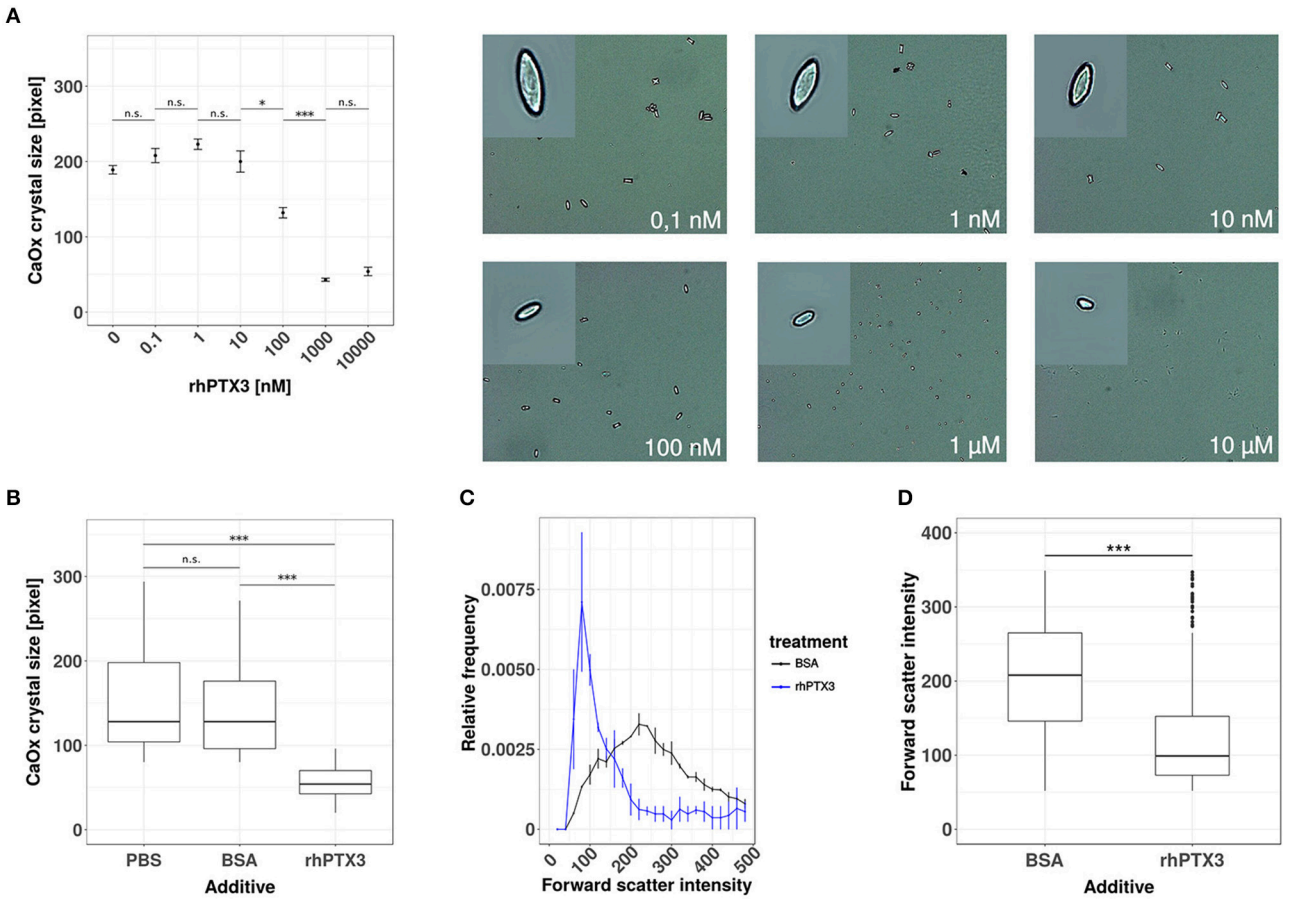

FIGURE 1 | Recombinant human PTX3 inhibits supersaturation-induced CaOx crystal aggregation. **(A)** Calcium oxalate crystals were generated *in chemico* in the presence of increasing concentrations of rhPTX3 and crystal size was measured microscopically 24 h later. **(B)** The effect of 1 μM rhPTX3 on microscopically measured calcium oxalate crystal size was compared to equimolar bovine serum albumin (BSA) and PBS. **(C,D)** Calcium oxalate crystals generated in the presence of 1 μM BSA or equimolar rhPTX3 were compared for their forward scatter (FSC) signal intensity by flow cytometry and displayed for **(C)** relative frequency of FSC and **(D)** overall FSC intensity. Data are from three independent experiments and represent means ± SEM in **(A)**. n.s., not significant; $^{*}p < 0.05$, $^{***}p < 0.001$ between groups as indicated.

ENSG00000163661-PTX3/cell), no epithelial PTX3 positivity using immunohistochemistry in healthy kidney samples from three different donors (data available at https://www.proteinatlas.org/ENSG00000163661-PTX3/tissue/kidney#imid_18912581) and reports negative staining results in 12 renal cell carcinoma samples (data available at https://www.proteinatlas.org/ENSG00000163661-PTX3/ pathology). Consistent with this scenario in humans and previous findings in mice (5), no staining was observed for PTX3 in the kidney of normal mice. However, a remarkable induction of tubular PTX3 expression was apparent upon feeding mice an oxalate-rich diet (**Figure 2A**). Specificity of the immunostaining was validated using an identical staining protocol on renal sections of *Ptx3*-deficient mice (**Figure 2A**). Consistent with these findings, western blot analyses of urine samples from healthy mice on normal chow diet could not detect the PTX3 protein, whereas those performed on mice with diet-induced hyperoxaluria clearly showed it in the urine (**Figure 2B**). Thus, renal tubular cells have the capacity to express PTX3 and secrete it into the urine, e.g., during hyperoxaluria.

Lack of PTX3 Induces Hyperoxaluria-Induced Nephrocalcinosis in Non-susceptible B6;129SV Mice

Having shown that PTX3 is present in the urine during hyperoxaluria, we sought to design an experiment that could examine its putative role as an inhibitor of CaOx crystallization. We selected the B6;129-Ptx3^{tm1Mant} mice that has global PTX3-deficiency to unravel the role of this pentraxin in CaOx crystal aggregation-related disease, i.e., in a model resembling the kidney phenotype of primary hyperoxaluria type I or other forms of progressive nephrocalcinosis. *Ptx3*$^{-/-}$ or *Ptx3*$^{+/+}$ littermates from heterozygous breeders were fed with a sodium oxalate-rich diet for 3 weeks. Despite the equal induction of hyperoxaluria in both genotypes (**Figure 3A**), only the *Ptx3*-deficient mice developed a nephrocalcinosis (**Figures 3B,C**). X-ray diffraction on pulverized and freeze dried murine *Ptx3*$^{-/-}$ kidney tissue, that were fed for 3 weeks with oxalate chow, confirmed the presence of calcium oxalate monohydrate crystals in the kidneys,

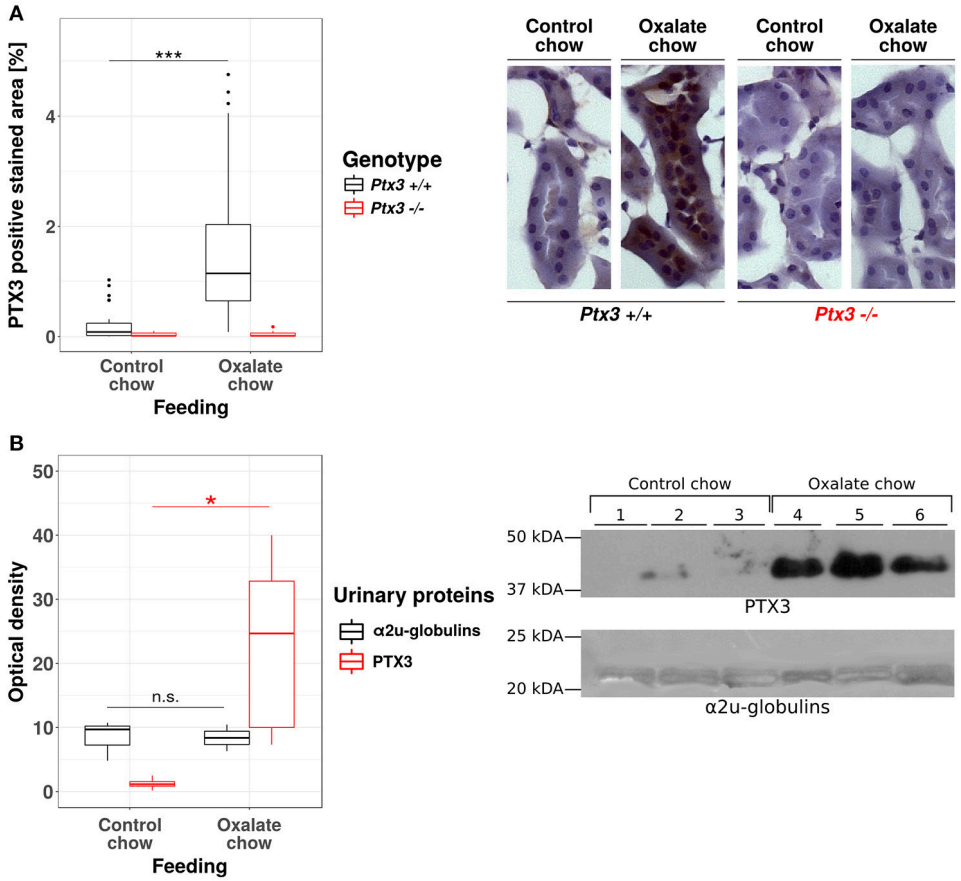

FIGURE 2 | Hyperoxaluria-induced nephrocalcinosis is associated with tubular PTX3 secretion. Female PTX3-competent ($Ptx3^{+/+}$) and -deficient ($Ptx3^{-/-}$) animals with 10–12 weeks of age received either control or oxalate chow for 3 weeks ($n = 5$). **(A)** Tubular expression of PTX3 was analyzed by immunohistochemical staining in frozen kidney sections and quantified as positive stained area per section in percent. **(B)** Detection of PTX3 in whole urine samples by immunoblotting (25 µg protein/lane, upper right). Ponceau Red staining shows major urinary proteins (mainly a2u-globulins, ~20 kDa, lower right) as a loading control. Optical density of the immunoreactive and Ponceau Red stained bands was quantified by ImageJ (NIH, Bethesda, MD). Data are from two independent experiments. n.s., not significant; $^{*}p < 0.05$, $^{***}p < 0.001$ between groups as indicated.

as judged based on the diffraction angle pattern (**Figure 3D**). Therefore, the B6;129 mice were not susceptible *per se* to hyperoxaluria-induced nephrocalcinosis, however deletion of the *ptx3* gene was sufficient to induce nephrocalcinosis in these animals, thus rendering them similar to other strains that are prone to nephrocalcinosis (43).

Lack of PTX3 Induces Hyperoxaluria-Induced Progressive CKD in Non-susceptible B6;129 Mice

A detailed phenotype analysis revealed profound and progressive nephrocalcinosis-related tubular injury in Periodic acid-Schiff (PAS)-stained kidney sections (**Figures 4A,B**) with CaOx crystal plugs (**Figure 4C**) in dilated tubules in $Ptx3^{-/-}$ but not in $Ptx3^{+/+}$ B6;129 mice. Tissue remodeling was further obvious from diffuse cortical and medullary interstitial fibrosis as indicated by interstitial positivity for smooth muscle actin (**Figures 4D,E**). Diffuse interstitial leukocyte infiltrates as assessed by flow cytometry from whole kidney homogenates (**Figure 4F**) indicated ongoing inflammatory processes. Finally, renal excretory function was assessed by measuring glomerular filtration rate (GFR) in awake and unrestrained mice using FITC-sinistrin injection and quantifying vascular FITC clearance kinetics with a transdermal detector (**Figure 4G**). $Ptx3^{-/-}$ and $Ptx3^{+/+}$ mice showed identical GFR before onset of oxalate diet feeding. While GFR remained constant in $Ptx3^{+/+}$ mice over the entire feeding period, $Ptx3^{-/-}$ mice showed a linear decline of GFR as previously reported for susceptible mouse strains (43). Thus, *Ptx3*-deficient mice display the full phenotype of hyperoxaluria-induced nephrocalcinosis and progressive CKD. Together with the *in vitro* data described above, we conclude that PTX3 is an endogenous inhibitor of CaOx crystal aggregation, nephrocalcinosis and CKD during hyperoxaluria.

PTX3 Abolishes Crystal Adhesion Molecule Expression *in vitro* and *in vivo*

Based on the data gathered from our *in vitro* and *in vivo* experiments so far, we assumed that PTX3 opsonizes small

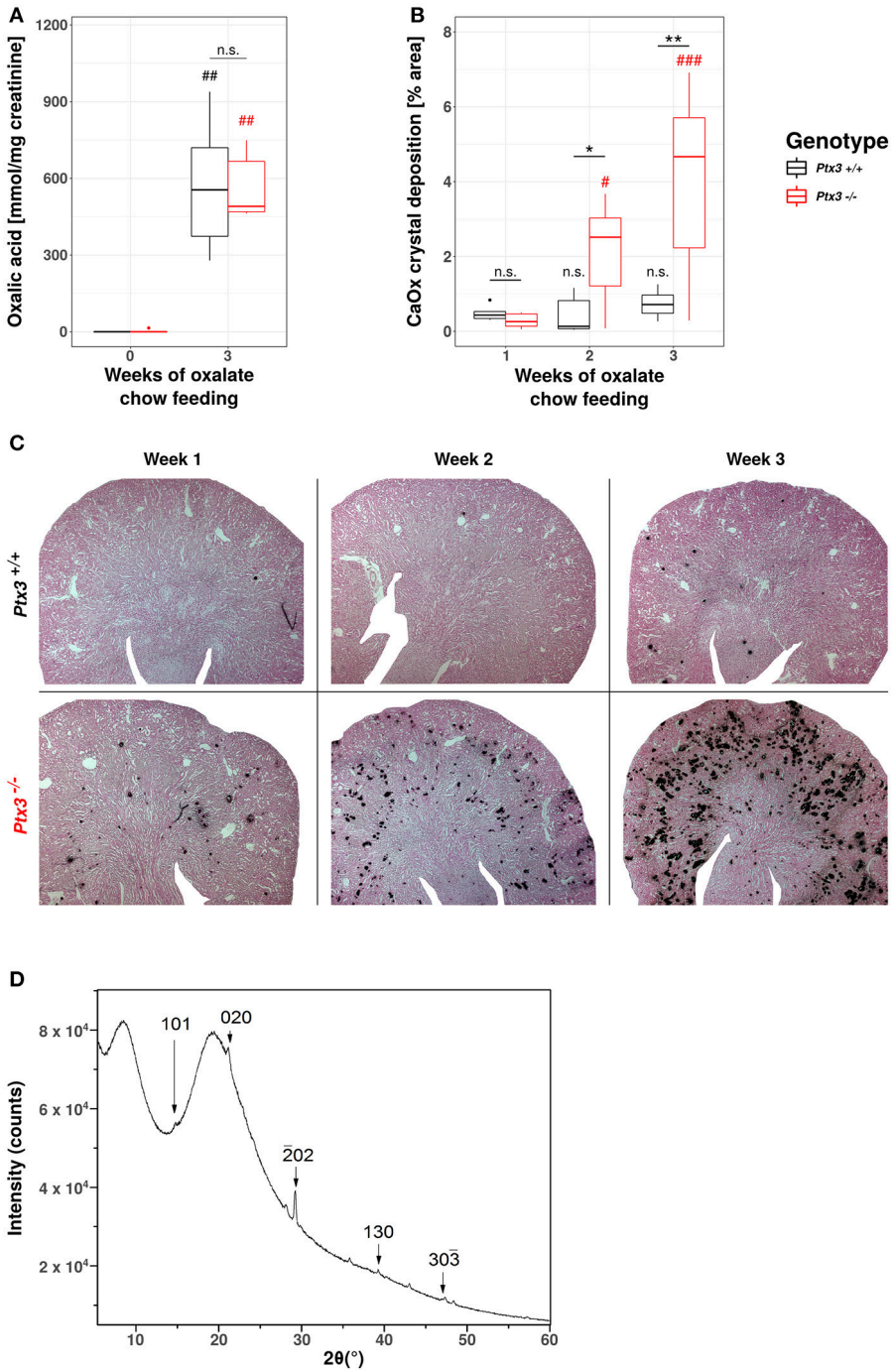

FIGURE 3 | Lack of PTX3 induces hyperoxaluria-induced nephrocalcinosis in non-susceptible B6;129SV mice. Female PTX3-competent ($Ptx3^{+/+}$) and -deficient ($Ptx3^{-/-}$) animals with 10–12 weeks of age received oxalate chow for 3 weeks ($n = 9$). **(A)** Oxalic acid levels in urine at baseline and after 3 weeks of oxalate chow. **(B)** Quantification of calcium oxalate crystal deposition was conducted using Pizzolato's method on formalin fixed kidney sections as shown in **(C)**. **(D)** Analysis of $PTX3^{-/-}$ kidneys by X-ray diffraction consistent with calcium-oxalate monohydrate crystals. Data are from four independent experiments. n.s., not significant; $^{*}p < 0.05$, $^{**}p < 0.01$ vs. wild type and respective #, ##, and ### vs. week 1 as indicated.

CaOx crystals and thereby inhibits further crystal growth and aggregation, which would result *in vivo* in crystal plug formation, kidney injury and progressive CKD. Nevertheless, nephrocalcinosis does not solely depend on the crystal aggregation, but also on the adhesion of crystals to the luminal side of tubular cells, a process that is enabled by crystal adhesion

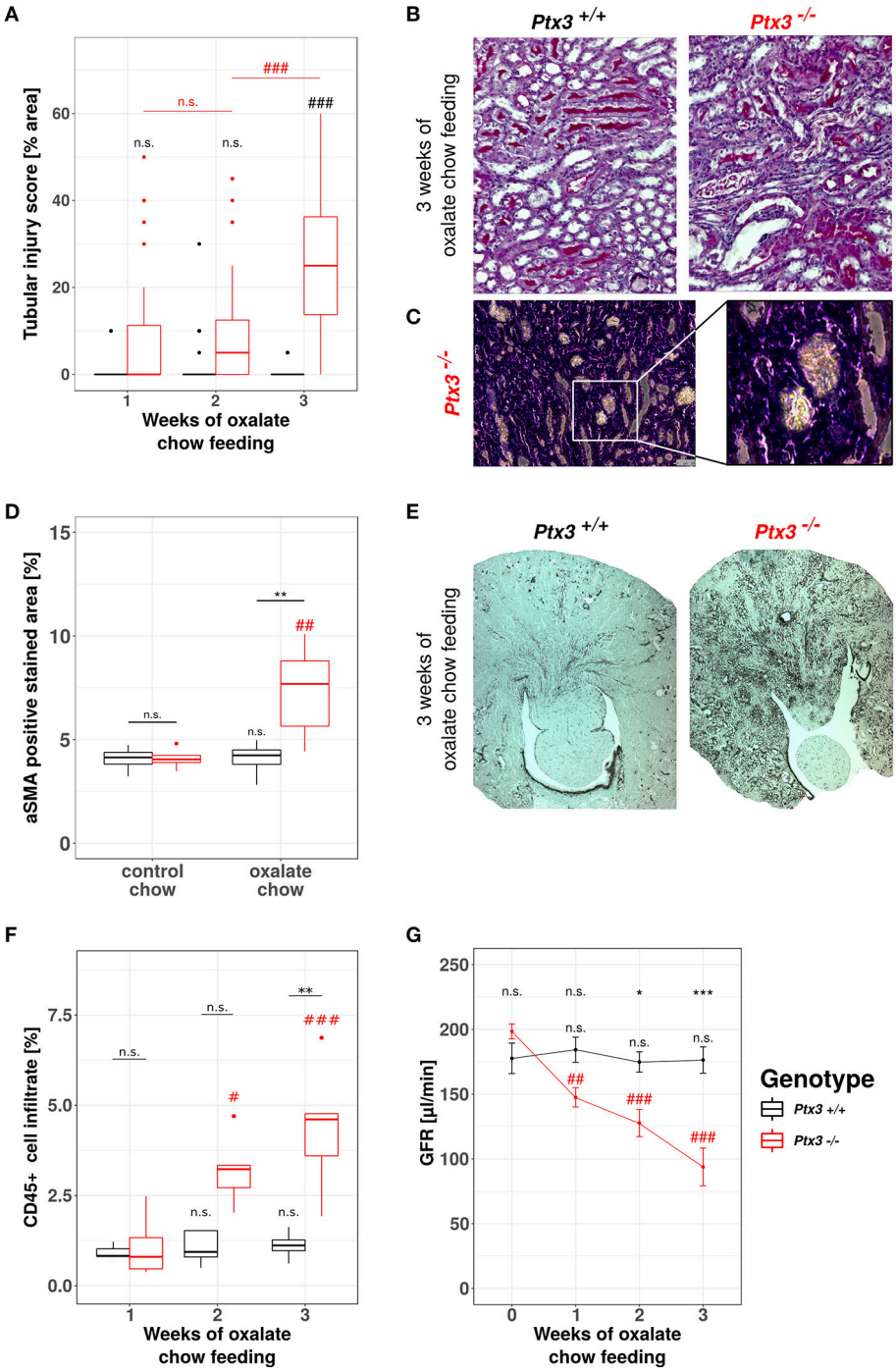

FIGURE 4 | Lack of PTX3 induces hyperoxaluria-induced progressive CKD in non-susceptible B6;129 mice. *Ptx3*$^{+/+}$ and *Ptx3*$^{-/-}$ female littermates (10–12 weeks of age) were fed with oxalate chow for 3 weeks ($n = 9$). **(A)** Quantification of tubular injury was conducted using PAS-stained kidney sections as shown in **(B)**. **(C)** Phase contrast image of crystal plugs in H&E-stained kidney section in 200× (left) and 400× (right) magnification. **(D)** Quantification of αSMA-positive area in kidney sections after 3 weeks of either control or oxalate chow feeding as shown in **(E)**. **(F)** Percentage of CD45^{+} cells within whole kidney cell suspension assessed by flow cytometry. **(G)** GFR assessed by transcutaneous measurement of FITC-sinistrin from subcutaneous capillaries at weeks 0, 1, 2, and 3 after onset of high oxalate diet in both genotypes. Data are from four independent experiments and represent means ± SEM in **(G)**. n.s., not significant; *$p < 0.05$, **$p < 0.01$, ***$p < 0.001$ vs. wild type and respective #, ##, and ### vs. week 1 as indicated.

molecules expressed on the cell surface, e.g., CD44 and annexin II. To address this point *in vitro*, we isolated primary murine proximal tubular cells from *PTX3*$^{+/+}$ and *PTX3*$^{-/-}$ littermates with 3 weeks of age and stimulated them with PBS or 500 μg/ml CaOx crystals (1–2 μM size). After 24 h total RNA was isolated, transcribed to cDNA and *Cd44* and *Anxa2* expression levels were quantified by qPCR (**Figures 5A,B**). Expression of both mRNAs was induced in tubular cells of PTX3-deficient mice stimulated with crystals only, whereas PTX3-competent cells did not upregulate the expression of either adhesion molecule. Similarly, i*n vivo*, after 3 weeks of control or oxalate chow diet, the expression of CD44 and annexin II was upregulated in tubular cells of *Ptx3*-deficient mice exposed to the oxalate chow only (**Figures 5C–F**). From these findings we conclude, that PTX3 not only inhibits CaOx crystal growth, but also abolishes the upregulation of crystal adhesion molecules after CaOx crystal challenge *in vitro* and *in vivo*, thereby additionally counteracting the development of nephrocalcinosis and CKD under hyperoxaluric conditions.

Development of Nephrocalcinosis and CKD Under Hyperoxaluric Conditions Is Strain and Sex Dependent

Our data from this and prior studies (43) suggest that the model of hyperoxaluria-induced nephrocalcinosis might be strain-dependent. To address this point, we compared the phenotypes of hyperoxaluric and control male and female mice on C57BL/6N, BALB/c, and CD-1 backgrounds, respectively. Pizzolato's staining method for CaOx crystals revealed, that out-bred CD-1 mice were not susceptible to nephrocalcinosis in our model (**Figures 6A,B**). In BALB/c mice, only males displayed CaOx crystal deposition, whereas females were protected. C57BL/6N mice of both sexes were susceptible to hyperoxaluria-induced nephrocalcinosis. In line with the presence of CaOx deposits in the kidneys, only BALB/c male as well as male and female C57BL/6N animals displayed tubular injury in PAS-stained sections, although the degree of injury was less profound in BALB/c compared to C57BL/6N (**Figures 6C,D**). Remarkably only hyperoxaluric C57BL/6N animals showed signs of fibrotic tissue remodeling, as assessed by collagen I-stained sections (**Figures 6E,F**), whereas BALB/c male mice did not. Characterizing the excretory kidney function we measured plasma levels of creatinine (**Figure 6G**), urea nitrogen (**Figure 6H**) and phosphorus (**Figure 6I**). Hyperoxaluric C57BL/6N mice of both sexes showed significantly increased levels of all three markers, whereas hyperoxaluric BALB/c male mice did not develop hyperphosphatemia and displayed lower levels of plasma creatinine and BUN compared to C57BL/6N. Based on this data we questioned whether the dependency of crystal formation from sex and strain was associated with the intrarenal levels of the PTX3 protein. Immunohistochemistry revealed a downregulation of PTX3 in male and female C57BL/6N mice fed with high oxalate diet compared to control animals, a phenomenon partly observed in male BALB/c animals also, although to a lesser extend (**Supplementary Figures 1A,B**). Non-crystal-forming female BALB/c and CD-1 mice of both sexes did not show PTX3 regulation. The animals with high oxalate diet which showed crystal deposition in the kidney were negative for PTX3, as shown using immunohistochemistry (**Supplementary Figures 1C,D**) and Western blotting in urine (**Supplementary Figures 1E,F**).

We conclude that genetic factors control susceptibility for hyperoxaluria-related nephrocalcinosis and that PTX3 is an endogenous inhibitory factor preventing nephrocalcinosis and its deterious consequences, e.g., by limiting crystal growth and by induction of crystal adhesion molecules.

DISCUSSION

We had speculated that the long pentraxin PTX3, an opsonin known to interact with dead cells and other extracellular microparticles, would affect CaOx crystal aggregation and growth, central pathomechanisms in kidney stone disease and nephrocalcinosis. Our data revealed that recombinant PTX3 limits CaOx crystal aggregation *in vitro*. Furthermore, during hyperoxaluria *in vivo* renal tubular cells secrete PTX3 which serves as an endogenous inhibitor of intrarenal crystal aggregation and adhesion, nephrocalcinosis, kidney injury, and subsequent CKD. Although not regulated in all investigated strains and sexes in the same manner, PTX3 protein levels associated with a lack of crystal formation in high oxalate diet exposed animals, further supporting a functional role of PTX3 as a calcium oxalate crystallization inhibitor. Our study identified a novel role of the opsonin and immune regulator PTX3 as a modulator of CaOx crystal aggregation and adhesion. Our data showed that PTX3 is one of several endogenous inhibitors of stone formation in nephrocalcinosis and potentially in urolithiasis or other crystallopathies.

The PTX3 protomer subunit comprises an N-terminal region, unrelated to any known protein structure, and a C-terminal domain, homologous to the short pentraxins CRP and SAP. In our study, we did not investigated which domain of the PTX3 protein mediates the inhibitory functions described above. This will be the subject of future investigations. In this regard, it is worth noting that other proteins, that are known to inhibit growth and aggregation of calcium oxalate crystals, e.g., Tamm-Horsfall glycoprotein, a_1-microglobulin or prothrombin fragment 1 (44), do not share well-characterized homologous amino acid sequences with PTX3. In the past scientific approaches to identify proteins with function in stone formation were usually conducted by characterizing protein composition of urinary stones (45, 46). In doing so, the possible contribution of carbohydrate side chains of proteins was discussed (45). Subsequent research supported the notion that protein-beared oligosaccharides could be involved in the overall inhibitory effect of glycoproteins on crystal growth, e.g., sialic acid side chains on Tamm-Horsfall protein (47, 48). The most efficient modifiers of calcium stones have a large number of carboxylic, hydroxyl, sulfate or phosphate functions on their structure (49). The PTX3 protein has a single N-glycosylation site in the C-terminal domain that is occupied by fucosylated and sialylated complex type sugars (37, 38). This post-translational

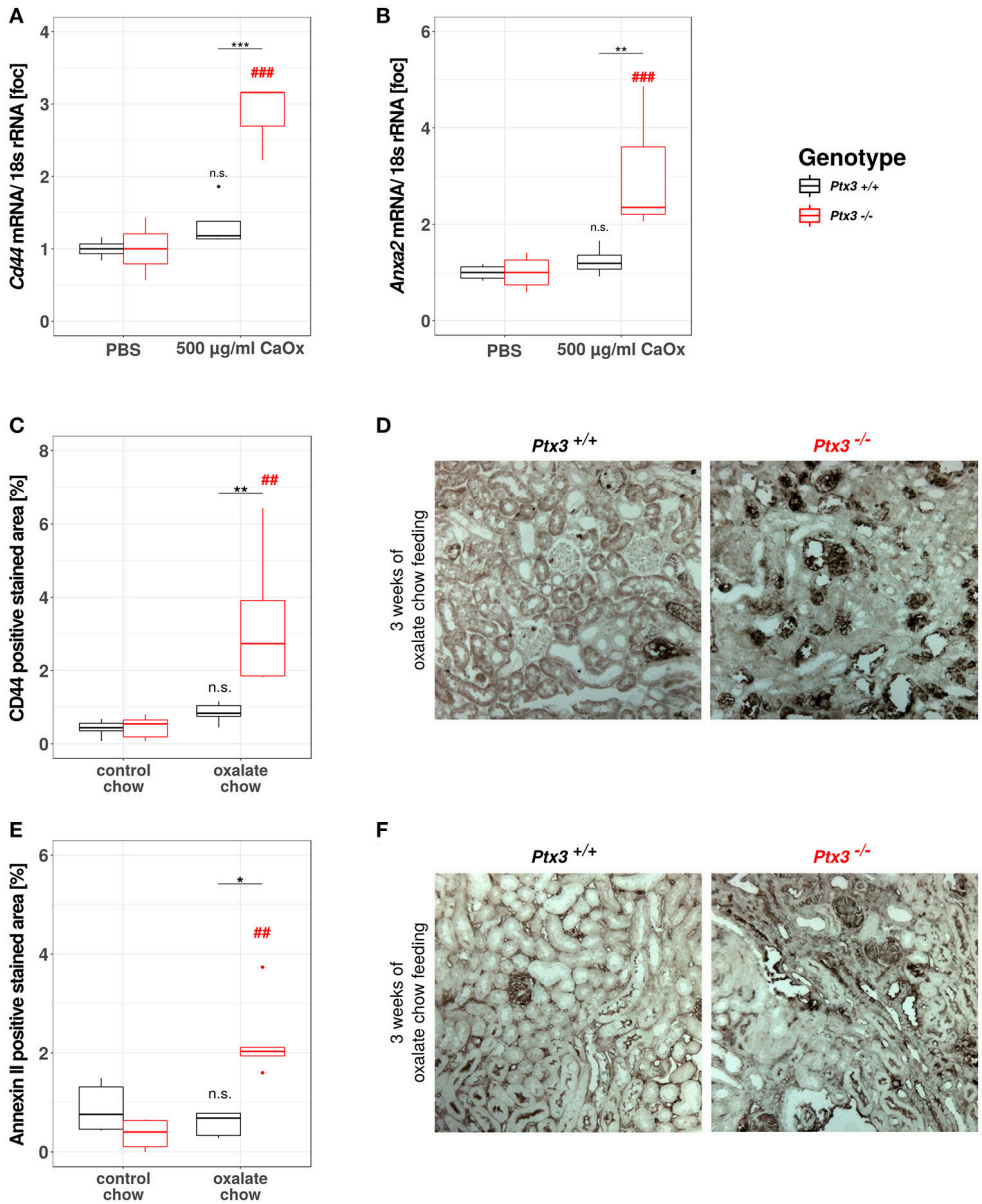

FIGURE 5 | PTX3 abolishes crystal adhesion molecule expression *in vitro* and *in vivo*. **(A,B)** Primary murine proximal tubular cells were isolated from $Ptx3^{+/+}$ and $Ptx3^{-/-}$ littermate mice with 3 weeks of age and stimulated with PBS and 500 µg/ml CaOx crystals, respectively ($n = 4$). Total RNA was isolated and transcribed to cDNA. Subsequent qPCR for **(A)** Cd44 and **(B)** Anxall expression was conducted. **(C–F)** $Ptx3^{+/+}$ and $Ptx3^{-/-}$ female littermates (10–12 weeks of age) were fed with oxalate chow for 3 weeks and formalin kidney sections were stained for **(C,D)** CD44 and **(E,F)** Annexin II, respectively ($n = 5$). n.s., not significant; $^{*}p < 0.05$, $^{**}p < 0.01$, $^{***}p < 0.001$ vs. wild type and respective ## and ### vs. PBS as indicated.

modification has been documented to affect the binding of PTX3 to a number of ligands, including complement components (37, 50) and P-selectin (51), thereby effectively altering the immune-modulatory properties of PTX3. It is worth noting here that throughout our study a recombinant preparation of PTX3 from Per.C6 cells was used, which is N-linked glycosylated (based on SDS-PAGE of the PNGase F-treated protein; data not shown). However, we cannot rule out that the glycosidic moiety of the Per.C6-derived protein might differ from that of the CHO-expressed PTX3 (i.e., that was used in previous reports). Although beyond the scopes of the study, this is an interesting point that deserves further investigations. Nonetheless, based on the body of literature available, it appears licit to speculate that the glycosylation status of PTX3 (with major regard to fucose and sialic acid-content) might influence the protein's properties as an inhibitor of crystal growth.

Another possible route of action for PTX3 that needs further investigation, is related to its association with TNF-α

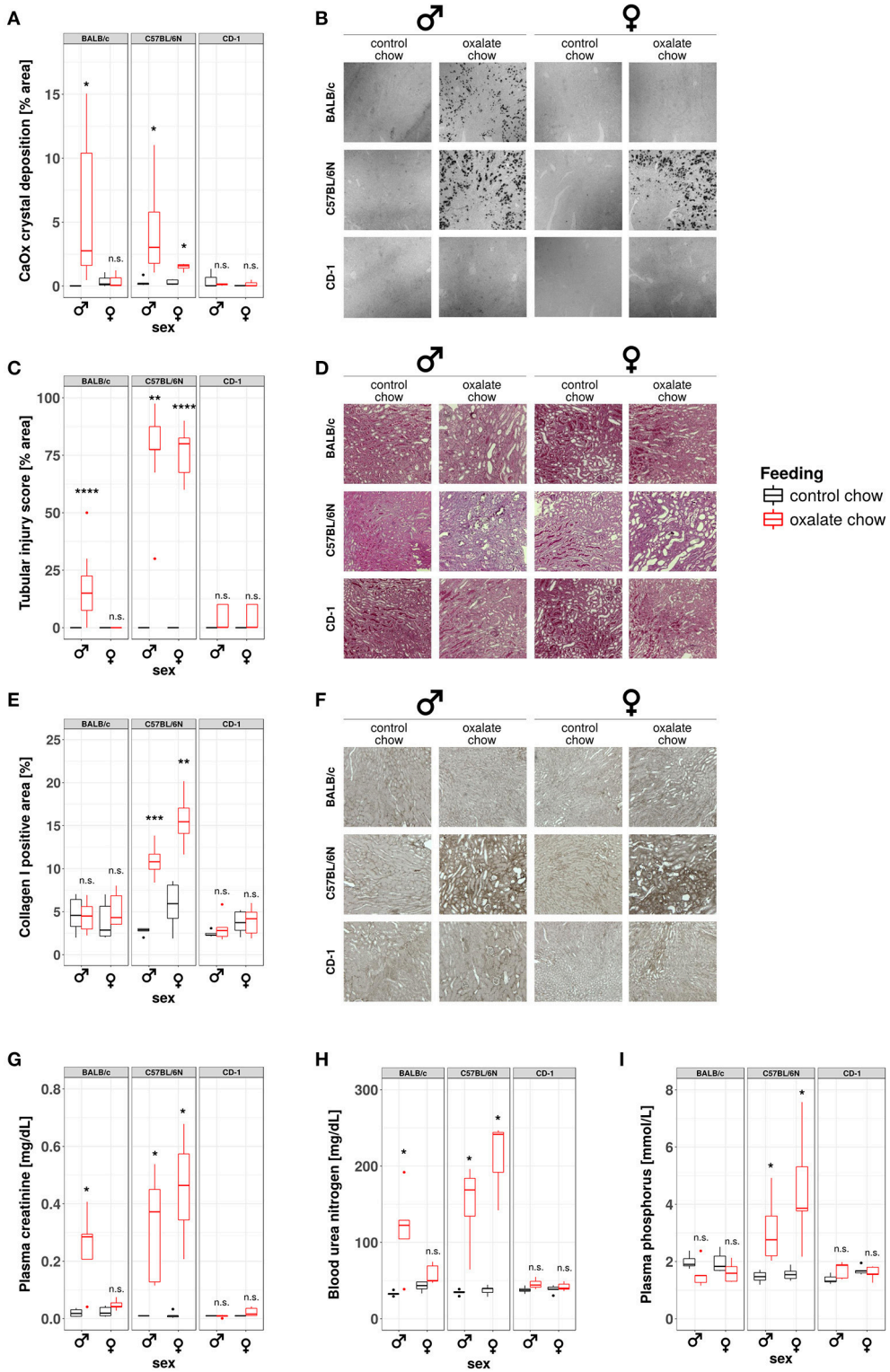

FIGURE 6 | Development of nephrocalcinosis and CKD under hyperoxaluric conditions is strain and sex dependent. Male and female BALB/c, C57BL/6N, and CD-1 mice (8 weeks of age) were fed with control or oxalate chow for 3 weeks ($n = 5$). **(A)** Quantification of calcium oxalate crystal deposition was conducted using Pizzolato's method on formalin fixed kidney sections as shown in **(B)**. **(C)** Quantification of tubular injury was conducted using PAS-stained formalin fixed kidney sections as shown in **(D)**. **(E)** Quantification of Collagen I deposition was conducted using Collagen I-stained formalin fixed kidney sections as shown in **(F)**. **(G)** Plasma creatinine, **(H)** blood urea nitrogen, and **(I)** plasma phosphorus were analyzed Cobas Integra 800 autoanalyzer. n.s., not significant; $^{*}p < 0.05$, $^{**}p < 0.01$, $^{***}p < 0.001$, $^{****}p < 0.0001$ between treatment groups.

signaling. We were previously able to show, that crystal adhesion to the luminal membrane of renal tubules requires TNFR signaling (28). The connection between TNF-α and PTX3 is well-established and indicates that PTX3 expression is a downstream event of TNF-α signaling (52), but also that PTX3 itself can inhibit TNF-α induced transcription factor activation (53). Hence, altered TNFR signaling might be involved in the phenotype observed in *Ptx3*-deficient mice.

Although technically feasible, we did not consider to recover the wild type mouse nephropathy phenotype by reconstituting the lack of PTX3 in *Ptx3*-deficient mice by injecting recombinant PTX3 because the PTX3 protein octamer is too large to pass the glomerular filter (40). Without a chance of reaching the tubular lumen, exogenous administered PTX3 cannot exert protective effects under hyperoxaluric conditions, which greatly limits its potential usefulness as a therapeutic intervention.

Nevertheless, we identified PTX3 as a previously unknown endogenous protein inhibitor of intrarenal CaOx crystal growth and adhesion (49). The field agrees that nephrocalcinosis, kidney stone disease and urolithiasis do not have a monogenic cause (54). Rather an increasing list of candidate genes is assembled by whole genome genotyping approaches using nephrolithiasis patient cohorts (55, 56). Our data suggest to include *Ptx3* in the list of candidate genes, that might contribute to a better understanding of stone diseases and prove useful in future patient diagnosis and management. Additionally, the investigation of different strains and sexes revealed, that decreased PTX3 protein expression associates with stone formation in some animals (C57BL/6N male and female), whereas other animals, that are not susceptible for hyperoxaluria-induced nephrocalcinosis, did either not show any PTX3 protein regulation (CD-1 male and female) or upregulated PTX3 under hyperoxaluric conditions (*Ptx3*-competent mice of the mixed B6;129 background). These *in vivo* observations might serve as a hint for the clinical setting, where haplotype compositions of each patient differ and some stone formers might show differences in PTX3 protein regulation, whereas others do not. PTX3 polymorphisms have already been shown to greatly influence the susceptibility of patients to aspergillosis, probably due to mRNA instability in some SNPs (57). Our data provide the rational for a similar study regarding kidney stone patients.

We reported the model of experimental hyperoxaluria-induced nephrocalcinosis to be valuable and clinically relevant for CKD research in male and female C57BL/6N mice (43). Next, the absence of nephrocalcinosis in $Ptx3^{+/+}$ animals on B6;129 background 3 weeks after model induction prompted us to study issues of strain and sex dependency in this model. With both sex and background affecting CaOx deposition with different degrees we believe that this model became even more valuable for studying mechanisms and risk factors related to kidney stone diseases. *In silico* comparison and transcriptome analysis of different murine strains and sexes available are very likely to draw a very precise picture on disease related genetic risk factors and possible therapeutic targets.

For CKD research—apart from the unique pathomechanisms only found in crystallopathies—strain and sex dependency of the model point out that researchers need to apply great care when using genetically-modified organisms, that were generated from different backgrounds or not completely backcrossed. Also, this does not only hold true for hyperoxaluria-induced nephrocalcinosis, but for a variety of other renal inflammatory models and conditions, e.g., thioglycolate-induced peritonitis (58), inflammatory response and albuminuria in response to albumin-overload (59), anti-GBM glumerulonephritis (60) as well as response to nephrotoxins (61).

In summary, the opsonin and immune regulator PTX3 also modulates CaOx crystal aggregation and adhesion to tubular cell membranes and is therefore one of several endogenous inhibitors of stone formation in nephrocalcinosis and potentially in urolithiasis or other crystallopathies.

MATERIALS AND METHODS

Animal Studies

BALB/c, C57BL/6N, and CD-1 mice were purchased from Charles River Laboratories (Sulzfeld, Germany). *Ptx3*-deficient mice in the B6;129 background were obtained from Alberto Mantovani/ Charles River Italy and were generated as previously described (62). Mice were co-housed in groups of five in filter top cages with unlimited access to food and water. Cages, nestlets, food, and water were sterilized by autoclaving before use. Eight-to-twelve-weeks-old male mice were used for experiments. Oxalate diet was prepared by adding 50 μmol/g sodium oxalate to a calcium-free standard diet (Ssniff, Soest, Germany) as previously described (43, 63). Mice were sacrificed at day 7, 14, and 21 after starting oxalate diet. Plasma and urine samples were collected and GFR was measured at different time points before cervical dislocation. Urine was immediately acidified for oxalate estimations or centrifuged for 10 min at 10,000 g for cellular component removal and stored at −80°C. One part of each kidney was fixed in formalin and subsequently embedded in paraffin for histological analysis. All experimental procedures were approved by the local government authorities.

Assessment of Renal Injury

Kidney sections of 2 μm were stained with periodic acid-Schiff (PAS) reagent, and the tubular injury was scored by assessing the percentage of necrotic tubules and presence of tubular casts. Pizzolato's staining was used to visualize CaOx crystals and crystal deposit formation in the kidney was evaluated as described (43). Fibrotic areas were identified by immunostaining for αSMA (Dako GmbH, Germany) and collagen I (Abcam, Cambridge, UK). The expression of crystal adhesion molecules e.g., CD44 and Annexin II was identified by immunostaining for CD44 and Annexin II (both Abcam, Cambridge, UK). PTX3 expression was identified in paraformaldehyde-fixated and cryo-cut tissue samples using a polyclonal rabbit anti-human PTX3 antibody (Enzo Life Sciences, Farmingdale, USA).

Quantification of Pizzolato's silver stain and immunostainings was done using Image J software. All assessments were performed by an observer blinded to the experimental condition. Plasma BUN, creatinine and phosphorus levels were measured using a Cobas Integra 800 autoanalyzer (Roche, Mannheim, Germany).

Assessing the signal intensity of the PTX3 staining in C57BL/6N, BALB/c, and CD-1 animals was not feasible using ImageJ, as big calcium oxalate crystal deposits were visible in the cryosections, showing the same level of contrast as the immunostaining. Hence, PTX3 staining was semi-quantitatively assessed using a scoring system where a strong positive signal was scored with a value of 2, a weak signal with a value of 1 and absence of signal with a value of 0. This evaluation was conducted independently for the cortex, medulla and papilla of one kidney section and the overall score resulted from the sum of all values, possibly raging of 0 to 6.

Transcutaneous Measurement of Glomerular Filtration Rate (GFR) in Conscious Mice

For GFR measurement mice were anesthetized with isoflurane and a miniaturized imager device built from two light-emitting diodes, a photodiode and a battery (MediBeacon, Mannheim, Germany) was mounted via a double-sided adhesive tape onto the shaved animals' neck (64). For the duration of recording (∼1.5 h) each animal was conscious and kept in a single cage. Prior to the intravenous injection of 150 mg/kg FITC-sinistrin (MediBeacon, Mannheim, Germany), the skin's background signal was recorded for 5 min. After removing the imager device the data were analyzed using MPD Lab software (MediBeacon, Mannheim, Germany). The GFR [μl/min] was calculated from the decrease of fluorescence intensity over time (i.e., plasma half-life of FITC-sinistrin) using a two-compartment model, the animals body weight and an empirical conversion factor (64).

X-ray Diffraction Analysis of Intrarenal Crystals

The analysis of the freeze dryed mouse kidney tissue by X-ray powder diffraction was performed with an Empyrean setup from PANalytical. A Cu x-ray tube (line source of 12 × 0.04 mm^2) provided CuKa radiation with $l = 0.1542$ nm. The Kb line was removed by a Ni filter. Source and detector moved in the vertical direction around a fixed horizontal sample. After passing a divergence slit of 1/8° and an anti-scatter slit of 1/4°, the beam reached the sample at the center of a phi-chi-z stage. In the Bragg-Bretano geometry used, the beam was refocused at a secondary divergence slit of 1/4°. Finally, the signal was recorded by a pixel detector (256 × 256 pixels of 55 μm) as a function of the scattering angle 2θ. Subsequently, the peak positions were calculated from $q = 2\pi/d = (4\pi/\lambda)\ \sin\theta$, in which **q** is the scattering vector. The detector was used in a scanning geometry that allowed all rows to be used simultaneously.

Flow Cytometry

Whole kidneys were chopped and digested for 30 min at 37°C using a collagenase and DNase I solution (both Sigma-Aldrich, Taufkirchen, Germany). Samples were further strained through a 70 μm mesh and washed with PBS. Dead cells were excluded from analysis using the Zombie NIR™ Fixable Viability Kit according to the manufacturer's instructions and as described before (65). $CD45^+$ positive cells were identified using a PE-Cy™5 labeled antibody (clone 30-F11, BD Biosciences, Franklin Lakes, USA). Analysis was conducted using FlowJo v10.0.

TABLE 1 | Primer sequences for qPCR.

Target		Primer sequence
CD44	Forward	5′-AGCGGCAGGTTACATTCAAA-3′
	Reverse	5′-CAAGTTTTGGTGGCACACAG-3′
Annexin II	Forward	5′-GCACATTGCTGCGGTTTGTCAG-3′
	Reverse	5′-CACCAACTTCGATGCTGAGAGG-3′
18s RNA	Forward	5′-GCAATTATTCCCCATGAACG-3′
	Reverse	5′-AGGGCCTCACTAAACCATCC-3′

Cell Culture Studies

Primary tubular epithelial cells (pTECs) were isolated from kidneys of mice with 3 weeks of age and were maintained in DMEM/F12 containing 10% fetal calf serum, 1% penicillin–streptomycin, 125 ng/ml prostaglandin E1 (Calbiochem, Darmstadt, Germany), 25 ng/ml EGF, 1.8 μg/ml l-thyroxine, 3.38 ng/ml hydrocortisone and 2.5 mg/ml of insulin-transferrin-sodium selenite supplement (I-T-SS) (all from Sigma-Aldrich, Taufkirchen, Germany unless mentioned) as previously described (66, 67). All cells were cultured in an incubator at 37°C, 5%CO_2, and stimulated with crystals of CaOx (1–2 μm size; Alfa Aesar, Karlsruhe, Germany).

RNA Preparation and Real-Time Quantitative PCR

Total RNA was isolated from pTECs using a Qiagen RNA extraction kit (Düsseldorf, Germany) following the manufacturer's instructions. After quantification RNA quality was assessed using agarose gels. From isolated RNA, cDNA was prepared using reverse transcriptase (Superscript II; Invitrogen, Carlsbad, USA). Real-time quantitative PCR (qPCR) was performed using SYBRGreen PCR master mix and was analyzed with a Light Cycler 480 (Roche, Mannheim, Germany). All gene expression values were normalized using 18S rRNA as a housekeeping gene. All primers used for amplification were from Metabion (Martinsried, Germany), and are listed in **Table 1**.

Immunoblotting

After determination of protein concentrations in urine samples, 50 μg of the protein solution was mixed with 4× sodium dodecyl sulfate loading buffer and was denatured at 95°C for 5 min for western blot analysis. Proteins were then separated by sodium dodecyl sulfate-polyacrylamide gel electrophoresis and transferred to a polyvinylidene difluoride membrane. Non-specific binding to the membrane was blocked for 1 h at room temperature with 5% non-fat milk in tris-buffered saline. The membranes were then incubated overnight at 4°C with a primary antibody for PTX3 (clone 2C3, Hycult Biotechs, Plymouth

Meeting, USA) followed by incubation with a secondary rabbit anti-mouse IgG HRP-labeled antibody. Immunostained bands were detected using a chemiluminescence kit (ECL kit, GE Healthcare, Cardiff, UK). Equal loading of urinary proteins was visualized by Ponceau Red staining (1 h at RT). Stain intensities for both stainings were further analyzed by densitometry (Image J). Murine PTX3 from urine samples as well as the recombinant PTX3 positive control showed the expected band around 45 kDa.

In Chemico Generation and Characterization of Calcium Oxalate Crystals

Calcium oxalate crystals of defined size and shape were generated as described elsewhere (68). In short, 10 mM sodium oxalate and 1 mM calcium chloride solutions were prepared using a 10 mM TRIS-HCl buffer (pH 7.3). For CaOx crystal generation 1 volume sodium oxalate solution was incubated over night at 4°C with 0.5 volume of either PBS or rhPTX3 in different concentrations. Next, 1 volume calcium chloride solution was added and kept at 4°C for 24 h. CaOx crystal size in the different preparations was assessed using bright light microscopy or flow cytometry.

Recombinant Human PTX3

Human PTX3 was recombinantly expressed in a PerC6 human cell line. Briefly, Per.C6 cells (Crucell, Leiden, The Netherlands) were stably transfected with a plasmid vector (pcDNA2001Neo-hPTX3) carrying the human PTX3 cDNA under control of the CMV promoter. After transfection, a highly producing clone was selected and expanded for protein expression. The recombinant protein was purified from conditioned medium using a multi-step chromatography strategy as previously described (69). Protein homogeneity in the end-product was assessed by analytical size exclusion chromatography (SEC), SDS-PAGE and immunoblotting (39). N-linked glycosylation of the purified protein was investigated using PNGase F (Sigma Aldrich) as previously described (37).

Statistical Analysis

Data are presented as mean with SEM or as boxplot statistics. Prior to every other statistical analysis, data were checked for normal distribution (Shapiro-Wilk test), homoscedasticity (Levene's test) and outliers (Grubb's test). Normally distributed and homoscedastic data sets were tested for statistical significant differences via ANOVA and *post-hoc* Bonferroni's correction was used for multiple comparisons. Heteroscedastic data were corrected following Games-Howell's *post-hoc* test. Not normally distributed data sets were compared using Kruskal-Wallis and Nemenyi testing. A value of $p < 0.05$ was considered to indicate statistical significance. *P*-values were indicated as $p > 0.05$ n.s., $p < 0.05$ * (or #), $p < 0.01$ ** (or ##), $p < 0.001$ *** (or ###).

ETHICS STATEMENT

All experimental procedures were carried out according to the German Animal Care and Ethics legislation and were approved by the local governmental authorities, i.e., the Ethical Committee of the Regierung von Oberbayern, permit no. (AZ) 55.2-1-54-2532-63-12 and 55.2-1-54-2532-143-13.

AUTHOR CONTRIBUTIONS

JM: design and conduction of experiments, data analysis, manuscript preparation; SM: design and conduction of experiments, data analysis; JM and SM contributed equally to the project; SS: flow cytometry conduction and analysis; LA: western blot conduction and analysis; ZZ: immunhistochemistry analysis; PB: X-ray diffraction conduction and analysis, manuscript preparation; KR: X-ray diffraction conduction and analysis; AI: provision of recombinant protein, experimental design, and manuscript preparation; CG: provision of transgenic animals, recombinant protein, PTX3 immunohistochemistry; AM: provision of transgenic animals, recombinant protein, PTX3 immunohistochemistry; H-JA: experimental design, data analysis, funding, manuscript preparation.

ACKNOWLEDGMENTS

The study was funded by the Deutsche Forschungsgemeinschaft (MU 3906/1-1, AN372/11-2, 16-2, and 24-1). This work was performed in part at the Center for Chemical Polymer Technology CPT, which was supported by the EU and the federal state of North Rhine-Westphalia (grant EFRE 30 00883 02). The expert technical support of Dan Draganovici, Jana Mandelbaum and Fabio Pasqualini is gratefully acknowledged. Parts of this work are presented in the thesis project of JM at the Medical Faculty of the University of Munich.

SUPPLEMENTARY MATERIAL

The Supplementary Material for this article can be found online at: https://www.frontiersin.org/articles/10.3389/fimmu.2018.02173/full#supplementary-material

Supplementary Figure 1 | PTX3 protein expression under hyperoxaluric conditions in different strains and sexes. Male and female BALB/c, C57BL/6N, and CD-1 mice (8 weeks of age) were fed with control or oxalate chow for 3 weeks ($n = 5$). **(A)** Scoring PTX3 positivity was performed on PTX3 immunostained cryosections as shown in **(B)**. Calcium oxalate crystal deposits are indicated with asterisks. **(C–F)** The figures include only those animals from the study, that were exposed to oxalate diet, not the control animals. **(C)** Comparing PTX3 staining scores between animals developing crystal deposition and those that did not, based on PTX3 immunohistochemistry on cryosections and Pizzolato's staining for oxalate crystals on paraffin sections **(D)**. **(E)** Comparing optical densities of immunoblots for PTX3 from urine samples (25 μg protein/lane) analogous to **(C,D)**. **(F)** Western blot for PTX3 (~45 kDa, upper panel) and Ponceau Red staining for major urinary proteins (mainly a2u-globulins, ~20 kDa, lower panel) as a loading control. Data are from one experiment. n.s., not significant; *$p < 0.05$, **$p < 0.01$, ****$p < 0.0001$ between groups as indicated.

REFERENCES

1. Erreni M, Manfredi AA, Garlanda C, Mantovani A, Rovere-Querini P. The long pentraxin PTX3: a prototypical sensor of tissue injury and a regulator of homeostasis. *Immunol Rev.* (2017) 280:112–25. doi: 10.1111/imr.12570
2. Bottazzi B, Doni A, Garlanda C, Mantovani A. An integrated view of humoral innate immunity: pentraxins as a paradigm. *Annu Rev Immunol.* (2010) 28:157–83. doi: 10.1146/annurev-immunol-030409-101305
3. Bottazzi B, Garlanda C, Salvatori G, Jeannin P, Manfredi A, Mantovani A. Pentraxins as a key component of innate immunity. *Curr Opin Immunol.* (2006) 18:10–5. doi: 10.1016/j.coi.2005.11.009
4. Nauta AJ, de Haij S, Bottazzi B, Mantovani A, Borrias MC, Aten J, et al. Human renal epithelial cells produce the long pentraxin PTX3. *Kidney Int.* (2005) 67:543–53. doi: 10.1111/j.1523-1755.2005.67111.x
5. Jaillon S, Moalli F, Ragnarsdottir B, Bonavita E, Puthia M, Riva F, et al. The humoral pattern recognition molecule PTX3 is a key component of innate immunity against urinary tract infection. *Immunity* (2014) 40:621–32. doi: 10.1016/j.immuni.2014.02.015
6. Diniz SN, Nomizo R, Cisalpino PS, Teixeira MM, Brown GD, Mantovani A, et al. PTX3 function as an opsonin for the dectin-1-dependent internalization of zymosan by macrophages. *J Leukoc Biol.* (2004) 75:649–56. doi: 10.1189/jlb.0803371
7. Baruah P, Dumitriu IE, Peri G, Russo V, Mantovani A, Manfredi AA, et al. The tissue pentraxin PTX3 limits C1q-mediated complement activation and phagocytosis of apoptotic cells by dendritic cells. *J Leukoc Biol.* (2006) 80:87–95. doi: 10.1189/jlb.0805445
8. Jaillon S, Jeannin P, Hamon Y, Frémaux I, Doni A, Bottazzi B, et al. Endogenous PTX3 translocates at the membrane of late apoptotic human neutrophils and is involved in their engulfment by macrophages. *Cell Death Differ.* (2009) 16173:465–74. doi: 10.1038/cdd.2008.173
9. Rovere P, Peri G, Fazzini F, Bottazzi B, Doni A, Bondanza A, et al. The long pentraxin PTX3 binds to apoptotic cells and regulates their clearance by antigen-presenting dendritic cells. *Blood* (2000) 96:4300–6.
10. van Rossum AP, Fazzini F, Limburg PC, Manfredi AA, Rovere-Querini P, Mantovani A, et al. The prototypic tissue pentraxin PTX3, in contrast to the short pentraxin serum amyloid P, inhibits phagocytosis of late apoptotic neutrophils by macrophages. *Arthritis Rheum.* (2004) 50:2667–74. doi: 10.1002/art.20370
11. Mulay SR, Anders H-J. Crystallopathies. *N Engl J Med.* (2016) 374:2465–76. doi: 10.1056/NEJMra1601611
12. Franklin BS, Mangan MS, Latz E. Crystal formation in inflammation. *Annu Rev Immunol.* (2016) 34:173–202. doi: 10.1146/annurev-immunol-041015-055539
13. Strowig T, Henao-Mejia J, Elinav E, Flavell R. Inflammasomes in health and disease. *Nature* (2012) 481:278–86. doi: 10.1038/nature10759
14. Mulay SR, Kulkarni OP, Rupanagudi KV, Migliorini A, Darisipudi MN, Vilaysane A, et al. Calcium oxalate crystals induce renal inflammation by NLRP3-mediated IL-1β secretion. *J Clin Invest.* (2013) 123:236–46. doi: 10.1172/JCI63679
15. Worcester EM, Coe FL. Clinical practice. Calcium kidney stones. *N Engl J Med.* (2010) 363:954–63. doi: 10.1056/NEJMcp1001011
16. Hoppe B. An update on primary hyperoxaluria. *Nat Rev Nephrol.* (2012) 8:467–75. doi: 10.1038/nrneph.2012.113
17. Bhasin B. Primary and secondary hyperoxaluria: understanding the enigma. *World J Nephrol.* (2015) 4:235. doi: 10.5527/wjn.v4.i2.235
18. Aggarwal KP, Narula S, Kakkar M, Tandon C. Nephrolithiasis: molecular mechanism of renal stone formation and the critical role played by modulators. *Biomed Res Int.* (2013) 2013:292953. doi: 10.1155/2013/292953
19. Baumann JM, Affolter B. From crystalluria to kidney stones, some physicochemical aspects of calcium nephrolithiasis. *World J Nephrol.* (2014) 3:256–67. doi: 10.5527/wjn.v3.i4.256
20. Asselman M, Verhulst A, De Broe ME, Verkoelen CF. Calcium oxalate crystal adherence to hyaluronan-, osteopontin-, and CD44-expressing injured/regenerating tubular epithelial cells in rat kidneys. *J Am Soc Nephrol.* (2003) 14:3155–66. doi: 10.1097/01.ASN.0000099380.18995.F7
21. Wesson JA, Ward MD. Role of crystal surface adhesion in kidney stone disease. *Curr Opin Nephrol Hypertens.* (2006) 15:386–93. doi: 10.1097/01.mnh.0000232879.50716.6f
22. Sheng X, Jung T, Wesson JA, Ward MD. Adhesion at calcium oxalate crystal surfaces and the effect of urinary constituents. *Proc Natl Acad Sci USA.* (2005) 102:267–72. doi: 10.1073/pnas.0406835101
23. Lieske JC, Swift H, Martin T, Patterson B, Toback FG. Renal epithelial cells rapidly bind and internalize calcium oxalate monohydrate crystals. *Proc Natl Acad Sci USA.* (1994) 91:6987–91. doi: 10.1073/pnas.91.15.6987
24. Sheng X, Ward MD, Wesson JA. Adhesion between molecules and calcium oxalate crystals: critical interactions in kidney stone formation. *J Am Chem Soc.* (2003) 125:2854–5. doi: 10.1021/ja029575h
25. Sheng X, Ward MD, Wesson JA. Crystal surface adhesion explains the pathological activity of calcium oxalate hydrates in kidney stone formation. *J Am Soc Nephrol.* (2005) 16:1904–8. doi: 10.1681/ASN.2005040400
26. Verhulst A, Asselman M, Persy VP, Schepers MSJ, Helbert MF, Verkoelen CF, et al. Crystal retention capacity of cells in the human nephron: involvement of CD44 and its ligands hyaluronic acid and osteopontin in the transition of a crystal binding- into a nonadherent epithelium. *J Am Soc Nephrol.* (2003) 14:107–15. doi: 10.1097/01.ASN.0000038686.17715.42
27. Kumar V, Farell G, Deganello S, Lieske JC. Annexin II is present on renal epithelial cells and binds calcium oxalate monohydrate crystals. *J Am Soc Nephrol.* (2003) 14:289–97. doi: 10.1097/01.ASN.0000046030.24938.0A
28. Mulay SR, Eberhard JN, Desai J, Marschner JA, Kumar SVR, Weidenbusch M, et al. Hyperoxaluria requires TNF receptors to initiate crystal adhesion and kidney stone disease. *J Am Soc Nephrol.* (2016) 28:761–8. doi: 10.1681/ASN.2016040486
29. Cochat P, Rumsby G. Primary hyperoxaluria. *N Engl J Med.* (2013) 369:649–58. doi: 10.1056/NEJMra1301564
30. Mulay SR, Anders H-J. Crystal nephropathies: mechanisms of crystal-induced kidney injury. *Nat Rev Nephrol.* (2017) 13:226–40. doi: 10.1038/nrneph.2017.10
31. Edyvane KA, Ryall RL, Marshall VR. The influence of serum and serum proteins on calcium oxalate crystal growth and aggregation. *Clin Chim Acta* (1986) 157:81–7. doi: 10.1016/0009-8981(86)90320-7
32. Ratkalkar VN, Kleinman JG. Mechanisms of stone formation. *Clin Rev Bone Miner Metab.* (2011) 9:187–97. doi: 10.1007/s12018-011-9104-8
33. Steiger S, Grill JF, Ma Q, Bäuerle T, Jordan J, Smolle M, et al. Anti-transforming growth factor β IgG elicits a dual effect on calcium oxalate crystallization and progressive nephrocalcinosis-related chronic kidney disease. *Front Immunol.* (2018) 9:619. doi: 10.3389/fimmu.2018.00619
34. Ryall RL, Chauvet MC, Grover PK. Intracrystalline proteins and urolithiasis: a comparison of the protein content and ultrastructure of urinary calcium oxalate monohydrate and dihydrate crystals. *BJU Int.* (2005) 96:654–63. doi: 10.1111/j.1464-410X.2005.05701.x
35. Nancollas GH, Gardner GL. Kinetics of crystal growth of calcium oxalate monohydrate. *J Cryst Growth* (1974) 21:267–76. doi: 10.1016/0022-0248(74)90014-1
36. Liu J, Jiang H, Liu X-Y. How does bovine serum albumin prevent the formation of kidney stone? A kinetics study. *J Phys Chem B* (2006) 110:9085–9. doi: 10.1021/jp057403b
37. Inforzato A, Peri G, Doni A, Garlanda C, Mantovani A, Bastone A, et al. Structure and function of the long pentraxin PTX3 glycosidic moiety: fine-tuning of the interaction with C1q and complement activation. *Biochemistry* (2006) 45:11540–51. doi: 10.1021/bi0607453
38. Inforzato A, Reading PC, Barbati E, Bottazzi B, Garlanda C, Mantovani A. The "sweet" side of a long pentraxin: how glycosylation affects PTX3 functions in innate immunity and inflammation. *Front Immunol.* (2012) 3:1–12. doi: 10.3389/fimmu.2012.00407
39. Inforzato A, Rivieccio V, Morreale AP, Bastone A, Salustri A, Scarchilli L, et al. Structural characterization of PTX3 disulfide bond network and its multimeric status in cumulus matrix organization. *J Biol Chem.* (2008) 283:10147–61. doi: 10.1074/jbc.M708535200
40. Inforzato A, Baldock C, Jowitt TA, Holmes DF, Lindstedt R, Marcellini M, et al. The angiogenic inhibitor long pentraxin PTX3 forms an asymmetric

octamer with two binding sites for FGF2. *J Biol Chem.* (2010) 285:17681–92. doi: 10.1074/jbc.M109.085639
41. Thul PJ, Åkesson L, Wiking M, Mahdessian D, Geladaki A, Ait Blal H, et al. A subcellular map of the human proteome. *Science* (2017) 356. doi: 10.1126/science.aal3321
42. Uhlén M, Fagerberg L, Hallström BM, Lindskog C, Oksvold P, Mardinoglu A, et al. Proteomics. Tissue-based map of the human proteome. *Science* (2015) 347:1260419. doi: 10.1126/science.1260419
43. Mulay SR, Eberhard JN, Pfann V, Marschner JA, Darisipudi MN, Daniel C, et al. Oxalate-induced chronic kidney disease with its uremic and cardiovascular complications in C57BL/6 mice. *Am J Physiol Physiol.* (2016) 310:F785–95. doi: 10.1152/ajprenal.00488.2015
44. Grover PK, Moritz RL, Simpson RJ, Ryall RL. Inhibition of growth and aggregation of calcium oxalate crystals *in vitro*–a co mparison of four human proteins. *Eur J Biochem.* (1998) 253:637–44. doi: 10.1046/j.1432-1327.1998.2530637.x
45. Nakagawa Y, Margolis H. Purification and characterization of a calcium oxalate monohydrate crystal growth inhibitor from human kidney tissue culture medium. *J Biol Chem.* (1981) 256:3936–3944.
46. Worcester M. Urinary calcium oxalate crystal growth inhibitors. *J Am Soc Nephrol.* (1994) 5:S46–53.
47. Chen WC, Lin HS, Chen HY, Shih CH, Li CW. Effects of Tamm-Horsfall protein and albumin on calcium oxalate crystallization and importance of sialic acids. *Mol Urol.* (2001) 5:1–5. doi: 10.1089/109153601750124186
48. Viswanathan P, Rimer JD, Kolbach AM, Ward MD, Kleinman JG, Wesson JA. Calcium oxalate monohydrate aggregation induced by aggregation of desialylated Tamm-Horsfall protein. *Urol Res.* (2011) 39:269–82. doi: 10.1007/s00240-010-0353-7
49. Alamani BG, Rimer JD. Molecular modifiers of kidney stones. *Curr Opin Nephrol Hypertens.* (2017) 26:1. doi: 10.1097/MNH.0000000000000330
50. Gout E, Moriscot C, Doni A, Dumestre-Pérard C, Lacroix M, Pérard J, et al. M-ficolin interacts with the long pentraxin PTX3: a novel case of cross-talk between soluble pattern-recognition molecules. *J Immunol.* (2011) 186:5815–22. doi: 10.4049/jimmunol.1100180
51. Deban L, Russo RC, Sironi M, Moalli F, Scanziani M, Zambelli V, et al. Regulation of leukocyte recruitment by the long pentraxin PTX3. *Nat Immunol.* (2010) 11:328–34. doi: 10.1038/ni.1854
52. Lee TH, Lee GW, Ziff EB, Vilcek J. Isolation and characterization of eight tumor necrosis factor-induced gene sequences from human fibroblasts. *Mol Cell Biol.* (1990) 10:1982–8. doi: 10.1128/MCB.10.5.1982
53. Shiraki A, Kotooka N, Komoda H, Hirase T, Oyama J, Node K. Pentraxin-3 regulates the inflammatory activity of macrophages. *Biochem Biophys Rep.* (2016) 5:290–95. doi: 10.1016/j.bbrep.2016.01.009
54. Vasudevan V, Samson P, Smith AD, Okeke Z. The genetic framework for development of nephrolithiasis. *Asian J Urol.* (2017) 4:18–26. doi: 10.1016/j.ajur.2016.11.003
55. Rungroj N, Nettuwakul C, Sudtachat N, Praditsap O, Sawasdee N, Sritippayawan S, et al. A whole genome SNP genotyping by DNA microarray and candidate gene association study for kidney stone disease. *BMC Med Genet.* (2014) 15:50. doi: 10.1186/1471-2350-15-50
56. Wolf MTF, Zalewski I, Martin FC, Ruf R, Müller D, Hennies HC, et al. Mapping a new suggestive gene locus for autosomal dominant nephrolithiasis to chromosome 9q33.2-q34.2 by total genome search for linkage. *Nephrol Dial Transplant.* (2005) 20:909–14. doi: 10.1093/ndt/gfh754
57. Cunha C, Aversa F, Lacerda JF, Busca A, Kurzai O, Grube M, et al. Genetic PTX3 deficiency and aspergillosis in stem-cell transplantation. *N Engl J Med.* (2014) 370:421–32. doi: 10.1056/NEJMoa1211161
58. Hoover-Plow JL, Gong Y, Shchurin A, Busuttil SJ, Schneeman TA, Hart E. Strain and model dependent differences in inflammatory cell recruitment in mice. *Inflamm Res.* (2008) 57:457–63. doi: 10.1007/s00011-008-7062-5
59. Ishola DA, van der Giezen DM, Hahnel B, Goldschmeding R, Kriz W, Koomans HA, et al. In mice, proteinuria and renal inflammatory responses to albumin overload are strain-dependent. *Nephrol Dial Transplant.* (2006) 21:591–7. doi: 10.1093/ndt/gfi303
60. Reynolds J. Strain differences and the genetic basis of experimental autoimmune anti-glomerular basement membrane glomerulonephritis. *Int J Exp Pathol.* (2011) 92:211–7. doi: 10.1111/j.1365-2613.2011.00763.x
61. Rabe M, Schaefer F. Non-transgenic mouse models of kidney disease. *Nephron* (2016) 133:53–61. doi: 10.1159/000445171
62. Garlanda C, Hirsch E, Bozza S, Salustri A, De Acetis M, Nota R, et al. Non-redundant role of the long pentraxin PTX3 in anti-fungal innate immune response. *Nature* (2002) 420:182–6. doi: 10.1038/nature01195
63. Knauf F, Asplin JR, Granja I, Schmidt IM, Moeckel GW, David RJ, et al. NALP3-mediated inflammation is a principal cause of progressive renal failure in oxalate nephropathy. *Kidney Int.* (2013) 84:895–901. doi: 10.1038/ki.2013.207
64. Schreiber A, Shulhevich Y, Geraci S, Hesser J, Stsepankou D, Neudecker S, et al. Transcutaneous measurement of renal function in conscious mice. *Am J Physiol Renal Physiol.* (2012) 303:F783–8. doi: 10.1152/ajprenal.00279.2012
65. Ma Q, Steiger S, Anders H-J. Sodium glucose transporter-2 inhibition has no renoprotective effects on non-diabetic chronic kidney disease. *Physiol Rep.* (2017) 5:e13228. doi: 10.14814/phy2.13228
66. Hagemann JH, Thomasova D, Mulay SR, Anders H-JJ. Nrf2 signalling promotes *ex vivo* tubular epithelial cell survival and regeneration via murine double minute (MDM)-2. *Nephrol Dial Transplant.* (2013) 28:2028–37. doi: 10.1093/ndt/gft037
67. Terryn S, Jouret F, Vandenabeele F, Smolders I, Moreels M, Devuyst O, et al. A primary culture of mouse proximal tubular cells, established on collagen-coated membranes. *AJP Ren Physiol.* (2007) 293:F476–85. doi: 10.1152/ajprenal.00363.2006
68. Thongboonkerd V, Semangoen T, Chutipongtanate S. Factors determining types and morphologies of calcium oxalate crystals: molar concentrations, buffering, pH, stirring and temperature. *Clin Chim Acta* (2006) 367:120–31. doi: 10.1016/j.cca.2005.11.033
69. Rivieccio V, Esposito A, Bellofiore P, Palladino P, Sassano M, Colombo M, et al. High-level expression and efficient purification of recombinant human long pentraxin PTX3 in Chinese hamster ovary cells. *Protein Expr Purif.* (2007) 51:49–58. doi: 10.1016/j.pep.2006.07.009

Conflict of Interest Statement: The authors declare that the research was conducted in the absence of any commercial or financial relationships that could be construed as a potential conflict of interest.

frontiers in Immunology

REVIEW
published: 29 January 2018
doi: 10.3389/fimmu.2018.00103

Macrophage Recognition of Crystals and Nanoparticles

Masafumi Nakayama[1,2]*

[1] Frontier Research Institute for Interdisciplinary Sciences, Tohoku University, Sendai, Japan, [2] PRESTO, Japan Science and Technology Agency, Kawaguchi, Japan

Inhalation of exogenous crystals such as silica, asbestos, and carbon nanotubes can cause lung fibrosis and cancer. Endogenous crystals such as monosodium urate, cholesterol, and hydroxyapatite are associated with pathogenesis of gout, atherosclerosis, and osteoarthritis, respectively. These crystal-associated-inflammatory diseases are triggered by the macrophage NLRP3 inflammasome activation and cell death. Therefore, it is important to understand how macrophages recognize crystals. However, it is unlikely that macrophages have evolutionally acquired receptors specific for crystals or recently emerged nanoparticles. Several recent studies have reported that some crystal particles are negatively charged and are recognized by scavenger receptor family members in a charge-dependent manner. Alternatively, a model for receptor-independent phagocytosis of crystals has also been proposed. This review focuses on the mechanisms by which macrophages recognize crystals and nanoparticles.

Keywords: macrophages, phagocytosis, crystals, nanoparticles, inflammation, scavenger receptors

OPEN ACCESS

Edited by:
Hans-Joachim Anders, Ludwig-Maximilians-Universität München, Germany

Reviewed by:
Nicolas Riteau, National Institutes of Health (NIH), United States
Niels Olsen Saraiva Camara, University of São Paulo, Brazil
Orestes Foresto-Neto, University of São Paulo, Brazil

***Correspondence:**
Masafumi Nakayama
mnakayama@fris.tohoku.ac.jp

Specialty section:
This article was submitted to Inflammation, a section of the journal Frontiers in Immunology

Received: *22 November 2017*
Accepted: *12 January 2018*
Published: *29 January 2018*

Citation:
Nakayama M (2018) Macrophage Recognition of Crystals and Nanoparticles. Front. Immunol. 9:103. doi: 10.3389/fimmu.2018.00103

INTRODUCTION

Phagocytosis of crystals such as silica, asbestos, monosodium urate (MSU), and hydroxyapatite by macrophages was initially observed by electron microscopy about 40 years ago (1–4). These early studies showed that upon phagocytosis, crystals are not digested but instead cause lysosomal damage. Although the underlying mechanism was unclear, this process was referred to as "frustrated phagocytosis" and was implicated in the pathogenesis of inflammatory diseases such as fibrosis and cancer (5).

Recent studies have revealed that silica and asbestos induce IL-1β secretion *via* NLRP3 inflammasome activation in macrophages (6–8). Likewise, various crystals such as MSU, hydroxyapatite, cholesterol, and alum crystals, and nanomaterials such as TiO_2 nanoparticles and carbon nanotubes (CNTs) have also been reported to induce NLRP3 inflammasome activation in macrophages (7, 9–12). The molecular mechanism for inflammasome activation has been extensively studied and is well summarized in several recent reviews (6, 13–15). Briefly, at least two signals are required for the activation of NLRP3 inflammasome. The first signal (signal 1) is mediated *via* pathogen-associated molecular patterns, damage-associated molecular patterns (DAMPs), or cytokines that trigger nuclear factor-κB (NF-κB)-mediated upregulation of NLRP3 along with pro-IL-1β (**Figure 1**). The second signal (signal 2) stimulates the assembly of a complex of multiple proteins including NLRP3, ASC, and pro-caspase-1, resulting in the activation of caspase-1. Subsequently, active caspase-1 processes pro-IL-1β to mature IL-1β, which is then released into the extracellular environment through damaged membranes of dying macrophages (**Figure 1**).

Upon recognition of crystals, macrophage surface receptors transmit signal 1 and/or 2. It is also proposed that the receptor-independent recognition of crystals transmits signal 2. This review summarizes and discusses the recent findings regarding the recognition of crystals and nanoparticles by macrophages.

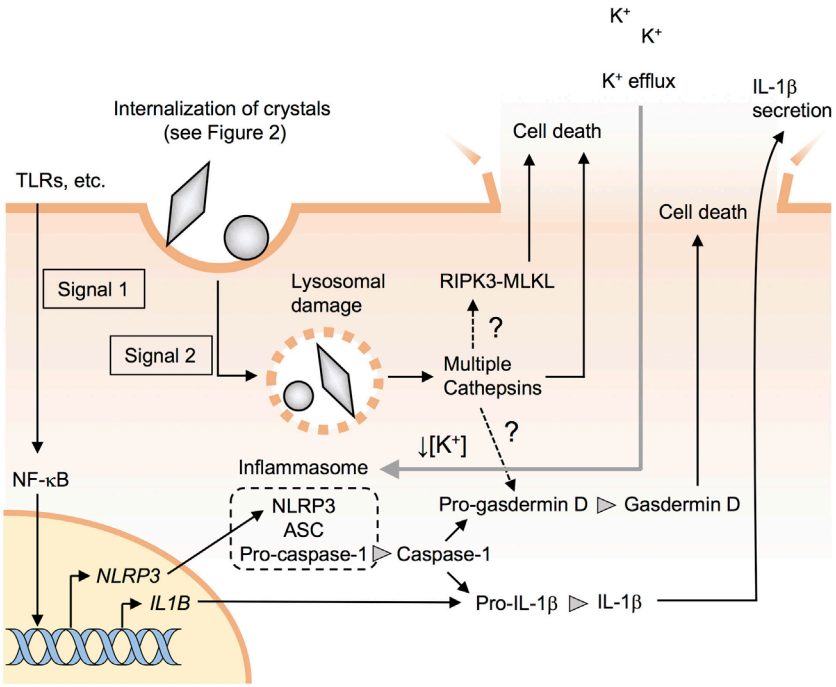

FIGURE 1 | Particle-induced NLRP3 inflammasome activation and cell death. Signal 1 induces pro-IL-1β along with NLRP3 through the nuclear factor-kappa B (NF-κB) pathway. Signal 2 causes lysosomal damages and stimulates the assembly of a complex of multiple proteins including NLRP3, ASC, and procaspase-1, resulting in the formation of inflammasomes. Active caspase-1 processes pro-IL-1β and pro-gasdermin D to mature IL-1β and gasdermin D. Lysosomal damage results in the release of the lysosomal enzyme cathepsins, which may induce NLRP3 inflammasome-independent pyroptotic cell death. Receptor-interacting serine/threonine kinase-mixed-lineage kinase domain-like protein (RIPK3-MLKL) pathway is involved in crystal-induced necroptosis in epithelial cells but not in macrophages.

MACROPHAGE SURFACE RECEPTORS

Macrophages express a wide variety of cell-surface receptors in order to recognize and internalize pathogenic particles such as bacteria and apoptotic cells (16–20). For instance, class A scavenger receptors such as SR-A1 (also known as MSR) and MARCO (proposed to be renamed as SR-A6) and class B scavenger receptors such as SR-B1 and CD36 (proposed to be renamed as SR-B2) bind to various polyanionic particles such as bacteria and apoptotic cells (18, 21). Fc receptors such as FcγRIII and complement receptors (CRs) such as CR3 internalize IgG- and complement-opsonized particles, respectively (22, 23), while C-type lectins such as Dectin-1 (also called Clec7a), Mincle (also called Clec4e), and MICL (also called Clec12a) recognize fungi-, mycobacteria-, or dying host cell-associated molecules (17, 24).

Given that it is unlikely that macrophages have acquired the specific ability to recognize crystals and recently emerged nanoparticles through evolution, the abovementioned receptors and opsonins may be responsible for the recognition of such inorganic particles. A common feature of organic particles such as bacteria and apoptotic cells and inorganic particles such as MSU, silica, and titanium is that they have negatively charged surfaces (25, 26), which could be favored by class A and class B scavenger receptors. By contrast, while organic particles harbor various ligands (protein, lipid, etc.) on their surface, the surface of a crystal is remarkably uniform. Therefore, an alternative model for receptor-independent phagocytosis of crystals has also been proposed (27). The mechanisms underlying the recognition of each particle by macrophages are discussed below.

RECOGNITION OF EXOGENOUS CRYSTALS AND NANOMATERIALS BY MACROPHAGES

Silica (SiO_2) and Titanium (TiO_2) Particles

Silica, which comprises about 60% of the Earth's crust, is a major component of sand and rocks and thus is contained in dust and air pollutants (28, 29). Therefore, it can be assumed that most organisms are exposed to crystalline silica (30, 31), and prolonged inhalation of large amounts of crystalline silica dust is known to cause lung fibrosis and cancer (8).

Compared with crystalline silica, amorphous silica is biocompatible and is contained in various foods and medicines (32). However, recent studies have shown that nanoparticles (diameter <100 nm), but not micro-sized particles, can trigger inflammation (32–34). Silica and titanium nanoparticles are the most frequently used nanomaterials (35), and titanium nanoparticles have also been reported to trigger inflammation (36, 37). Under physiological conditions, nanoparticles tend to aggregate irreversibly, resulting in particles of submicron or micrometer size in order to reduce their high surface energy

(26, 38, 39). Nevertheless, their toxicity largely depends on their primary size and not on the secondary aggregate size (34, 40) with smaller particles being more toxic. However, the molecular mechanism underlying size-dependent toxicity remains largely unknown.

Class A scavenger receptors such as SR-A1 and MARCO are known to bind to silica and titanium particles (**Figure 2**) (41); however, given that SR-A1- and MARCO-deficient mice and macrophages still show inflammatory responses to these particles (42–44), it seems likely that additional receptor(s) may be involved. Using unbiased functional screening, our laboratory recently identified the class B scavenger receptor member 1 (SR-B1) as a novel silica receptor (**Figure 2**) (26). In contrast to SR-A1 and MARCO, which bind to both silica and titanium particles (41), SR-B1 binds to silica but not to titanium particles (26). Moreover, SR-B1-deficient macrophages showed impaired internalization of silica and subsequent inflammasome activation (26). However, since SR-B1 binds to both crystalline and amorphous silica irrespective of particle size (26), the recognition by SR-B1 does not account for the size-dependent toxicity of silica particles. On the other hand, Nishijima et al. have recently shown that anti-SR-A1 mAb inhibits THP-1 cell-inflammatory responses to 50-nm silica particles, but not to other sizes of silica particles, suggesting that the recognition by SR-A1 may account for the size-dependent toxicity of silica (45).

The class B scavenger receptor CD36 also binds to silica particles (**Figure 2**) (26); however, CD36 is not involved in silica-induced acute lung inflammation in mice (26, 46). This is probably due to the marginal expression of CD36 on resident alveolar macrophages (26, 47). Nevertheless, since CD36 is expressed on inflammatory macrophages infiltrating alveolar spaces (47), CD36 may contribute to the chronic lung inflammation.

Because scavenger receptors have only a short cytoplasmic tail (18), they probably work as tethering receptors rather than as signaling receptors following particle recognition. Therefore, co-receptors may also be required in order to internalize particles. Indeed, the ectopic expression of SR-A1 or SR-B1 on non-phagocytic cells enables these cells to bind, but not internalize, to silica particles (26). It has been reported that a chemical inhibitor of Mer receptor tyrosine kinase (MerTK) inhibits IL-1β secretion from THP-1 cells, which use SR-A1 to recognize silica particles. This suggests that MerTK works as a co-receptor of the scavenger receptor (45). Therefore, it would be intriguing to address whether the co-expression of MerTK and the scavenger receptor impart cells with the ability to internalize silica particles.

Asbestos and CNTs

It is well known that the prolonged inhalation of large amounts of asbestos causes mesothelioma and lung cancer (48). Like silica, asbestos is also efficiently internalized by macrophages, resulting in NLRP3 inflammasome activation and cell death (49). Since asbestos is a silicate mineral, asbestos may also bind to scavenger receptors. Murthy et al. reported that MARCO-deficient mice show less fibrosis following exposure to chrysotile asbestos (50). Although the authors did not show the direct binding of MARCO to asbestos, these data suggest that MARCO may contribute to asbestos-induced lung fibrosis.

Carbon nanotubes are a highly representative product of nanotechnology (51), and although the worldwide production of CNTs

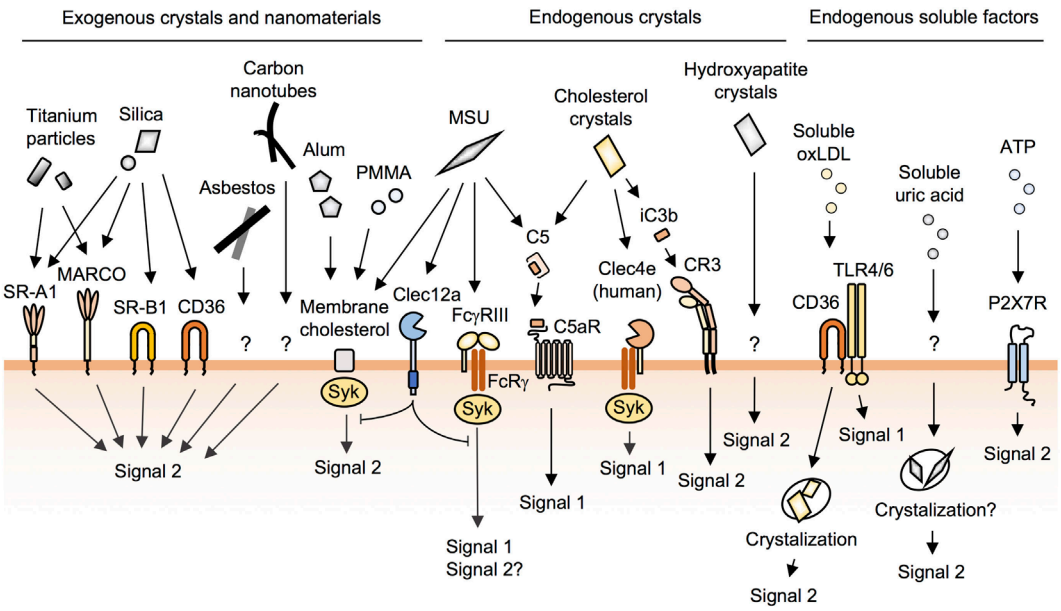

FIGURE 2 | The recognition of crystals and nanoparticles on the macrophage surface. Macrophages recognize and internalize crystals and nanoparticles through cell-surface receptors and membrane cholesterol. Silica particles are recognized by SR-A1, MARCO, SR-B1, and CD36. Alum, poly(methyl methacrylate) (PMMA), and monosodium urate (MSU) crystals bind directly to membrane cholesterol to be internalized. MSU and cholesterol crystals activate complement pathways. Soluble oxidized low-density lipoprotein (oxLDL) is internalized by CD36 and then crystallized in phagosomes. P2X7R does not cause lysosomal damage. In addition to these, many unknown pathways of phagocytosis remain to be identified.

is less than that of silica and titanium nanoparticles (35, 51), the production of CNTs has been increasing drastically year after year as they are applied to a wide variety of commercial products including rechargeable batteries and automotive parts (51). Electron microscopy reveals that some CNTs have a needle-like structure reminiscent of asbestos (52, 53). Indeed, recent animal studies have shown that these CNTs have asbestos-like pathogenic behavior (9, 54). For instance, a seminal study by Poland et al. showed that the intraperitoneal injection with multi-walled CNTs (MWCNTs) as well as asbestos causes massive granulomatous inflammation in the diaphragms of wild-type mice (55). Furthermore, Takagi et al. showed that the intraperitoneal injection of MWCNT caused mesothelioma in $p53^{+/-}$ mice (56), while Palomaki et al. found that CNTs and asbestos induce NLPR3 inflammasome activation in human macrophages (57). However, it remains unknown how macrophages recognize CNTs on their cell surface.

Alum Crystals

Alums (aluminum adjuvants) are widely used for vaccination in both humans and animals (58). It has been reported that upon being internalized, alum activates NLRP3 inflammasomes, which are essential for alum-induced acute inflammation (59, 60). However, recent studies have proposed that the adjuvant effect of alum is mediated *via* NLRP3-independent phagocyte cell death (**Figure 1**) (61, 62). This occurs when dying cells release their intracellular contents, some of which trigger innate immune responses. Specifically, alum-induced Th2 responses have been reported to be mediated *via* host DNA and uric acid (61, 62). On the other hand, it has been reported that NLRP3 is expressed in the nuclei of Th2 cells and works as a transcriptional regulator of Th2 differentiation (63). Thus, the requirement of NLRP3 for Th2 responses remains controversial.

Shi and colleagues have reported that the phagocytosis of alum as well as MSU crystals (discussed below) is not mediated by cell-surface receptors (64, 65). By using atomic force microscopy, they showed that alum directly binds to membrane lipids, and this lipid ligation activates Syk and PI3K (**Figure 2**) (64, 65).

In addition to the direct recognition of crystals and nanoparticles by macrophage receptors and membrane cholesterol, these particles may also be *opsonized* and recognized indirectly by macrophages. Indeed, nanoparticles are absorbed by various plasma proteins called the protein corona (66–68). For instance, it has been reported that albumin and complement bind to silica nanoparticles (69), although it remains unknown whether the protein corona contributes to phagocytosis. Some *in vitro* studies have shown that the protein corona does not enhance but rather suppresses the phagocytosis of nanoparticles by macrophages (70, 71). As discussed below, endogenous crystals such as MSU and cholesterol activate complement pathways.

RECOGNITION OF ENDOGENOUS CRYSTALS BY MACROPHAGES

MSU Crystals

Dying cells release uric acid, and these crystals trigger inflammation (72). In addition, the saturation of uric acid in body fluids results in the formation of MSU crystals, which trigger macrophage NLRP3 inflammasome activation and are associated with the pathogenesis of gout (10, 73). Early studies reported that MSU crystals activate complement pathways (74, 75), and this has been confirmed by a recent study which showed that MSU and cholesterol crystals (discussed below), but not silica or alum, activate complement pathways (76). Although MSU-activated C5a binds to C5aR, a G protein-coupled receptor (**Figure 2**), to activate signal 1 (**Figure 1**) in human monocytes (76), C5aR was not found to contribute to the phagocytosis of MSU (76).

FcγRIII (CD16) has been reported to bind to MSU directly, resulting in the activation of the Syk pathway in human neutrophils (**Figure 2**) (77). FcγRIII associates with the FcRγ chain, and this receptor complex is a well-characterized phagocytic receptor for IgG-opsonized particles (22); however, the internalization of MSU by FcγRIII has not been demonstrated. Although we and others have observed that MSU crystals have negatively charged surfaces (26, 27), we failed to observe the binding of MSU crystals to scavenger receptors, which can bind to polyanionic particles (26). These results suggest that scavenger receptors may recognize not only surface charges but also shapes and/or substances of particles. Phagocytic receptors for MSU crystals remain to be identified.

Shi and colleagues proposed that MSU crystals bind directly to plasma membrane cholesterols, a driving force for their internalization (**Figure 2**) (65). This group also proposed that the receptor-independent model can be applied for alum (64) and biomaterial microspheres of poly(methyl methacrylate) (**Figure 2**) (78). While this is an attractive model for understanding the recognition of crystals and nanoparticles with uniform surfaces by phagocytes, it remains unknown why these particles preferentially bind to phagocytes when cholesterol is present in the membrane of all cell types.

Clec12a (also called MICL, DCAL2, and CLL-1), a C-type lectin receptor, has been recently reported to recognize MSU, but not other particles such as polystyrene, silica, or zymosan (**Figure 2**) (79). Clec12a has an ITIM in its cytoplasmic domain, and the activation of this receptor has been shown to inhibit Syk signaling. Moreover, Clec12a-deficient mice showed enhanced inflammation in response to MSU (79), although it remains unknown whether Clec12a suppresses phagocytosis of MSU.

A recent study has shown that soluble uric acid also triggers NLRP3 inflammasome activation, although the authors do not exclude the possibility that this activation could be caused by undetectable microcrystals of uric acid (80). It is also possible that internalized soluble uric acid is crystallized in phagocytes just like soluble oxidized LDL as described below (81) (**Figure 2**). Either way, this finding may propose that uric acid released from dying cells or hyperuricemia directly causes inflammation without crystal deposition.

Cholesterol Crystals

Cholesterol accumulation leads to the formation of crystals, which have been shown to be engulfed by macrophages in atherosclerotic sinus lesions (12), leading to pro-inflammatory

responses through NLRP3 inflammasome activation (10, 82). In addition, early studies have shown that cholesterol crystals as well as MSU crystals activate complement pathways (83, 84). Recently, Samstad et al. showed that cholesterol crystals activate the C5a and the C5aR pathways leading to the upregulation of CR3 (CD11b and CD18 complexes) (**Figure 2**) (85). Mechanistically, C5aR, a G-protein-coupled receptor, activates ERK and NF-κB pathways (signal 1) (86). These pathways lead to the induction of the expression of CR3, a phagocytic receptor for iC3b-tagged particles (19), which contributes to the phagocytosis of cholesterol crystals (signal 2) (85). Indeed, this group showed that the inhibition of C5 or C3 reduces the phagocytosis of cholesterol crystals by human monocytes (85, 87).

The human, but not mouse, C-type lectin Mincle (also called Clec4e) has been shown to have a cholesterol recognition amino acid consensus (CRAC) motif in its extracellular domain (88). Through this CRAC motif, human Mincle binds to cholesterol crystals, resulting in the activation of pro-inflammatory signals *via* the associated FcRγ chain (**Figure 2**) (88). Although the FcRγ chain is able to mediate a phagocytic signal (22), it remains unknown whether human Mincle is involved in the phagocytosis of cholesterol crystals.

In addition to cholesterol crystals, soluble oxidized low-density lipoprotein (oxLDL) is internalized by macrophages, and the crystals are then nucleated, resulting in the lysosomal disruption and activation of the NLRP3 inflammasome (81, 82). CD36 is a receptor for oxLDL and is essential for both signal 1 (NF-κB activation in conjunction with TLR4 and -6) and signal 2 (internalization of oxLDL), resulting in NLRP3 inflammasome activation (**Figures 1** and **2**) (81, 89).

Hydroxyapatite Crystals

Hydroxyapatite, a basic calcium phosphate crystal, is a major component of bones and teeth. The ectopic deposition of these crystals is predominantly observed in osteoarthritis (OA) joints and is implicated in the pathogenesis of OA (10, 90). In addition, synthetic hydroxyapatite crystals are the widely used biomaterials, although it has been shown that these crystals can trigger local inflammation upon being released from implanted prosthetics (91). Recent studies have reported that hydroxyapatite crystals are internalized by macrophages through unknown mechanisms where they trigger NLRP3 inflammasome activation (**Figure 2**) (92, 93). NLRP3 is essential for crystal-induced IL-1β secretion *in vitro*; however, the requirement for NLRP3 is only partial in mouse models of arthritis (92, 94) as shown in NLRP3-deficient mice where various crystals such as silica and alum still induce macrophage cell death and inflammation (discussed below). Thus, hydroxyapatite crystal-induced arthritis may be mediated *via* NLRP3-independent macrophage death.

PARTICLE-INDUCED CELL DEATH AND DISEASES

Crystals cause lysosomal damages, resulting in the release of the lysosomal enzyme cathepsins to cytosol (95), which is the upstream of NLRP3 inflammasome activation (**Figure 1**). Rock and colleagues have recently shown that multiple cathepsins including cathepsins b, l, x, and s contribute to NLRP3- and caspase-1-independent cell death (**Figure 1**) (96). However, the downstream mechanisms of action of the cathepsins remain unknown. It would be intriguing to address whether cathepsins directly cause membrane damage or activate pore-forming proteins such as gasdermin D (97–99). It has also been reported that receptor-interacting serine/threonine kinase-3 and mixed-lineage kinase domain-like protein-mediated necroptosis pathways (100) are involved in crystal-induced cell death in epithelial cells (101) but not in macrophages (**Figure 1**) (96, 102).

Dying cells release DAMPs such as uric acid and ATP (72). As mentioned earlier, uric acid induces inflammation (80). ATP, which is released from pannexin-1, binds to P2X7 receptor to induce cell death and NLRP3 inflammasome activation without causing lysosomal damage (**Figure 2**) (103). Besides DAMPs, dying macrophages release internalized crystals, which could induce cell death of the neighboring macrophages. This sequential cell death may be more crucial than NLRP3 inflammasome activation in the pathogenesis of crystal-induced chronic inflammation and fibrosis such as arthritis (92, 94), silicosis (104), and asbestosis (105) as these diseases develop in NLRP3-deficient mice.

CONCLUSION

Crystals such as silica, asbestos, and MSU cause inflammatory diseases through macrophage activation and cell death. As discussed here, macrophages have been found to recognize crystals *via* cell-surface receptors and/or membrane cholesterol, although these pathways account for only a fraction of crystal phagocytosis. Therefore, many unknown pathways of phagocytosis remain to be identified. While phagocytosis and subsequent lysosomal damage appear to be essential for the pathogenesis of particle-induced-inflammatory diseases, it remains unknown how the physicochemical properties (element, size, etc.) of particles impact lysosomal damage. A better understanding of the molecular mechanisms underlying particle-induced inflammation will provide opportunities not only for the development of therapeutic approaches for incurable silicosis and asbestosis but also for the development of safer nanomaterials in the future.

AUTHOR CONTRIBUTIONS

The author confirms being the sole contributor of this work and approved it for publication.

FUNDING

This work was supported by Grants in Aid for Scientific Research (B) #16H02960 from the Japan Society for the Promotion of Science (JSPS) and by PRESTO #JPMJPR17H9 from the Japan Science and Technology Agency (JST).

REFERENCES

1. Maurer KH, Schumacher HR. Hydroxyapatite phagocytosis by human polymorphonuclear leucocytes. *Ann Rheum Dis* (1979) 38:84–8. doi:10.1136/ard.38.1.84
2. Policard A, Collet A, Giltaireralyte L. [Electron microscopy study of the phagocytosis of silica particles]. *Rev Hematol* (1955) 10:674–88.
3. Schumacher HR, Phelps P. Sequential changes in human polymorphonuclear leukocytes after urate crystal phagocytosis. An electron microscopic study. *Arthritis Rheum* (1971) 14:513–26. doi:10.1002/art.1780140411
4. Suzuki Y, Churg J. Structure and development of the asbestos body. *Am J Pathol* (1969) 55:79–107.
5. Archer VE. Carcinogenicity of fibers and films: a theory. *Med Hypotheses* (1979) 5:1257–62. doi:10.1016/0306-9877(79)90008-2
6. Broz P, Dixit VM. Inflammasomes: mechanism of assembly, regulation and signalling. *Nat Rev Immunol* (2016) 16:407–20. doi:10.1038/nri.2016.58
7. Franklin BS, Mangan MS, Latz E. Crystal formation in inflammation. *Annu Rev Immunol* (2016) 34:173–202. doi:10.1146/annurev-immunol-041015-055539
8. Leung CC, Yu IT, Chen W. Silicosis. *Lancet* (2012) 379:2008–18. doi:10.1016/S0140-6736(12)60235-9
9. Donaldson K, Murphy FA, Duffin R, Poland CA. Asbestos, carbon nanotubes and the pleural mesothelium: a review of the hypothesis regarding the role of long fibre retention in the parietal pleura, inflammation and mesothelioma. *Part Fibre Toxicol* (2010) 7:5. doi:10.1186/1743-8977-7-5
10. Mulay SR, Anders HJ. Crystallopathies. *N Engl J Med* (2016) 374:2465–76. doi:10.1056/NEJMra1601611
11. Rock KL, Kataoka H, Lai JJ. Uric acid as a danger signal in gout and its comorbidities. *Nat Rev Rheumatol* (2013) 9:13–23. doi:10.1038/nrrheum.2012.143
12. Tall AR, Yvan-Charvet L. Cholesterol, inflammation and innate immunity. *Nat Rev Immunol* (2015) 15:104–16. doi:10.1038/nri3793
13. Gross O, Thomas CJ, Guarda G, Tschopp J. The inflammasome: an integrated view. *Immunol Rev* (2011) 243:136–51. doi:10.1111/j.1600-065X.2011.01046.x
14. Latz E, Xiao TS, Stutz A. Activation and regulation of the inflammasomes. *Nat Rev Immunol* (2013) 13:397–411. doi:10.1038/nri3452
15. Rathinam VA, Fitzgerald KA. Inflammasome complexes: emerging mechanisms and effector functions. *Cell* (2016) 165:792–800. doi:10.1016/j.cell.2016.03.046
16. Bournazos S, Ravetch JV. Fcgamma receptor function and the design of vaccination strategies. *Immunity* (2017) 47:224–33. doi:10.1016/j.immuni.2017.07.009
17. Ishikawa E, Mori D, Yamasaki S. Recognition of mycobacterial lipids by immune receptors. *Trends Immunol* (2017) 38:66–76. doi:10.1016/j.it.2016.10.009
18. PrabhuDas MR, Baldwin CL, Bollyky PL, Bowdish DME, Drickamer K, Febbraio M, et al. A consensus definitive classification of scavenger receptors and their roles in health and disease. *J Immunol* (2017) 198:3775–89. doi:10.4049/jimmunol.1700373
19. Taylor PR, Martinez-Pomares L, Stacey M, Lin HH, Brown GD, Gordon S. Macrophage receptors and immune recognition. *Annu Rev Immunol* (2005) 23:901–44. doi:10.1146/annurev.immunol.23.021704.115816
20. Underhill DM, Goodridge HS. Information processing during phagocytosis. *Nat Rev Immunol* (2012) 12:492–502. doi:10.1038/nri3244
21. Canton J, Neculai D, Grinstein S. Scavenger receptors in homeostasis and immunity. *Nat Rev Immunol* (2013) 13:621–34. doi:10.1038/nri3515
22. Bournazos S, DiLillo DJ, Ravetch JV. The role of Fc-FcgammaR interactions in IgG-mediated microbial neutralization. *J Exp Med* (2015) 212:1361–9. doi:10.1084/jem.20151267
23. Ricklin D, Reis ES, Lambris JD. Complement in disease: a defence system turning offensive. *Nat Rev Nephrol* (2016) 12:383–401. doi:10.1038/nrneph.2016.70
24. Dambuza IM, Brown GD. C-type lectins in immunity: recent developments. *Curr Opin Immunol* (2015) 32:21–7. doi:10.1016/j.coi.2014.12.002
25. Cho WS, Duffin R, Thielbeer F, Bradley M, Megson IL, Macnee W, et al. Zeta potential and solubility to toxic ions as mechanisms of lung inflammation caused by metal/metal oxide nanoparticles. *Toxicol Sci* (2012) 126:469–77. doi:10.1093/toxsci/kfs006
26. Tsugita M, Morimoto N, Tashiro M, Kinoshita K, Nakayama M. SR-B1 is a silica receptor that mediates canonical inflammasome activation. *Cell Rep* (2017) 18:1298–311. doi:10.1016/j.celrep.2017.01.004
27. Shi Y, Mucsi AD, Ng G. Monosodium urate crystals in inflammation and immunity. *Immunol Rev* (2010) 233:203–17. doi:10.1111/j.0105-2896.2009.00851.x
28. Moreno T, Reche C, Rivas I, Cruz Minguillon M, Martins V, Vargas C, et al. Urban air quality comparison for bus, tram, subway and pedestrian commutes in Barcelona. *Environ Res* (2015) 142:495–510. doi:10.1016/j.envres.2015.07.022
29. Pozzi R, De Berardis B, Paoletti L, Guastadisegni C. Inflammatory mediators induced by coarse (PM2.5-10) and fine (PM2.5) urban air particles in raw 264.7 cells. *Toxicology* (2003) 183:243–54. doi:10.1016/S0300-483X(02)00545-0
30. Brauer M, Avila-Casado C, Fortoul TI, Vedal S, Stevens B, Churg A. Air pollution and retained particles in the lung. *Environ Health Perspect* (2001) 109:1039–43. doi:10.1289/ehp.011091039
31. WHO. *Elimination of Silicosis GOHNET News Letter*. (2007). p. 1–20. Available from: http://www.who.int/occupational_health/publications/newsletter/gohnet12e.pdf
32. Merget R, Bauer T, Kupper HU, Philippou S, Bauer HD, Breitstadt R, et al. Health hazards due to the inhalation of amorphous silica. *Arch Toxicol* (2002) 75:625–34. doi:10.1007/s002040100266
33. Huh D, Matthews BD, Mammoto A, Montoya-Zavala M, Hsin HY, Ingber DE. Reconstituting organ-level lung functions on a chip. *Science* (2010) 328:1662–8. doi:10.1126/science.1188302
34. Kusaka T, Nakayama M, Nakamura K, Ishimiya M, Furusawa E, Ogasawara K. Effect of silica particle size on macrophage inflammatory responses. *PLoS One* (2014) 9:e92634. doi:10.1371/journal.pone.0092634
35. Mitrano DM, Motellier S, Clavaguera S, Nowack B. Review of nanomaterial aging and transformations through the life cycle of nano-enhanced products. *Environ Int* (2015) 77:132–47. doi:10.1016/j.envint.2015.01.013
36. Shi H, Magaye R, Castranova V, Zhao J. Titanium dioxide nanoparticles: a review of current toxicological data. *Part Fibre Toxicol* (2013) 10:15. doi:10.1186/1743-8977-10-15
37. Yazdi AS, Guarda G, Riteau N, Drexler SK, Tardivel A, Couillin I, et al. Nanoparticles activate the NLR pyrin domain containing 3 (Nlrp3) inflammasome and cause pulmonary inflammation through release of IL-1alpha and IL-1beta. *Proc Natl Acad Sci U S A* (2010) 107:19449–54. doi:10.1073/pnas.1008155107
38. Lison D, Vietti G, van den Brule S. Paracelsus in nanotoxicology. *Part Fibre Toxicol* (2014) 11:35. doi:10.1186/s12989-014-0035-7
39. Tsugita M, Morimoto N, Nakayama M. SiO_2 and TiO_2 nanoparticles synergistically trigger macrophage inflammatory responses. *Part Fibre Toxicol* (2017) 14:11. doi:10.1186/s12989-017-0192-6
40. Rabolli V, Lison D, Huaux F. The complex cascade of cellular events governing inflammasome activation and IL-1beta processing in response to inhaled particles. *Part Fibre Toxicol* (2016) 13:40. doi:10.1186/s12989-016-0150-8
41. Thakur SA, Hamilton RF Jr, Holian A. Role of scavenger receptor a family in lung inflammation from exposure to environmental particles. *J Immunotoxicol* (2008) 5:151–7. doi:10.1080/15476910802085863
42. Arredouani M, Yang Z, Ning Y, Qin G, Soininen R, Tryggvason K, et al. The scavenger receptor MARCO is required for lung defense against pneumococcal pneumonia and inhaled particles. *J Exp Med* (2004) 200:267–72. doi:10.1084/jem.20040731
43. Beamer CA, Holian A. Scavenger receptor class A type I/II (CD204) null mice fail to develop fibrosis following silica exposure. *Am J Physiol Lung Cell Mol Physiol* (2005) 289:L186–95. doi:10.1152/ajplung.00474.2004
44. Thakur SA, Beamer CA, Migliaccio CT, Holian A. Critical role of MARCO in crystalline silica-induced pulmonary inflammation. *Toxicol Sci* (2009) 108:462–71. doi:10.1093/toxsci/kfp011
45. Nishijima N, Hirai T, Misato K, Aoyama M, Kuroda E, Ishii KJ, et al. Human scavenger receptor A1-mediated inflammatory response to silica particle exposure is size specific. *Front Immunol* (2017) 8:379. doi:10.3389/fimmu.2017.00379
46. Hamilton RF Jr, Thakur SA, Mayfair JK, Holian A. MARCO mediates silica uptake and toxicity in alveolar macrophages from C57BL/6 mice. *J Biol Chem* (2006) 281:34218–26. doi:10.1074/jbc.M605229200
47. Lagasse HA, Anidi IU, Craig JM, Limjunyawong N, Poupore AK, Mitzner W, et al. Recruited monocytes modulate malaria-induced lung injury through CD36-mediated clearance of sequestered infected erythrocytes. *J Leukoc Biol* (2016) 99:659–71. doi:10.1189/jlb.4HI0315-130RRR
48. Mossman BT, Gee JB. Asbestos-related diseases. *N Engl J Med* (1989) 320:1721–30. doi:10.1056/NEJM198906293202604

49. Dostert C, Petrilli V, Van Bruggen R, Steele C, Mossman BT, Tschopp J. Innate immune activation through Nalp3 inflammasome sensing of asbestos and silica. *Science* (2008) 320:674–7. doi:10.1126/science.1156995
50. Murthy S, Larson-Casey JL, Ryan AJ, He C, Kobzik L, Carter AB. Alternative activation of macrophages and pulmonary fibrosis are modulated by scavenger receptor, macrophage receptor with collagenous structure. *FASEB J* (2015) 29:3527–36. doi:10.1096/fj.15-271304
51. De Volder MF, Tawfick SH, Baughman RH, Hart AJ. Carbon nanotubes: present and future commercial applications. *Science* (2013) 339:535–9. doi:10.1126/science.1222453
52. Murr LE, Soto KF. TEM comparison of chrysotile (asbestos) nanotubes and carbon nanotubes. *J Sci Mater* (2004) 39:4941–7. doi:10.1023/B:Jmsc.0000035342.99587.96
53. Service RF. Nanotoxicology. Nanotechnology grows up. *Science* (2004) 304:1732–4. doi:10.1126/science.304.5678.1732
54. Vietti G, Lison D, van den Brule S. Mechanisms of lung fibrosis induced by carbon nanotubes: towards an adverse outcome pathway (AOP). *Part Fibre Toxicol* (2016) 13:11. doi:10.1186/s12989-016-0123-y
55. Poland CA, Duffin R, Kinloch I, Maynard A, Wallace WA, Seaton A, et al. Carbon nanotubes introduced into the abdominal cavity of mice show asbestos-like pathogenicity in a pilot study. *Nat Nanotechnol* (2008) 3:423–8. doi:10.1038/nnano.2008.111
56. Takagi A, Hirose A, Nishimura T, Fukumori N, Ogata A, Ohashi N, et al. Induction of mesothelioma in p53± mouse by intraperitoneal application of multi-wall carbon nanotube. *J Toxicol Sci* (2008) 33:105–16. doi:10.2131/jts.33.105
57. Palomaki J, Valimaki E, Sund J, Vippola M, Clausen PA, Jensen KA, et al. Long, needle-like carbon nanotubes and asbestos activate the NLRP3 inflammasome through a similar mechanism. *ACS Nano* (2011) 5:6861–70. doi:10.1021/nn200595c
58. Lindblad EB. Aluminium adjuvants—in retrospect and prospect. *Vaccine* (2004) 22:3658–68. doi:10.1016/j.vaccine.2004.03.032
59. Eisenbarth SC, Colegio OR, O'Connor W, Sutterwala FS, Flavell RA. Crucial role for the Nalp3 inflammasome in the immunostimulatory properties of aluminium adjuvants. *Nature* (2008) 453:1122–6. doi:10.1038/nature06939
60. Hornung V, Bauernfeind F, Halle A, Samstad EO, Kono H, Rock KL, et al. Silica crystals and aluminum salts activate the NALP3 inflammasome through phagosomal destabilization. *Nat Immunol* (2008) 9:847–56. doi:10.1038/ni.1631
61. Kool M, Willart MA, van Nimwegen M, Bergen I, Pouliot P, Virchow JC, et al. An unexpected role for uric acid as an inducer of T helper 2 cell immunity to inhaled antigens and inflammatory mediator of allergic asthma. *Immunity* (2011) 34:527–40. doi:10.1016/j.immuni.2011.03.015
62. Marichal T, Ohata K, Bedoret D, Mesnil C, Sabatel C, Kobiyama K, et al. DNA released from dying host cells mediates aluminum adjuvant activity. *Nat Med* (2011) 17:996–1002. doi:10.1038/nm.2403
63. Bruchard M, Rebe C, Derangere V, Togbe D, Ryffel B, Boidot R, et al. The receptor NLRP3 is a transcriptional regulator of TH2 differentiation. *Nat Immunol* (2015) 16:859–70. doi:10.1038/ni.3202
64. Flach TL, Ng G, Hari A, Desrosiers MD, Zhang P, Ward SM, et al. Alum interaction with dendritic cell membrane lipids is essential for its adjuvanticity. *Nat Med* (2011) 17:479–87. doi:10.1038/nm.2306
65. Ng G, Sharma K, Ward SM, Desrosiers MD, Stephens LA, Schoel WM, et al. Receptor-independent, direct membrane binding leads to cell-surface lipid sorting and Syk kinase activation in dendritic cells. *Immunity* (2008) 29:807–18. doi:10.1016/j.immuni.2008.09.013
66. Caracciolo G, Farokhzad OC, Mahmoudi M. Biological identity of nanoparticles *in vivo*: clinical implications of the protein corona. *Trends Biotechnol* (2017) 35:257–64. doi:10.1016/j.tibtech.2016.08.011
67. Hadjidemetriou M, Kostarelos K. Nanomedicine: evolution of the nanoparticle corona. *Nat Nanotechnol* (2017) 12:288–90. doi:10.1038/nnano.2017.61
68. Lundqvist M, Stigler J, Elia G, Lynch I, Cedervall T, Dawson KA. Nanoparticle size and surface properties determine the protein corona with possible implications for biological impacts. *Proc Natl Acad Sci U S A* (2008) 105:14265–70. doi:10.1073/pnas.0805135105
69. Tenzer S, Docter D, Kuharev J, Musyanovych A, Fetz V, Hecht R, et al. Rapid formation of plasma protein corona critically affects nanoparticle pathophysiology. *Nat Nanotechnol* (2013) 8:772–81. doi:10.1038/nnano.2013.181
70. Mirshafiee V, Kim R, Park S, Mahmoudi M, Kraft ML. Impact of protein pre-coating on the protein corona composition and nanoparticle cellular uptake. *Biomaterials* (2016) 75:295–304. doi:10.1016/j.biomaterials.2015.10.019
71. Yan Y, Gause KT, Kamphuis MM, Ang CS, O'Brien-Simpson NM, Lenzo JC, et al. Differential roles of the protein corona in the cellular uptake of nanoporous polymer particles by monocyte and macrophage cell lines. *ACS Nano* (2013) 7:10960–70. doi:10.1021/nn404481f
72. Kono H, Rock KL. How dying cells alert the immune system to danger. *Nat Rev Immunol* (2008) 8:279–89. doi:10.1038/nri2215
73. So AK, Martinon F. Inflammation in gout: mechanisms and therapeutic targets. *Nat Rev Rheumatol* (2017) 13:639–47. doi:10.1038/nrrheum.2017.155
74. Giclas PC, Ginsberg MH, Cooper NR. Immunoglobulin G independent activation of the classical complement pathway by monosodium urate crystals. *J Clin Invest* (1979) 63:759–64. doi:10.1172/JCI109360
75. Hasselbacher P. C3 activation by monosodium urate monohydrate and other crystalline material. *Arthritis Rheum* (1979) 22:571–8. doi:10.1002/art.1780220603
76. An LL, Mehta P, Xu L, Turman S, Reimer T, Naiman B, et al. Complement C5a potentiates uric acid crystal-induced IL-1beta production. *Eur J Immunol* (2014) 44:3669–79. doi:10.1002/eji.201444560
77. Barabe F, Gilbert C, Liao N, Bourgoin SG, Naccache PH. Crystal-induced neutrophil activation VI. Involvement of FcgammaRIIIB (CD16) and CD11b in response to inflammatory microcrystals. *FASEB J* (1998) 12:209–20.
78. Malik AF, Hoque R, Ouyang X, Ghani A, Hong E, Khan K, et al. Inflammasome components Asc and caspase-1 mediate biomaterial-induced inflammation and foreign body response. *Proc Natl Acad Sci U S A* (2011) 108:20095–100. doi:10.1073/pnas.1105152108
79. Neumann K, Castineiras-Vilarino M, Hockendorf U, Hannesschlager N, Lemeer S, Kupka D, et al. Clec12a is an inhibitory receptor for uric acid crystals that regulates inflammation in response to cell death. *Immunity* (2014) 40:389–99. doi:10.1016/j.immuni.2013.12.015
80. Braga TT, Forni MF, Correa-Costa M, Ramos RN, Barbuto JA, Branco P, et al. Soluble uric acid activates the NLRP3 inflammasome. *Sci Rep* (2017) 7:39884. doi:10.1038/srep39884
81. Sheedy FJ, Grebe A, Rayner KJ, Kalantari P, Ramkhelawon B, Carpenter SB, et al. CD36 coordinates NLRP3 inflammasome activation by facilitating intracellular nucleation of soluble ligands into particulate ligands in sterile inflammation. *Nat Immunol* (2013) 14:812–20. doi:10.1038/ni.2639
82. Duewell P, Kono H, Rayner KJ, Sirois CM, Vladimer G, Bauernfeind FG, et al. NLRP3 inflammasomes are required for atherogenesis and activated by cholesterol crystals. *Nature* (2010) 464:1357–61. doi:10.1038/nature08938
83. Hasselbacher P, Hahn JL. Activation of the alternative pathway of complement by microcrystalline cholesterol. *Atherosclerosis* (1980) 37:239–45. doi:10.1016/0021-9150(80)90009-X
84. Vogt W, von Zabern I, Damerau B, Hesse D, Luhmann B, Nolte R. Mechanisms of complement activation by crystalline cholesterol. *Mol Immunol* (1985) 22:101–6. doi:10.1016/S0161-5890(85)80003-1
85. Samstad EO, Niyonzima N, Nymo S, Aune MH, Ryan L, Bakke SS, et al. Cholesterol crystals induce complement-dependent inflammasome activation and cytokine release. *J Immunol* (2014) 192:2837–45. doi:10.4049/jimmunol.1302484
86. Kolev M, Le Friec G, Kemper C. Complement—tapping into new sites and effector systems. *Nat Rev Immunol* (2014) 14:811–20. doi:10.1038/nri3761
87. Pilely K, Rosbjerg A, Genster N, Gal P, Pal G, Halvorsen B, et al. Cholesterol crystals activate the lectin complement pathway *via* ficolin-2 and mannose-binding lectin: implications for the progression of atherosclerosis. *J Immunol* (2016) 196:5064–74. doi:10.4049/jimmunol.1502595
88. Kiyotake R, Oh-Hora M, Ishikawa E, Miyamoto T, Ishibashi T, Yamasaki S. Human Mincle binds to cholesterol crystals and triggers innate immune responses. *J Biol Chem* (2015) 290:25322–32. doi:10.1074/jbc.M115.645234
89. Stewart CR, Stuart LM, Wilkinson K, van Gils JM, Deng J, Halle A, et al. CD36 ligands promote sterile inflammation through assembly of a toll-like receptor 4 and 6 heterodimer. *Nat Immunol* (2010) 11:155–61. doi:10.1038/ni.1836
90. McCarthy GM, Cheung HS. Point: hydroxyapatite crystal deposition is intimately involved in the pathogenesis and progression of human osteoarthritis. *Curr Rheumatol Rep* (2009) 11:141–7. doi:10.1007/s11926-009-0020-6

91. Laquerriere P, Grandjean-Laquerriere A, Jallot E, Balossier G, Frayssinet P, Guenounou M. Importance of hydroxyapatite particles characteristics on cytokines production by human monocytes *in vitro*. *Biomaterials* (2003) 24:2739–47. doi:10.1016/S0142-9612(03)00089-9
92. Jin C, Frayssinet P, Pelker R, Cwirka D, Hu B, Vignery A, et al. NLRP3 inflammasome plays a critical role in the pathogenesis of hydroxyapatite-associated arthropathy. *Proc Natl Acad Sci U S A* (2011) 108:14867–72. doi:10.1073/pnas.1111101108
93. Pazar B, Ea HK, Narayan S, Kolly L, Bagnoud N, Chobaz V, et al. Basic calcium phosphate crystals induce monocyte/macrophage IL-1beta secretion through the NLRP3 inflammasome *in vitro*. *J Immunol* (2011) 186:2495–502. doi:10.4049/jimmunol.1001284
94. Joosten LA, Ea HK, Netea MG, Busso N. Interleukin-1beta activation during acute joint inflammation: a limited role for the NLRP3 inflammasome *in vivo*. *Joint Bone Spine* (2011) 78:107–10. doi:10.1016/j.jbspin.2010.11.004
95. Kroemer G, Jaattela M. Lysosomes and autophagy in cell death control. *Nat Rev Cancer* (2005) 5:886–97. doi:10.1038/nrc1738
96. Orlowski GM, Sharma S, Colbert JD, Bogyo M, Robertson SA, Kataoka H, et al. Frontline science: multiple cathepsins promote inflammasome-independent, particle-induced cell death during NLRP3-dependent IL-1beta activation. *J Leukoc Biol* (2017) 102:7–17. doi:10.1189/jlb.3HI0316-152R
97. Ding J, Wang K, Liu W, She Y, Sun Q, Shi J, et al. Pore-forming activity and structural autoinhibition of the gasdermin family. *Nature* (2016) 535:111–6. doi:10.1038/nature18590
98. Kayagaki N, Stowe IB, Lee BL, O'Rourke K, Anderson K, Warming S, et al. Caspase-11 cleaves gasdermin D for non-canonical inflammasome signalling. *Nature* (2015) 526:666–71. doi:10.1038/nature15541
99. Shi J, Zhao Y, Wang K, Shi X, Wang Y, Huang H, et al. Cleavage of GSDMD by inflammatory caspases determines pyroptotic cell death. *Nature* (2015) 526:660–5. doi:10.1038/nature15514
100. Weinlich R, Oberst A, Beere HM, Green DR. Necroptosis in development, inflammation and disease. *Nat Rev Mol Cell Biol* (2017) 18:127–36. doi:10.1038/nrm.2016.149
101. Mulay SR, Desai J, Kumar SV, Eberhard JN, Thomasova D, Romoli S, et al. Cytotoxicity of crystals involves RIPK3-MLKL-mediated necroptosis. *Nat Commun* (2016) 7:10274. doi:10.1038/ncomms10274
102. Jacobson LS, Lima H Jr, Goldberg MF, Gocheva V, Tsiperson V, Sutterwala FS, et al. Cathepsin-mediated necrosis controls the adaptive immune response by Th2 (T helper type 2)-associated adjuvants. *J Biol Chem* (2013) 288:7481–91. doi:10.1074/jbc.M112.400655
103. Di Virgilio F, Dal Ben D, Sarti AC, Giuliani AL, Falzoni S. The P2X7 receptor in infection and inflammation. *Immunity* (2017) 47:15–31. doi:10.1016/j.immuni.2017.06.020
104. Chow MT, Tschopp J, Moller A, Smyth MJ. NLRP3 promotes inflammation-induced skin cancer but is dispensable for asbestos-induced mesothelioma. *Immunol Cell Biol* (2012) 90:983–6. doi:10.1038/icb.2012.46
105. Re SL, Giordano G, Yakoub Y, Devosse R, Uwambayinema F, Couillin I, et al. Uncoupling between inflammatory and fibrotic responses to silica: evidence from MyD88 knockout mice. *PLoS One* (2014) 9:e99383. doi:10.1371/journal.pone.0099383

Conflict of Interest Statement: The author declares that the research was conducted in the absence of any commercial or financial relationships that could be construed as a potential conflict of interest.

frontiers in Immunology

MINI REVIEW
published: 28 May 2018
doi: 10.3389/fimmu.2018.01145

Disease-Associated Particulates and Joint Inflammation; Mechanistic Insights and Potential Therapeutic Targets

*Olwyn R. Mahon and Aisling Dunne**

School of Biochemistry and Immunology, School of Medicine, Trinity College Dublin, Trinity Biomedical Sciences Institute, The University of Dublin, Dublin, Ireland

It is now well established that intra-articular deposition of endogenous particulates, such as osteoarthritis-associated basic calcium phosphate crystals, gout-associated monosodium urate crystals, and calcium deposition disease-associated calcium pyrophosphate crystals, contributes to joint destruction through the production of cartilage-degrading enzymes and pro-inflammatory cytokines. Furthermore, exogenous wear-debris particles, generated from prosthetic implants, drive periprosthetic osteolysis which impacts on the longevity of total joint replacements. Over the last few years, significant insight has been gained into the mechanisms through which these particulates exert their effects. Not only has this increased our understanding of the pathological processes associated with crystal deposition but it has also led to the identification of a number of therapeutic targets to treat particulate-associated disease. In this review, we discuss recent developments regarding the cellular events triggered by joint-associated particulates, as well as future directions in therapy for particulate-related arthropathies.

Keywords: particulates, osteoarthritis, gout, calcium deposition disease, joint inflammation

OPEN ACCESS

Edited by:
Shrikant R. Mulay, Ludwig-Maximilians-Universität München, Germany

Reviewed by:
Christian Maueröder, VIB-UGent Center for Inflammation Research (IRC), Belgium
Anna Scanu, Università degli Studi di Padova, Italy
Onkar Prakash Kulkarni, Birla Institute of Technology and Science, India

***Correspondence:**
Aisling Dunne
aidunne@tcd.ie

Specialty section:
This article was submitted to Inflammation, a section of the journal Frontiers in Immunology

Received: *29 March 2018*
Accepted: *07 May 2018*
Published: *28 May 2018*

Citation:
Mahon OR and Dunne A (2018) Disease-Associated Particulates and Joint Inflammation; Mechanistic Insights and Potential Therapeutic Targets. Front. Immunol. 9:1145. doi: 10.3389/fimmu.2018.01145

INTRODUCTION

Immune responses driven by microparticles are implicated in the pathogenesis of a number of inflammatory diseases, including atherosclerosis, silicosis, and asbestosis (1). In the joint, endogenous crystals, including uric acid and calcium-containing crystals, are formed as a result of dysregulated metabolic processes. These particulates are associated with gout, calcium pyrophosphate deposition (CPPD) disease, and osteoarthritis (OA), and a number of studies have demonstrated that they contribute to synovial inflammation, cartilage destruction, and subchondral bone remodeling (2–5). In cases of severe joint degeneration, total joint replacement (TJR) is the only remaining option to improve pain and ambulation in patients. However, the gradual wear of orthopedic implants over time results in the generation of particulate matter derived from various components of the prosthesis. The presence of these particles is associated with periprosthetic osteolysis which is characterized by inflammation and osteoclastic resorption of bone surrounding the implant (6, 7). Examination of the cell types and pathways activated following crystal deposition has shed light on the pathogenesis of crystal-related arthropathies and peri-implant inflammation, all of which are steadily becoming more prevalent as the lifespan of the general population increases. In this review, we discuss the molecular mechanisms underlying particulate matter-induced inflammatory and catabolic processes in the joint. We also highlight potential therapeutic targets for the treatment of particulate matter-induced inflammation.

MONOSODIUM URATE (MSU) CRYSTALS AND GOUT

Gout is a chronic inflammatory disease characterized by high serum urate concentrations (>6.8 mg/dL) which in turn leads to MSU crystal deposition in joints and peri-articular tissues. While genetic and environmental factors contribute to the development of hyperuricaemia, the underexcretion of urate by specialized transporters in the gastrointestinal tract and kidney is considered a leading cause of elevated serum urate levels (8, 9). The precise mechanism(s) leading to MSU-crystal formation is not entirely understood; however, peripheral temperature, tissue pH, and synovial fluid components are all thought to play a contributory role when serum urate levels exceed maximal solubility. Clinical features of gout include acute inflammatory flares that tend to resolve spontaneously and, if untreated, can eventually advance to chronic gouty arthritis which is characterized by chronic inflammation and the formation of granulomatous lesions, known as tophi (10–12). Current treatments include urate lowering drugs, NSAID administration, and dietary modification; however, ongoing research into the mechanisms surrounding MSU crystal-induced cell activation has led to the identification of a number of novel targets that may also limit inflammation.

Monosodium urate crystals induce matrix metalloprotease (MMP) expression by chondrocytes (13), prostaglandin, and CCL2 production by fibroblasts and synoviocytes (14) and TGFβ1, IL-6, tumor necrosis factor (TNF)-α, and IL-8 secretion by monocytes (15–17). However, the acute joint inflammation observed during flare-ups is primarily driven by macrophage derived IL-1β, *via* activation of NOD-like receptor related protein 3 (NLRP3). MSU crystals are, therefore, classified as "danger signals" and, together with extracellular ATP and CPPD crystals, were the first endogenous activators of NLRP3 identified (18). Persistent NLRP3 activation has been linked to the pathogenesis of a number of inflammatory diseases and has been reviewed in detail elsewhere (19, 20). Briefly, activation of NLRP3 results in the assembly of a large multiprotein complex called the inflammasome which is involved in the processing of pro-IL-1 β and pro-IL-18 into their active forms. A "priming signal" (signal 1) upregulates expression of pro IL-1β/pro-IL-18 as well as components of the inflammasome complex and is mediated, for example, by TLR agonists. A second signal (Signal 2), caused by a disruption in cellular homeostasis, results in assembly of a complex comprised of NLRP3 oligomers and the adapter protein, ASC. Inactive pro-caspase-1 is recruited to the complex where it undergoes auto-activation and catalyzes the cleavage of pro-IL-1 β and pro-IL-18 into their mature forms which are secreted from the cell (21, 22). In the context of gout, a number of endogenous molecules, including free fatty acids, have been proposed to act as a priming signal, while MSU crystals act as signal 2 (23).

Crystal-induced inflammasome activation is linked to lysosomal rupture, ROS production and ATP driven P2X7-dependent pore formation (24). Potassium efflux is also involved in NLRP3 activation, and it has been proposed that fusion of MSU crystal-containing phagosomes with acidic lysosomes causes a massive release of sodium ions from the phagolysosome which is balanced by passive water influx. The accompanying drop in intracellular potassium concentration in turn drives NLRP3 assembly/activation (25). Targeting these aspects of NLRP3 inflammasome activation is currently being explored as a means of limiting the pathological effects of MSU crystals. For example, the ketone body, b-hydroxybutyrate, which specifically inhibits NLRP3 inflammasome activation *via* potassium efflux blockade, and the naturally derived antioxidant, sulforaphane, have been shown to attenuate MSU-induced responses in murine models of gout (26, 27). Furthermore, the anti-inflammatory phytochemical, caffeic acid phenyl ester, was shown to suppress MSU crystal-induced IL-1β production *in vivo* by directly blocking NLRP3/ASC interactions (28). It is worth noting that neutrophil-derived serine proteases are also capable of processing pro-IL-1β; therefore, direct neutralization of IL-1β may be of greater benefit in some patients (29). Indeed, canakinumab (anti-IL-1β) is recommended for the treatment of acute flares when other anti-inflammatory drugs are ineffective.

Targeting upstream of NLRP3 activation is also a possibility and recent studies have provided insight into the cellular events triggered upon binding of MSU crystals to the cell membrane. Barabe et al. demonstrated that MSU crystals bind directly to the surface Fc receptor, FcgRIII, in human neutrophils (30) while Desaulniers et al. demonstrated that MSU crystals trigger activation of the downstream signaling molecule, Syk (31). It was subsequently demonstrated that Syk is a substrate of conventional PKCs, which are activated in a Src kinase-dependant manner (32). Phosphorylation of Syk by PKC facilitates the interaction of Syk with PI3 kinase driving subsequent phagocytosis of MSU crystals (33). These effects may, however, be cell-type specific as it was later demonstrated that Syk is activated by MSU crystals in a receptor-independent manner in dendritic cells, *via* a process known as membrane affinity-triggered signaling (MATS) (34). This involves direct binding of particulate matter to the cell membrane which results in clustering of lipid rafts and aggregation of proteins that are partitioned into membrane lipids. Atomic force microscopy confirmed the direct interaction of MSU crystals with cell-surface lipids, particularly cholesterol. This in turn leads to aggregation of immunoreceptor tyrosine-based activation motif-containing molecules which then recruit and activate Syk (35). Inhibition of Src family kinases prevented MSU-induced Syk phosphorylation while PI3 kinase was found to be activated downstream of Syk; however, unlike neutrophils, surface receptors were not required for this interaction as treatment with pronase had no effect on MSU uptake (34).

While Syk inhibitors can attenuate MSU-induced IL-1β production *in vitro* (36), it remains to be seen whether direct intra-articular administration of Syk inhibitors can ameliorate the effects of MSU crystals in a clinical setting. Indeed a number of kinases are likely to be activated downstream of Syk. Of note, the broad spectrum tyrosine kinase inhibitor, imatinib mesylate, was recently shown to suppress MSU crystal-induced synovial inflammation in an acute gouty arthritis model (37).

Neutrophil necroptosis, a regulated form of necrosis, has also been implicated in MSU-induced responses (38, 39). In contrast to apoptosis, necroptosis occurs independently of caspase activation and may exacerbate inflammation *via* the release of additional danger signals (40). Receptor interacting protein kinase-1,

RIP3, and mixed lineage kinase domain-like (MLKL), play key roles in necroptosis. Targeting RIP1 and MLKL was shown to suppress MSU-induced cell death *in vitro* while MLKL-deficient mice lacked tophus formation in a gouty arthritis model, providing further confirmation of the involvement of the RIP1-RIP3-MLKL axis (38). Neutrophil extracellular traps (NETs) are formed during MSU-induced necroptosis but whether this is an active process or a passive consequence of unregulated necrosis has yet to be determined and is discussed in more detail in Ref. (41). While it was previously reported that ROS production is required for macroscopic aggregation of NETs and crystals (42), a recent study by Chatfield et al., involving direct quantitation of key aspects of NET formation, has demonstrated that ROS production is dispensable for MSU-induced NET formation in human neutrophils (43). Furthermore, neutrophils from patients with a functional NOX2 deficiency are capable of producing NETs in response to MSU crystal stimulation (44).

Neutrophil extracellular traps have been detected in synovial fluid from acutely inflamed joints of gouty patients and also surrounding crystals in non-inflamed tophi of chronic gout patients (43). NETs are released by neutrophils to trap and kill invading microbes during infection and neutrophil granule proteases have been shown to activate cytokines such as IL-1α and IL-33 (45); however, it has been suggested that they may actually play a pro-resolving role in acute gout *via* degradation of pro-inflammatory cytokines and chemokines (42). Further study is clearly required to fully appreciate the role of neutrophil-mediated processes in the pathogenesis of gout. The cell types and mediators of MSU-induced inflammation are highlighted in **Figure 1**.

CALCIUM-CONTAINING CRYSTALS IN OA AND CPPD DISEASE

Basic calcium phosphate (BCP) crystals, of which the hydroxyapatite (HA) form is most prevalent, are found in 70% of total OA cases where their concentration closely correlates with the extent of cartilage degradation and lesion severity (46, 47). They are thought to form as a result of dysregulated ossification processes (48) and, given that crystal deposition does not occur in healthy cartilage, it is becoming more widely accepted that cartilage calcification plays a pathogenic role in OA (3). Like MSU crystals, BCP crystals are now considered a "danger signal" as they can activate a number of cell types and contribute to joint degeneration through the production of cartilage-degrading proteases and pro-inflammatory mediators. Early studies demonstrated that BCP crystals drive MMP and inflammatory gene expression in fibroblasts (49, 50), while more recent studies have focused on their effects on macrophages, chondrocytes, and osteoclasts (51–54). Macrophage derived-IL-1β has been given a lot of consideration in the context of BCP crystals and OA, and while BCP crystals induce potent IL-1β production *in vitro*, reports from *in vivo* studies have been conflicting (55, 56). Indeed, Nasi et al. recently demonstrated that neither IL-1α nor IL-1β mediate the pathology seen in the murine menisectomy model of OA (57), a finding that may explain the lack of efficacy of IL-1 inhibitors in human OA. Based on these studies, focus has shifted to other potential targets including IL-6 which is produced by chondrocytes in response to BCP stimulation and acts in an autocrine manner to promote calcium-containing crystal formation and upregulation of genes involved in calcification (51).

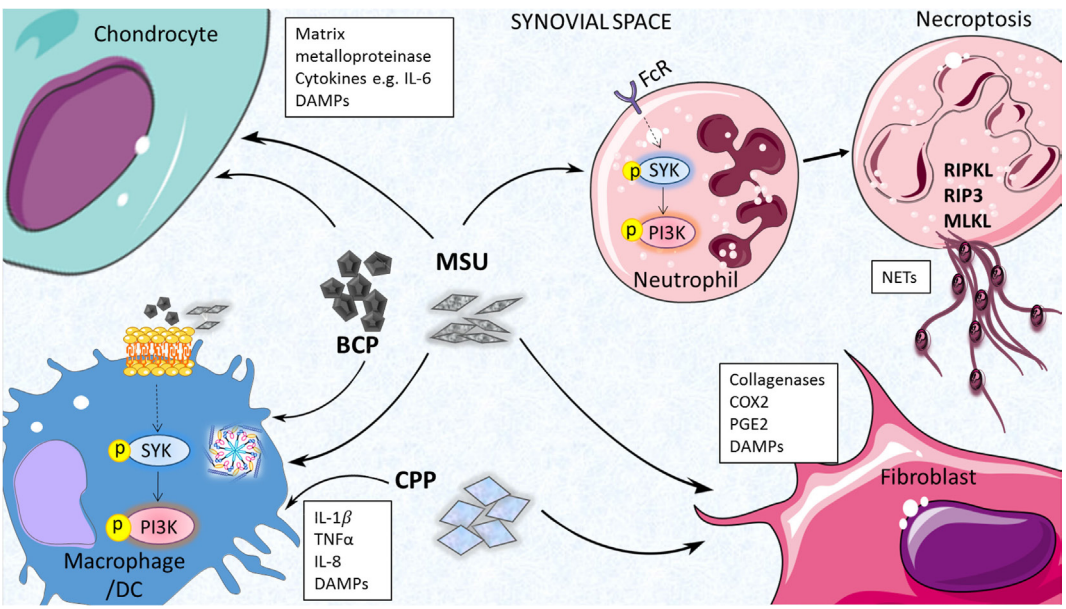

FIGURE 1 | Inflammatory processes driven by endogenous joint-associates particulates. Monosodium urate (MSU), basic calcium phosphate (BCP) and calcium pyrophosphate (CPP) crystals can act on a number of cell types in the joint to drive pro-inflammatory cytokine production, matrix metalloprotease (MMP) expression, and release of additional damage-associated molecular patterns (DAMPs) that contribute further to joint inflammation and cartilage destruction. Inflammasome activation, membrane affinity-triggered signaling, and neutrophil-mediated neutrophil extracellular trap (NET) formation have been implicated in these responses.

We recently demonstrated that, like MSU crystals, BCP crystals also activate, Syk, and its downstream interacting partner, PI3K, in primary macrophages, and that pharmacological inhibition of these kinases leads to reduced MMP expression and pro-inflammatory cytokine production (53, 54). Whether Syk and/or PI3K activity is heightened in OA joints is yet to be determined, however, targeting membrane-proximal events induced by BCP crystals is a therapeutic option worth exploring. We have also demonstrated that both MSU and BCP crystals may contribute to bone erosion *via* inhibition of anti-osteoclastogenic cytokine signaling (58); therefore, targeting synovial inflammation induced by crystal deposition may suppress early destructive processes, while targeting the osteoclastogenic effects of crystals may suppress excessive bone remodeling. Indeed, preventing the actual intra-articular deposition of calcium crystals, as recently demonstrated by Nasi et al. using sodium thiosulphate, could limit inflammatory responses at the outset (59).

Pathological calcification is also a feature of CPPD disease. Acute CPPD disease is caused by the deposition of calcium pyrophosphate (CPP) crystals and is accompanied by symptoms overlapping with acute gouty arthritis, hence it is often referred to as pseudogout [reviewed in Ref. (5)]. A local excess of pyrophosphate (PPi) has been observed in the cartilage of affected patients and it is believed that high levels of extracellular PPi complex with calcium in the chondrocyte pericellular matrix to form CPP crystals. Like MSU crystals, CPPD crystals are phagocytosed by macrophages leading to NLRP3 dependent IL-1β processing and secretion and there is some evidence to suggest that anti-IL-1 therapies may be of benefit to patients (18). CPPD crystals have also been shown to drive the formation of NETs *in vitro* (60); however, whether this contributes to joint inflammation or plays a pro-resolving role *in vivo* has yet to be determined. Cartilage destruction is driven largely by the action of MMPs produced by synovial fibroblasts and chondrocytes and in patients with severe disease, joint replacement may be required. One potential therapeutic target for CPPD disease that has received a lot of attention of late is the multipass membrane protein, ANK (protein product of the progressive ankylosis gene), which regulates levels of inorganic phosphate. A gain of function mutation in human ANK is associated with familial cases of CPPD while expression of the protein was found to be increased in the cartilage of patients with sporadic CPPD disease (61). Given the potential link between crystal deposition and ANK activity, modulation of this pathway may be of benefit for the treatment, not just of pseudogout, but other arthopathies involving pathological CPP deposition.

WEAR-DEBRIS PARTICLES AND PERIPROSTHETIC OSTEOLYSIS

Total joint replacement is a highly successful procedure used to alleviate pain and restore function in individuals suffering from end-stage joint disease. Implants are commonly composed of a metal, e.g., titanium or ultra-high-molecular-weight polyethylene, and are coated with a bioceramic, such as HA, to enhance integration with surrounding bone. The implant is then typically fixed into place with poly-methyl methacrylate (PMMA) bone cement. While excellent patient outcomes are associated with this procedure, revision surgeries are often required due to the limited lifespan of orthopedic devices. The gradual wear and tear of implants over time results in the continuous generation of wear-debris particles from the articulating surface of the prosthesis (62). Due to their insoluble nature, most wear particles are resistant to digestion by macrophages and thus, a chronically activated macrophage population persists in the joint (63). This then culminates in periprosthetic osteolysis which is characterized by the osteoclastic resorption and degradation of bone surrounding the implant, a process that ultimately leads to aseptic implant loosening (64–66).

A number of cell types, including osteoclasts, fibroblasts, and osteoblasts, have been implicated in wear-debris induced osteolysis (**Figure 2**) (67, 68). More recently, various types of nanoparticles have been shown to act on neutrophils, inducing the formation of NETs (69–73). For example, Vitkov et al. demonstrated that PMN cells incubated with sandblasted large-grit acid etched (SLA) implants undergo histone citrullination, nuclear swelling, and chromatin alterations (70), while Muñoz et al. demonstrated that carbon and polystyrene nanopowders increase NET formation in a size-dependent manner (72). Macrophages play a key role in osteolysis where particle uptake culminates in a chronic inflammatory state mediated by cytokines, such as IL-1, IL-6, TNF-α, and RANKL, which can also contribute to osteoclast differentiation and thus exacerbate bone resorption (74–78). Chemokine production is also central to wear-debris particle-induced inflammatory responses (79). For example, MIF, MCP1, MIP 1α RANTES, and IL-8 levels are elevated in macrophages in response to PMMA and titanium particles (80–82), while fibroblasts produce elevated levels of MCP-1 after exposure to titanium and PMMA particles (83).

Like other disease-associated particulates, it is likely that wear-debris particles are binding to scavenger receptors on the cell surface or are inducing MATS. We have recently demonstrated that this is the case for HA and PMMA particles and that inhibition of Syk prevented wear particle-induced M1 macrophage polarization *in vitro* (84). Indeed, modulation of macrophage phenotype has been suggested as a potential therapeutic avenue for periprosthetic osteolysis and administration of the M2 polarizing cytokine, IL-4, has shown some efficacy, at least in murine models (85, 86). There are, however, no drugs specifically approved for the prevention of periprosthetic osteolysis. Bisphosphonates have been shown to inhibit enzymes in the mevalonate pathway which results in apoptosis of osteoclasts (68). They are commonly used for metabolic bone diseases (87) and several experimental studies have demonstrated a significant decrease in osteolysis/bone resorption after treatment with these compounds (88, 89). Modulating pro-inflammatory cytokine production may also prove beneficial for osteolysis patients assuming inflammation is targeted prior to extensive bone damage. Bortezomib (Bzb) is a reversible 26S proteasome inhibitor currently approved for the treatment of relapsed/refractory multiple myeloma (90). As well as antitumor effects, it has been shown to limit inflammation and bone resorption in arthritis models (91, 92). Bzb inhibits NF-κB, a master regulator of inflammation, by blocking degradation of the NF-κB inhibitor,

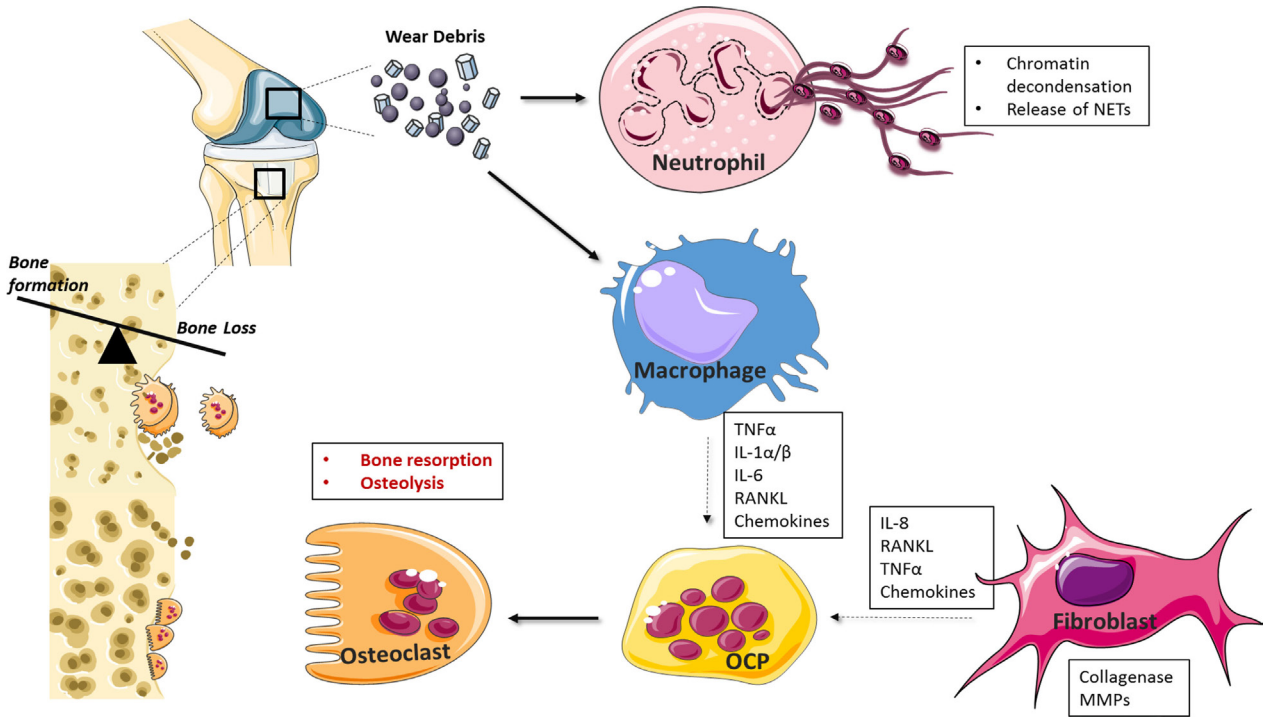

FIGURE 2 | Cellular mediators of periprosthetic osteolysis. Wear-debris particles generated from prostheses activate resident and infiltrating macrophages, fibroblasts, and neutrophils at the site of implantation. Neutrophil recognition of biomaterials drives neutrophil extracellular trap (NET) formation while macrophage and fibroblast-induced chemokine production facilitates further leukocyte recruitment to the implant interface. Cytokines, such as tumor necrosis factor (TNF)-α and IL-1, drive inflammation and, together with RANKL, can induce the differentiation of osteoclast precursor cells (OCPs) into activated bone resorbing cells. Matrix metalloprotease (MMPs) and collagenases contribute further to catabolic processes and aseptic implant loosening.

IkB. Mao et al. recently demonstrated that Bzb can inhibit titanium particle-induced inflammation in murine macrophages, a finding that warrants further *in vivo* study as it may have implications for the treatment of periprosthetic inflammation.

Finally, autophagy is associated with a number of physiological processes including basal inhibition of inflammation (93). Crișan et al. recently demonstrated that uric acid can inhibit autophagy, a finding that has implications not just for gout but other diseases associated with elevated uric acid levels including cancer and type 2 diabetes (94). Indeed, titanium particles can downregulate the expression of osteocyte-derived IFNβ in an autophagy-dependent manner (95). IFNβ is a negative regulator of osteoclastogenesis (96); therefore, therapeutic interventions to boost autophagy, for example with mTOR inhibitors or naturally derived autophagy inducers such as trehalose (97), may be of benefit for both gout and osteolysis patients.

CONCLUSION

While much progress has been made in elucidating the events contributing to crystal deposition diseases, the complex nature of these conditions has hampered the development of effective treatments. Urate-lowering drugs have proven efficacy in gout; however; in the case of OA, and in some instances, CPPD disease, TJR remains the only option for patients with significant joint destruction. This in itself is associated with the added complication of periprosthetic osteolysis and potential implant failure. The development of more durable biomaterials with low immunogenicity may prevent the occurrence of periprosthetic inflammation, while the identification of successful disease-modifying drugs for severe arthropathies may relinquish the need for joint replacement in the first instance. Therefore, gaining a better understanding of the inflammatory and destructive processes driven by disease-associated particulates, coupled with advances in disease monitoring technology, will be of huge benefit for the development of future prevention/treatment strategies.

AUTHOR CONTRIBUTIONS

AD conceived and wrote the paper with contribution from OM.

FUNDING

This work was supported by the Health Research Board, Ireland (HRA-POR-2014-582).

REFERENCES

1. Nakayama M. Macrophage recognition of crystals and nanoparticles. *Front Immunol* (2018) 9:103. doi:10.3389/fimmu.2018.00103
2. Pascart T, Lioté F. Gout: state of the art after a decade of developments. *Rheumatology* (2018) 1–18. doi:10.1093/rheumatology/key002
3. Conway R, McCarthy GM. Calcium-containing crystals and osteoarthritis: an unhealthy alliance. *Curr Rheumatol Rep* (2018) 20:13. doi:10.1007/s11926-018-0721-9
4. So A, Busso N. Osteoarthritis: crystal-gazing into the pathogenesis of osteoarthritis. *Nat Rev Rheumatol* (2011) 7:688–9. doi:10.1038/nrrheum.2011.165
5. Rosenthal AK, Ryan LM. Calcium pyrophosphate deposition disease. *N Engl J Med* (2016) 374:2575–84. doi:10.1056/NEJMra1511117
6. Beck RT, Illingworth KD, Saleh KJ. Review of periprosthetic osteolysis in total joint arthroplasty: an emphasis on host factors and future directions. *J Orthop Res* (2012) 30:541–6. doi:10.1002/jor.21554
7. Sukur E, Akman YE, Ozturkmen Y, Kucukdurmaz F. Particle disease: a current review of the biological mechanisms in periprosthetic osteolysis after hip arthroplasty. *Open Orthop J* (2016) 10:241–51. doi:10.2174/1874325001610010241
8. Dalbeth N, Merriman TR, Stamp LK. Gout. *Lancet* (2016) 388:2039–52. doi:10.1016/S0140-6736(16)00346-9
9. Kuo C-F, Grainge MJ, Zhang W, Doherty M. Global epidemiology of gout: prevalence, incidence and risk factors. *Nat Rev Rheumatol* (2015) 11:649. doi:10.1038/nrrheum.2015.91
10. Dalbeth N, Pool B, Gamble GD, Smith T, Callon KE, McQueen FM, et al. Cellular characterization of the gouty tophus: a quantitative analysis. *Arthritis Rheum* (2010) 62:1549–56. doi:10.1002/art.27356
11. Dalbeth N, Clark B, Gregory K, Gamble G, Sheehan T, Doyle A, et al. Mechanisms of bone erosion in gout: a quantitative analysis using plain radiography and computed tomography. *Ann Rheum Dis* (2009) 68:1290–5. doi:10.1136/ard.2008.094201
12. Ragab G, Elshahaly M, Bardin T. Gout: an old disease in new perspective – a review. *J Adv Res* (2017) 8:495–511. doi:10.1016/j.jare.2017.04.008
13. Liu R, Lioté F, Rose DM, Merz D, Terkeltaub R. Proline-rich tyrosine kinase 2 and Src kinase signaling transduce monosodium urate crystal-induced nitric oxide production and matrix metalloproteinase 3 expression in chondrocytes. *Arthritis Rheum* (2004) 50:247–58. doi:10.1002/art.11486
14. Scanu A, Oliviero F, Gruaz L, Sfriso P, Pozzuoli A, Frezzato F, et al. High-density lipoproteins downregulate CCL2 production in human fibroblast-like synoviocytes stimulated by urate crystals. *Arthritis Res Ther* (2010) 12:R23. doi:10.1186/ar2930
15. Yagnik DR, Evans BJ, Florey O, Mason JC, Landis RC, Haskard DO. Macrophage release of transforming growth factor beta1 during resolution of monosodium urate monohydrate crystal-induced inflammation. *Arthritis Rheum* (2004) 50:2273–80. doi:10.1002/art.20317
16. Martin WJ, Walton M, Harper J. Resident macrophages initiating and driving inflammation in a monosodium urate monohydrate crystal-induced murine peritoneal model of acute gout. *Arthritis Rheum* (2009) 60:281–9. doi:10.1002/art.24185
17. Terkeltaub R, Zachariae C, Santoro D, Martin J, Peveri P, Matsushima K. Monocyte-derived neutrophil chemotactic factor/interleukin-8 is a potential mediator of crystal-induced inflammation. *Arthritis Rheum* (1991) 34:894–903. doi:10.1002/art.1780340716
18. Martinon F, Pétrilli V, Mayor A, Tardivel A, Tschopp J. Gout-associated uric acid crystals activate the NALP3 inflammasome. *Nature* (2006) 440:237–41. doi:10.1038/nature04516
19. Place DE, Kanneganti T-D. Recent advances in inflammasome biology. *Curr Opin Immunol* (2018) 50:32–8. doi:10.1016/j.coi.2017.10.011
20. Malik A, Kanneganti T-D. Inflammasome activation and assembly at a glance. *J Cell Sci* (2017) 130:3955–63. doi:10.1242/jcs.207365
21. Yamin TT, Ayala JM, Miller DK. Activation of the native 45-kDa precursor form of interleukin-1-converting enzyme. *J Biol Chem* (1996) 271:13273–82. doi:10.1074/jbc.271.22.13273
22. Thornberry NA, Bull HG, Calaycay JR, Chapman KT, Howard AD, Kostura MJ, et al. A novel heterodimeric cysteine protease is required for interleukin-1βprocessing in monocytes. *Nature* (1992) 356:768–74. doi:10.1038/356768a0
23. Joosten LAB, Netea MG, Mylona E, Koenders MI, Malireddi RKS, Oosting M, et al. Engagement of fatty acids with toll-like receptor 2 drives interleukin-1β production via the ASC/caspase 1 pathway in monosodium urate monohydrate crystal-induced gouty arthritis. *Arthritis Rheum* (2010) 62:3237–48. doi:10.1002/art.27667
24. Gong T, Yang Y, Jin T, Jiang W, Zhou R. Orchestration of NLRP3 inflammasome activation by ion fluxes. *Trends Immunol* (2018) 39:393–406. doi:10.1016/j.it.2018.01.009
25. Schorn C, Frey B, Lauber K, Janko C, Strysio M, Keppeler H, et al. Sodium overload and water influx activate the NALP3 inflammasome. *J Biol Chem* (2011) 286:35–41. doi:10.1074/jbc.M110.139048
26. Goldberg EL, Asher JL, Molony RD, Shaw AC, Zeiss CJ, Wang C, et al. β-Hydroxybutyrate deactivates neutrophil NLRP3 inflammasome to relieve gout flares. *Cell Rep* (2017) 18:2077–87. doi:10.1016/j.celrep.2017.02.004
27. Yang G, Yeon SH, Lee HE, Kang HC, Cho YY, Lee HS, et al. Suppression of NLRP3 inflammasome by oral treatment with sulforaphane alleviates acute gouty inflammation. *Rheumatology* (2018) 57:727–36. doi:10.1093/rheumatology/kex499
28. Lee HE, Yang G, Kim ND, Jeong S, Jung Y, Choi JY, et al. Targeting ASC in NLRP3 inflammasome by caffeic acid phenethyl ester: a novel strategy to treat acute gout. *Sci Rep* (2016) 6:38622. doi:10.1038/srep38622
29. Netea MG, Simon A, van de Veerdonk F, Kullberg B-J, Van der Meer JWM, Joosten LAB. IL-1β processing in host defense: beyond the inflammasomes. *PLoS Pathog* (2010) 6:e1000661. doi:10.1371/journal.ppat.1000661
30. Barabe F, Gilbert C, Liao N, Bourgoin SG, Naccache PH. Crystal-induced neutrophil activation VI. Involvement of Fc{gamma}RIIIB (CD16) and CD11b in response to inflammatory microcrystals. *FASEB J* (1998) 12:209–20. doi:10.1096/fasebj.12.2.209
31. Desaulniers P, Fernandes M, Gilbert C, Bourgoin SG, Naccache PH. Crystal-induced neutrophil activation. VII. Involvement of Syk in the responses to monosodium urate crystals. *J Leukoc Biol* (2001) 70:659–68. doi:10.1189/jlb.70.4.659
32. Popa-Nita O, Proulx S, Paré G, Rollet-Labelle E, Naccache PH. Crystal-induced neutrophil activation: XI. Implication and novel roles of classical protein kinase C. *J Immunol* (2009) 183:2104–14. doi:10.4049/jimmunol.0900906
33. Popa-Nita O, Rollet-Labelle E, Thibault N, Gilbert C, Bourgoin SG, Naccache PH. Crystal-induced neutrophil activation. IX. Syk-dependent activation of class Ia phosphatidylinositol 3-kinase. *J Leukoc Biol* (2007) 82:763–73. doi:10.1189/jlb.0307174
34. Ng G, Sharma K, Ward SM, Desrosiers MD, Stephens LA, Schoel WM, et al. Receptor-independent, direct membrane binding leads to cell-surface lipid sorting and Syk kinase activation in dendritic cells. *Immunity* (2008) 29:807–18. doi:10.1016/j.immuni.2008.09.013
35. Shi Y, Mucsi AD, Ng G. Monosodium urate crystals in inflammation and immunity. *Immunol Rev* (2010) 233:203–17. doi:10.1111/j.0105-2896.2009.00851.x
36. Lin Y-C, Huang D-Y, Wang J-S, Lin Y-L, Hsieh S-L, Huang K-C, et al. Syk is involved in NLRP3 inflammasome-mediated caspase-1 activation through adaptor ASC phosphorylation and enhanced oligomerization. *J Leukoc Biol* (2015) 97:825–35. doi:10.1189/jlb.3HI0814-371RR
37. Reber LL, Starkl P, Balbino B, Sibilano R, Gaudenzio N, Rogalla S, et al. The tyrosine kinase inhibitor imatinib mesylate suppresses uric acid crystal-induced acute gouty arthritis in mice. *PLoS One* (2017) 12:e0185704. doi:10.1371/journal.pone.0185704
38. Desai J, Kumar SV, Mulay SR, Konrad L, Romoli S, Schauer C, et al. PMA and crystal-induced neutrophil extracellular trap formation involves RIPK1-RIPK3-MLKL signaling. *Eur J Immunol* (2016) 46:223–9. doi:10.1002/eji.201545605
39. Desai J, Mulay SR, Nakazawa D, Anders HJ. Matters of life and death. How neutrophils die or survive along NET release and is "NETosis" = necroptosis? *Cell Mol Life Sci* (2016) 73:2211–9. doi:10.1007/s00018-016-2195-0
40. Garg AD, Galluzzi L, Apetoh L, Baert T, Birge RB, Bravo-San Pedro JM, et al. Molecular and translational classifications of DAMPs in immunogenic cell death. *Front Immunol* (2015) 6:588. doi:10.3389/fimmu.2015.00588
41. Konig MF, Andrade F. A critical reappraisal of neutrophil extracellular traps and NETosis mimics based on differential requirements for protein citrullination. *Front Immunol* (2016) 7:461. doi:10.3389/fimmu.2016.00461
42. Schauer C, Janko C, Munoz LE, Zhao Y, Kienhöfer D, Frey B, et al. Aggregated neutrophil extracellular traps limit inflammation by degrading cytokines and chemokines. *Nat Med* (2014) 20:511–7. doi:10.1038/nm.3547

43. Chatfield SM, Grebe K, Whitehead LW, Rogers KL, Nebl T, Murphy JM, et al. Monosodium urate crystals generate nuclease-resistant neutrophil extracellular traps via a distinct molecular pathway. *J Immunol* (2018) 200: 1802–16. doi:10.4049/jimmunol.1701382
44. Van Der Linden M, Westerlaken GHA, Van Der Vlist M, Van Montfrans J, Meyaard L. Differential signalling and kinetics of neutrophil extracellular trap release revealed by quantitative live imaging. *Sci Rep* (2017) 7:6529. doi:10.1038/s41598-017-06901-w
45. Clancy DM, Sullivan GP, Moran HBT, Henry CM, Reeves EP, McElvaney NG, et al. Extracellular neutrophil proteases are efficient regulators of IL-1, IL-33, and IL-36 cytokine activity but poor effectors of microbial killing. *Cell Rep* (2018) 22:2809–17. doi:10.1016/j.celrep.2018.02.062
46. Ea HK, Nguyen C, Bazin D, Bianchi A, Guicheux J, Reboul P, et al. Articular cartilage calcification in osteoarthritis: insights into crystal-induced stress. *Arthritis Rheum* (2011) 63:10–8. doi:10.1002/art.27761
47. Stack J, McCarthy G. Basic calcium phosphate crystals and osteoarthritis pathogenesis: novel pathways and potential targets. *Curr Opin Rheumatol* (2016) 28:122–6. doi:10.1097/BOR.0000000000000245
48. Dreier R. Hypertrophic differentiation of chondrocytes in osteoarthritis: the developmental aspect of degenerative joint disorders. *Arthritis Res Ther* (2010) 12:216. doi:10.1186/ar3117
49. McCarthy GM, Augustine JA, Baldwin AS, Christopherson PA, Cheung HS, Westfall PR, et al. Molecular mechanism of basic calcium phosphate crystal-induced activation of human fibroblasts: role of nuclear factor κB, activator protein 1, and protein kinase C. *J Biol Chem* (1998) 273:35161–9. doi:10.1074/jbc.273.52.35161
50. Reuben PM, Brogley MA, Sun Y, Cheung HS. Molecular mechanism of the induction of metalloproteinases 1 and 3 in human fibroblasts by basic calcium phosphate crystals. *J Biol Chem* (2002) 277:15190–8. doi:10.1074/jbc.M200278200
51. Nasi S, So A, Combes C, Daudon M, Busso N. Interleukin-6 and chondrocyte mineralisation act in tandem to promote experimental osteoarthritis. *Ann Rheum Dis* (2016) 75:1372–9. doi:10.1136/annrheumdis-2015-207487
52. Pazar B, Ea H-K, Narayan S, Kolly L, Bagnoud N, Chobaz V, et al. Basic calcium phosphate crystals induce monocyte/macrophage IL-1 secretion through the NLRP3 inflammasome in vitro. *J Immunol* (2011) 186:2495–502. doi:10.4049/jimmunol.1001284
53. Corr EM, Cunningham CC, Helbert L, McCarthy GM, Dunne A. Osteoarthritis-associated basic calcium phosphate crystals activate membrane proximal kinases in human innate immune cells. *Arthritis Res Ther* (2017) 19:23. doi:10.1186/s13075-017-1225-0
54. Cunningham CC, Mills E, Mielke LA, O'Farrell LK, Lavelle E, Mori A, et al. Osteoarthritis-associated basic calcium phosphate crystals induce pro-inflammatory cytokines and damage-associated molecules via activation of Syk and PI3 kinase. *Clin Immunol* (2012) 144:228–36. doi:10.1016/j.clim.2012.06.007
55. Jin C, Frayssinet P, Pelker R, Cwirka D, Hu B, Vignery A, et al. NLRP3 inflammasome plays a critical role in the pathogenesis of hydroxyapatite-associated arthropathy. *Proc Natl Acad Sci U S A* (2011) 108:14867–72. doi:10.1073/pnas.1111101108
56. Ea H-K, Chobaz V, Nguyen C, Nasi S, van Lent P, Daudon M, et al. Pathogenic role of basic calcium phosphate crystals in destructive arthropathies. *PLoS One* (2013) 8:e57352. doi:10.1371/journal.pone.0057352
57. Nasi S, Ea HK, So A, Busso N. Revisiting the role of interleukin-1 pathway in osteoarthritis: interleukin-1α and -1β, and NLRP3 inflammasome are not involved in the pathological features of the murine menisectomy model of osteoarthritis. *Front Pharmacol* (2017) 8:282. doi:10.3389/fphar.2017.00282
58. Cunningham CC, Corr EM, McCarthy GM, Dunne A. Intra-articular basic calcium phosphate and monosodium urate crystals inhibit anti-osteoclastogenic cytokine signalling. *Osteoarthritis Cartilage* (2016) 24:2141–52. doi:10.1016/j.joca.2016.07.001
59. Nasi S, Ea HK, Lioté F, So A, Busso N. Sodium thiosulfate prevents chondrocyte mineralization and reduces the severity of murine osteoarthritis. *PLoS One* (2016) 11:e0158196. doi:10.1371/journal.pone.0158196
60. Pang L, Hayes CP, Buac K, Yoo D-G, Rada B. Pseudogout-associated inflammatory calcium pyrophosphate dihydrate microcrystals induce formation of neutrophil extracellular traps. *J Immunol* (2013) 190:6488–500. doi:10.4049/jimmunol.1203215
61. Uzuki M, Sawai T, Ryan LM, Rosenthal AK, Masuda I. Upregulation of ANK protein expression in joint tissue in calcium pyrophosphate dihydrate crystal deposition disease. *J Rheumatol* (2014) 41:65–74. doi:10.3899/jrheum.111476
62. Nich C, Takakubo Y, Pajarinen J, Ainola M, Salem A, Sillat T, et al. Macrophages – key cells in the response to wear debris from joint replacements. *J Biomed Mater Res A* (2013) 101:3033–45. doi:10.1002/jbm.a.34599
63. Schmalzried TP, Jasty M, Harris WH. Periprosthetic bone loss in total hip arthroplasty. Polyethylene wear debris and the concept of the effective joint space. *J Bone Joint Surg Am* (1992) 74:849–63. doi:10.2106/00004623-199274060-00006
64. Laquerriere P, Grandjean-Laquerriere A, Jallot E, Balossier G, Frayssinet P, Guenounou M. Importance of hydroxyapatite particles characteristics on cytokines production by human monocytes in vitro. *Biomaterials* (2003) 24:2739–47. doi:10.1016/S0142-9612(03)00089-9
65. Howie DW, Neale SD, Haynes DR, Holubowycz OT, McGee MA, Solomon LB, et al. Periprosthetic osteolysis after total hip replacement: molecular pathology and clinical management. *Inflammopharmacology* (2013) 21:389–96. doi:10.1007/s10787-013-0192-6
66. Bitar D, Parvizi J. Biological response to prosthetic debris. *World J Orthop* (2015) 6:172. doi:10.5312/wjo.v6.i2.172
67. Purdue PE, Koulouvaris P, Nestor BJ, Sculco TP. The central role of wear debris in periprosthetic osteolysis. *HSS J* (2006) 2:102–13. doi:10.1007/s11420-006-9003-6
68. Noordin S, Masri B. Periprosthetic osteolysis: genetics, mechanisms and potential therapeutic interventions. *Can J Surg* (2012) 55:408–17. doi:10.1503/cjs.003711
69. Farrera C, Bhattacharya K, Lazzaretto B, Andon FT, Hultenby K, Kotchey GP, et al. Extracellular entrapment and degradation of single-walled carbon nanotubes. *Nanoscale* (2014) 6:6974–83. doi:10.1039/c3nr06047k
70. Vitkov L, Krautgartner W-D, Obermayer A, Stoiber W, Hannig M, Klappacher M, et al. The initial inflammatory response to bioactive implants is characterized by NETosis. *PLoS One* (2015) 10:e0121359. doi:10.1371/journal.pone.0121359
71. Jhunjhunwala S, Aresta-DaSilva S, Tang K, Alvarez D, Webber MJ, Tang BC, et al. Neutrophil responses to sterile implant materials. *PLoS One* (2015) 10:e0137550. doi:10.1371/journal.pone.0137550
72. Muñoz LE, Bilyy R, Biermann MHC, Kienhöfer D, Maueröder C, Hahn J, et al. Nanoparticles size-dependently initiate self-limiting NETosis-driven inflammation. *Proc Natl Acad Sci U S A* (2016) 113:E5856–65. doi:10.1073/pnas.1602230113
73. Biermann MHC, Podolska MJ, Knopf J, Reinwald C, Weidner D, Maueröder C, et al. Oxidative burst-dependent NETosis is implicated in the resolution of necrosis-associated sterile inflammation. *Front Immunol* (2016) 7:557. doi:10.3389/fimmu.2016.00557
74. Abu-Amer Y, Darwech I, Clohisy JC. Aseptic loosening of total joint replacements: mechanisms underlying osteolysis and potential therapies. *Arthritis Res Ther* (2007) 9:S6. doi:10.1186/ar2170
75. Purdue PE. Alternative macrophage activation in periprosthetic osteolysis. *Autoimmunity* (2008) 41:212–7. doi:10.1080/08916930701694626
76. Wooley PH, Morren R, Andary J, Sud S, Yang SY, Mayton L, et al. Inflammatory responses to orthopaedic biomaterials in the murine air pouch. *Biomaterials* (2002) 23:517–26. doi:10.1016/S0142-9612(01)00134-X
77. St Pierre CA, Chan M, Iwakura Y, Ayers DC, Kurt-Jones EA, Finberg RW. Periprosthetic osteolysis: characterizing the innate immune response to titanium wear-particles. *J Orthop Res* (2010) 28:1418–24. doi:10.1002/jor.21149
78. Horowitz SM, Doty SB, Lane JM, Burstein AH. Studies of the mechanism by which the mechanical failure of polymethylmethacrylate leads to bone resorption. *J Bone Joint Surg Am* (1993) 75:802–13. doi:10.2106/00004623-199306000-00002
79. Gu Q, Shi Q, Yang H. The role of TLR and chemokine in wear particle-induced aseptic loosening. *J Biomed Biotechnol* (2012) 2012:596870. doi:10.1155/2012/596870
80. Lind M, Trindade MCD, Schurman DJ, Goodman SB, Smith RL. Monocyte migration inhibitory factor synthesis and gene expression in particle-activated macrophages. *Cytokine* (2000) 12:909–13. doi:10.1006/cyto.1999.0647
81. Kaufman AM, Alabre CI, Rubash HE, Shanbhag AS. Human macrophage response to UHMWPE, TiAlV, CoCr, and alumina particles: analysis of

multiple cytokines using protein arrays. *J Biomed Mater Res A* (2008) 84:464–74. doi:10.1002/jbm.a.31467
82. Nakashima Y, Sun DH, Trindade MC, Chun LE, Song Y, Goodman SB, et al. Induction of macrophage C-C chemokine expression by titanium alloy and bone cement particles. *J Bone Joint Surg Br* (1999) 81:155–62. doi:10.1302/0301-620X.81B1.0810155
83. Yaszay B, Trindade MCD, Lind M, Goodman SB, Smith RL. Fibroblast expression of C-C chemokines in response to orthopaedic biomaterial particle challenge in vitro. *J Orthop Res* (2001) 19:970–6. doi:10.1016/S0736-0266(01)00003-1
84. Mahon OR, O'Hanlon S, Cunningham CC, McCarthy GM, Hobbs C, Nicolosi V, et al. Orthopaedic implant materials drive M1 macrophage polarization in a spleen tyrosine kinase- and mitogen-activated protein kinase-dependent manner. *Acta Biomater* (2018) 65:426–35. doi:10.1016/j.actbio.2017.10.041
85. Rao AJ, Gibon E, Ma T, Yao Z, Smith RL, Goodman SB. Acta biomaterialia revision joint replacement, wear particles, and macrophage polarization. *Acta Biomater* (2012) 8:2815–23. doi:10.1016/j.actbio.2012.03.042
86. Sato T, Pajarinen J, Behn A, Jiang X, Lin T, Loi F, et al. The effect of local IL-4 delivery or CCL2 blockade on implant fixation and bone structural properties in a mouse model of wear particle induced osteolysis. *J Biomed Mater Res A* (2016) 104:2255–62. doi:10.1002/jbm.a.35759
87. Fleisch HA. Bisphosphonates: preclinical aspects and use in osteoporosis. *Ann Med* (1997) 29:55–62. doi:10.3109/07853899708998743
88. Trevisan C, Nava V, Mattavelli M, Parra CG. Bisphosphonate treatment for osteolysis in total hip arthroplasty. A report of four cases. *Clin Cases Miner Bone Metab* (2013) 10:61–4. doi:10.11138/ccmbm/2013.10.1.061
89. Teng S, Yi C, Krettek C, Jagodzinski M. Bisphosphonate use and risk of implant revision after total hip/knee arthroplasty: a meta-analysis of observational studies. *PLoS One* (2015) 10:e0139927. doi:10.1371/journal.pone.0139927
90. Richardson PG, Barlogie B, Berenson J, Singhal S, Jagannath S, Irwin D, et al. A phase 2 study of bortezomib in relapsed, refractory myeloma. *N Engl J Med* (2003) 348:2609–17. doi:10.1056/NEJMoa030288
91. Yannaki E, Papadopoulou A, Athanasiou E, Kaloyannidis P, Paraskeva A, Bougiouklis D, et al. The proteasome inhibitor bortezomib drastically affects inflammation and bone disease in adjuvant-induced arthritis in rats. *Arthritis Rheum* (2010) 62:3277–88. doi:10.1002/art.27690
92. Lee SW, Kim JH, Park YB, Lee SK. Bortezomib attenuates murine collagen-induced arthritis. *Ann Rheum Dis* (2009) 68:1761–7. doi:10.1136/ard.2008.097709
93. Cadwell K. Crosstalk between autophagy and inflammatory signalling pathways: balancing defence and homeostasis. *Nat Rev Immunol* (2016) 16:661–75. doi:10.1038/nri.2016.100
94. Crişan TO, Cleophas MCP, Novakovic B, Erler K, van de Veerdonk FL, Stunnenberg HG, et al. Uric acid priming in human monocytes is driven by the AKT-PRAS40 autophagy pathway. *Proc Natl Acad Sci U S A* (2017) 114:5485–90. doi:10.1073/pnas.1620910114
95. Wang Z, Deng Z, Gan J, Zhou G, Shi T, Wang Z, et al. TiAl6V4particles promote osteoclast formation via autophagy-mediated downregulation of interferon-beta in osteocytes. *Acta Biomater* (2017) 48:489–98. doi:10.1016/j.actbio.2016.11.020
96. Hayashida C, Ito J, Nakayachi M, Okayasu M, Ohyama Y, Hakeda Y, et al. Osteocytes produce interferon-beta as a negative regulator of osteoclastogenesis. *J Biol Chem* (2014) 289:11545–55. doi:10.1074/jbc.M113.523811
97. Towers CG, Thorburn A. Therapeutic targeting of autophagy. *EBioMedicine* (2016) 14:15–23. doi:10.1016/j.ebiom.2016.10.034

Conflict of Interest Statement: The authors declare that the research was conducted in the absence of any commercial or financial relationships that could be construed as a potential conflict of interest.

frontiers in Immunology

ORIGINAL RESEARCH
published: 22 May 2018
doi: 10.3389/fimmu.2018.01115

Tannic Acid-Modified Silver and Gold Nanoparticles as Novel Stimulators of Dendritic Cells Activation

*Piotr Orlowski[1], Emilia Tomaszewska[2], Katarzyna Ranoszek-Soliwoda[2], Marianna Gniadek[3], Olga Labedz[3], Tadeusz Malewski[4], Julita Nowakowska[5], Grzegorz Chodaczek[6], Grzegorz Celichowski[2], Jaroslaw Grobelny[2] and Malgorzata Krzyzowska[1,6]**

[1] Military Institute of Hygiene and Epidemiology, Warsaw, Poland, [2] Department of Materials Technology and Chemistry, Faculty of Chemistry, University of Lodz, Lodz, Poland, [3] Faculty of Chemistry, University of Warsaw, Warsaw, Poland, [4] Museum and Institute of Zoology, Polish Academy of Science, Warsaw, Poland, [5] Laboratory of Electron and Confocal Microscopy, Faculty of Biology, University of Warsaw, Warsaw, Poland, [6] Wroclaw Research Centrum EIT+, Wroclaw, Poland

OPEN ACCESS

Edited by:
Hans-Joachim Anders, Ludwig-Maximilians-Universität München, Germany

Reviewed by:
Gordana Leposavić, University of Belgrade, Serbia
Santhosh V. Kumar, Murdoch Childrens Research Institute, Australia
Jyaysi Desai, Leiden University Medical Center, Netherlands

***Correspondence:**
Malgorzata Krzyzowska
krzyzowskam@yahoo.com

Specialty section:
This article was submitted to Inflammation, a section of the journal Frontiers in Immunology

Received: *11 February 2018*
Accepted: *03 May 2018*
Published: *22 May 2018*

Citation:
Orlowski P, Tomaszewska E, Ranoszek-Soliwoda K, Gniadek M, Labedz O, Malewski T, Nowakowska J, Chodaczek G, Celichowski G, Grobelny J and Krzyzowska M (2018) Tannic Acid-Modified Silver and Gold Nanoparticles as Novel Stimulators of Dendritic Cells Activation. Front. Immunol. 9:1115. doi: 10.3389/fimmu.2018.01115

Silver nanoparticles (AgNPs) are promising new antimicrobial agents against a wide range of skin and mucosal pathogens. However, their interaction with the immune system is currently not fully understood. Dendritic cells (DCs) are crucial during development of T cell-specific responses against bacterial and viral pathogens. We have previously shown that tannic acid-modified silver nanoparticles (TA-AgNPs) consist of a promising microbicide against HSV-2. The aim of this study was to compare the ability of TA-AgNPs or TA-AuNPs of similar sizes (TA-Ag/AuNPs) to induce DCs maturation and activation in the presence of HSV-2 antigens when used at non-toxic doses. First, we used JAWS II DC line to test toxicity, ultrastructure as well as activation markers (MHC I and II, CD40, CD80, CD86, PD-L1) and cytokine production in the presence of TA-Ag/AuNPs. Preparations of HSV-2 treated with nanoparticles (TA-Ag/AuNPs-HSV-2) were further used to investigate HSV-2 antigen uptake, activation markers, TLR9 expression, and cytokine production. Additionally, we accessed proliferation and activation of HSV-2-specific T cells by DCs treated with TA-AgNP/AuNPs-HSV-2. We found that both TA-AgNPs and TA-AuNPs were efficiently internalized by DCs and induced activated ultrastructure. Although TA-AgNPs were more toxic than TA-AuNPs in corresponding sizes, they were also more potent stimulators of DCs maturation and TLR9 expression. TA-Ag/AuNPs-HSV-2 helped to overcome inhibition of DCs maturation by live or inactivated virus through up-regulation of MHC II and CD86 and down-regulation of CD80 expression. Down-regulation of CD40 expression in HSV-2-infected DCs was reversed when HSV-2 was treated with TA-NPs sized >30 nm. On the other hand, small-sized TA-AgNPs helped to better internalize HSV-2 antigens. HSV-2 treated with both types of NPs stimulated activation of JAWS II and memory CD8+ T cells, while TA-AgNPs treatment induced IFN-γ producing CD4+ and CD8+ T cells. Our study shows that TA-AgNPs or TA-AuNPs are good activators of DCs, albeit their final effect upon maturation and activation may be metal and size dependent. We conclude that TA-Ag/AuNPs consist of a novel class of nano-adjuvants, which can help to overcome virus-induced suppression of DCs activation.

Keywords: silver nanoparticles, gold nanoparticles, dendritic cells, HSV-2, tannic acid

INTRODUCTION

Nanoparticles (NPs) are increasingly recognized for their potential applications in cosmetics, pharmaceuticals, and medicine (1–5). The small size of NPs enables them to infiltrate tissues including lymphoid tissues and subsequently target immune cells, which makes them potentially useful in immunotherapies (6). Conjugation of NPs with biologically active compounds may further lead to new advantageous properties, better biodistribution, and bioactivity.

Dendritic cells (DCs) induce immunity (cellular and humoral) through response to foreign pathogens by activation of cellular immune response. In the periphery, DCs exist in immature state and are activated and differentiated into mature DCs through the recognition of antigens (7, 8). After antigen capture, DCs acquire a mature phenotype, lose their endocytic and phagocytic receptors, and migrate to lymphoid organs for T cells priming (7, 8). Taking into account the fact that DCs are present throughout the body, they consist, together with other mechanisms of the adaptive immune response, the first line of encounter of the immune system with NPs.

Metallic NPs (MeNPs) are relatively non-biodegradable, have rigid structures, and possess simple synthesis methodology. Different MeNPs (gold, silver, and nickel) have been used in conjunction with several Ag for distinct microorganisms and showed the ability to generate humoral and cytotoxic responses (9–12). A number of reports have indicated that gold NPs (AuNPs) facilitate delivery of antigens and adjuvants to the immune system, promote the therapeutic effect, and possess an adjuvant effect on their own (9–11). AuNPs accumulate in DCs and B cells of the spleen after intravenous injection (6). Furthermore, AgNPs also show a significant adjuvant effect mainly due to the recruitment and activation of local leukocytes, especially of macrophages (13). On the other hand, DCs exposed to silver NPs (AgNPs) show a decrease in cell viability and production of reactive oxygen species (ROS) but no production of inflammatory cytokines such as TNF-α or IL-1β (14).

In our previous work, we demonstrated antiviral properties of tannic acid modified-AgNPs (TA-AgNPs) both *in vitro* and *in vivo* using the murine model of intravaginal HSV-2 infection (15). The antiviral mechanism of TA-AgNPs involved blocking of virus attachment, entry, and induction of anti-viral cytokine and chemokine production. Cytokine and chemokine production during HSV-2 infection showed time and size-related differences for treatment with each NP type (15). Furthermore, TA-AgNPs also showed size-dependent immunomodulatory properties against uninfected monocytes and keratinocytes (16, 17).

Herpes simplex virus (HSV) causes a contagious infection that affects approximately 60% to 95% of adults worldwide. HSV-1 is associated mainly with infections of the mouth, pharynx, face, eye, and central nervous system (CNS), while HSV-2 is associated with infections of the anogenital region. HSV-1 and -2 persist in the body by becoming latent in the cell bodies of nerves and after the initial or primary infection (18). Currently, the only way of herpes treatment is the use of antiviral drugs, blocking viral replication. Given the sub-optimal performance of HSV vaccine candidates to date and the role of DCs in priming cellular responses, a more directed approach specifically targeted at DCs may be required to improve vaccine efficacy (19). One possible solution is to target DCs with appropriate antigens/adjuvants. Since NPs possessing anti-viral and immunomodulatory activities can be engulfed by DCs and used as "antigen delivery/enhancement system," they can also play a role of the locally applied adjuvants (20, 21).

In the present study, we showed how differently sized TA-AgNPs and -AuNPs, applied at the non-toxic concentrations, influence maturation of JAWS II mouse DCs line, production of cytokines, and expression of TLR9. Furthermore, we showed that NPs treatment of HSV-2 can overcome inhibited maturation of DCs, increase antigen uptake as well as activation of HSV-2 specific memory T cells as well as INF-γ producing CD4+ and CD8+ T cells.

MATERIALS AND METHODS

Ethics Statement

This study was performed in strict accordance with the recommendations of the Polish Act of 21 January 2005 on animal experiments (OJ no. 33, item 289) and Directive 2010/63/EU of the European Parliament and the Council of 22 September 2010 on the protection of animals used for scientific purposes. The protocol was approved by the 4th Local Committee on the Ethics of Animal Experiments in Warsaw, Poland (Permit Number: 51/2013).

Synthesis of AuNPs and AgNPs

Materials and Methods of Synthesis

Gold (III) chloride hydrate ($HAuCl_4 \cdot H_2O$, Sigma-Aldrich, St. Louis, MO, USA, ≥ 49% Au basis), silver nitrite ($AgNO_3$; Sigma-Aldrich, 99.999% metal basis), sodium citrate ($C_6H_5Na_3O_7 \cdot 2H_2O$, Sigma-Aldrich, ≥99%), ammonium citrate tribasic ($C_6H_{17}N_3O_7$, Sigma-Aldrich, ≥ 97%), tannic acid ($C_{76}H_{52}O_{46}$, Fluka, Seelze, Germany), and sodium borohydride ($NaBH_4$, Fluka, ≥99%) were used without additional purification. For all experiments, deionized water was obtained from Deionizer Millipore Simplicity UV system (specific resistivity of water was 18.2 MΩ cm, Millipore, Merck, Warsaw, Poland). All AuNPs and AgNPs colloids were stored at darkness and filtered through a 0.1 μm polyvinylidene fluoride (PVDF) membrane before use in biological tests.

Synthesized NPs were characterized using scanning transmission electron microscopy (STEM), dynamic light scattering (DLS), and UV-Vis spectroscopy. STEM measurements were performed using scanning electron microscope Nova NanoSEM 450, accelerating voltage of 30 kV (FEI, Hillsboro, OR, USA) equipped with a detector for transmitted electron acquisition (STEM II). Samples for STEM were prepared as follows: a drop of colloid was deposited onto a carbon-coated copper grid (300 mesh) and left for solvent evaporation under ambient conditions. The DLS and Zeta potential measurements were carried out using Nano ZS Zetasizer system (Malvern Instruments, Malvern, Great Britain) with the He−Ne laser (633 nm) as the light source (scattering angle 173°, measurement temperature

25°C; medium viscosity 0.887 mPa·s, material refractive index 1.330). DLS measurements were performed in disposable quartz cuvettes and Zeta potential measurements in disposable folded capillary zeta cells (DTS 1070). For analysis of Zeta potential measurements, the Smoluchowski model was applied (22). The UV−vis spectra were recorded with the spectrophotometer USB2000 + detector (miniature fiber optic spectrometer) Ocean Optics, HL-2000 (tungsten halogen light sources) using quartz cuvettes (Ocean Optics, Winter Park, FL, USA).

Gold Nanoparticles

AuNPs with the size of 10 nm, 34 nm, and 62 nm and weight concentration of Au in colloid equal to 100 ppm were synthesized in water by reduction of gold (III) chloride hydrate. The synthesis procedures were described in our previous work (17). Briefly, an aqueous solution of gold (III) chloride hydrate was boiled and vigorously stirred under reflux. Next, a mixture of aqueous solutions of sodium/ammonium citrate and/or tannic acid was added into the solution. The amounts of reagents used for syntheses are summarized in **Table 1**. After the reducing mixture changed color to red indicating the formation of AuNPs, the colloids were stirred for additional 15 min under reflux and cooled down to a room temperature.

Silver Nanoparticles

Silver nanoparticles (100 ppm) with the size of 10 nm, 37 nm, and 59 nm were synthesized in water by the chemical reduction method. The synthesis procedures were described previously (17) and were as follows: a reducing mixture was added to the aqueous solution of silver nitrite heated to the boiling point under reflux (except for AgNPs 10 nm, where the aqueous solution of silver nitrite at room temperature was used). The amounts of reagents used for syntheses are summarized in **Table 2**. After a few minutes, the color of the solution changed to brownish indicating the formation of AgNPs. The mixture was stirred for additional 15 min.

TABLE 1 | The amounts of reagents used for the syntheses of AuNPs.

Size of AuNPs	Gold (III) chloride hydrate	Reducing mixture
10 nm	94.4 g, 0.018 wt%	Sodium citrate (3.9 g, 1 wt%) Tannic acid (1.7 g, 1 wt%)
34 nm	96.2 g, 0.018 wt%	Tannic acid (3.8 g, 5 wt%)
62 nm	97.8 g, 0.018 wt%	Tribase ammonium citrate (2.2 g, 2 wt%)

TABLE 2 | The amounts of reagents used for the syntheses of AgNPs.

Size of AgNPs	Silver nitrite	Reducing mixture
10 nm	94.5 g, 0.0166 wt%	Tannic acid (0.6 g, 5 wt%) Sodium citrate (4.2 g, 4 wt%) Sodium borohydride (0.7 g, 2 wt%)
37 nm	95.2 g, 0.0165 wt%	Tannic acid (0.6 g, 5 wt%) Sodium citrate (4.2 g, 4 wt%)
59 nm	97.60 g, 0.0161 wt%	Tannic acid (1.3 g, 5 wt%) Sodium citrate (1.1 g, 4 wt%)

Virus

HSV-2 strain 333 was grown and titrated (PFU/ml) in African green monkey kidney cells (GMK-AH1). The heat-inactivated virus was prepared by heating the virus suspended in a complete cell culture medium at 56°C for 60 min. For UV inactivation, virus suspension was exposed in sterile conditions to UV lamp for 45 min on ice. No viral particles were detected by plaque assay in the supernatants of cell cultures treated with UV- or heat-inactivated HSV-2. For inactivation of HSV-2 with NPs, a virus inoculum was pre-incubated with 2.5 μg/ml of silver or AuNPs for 1 h, as described previously (15).

Cell Lines, Bone-Marrow Derived DCs (BMDCs), and Treatment With NPs

African green monkey kidney cells (GMK-AH1) were a gift from the Swedish Institute for Infectious Disease Control, Stockholm, and were cultured in MEM alpha modification (α-MEM) supplemented with 10% heat inactivated fetal bovine serum (HI-FBS), 100 U/ml penicillin, and 100 μg/ml streptomycin B (Gibco by Thermo Fisher Scientific, MA, USA) in standard conditions (37°C, 5% CO_2). The immature DCs (JAWSII) were purchased from American Type Culture Collection (ATCC, CRL-11904, Rockville, MD, USA) and were grown in α-MEM with deoxy- and ribonucleosides, supplemented with 20% HI-FBS, 4 mM L-glutamine, 1 mM sodium pyruvate, 100 U/ml penicillin, 100 μg/ml streptomycin (Gibco), and 5 ng/ml murine granulocyte macrophage colony-stimulating factor (GM-CSF) (Sigma-Aldrich), in standard conditions.

JAWSII cells were seeded into 24-well plates at a density of 5×10^4/ml for 24 h before exposure to NPs at the concentration from 0.5 to 10 μg/ml or infection with HSV-2, heat inactivated HSV-2, or HSV-2 inactivated with 2.5 μg/ml NPs at the multiplicity of infection (MOI) 0.5–1. After another 24 h, the cells were used for further analyses. Lipopolysaccharide (LPS, Sigma-Aldrich), a TLR-4 ligand, or polyinosinic-polycytidylic acid potassium salt (Poly I:C) (Sigma-Aldrich), a TLR-3 ligand, at the concentration of 10 μg/ml and 5 μg/ml, respectively, were used as positive control.

To inhibit NPs uptake in some experiments, the following inhibitors were used for 1 h: 10 μg/ml monodansyl cadeverine (MDC), 200 μM genistein, 10 μg/ml colchicine, 400 nM wortmannin, and 5 μg/ml cytochalasin D (CChD, Sigma-Aldrich), then washed out. Subsequently, the cells were exposed to 2.5 μg/ml NPs for 6 h. Concentrations of inhibitors were chosen on the basis of lack of toxic effects measured by tests described below.

Primary cultures of BMDCs were prepared by culturing bone marrow cells isolated from C57BL6 mice in the D-MEM (Gibco) culture medium supplemented with 25 ng/ml GM-CSF and 15 ng/ml IL-4 (Gibco), 4,500 mg/l glucose, antibiotics (penicillin and streptomycin), L-glutamine, 10% fetal bovine serum (Gibco) for 5 days. At day 5, primary cultures of DCs were washed and subjected to treatment, as described above. All experiments were performed at least in triplicates.

Toxicity Assessment

To determine cell apoptosis or necrosis, Apoptosis Detection kit was used (Beckton Dickinson, Franklin Lakes, NJ, USA). The kit distinguishes apoptotic from necrotic cells by detecting apoptotic

asymmetry of the cell membrane with annexin V-FITC, while necrotic cells are labeled with red-fluorescent propidium iodide (PI). Briefly, after exposure to NPs, cells were collected, washed with PBS, and then suspended in staining solution containing 5 μg/ml of annexin V and 1 μg/ml of PI, incubated for 10 min in 4°C, and analyzed in FACS Calibur using CellQuest programme (Beckton Dickinson). Apoptotic cells were defined as the percentage of annexin V-FITC positive cells, while necrotic cells were defined as the percentage of PI positive cells.

To assess the mitochondrial potential after NPs treatment, the cells were stained with 5,5′,6,6′-tetrachloro-1,1′,3′-teraethylbenzimidazolylcarbocyanine iodide (JC-1, Sigma-Aldrich). For staining, cells were harvested and incubated with α-MEM supplemented with 20% FBS and 5 μg/ml JC-1 at 37°C for 15 min. Cells were then washed two times in PBS and analyzed in FACS Calibur using CellQuest program (Beckton-Dickinson) for the percentage of cells with a decrease in red to green fluorescence intensity ratio. The Neutral red test was performed as described previously (16). The viability of cells was expressed as a percentage of the control, untreated cells (100%).

Transmission Electron Microscopy (TEM) and Scanning Electron Microscopy (SEM) Imaging

For TEM imaging of JAWS II ultrastructure, cells were collected, fixed, and processed as described previously (17). Ultrathin sections (70–90 nm) were cut on a Ultracut E microtome (Reichert-Jung, Austria). The images were acquired using Zeiss Libra 120 transmission electron microscopy (Zeiss, Jena, Germany).

Scanning electron microscopy images of the cells surfaces were obtained by incubating JAWSII with 5 μg/ml of NPs for 3 h, then the cells were fixed with warm 2.5% glutaraldehyde in 0.1 M phosphate buffer pH 7.2 for 20 min, as described in Ref. (17) and acquired using FE-SEM Merlin (Zeiss, Jena, Germany).

Confocal Imaging

For microscopic detection of NPs, cells were plated on slides at a density of 1×10^5/ml for 18 h before exposure to NPs. After 24 h of exposure to 5 μg/ml of TA-AgNPs or TA-AuNPs, the medium was discarded and the cells were fixed with 4% paraformaldehyde (PFA) in PBS (Sigma-Aldrich), washed twice with PBS and stained with LysoTracker™ Red DND-99 (Thermo Fisher Scientific) according to the manufacturer′s protocol. The images were captured on an upright Leica SP8 resonant scanning confocal system (Leica Microsystem, Wetzlar, Germany). Stacks of confocal 8-bit images with a pixel size of 0.186 μm and a 0.5 μm Z step were acquired using 40× oil immersion objective (NA 1.30). The pinhole was set to 1 AU. Nanoparticles were visualized in a reflection mode using a 638 nm laser line. DNA signal from Hoechst 33342 was excited using a 405 nm laser line and 460–490 nm emission range was collected. Lysosomes were stained in live cells with LysoTracker Red DND-99 (excitation with a 552 nm laser line and recorded emission was 561–618 nm). The acquisition was performed in a sequential mode. Images showing equatorial optical sections were analyzed in Fiji/ImageJ software (National Institutes of Health, USA), and Manders' Colocalization Coefficients were calculated in thresholded images.

Flow Cytometry Phenotypic Analysis, High Content Screening (HCS), and Measurement of Cytokines

After treatments, cells were collected, washed with PBS containing 2% FBS, and blocked with anti-mouse CD16/CD32 (clone 93; eBioscience, San Diego, CA, USA) on ice for 10 min. After washing, cells were stained using anti-MHC I-FITC (clone 34-1-2 S; eBioscience), anti-CD80-PE (clone 16-10 A1; eBioscience), anti-CD40-FITC (clone HM40-3; eBioscience), anti-MHC II-PE (clone M5/114.15.2; eBioscience), anti-CD86-FITC (clone GL1; eBioscience), anti-PD-L1-PE (clone MIH5; eBioscience), anti-CD3e-Alexa Fluor 488 (clone 145-2C11; eBioscience), anti-CD4-PE (clone GK1.5; eBioscience), anti-CD8-BV421 (clone 53-6.7; Becton Dickinson), anti-CD44-APC (clone IM7; eBioscience), and anti-CD69-APC (clone H1.2F3; eBioscience). Following the immunolabelling for the extracellular markers, cells were fixed with Perm/Wash buffer (BD Bioscience) and were incubated with anti-IFN-γ APC-Cy7 (clone-XMG1.2; eBioscience). The stained cell suspensions were analyzed in FACS Calibur or FACS Verse for the percentage of positively stained cells or the mean fluorescence intensity.

For measurement of HSV-2 antigens incorporated 6 h post infection (p. i.), we used HCS. After infection, cells were fixed with acetone–methanol mixture, air dried, and kept until antigen detection at −20°C. After rehydration in PBS, cells were stained with FITC-conjugated anti-HSV-1/HSV-2 polyclonal antibody (Dako, Glostrup, Denmark). Nuclei were stained with Hoechst 33342 (Sigma-Aldrich). Images were obtained and analyzed by ArrayScan™ XTI High Content Platform equipped with HCS Studio™ 2.0 Cell Analysis Software (Thermo Fisher Scientific).

We used Cytometric Bead Array (CBA) Mouse Th1/Th2/Th17 Kit (IL-10, IL-17A, TNF, IFN-γ, IL-6, IL-4, IL-2) (Beckton Dickinson) to measure cytokines from culture supernatants by flow cytometry according to the manufacturer′s protocol. The results are presented as means of assays performed in triplicates. Data were analyzed using FCAP 0.1 BD Cytometric Bead Array and BD Array 1.4 software assay (Beckton Dickinson).

TLR9 mRNA Levels

Total RNA was extracted with the Universal RNA Purification Kit (Eurx, Gdansk, Poland), following the manufacturer′s protocol. The amount of total RNA extracted and its purification from protein and polysaccharides was determined with a NanoDrop 2000 spectrophotometer (Thermo Fisher Scientific). RNA integrity was verified electrophoretically in a 1.5% agarose gel stained with ethidium bromide. Only samples that satisfied both the quality and integrity requirements were used in subsequent experiments. Three high-quality RNA samples (i.e., biological replicates) were obtained for each condition. Reverse transcription was carried out using Enhanced Avian HS RT-PCR Kit (Sigma-Aldrich), in line with the manufacturer′s instructions. To analyze expression of tlr9 gene, we used the primers 5′GCCACATTCTATACAGGGATTGG3′ and

5′GCCACATTCTATACAGGGATTGG3′, Gapdh was used as a reporter gene in our experiment. Real-time PCRs were performed in the RotorGene 6000 system (Qiagen, Hilden, Germany). Reactions were carried out using LuminoCt SYBR Green qPCR Master Mix (Sigma-Aldrich), while cycle threshold (Ct) estimates were obtained using the relative quantification module in the software package. Fluorescence data were analyzed subsequently using the Tm calling module in the RotorGene 6000 software. The $2^{\Delta\Delta Ct}$ method was used in calculating the relative ratio, but instead of value 2, the correct amplification efficiency was used (23). We used a noise-resistant iterative nonlinear regression algorithm (Real-time PCR miner; www.miner.ewindup.info) to determine the efficiency of the PCR reaction (24). Levels of mRNA were counted from three PCR reactions for each sample.

Mice Challenge and T-Cells Activation Assay

Female C57BL/6 mice were challenged every 30 days subcutaneously with 2.5×10^4 PFU of UV inactivated HSV-2. After 240 days, and two weeks after the last challenge, the mice were sacrificed and spleens were isolated to obtain single cell suspensions. T-lymphocytes were isolated using MACS Pan-T Cell Isolation Kit according to the manufacturer′s protocol (Miltenyi Biotec, Surrey, UK). The isolated T cells were stained with carboxyfluorescein succinimidyl ester (CFSE) (Sigma-Aldrich). Briefly, cells washed with PBS were incubated with 5 μM CFSE, then washed twice with 2% FBS/PBS. JAWSII were seeded for 24 h in U-bottomed 96-plates at the density of 1×10^4/well and infected with HSV-2, heat-inactivated HSV-2 or exposed to HSV-2 treated with NPs as described above. Twenty-four hour post-infection/treatment medium was replaced to RPMI supplemented with 10% HI-FBS, 100 U/ml penicillin, 100 μg/ml streptomycin (Gibco), and then co-cultured with 10^5/well T cells. After 72 h, T cells proliferation was analyzed in FACS Calibur as described above.

T Cell Proliferation Assay

T cell proliferation was measured using Cell Proliferation ELISA BrdU colorimetric kit (Roche, Basel, Switzerland). Briefly, isolated T-cells were seeded into 96-well flat bottom plates at the density of 10^5 cells per well in the medium described above, containing 2.5 μg/ml of TA-AgNPs or TA-AuNPs with or without 5 μg/ml concanavalin A (Sigma-Aldrich). After 48 h of incubation bromodeoxyuridine (BrdU) was added to a final concentration of 100 μM, and cells were incubated for additional 24 h. Next, the cells were fixed and incorporated BrdU was detected according to the manufacturer′s protocol.

Statistical Methods

Data are presented as the mean ± standard error of the mean (S.E.M.) from at least three independent experiments. Data were analyzed using a two-tailed paired Student′s *t*-test (normal distribution) or non-parametric Kruskal–Wallis and Wilcoxon tests were applied using Biostat 2009 software. In every analysis, values of $p \leq 0.05$ were considered significant.

RESULTS

NPs Characterization

Before biological tests, AuNPs and AgNPs were precisely characterized. Briefly, the shape and size of metallic core of NPs were determined with STEM technique, the hydrodynamic size of NPs (the size of a metallic core along with substances present on the NPs surface) was measured with DLS technique and the colloidal stability of NPs was studied with DLS, UV–vis spectroscopy, and Zeta potential measurements.

The STEM images along with the DLS size distribution histograms and UV–vis spectra of AuNPs and AgNPs are presented in **Figures 1A–F** (AuNPss and AgNPs, respectively). The size of a metallic core of AuNPs is 5 ± 1 nm (**Figure 1A**), 24 ± 3 nm (**Figure 1B**), and 58 ± 7 nm (**Figure 1C**), and the size of a metallic core of AgNPs: 6 ± 2 nm (**Figure 1D**), 27 ± 7 nm (**Figure 1E**), and 45 ± 8 nm (**Figure 1F**). The hydrodynamic size of NPs is: 10 ± 2 nm (**Figure 1A**), 34 ± 7 nm (**Figure 1B**), 62 ± 10 nm (**Figure 1C**), 10 ± 2 nm (**Figure 1D**), 37 ± 7 nm (**Figure 1E**), and 59 ± 10 nm (**Figure 1F**). Any other peaks from agglomerates or aggregates of NPs were not detected in all cases, which confirm the monodispersity and colloidal stability of all samples. The differences between the hydrodynamic size of NPs measured in DLS technique and the size of metallic core measured in STEM technique correspond to the shell of stabilizers adsorbed on NPs surface. The shell of stabilizers adsorbed on NPs surface consist of complexes of tannic acid and sodium citrate (25), which are involved in the synthesis of NPs and its further stabilization in a colloidal solution. The absorption peaks maxima recorded by UV–vis spectroscopy were located at wavelengths characteristic for AuNPs at: 520 nm, 518 nm, and 528 nm (samples A, B, and C, respectively) and for AgNPs at: 407 nm, 405 nm, and 427 nm (samples D, E, and F, respectively). The negative values of Zeta potential confirmed high storage stability of all colloids (−26 ± 6 mV, −32 ± 1 mV, −51 ± 5 mV, −31 ± 7 mV, −58 ± 2 mV, and −56 ± 2 mV for sample A, B, C, D, E, and F, respectively). DLS results along with the UV–vis spectra and Zeta potential measurements confirm high stability of all investigated colloids. The overall results of AuNPs and AgNPs characterization are shown in **Table 3**.

Toxicity of NPs Is Size, Concentration, and Metal Dependent

The apoptosis/necrosis assay at 24 h of exposure to NPs showed that toxicity of NPs was size and concentration dependent but also metal dependent. We found that TA-AgNPs are more toxic than TA-AuNPs, with more necrotic than apoptotic cells at ≥5 μg/ml (**Figure 2**). Only the highest concentrations of the smallest TA-AgNPs and TA-AuNPs caused significant apoptosis ($p \leq 0.01$) (**Figures 2A,B**). The significant increase of the necrotic cells was observed at 10 μg/ml for all tested TA-AgNPs (35.05 ± 3% for 10 nm, 26.64 ± 2.26% for 37 nm, and 20.88 ± 1.9% for 59 nm) ($p \leq 0.05$) (**Figure 2C**). On the other hand, the significant increase in the percentage of necrotic cells for TA-AuNPs treatments was observed only for 10 nm at the 10 μg/ml (51.8 ± 3.09% in comparison to 39.39 ± 2.26% for control) ($p = 0.034$) (**Figure 2D**).

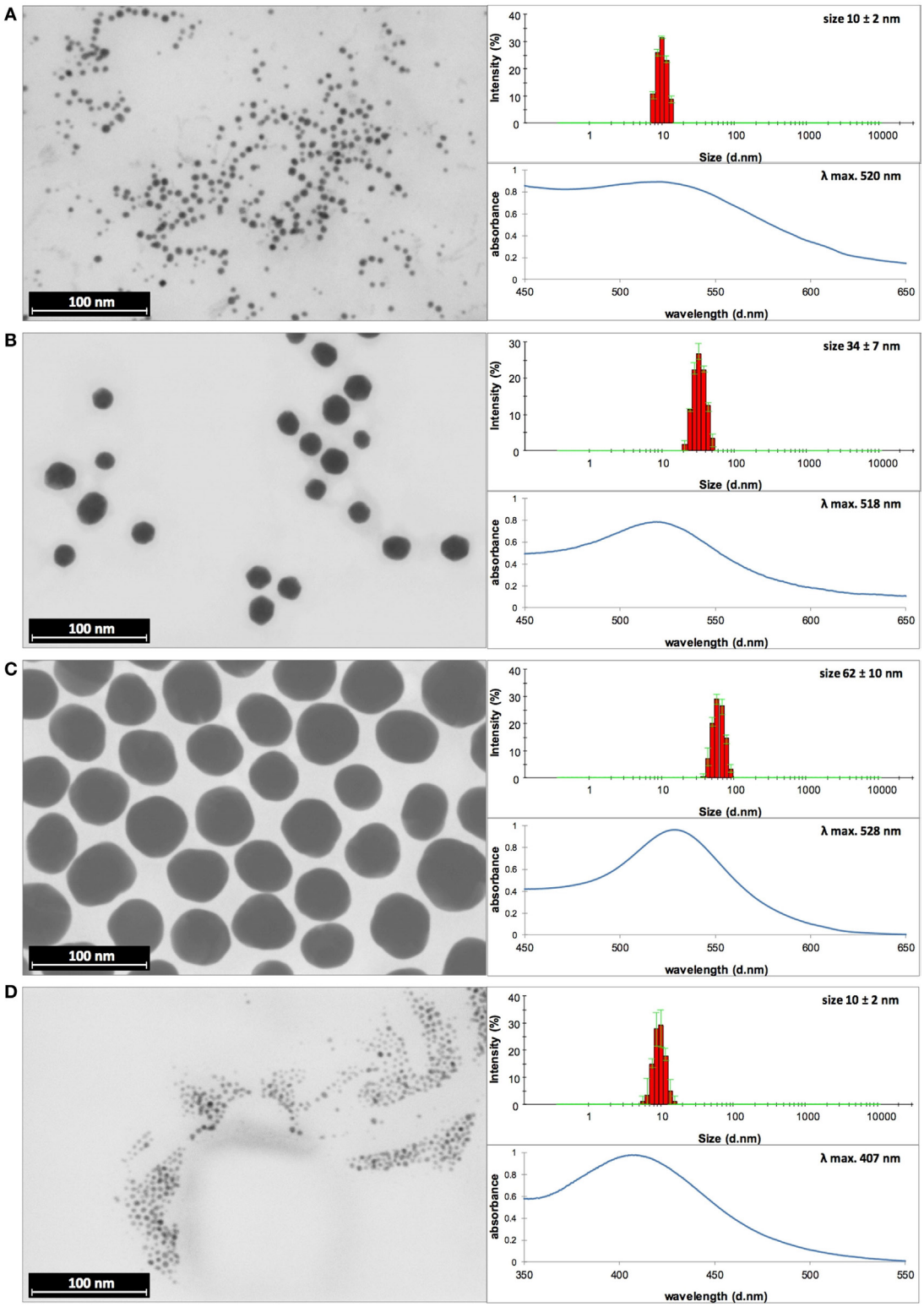

FIGURE 1 | Continued

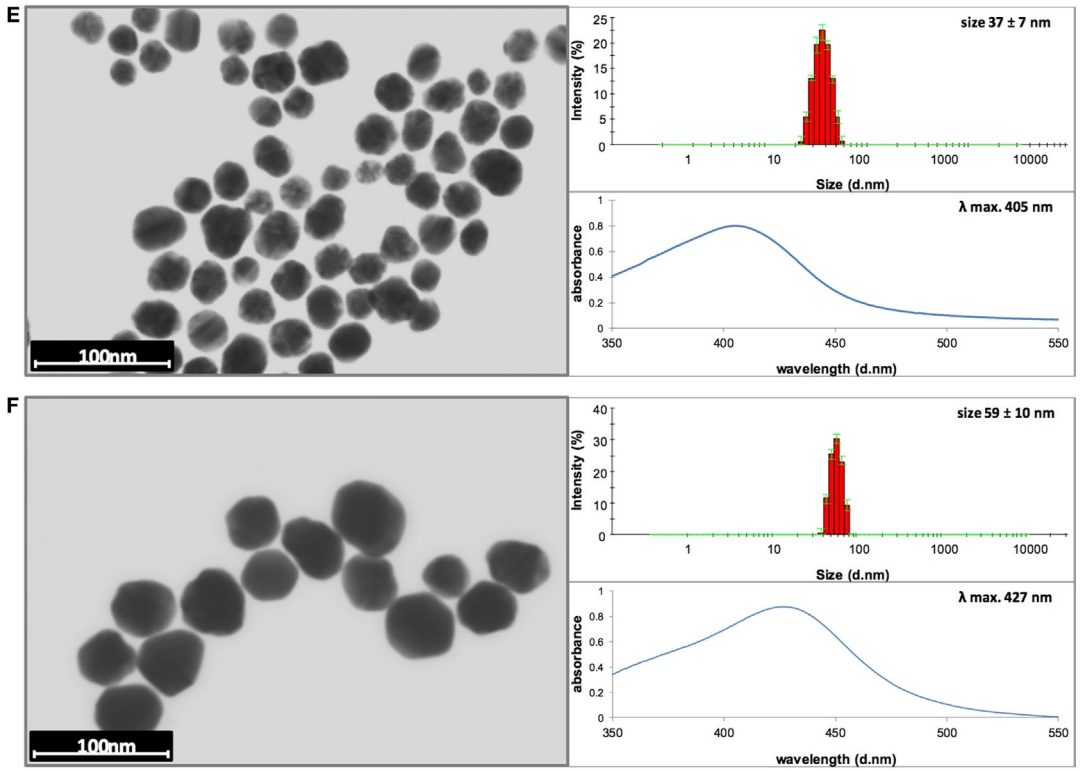

FIGURE 1 | Dynamic light scattering (DLS) histograms, UV–vis, and scanning transmission electron microscopy images with size distribution histograms of AuNPs sized **(A)** 10 nm, **(B)** 34 nm, and **(C)** 62 nm, and AgNPs sized **(D)** 10 nm, **(E)** 37 nm, and **(F)** 59 nm.

TABLE 3 | The overall results of AuNPs and AgNPs characterization.

Sample	STEM size (nm)	DLS size (nm)	UV–vis λ_{max} (nm)	Zeta potential (mV)
AuNPs				
A	5 ± 1	10 ± 2	520	−26 ± 6
B	24 ± 3	34 ± 7	518	−32 ± 1
C	58 ± 7	62 ± 10	528	−51 ± 5
AgNPs				
D	6 ± 2	10 ± 2	407	−31 ± 7
E	27 ± 7	37 ± 7	405	−58 ± 2
F	45 ± 8	59 ± 10	427	−56 ± 2

The mitochondrial potential after 24 h of treatment with TA-AgNPs or TA-AuNPs was determined using the JC-1 assay (**Figures 2E,F**). The decrease of mitochondrial potential was observed for all tested TA-AgNPs at ≥5 μg/ml and only for 62 nm TA-AuNPs at 10 μg/ml ($p \leq 0.05$). Again, the strongest toxic effect was observed for 10 nm TA-AgNPs treatment—at 10 μg/ml, we observed 48.19 ± 11.08% cells with decreased mitochondrial potential in comparison to 37.32 ± 4.9% for 37 nm TA-AgNPs and 32.43 ± 0.29% for 59 nm TA-AgNPs (**Figures 2E,F**). These data suggest mitochondrial potential disruption and necrosis rather than apoptosis as the main toxic effects of tested NPs.

Toxicity tests in endothelial cells from mouse peripheral lymph nodes HECa10 showed results similar to those obtained in JAWS II, indicating metal- and size-dependent toxicity. We found 10 nm TA-AgNPs already toxic at 2.5 μg/ml, while for other NPs, toxicity started from 5 μg/ml (10 nm TA-AuNPs) or 10 μg/ml (all remaining NPs) (Table S1 in Supplementary Material).

Uptake of NPs and Impact on Cellular Ultrastructure

To assess the influence of NPs upon morphology and ultrastructure of DCs, we used SEM (**Figures 3** and **4**). After 3 h of treatment with all tested NPs at 5 μg/ml, DCs showed an activated morphology (**Figures 3A** and **4A**)—the cells became less rounded and more adherent in comparison to the untreated control cells (**Figures 3A** and **4A**). Surface ultrastructure of cells exposed to NPs showed numerous microvilli of various length and lamellipodia with funnel configuration decorated with single or small groups of NPs (**Figures 3A** and **4A**). These structures indicate phagocytosis and endocytosis as the main mechanism of NPs uptake. The activated morphology of DCs is retained at 24 h of exposure to NPs (**Figures 3B** and **4B**).

To investigate intracellular localization of NPs in exposed cells, we employed TEM (**Figures 3B** and **4B**). The 24 h exposure of JAWS II cells to NPs at the concentration of 2.5 μg/ml led to accumulation of NPs mainly within vesicles filled with an electron dense content. We found that intracellular sizes of all tested AgNPs were below the synthesis dimensions (**Figure 3B**) in contrast to

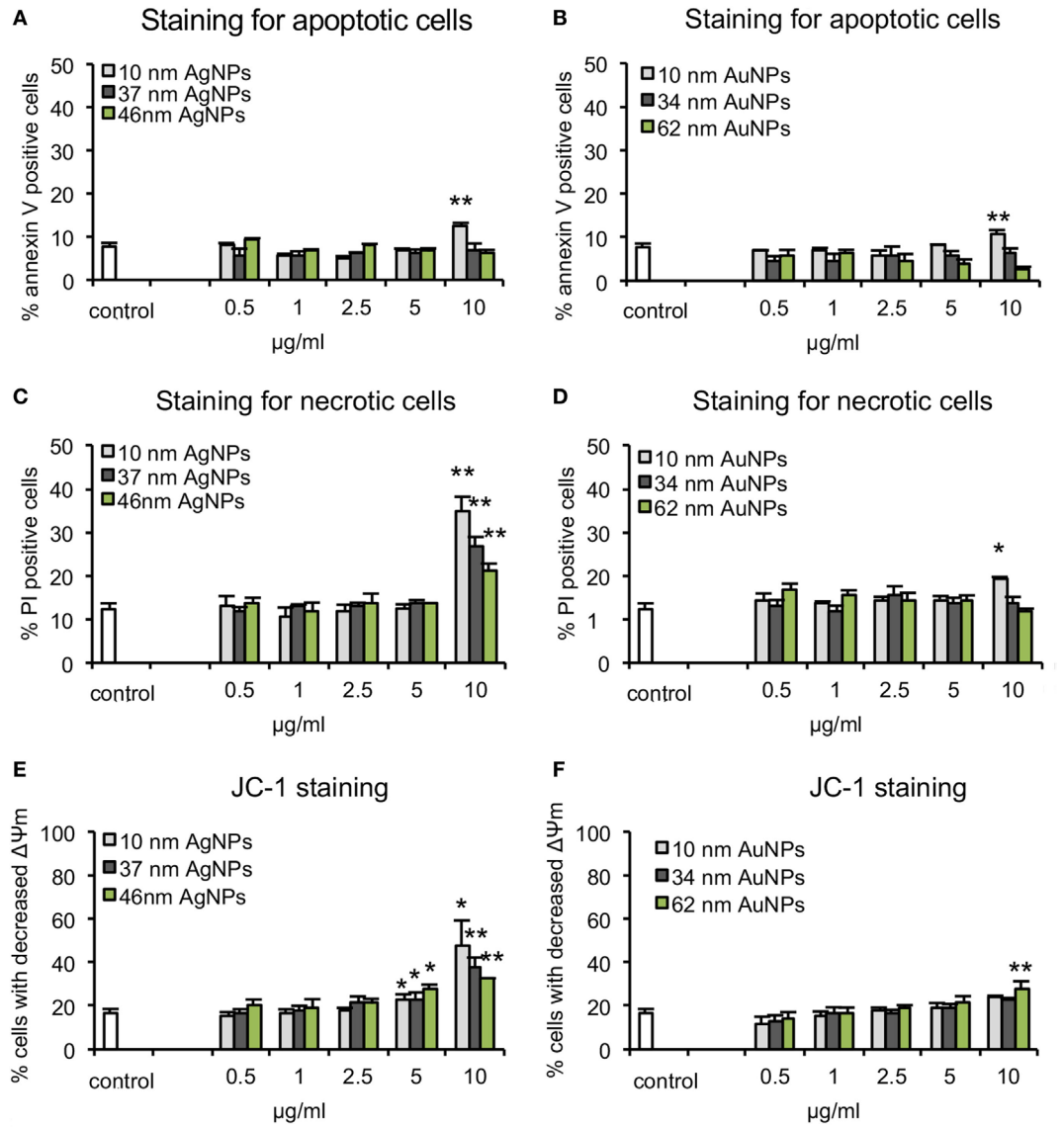

FIGURE 2 | Cytotoxicity assays in JAWSII cell line at 24 h of exposure to AgNPs sized 10 nm, 37 nm, and 59 nm, and AuNPs sized 10 nm, 34 nm, and 62 nm at 0.5–10 µg/ml. **(A,B)** Percentage of annexin V-positive (apoptotic) cells. **(C,D)** Percentage of PI positive (necrotic) cells. **(E,F)** Decrease in mitochondrial potential expressed as the percentage of cells with decreased mitochondrial potential Each bar represents the mean from five experiments ($N = 5$) ± S.E.M., *Significant differences with $p \leq 0.05$, **$p \leq 0.01$.

TA-AuNPs with the unchanged sizes (**Figure 4B**). TA-AgNPs of 10 nm and 37 nm as well as TA-AuNPs of 10 nm and 34 nm were localized as attached to inner vesicles membrane (**Figures 3B** and **4B**, respectively) whereas 59 nm TA-AgNPs were found as small groups of particles dispersed in vesicles (**Figure 3B**). Single 62 nm TA-AuNPs were thoroughly distributed in the vesicles content (**Figure 4B**).

To test if NPs are degraded in lysosomes, we stained cells with LysoTracker (**Figure 5**). The analyses showed that co-localization of TA-Ag/AuNPs with lysosomes was lower in comparison to localization in non-acidic compartments both at 6 and 24 h of incubation (**Figures 5A,B**). The highest co-localization with lysosomes was observed for 37 nm and 59 nm TA-AgNPs, 10 nm and 62 nm TA-AuNPs at 24 h (**Figure 5B**). **Figure 5C** shows localization of TA-Ag/AuNPs in JAWS stained for lysosomes. The NPs are visualized in red by the light reflected from their surface. Therefore, the higher surface to volume ratio, the higher signal (**Figure 5C**).

To further understand the mechanism of NPs uptake, we used pharmacological inhibitors of clathrin-mediated endocytosis (MDC), caveolae/lipid raft-mediated endocytosis (genistein), colchicine (pinocytosis), fluid-phase endocytosis (wortmannin), phagocytosis, and macropinocytosis (CChD). Of all used inhibitors, only MDC and CChD significantly inhibited uptake of all NPs at 6 hours of incubation ($p \leq 0.05$) (**Figure 5D**).

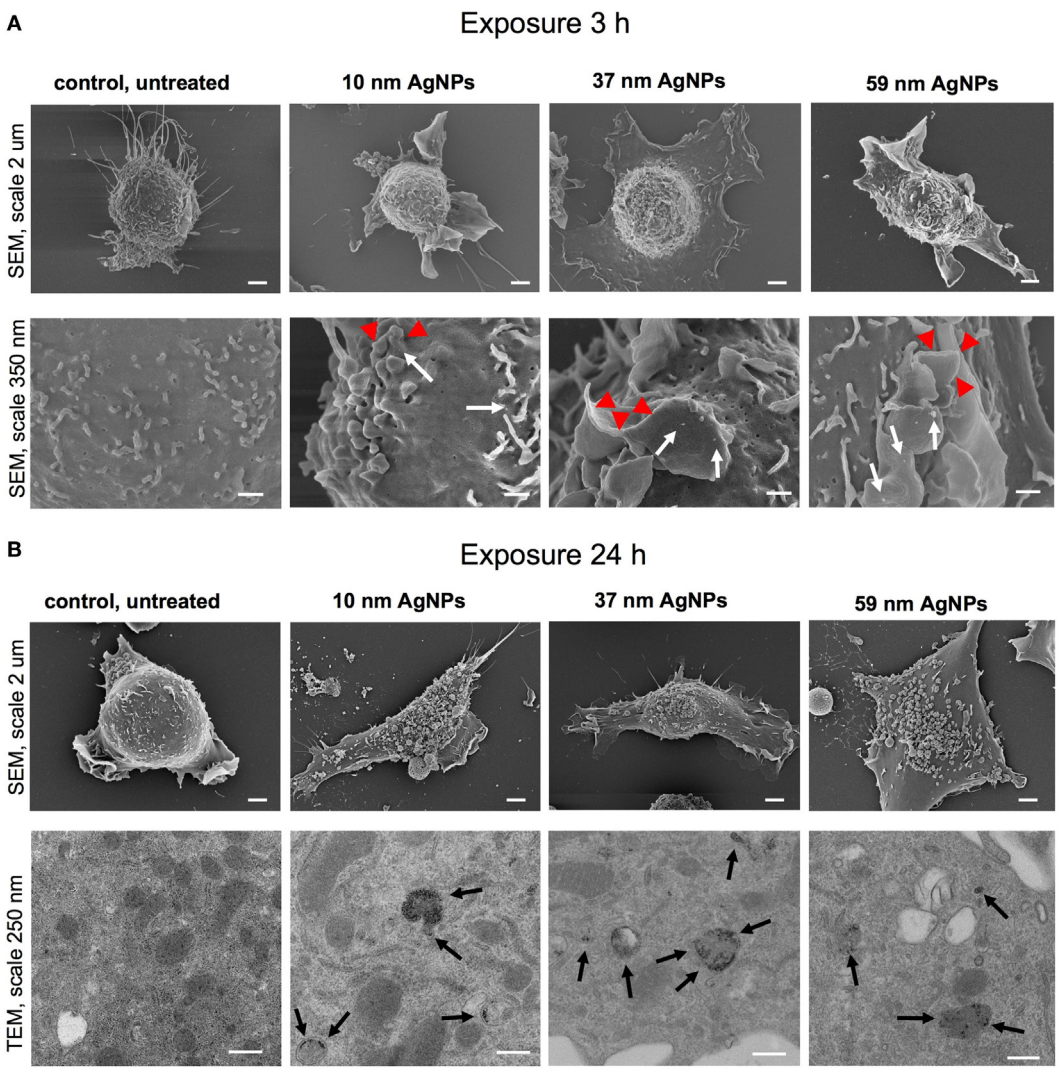

FIGURE 3 | Scanning electron microscopy (SEM) and transmission electron microscopy (TEM) images of JAWS II cell line after 3 **(A)** and 24 h **(B)** of incubation with 5 μg/ml 10, 37, and 59 nm TA-AgNPs. White arrows indicate deposition of NPs, red arrowheads indicate lamellipodia, while black arrows point to intracellular deposits of AgNPs. Bars 2 μm, 250 nm and 350 nm are indicated.

Effect of NPs on Expression of Surface Activation Markers

During activation and maturation, DCs change their morphology and up-regulate surface activation markers. To check the influence of NPs on maturation of DCs, we measured expression levels of MHC class I/II and CD40, CD80, and CD86 co-stimulatory molecules after 24 h treatment with NPs at the non-toxic dose of 2.5 μg/ml (**Figure 6**), but also at 6 h after treatment with NPs and inhibitors of endocytosis and phagocytosis—MDC and CChD (**Figure 7**). Lipopolysaccharide was used to stimulate DCs maturation in the positive control. For JAWS II, MHC I and CD80 expression is present on all cells, while MHC II, CD40, and CD86 are detected only for the percentage of cell culture. However, these cells show different characteristics of activation markers in response to NPs modified with tannic acid. While for MHC I and CD86, activation was observed as an increased or decreased percentage of cells expressing a particular marker, for CD40, CD80, and MHC II, activation was showed as changes in the mean fluorescence intensity (MFI). All tested NPs significantly decreased the percentage of MHC I positive cells ($p \leq 0.01$) (**Figure 6A**). We observed 59.16 ± 2.24% and 61.49 ± 8.9% MHC I positive cells for small (S, 10 nm and 10 nm) TA-AgNPs and TA-AuNPs, 62.08 ± 3.06% and 66.84 ± 2.39% for medium (M, 37 nm and 34 nm) TA-AgNPs and TA-AuNPs, 62.13 ± 3.73% and 65.46 ± 3.75% for large (L, 59 nm and 62 nm) TA-AgNPs and TA-AuNPs, respectively, in comparison to control untreated cells (79.1 ± 1.19%) and LPS-stimulated positive control (89.04 ± 1.81%) ($p = 0.002$) (**Figure 6A**). MDC and CChD significantly reduced MHC I expression in control JAWS II cells at 6 h ($p \leq 0.01$) (**Figure 7A**), which can be contributed to the individual sensitivity of this cell line to phagocytosis and endocytosis inhibitors. However, only treatment with MDC led to

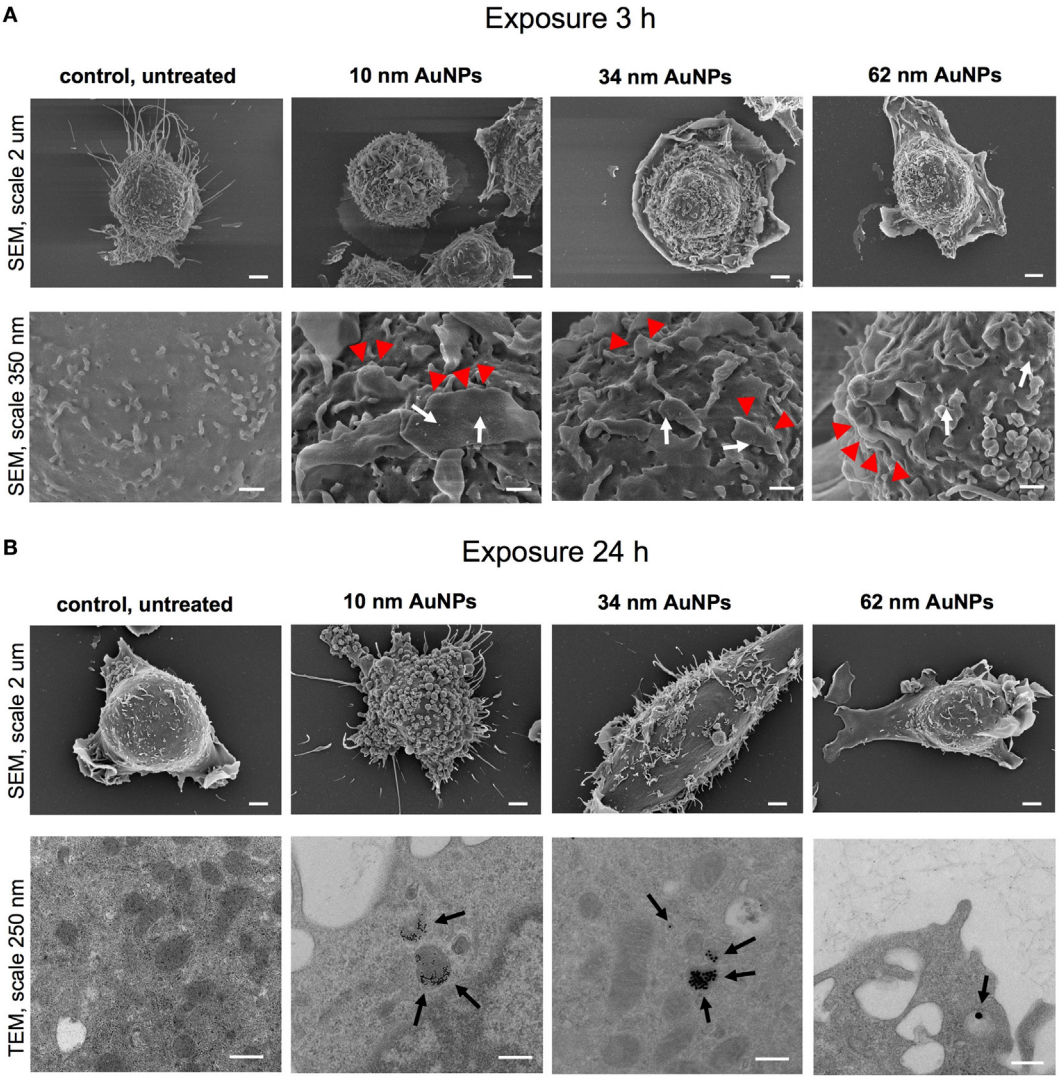

FIGURE 4 | Scanning electron microscopy (SEM) and transmission electron microscopy (TEM) images of JAWS II cell line after 3 **(A)** and 24 h **(B)** of incubation with 5 μg/ml 10, 34, and 62 TA-AuNPs. White arrows indicate deposition of NPs, red arrowheads indicate lamellipodia, while black arrows point to intracellular deposits of AuNPs. Bars 2 μm, 250 nm and 350 nm are indicated.

further significant decrease in MHC I expression in cells treated with all sizes of TA-Ag/AuNPs in comparison to MDC-treated control cells at 6 h ($p \leq 0.05$) (**Figure 7A**). In contrast, all NPs except for 10 nm TA-AuNPs significantly increased MHC II expression, at the level similar to LPS stimulation (339.36 ± 4.68 MFI), in comparison to untreated control (233.93 ± 18.15 MFI) ($p \leq 0.05$) (**Figure 6B**). Significant increase of MHC II expression was also observed for cells treated with CChD, both control and NPs-treated at 6 h ($p \leq 0.05$) (**Figure 7B**).

Analysis of CD40 revealed that DCs exposed to TA-AgNPs increase expression of this marker (**Figure 5C**). Stimulation with 10 nm TA-AgNPs led to a two-fold increase of CD40 expression in comparison to untreated control cells (431.69 ± 67.81 MFI and 209.36 ± 20.18 MFI, respectively) ($p \leq 0.01$). Exposure to 37 nm and 59 nm TA-AgNPs increased CD40 expression to 354.39 ± 65.83 MFI ($p \leq 0.01$) and 317.23 ± 58.83 MFI ($p \leq 0.05$), respectively. No significant changes were observed upon TA-AuNPs or LPS treatment ($p \geq 0.05$) (**Figure 6C**).

Interestingly, NPs-treated cells subjected to MDC significantly up-regulated CD40 expression in comparison to control and MDC-treated control ($p \leq 0.05$), except for 59 nm TA-AgNPs (**Figure 7C**). CChD did not influence CD40 expression in NPs-treated cells (**Figure 7C**).

Up-regulation of CD86 expression was found during LPS, TA-AgNPs, and 10 nm TA-AuNPs treatment (**Figure 6D**). Treatment with 10 nm TA-AgNPs or TA-AuNPs led to a three- and two-fold increase in CD86 expression (36.51 ± 3.83% and 25.21 ± 3.91%, respectively) in comparison to control (13.78 ± 0.96%). Interestingly, treatment with 37 nm TA-AgNPs elevated CD86 expression five-fold (80.46 ± 3.84%) in comparison to untreated control cells

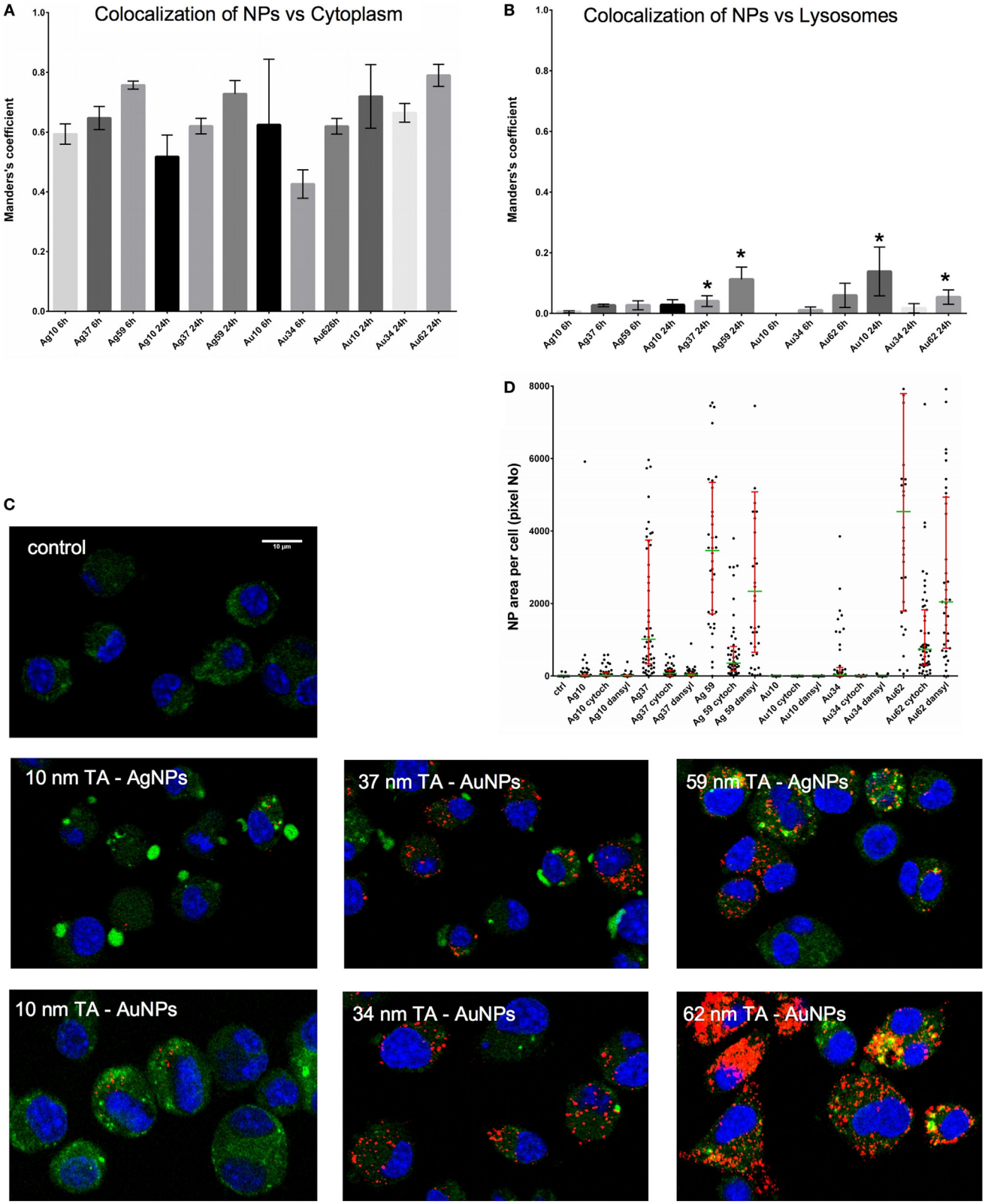

FIGURE 5 | Intracellular localization of TA-Ag/AuNPs. The Manders' coefficients for co-localization of TA-Ag/AuNPs and cytoplasm **(A)** or lysosomes **(B)** in JAWS II cell culture exposed to 10 nm, 37 nm, 59 nm TA-AgNPs and 10 nm, 34 nm, 62 nm TA-AuNPs for 24 h at 2.5 µg/ml. *Significant differences with $p \leq 0.05$. **(C)** Representative images for lysosomes (green), nanoparticles (NPs) (red) and nuclei (blue) in cells exposed to NPs, as described above. **(D)** NPs content in cells subjected to pretreatment with 10 µg/ml monodansyl cadeverine and 5 µg/ml cytochalasin D, and then to incubation with TA-Ag/AuNPs at 2.5 µg/ml for 6 h.

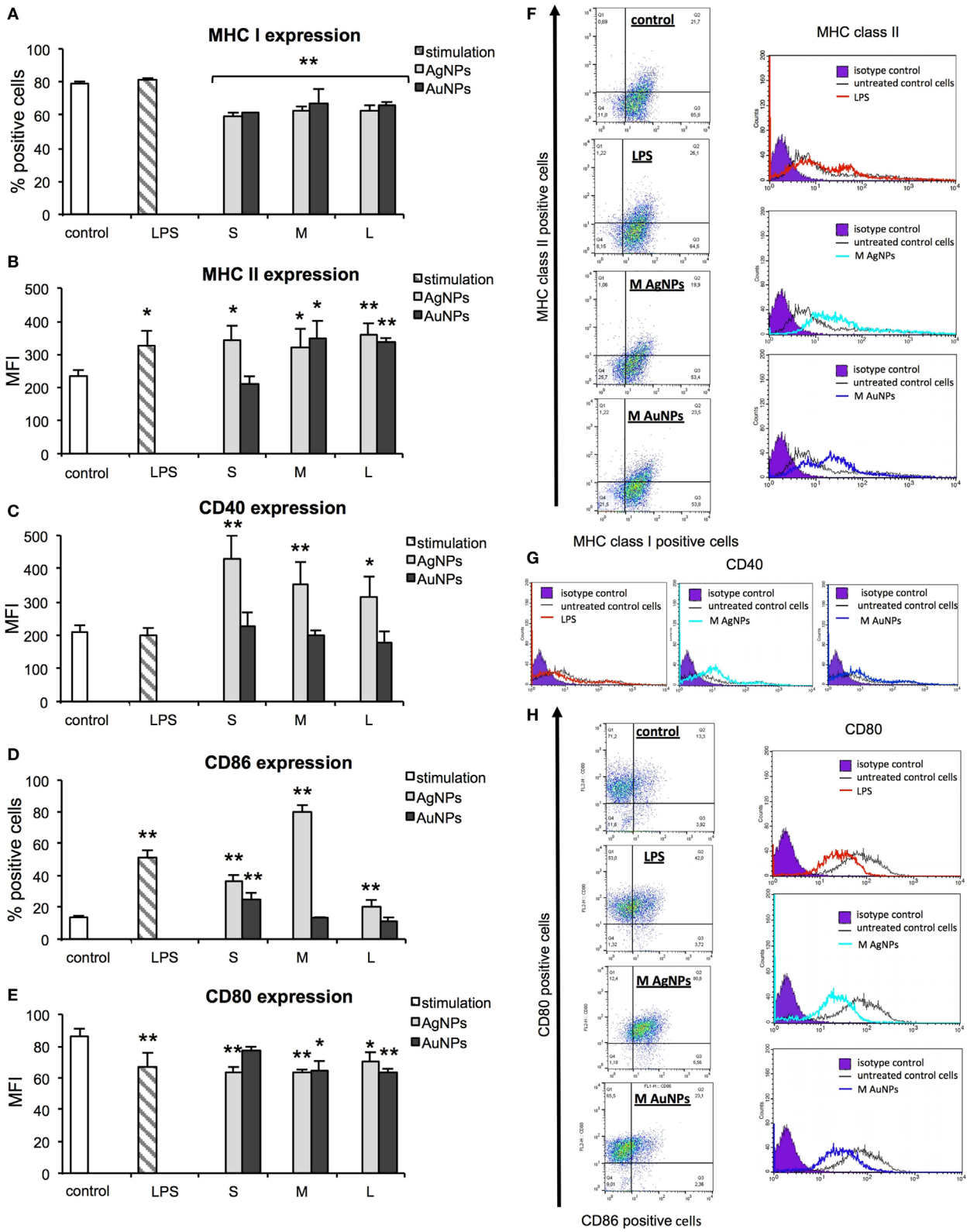

FIGURE 6 | Effect of nanoparticles (NPs) on expression of surface activation markers. MHC class I **(A)**, MHC class II **(B)**, CD40 **(C)**, CD86 **(D)**, and CD80 **(E)** from 5 experiments ($N = 5$) ± S.E.M. **(F)** Representative dot plots (left panel) for MHC I and MHC II expression and representative histograms for MHC II expression. **(G)** Representative histograms for CD40 expression. **(H)** Representative dot plots for CD80 and CD86 expression (left panel) and representative histograms for CD86 expression (right panel). *Significant differences with $p \leq 0.05$, **$p \leq 0.01$.

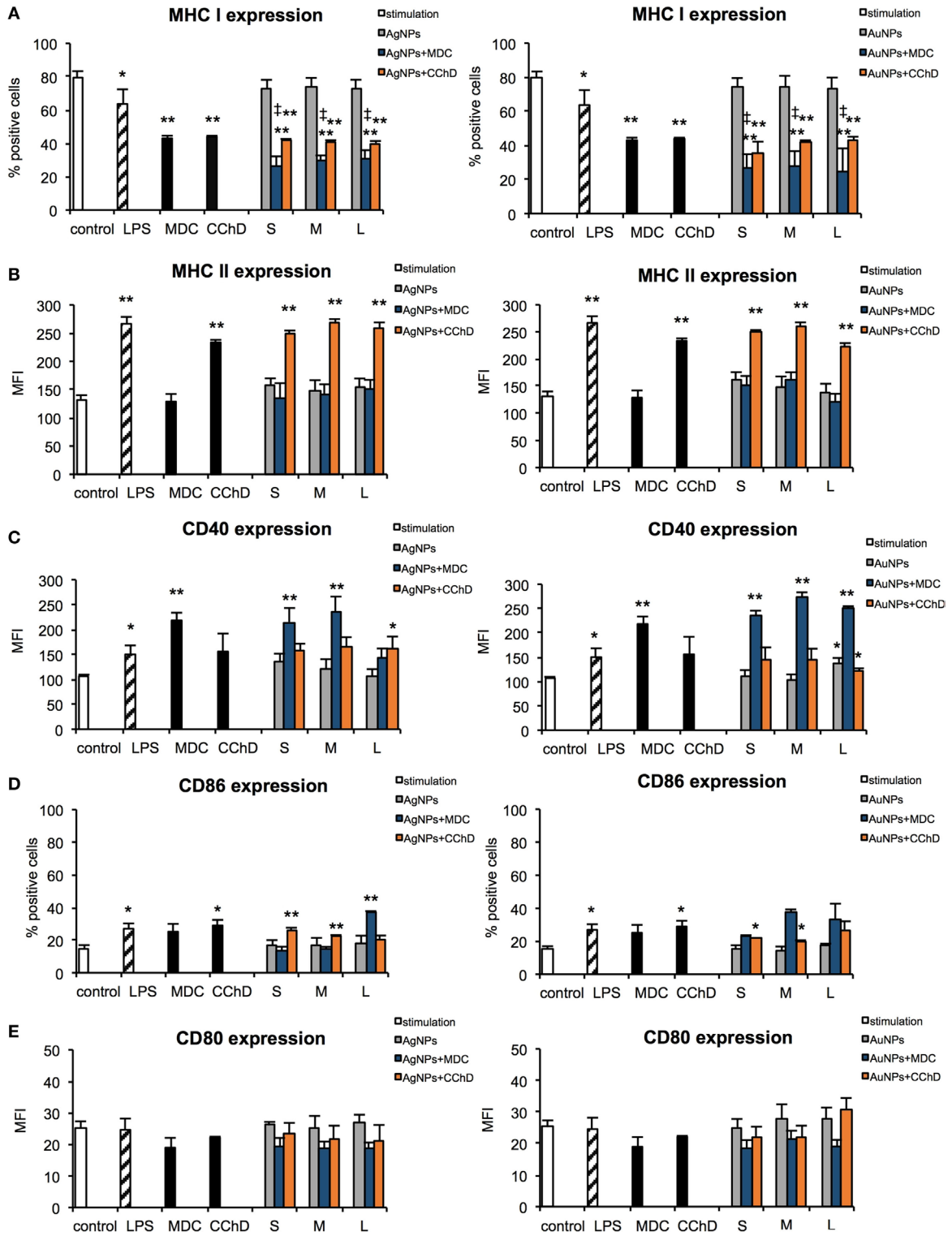

FIGURE 7 | Effect of nanoparticles (NPs) on expression of surface activation markers in the presence of endocytosis and phagocytosis inhibitors. MHC class I **(A)**, MHC class II **(B)**, CD40 **(C)**, CD86 **(D)**, and CD80 **(E)** expression on the JAWS II cells after 6 h exposure to 2.5 μg/ml 10 nm (S), 37 nm (M), 59 nm (L) TA-AgNPs and 10 nm (S), 34 nm (M), 62 nm (L) TA-AuNPs with or without pretreatment with 10 μg/ml monodansyl cadeverine (MDC), and 5 μg/ml cytochalasin D (CChD). Each bar represents the mean from three experiments ($N = 3$) ± S.E.M. *Significant differences with $p \leq 0.05$, **$p \leq 0.01$ in comparison to untreated control, ‡Significant differences with $p \leq 0.05$ in comparison to inhibitor treatment.

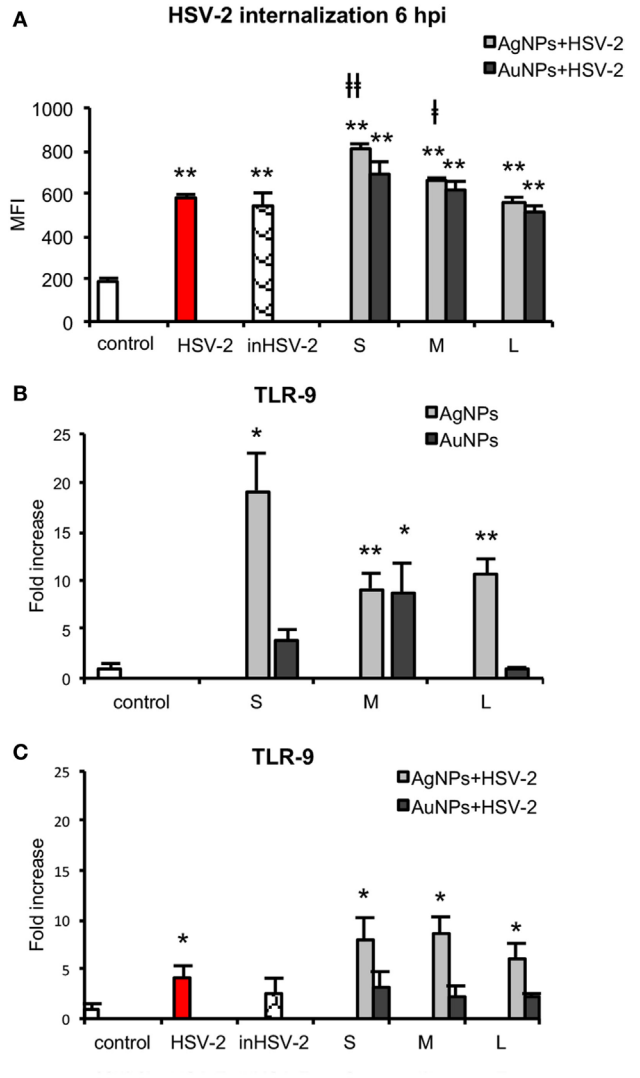

FIGURE 8 | Nanoparticles (NPs) stimulate uptake of viral antigens and expression of TLR9. **(A)** Presence of HSV-2 antigens in JAWS II cells after 6 h exposure to HSV-2, inactivated HSV-2, or NPs-treated HSV-2. TLR 9 expression in NPs- and HSV-NPs-treated JAWS II cells. The cells were exposed to 2.5 μg/ml of **(B)** TA-Ag/AuNP, **(C)** TA-AgNPs or TA-AuNPs-treated HSV-2. Each bar represents the mean from three experiments ($N = 3$) ± S.E.M. *Significant differences with $p \leq 0.05$, **$p \leq 0.01$ in relation to untreated control, ǂ$p \leq 0.05$, and ǂǂ$p \leq 0.01$ calculated in relation to the HSV-2 infected control.

(13.78 ± 0.96%) ($p = 0.0000$). No significant influence upon CD86 expression was found for cells treated with MDC, both control and NPs-treated at 6 h ($p > 0.05$) (**Figure 7D**).

A significant decrease in CD80 expression levels was observed upon LPS treatment (66.42 ± 9.37 MFI) as well as for 10 nm (62.94 ± 3.89 MFI), 37 nm (63.42 ± 1.79 MFI), and 59 nm (69.99 ± 6.12) TA-AgNPs treatment when compared with control cells (86.19 ± 4.79 MFI) ($p \leq 0.01$) (**Figure 6E**). Significantly decreased expression of CD80 was also observed during exposure to 34 and 62 TA-AuNPs (64.08 ± 6.49 MFI and 63.48 ± 2.25 MFI, respectively) ($p \leq 0.01$) (**Figure 6E**). No significant influence upon CD80 expression was found for cells treated with MDC, both control and NPs-treated at 6 h ($p > 0.05$) (**Figure 7E**).

Programmed death-ligand 1 (PD-L1) has been postulated to play a crucial role in suppressing lymphocyte activation (26). Here, we tested if TA-NPs treatment has any influence upon PD-L1 expression in JAWS II cells, but we found no significant differences (data not shown).

To check for relevance with *in vivo* conditions, we performed follow-up experiments with BMDCs cultures obtained from C57BL/6 mice. All sizes of TA-AgNPs significantly decreased percentages of MHC I positive BMDCs ($p \leq 0.05$), while this tendency was insignificant for TA-AuNPs treated cells ($p > 0.05$) (Figure S1A in Supplementary Material). BMDCs treated with all sizes of TA-AgNPs/AuNPs significantly increased MHC II expression, at the level similar to LPS stimulation in comparison to untreated control ($p \leq 0.05$) (Figure S1B in Supplementary Material). As for JAWS II cells, BMDCs exposed to TA-AgNPs significantly increased expression of CD40 ($p \leq 0.05$) (Figure S1C in Supplementary Material). A decrease in CD80 expression levels was observed upon LPS treatment and treatment with all sizes of TA-AgNPs/AuNPs ($p \leq 0.05$) (Figure S1D in Supplementary Material) except for 10 nm and 37 nm TA-AgNPs, due to a high distribution of individual results. For CD86 expression, we did not observe any significant differences in the expression patterns after exposure to TA-AgNPs/AuNPs ($p > 0.05$) (Figure S1D in Supplementary Material).

NPs Stimulate Uptake of Viral Antigens

In our previous work, we showed that 1 h pre-incubation of HSV-2 inoculum with 2.5 μg/ml TA-NPs resulted in complete inhibition of infection *in vitro* (15). Here, we examined if TA-NPs-treated HSV-2 (HSV) can induce DCs maturation. First, we studied the level of TA-NPs-treated HSV-2 (NPs-HSV) uptake by JAWS II cells in comparison to non-treated HSV-2 and heat inactivated HSV-2 (inHSV) (**Figure 8A**). The antigen uptake after 6 h post infection (p. i.) for HSV and inHSV was observed at the similar level (578.84 ± 15.67 MFI and 541.06 ± 60.78 MFI, respectively). A six-hour incubation of JAWS II with 2.5 μg/ml TA-NPs-HSV resulted in a significant internalization of viral antigens in the presence of S and M AgNPs-HSV ($p \leq 0.05$) in comparison to HSV-2 infected control. The highest observed antigen uptake was found for S TA-AgNPs-HSV (809.89 ± 21.79 MFI) ($p = 0.0005$) (**Figure 8A**). Blockage of the virus surface by L TA-AgNPs and all tested TA-AuNPs did not influence the uptake of viral antigens in comparison to infection with untreated HSV-2.

TLR9 Expression

TLR9 is expressed within the endoplasmic compartment and recognizes CpG DNA motifs (27). Since we observed higher internalization of HSV-2 treated with NPs, we measured the level of TLR9 mRNA in the treated JAWS II cells. After exposure of DCs to TA-AgNPs, the level of TLR9 mRNA significantly increased inversely with their size (**Figure 8B**). Exposure to 10 nm TA-AgNPs induced 26.02 ± 3.82-fold higher expression of TLR9 mRNA in comparison to control cells ($p = 0.046$) (**Figure 8B**). The 37 nm and 59 nm TA-AgNPs caused 9.19 ± 1.53 and 10.54 ± 1.66-fold increase of TLR9 mRNA level in comparison

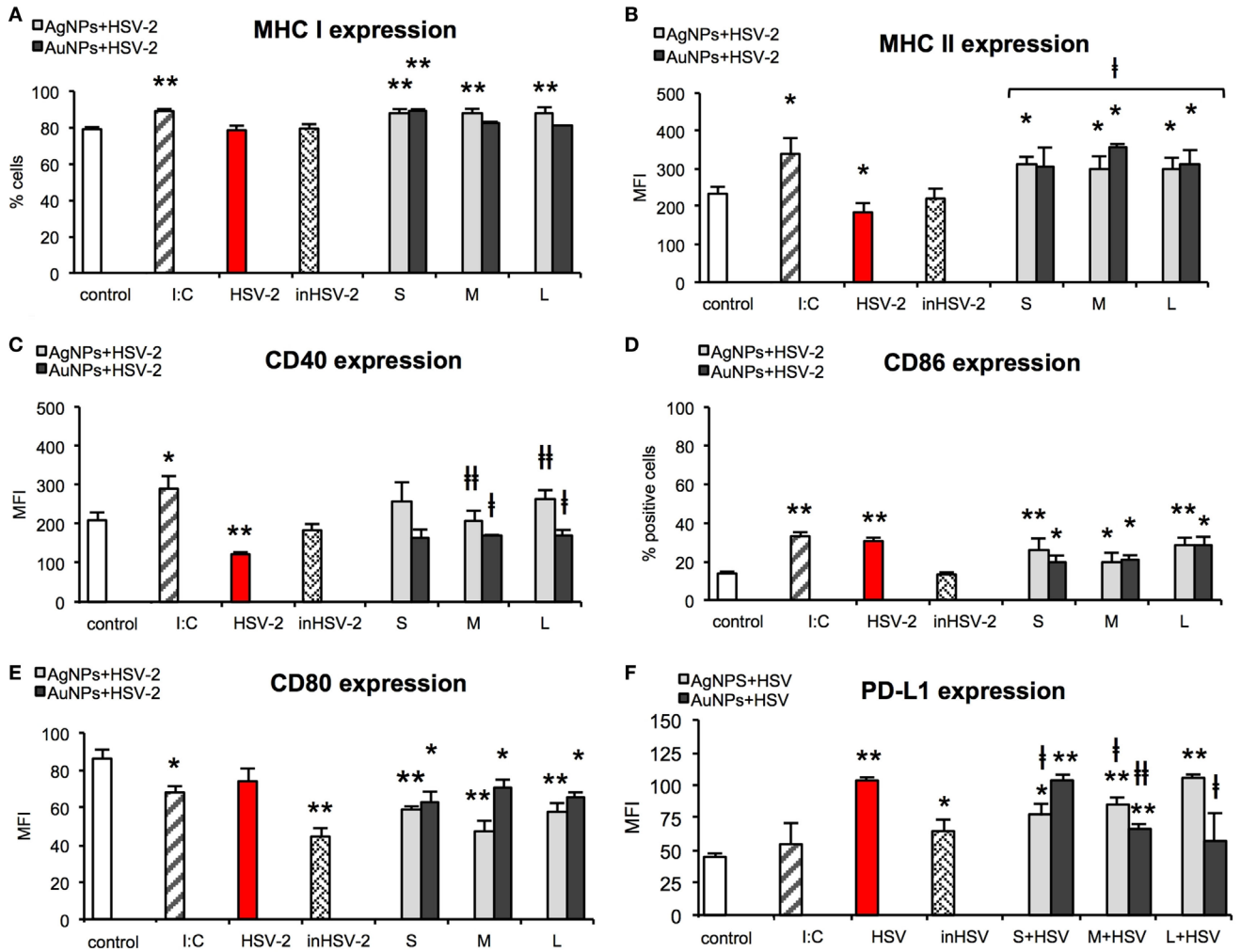

FIGURE 9 | Nanoparticles (NPs)-treated HSV-2 stimulate maturation of dendritic cells (DCs). MHC class I **(A)**, MHC class II **(B)**, CD40 **(C)**, CD86 **(D)**, CD80 **(E)**, and PD-L1 **(F)** expression on the JAWS II cells after 24 h exposure to HSV-2 treated with 2.5 μg/ml of 10 nm (S), 37 nm (M), 59 nm (L) TA-AgNPs and 10 nm (S), 34 nm (M), 62 nm (L) TA-AuNPs. Each bar represents the mean from 5 experiments ($N = 5$) ± S.E.M. *Significant differences with $p \leq 0.05$, **$p \leq 0.01$ in relation to untreated control, ǂ$p \leq 0.05$, and ǂǂ$p \leq 0.01$ calculated in relation to the HSV-2 infected control.

to control, respectively ($p \leq 0.01$). Only 37-nm-sized TA-AuNPs caused a significant increase in the TLR9 mRNA level (8.86 ± 2.9) ($p = 0.0280$). Infection of JAWS II cells led to 4.11 ± 1.23 higher level of TLR9 mRNA in comparison to uninfected control cells ($p = 0.039$) (**Figure 8B**). During exposure of JAWS II cells to HSV-2 treated with TA-AgNPs, we observed an increased synthesis of mRNA ($p \leq 0.05$) (**Figure 8C**). None of TA-AuNPs-treated HSV-2 significantly induced the synthesis of TLR9 mRNA level in comparison to untreated control ($p \geq 0.05$) (**Figure 8C**).

NPs Treated HSV-2 Stimulate Maturation of DCs

Taking into account the fact that HSV-2 infection inhibits DCs maturation and thus results in a poor development of the specific immune response (28), we examined the impact of HSV-2 treated with NPs on the activation markers at 24 h post infection (p. i.). For all tested AgNPs-treated HSV-2, MHC class I expression was significantly higher in comparison to control cells and stayed at the level similar to that observed for positive poly (I:C) stimulated control ($p \leq 0.01$) (**Figure 9A**). Following infection with TA-AuNPs-HSV-2, only 10 nm TA-AuNPs-HSV-2 significantly increased MHC I expression ($p \leq 0.01$). HSV-2 infection significantly decreased MHC II expression in comparison to untreated control (184.63 ± 14.35% and 233.93 ± 14.15%, respectively) ($p = 0.016$) (**Figure 9B**). On the contrary, exposure to TA-AgNPs-treated HSV-2 resulted in a significant up-regulation of MHC II expression in comparison to untreated control and HSV-2 infected cells ($p \leq 0.05$). Only exposure to M and L TA-AuNPs-treated HSV-2 caused a significant up-regulation of MHC II expression (354.47 ± 10.78 MFI and 313.98 ± 35.36 MFI, respectively) in comparison to untreated and HSV-2 infected cells ($p \leq 0.05$).

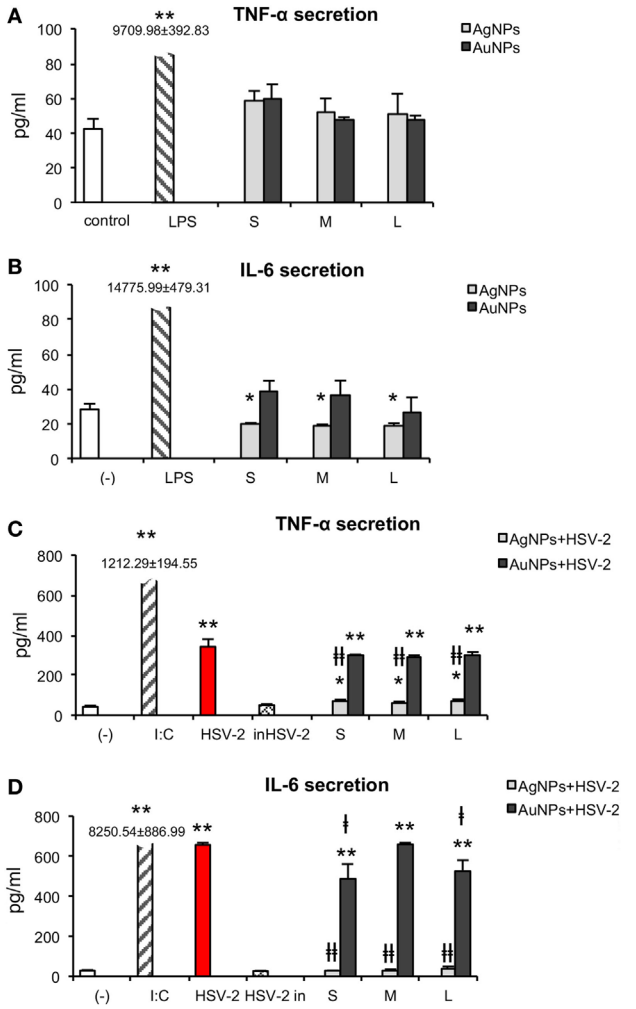

FIGURE 10 | Effect of nanoparticles (NPs) and NPs-treated-HSV-2 on cytokine secretion. TNF-α **(A)** and IL-6 **(B)** production in JAWS II cells exposed to 2.5 μg/ml NPs for 24 h. **(C)** TNF-α and **(D)** IL-6 production in JAWS II cells exposed to NPs-treated HSV-2 for 24 h. Each bar represents the mean from 3 experiments ($N = 3$) ± S.E.M. *Significant differences with $p \leq 0.05$, ** $p \leq 0.01$ in relation to untreated control, ǂ$p \leq 0.05$, and ǂǂ$p \leq 0.01$ calculated in relation to the HSV-2 infected control.

HSV-2 infection also led to a significant decrease in CD40 expression (122.26 ± 5.41 MFI) in comparison to untreated control cells (209.36 ± 20.18 MFI) ($p = 0.0075$) (**Figure 9C**). However, cells exposed to HSV-2 treated with M and L TA-AgNPs showed significantly higher CD40 expression than HSV-2 infected cells (122.26 ± 5.41 MFI) ($p \leq 0.01$). Also, cells exposed to HSV-2 treated with M and L TA-AuNPs showed significantly higher expression of CD40 (167.42 ± 4.17 MFI and 172.01 ± 12.69 MFI) in comparison to infected cells (122.26 ± 5.41 MFI) ($p \leq 0.05$).

HSV infection of JAWS II cells resulted in a significant up-regulation of CD86 expression (30.07 ± 1.75%, $p = 0.0000$), as that observed for poly (I:C) stimulated control (33.06 ± 2.12%, $p = 0.0000$) in comparison to untreated control cells (13.78 ± 0.96%) (**Figure 9D**). All NPs-treated HSV-2 preparations significantly increased CD86 expression in comparison to untreated control cells ($p \leq 0.05$). The lowest up-regulation of CD86 expression was observed for M TA-AgNPs and S/M AuNPs treated HSV-2 (20.2 ± 4.3%, 20.05 ± 3.03%, and 20.42 ± 2.8%, respectively) ($p \leq 0.05$).

CD80 expression was significantly decreased upon poly (I:C) stimulation in comparison to untreated control (68.03 ± 3.42 MFI and 86.19 ± 4.79 MFI, respectively) ($p = 0.0179$) (**Figure 9E**). Inactivated HSV-2 was the strongest down-regulator of CD80 expression (44.38 ± 4.46) ($p = 0.0015$). All NPs-treated HSV-2 significantly downregulated expression of CD80. We observed stronger down-regulation of CD80 expression on the cells exposed to TA-AgNPs-HSV-2 than on the cells exposed to TA-AuNPs-HSV-2 preparations ($p \leq 0.01$ and $p \leq 0.05$, respectively) (**Figure 9E**).

Here, we checked if NPs-treated HSV-2 was able to influence the level of PD-L1 expression on JAWS II (**Figure 9F**). HSV-2 infection of JAWS II resulted in a significant up-regulation of PD-L1 (103.53 ± 2.36 MFI) in comparison to untreated control cells (44.68 ± 2.7 MFI) ($p = 0.0000$). We observed a size-dependent influence of TA-AgNPs-treated HSV-2 upon PD-L1 expression with PD-L1 expression increasing together with the size of AgNPs used for HSV-2 inactivation ($p \leq 0.01$) (**Figure 9F**). Interestingly, treatment of HSV-2 with S/M TA-AgNPs led to PD-L1 expression which was lower than that this observed on HSV-2 infected DCs ($p \leq 0.05$) (**Figure 9F**). For AuNPs-treated HSV-2, we observed a reversed correlation—PD-L1 expression decreased with the increasing size of AuNPs and the highest expression of PDL-1 was detected in S AuNPs-HSV-2-treated cells (**Figure 9F**). Furthermore, only M and L TA-AuNPs-treated HSV-2 preparations led to PD-L1 expression lower than that this observed for HSV-2 infection ($p \leq 0.05$) (**Figure 9F**).

Polymyxin B had no significant influence upon expression of MHC I, MHC II, CD80, CD86 in DCs subjected to TA-NPs-treated HSV-2, except for CD40, expression of which was significantly down-regulated upon polymyxin B addition (Table S2 in Supplementary Material). Significant decrease in CD40 expression was observed for HSV-2 treated with TA-AgNPs, and 63 nm TA-AuNPs ($p \leq 0.05$) (Table S2 in Supplementary Material).

Effect of NPs and NPs Treated HSV-2 on Cytokine Secretion

During activation and maturation, DCs change the profile of produced cytokines. We measured secretion of IL-10, IL-17A, TNF-α, IFN-γ, IL-6, IL-4, and IL-2 by JAWS II subjected to HSV-2 treated with TA-Ag/AuNPs using the CBA. We were not able to detect IL-10, IL17A, IFN-γ, IL-4, or IL-2 in the supernatants from stimulated or control cells. Exposure to all NPs did not cause any significant change in TNF-α secretion in comparison to untreated control (**Figure 10A**) ($p \geq 0.05$). IL-6 measurement showed a significant decrease upon treatment with S, M, and L TA-AgNPs (19.85 ± 0.55 pg/ml, 18.94 ± 0.69 pg/ml, and 19.2 ± 1 pg/ml, respectively) in comparison to untreated control cells (28.19 ± 3.22 pg/ml) ($p \leq 0.01$) (**Figure 10B**).

HSV-2 infection of JAWS II significantly increased TNF-α production to 342.23 ± 37.59 pg/ml in comparison to 42.34 ± 5.89 pg/ml produced by untreated control cells ($p = 0.0007$) (**Figure 10C**).

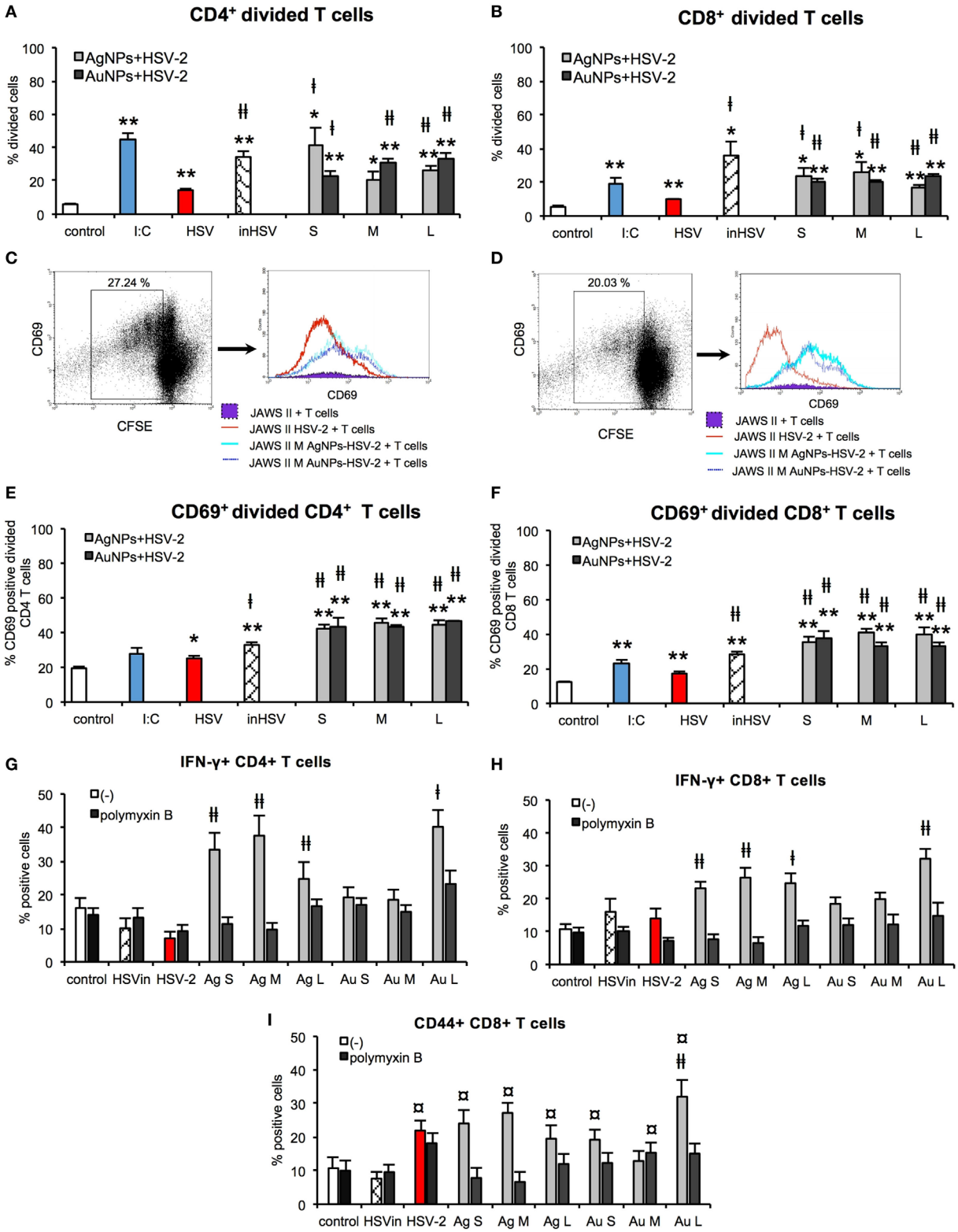

FIGURE 11 | Nanoparticles (NPs) enhance the ability of dendritic cells (DCs) to activate T cells *in vitro*. Percentage of divided CD4+ **(A)** and CD8+ T cells **(B)**. Representative dot plots and histogram plots of CD69+ CD4+ **(C)** and CD69+ CD8+ **(D)** divided T cells. Percentage of CD69+ divided CD4+ **(E)** and CD69+ divided CD8+ T cells **(F)**. Percentage of IFN-γ+ CD4+ **(G)** and IFN-γ+ CD8+ T cells with or without 10 μg/ml polymyxin B **(H)**. Percentage of CD44+ CD8+ T cells with or without 10 μg/ml polymyxin B **(I)**. Each bar represents the mean from 3 experiments ($N = 3$) ± S.E.M. *Significant differences with $p \leq 0.05$, **$p \leq 0.01$ in relation to untreated control, ‡$p \leq 0.05$, and ‡‡$p \leq 0.01$ calculated in relation to the HSV-2 infected control. ¤$p \leq 0.01$ calculated in relation to the inactivated HSV-2.

We did not observe any significant changes in TNF-α secretion upon stimulation with HSV-2 ($p \geq 0.05$). Exposure to TA-AgNPs-treated HSV-2 caused significantly higher secretion of TNF-α, for all NPs sizes, in comparison to non-stimulated control ($p \leq 0.05$), but it was significantly lower for all tested TA-AgNPs sizes in comparison to HSV-2 infected cells (71.01 ± 7.26 pg/ml for S, 64.18 ± 4.16 for M, and 74.32 ± 574 pg/ml for L TA-AgNPs-HSV-2) ($p \leq 0.01$). On the other hand, stimulation with TA-AuNPs-treated HSV-2 significantly increased secretion of TNF-α at similar levels for all tested sizes ($p \leq 0.01$). The observed increase was higher in TA-AuNPs-HSV-2 than in TA-AgNPs-HSV-2-treated cells. Interleukin 6 was produced during HSV-2 infection (656.45 ± 10.06 pg/ml), although at the level lower than in poly I:C stimulated control cells (8,250.42 ± 886.99 pg/ml) ($p = 0.0000$) (**Figure 10D**). In comparison to HSV-2 infected cells, all TA-AgNPs-HSV-2 preparations decreased IL-6 production ($p \leq 0.01$) to the level observed in the unstimulated control (**Figure 10D**). TA-AuNPs-treated HSV-2 caused strong IL-6 production in comparison to untreated cells ($p \leq 0.01$) (**Figure 10D**). Only S and L TA-AuNP-HSV-2 preparations significantly decreased production of IL-6 in comparison to HSV-2 infected cells ($p \leq 0.05$) (**Figure 10D**).

NPs Enhance the Ability of DCs to Activate Antigen-Specific T Cells *In Vitro*

Development of adaptive immune response depends on the effective antigen presentation by APCs to naïve T cells. Here, we examined the ability of JAWS II exposed to TA-NPs-treated HSV-2 to activate splenic $CD4^+$ and $CD8^+$ T cells isolated from mice challenged with UV-inactivated HSV-2 (**Figure 11**). Treatment of JAWS II cells with untreated HSV-2 and heat inactivated HSV-2 resulted in induction of $CD4^+$ and $CD8^+$ T cells proliferation, with higher induction of CD4+ T cells than CD8+ T cells ($p \leq 0.01$) (**Figures 11A,B**). Significant increase of $CD4^+$ cells was observed if JAWS II were exposed to S and L TA-AgNPs-treated HSV-2 in comparison to HSV-2 infection ($p \leq 0.05$) (**Figure 11A**). M TA-AgNPs-treated HSV-2 induced CD4+ T cells proliferation ($p \leq 0.05$) (**Figure 11A**), albeit only in comparison to uninfected cells. JAWS II stimulated with all TA-AuNPs-treated HSV-2 induced significant proliferation of $CD4^+$ cells in comparison to HSV-2 infected cells ($p \leq 0.05$) (**Figure 11A**).

JAWS II cells exposed to all TA-NPs-HSV induced significantly higher proliferation of $CD8^+$ cells in comparison to HSV-2 infected control ($p \leq 0.05$) (**Figure 11B**). CD69 was used as a marker of early T cell activation in the population of divided cells. Dendritic cells subjected to all TA-NPs-HSV significantly induced expression of CD69 in divided $CD4^+$ and $CD8^+$ T cells in comparison to HSV-2 infected control cells ($p \leq 0.01$) (**Figures 11C–F**). Furthermore, JAWS II cells exposed to all sizes of TA-AgNPs-HSV and L TA-AuNPs induced significantly higher percentages of IFN-γ CD4+ and CD8+ T cells in comparison to HSV-2 infected control or control cells treated with inactivated HSV-2 ($p \leq 0.05$) (**Figures 11G,H**). Also, percentages of memory CD44+ CD8+ T cells in co-cultures with DCs exposed to all NPs-HSV-2 were significantly increased in comparison DCs stimulated with inactivated HSV-2 ($p \leq 0.05$) (**Figure 11I**). However, only treatment of DCs with all sizes of TA-AgNPs-HSV and L TA-AuNPs induced significantly higher percentages of CD44+ CD8+ T cells in comparison to HSV-2 infected control ($p \leq 0.05$) (**Figure 11I**). Treatment with polymyxin B significantly blocked activation of T cells.

DIRECT EFFECT OF NPs AND T CELLS

In our experiments with co-culture of DCs with T cells, the NPs were not present—they were washed out before addition of T cells. However, taking into account possibility of T cells coming into contact with NPs, we checked direct effects of TA-Ag/AuNPs on T cells. For T cells exposed to TA-modified 10 nm, 37 nm, and 59 nm AgNPs, the EC50 values were as follows: 11.22 ± 1.41 μg/ml, 17.85 ± 1.46 μg/ml, and 27.69 ± 4.77 μg/ml, respectively. For exposure of T cells to TA-modified 10 nm, 34 nm, and 62 nm AuNPs, EC50 values were 29.03 ± 2.95 μg/ml, 16.69 ± 0.15 μg/ml and 17.93 ± 0.55 μg/ml, respectively. To access how direct contact with NPs may influence T cell proliferation, we cultured T cells for 72 h with or without concanavalin A in the presence of 2.5 μg/ml TA-Ag/AuNPs and accessed T cell proliferation. Our data show that although all sizes of TA-AgNPs significantly decrease spontaneous proliferation of T cell cultures ($p \leq 0.01$) (**Figure 12A**), only 10 nm TA-AgNPs can significantly decrease proliferation induced by concanavalin A ($p \leq 0.01$) (**Figure 12A**). No significant influence of TA-AuNPs upon spontaneous or concanavalin-induced proliferation was observed (**Figure 12B**).

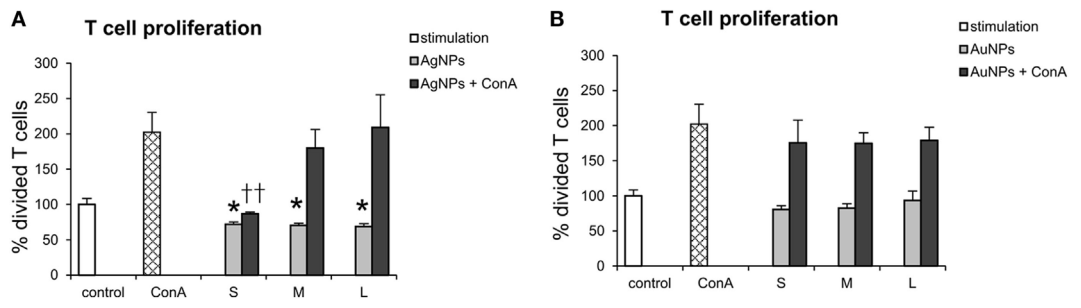

FIGURE 12 | Direct effect of nanoparticles (NPs) on proliferation of T cells. T cell cultures with or without concanavalin A (ConA) were cultured with 2.5 μg/ml of **(A)** 10 nm (S), 37 nm (M), 59 nm (L) TA-AgNPs and **(B)** 10 nm (S), 34 nm (M), 62 nm (L) TA-AuNPs for 72 h. Each bar represents the mean from 3 experiments ($N = 3$) ± S.E.M. *Significant differences with $p \leq 0.01$, ††$p \leq 0.01$ calculated in relation to concanavalin A-treated control.

DISCUSSION

Taking into account an increasing interest in NPs as a new class of microbicides, the aim of this work was to check whether anti-viral activity of TA-AgNPs is followed by an adjuvant and immune-stimulatory effect. Various papers have demonstrated that metal NPs such as silver, gold, and iron oxide enhance the immunogenicity of antigens (9, 13, 20, 29). Therefore, apart from other applications of NPs, they can also be used as immune modulators. The material from which an NP is made as well as size, shape, and surface coating has a direct influence on the functions of APCs (9). Most studies use negatively charged citrate-coated NPs (9, 29), but the higher hydrophobicity of AuNP was shown to activate the innate immune system (TNF-α secretion) (30). Tannins are water-soluble phenol derivatives naturally synthesized and accumulated by higher plants as secondary metabolic products. Tannic acid (penta-m-digalloyl glucose) is the simplest and principal hydrolyzable tannin shown to exert anti-oxidative, anti-inflammatory, and antiviral properties (31, 32). It is known that the polyphenolic nature of tannic acid (hydrophobic core and hydrophilic shell) is the feature responsible for its interaction with cellular surface proteins (33). In our previous work, we showed that TA-AgNPs induced production of cytokines and chemokines by keratinocytes and macrophages (16), but also decreased inflammatory response induced by TNF-α and LPS (17). Additionally, TA-AgNPs directly interact with the surface of HSV-2 leading to a significant decrease in viral titers during both *in vitro* and *in vivo* infections (15). Treatment of the HSV-2 infected mucosal tissue with TA-AgNPs resulted not only in the decreased viral titers (15) but also in higher anti-HSV-2 antibody titers during recovery stage as shown by seroneutralisation tests (unpublished data). For HSV-2, the submucosal DCs present viral antigens to CD4+ T cells in the draining lymph nodes and help to generate the protective immune responses (28). HSV-2 treated in the mucosal tissue with TA-AgNPs may be effectively internalized by migratory DCs and activate them to present and prime CD4+ T cells.

Therefore, we used TA-AgNPs and -AuNPs of similar sizes to compare their immune-stimulatory and adjuvant effects in JAWS II mouse DCs exposed to TA-Ag/AuNPs, but also to NPs-treated HSV-2. This cell line has stable characteristics of DCs and is able to grow at high density without limitations of BMDCs cultures (34).

Gold nanoparticles are inert and non-toxic, while AgNPs are known to release silver ions, which can further influence cellular metabolism (35–39). Both types of NPs can be easily taken up by DCs and other phagocyting cells leading to their activation. As shown previously, toxicity of NPs modified with tannic acid can vary with the cell type, cellular uptake, and size (16, 17). Here, we show that TA-AgNPs and TA-AuNPs also demonstrate material- and size-dependent toxicity against JAWS II cells with AgNPs being more toxic than AuNPs. Similar tendency was observed in HECa10 cells, which showed relatively small toxicity starting from 5 μg/ml, proving TA-NPs > 30 nm safety for the local use such as injections. These results are consistent with previous reports (38, 39) and the data showed for RAW 264.7 mouse monocytic cell line exposed to TA-AuNPs (40). Toxicity of TA-AuNPs was previously observed for concentrations starting from 10 μg/ml (40). Postulated by Park et al. the Trojan-horse mechanism of AgNPs cytotoxicity involves release of silver ions from the surface of NPs in acidified compartments. The released ions induce ROS production triggering activation of immune cells through stress signals and secreted cytokines (i.e., TNF-α) (39). In our study, all TA-AgNPs showed reduced sizes in TEM images in comparison to their initial dimensions, indicating partial decomposition of TA-AgNPs by JAWS II cells and release of silver ions. Interestingly, when compared with the toxicity observed in RAW 264.7 mouse monocyte line exposed to TA-AgNPs, the same NPs demonstrate lower toxicity against DC line and no production of TNF-α (16). This may be due to a lower acidification of compartments occupied by NPs leading to a lower release of silver ions in DCs.

Nanoparticles have been shown to enter the cell via four types of pathways: clathrin/caveolar-mediated endocytosis, phagocytosis, macropinocytosis, and pinocytosis. JAWS II DCs treated with both AgNPs and AuNPs demonstrated activated morphology with numerous microvilli and funnel configured lamellipodia decorated with NPs, characteristic for macropinocytosis and endocytosis (41, 42). Since JAWS II express receptors for negatively charged molecules (i.e., DEC-205) (42) and all tested NPs have negative charge, JAWS II cells utilize receptor-mediated endocytosis for NP internalization, a pathway important for DC activation (41, 42). Furthermore, we found that inhibitor of clathrin-mediated endocytosis blocked uptake of TA-Ag/AuNPs. Clathrin- and caveolin-mediated endocytosis and phagocytosis are believed to be typical pathways for uptake of NPs by actively phagocyting cells such as DCs (43). After 24 h exposure, NPs were localized mainly within electron-dense vacuoles attached to the inner vacuole membrane. Such pattern was also observed by Yen et al., but only for AuNPs (44). Internalization of TA-Ag/AuNPs was also influenced by CChD, an inhibitor of phagocytosis and macropinocytosis. The macropinocytosis pathway is a non-specific process to internalize fluids and particles together into the cell. The phagocytosis pathway is actin-dependent and restricted to professional phagocytes, such as macrophages, DCs, and neutrophils. Phagocytosis is used to internalize particles bigger than 0.5 μm. Most NPs tend to aggregate in biological solutions, increasing their overall size. Thus, we cannot exclude that tannic acid-modified NPs used in this study form aggregates in biological fluids. However, by forming aggregates with viral antigens, tannic acid-modified NPs may help to internalize viral antigens and help to present them to immune competent cells.

Efficient antigen presentation requires presence of the MHC class I or II, but also a second signal from the co-stimulatory molecules (45). Here, JAWS II exposed to non-toxic doses of all tested NPs decreased MHC class I expression and up-regulated MHC class II. The MHC II molecules are essential for the antigen presentation by APC to the naive T cell, which is followed by the activation of the adaptive immune response. Xu et al. (13) showed that non-toxic doses of AgNPs up-regulated MHC II expression on murine macrophages, while in the study by Tomić et al. (46) unmodified AuNPs of 10 and 50 nm had no effect upon CD83, CD86, and MHC II activation and suppressed LPS-induced up-regulation of MHC II, CD83, and CD86. When an NP enters a

biological environment, it comes into contact with a biofluid that contains a diverse mixture of proteins. A subset of these proteins will adsorb to its surface, forming a protein "corona" (47). It is believed that composition of this corona largely defines the biological identity and activity of the particle (47). In this study, we used tannic acid-modified NPs, which can result in different composition of the protein corona and thus different reaction of immune competent cells, in comparison to unmodified AgNPs or AuNPs. Interestingly, stimulation of JAWS II cells with all tested TA-AgNPs increased expression of CD40 and CD86, while only 10 nm AuNPs increased CD86 expression. In contrast, all tested NPs down-regulated expression of CD80. The experiments with endocytosis and phagocytosis inhibitors showed that contact with the surface of tannic acid-modified NPs is important for early down-regulation of MHC I expression but does not lead to early activation of DCs. Internalization of TA-Au/AgNPs is clearly important for further activation of DCs. Therefore, we can hypothesize that later changes in CD40, CD80, CD86, and MHC II expression and activation status is related with the metal type and size and requires NPs internalization. As mentioned above, AgNPs can undergo decomposition in acid cellular compartments and thus influence DCs activation.

The follow-up experiments with BMDCs cultures obtained from C57BL/6 mice generally followed the pattern observed for JAWS II cells (Figure S1 in Supplementary Material). However, we did not detect any differences for CD86 expression and a high distribution of individual results for CD80. This confirms utility of JAWS II cell line for studies of DCs biology.

Previously, we have shown that TA-AgNPs exert a size-dependent inhibition of infection by blockage of HSV-2 attachment and penetration, with small NPs being the most effective (15). JAWS II cells exposed to HSV-2 treated with 10 and 37 nm TA-AgNPs internalized HSV-2 antigens more efficiently than live or inactivated HSV-2. Here, the NPs are modified with tannic acid, which further increases their interaction with proteins and apparently helps to form aggregates with viral proteins, which are further internalized. Furthermore, silver NPs better exposed viral antigens to host receptors than AuNPs of the same size, which suggest the effect of the silver upon antigens internalization. This is in contrast to the paper by Xu et al. reporting that AgNPs did not act as a cargo for the cellular delivery of the antigens to macrophages, and the adjuvant effect of AgNPs was mainly ascribed to the recruitment and activation of local leukocytes (13). Again, AgNPs used by Xu et al. are unmodified NPs (13).

Toll-like receptors belong to the pattern-recognition receptors (PRRs) and are crucial during recognition of pathogens by DCs to trigger adaptive immune response (27, 48). HSV-2 is detected by PRRs through glycoproteins, RNA, and genomic DNA (49). TLR9 is expressed mainly within endosomal compartment and recognizes CpG motifs in viral DNA and it has been demonstrated that it is involved in HSV recognition (49). Response to CpG-DNA recognized by TLR9 leads to up-regulation of MHC class II and CD40, CD80, and CD86 co-stimulatory molecules (27, 48). In this study, elevated levels of TLR9 mRNA were found during stimulation with all TA-AgNPs and 34 nm TA-AuNPs alone. Only TA-AgNPs-treated HSV-2 was able to activate TLR9 expression indicating that AgNPs rather than AuNPs allow for better recognition of viral DNA.

While HSV-2 infection of DCs inhibits their maturation and thus results in a poor development of the specific immune response, inactivated HSV-2 has also been shown to be a poor antigen for immature DCs (19). In our studies, HSV-2 infection of JAWS II mouse DC line resulted in down-regulation of CD40 and MHC class II but not CD86 or CD80, while inactivated HSV-2 had little influence on activation of DCs. As shown in **Figure 9,** both AgNPs and AuNPs can help to present viral antigens through MHC class II, while AgNPs can help to cross-present viral antigens to CD8+ T cells though stimulation of MHC I expression. HSV-2 treated with TA-AgNPs of all sizes and small TA-AuNPs were better stimulants of MHC I expression than bigger TA-AuNPs. MHC class I is present on all nuclear cells presenting self-antigens. However, DCs are able to cross-present captured antigens in the context of MHC class I to CD8+ T-cells, which is of importance for anti-HSV-2 response (49–51). Furthermore, all preparations of HSV-2 treated with NPs up-regulated expression of MHC class II in comparison to cells infected with live or inactivated virus.

Furthermore, NPs can also help to overcome inhibition of DCs maturation by live or inactivated virus due to up-regulation of co-stimulatory molecules, necessary for effective antigen presentation. All NPs-treated HSV-2 retained CD86 expression and down-regulated CD80 expression in comparison to infection with live HSV-2. Down-regulation of CD40 expression in HSV-2 infection of DCs was overcome when HSV-2 was treated with NP sized >30 nm. Ligation of PD-L1 to its receptor PD-1 inhibits activation and expansion of CD8+ T cells, rendering them dysfunctional. Infection of DCs with live HSV-2 leads to an up-regulation of PD-L1 expression, as shown by Krzyzowska et al. (52). Here, PD-L1 expression was conversely related with TA-AgNPs size, while an opposite effect was observed for TA-AuNPs.

Interestingly, TA-AgNPs-treated HSV-2 elicited significantly lower TNF-α inflammatory response as well as decreased IL-6 production in comparison to live HSV-2 (**Figure 10**). Reduced secretion of IL-6 during antigen presentation may lead to development of CD4+ Th2-dependent response which is important during infection of mucous membranes (53). It has been shown that high titers of specific anti-HSV antibodies decrease the risk of recurrent intravaginal infection (54).

Co-culture of HSV-2 infected JAWS II cells with T cells obtained from UV-HSV-2 challenged mice confirmed inhibitory effects of HSV-2 infection on JAWS II maturation. HSV-2 infected DCs showed the lowest ability to stimulate proliferation of antigen-specific T cells in comparison to heat-inactivated HSV-2. In contrast, treatment of HSV-2 with all tested NPs stimulated JAWS II DCs to induction of T cell proliferation. We can therefore conclude that tannic acid NPs-treated HSV-2 help to present viral antigens to antigen-specific memory T cells and effectively activate both CD4+ and CD8+ T cells. Upon T cells activation, CD69 is usually expressed only up-to 48 h, then rapidly down-regulated. However, we still observed up-regulation of CD69 on T cells after 72 h of co-culture with NPs-HSV stimulated JAWS II. These data are in agreement with those obtained by Fazekas De St Groth showing that T cells destined to divide will express CD69 (55). Furthermore, co-cultures of antigen-specific T cells with DCs stimulated with

NPs-treated HSV-2 showed that TA-AgNPs of all sizes and only large TA-AuNPs lead to significant increase in CD4+ IFN-γ+ cells, indicating that TA-NPs can help to stimulate Th1 response. This was followed in this study by a significant increase in CD8+ IFN-γ+ T cells, important for cytotoxic response to virus-infected cells. Additionally, we found that all TA-NPs were better stimulants of memory CD8+ T cells in comparison to inactivated HSV-2, while all AgNPs and only large AuNPs were better stimulants of memoryCD8+ T cell proliferation than live HSV-2. Recent study by Srivastava et al. showed that mobilization of functional protective memory CD8+ T cells within the site of infection protects from acute and recurrent genital herpes infection (56). CD8+ T cell response to HSV infection requires CD4+ T cells and CD40L-CD40 interactions with DCs cells (57). The presence of polymyxin B sulphate influenced induction of CD40 expression on DCs upon TA-NPs-HSV-2 treatment. Since this antibiotic consists of a cyclic heptapeptide tripeptide side chain and a fatty acid tail, it can interact with hydrophobic moieties of tannic acid. However, the exact character of polymyxin B–TA-NPs-HSV-2 interaction is unknown and probably complex.

Interestingly, TA-Ag/AuNPs added directly to T cell cultures, had no effect upon proliferation of activated T cells, except for 10 nm AgNPs. This is in contrast to the results of work by Devanabanda et al., where gold and silver sized 30 and 60 nm significantly affected concanavalin A stimulated responses of murine splenic lymphocytes (58). However, concentrations used in this study were approximately 10 times lower. This indicates that TA-AgNPs or TA-AuNPs do not inhibit activated T cells.

For HSV-2, the pathway to antigen presentation is complex involving multiple types of DCs. The virus first infects LCs, which undergo apoptosis and are taken up by bystander DCs. The migratory DCs carry HSV antigen out of the tissue and are essential for T-cell priming in the lymph node (28). Taking into account the use of TA-AgNPs as microbicides, we can therefore conclude that upon treatment of primary infection, AgNPs-treated HSV-2 may be effectively internalized by migratory DCs, activate them to present and prime CD4+ and CD8+ T cells. During secondary infection, NPs-treated HSV-2 antigens can effectively activate antigen-specific memory T cells.

We found TA-AgNPs as better stimulators of DCs maturation than TA-AuNPs which is probably due to their higher bioactivity. There are also many studies showing that AgNPs directly stimulate the innate immune system (30, 47). Another possibility is that both metals activate different cellular pathways related with antigen presentation and DC activation as shown here for expression of cytokines and TLR9. Furthermore, we also showed for the first time that tannic acid modification of AgNPs indeed helped to internalize antigens.

In summary, increased immunogenicity of NPs-treated HSV-2 may contribute not only to a faster healing of mucous membrane infection after treatment with TA-AgNPs but also for better development of specific immune response which may cause higher resistance to recurrent infection. Since mucous membranes are attractive targets for vaccines and AgNPs or AuNPs are relatively biocompatible, we can speculate that our results may provide data for preliminary studies on nano-metal-based class of nano-adjuvants.

ETHICS STATEMENT

This study was performed in strict accordance with the recommendations of the Polish Act of 21 January 2005 on animal experiments (OJ no. 33, item 289) and Directive 2010/63/EU of the European Parliament and the Council of 22 September 2010 on the protection of animals used for scientific purposes. The protocol was approved by the 4th Local Committee on the Ethics of Animal Experiments in Warsaw, Poland (Permit Number: 51/2013).

AUTHOR CONTRIBUTIONS

PO, MK, GC, and JG contributed conception and design of the study; PO, ET, KR-S, TM, and GC performed lab experiments; MG, OL, and JN performed TEM analysis; GC performed confocal imaging; PO wrote the first draft of the manuscript; ET, KR-S, GC, JG, MK, TM, MG, OL, and GC wrote sections of the manuscript. All the authors have read and approved of the final manuscript.

ACKNOWLEDGMENTS

We would like to thank Miroslaw Sobczak, the Head of Department of Botany at Warsaw University of Life Sciences (SGGW) for valuable tips and support in preparation of the samples for transmission electron microscopy. We would also like to thank Professor Nadzieja Drela and Dr. Ewelina Kiernozek from Institute of Zoology at University of Warsaw for the support during cytometric analysis.

FUNDING

This work was supported by the National Science Centre Poland grant no. DEC- 2012/05/N/NZ6/01757.

SUPPLEMENTARY MATERIAL

The Supplementary Material for this article can be found online at https://www.frontiersin.org/articles/10.3389/fimmu.2018.01115/full#supplementary-material.

REFERENCES

1. Cheng D, Yang J, Zhao Y. Antibacterial materials of silver nanoparticles application in medical appliances and appliances for daily use. *Chin Med Equip J* (2004) 4:26–32.
2. Arvizo R, Bhattacharya R, Mukherjee P. Gold nanoparticles: opportunities and challenges in nanomedicine. *Expert Opin Drug Deliv* (2010) 7:753–63. doi:10.1517/17425241003777010
3. Tolaymat TM, El Badawy AM, Genaidy A, Scheckel KG, Luxton TP, Suidan M. An evidence-based environmental perspective of manufactured silver nanoparticle in syntheses and applications: a systematic review and appraisal of peerreviewed scientific papers. *Sci Total Environ* (2010) 408:999–1006. doi:10.1016/j.scitotenv.2009.11.003
4. Shahverdi RA, Fakhimi A, Shahverdi HR, Minaian S. Synthesis and effect of silver nanoparticles on the antibacterial activity of different antibiotics against

Staphyloccocus aureus and *Escherichia coli*. *Nanomedicine* (2007) 3:168–71. doi:10.1016/j.nano.2007.02.001
5. Wright JB, Lam K, Buret AG, Olson ME, Burrell RE. Early healing events in a porcine model of contaminated wounds: effects of nanocrystalline silver on matrix metalloproteinases, cell apoptosis, and healing. *Wound Repair Regen* (2002) 10:141–51. doi:10.1046/j.1524-475X.2002.10308.x
6. Almeida JP, Lin AY, Langsner RJ, Eckels P, Foster AE, Drezek RA. In vivo immune cell distribution of gold nanoparticles in naive and tumor bearing mice. *Small* (2014) 10:812–9. doi:10.1002/smll.201301998
7. Wilson NS, Young LJ, Kupresanin F, Naik SH, Vremec D, Heath WR, et al. Normal proportion and expression of maturation markers in migratory dendritic cells in the absence of germs or toll-like receptor signaling. *Immunol Cell Biol* (2008) 86:200–5. doi:10.1038/sj.icb.7100125
8. Lutz MB, Schuler G. Immature, semi-mature and fully mature dendritic cells: which signals induce tolerance or immunity? *Trends Immunol* (2002) 23:444–9. doi:10.1016/S1471-4906(02)02281-0
9. Niikura K, Matsunaga T, Suzuki T, Kobayashi S, Yamaguchi H, Orba Y, et al. Gold nanoparticles as a vaccine platform: influence of size and shape on immunological responses in vitro and in vivo. *ACS Nano* (2013) 7:3926–38. doi:10.1021/nn3057005
10. Safari D, Marradi M, Chiodo F, Th Dekker HA, Shan Y, Adamo R, et al. Gold nanoparticles as carriers for a synthetic *Streptococcus pneumoniae* type 14 conjugate vaccine. *Nanomedicine (Lond)* (2012) 7:651–62. doi:10.2217/nnm.11.151
11. Rodriguez-Del Rio E, Marradi M, Calderon-Gonzalez R, Frande-Cabanes E, Penades S, Petrovsky N, et al. A gold glyco-nanoparticle carrying a Listeriolysin O peptide and formulated with advax delta inulin adjuvant induces robust T-cell protection against listeria infection. *Vaccine* (2015) 33:1465–73. doi:10.1016/j.vaccine.2015.01.062
12. Fischer NO, Infante E, Ishikawa T, Blanchette CD, Bourne N, Hoeprich PD, et al. Conjugation to nickel-chelating nanolipoprotein particles increases the potency and efficacy of subunit vaccines to prevent West Nile encephalitis. *Bioconjug Chem* (2010) 21:1018–22. doi:10.1021/bc100083d
13. Xu Y, Tang H, Liu JH, Wang H, Liu Y. Evaluation of the adjuvant effect of silver nanoparticles both in vitro and in vivo. *Toxicol Lett* (2013) 21:42–8. doi:10.1016/j.toxlet.2013.02.010
14. Kang K, Jung H, Lim JS. Cell death by polyvinylpyrrolidine-coated silver nanoparticles is mediated by ROS-dependent signaling. *Biomol Ther (Seoul)* (2012) 20:399–405. doi:10.4062/biomolther.2012.20.4.399
15. Orlowski P, Tomaszewska E, Gniadek M, Baska P, Nowakowska J, Sokolowska J, et al. Tannic acid modified silver nanoparticles show antiviral activity in herpes simplex virus type 2 infection. *PLoS One* (2014) 9(8):e104113. doi:10.1371/journal.pone.0104113
16. Orlowski P, Krzyzowska M, Zdanowski R, Winnicka A, Nowakowska J, Stankiewicz W, et al. Assessment of in vitro cellular responses of monocytes and keratinocytes to tannic acid modified silver nanopartilces. *Toxicol In Vitro* (2013) 27:1798–808. doi:10.1016/j.tiv.2013.05.010
17. Orlowski P, Soliwoda K, Tomaszewska E, Bien K, Fruba A, Gniadek M, et al. Toxicity of tannic acid-modified silver nanoparticles in keratinocytes: potential for immunomodulatory applications. *Toxicol In Vitro* (2016) 35:43–54. doi:10.1016/j.tiv.2016.05.009
18. Steiner I. Human herpes viruses latent infection in the nervous system. *Immunol Rev* (1996) 152:157–73. doi:10.1111/j.1600-065X.1996.tb00915.x
19. Cappel R. Comparison of the humoral and cellular immune responses after immunization with live, UV inactivated herpes simplex virus and a subunit vaccine and efficacy of these immunizations. *Arch Virol* (1976) 52:29–35. doi:10.1007/BF01317862
20. Irvine DJ, Swartz MA, Szeto GL. Engineering synthetic vaccines using cues from natural immunity. *Nat Mater* (2013) 12:978–90. doi:10.1038/nmat3775
21. He Q, Mitchell AR, Johnson SL, Wagner-Bartak C, Morcol T, Bell SJ. Calcium phosphate nanoparticle adjuvant. *Clin Diagn Lab Immunol* (2000) 7:899–903.
22. Lyklema J. Electrokinetics after Smoluchowski. *Colloids Surf A Physicochem Eng Aspects* (2003) 222(1–3):5–14. doi:10.1016/S0927-7757(03)00217-6
23. Livak KJ, Schmittgen TD. Analysis of relative gene expression data using real-time quantitive PCR and the 2(-Delta Delta C(T)) method. *Methods* (2001) 25:402–8. doi:10.1006/meth.2001.1262
24. Zhao S, Fernald SD. Comprehensive algorithm for quantitative real-time polymerase chain reaction. *J Comput Biol* (2005) 12:1045–62. doi:10.1089/cmb.2005.12.1047
25. Ranoszek-Soliwoda K, Tomaszewska E, Socha E, Krzyczmonik P, Ignaczak A, Orlowski P, et al. The role of tannic acid and sodium citrate in the synthesis of silver nanoparticles. *J Nanopart Res* (2017) 19(8):273. doi:10.1007/s11051-017-3973-9
26. Freeman GJ, Long AJ, Iwai Y, Bourque K, Chernova T, Nishimura H, et al. Engagement of the PD-1 immunoinhibitory receptor by a novel B7 family member leads to negative regulation of lymphocyte activation. *J Exp Med* (2000) 192:1027–34. doi:10.1084/jem.192.7.1027
27. Takeda K, Akira S. Toll-like receptors in innate immunity. *Int Immunol* (2015) 109:14.12.1–10. doi:10.1002/0471142735.im1412s109
28. Kim M, Truong NR, James V, Bosnjak L, Sandgren KJ, Harman AN, et al. Relay of herpes simplex virus between Langerhans cells and dermal dendritic cells in human skin. *PLoS Pathog* (2015) 11(4):e1004812. doi:10.1371/journal.ppat.1004812
29. Pusic K, Aguilar Z, Mcloughlin J, Kobuch S, Xu H, Tsang M, et al. Iron oxide nanoparticles as a clinically acceptable delivery platform for a recombinant blood-stage human malaria vaccine. *FASEB J* (2013) 27:1153–66. doi:10.1096/fj.12-218362
30. Moyano DF, Goldsmith M, Solfiell DJ, Landesman-Milo D, Miranda OR, Peer D, et al. Nanoparticle hydrophobicity dictates immune response. *J Am Chem Soc* (2012) 134:3965–7. doi:10.1021/ja2108905
31. Buzzini P, Arapitsas P, Goretti M, Branda E, Turchetti B, Pinelli P, et al. Antimicrobial and antiviral activity of hydrolysable tannins. *Mini Rev Med Chem* (2008) 8:1179–87. doi:10.2174/138955708786140990
32. Karuppagounder V, Arumugam S, Thandavarayan RA, Pitchaimani V, Sreedhar R, Afrin R, et al. Tannic acid modulates NFκB signaling pathway and skin inflammation in NC/Nga mice through PPARγ expression. *Cytokine* (2015) 76:206–13. doi:10.1016/j.cyto.2015.05.016
33. Obreque-Slier E, Mateluna C, Peña-Neira A, López-Solís R. Quantitative determination of interactions between tannic acid and a model protein using diffusion and precipitation assays on cellulose membranes. *J Agric Food Chem* (2010) 58:8375–9. doi:10.1021/jf100631k
34. MacKay VLM, Moore EE. *Immortalized Dendritic Cells*. United States patent 5 648 219. (1997).
35. Niidome T, Yamagata M, Okamoto Y, Akiyama Y, Takashi H, Kawano T, et al. PEG – modified gold nanorods with a stealth character for in vivo applications. *J Control Release* (2006) 114:343–7. doi:10.1016/j.jconrel.2006.06.017
36. Mironava T, Hadjiargyrou M, Simon M, Jurukovski V, Rafailovich MH. Gold nanoparticles cellular toxicity and recovery: effect of size, concentration and exposure time. *Nanotoxicology* (2010) 4:120–37. doi:10.3109/17435390903471463
37. Pernodet N, Fang X, Sun Y, Bakhtina A, Ramakrishnan A, Sokolov J, et al. Adverse effects of citrate/gold nanoparticles on human dermal fibroblasts. *Small* (2006) 6:766–73. doi:10.1002/smll.200500492
38. Johnston HJ, Hutchinson G, Christensen FM, Peters S, Hankin S, Stone V. A review of the in vivo and in vitro toxicity of silver and gold particulates: particle attributes and biological mechanisms responsible for the observed toxicity. *Crit Rev Toxicol* (2010) 40:328–46. doi:10.3109/10408440903453074
39. Park EJ, Yi J, Kim Y, Choi K, Park K. Silver nanoparticles induce cytotoxicity by a Trojan-horse type mechanism. *Toxicol In Vitro* (2010) 24:872–8. doi:10.1016/j.tiv.2009.12.001
40. Krzyzowska M, Tomaszewska E, Ranoszek-Soliwoda K, Bien K, Orlowski P, Celichowski G, et al. Tannic acid modification of metal nanoparticles: possibility for new antiviral applications. In: Andronescu E, Mihai Grumezescu AM, editors. *Nanostructures for Oral Medicine*. New York, USA: Elsevier Inc. (2017). p. 335–63.
41. Verdijk P, van Veelen PA, de Ru AH, Hensbergen PJ, Mizuno K, Koerten HK, et al. Morphological changes during dendritic cell maturation correlate with cofilin activation and translocation to the cell membrane. *Eur J Immunol* (2004) 34:156–64. doi:10.1002/eji.200324241
42. Canton I, Battaglia G. Endocytosis at the nanoscale. *Chem Soc Rev* (2012) 41:2718–39. doi:10.1039/c2cs15309b
43. Wang H, Wu L, Reihard BM. Scavenger receptor mediated endocytosis of silver nanoparticles into J774A.1 macrophages is heterogeneous. *ACS Nano* (2012) 6:7122–32. doi:10.1021/nn302186n

44. Yen HJ, Hsu S, Tsai CL. Cytotoxicity and immunological response of gold and silver nanoparticles of different sizes. *Small* (2009) 5:1553–61. doi:10.1002/smll.200900126
45. Guermonprez P, Valladeau J, Zitvogel L, Thery C, Amigorena S. Antigen presentation and T cell stimulation by dendritic cells. *Annu Rev Immunol* (2001) 20:621–67. doi:10.1146/annurev.immunol.20.100301.064828
46. Tomić S, Dokić J, Vasilijić S, Ogrinc N, Rudolf R, Pelicon R, et al. Size-dependent effects of gold nanoparticles uptake on maturation and antitumor functions of human dendritic cells in vitro. *PLoS One* (2014) 9(5):e96584. doi:10.1371/journal.pone.0096584
47. Cedervall T, Lynch I, Lindman S, Berggård T, Thulin E, Nilsson H, et al. Understanding the nanoparticle-protein corona using methods to quantify exchange rates and affinities of proteins for nanoparticles. *Proc Natl Acad Sci U S A* (2007) 104:2050–5. doi:10.1073/pnas.0608582104
48. Werling D, Jungi TW. Toll-like receptors linking innate and adaptive immune response. *Vet Immunol Immunopathol* (2003) 91:1–12. doi:10.1016/S0165-2427(02)00228-3
49. Paludan SR, Bowie AG, Horan KA, Fitzgerald KA. Recognition of herpesviruses by the immune system. *Nat Rev Immunol* (2011) 11:143–54. doi:10.1038/nri2937
50. Ackerman AL, Cresswell P. Cellular mechanism governing cross-presentation of exogenious antigens. *Nat Immunol* (2004) 5:678–84. doi:10.1038/ni1082
51. Burgdorf S, Scholz C, Kautz A. Spatial and mechanistic separation of cross-presentation and endogenious antigen presentation. *Nat Immunol* (2008) 9:558–66. doi:10.1038/ni.1601
52. Krzyzowska M, Orlowski P, Baska P, Bodera P, Zdanowski R, Stankiewicz W. Role of Fas/FasL signaling in regulation of anti-viral response during HSV-2 vaginal infection in mice. *Immunobiology* (2014) 219:932–43. doi:10.1016/j.imbio.2014.07.021
53. Mayer A, Debuisson D, Denanglaire S, Eddahri F, Fievez L, Hercor M, et al. Antigen presenting cell-derived IL-6 restricts Th2-cell differentiation. *Eur J Immunol* (2014) 44:3252–62. doi:10.1002/eji.201444646
54. Eis-Hubinger AM, Schmidt DS, Schneweis KE. Anti-glycoprotein B monoclonal antibody protects T-cell depleted mice against herpes simplex virus infection by inhibition of virus replication at the inoculated mucous membranes. *J Gen Virol* (1993) 74:379–85. doi:10.1099/0022-1317-74-3-379
55. Fazekas de St Groth B, Smith AL, Higgins CA. T cell activation: in vivo veritas. *Immunol Cell Biol* (2004) 82:260–8. doi:10.1111/j.0818-9641.2004.01243.x
56. Srivastava R, Hernández-Ruiz M, Khan AA, Fouladi MA, Kim GJ, Ly VT, et al. CXCL17 chemokine-dependent mobilization of CXCR8+CD8+ effector memory and tissue-resident memory T cells in the vaginal mucosa is associated with protection against genital herpes. *J Immunol* (2018) 200(8):2915–26. doi:10.4049/jimmunol.1701474
57. Greyer M, Whitney PG, Stock AT, Davey GM, Tebartz C, Bachem A, et al. T Cell help amplifies innate signals in CD8(+) DCs for optimal CD8(+) T cell priming. *Cell Rep* (2016) 14(3):586–97. doi:10.1016/j.celrep.2015.12.058
58. Devanabanda M, Latheef SA, Madduri R. Immunotoxic effects of gold and silver nanoparticles: inhibition of mitogen-induced proliferative responses and viability of human and murine lymphocytes in vitro. *J Immunotoxicol* (2016) 13(6):897–902. doi:10.1080/1547691X.2016.1234522

Conflict of Interest Statement: The authors declare that the research was conducted in the absence of any commercial or financial relationships that could be construed as a potential conflict of interest.

frontiers in Immunology

MINI REVIEW
published: 03 July 2018
doi: 10.3389/fimmu.2018.01534

Therapeutic Prospects of Extracellular Vesicles in Cancer Treatment

*Daria S. Chulpanova[1], Kristina V. Kitaeva[1], Victoria James[2], Albert A. Rizvanov[1] and Valeriya V. Solovyeva[1]**

[1] Institute of Fundamental Medicine and Biology, Kazan Federal University, Kazan, Russia, [2] School of Veterinary Medicine and Science, University of Nottingham, Nottingham, United Kingdom

Extracellular vesicles (EVs) are released by all cells within the tumor microenvironment, such as endothelial cells, tumor-associated fibroblasts, pericytes, and immune system cells. The EVs carry the cargo of parental cells formed of proteins and nucleic acids, which can convey cell-to-cell communication influencing the maintenance and spread of the malignant neoplasm, for example, promoting angiogenesis, tumor cell invasion, and immune escape. However, EVs can also suppress tumor progression, either by the direct influence of the protein and nucleic acid cargo of the EVs or *via* antigen presentation to immune cells as tumor-derived EVs carry on their surface some of the same antigens as the donor cells. Moreover, dendritic cell-derived EVs carry major histocompatibility complex class I and class II/peptide complexes and are able to prime other immune system cell types and activate an antitumor immune response. Given the relative longevity of vesicles within the circulation and their ability to cross blood–brain barriers, modification of these unique organelles offers the potential to create new biological-tools for cancer therapy. This review examines how modification of the EV cargo has the potential to target specific tumor mechanisms responsible for tumor formation and progression to develop new therapeutic strategies and to increase the efficacy of antitumor therapies.

Keywords: extracellular vesicles, tumor microenvironment, tumor cells, immune cells, stromal cells, vaccination, cancer therapy

OPEN ACCESS

Edited by:
Martin Herrmann, Universitätsklinikum Erlangen, Germany

Reviewed by:
Silvano Sozzani, University of Brescia, Italy
Dalil Hannani, UMR5525 Techniques de l'Ingénierie Médicale et de la Complexité Informatique, Mathématiques et Applications, Grenoble (TIMC-IMAG), France
Giovanna Schiavoni, Istituto Superiore di Sanità, Italy

****Correspondence:***
Valeriya V. Solovyeva
solovyovavv@gmail.com

Specialty section:
This article was submitted to Molecular Innate Immunity, a section of the journal Frontiers in Immunology

Received: *23 March 2018*
Accepted: *21 June 2018*
Published: *03 July 2018*

Citation:
Chulpanova DS, Kitaeva KV, James V, Rizvanov AA and Solovyeva VV (2018) Therapeutic Prospects of Extracellular Vesicles in Cancer Treatment. Front. Immunol. 9:1534. doi: 10.3389/fimmu.2018.01534

INTRODUCTION

Extracellular vesicles (EVs) are of particular interest due to their ability to mediate intercellular communication, influencing multiple cellular processes. EVs can be categorized based upon their biogenesis and divided into exosomes, microvesicles (MVs), and apoptotic bodies (ABs) (1, 2). Exosomes are small vesicles 40–100 nm in diameter, formed as part of the endocytic pathway. Exosomes carry the donor cell cargo, represented by various proteins and nucleic acids [DNA, mRNA, miRNA, and other non-coding RNAs (ncRNAs)] (**Figure 1C**) (3, 4). Exosomes are stable in biological fluids and small enough to pass through the blood–brain barrier (5). MVs have a diameter of 100–1,000 nm and are released by directly budding from the plasma membrane (6). MVs also carry cargos of proteins and nucleic acids, although their functional roles in cell-to-cell communication remains less well studied than the exosome population (7). In contrast to exosomes and MVs, which are formed continuously by cells, ABs are formed as part of the fragmentation process of cells undergoing apoptosis, the process of programmed cell death (1) (**Figure 1A**).

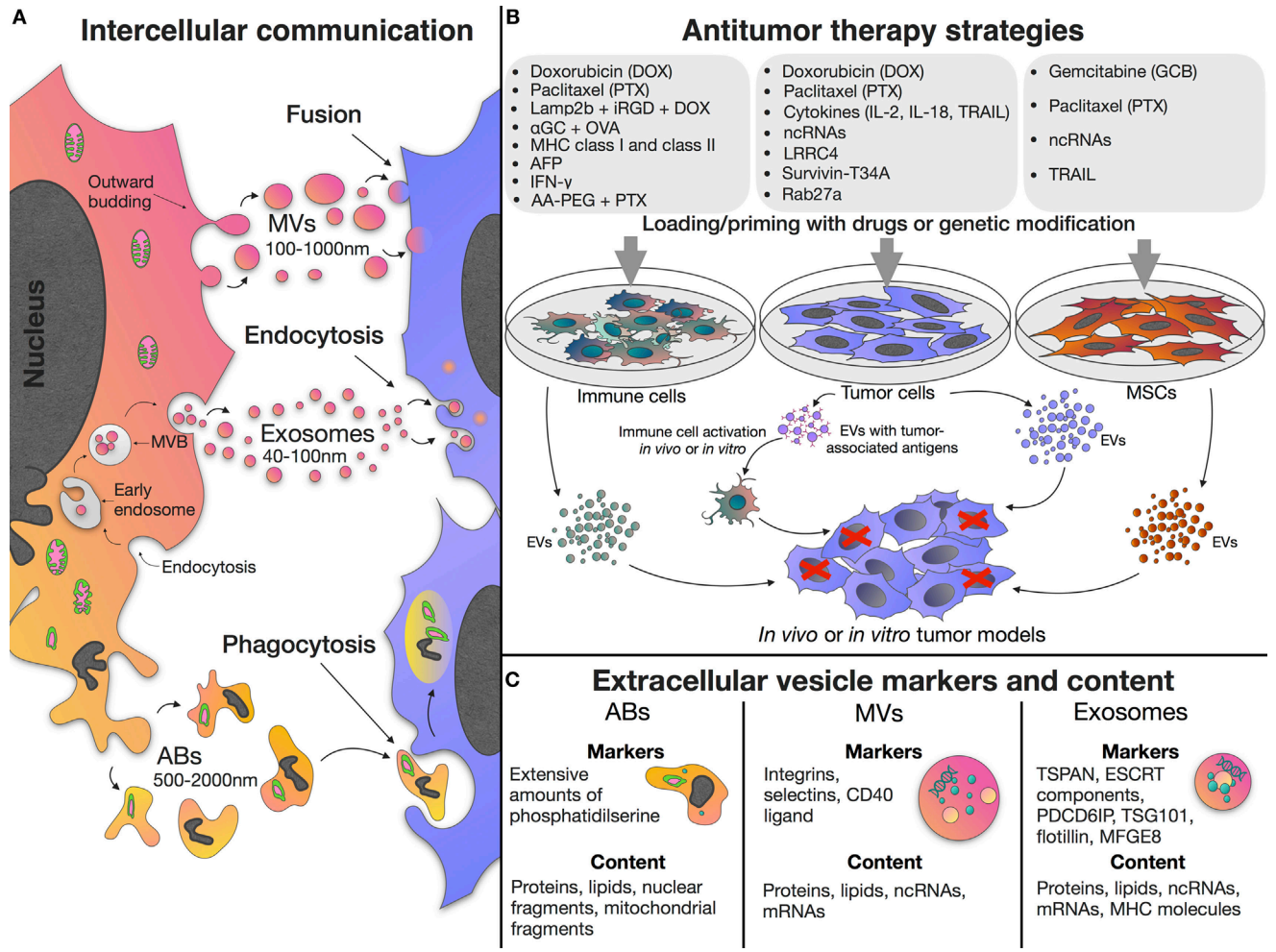

FIGURE 1 | Extracellular vesicle (EV) properties and application in antitumor treatment. **(A)** EVs can be classified based upon their biogenesis and are divided into exosomes, microvesicles (MVs), and apoptotic bodies (ABs). Exosomes are formed as part of the endocytic pathway by inward budding of endosomal membranes, resulting in accumulation of early endosomes and formation of large multivesicular bodies (MVBs) which release their contents (exosomes) into the extracellular space. MVs are released by directly budding from the plasma membrane. ABs are formed as part of the fragmentation process of cells undergoing apoptosis. **(B)** EVs derived from native or primed/genetically modified cells can be used in antitumor treatment. **(C)** Different types of EVs contain various proteins, lipids, and nucleic acids and have specific membrane markers. Exosomes have tetraspanin (such as TSPAN29 or TSPAN30), endosomal sorting complex required for transport (ESCRT) components, milk fat globule-EGF factor 8 protein (MFGE8), programmed cell death 6 interacting protein (PDCD6IP), tumor susceptibility gene 101 protein (TSG101), and flotillin molecules on their surface. Exosome content include mRNAs, microRNAs, and other non-coding RNAs (ncRNAs), cytoplasmic and membrane proteins including receptors and major histocompatibility complex (MHC) molecules. MVs carry integrins, selectins, and CD40 ligand on their surface, and also contain mRNAs, microRNAs, ncRNAs, cytoplasmic and membrane proteins. ABs have extensive amounts of phosphatidylserine and contain various parts of the apoptotic cell such as proteins, lipids, nuclear fragments, and cell organelles. Cargo and biogenesis of EVs have been comprehensively discussed elsewhere (8, 9).

The tumor microenvironment is often a very complex and dynamic niche containing not only neoplastic cells but also a multitude of non-malignant stromal cells such as endothelial cells, tumor-associated fibroblasts, pericytes, and immune cells (10). In addition to stromal cells, the extracellular matrix and surrounding tumor adipose tissue also make an important contribution to tumor progression as they contain adipocytes and progenitor cells [preadipocytes and mesenchymal stem cells (MSCs)] (10, 11), as well as a variety of soluble cytokines, growth factors, and metabolites produced the stromal cells within the tumor microenvironment (10, 12). As EVs are believed to mediate cell-to-cell communication in the tumor microenvironment and induce phenotypic modification in recipient cells, there is a growing interest in the potential role of EVs as key mediators of tumor progression and the spread of malignant neoplasm (13–16). Since EV functions are related to the donor cell type and the imparted cargo of proteins and nucleic acids, EVs of different origins exhibit different features. However, as these have been comprehensively discussed elsewhere (17), this review focuses on the use and efficacy of EVs as antitumor therapies. For instance, as a result of the unique properties of MSCs, the EVs produced by stem cells retain the ability to migrate toward tumor niches (18), they also posses the same low immunogenicity of the donor MSCs (19). Therefore, the use of MSC-derived EVs as non-cell

structures, in place of MSCs themselves, allows the avoidance of the risk of unlimited cell growth, undesirable transformation, and potential tumor formation (20). The ability to act as multi-signal messengers makes EVs a prospective new class of therapeutic agents to modulate the processes occurring in the tumor microenvironment (21) (**Figure 1B**).

TUMOR CELL-DERIVED EVs

Intercellular EV-mediated signaling by tumor cells has been linked with maintain angiogenesis, invasion, immune escape (22) and to develop an aggressive phenotype and chemo- and radiotherapy resistance (16, 23–25). The extent of the contribution of EVs in tumor maintenance has been demonstrated through the study of EV inhibition, following which malignancy is suppressed and cancer cells show enhanced sensitivity to proton-pump inhibitor (omeprazole) and cisplatin (26, 27). As EV traffic is regulated by an acidic microenvironment, a common feature of all solid tumors, altering intracellular pH is an effective means of modulating exosome release. Changes in intracellular pH alters the lipid composition of the cells membrane and subsequently modulates both exosome release and fusion/uptake (28). In addition, the lower extracellular pH can promote tumor resistance to cytotoxic drugs through neutralization of those antitumor drugs that are weak bases or isolating drugs in acidic vesicles and/or eliminating them through an exocytotic pathway (29).

Extracellular vesicles may also promote tumor progression through the transfer of their specific cargos, for example, during the formation of a pre-metastatic niche (PMN), where the transfer of EV-cargos to stromal cells, induce molecular and cellular changes that promote PMN development (30, 31). For example, the tumor exosomal transport of miR-494 and miR-542p to stromal cells and lung fibroblasts leads to cadherin-17 downregulation and matrix metalloproteinase upregulation (30), while proangiogenic RNAs contained within MVs trigger angiogenesis to promote PMN formation (32).

The ability of tumor cell-derived EVs to fuse with recipient cells through endocytosis and release their cargo into the recipient cell cytoplasm makes EVs a promising biological vector for targeted delivery of various antitumor agents (33). This is exemplified by the use of EVs derived from LNCaP and PC-3 prostate cancer cell lines modified to transport paclitaxel (PTX) into recipient cells through the endocytic pathway, significantly increasing PTX cytotoxicity *in vitro* (33). Furthermore, U-87 MG (brain neuronal glioblastoma–astrocytoma) derived EVs primed with doxorubicin (DOX) or PTX significantly decreased the viability of recipient U-87 MG cells by 70 and 50%, respectively, at the highest tested concentration of exosomes (200 μg/mL) *in vitro* (34).

Tumor-derived EVs can be used for therapeutic drug delivery to reduce systemic toxicity by targeting the tumor microenvironment. It was shown that *in vitro* and *in vivo*, doxorubicin-loaded exosomes (exoDOX) derived from MDA-MB-231 (breast adenocarcinoma) and HCT-116 (colorectal carcinoma) cell lines did not reduce DOX efficacy. Simultaneously, exoDOX treated nude mice did not show the cardiotoxicity observed in their free-DOX-treated counterparts. Mass spectrometry confirmed that DOX accumulation in the heart was reduced by approximately 40% when DOX was delivered *via* exosomes (exoDOX) (35). The reduced cardiotoxicity achieved when delivering DOX *via* modified exosomes would allow for a higher concentration of exoDOX to be used, thus offering the potential to increase DOX efficacy. Similar findings have also been reported for *in vivo* models of breast (MDA-MB-231) and ovarian (STOSE) cancer (36).

Tumor cell-derived EVs carry on their surface the same antigens as the cell that produced them (the donor cell), such as HER2/*neu*, melan-A, Silv, carcinoembryonic antigen (CEA), mesothelin, and others (37). Thus, they can act to prime immune cells by antigen presentation. The delivery of dendritic cells (DCs) *in vitro* primed with exosomes isolated from the mesothelioma cell line AB1 within a BALB/c mouse mesothelioma model, resulted in increased mean and overall survival times *in vivo* (38). Similarly, DCs primed with exosomes isolated from rat glioblastoma cells, induced a strong antitumor response and significantly increased median survival times in glioblastoma-bearing rats when used in combination with α-galactosylceramide (39).

The efficacy of priming immune cells can be improved by combining their use with immune cell stimulating drugs. For instance, exosomes derived from the pancreatic cancer cell line UNKC6141 were co-delivered with DCs (DCs/Exo) to UNKC16141 xenograft mice. Tumor onset was delayed in these animals and subsequently a significant increase in survival was observed. When the same assay was repeated, but with the inclusion of all-transretinoic acid (ATRA) alongside the delivery of DCs/Exo, increased lymphocyte proliferation within lymph nodes was reported which coincided with increased cytotoxic T-cell activity in comparison with untreated or DCs/Exo only treated animals. However, the inclusion of ATRA had no further effect on prolonging survival and only modest changes in metastasis to distant organs were observed. The combination of DCs/Exo with sunitinib in these animal models also led to an increase in cytotoxic activity which in these assays did lead to significantly prolonged survival times in DCs/Exo/sunitinib compared to animals treated only with free sunitinib therapy. Similar increases in survival time and a reduction in metastatic spread was also observed when DCs/Exo use was combined with gemcitabine treatment (40).

To increase the therapeutic potential and immunogenicity of EV-based tumor vaccines, tumor cells producing the EVs can be modified to express specific cytokine/chemokine genes that have an immunomodulating effect. Dai et al. reported that exosomes derived from LS-174T cells genetically modified to express IL-18 CEA (Exo/IL-18), had a more pronounced effect on specific antitumor immunity when compared with exosomes from native LS-174T cells. Exo/IL-18 promoted proliferation of peripheral blood mononuclear cells and induced cytokine secretion by T-lymphocytes and DC *in vitro*, as well as inducing the phenotypic and functional maturation of DCs (41). Similar results were obtained by Yang et al. using *in vivo* experiments, whereby exosomes were derived from IL-2-modified ovalbumin (OVA)-expressing EL-4 lymphoma cells (Exo/IL-2). Vaccination of C57BL/C mice with Exo/IL-2 more effectively inhibited tumor growth (42).

The modification of tumor cells through the aberrant expression of tumor suppressor genes, apoptosis inductors, and ncRNAs has also been shown to impart a potential therapeutic benefit to the resulting EVs. YUSAC 2 melanoma cells were engineered

to overexpress a dominant-negative mutant form of Survivin (Survivin-T34A). Exosomes derived from Survivin-T34A-modified YUSAC 2 cells, in combination with gemcitabine, significantly increased apoptosis in pancreatic adenocarcinoma MIA PaCa-2 cells in comparison with gemcitabine alone (43). Rivoltini et al. showed that exosomes derived from K562 leukemia cells modified with TNF-related apoptosis-inducing ligand (TRAIL) [TRAIL(+) exosomes], induced apoptosis in TRAIL-death receptor (DR)5(+) SUDHL4 lymphoma and INT12 melanoma cells *in vitro*. In *in vivo* experiments of TRAIL(+) exosomes demonstrated homing of the exosomes to the tumor sites and significant suppression of tumor growth by 58% in SUDHL4-B-cell lymphoma bearing mice (44). Li et al. investigated exosomes derived from glioblastoma multiforme (GBM) cells with overexpression of the tumor suppressor gene LRRC4 (Exo/LRRC4). Exo/LRRC4 induced significant chemotaxis and expansion of $CD4^+CCR4^+$ T cells, inhibited the proportion of Ti-Treg cells, and promoted Ti-Teff cell expansion through cytokines release *in vitro* (45).

The Rab GTPases control many stages of membrane trafficking, including the formation and release of vesicles. Ostrowski et al. identified Rab GTPases Rab2b, Rab9a, Rab5a, Rab27a, and Rab27b that promote exosome secretion in HeLa cells (46), indicating the possibility of manipulating the secretion of Rab proteins to control exosome production. Exosomes, derived from Rab27a-overexpressing A549 cells (exo/Rab27a), exhibited the ability to regulate major histocompatibility complex (MHC) class II molecules and co-stimulatory molecules CD80 and CD86 on DCs. Furthermore, DCs primed with exosomes derived from Rab27-overexpressing A549 cells significantly increased $CD4^+$ T cell proliferation *in vitro*. *In vivo* immunization with exo/Rab27a inhibited tumor growth in a tumor mouse model (47).

At present ncRNAs are actively being studied as potential antitumor agents. However, when developing miRNA-based therapies there are problems with specific targeting of tumor cells and target cells within the tumor microenvironment. Tumor-derived EVs can be used for delivering a variety of potentially therapeutic ncRNAs, for instance miR-134 (48), miR-29a, and miR-29c microRNAs (49), as well as short interfering RNAs (siRNAs) (50) (**Table 1**).

IMMUNE CELL-DERIVED EVs

Exosomes from immature dendritic cells (imDCs) can be used to deliver chemotherapeutic agents such as DOX. For instance, imDCs were modified to express lysosome-associated membrane protein 2 (Lamp2b) fused to the αv-integrin-specific iRGD peptide. It was shown that modified imDC-derived exosomes (Exo/iRGD) loaded with DOX, effectively targeted and delivered DOX to $\alpha v\text{-integrin}^+$ MDA-MB-231 breast cancer cells *in vitro*. Exo/iRGD intravenous injection in BALB/c mice led to inhibition of breast tumor cell growth without any apparent toxic effects (52).

A new approach for cancer immunotherapy is the combination of exosomes and the invariant NKT immune cell ligand α-galactosylceramide (αGC) (53). Loaded with αGC and OVA-model antigen exosomes induced potent NK and γδ T-cell innate immune responses *in vitro* and *in vivo*. In an OVA-expressing mouse model of melanoma treatment of tumor-bearing mice with αGC/OVA-loaded exosomes decreased tumor growth, increased antigen-specific $CD8^+$ T-cell tumor infiltration, and increased median survival, relative to control mice immunized with soluble αGC + OVA alone (53). Similarly, exosomes derived from α-fetoprotein (AFP)-expressing DCs (DEXAFP) intravenously injected into hepatocarcinoma-bearing C57BL6 mice prolonged survival to 57 days in 100% of DEXAFP-treated mice (55).

Without modification, DC-derived exosomes alone carry MHC class I and class II/peptide complexes capable of leading to the priming of $CD8^+$ and $CD4^+$ T cells, respectively, and subsequent T cell-dependent tumor rejection (13, 54). DC-derived exosomes have also been reported to trigger NK cell proliferation and activation *in vitro* and in patients, by trans-presentation of IL-15 by IL-15Rα. This mechanism of action was shown to significantly reduce the number of lung metastases *in vivo*. Combination of DC-derived exosomes with IL-15Rα and rhIL-15 molecules led to NK cell proliferation and activation and significantly enhanced IFNγ secretion by NK cells *in vitro* (54).

Phase I clinical trials have demonstrated the safety of using DC-derived exosomes in patients with metastatic melanoma (69) and lung cancer (70). Phase II trials in non-small cell carcinoma patients using modified IFN-γ expressing DCs to produce exosomes have reported an increase in NKp30-dependent NK cell functions, and 32% of participants experienced stabilization for more than 4 months (56).

In addition to DCs, macrophages have also been studied as a source of EVs of potential therapeutic benefit. Derived from RAW 264.7 macrophages, vesicles loaded with PTX (exoPTX) were reported to significantly increase drug cytotoxicity (more than 50 times) in multidrug resistance (MDR) MDCKMDR1, MDCKwt, and 3LL-M27 cells *in vitro*. Furthermore, when delivered into the airway of mice modeling Lewis lung carcinoma pulmonary metastases, exoPTX were found to have a potent anticancer effect (57). For PTX targeted delivery macrophages can be modified with aminoethylanisamide-polyethylene glycol (AA-PEG) a vector moiety to target the σ-receptor which is overexpressed by lung cancer cells (58). Jang et al. developed a bioinspired exosome-mimetic nanovesicles that can be modified to deliver DOX, gemcitabine, or carboplatin to the tumor tissue after systemic administration. Chemotherapeutic-loaded nanovesicles, derived from monocytes or macrophages, induced TNF-α-stimulated endothelial cell (HUVECs) death in a dose-dependent manner *in vitro*. DOX-loaded nanovesicles increased apoptosis and reduced the number of proliferating cells in CT26 colorectal cancer murine models (59) (**Table 1**).

MSC-DERIVED EVs

Extracellular vesicles released from MSCs have been reported to exhibit variable effects on tumor growth, indicating the influence of EVs is dependent on cargo and the donor cell type (71, 72). Delivered by MSC-derived exosomes molecules of different types of RNA can induce adipogenesis, angiogenesis, apoptosis, and proteolysis in recipient cells (15). Exosomes from gastric cancer-derived MSCs were found to deliver miR-221 to HGC-27 gastric cancer cells, promoting their proliferation and migration *in vitro* (73). Other biomolecules carried by exosomes such as oncogenic proteins, cytokines, adhesion molecules, and anti-apoptotic

TABLE 1 | The use of extracellular vesicles (EVs) with or without modified cargo for antitumor therapy.

Vesicle source	Vesicle type	Purification strategy	Cargo	Mechanism of action	Model	Reference
Cancer cells						
Glioblastoma–astrocytoma U-87 MG cells	Exosomes	Exosome isolation reagent (Invitrogen)	DOX or PTX	Cell viability decrease	*In vitro* U-87 MG cell culture	(34)
LNCaP and PC-3 prostate cancer cells	Exosomes and microvesicles	Differential centrifugation	PTX	PTX cytotoxic effect increase	*In vitro* PC-3 and LNCaP cell culture	(33)
MDA-MB-231 and HCT-116 cell lines	Exosomes	ExoQuick-TC™ solution (System BioSciences)	DOX	Cardio toxicity decrease, DOX efficacy increase	MDA-MB-231 cell mice model *in vivo*	(35)
MDA-MB-231 and STOSE cell lines	Exosomes	AB cell culture-nanovesicles solution (AB ANALITICA)	DOX		Breast MDA-MB-231 and ovarian STOSE mouse tumors *in vivo*	(36)
Oral cancer cells	Exosomes	Ultrafiltration and affinity chromatography	Tumor-associated antigens	NK cell proliferation and NK cell cytotoxicity increase	*In vitro* NK cell culture	(51)
Mouse malignant mesothelioma (MM) AB1 cells	Exosomes	Stepwise ultracentrifugation	Tumor-associated antigens	Exosome-loaded dendritic cell (DC) increased median and overall survival	AB1 tumor BALB/c mice model *in vivo*	(38)
Rat glioblastoma	Exosomes	ExoRNeasy Serum/Plasma Maxi Kit (Qiagen)	Tumor-associated antigens + α-galactosylceramide	Exosomes pulsed DCs increased median survival time	Glioblastoma-bearing rat model *in vivo*	(39)
UNKC6141 (pancreatic cancer) cells	Exosomes	Sucrose gradients ultracentrifugation	Tumor-associated antigens	Exosome-loaded DCs delayed tumor onset and increased survival time	UNKC6141-bearing mice	(40)
				DCs/Exo + all-transretinoic acid increased proliferation of lymph node cells and cytotoxic T cell activity		
				DCs/Exo and sunitinib prolonged survival time		
				DCs/Exo + gemcitabine prolonged survival time		
Carcinoembryonic antigen (CEA)-expressing LS-174T tumor cells	Exosomes	Sucrose gradients ultracentrifugation	IL-18	Maturation of DCs and induction of CEA-specific $CD8^+$ CTL	DCs and CTL cells *in vitro*	(41)
OVA-expressing EL-4 lymphoma cells	Exosomes	Sucrose gradients ultracentrifugation	IL-2	Immune response induction and tumor growth inhibition	C57BL/C mice model *in vivo*	(42)
YUSAC 2 melanoma cells	Exosomes	Sucrose gradients ultracentrifugation	Survivin-T34A (Survivin blocking protein)	Caspase activation and apoptosis induction	Pancreatic cancer cells *in vitro*	(43)
K562 leukemia cells	Exosomes	Differential centrifugation	TNF-related apoptosis-inducing ligand (TRAIL)	TRAIL-related apoptosis induction	SUDHL4 lymphoma and INT12 melanoma cells *in vitro*	(44)
				Tumor growth inhibition	SUDHL4-bearing mice	
A549 cells	Exosomes	Differential centrifugation	Rab27a	Maturation of major histocompatibility complex (MHC) class II molecules, CD80 and CD86. Inhibition of tumor growth	DCs *in vitro*, BALB/c mice model *in vivo*	(47)

(*Continued*)

TABLE 1 | Continued

Vesicle source	Vesicle type	Purification strategy	Cargo	Mechanism of action	Model	Reference
Glioblastoma multiforme (GBM) cells	Exosomes	Differential centrifugation	LRRC4	Chemotaxis and expansion of $CD4^+$ $CCR4^+$ T cells	GBM cells *in vitro*	(45)
Hs578T and Hs578Ts(i)8 cells	Exosomes	Filtration and ultracentrifugation	miR-134	Cellular migration and invasion reduction, drugs sensitivity enhancement	Hs578Ts(i)8 cells *in vitro*	(48)
SGC7901 cells	Microvesicles	Differential centrifugation	miR-29a and miR-29c	Angiogenesis and tumor growth suppression	Implanted with SGC7901 cells BALB/c mice *in vivo*	(49)
HeLa and HT1080 cells	Exosomes	Differential centrifugations and micro-filtration	Short interfering RNAs (siRNAs) against RAD51 and RAD52	Accumulation of the cells in S and G2/M phases of cell cycle and recipient cell death induction	HeLa cells *in vitro*	(50)
Immune cells						
DCs	Exosomes	Sucrose gradients ultracentrifugation	Lamp2b + iRGD + DOX	Tumor growth inhibition	MDA-MB-231 injected BALB/c nude mice model *in vivo*	(52)
DCs	Exosomes	Differential centrifugation	αGC + OVA	NK and γδ T-cell immune responses induction	Invariant NKT cells *in vitro*	(53)
				Tumor growth decrease	B16/OVA melanoma tumor model *in vivo*	
DCs	Exosomes	Ultrafiltration/diafiltration and sucrose gradients ultracentrifugation	MHC class I and class II	NK cell proliferation and activation, IFNγ secretion enhancement	NK cells *in vitro*	(54)
			MHC class I and class II	NK cell proliferation and activation by trans-presentation of IL-15 by IL-15Rα, number of metastases reduction	Mouse model *in vivo*	
DCs	Exosomes	Differential centrifugation	AFP	Survival rate prolongation	Tumor-bearing C57BL6 mice model *in vivo*	(55)
DCs	Exosomes	Ultrafiltration/diafiltration and sucrose gradients ultracentrifugation	IFN-γ	NKp30-dependent NK cell function enhancement	Advanced non-small cell lung cancer patients	(56)
RAW 264.7 macrophages	Exosomes	ExoQuick-TC™ solution (System BioSciences)	PTX	Drug cytotoxicity increase, inhibition of metastases growth	Resistant multidrug resistance cell culture *in vitro*, Lewis lung carcinoma mouse model *in vivo*	(57)
			AA-PEG + PTX	Suppression of metastases growth and survival time increase	*In vivo* C57BL/6 mice lung cancer model	(58)
Monocytes or macrophages	Exosome-mimetic nanovesicles	Iodixanol gradients ultracentrifugation	DOX	Apoptosis increase and number of proliferating cells reduction	*In vivo* model of mouse CT26 colorectal cancer	(59)
Mesenchymal stem cells (MSCs)						
MSCs	Exosomes	Differential centrifugation	Anti-miR-9	Temozolomide sensitivity increase	Temozolomide-resistant GBM cell culture *in vitro*	(60)

(*Continued*)

TABLE 1 | Continued

Vesicle source	Vesicle type	Purification strategy	Cargo	Mechanism of action	Model	Reference
MSCs	Exosomes	ExoQuick-TC™ solution (System BioSciences)	miR-146b	Tumor growth reduction	*In vivo* rat model of primary brain tumor	(61)
MSCs	Exosomes	Sucrose gradients ultracentrifugation	miR-124a	Viability and clonogenicity reduction	Glioma stem cell lines *in vitro*	(62)
				Prolonged survival rate	*In vivo* model of mouse GSC267 glioma	
Bone marrow MSCs (BM-MSCs)	Exosomes	ExoQuick-TC™ solution (System BioSciences)	miR-340	Tumor angiogenesis inhibition *via* the HGF/c-MET signaling pathway	Endothelial cell culture *in vitro*	(63)
MSCs	Exosomes	Differential centrifugation	Polo-like kinase 1 (PLK-1) siRNA	Cancer cell proliferation reduction by PLK-1 gene silencing	Bladder cancer cells *in vitro*	(64)
MSCs	Exosomes	ExoQuick-TC™ solution (System BioSciences)	miR-122	Antitumor efficacy of sorafenib increase	Hepatocellular carcinoma model *in vivo*	(65)
BM-MSCs	Microvesicles	Differential centrifugation	PTX	Tumor growth inhibition	Human pancreatic adenocarcinoma CFPAC-1 cells *in vitro*	(66)
MSCs	Microvesicles	Differential centrifugation	PTX or GCB	Tumor proliferation inhibition	Pancreatic cancer cells *in vitro*	(67)
MSCs	Exosomes	Sequential ultracentrifugation combined with 0.22 μm ultrafiltration	TRAIL	Apoptosis induction	M231 breast cancer cells and other cancer cell lines *in vitro*	(68)

proteins can also promote tumor progression (74–76), as well as increase tumor resistance to chemotherapy drugs (77).

Exosomes from bone marrow MSCs (BM-MSCs) can transfer miRNAs from the BM, particularly miR-23b, which promote dormancy in bone marrow-metastatic human breast cancer through the suppression of a target gene, MARCKS *in vivo* (78). In support of this, Lee et al. showed that MSC-derived exosomes can suppress human breast cancer angiogenesis by downregulating the expression of VEGF in tumor cells *in vitro* and *in vivo* (79).

In addition to the endogenous effects of MSC-EVs, MSC-derived MVs can be used as delivery vehicles for a variety of potential therapeutic agents, in particular ncRNAs. For example, injection of exosomes derived from miR-146-expressing MSCs into xenograft gliomas in primary brain tumor rat models cause a significant reduction in tumor growth (61). Treatment with MSC-derived exosomes containing miR-124a reduce the viability and clonogenicity of glioma stem cell lines *in vitro* and increase the survival rate in glioma mouse models up to 50% by silencing FOXA2 (62), while the loading of MSC exosomes with miR-143 acts to significantly reduce the migration of 143B osteosarcoma cells (80). Transfection of bone marrow stromal cells with miR-340 generates exosomes capable of inhibiting tumor angiogenesis *via* the HGF/c-MET signaling pathway in endothelial cells (63). MSC-derived EVs can also be used to alter the chemosensitivity of tumor cells. Delivery of anti-miR-9 to temozolomide-resistant GBM cells increases cell sensitivity to this drug (60). The sensitivity of hepatocellular carcinoma cells to chemotherapeutic agents (5-fluorouracil and sorafenib) can similarly be altered through the use of miR-122 loaded MSC exosomes *in vivo* (65). MSC-derived MVs can also be loaded with various siRNAs that target key genes driving tumorigenesis, for example, MSC exosomes carrying siRNAs against polo-like kinase 1 significantly reduce bladder cancer cell proliferation *in vitro* (64).

In addition to biomolecules, MSC-derived vesicles can be loaded with chemotherapeutic drugs. BM-MSC-derived MVs primed with high-dose PTX inhibited cell growth by 50% in human CFPAC-1 pancreatic adenocarcinoma cells *in vitro* (66). This finding was supported by the recent studies of Cocce et al., which showed antitumor activity of MSCs MVs loaded with PTX or gemcitabine (GCB) on pancreatic cancer cells *in vitro* (67).

Recent studies have also highlighted the potential to deliver TRAIL by MSC-EVs (MSCT). MSCT-EVs induced apoptosis in 11 cancer cell lines in a dose-dependent manner but showed no cytotoxicity in human bronchial epithelial cells *in vitro*. Interestingly TRAIL-primed EVs that contain 3.88 ng TRAIL/mL induced significantly more apoptosis in M231 breast cancer cells compared with 100 ng/mL of recombinant TRAIL. TRAIL delivery by MSC-EVs induced significant apoptosis in TRAIL resistant A549 lung adenocarcinoma cells in a dose-dependent manner *in vitro* (68) (**Table 1**).

CONCLUSION

Extracellular vesicles, which include groups of differing origins such as exosomes and MVs, are released by all cells within the tumor microenvironment during normal cellular activity. EVs carry variable cargos that reflect the composition of the donor

cells, these cargos can be transferred to neighboring cells and thus affect the processes occurring in those recipient cells and subsequently the tumor microenvironment as a whole. In addition to their endogenous ability to influence tumor progression, the ability to modify the EV content makes them a promising tool for cancer therapy. Surface antigens of tumor cell-derived vesicles can be used for immune cell priming. They can also be modified with various agents to directly affect tumor cells or modulate antitumor immunity. Genetic modifications can also be performed on MSC-derived vesicles, the main advantage of which is targeted cargo delivery to the tumor microenvironment. From priming the immune response to delivering ncRNAs and antitumor drugs, EVs provide a unique biological means of targeting tumors and their microenvironments, minimizing cytotoxic effects, and increasing the efficacy of treatments at lower drug doses (**Table 1**). However, despite these many advantages, EVs can have variable effects on tumor progression and the tumor microenvironment dependent upon their protein and nucleic acid cargos. One of the limitations of EV usage is the heterogeneity of the isolated population, since the size of exosomes and MVs overlap, and as yet it is not clear which population carries the greatest potential to elicit functional changes. Furthermore, the inconsistency of the EV cargo adds an additional caveat to their study and therapeutic use (81). In the case of drug loading, disadvantages include a low transfection efficiency, and, in the case of cell manipulation, there is a high dependence on cell division (82). Therefore, progressing their use as therapeutic tools requires full characterization of such disadvantages and limitations before the promise of MVs in clinical practice is achieved.

AUTHOR CONTRIBUTIONS

DC wrote the manuscript and made the table. KK created the figure. VJ edited the manuscript. DC, VS, and AR conceived the idea and edited the manuscript and table.

FUNDING

The work is performed according to the Russian Government Program of Competitive Growth of Kazan Federal University. VS was supported by the Russian Foundation for Basic Research (RFBR) grant 16-34-60201. AR was supported by state assignment 20.5175.2017/6.7 of the Ministry of Education and Science of Russian Federation and RFBR grant 18-04-01133.

REFERENCES

1. Elmore S. Apoptosis: a review of programmed cell death. *Toxicol Pathol* (2007) 35(4):495–516. doi:10.1080/01926230701320337
2. Gould SJ, Raposo G. As we wait: coping with an imperfect nomenclature for extracellular vesicles. *J Extracell Vesicles* (2013) 2(1):20389. doi:10.3402/jev.v2i0.20389
3. Valadi H, Ekstrom K, Bossios A, Sjostrand M, Lee JJ, Lotvall JO. Exosome-mediated transfer of mRNAs and microRNAs is a novel mechanism of genetic exchange between cells. *Nat Cell Biol* (2007) 9(6):654–9. doi:10.1038/ncb1596
4. Wu K, Sharma S, Venkat S, Liu K, Zhou X, Watabe K. Non-coding RNAs in cancer brain metastasis. *Front Biosci (Schol Ed)* (2016) 8:187–202. doi:10.2741/s457
5. Li X, Tsibouklis J, Weng T, Zhang B, Yin G, Feng G, et al. Nano carriers for drug transport across the blood-brain barrier. *J Drug Target* (2017) 25(1):17–28. doi:10.1080/1061186X.2016.1184272
6. Lee Y, El Andaloussi S, Wood MJ. Exosomes and microvesicles: extracellular vesicles for genetic information transfer and gene therapy. *Hum Mol Genet* (2012) 21(R1):R125–34. doi:10.1093/hmg/dds317
7. Wu K, Xing F, Wu SY, Watabe K. Extracellular vesicles as emerging targets in cancer: Recent development from bench to bedside. *Biochim Biophys Acta* (2017) 1868(2):538–63. doi:10.1016/j.bbcan.2017.10.001
8. Raposo G, Stoorvogel W. Extracellular vesicles: exosomes, microvesicles, and friends. *J Cell Biol* (2013) 200(4):373–83. doi:10.1083/jcb.201211138
9. Kalra H, Drummen GP, Mathivanan S. Focus on extracellular vesicles: introducing the next small big thing. *Int J Mol Sci* (2016) 17(2):170. doi:10.3390/ijms17020170
10. Wang M, Zhao J, Zhang L, Wei F, Lian Y, Wu Y, et al. Role of tumor microenvironment in tumorigenesis. *J Cancer* (2017) 8(5):761–73. doi:10.7150/jca.17648
11. Jordan BF, Gourgue F, Cani PD. Adipose tissue metabolism and cancer progression: novel insights from gut microbiota? *Curr Pathobiol Rep* (2017) 5(4):315–22. doi:10.1007/s40139-017-0154-6
12. Hanahan D, Weinberg RA. Hallmarks of cancer: the next generation. *Cell* (2011) 144(5):646–74. doi:10.1016/j.cell.2011.02.013
13. Andre F, Chaput N, Schartz NE, Flament C, Aubert N, Bernard J, et al. Exosomes as potent cell-free peptide-based vaccine. I. Dendritic cell-derived exosomes transfer functional MHC class I/peptide complexes to dendritic cells. *J Immunol* (2004) 172(4):2126–36. doi:10.4049/jimmunol.172.4.2126
14. Camussi G, Deregibus MC, Bruno S, Grange C, Fonsato V, Tetta C. Exosome/microvesicle-mediated epigenetic reprogramming of cells. *Am J Cancer Res* (2011) 1(1):98–110.
15. Eirin A, Riester SM, Zhu XY, Tang H, Evans JM, O'Brien D, et al. MicroRNA and mRNA cargo of extracellular vesicles from porcine adipose tissue-derived mesenchymal stem cells. *Gene* (2014) 551(1):55–64. doi:10.1016/j.gene.2014.08.041
16. Li XJ, Ren ZJ, Tang JH, Yu Q. Exosomal microRNA MiR-1246 promotes cell proliferation, invasion and drug resistance by targeting CCNG2 in breast cancer. *Cell Physiol Biochem* (2017) 44(5):1741–8. doi:10.1159/000485780
17. Yanez-Mo M, Siljander PR, Andreu Z, Zavec AB, Borras FE, Buzas EI, et al. Biological properties of extracellular vesicles and their physiological functions. *J Extracell Vesicles* (2015) 4:27066. doi:10.3402/jev.v4.27066
18. Kalimuthu S, Gangadaran P, Li XJ, Oh JM, Lee HW, Jeong SY, et al. In vivo therapeutic potential of mesenchymal stem cell-derived extracellular vesicles with optical imaging reporter in tumor mice model. *Sci Rep* (2016) 6:30418. doi:10.1038/srep30418
19. Chulpanova DS, Kitaeva KV, Tazetdinova LG, James V, Rizvanov AA, Solovyeva VV. Application of mesenchymal stem cells for therapeutic agent delivery in anti-tumor treatment. *Front Pharmacol* (2018) 9:259. doi:10.3389/fphar.2018.00259
20. Gomzikova MO, Rizvanov AA. Current trends in regenerative medicine: from cell to cell-free therapy. *BioNanoSci* (2017) 7:240–5. doi:10.1007/s12668-016-0348-0
21. Han L, Xu J, Xu Q, Zhang B, Lam EW, Sun Y. Extracellular vesicles in the tumor microenvironment: therapeutic resistance, clinical biomarkers, and targeting strategies. *Med Res Rev* (2017) 37(6):1318–49. doi:10.1002/med.21453
22. Aubertin K, Silva AK, Luciani N, Espinosa A, Djemat A, Charue D, et al. Massive release of extracellular vesicles from cancer cells after photodynamic treatment or chemotherapy. *Sci Rep* (2016) 6:35376. doi:10.1038/srep35376
23. Feng Q, Zhang C, Lum D, Druso JE, Blank B, Wilson KF, et al. A class of extracellular vesicles from breast cancer cells activates VEGF receptors and tumour angiogenesis. *Nat Commun* (2017) 8:14450. doi:10.1038/ncomms14450
24. Zhang S, Zhang Y, Qu J, Che X, Fan Y, Hou K, et al. Exosomes promote cetuximab resistance via the PTEN/Akt pathway in colon cancer cells. *Braz J Med Biol Res* (2017) 51(1):e6472. doi:10.1590/1414-431X20176472
25. Khan FM, Saleh E, Alawadhi H, Harati R, Zimmermann WH, El-Awady R. Inhibition of exosome release by ketotifen enhances sensitivity of cancer cells to doxorubicin. *Cancer Biol Ther* (2018) 19(1):25–33. doi:10.1080/15384047.2017.1394544
26. Guan XW, Zhao F, Wang JY, Wang HY, Ge SH, Wang X, et al. Tumor microenvironment interruption: a novel anti-cancer mechanism of proton-pump inhibitor in gastric cancer by suppressing the release of microRNA-carrying exosomes. *Am J Cancer Res* (2017) 7(9):1913–25.

27. Qin X, Yu S, Zhou L, Shi M, Hu Y, Xu X, et al. Cisplatin-resistant lung cancer cell-derived exosomes increase cisplatin resistance of recipient cells in exosomal miR-100-5p-dependent manner. *Int J Nanomedicine* (2017) 12:3721–33. doi:10.2147/IJN.S131516
28. Parolini I, Federici C, Raggi C, Lugini L, Palleschi S, De Milito A, et al. Microenvironmental pH is a key factor for exosome traffic in tumor cells. *J Biol Chem* (2009) 284(49):34211–22. doi:10.1074/jbc.M109.041152
29. Luciani F, Spada M, De Milito A, Molinari A, Rivoltini L, Montinaro A, et al. Effect of proton pump inhibitor pretreatment on resistance of solid tumors to cytotoxic drugs. *J Natl Cancer Inst* (2004) 96(22):1702–13. doi:10.1093/jnci/djh305
30. Rana S, Malinowska K, Zoller M. Exosomal tumor microRNA modulates premetastatic organ cells. *Neoplasia* (2013) 15(3):281–95. doi:10.1593/neo.122010
31. Costa-Silva B, Aiello NM, Ocean AJ, Singh S, Zhang H, Thakur BK, et al. Pancreatic cancer exosomes initiate pre-metastatic niche formation in the liver. *Nat Cell Biol* (2015) 17(6):816–26. doi:10.1038/ncb3169
32. Grange C, Tapparo M, Collino F, Vitillo L, Damasco C, Deregibus MC, et al. Microvesicles released from human renal cancer stem cells stimulate angiogenesis and formation of lung premetastatic niche. *Cancer Res* (2011) 71(15):5346–56. doi:10.1158/0008-5472.CAN-11-0241
33. Saari H, Lazaro-Ibanez E, Viitala T, Vuorimaa-Laukkanen E, Siljander P, Yliperttula M. Microvesicle- and exosome-mediated drug delivery enhances the cytotoxicity of Paclitaxel in autologous prostate cancer cells. *J Control Release* (2015) 220(Pt B):727–37. doi:10.1016/j.jconrel.2015.09.031
34. Yang T, Martin P, Fogarty B, Brown A, Schurman K, Phipps R, et al. Exosome delivered anticancer drugs across the blood-brain barrier for brain cancer therapy in *Danio rerio*. *Pharm Res* (2015) 32(6):2003–14. doi:10.1007/s11095-014-1593-y
35. Toffoli G, Hadla M, Corona G, Caligiuri I, Palazzolo S, Semeraro S, et al. Exosomal doxorubicin reduces the cardiac toxicity of doxorubicin. *Nanomedicine (Lond)* (2015) 10(19):2963–71. doi:10.2217/nnm.15.118
36. Hadla M, Palazzolo S, Corona G, Caligiuri I, Canzonieri V, Toffoli G, et al. Exosomes increase the therapeutic index of doxorubicin in breast and ovarian cancer mouse models. *Nanomedicine (Lond)* (2016) 11(18):2431–41. doi:10.2217/nnm-2016-0154
37. Clayton A, Mason MD. Exosomes in tumour immunity. *Curr Oncol* (2009) 16(3):46–9. doi:10.3747/co.v16i3.367
38. Mahaweni NM, Kaijen-Lambers ME, Dekkers J, Aerts JG, Hegmans JP. Tumour-derived exosomes as antigen delivery carriers in dendritic cell-based immunotherapy for malignant mesothelioma. *J Extracell Vesicles* (2013) 2(1):22492. doi:10.3402/jev.v2i0.22492
39. Liu H, Chen L, Liu J, Meng H, Zhang R, Ma L, et al. Co-delivery of tumor-derived exosomes with alpha-galactosylceramide on dendritic cell-based immunotherapy for glioblastoma. *Cancer Lett* (2017) 411:182–90. doi:10.1016/j.canlet.2017.09.022
40. Xiao L, Erb U, Zhao K, Hackert T, Zoller M. Efficacy of vaccination with tumor-exosome loaded dendritic cells combined with cytotoxic drug treatment in pancreatic cancer. *Oncoimmunology* (2017) 6(6):e1319044. doi:10.1080/2162402X.2017.1319044
41. Dai S, Zhou X, Wang B, Wang Q, Fu Y, Chen T, et al. Enhanced induction of dendritic cell maturation and HLA-A*0201-restricted CEA-specific CD8(+) CTL response by exosomes derived from IL-18 gene-modified CEA-positive tumor cells. *J Mol Med (Berl)* (2006) 84(12):1067–76. doi:10.1007/s00109-006-0102-0
42. Yang Y, Xiu F, Cai Z, Wang J, Wang Q, Fu Y, et al. Increased induction of antitumor response by exosomes derived from interleukin-2 gene-modified tumor cells. *J Cancer Res Clin Oncol* (2007) 133(6):389–99. doi:10.1007/s00432-006-0184-7
43. Aspe JR, Diaz Osterman CJ, Jutzy JM, Deshields S, Whang S, Wall NR. Enhancement of gemcitabine sensitivity in pancreatic adenocarcinoma by novel exosome-mediated delivery of the Survivin-T34A mutant. *J Extracell Vesicles* (2014) 3(1):23244. doi:10.3402/jev.v3.23244
44. Rivoltini L, Chiodoni C, Squarcina P, Tortoreto M, Villa A, Vergani B, et al. TNF-related apoptosis-inducing ligand (TRAIL)-armed exosomes deliver proapoptotic signals to tumor site. *Clin Cancer Res* (2016) 22(14):3499–512. doi:10.1158/1078-0432.CCR-15-2170
45. Li P, Feng J, Liu Y, Liu Q, Fan L, Liu Q, et al. Novel therapy for glioblastoma multiforme by restoring LRRC4 in tumor cells: LRRC4 inhibits tumor-infiltrating regulatory T cells by cytokine and programmed cell death 1-containing exosomes. *Front Immunol* (2017) 8:1748. doi:10.3389/fimmu.2017.01748
46. Ostrowski M, Carmo NB, Krumeich S, Fanget I, Raposo G, Savina A, et al. Rab27a and Rab27b control different steps of the exosome secretion pathway. *Nat Cell Biol* (2010) 12(1):19–30; sup 11–13. doi:10.1038/ncb2000
47. Li W, Mu D, Tian F, Hu Y, Jiang T, Han Y, et al. Exosomes derived from Rab27a-overexpressing tumor cells elicit efficient induction of antitumor immunity. *Mol Med Rep* (2013) 8(6):1876–82. doi:10.3892/mmr.2013.1738
48. O'Brien K, Lowry MC, Corcoran C, Martinez VG, Daly M, Rani S, et al. miR-134 in extracellular vesicles reduces triple-negative breast cancer aggression and increases drug sensitivity. *Oncotarget* (2015) 6(32):32774–89. doi:10.18632/oncotarget.5192
49. Zhang H, Bai M, Deng T, Liu R, Wang X, Qu Y, et al. Cell-derived microvesicles mediate the delivery of miR-29a/c to suppress angiogenesis in gastric carcinoma. *Cancer Lett* (2016) 375(2):331–9. doi:10.1016/j.canlet.2016.03.026
50. Shtam TA, Kovalev RA, Varfolomeeva EY, Makarov EM, Kil YV, Filatov MV. Exosomes are natural carriers of exogenous siRNA to human cells in vitro. *Cell Commun Signal* (2013) 11:88. doi:10.1186/1478-811X-11-88
51. Wang Y, Qin X, Zhu X, Chen W, Zhang J, Chen W. Oral cancer-derived exosomal NAP1 enhances cytotoxicity of natural killer cells via the IRF-3 pathway. *Oral Oncol* (2018) 76:34–41. doi:10.1016/j.oraloncology.2017.11.024
52. Tian Y, Li S, Song J, Ji T, Zhu M, Anderson GJ, et al. A doxorubicin delivery platform using engineered natural membrane vesicle exosomes for targeted tumor therapy. *Biomaterials* (2014) 35(7):2383–90. doi:10.1016/j.biomaterials.2013.11.083
53. Gehrmann U, Hiltbrunner S, Georgoudaki AM, Karlsson MC, Naslund TI, Gabrielsson S. Synergistic induction of adaptive antitumor immunity by codelivery of antigen with alpha-galactosylceramide on exosomes. *Cancer Res* (2013) 73(13):3865–76. doi:10.1158/0008-5472.CAN-12-3918
54. Viaud S, Terme M, Flament C, Taieb J, Andre F, Novault S, et al. Dendritic cell-derived exosomes promote natural killer cell activation and proliferation: a role for NKG2D ligands and IL-15Ralpha. *PLoS One* (2009) 4(3):e4942. doi:10.1371/journal.pone.0004942
55. Lu Z, Zuo B, Jing R, Gao X, Rao Q, Liu Z, et al. Dendritic cell-derived exosomes elicit tumor regression in autochthonous hepatocellular carcinoma mouse models. *J Hepatol* (2017) 67(4):739–48. doi:10.1016/j.jhep.2017.05.019
56. Besse B, Charrier M, Lapierre V, Dansin E, Lantz O, Planchard D, et al. Dendritic cell-derived exosomes as maintenance immunotherapy after first line chemotherapy in NSCLC. *Oncoimmunology* (2016) 5(4):e1071008. doi:10.1080/2162402X.2015.1071008
57. Kim MS, Haney MJ, Zhao Y, Mahajan V, Deygen I, Klyachko NL, et al. Development of exosome-encapsulated paclitaxel to overcome MDR in cancer cells. *Nanomedicine* (2016) 12(3):655–64. doi:10.1016/j.nano.2015.10.012
58. Kim MS, Haney MJ, Zhao Y, Yuan D, Deygen I, Klyachko NL, et al. Engineering macrophage-derived exosomes for targeted paclitaxel delivery to pulmonary metastases: in vitro and in vivo evaluations. *Nanomedicine* (2018) 14(1):195–204. doi:10.1016/j.nano.2017.09.011
59. Jang SC, Kim OY, Yoon CM, Choi DS, Roh TY, Park J, et al. Bioinspired exosome-mimetic nanovesicles for targeted delivery of chemotherapeutics to malignant tumors. *ACS Nano* (2013) 7(9):7698–710. doi:10.1021/nn402232g
60. Munoz JL, Bliss SA, Greco SJ, Ramkissoon SH, Ligon KL, Rameshwar P. Delivery of functional anti-miR-9 by mesenchymal stem cell-derived exosomes to glioblastoma multiforme cells conferred chemosensitivity. *Mol Ther Nucleic Acids* (2013) 2:e126. doi:10.1038/mtna.2013.60
61. Katakowski M, Buller B, Zheng X, Lu Y, Rogers T, Osobamiro O, et al. Exosomes from marrow stromal cells expressing miR-146b inhibit glioma growth. *Cancer Lett* (2013) 335(1):201–4. doi:10.1016/j.canlet.2013.02.019
62. Lang FM, Hossain A, Gumin J, Momin EN, Shimizu Y, Ledbetter D, et al. Mesenchymal stem cells as natural biofactories for exosomes carrying miR-124a in the treatment of gliomas. *Neuro Oncol* (2018) 20(3):380–90. doi:10.1093/neuonc/nox152
63. Umezu T, Imanishi S, Azuma K, Kobayashi C, Yoshizawa S, Ohyashiki K, et al. Replenishing exosomes from older bone marrow stromal cells with miR-340 inhibits myeloma-related angiogenesis. *Blood Adv* (2017) 1(13):812–23. doi:10.1182/bloodadvances.2016003251
64. Greco KA, Franzen CA, Foreman KE, Flanigan RC, Kuo PC, Gupta GN. PLK-1 silencing in bladder cancer by siRNA delivered with exosomes. *Urology* (2016) 91:242.e1–7. doi:10.1016/j.urology.2016.01.028

65. Lou G, Song X, Yang F, Wu S, Wang J, Chen Z, et al. Exosomes derived from miR-122-modified adipose tissue-derived MSCs increase chemosensitivity of hepatocellular carcinoma. *J Hematol Oncol* (2015) 8:122. doi:10.1186/s13045-015-0220-7
66. Pascucci L, Cocce V, Bonomi A, Ami D, Ceccarelli P, Ciusani E, et al. Paclitaxel is incorporated by mesenchymal stromal cells and released in exosomes that inhibit in vitro tumor growth: a new approach for drug delivery. *J Control Release* (2014) 192:262–70. doi:10.1016/j.jconrel.2014.07.042
67. Cocce V, Balducci L, Falchetti ML, Pascucci L, Ciusani E, Brini AT, et al. Fluorescent immortalized human adipose derived stromal cells (hASCs-TS/GFP+) for studying cell drug delivery mediated by microvesicles. *Anticancer Agents Med Chem* (2017) 17(11):1578–85. doi:10.2174/1871520617666170327113932
68. Yuan Z, Kolluri KK, Gowers KH, Janes SM. TRAIL delivery by MSC-derived extracellular vesicles is an effective anticancer therapy. *J Extracell Vesicles* (2017) 6(1):1265291. doi:10.1080/20013078.2017.1265291
69. Escudier B, Dorval T, Chaput N, Andre F, Caby MP, Novault S, et al. Vaccination of metastatic melanoma patients with autologous dendritic cell (DC) derived-exosomes: results of the first phase I clinical trial. *J Transl Med* (2005) 3(1):10. doi:10.1186/1479-5876-3-10
70. Morse MA, Garst J, Osada T, Khan S, Hobeika A, Clay TM, et al. A phase I study of dexosome immunotherapy in patients with advanced non-small cell lung cancer. *J Transl Med* (2005) 3(1):9. doi:10.1186/1479-5876-3-9
71. Huang WH, Chang MC, Tsai KS, Hung MC, Chen HL, Hung SC. Mesenchymal stem cells promote growth and angiogenesis of tumors in mice. *Oncogene* (2013) 32(37):4343–54. doi:10.1038/onc.2012.458
72. Ramdasi S, Sarang S, Viswanathan C. Potential of mesenchymal stem cell based application in cancer. *Int J Hematol Oncol Stem Cell Res* (2015) 9(2):95–103.
73. Wang M, Zhao C, Shi H, Zhang B, Zhang L, Zhang X, et al. Deregulated microRNAs in gastric cancer tissue-derived mesenchymal stem cells: novel biomarkers and a mechanism for gastric cancer. *Br J Cancer* (2014) 110(5):1199–210. doi:10.1038/bjc.2014.14
74. Zhu W, Huang L, Li Y, Zhang X, Gu J, Yan Y, et al. Exosomes derived from human bone marrow mesenchymal stem cells promote tumor growth in vivo. *Cancer Lett* (2012) 315(1):28–37. doi:10.1016/j.canlet.2011.10.002
75. Roccaro AM, Sacco A, Maiso P, Azab AK, Tai YT, Reagan M, et al. BM mesenchymal stromal cell-derived exosomes facilitate multiple myeloma progression. *J Clin Invest* (2013) 123(4):1542–55. doi:10.1172/JCI66517
76. Vallabhaneni KC, Penfornis P, Dhule S, Guillonneau F, Adams KV, Mo YY, et al. Extracellular vesicles from bone marrow mesenchymal stem/stromal cells transport tumor regulatory microRNA, proteins, and metabolites. *Oncotarget* (2015) 6(7):4953–67. doi:10.18632/oncotarget.3211
77. Ji R, Zhang B, Zhang X, Xue J, Yuan X, Yan Y, et al. Exosomes derived from human mesenchymal stem cells confer drug resistance in gastric cancer. *Cell Cycle* (2015) 14(15):2473–83. doi:10.1080/15384101.2015.1005530
78. Ono M, Kosaka N, Tominaga N, Yoshioka Y, Takeshita F, Takahashi RU, et al. Exosomes from bone marrow mesenchymal stem cells contain a microRNA that promotes dormancy in metastatic breast cancer cells. *Sci Signal* (2014) 7(332):ra63. doi:10.1126/scisignal.2005231
79. Lee JK, Park SR, Jung BK, Jeon YK, Lee YS, Kim MK, et al. Exosomes derived from mesenchymal stem cells suppress angiogenesis by down-regulating VEGF expression in breast cancer cells. *PLoS One* (2013) 8(12):e84256. doi:10.1371/journal.pone.0084256
80. Shimbo K, Miyaki S, Ishitobi H, Kato Y, Kubo T, Shimose S, et al. Exosome-formed synthetic microRNA-143 is transferred to osteosarcoma cells and inhibits their migration. *Biochem Biophys Res Commun* (2014) 445(2):381–7. doi:10.1016/j.bbrc.2014.02.007
81. Gilligan KE, Dwyer RM. Engineering exosomes for cancer therapy. *Int J Mol Sci* (2017) 18(6):1122. doi:10.3390/ijms18061122
82. Gresch O, Engel FB, Nesic D, Tran TT, England HM, Hickman ES, et al. New non-viral method for gene transfer into primary cells. *Methods* (2004) 33(2):151–63. doi:10.1016/j.ymeth.2003.11.009

Conflict of Interest Statement: The authors declare that the research was conducted in the absence of any commercial or financial relationships that could be construed as a potential conflict of interest.

frontiers in Immunology

ORIGINAL RESEARCH
published: 26 April 2018
doi: 10.3389/fimmu.2018.00874

Silicosis and Silica-Induced Autoimmunity in the Diversity Outbred Mouse

*Jessica M. Mayeux[1], Gabriela M. Escalante[1], Joseph M. Christy[1], Rahul D. Pawar[1], Dwight H. Kono[2] and Kenneth M. Pollard[1]**

[1] Department of Molecular Medicine, The Scripps Research Institute, La Jolla, CA, United States, [2] Department of Immunology and Microbiology, The Scripps Research Institute, La Jolla, CA, United States

Epidemiological studies have confidently linked occupational crystalline silica exposure to autoimmunity, but pathogenic mechanisms and role of genetic predisposition remain poorly defined. Although studies of single inbred strains have yielded insights, understanding the relationships between lung pathology, silica-induced autoimmunity, and genetic predisposition will require examination of a broad spectrum of responses and susceptibilities. We defined the characteristics of silicosis and autoimmunity and their relationships using the genetically heterogeneous diversity outbred (DO) mouse population and determined the suitability of this model for investigating silica-induced autoimmunity. Clinically relevant lung and autoimmune phenotypes were assessed 12 weeks after a transoral dose of 0, 5, or 10 mg crystalline silica in large cohorts of DO mice. Data were further analyzed for correlations, hierarchical clustering, and sex effects. DO mice exhibited a wide range of responses to silica, including mild to severe silicosis and importantly silica-induced systemic autoimmunity. Strikingly, about half of PBS controls were anti-nuclear antibodies (ANA) positive, however, few had disease-associated specificities, whereas most ANAs in silica-exposed mice showed anti-ENA5 reactivity. Correlation and hierarchical clustering showed close association of silicosis, lung biomarkers, and anti-ENA5, while other autoimmune characteristics, such as ANA and glomerulonephritis, clustered separately. Silica-exposed males had more lung inflammation, bronchoalveolar lavage fluid cells, IL-6, and autoantibodies. DO mice are susceptible to both silicosis and silica-induced autoimmunity and show substantial individual variations reflecting their genetic diverseness and the importance of predisposition particularly for autoimmunity. This model provides a new tool for deciphering the relationship between silica exposure, genes, and disease.

Keywords: silica, diversity outbred, autoimmunity, silicosis, autoantibody, inflammation, lung, environmental autoimmunity

OPEN ACCESS

Edited by:
Hans-Joachim Anders, Ludwig-Maximilians-Universität München, Germany

Reviewed by:
Takemi Otsuki, Kawasaki Medical School, Japan
Ping Chen, Georgetown University, United States
James Pestka, Michigan State University, United States

****Correspondence:***
Kenneth M. Pollard
mpollard@scripps.edu

Specialty section:
This article was submitted to Inflammation, a section of the journal Frontiers in Immunology

Received: *06 February 2018*
Accepted: *09 April 2018*
Published: *26 April 2018*

Citation:
Mayeux JM, Escalante GM, Christy JM, Pawar RD, Kono DH and Pollard KM (2018) Silicosis and Silica-Induced Autoimmunity in the Diversity Outbred Mouse. Front. Immunol. 9:874. doi: 10.3389/fimmu.2018.00874

INTRODUCTION

Crystalline silica is an abundant mineral found in rock, sand, and soil, and exposure is an environmental or occupational hazard in construction, mining, and other dusty trades (1, 2). Silicosis results from the inhalation and deposition of respirable crystalline silica in the lungs, which causes a range of pathologies, including inflammation, tissue damage, necrosis, and fibrosis (1–3). Silica exposure is also associated with autoimmunity [systemic lupus erythematosus (SLE), rheumatoid arthritis

(RA), and scleroderma] in humans, however, little is known of the mechanisms responsible (2, 4–11). Although these diseases occur predominantly in females (12), silica-induced autoimmunity is most often described following occupational exposure in males (8). While several human studies have found an association between the intensity of silica exposure with autoimmune disease and autoantibodies, silica-induced autoantibody production can occur without significant lung damage (13–15). Silica exposure results in more pronounced lung responses and exacerbates autoimmunity in susceptible mice; however, the limited animal studies of silica-induced autoimmunity have revealed little regarding the mechanisms involved (9, 16–19). This paucity of information is a significant barrier to furthering our understanding of how silica-mediated pathology leads to autoimmunity.

Genetic predisposition and environmental exposure to silica likely interact to drive susceptibility or resistance to silicosis and silica-induced autoimmunity. Disease features associated with silica exposure occur with variable frequency in humans suggesting a significant gene–environment interaction in both silicosis and silica-induced autoimmunity (2). A similar spectrum of disease features are found in murine silicosis, which exhibits a clear dose response (16, 20), however variation among inbred mouse strains suggests a strong genetic component. Although this variability of disease phenotypes is observed when multiple inbred mouse strains are exposed to silica, it is not found in any single inbred mouse strain because the restricted genetic content recapitulates only some features of disease (9, 16, 20). These animal studies suggest that many of the pathological features described in human silicosis and silica-induced autoimmunity are heavily influenced by genetic background. However, studies to elucidate the genetic contribution to disease have been hampered by the lack of animal models that exemplify the genetic heterogeneity of human populations.

One approach to broaden the genetic heterogeneity in murine studies is to use outbred strains, such as the diversity outbred (DO) mouse (21–24). The DO mouse is a heterogeneous stock derived from eight founder strains (A/J, C57BL/6J, 129S1/SvImJ, NOD/ShiLtJ, NZO/HiLtJ, CAST/EiJ, PWK/PhJ, and WSB/EiJ) that is maintained by randomized breeding. The DO exhibits significant phenotypic variability because it captures the same set of allelic variants as the eight founder strains (25) and is, therefore, well suited to model the range of immunological responses that follow exposure to environmental agents known to induce disease in humans (26, 27). The DO mouse also provides a powerful tool for genome-wide association studies that could better model the genetic heterogeneity of human populations than inbred mice for the study of silicosis and silica-induced autoimmunity.

In this study, we sought to determine if DO mice could be used to model the diversity of immunological and pathological changes found in human silicosis and silica-induced autoimmunity. Here, we identify biomarkers of silica-induced lung pathology and autoimmunity and describe the range of responses to silica in the DO mouse establishing it as a model of population-based silicosis and silica-induced autoimmunity. Biomarkers associated with human pulmonary silicosis, bronchoalveolar lavage fluid (BALF) cell numbers and protein, TGF-β, TNF-α, and lactate dehydrogenase (LDH) activity, were increased in silica-exposed mice. Silica-induced autoimmunity, including serum IgM, IgG, anti-nuclear antibodies (ANA), and anti-ENA (RNP and Sm) specificity were increased with silica exposure along with lupus-like glomerulonephritis. Significantly, our findings also suggest that expression of some features of autoimmunity do not closely reflect silica-induced lung pathology, and that male mice can display more severe parameters of both silicosis and autoimmunity. Finally, these results provide a new model to study the effects of genetic diversity on the pathogenesis of silicosis and silica-induced autoimmunity.

MATERIALS AND METHODS

Mice

Male and female DO mice (J:DO, Stock No: 009376) were purchased from Jackson Laboratory (Bar Harbor, ME, USA) and have been described previously (22). Handling and maintenance were performed under specific pathogen-free conditions at TSRI's Animal Facility. Experiments were carried out with 8- to 10-week-old animals. Animal rooms were kept at 68–72°F and 60–70% humidity, with a 12/12 h light–dark cycle, and sterilized cages were replaced each week with fresh water and food (autoclaved standard grain diet 7012, Teklad, Envigo, Madison, WI, USA) to which the mice had access *ad libitum*. Behavioral enrichments, such as paper breeder huts, goat chow, and nylabones, were provided as needed. All procedures were approved by The Scripps Research Institute Institutional Animal Care and Use Committee (IACUC).

Exposure to Crystalline Silica

Mice were exposed to a single dose of crystalline silica (Min-U-Sil-5, average particle size 1.5–2 μm; U.S. Silica Company, Frederick, MD, USA) by transoral (or oropharyngeal) instillation in a volume of 25 μl of PBS under isoflurane anesthesia. Briefly, mice were anesthetized and the tongue pulled forward and to the side (to block the swallow reflex) so that the silica solution is delivered into the back of the throat and aspirated into the lungs (28). A total of 210 8- to 10-week-old mice were exposed to crystalline silica, of which 90 received 5 mg and 120 received 10 mg. These doses were chosen based on calculations of human lifetime exposure to respirable crystalline silica and an equivalent exposure for mice, and represent approximately 60–120% of a human lifetime exposure at the recommended NIOSH exposure limit (19). A single instillation was used because of evidence of an association between the intensity of silica exposure and autoimmunity (8). A control group of 70 mice received PBS alone. Each treatment group consisted of equal numbers of male and female mice. Silica was acid washed in 1 M HCl at 100°C for 2 h and then autoclaved for 1 h at 121°C and allowed to dry (29). Immediately prior to use silica was disbursed by sonication. Use of crystalline silica was approved by The Scripps Research Institute Department of Environmental Health and Safety.

Bronchoalveolar Lavage and Lung Histology

Mice were sacrificed at 12 weeks post-exposure and BALF was collected. Total cell counts were determined using a Countess II

FL Automated Cell Counter (Thermo Fisher Scientific, Waltham, MA, USA) before BALF was stored at −80°C. Lungs were excised and fixed for 24 h in zinc formalin. Paraffin-embedding, sectioning (5 μm), and staining (hematoxylin and eosin and trichrome) were done by TSRI's Histology Core. Formalin fixed paraffin-embedded slides were scanned and images stored on Digital Image Hub (Slidepath, Dublin, Ireland). Lungs were scored under blinded conditions. The four right lobes and the single left lung was scored for the percent of the lobe affected by alveolitis (maximum score of 500) as well as peribronchitis and perivasculitis (maximum score of 500). A total lung score (TLS) (maximum score of 1,000) was determined by combining the amount of alveolitis, peribronchitis, and perivasculitis. The presence of silicosis was defined as a TLS greater than the mean plus 2 SDs of the PBS controls (9.6).

Immunofluorescence and ELISAs for Serum Immunoglobulins and Autoantibodies

Blood was collected from the retro-orbital sinus pre-silica exposure and at 4, 8, and 12 weeks post-exposure. Serum ANA were detected as previously described (30) using a 1:40 dilution of serum on Hep2 ANA slides as an initial screen (Innova Diagnostics, San Diego, CA, USA). Bound antibody was detected with goat anti-mouse IgG Alexa Fluor 488 (Life Technologies, Carlsbad, CA, USA). Slides were mounted using Vectashield Mounting Medium containing DAPI (Vectorlabs, Burlingame, CA, USA), and observed using an Olympus BH2 microscope. Digital images of ANA patterns were captured using a LEICA DFC 365 FX camera and analyzed using Leica Application Suite AF software (Leica Microsystems, Buffalo Grove, IL, USA).

Total serum IgG and IgM were measured by ELISA (30) as specified by the manufacturer (Immunology Consultants Laboratory, Portland, OR). To measure autoantibodies in the serum, ENA5 (designed for the detection of anti-Sm, -RNP, -SS-A (60 and 52 kDa), -SS-B, and -Scl-70 antibodies), anti-chromatin, anti-dsDNA, anti-SSA, anti-SSB, anti-RNP, and anti-Sm ELISA kits (QUANTA Lite ELISA Inova Diagnostics, San Diego, CA, USA) were modified to detect murine samples using a goat-anti mouse IgG HRP antibody (Thermo Fisher #62-6520). As calibrated mouse IgG of defined ANA specificities are not available the determination of antibody units in DO mice sera was achieved using human negative, low positive, and high positive controls and anti-human IgG HRP as described by the manufacturer (Innova Diagnostics). The units for each sample were calculated by dividing the average OD of the DO mouse sample by the average OD of the human Low Positive. The result was multiplied by the number of units assigned (by the manufacturer) to the human Low Positive (25 Units). Serum from MRL-*Fas*^{Lpr} mice was used as positive controls for reactivity of mouse sera for all ELISAs and a murine monoclonal antibody against chromatin, MoAb 2–3 (courtesy of Dr. Marc Monestier, Temple University, Philadelphia, PA, USA) was additionally used for the anti-chromatin ELISA. For the measurement of IgM RF, a sandwich ELISA was performed by coating IgG1κ (BD Pharmingen, San Diego, CA, USA) at 1 μg/ml onto NUNC plates (Thermo Fisher Scientific) and blocked with PBS containing 1 mg gelatin/ml. Serum was diluted 1:200, and bound RF detected with goat anti-mouse IgM HRP (Invitrogen, Carlsbad, CA, USA) at 1:1,000.

ELISA for Biomarkers in BALF

TNF-α (BioLegend, San Diego, CA, USA), IL-6 (BioLegend, San Diego, CA, USA), and activated TGF-β (R&D Systems, Minneapolis, MN, USA) were determined by ELISA according to the manufacturer's instructions. LDH activity was measured using a colorimetric assay (Sigma-Aldrich, St. Louis, MO, USA). Protein in BALF was determined using the Pierce BCA Protein Assay Kit (Thermo Fisher Scientific, Waltham, MA, USA).

Renal Pathology

Kidneys were fixed for 24 h in zinc formalin then paraffin sections (5 μm) were stained with Periodic Acid–Schiff (PAS). Slide images were stored on Digital Image Hub (Slidepath, Dublin, Ireland). Glomerulonephritis was scored on a 0–4 scale under blinded conditions (31). Proteinuria was determined using Roche Diagnostics Chemstrip 2 GP Urine Test Strips (Fisher Scientific).

Statistical Analysis

Unless otherwise noted, data are expressed as mean and SE. Statistical analysis was performed with GraphPad Software V6 (San Diego, CA, USA). Comparisons were performed using Kruskal–Wallis test or two-way ANOVA with Sidak's multiple comparisons. Correlations were calculated using pairwise deletion and reported in Spearman's correlation coefficient (r_s). Hierarchical Cluster Analysis was done using Cluster 3.0[1] and Java TreeView[2] using a relative change value for each phenotype. Briefly, relative change values were calculated using the equation: $\frac{s-s_{avg}}{s_{avg}}$, s = sample data point and s_{avg} = the average of the combined treatment samples (0, 5, and 10 mg). A one-dimensional self-organizing map was constructed along each axis (x-axis = samples, 20,000 iterations; y-axis = phenotypes, 100,000 iterations) followed by binary, agglomerative, hierarchical clustering using the Spearman Rank Correlation similarity metric, and a complete linkage clustering method. $P < 0.05$ was considered significant.

RESULTS

Silica Exposure and Lung Pathology

To determine the association of silicosis with autoimmunity, mice were given a single exposure to 0, 5, or 10 mg of crystalline silica and analyzed after 12 weeks. Silica exposure was well tolerated with no evidence of increased morbidity or any significant changes to whole body weight. Five animals died post exposure. Of these, two were PBS animals that died with mortal fighting-related wounds and three were silica-exposed animals with no fighting-related wounds, but all had high ANA positivity. One

[1]http://bonsai.hgc.jp/~mdehoon/software/cluster/software.htm (Accessed: July 6, 2017).
[2]http://jtreeview.sourceforge.net/ (Accessed: July 6, 2017).

silica-treated animal exhibited extreme morbidity and edema during the exposure period and was sacrificed early. Mice exposed to either dose of silica developed prominent alveolar, peribronchial, and perivascular inflammatory cell infiltrates containing varying amounts of lymphocytes, macrophages, and neutrophils. Accordingly, the total lung, alveolitis, and perivasculitis/bronchitis pathology scores in silica-exposed mice were much greater than unexposed controls and exhibited a strong dose response (**Figures 1A–D**). Furthermore, there was a wide range of responses to the silica consistent with the genetic diversity of DO mice.

Several pathologic findings occurred in only subsets of silica-exposed DO mice, including fibrosis, granulomas, and enlarged tracheobronchial lymph nodes. Fibrosis was seen in both the lungs and the draining tracheobronchial lymph nodes of silica-exposed mice primarily within granulomas (**Figures 1E,F**). Tracheobronchial lymph node hypertrophy was not observed in PBS mice, but was observed in 23% of mice receiving 10 mg silica ($p = 0.001$). The frequency and size of granulomas varied widely within each dosage group, but was much more frequent at the higher dose.

BALF Characteristics and Biomarkers of Silicosis

When corresponding BALF was examined, mean cell numbers and the percent of mice with elevated cell counts (greater than the mean + 2SD of PBS group) were substantially elevated in mice given 5 or 10 mg silica compared to PBS (**Figure 2A**; Table S1 in Supplementary Material). Furthermore, while the mean cell number was higher for the 10 versus 5 mg group, this did not reach statistical significance. Contrastingly, mean BALF protein levels and percent of mice with elevated protein levels were only increased in mice exposed to 10 mg of silica and unexpectedly mice receiving 5 mg of silica had slightly lower BALF protein

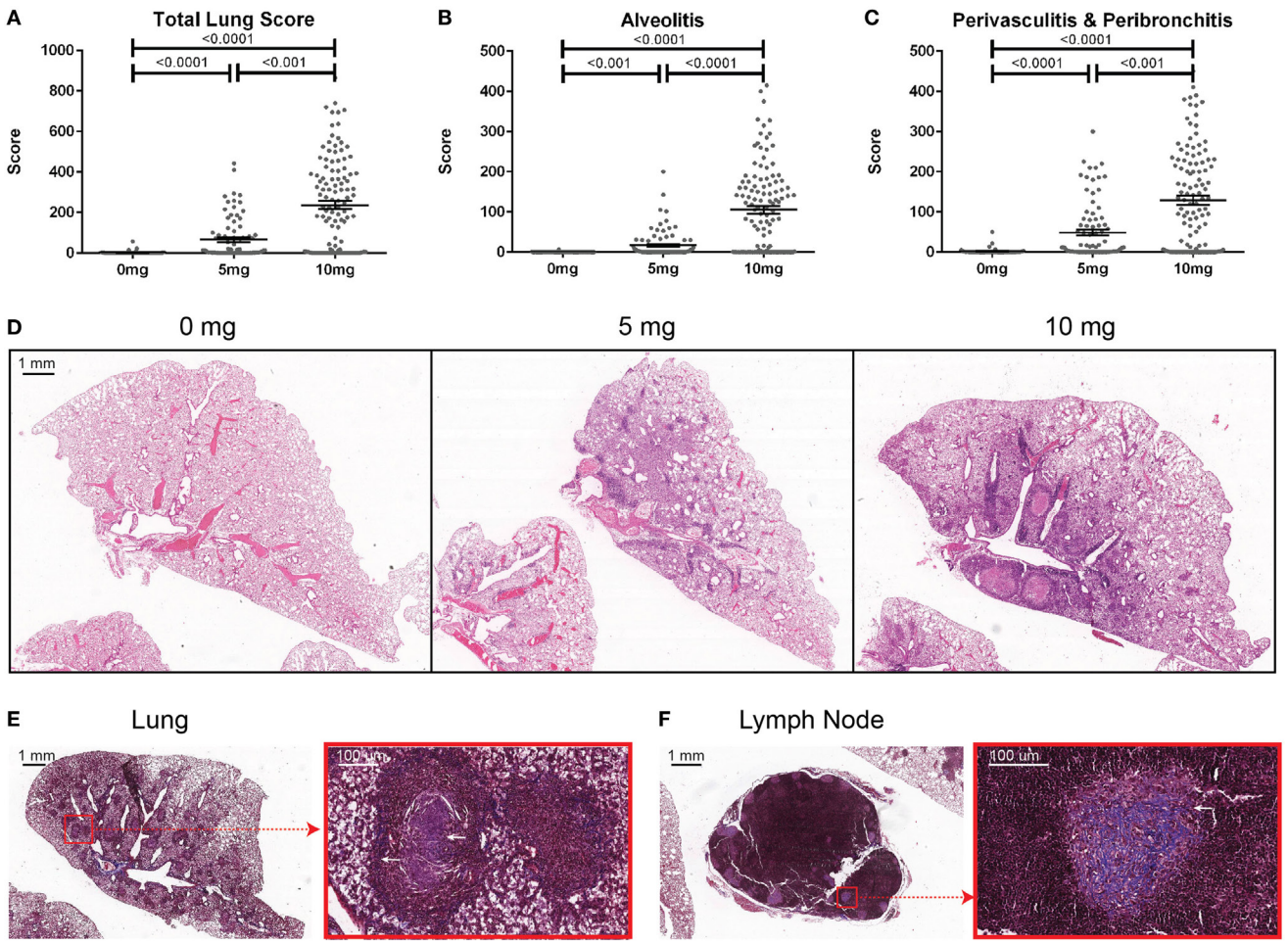

FIGURE 1 | Indices of silica-induced lung pathology in diversity outbred mice. Mice were exposed transorally to 0 mg ($n = 70$), 5 mg ($n = 90$), or 10 mg ($n = 120$) of crystalline silica in PBS for 12 weeks before H&E stained lung sections were reviewed and scored for **(A)** total lung score, **(B)** alveolitis, and **(C)** peribronchitis and perivasculitis. Images of slides with **(D)** H&E staining of the left lung lobe from mice exposed to 0 (left), 5 (middle), and 10 mg (right) of crystalline silica in PBS. Trichrome staining of the **(E)** left lung lobe and **(F)** tracheobronchial lymph node with white arrows indicating granulomas containing lattice-like fibrous connective tissue (inset with red outline).

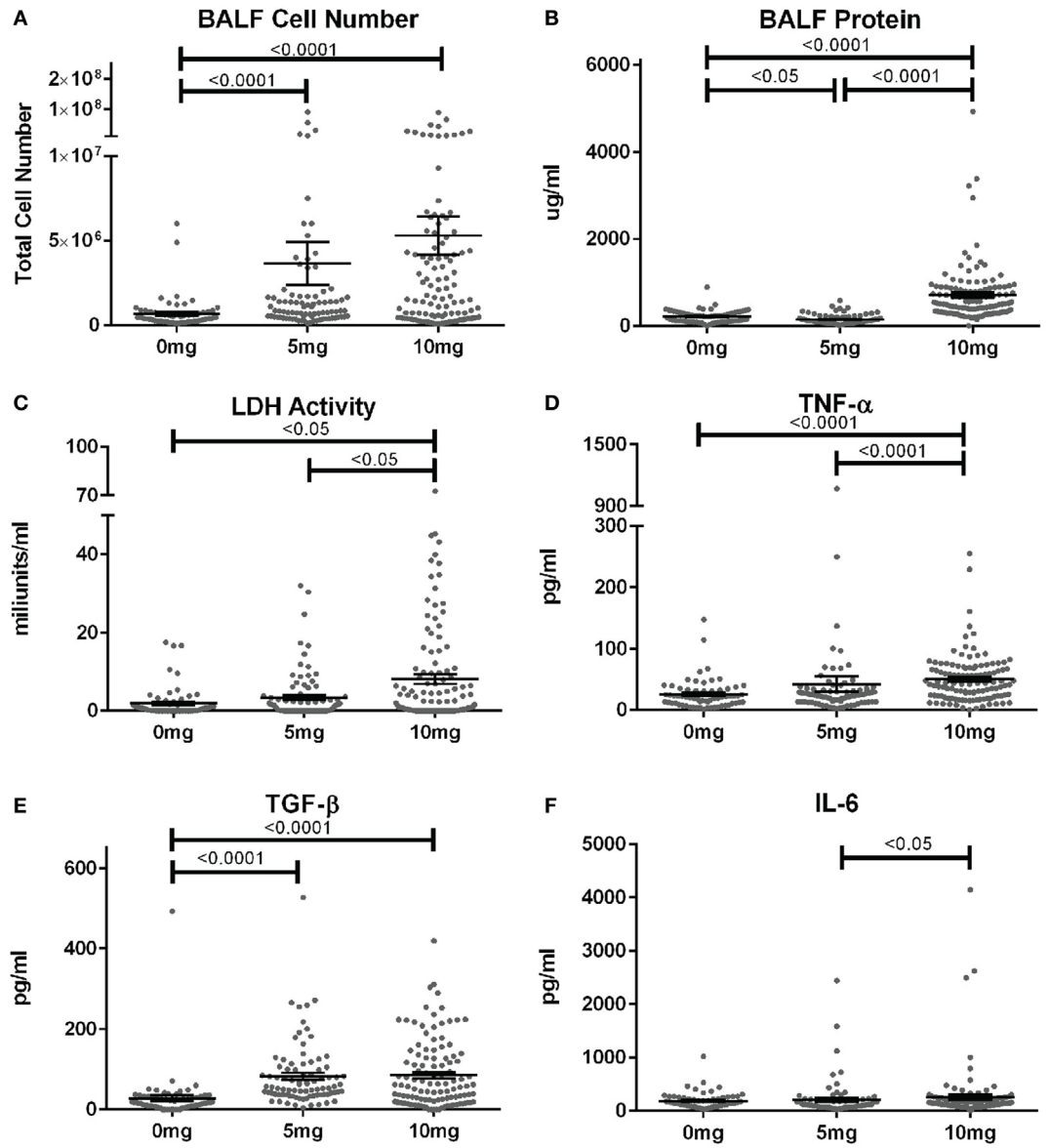

FIGURE 2 | Biomarkers of inflammation and fibrosis in bronchial alveolar lavage fluid (BALF) of silica-exposed diversity outbred mice. Mice were exposed transorally to crystalline silica in PBS (see **Figure 1**) before BALF was collected for the measurement of **(A)** BALF cell number, **(B)** BALF protein levels, **(C)** lactate dehydrogenase activity, **(D)** TNF-α, **(E)** TGF-β, and **(F)** IL-6.

levels than controls (**Figure 2B**). Thus, lower amounts of silica are sufficient to stimulate BALF cell increases, while higher doses are required to increase BALF protein levels.

We next determined whether BALF biomarkers of human silicosis (32) were also represented in silica-exposed DO mice. Indeed, mean levels of LDH activity, TNF-α, and TGF-β, but not IL-6 were elevated in mice exposed to silica (**Figures 2C–F**; Table S1 in Supplementary Material). Mean LDH activity increased with dose of silica, but only reached statistical significance with the 10 mg dose. Likewise, the percent of mice with elevated LDH activity was significantly higher in the 10 mg group. Similar findings were observed for TNF-α, however, the increases in mean values were only modest. In contrast, mean TGF-β levels were substantially higher in both silica dose groups. Taken together, our findings show that three of four reported BALF biomarkers for human pulmonary silicosis were elevated in a significant percentage of silica-exposed DO mice particularly at the higher exposure.

Autoimmunity

To assess the frequency of systemic autoimmunity induced by silica exposure in the DO population, we examined immunoglobulin and autoantibody levels, spleen size, and kidney pathology. Mean serum IgM and IgG levels were significantly elevated 12 weeks after exposure in mice given 10, but not 5 mg of silica when compared

to PBS controls, consistent with greater activation of the adaptive immune response with higher silica exposure (**Figures 3A,B**; Table S2 in Supplementary Material). Serial ANAs were measured prior to and every 4 weeks after PBS or silica exposure. Strikingly, 45% of mice in the PBS group became positive for ANA (≥1+) at 4 weeks (12–14 weeks of age) despite only two mice being ANA positive (both 1+) at the start of the experiment (**Figure 3F**; Table S2 in Supplementary Material). By 12 weeks, a similar 50% of PBS mice were ANA positive, however, the average ANA score was increased compared to 4 weeks ($p < 0.0001$). The 5 mg-exposed mice were 77% ANA positive at 4 weeks and 66% at 12 weeks. Mean ANA scores also increased over the course of the 12 weeks exposure ($p < 0.0001$) and were significantly higher than the PBS group ($p = 0.006$). In contrast, mice exposed to 10 mg of silica exhibited ANA positivity (50 and 53%, 4 and 12 weeks) and scores that were not significantly different from PBS controls.

Anti-nuclear antibodies specificities were further examined for IgG anti-chromatin and anti-ENA5 (Sm, RNP, SS-A 60 and 52 kDa, SS-B, and Scl-70). Anti-chromatin antibodies at 12 weeks were detected in only 3% (2/68), 16% (14/86), and 4% (5/118) of mice in the 0, 5, and 10 mg groups, respectively, a much lower percentage than ANAs (**Figure 4A**; Table S2 in Supplementary Material). In contrast, when ANA-positive mice were examined, silica exposure was associated with substantially higher levels and percentages of anti-ENA5 antibodies compared to unexposed controls ($p < 0.0001$) (**Figure 4C**). Most of the ENA5 reactivity

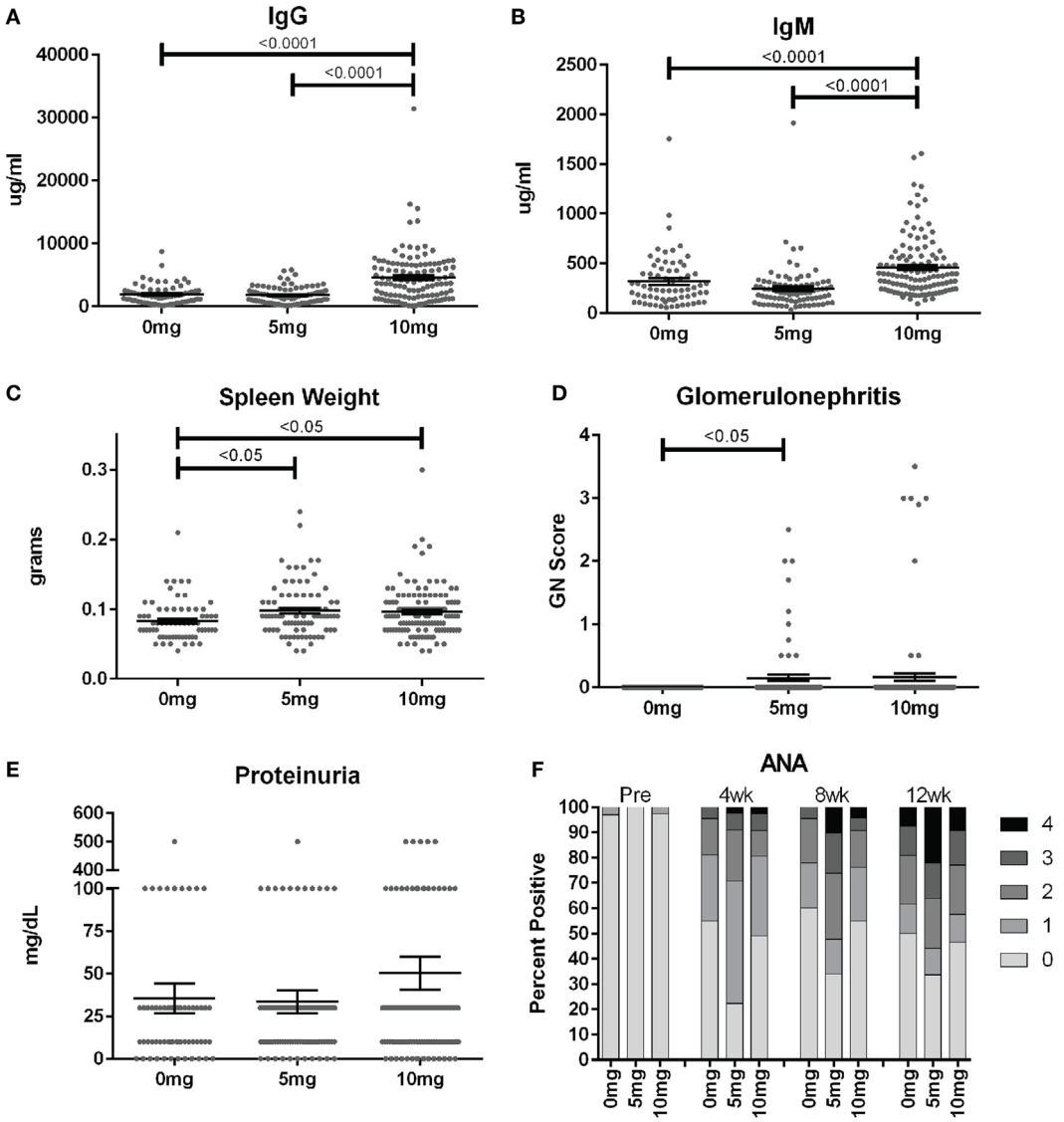

FIGURE 3 | Indices of silica-induced autoimmunity in diversity outbred mice. Mice were exposed transorally to crystalline silica in PBS (see **Figure 1**) before blood was collected for determination of serum **(A)** IgG and **(B)** IgM and **(C)** spleen weight. **(D)** Glomerulonephritis was determined by reviewing and scoring Periodic Acid–Schiff-stained kidney sections and **(E)** proteinuria was measured in the urine using Chemstrips. **(F)** Blood was collected prior to exposure and every 4 weeks thereafter for determination of serum anti-nuclear antibodies by immunofluorescence.

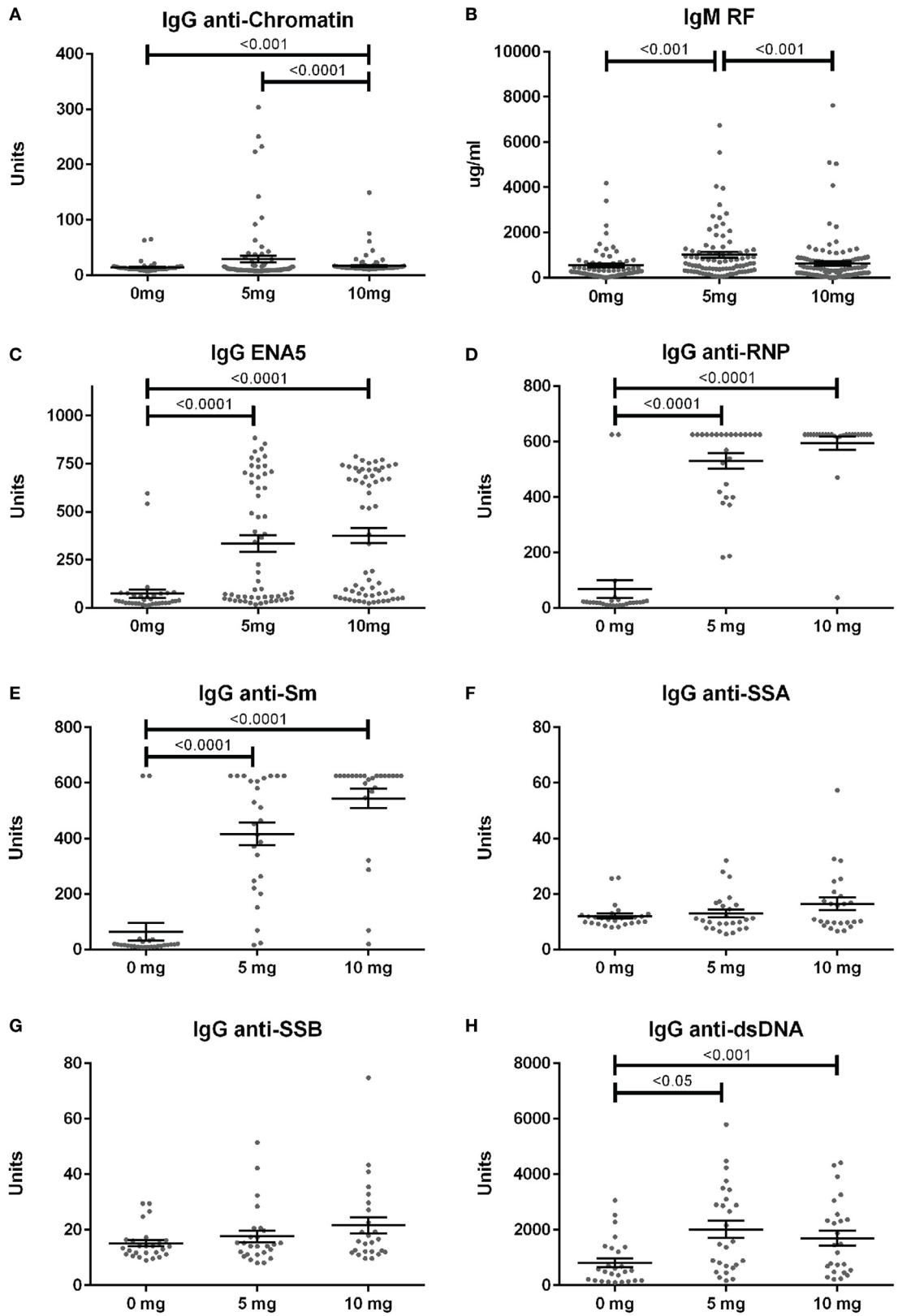

FIGURE 4 | Serum autoantibodies in silica-exposed diversity outbred mice. Mice were exposed transorally to crystalline silica in PBS (see **Figure 1**) before blood was collected for determination of serum autoantibodies: **(A)** IgG anti-chromatin, **(B)** IgM rheumatoid factor, **(C)** ENA5 [designed for the detection of IgG anti-Sm, -RNP, -SSA (60 and 52 kDa), -SSB, and -Scl-70 IgG antibodies], **(D)** IgG anti-RNP, **(E)** IgG anti-Sm, **(F)** IgG anti-SSA, **(G)** IgG anti-SSB, and **(H)** IgG anti-dsDNA.

was to RNP (85 and 96% for 5 and 10 mg exposures) and Sm (58 and 84%), whereas anti-SSA (60 and 52 kDa) (12 and 20%) and anti-SSB (15 and 28%) specificities were present, but occurred less frequently (**Figures 4D–G**). IgM rheumatoid factor (RF) and anti-dsDNA were also elevated in a subset of silica-exposed mice with higher levels present in mice exposed to the lower dose of silica (**Figures 4B,H**).

In addition to the serological changes, a modest increase in spleen weight was observed in both groups of silica-exposed mice compared to controls (**Figure 3C**). Glomerulonephritis ranging from mild to severe was also observed by histology in a few silica-exposed mice at both doses, but in none of the PBS mice (**Figure 3D**). Two of the mice with glomerulonephritis developed significant proteinuria at 12 weeks (**Figure 3E**).

Correlations Between Lung Pathology, Biomarkers of Silicosis, and Autoimmunity

We next looked for correlations between the severity of silica-induced lung pathology, biomarkers of silicosis in BALF, and autoimmune disease manifestations in silica-exposed mice at 12 weeks. A significant correlation with TLS was found for all biomarkers, except IL-6, with TGF-β and TNF-α having strong and LDH activity moderate Spearman's correlation coefficient (r_s) values (**Figure 5A**; Table S3 in Supplementary Material). Similarly, several immune parameters, including total IgG and IgM, anti-ENA5, and anti-chromatin exhibited moderate correlation with lung pathology (**Figure 5A**; Table S4 in Supplementary Material). As expected, the anti-ENA5 response was strongly correlated with anti-RNP and anti-Sm, the most common ENA5 autoantibodies induced by silica (**Figure 5A**).

Hierarchical clustering analysis was also performed to determine unbiased relationships between biomarkers of silicosis, BALF and lung pathology, and autoimmunity, as well as between PBS and silica-exposed DO mice. Accordingly, DO mice showed clear distinction between the 10 mg dose and other groups due in large part to greater severity of lung pathology, BALF cytokines, immunoglobulin levels, and ENA5 antibodies, while there was less demarcation of the 0 and 5 mg silica groups (**Figure 5B**, horizontal clustering). The pulmonary and autoimmune phenotypes were divided into four main groups: RF, pre-bleed ANA, and proteinuria (cluster a); ANA, anti-dsDNA, anti-SSA, anti-SSB, and glomerulonephritis (cluster b); BALF protein and IL-6, and serum IgG, IgM, and anti-chromatin (cluster c); and lung pathology, BALF cell numbers, TGF-β, TNF-α, LDH activity, and antibodies to ENA5, Sm, and RNP (cluster d) (**Figure 5B**, vertical clustering). These results confirmed the connection between lung and BALF pathology and with the development of anti-ENA5, specifically anti-RNP and anti-Sm (cluster d). The separate cluster c contained mainly other immunopathologic consequences of pulmonary silicosis and inflammation. Finally, cluster b consisted of manifestations associated with systemic autoimmune diseases,

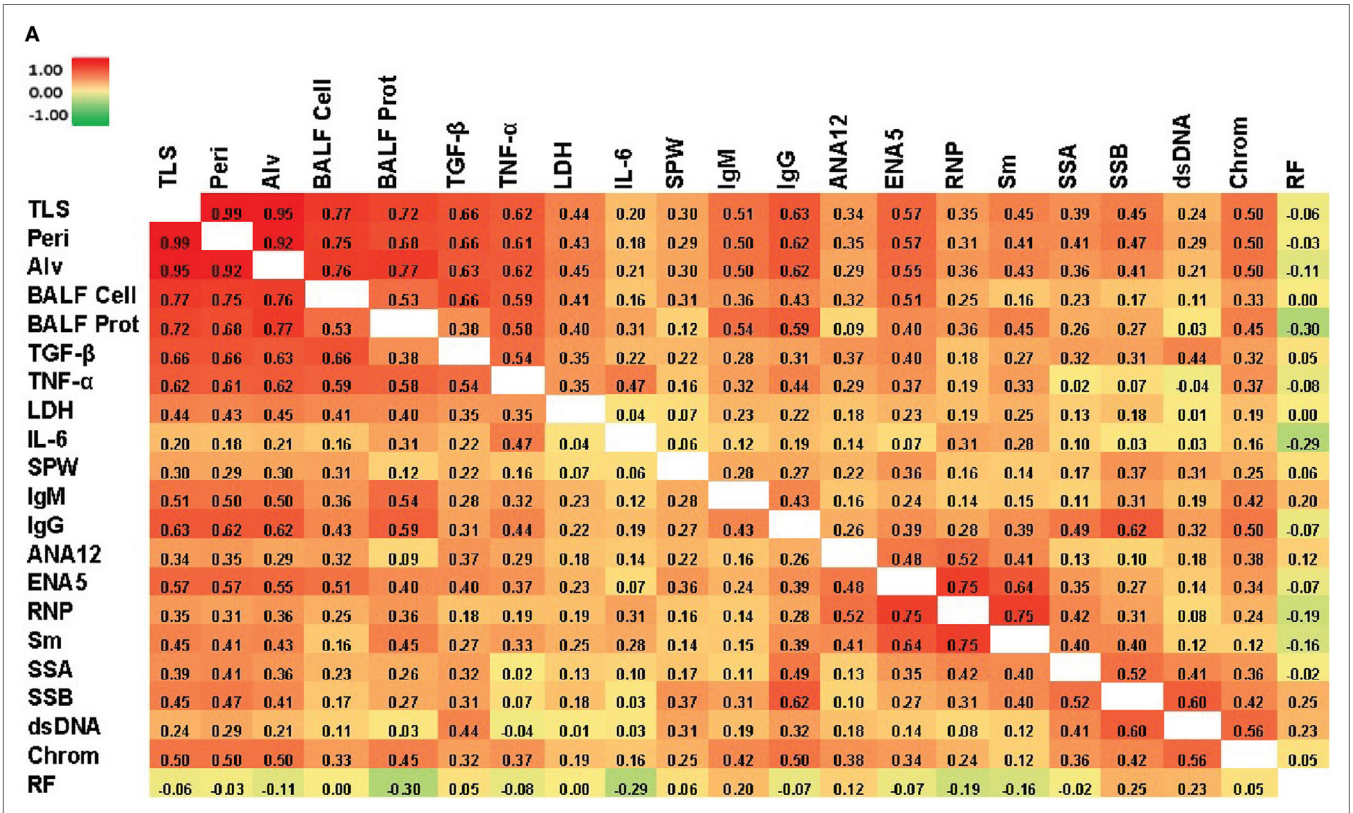

FIGURE 5 | Continued

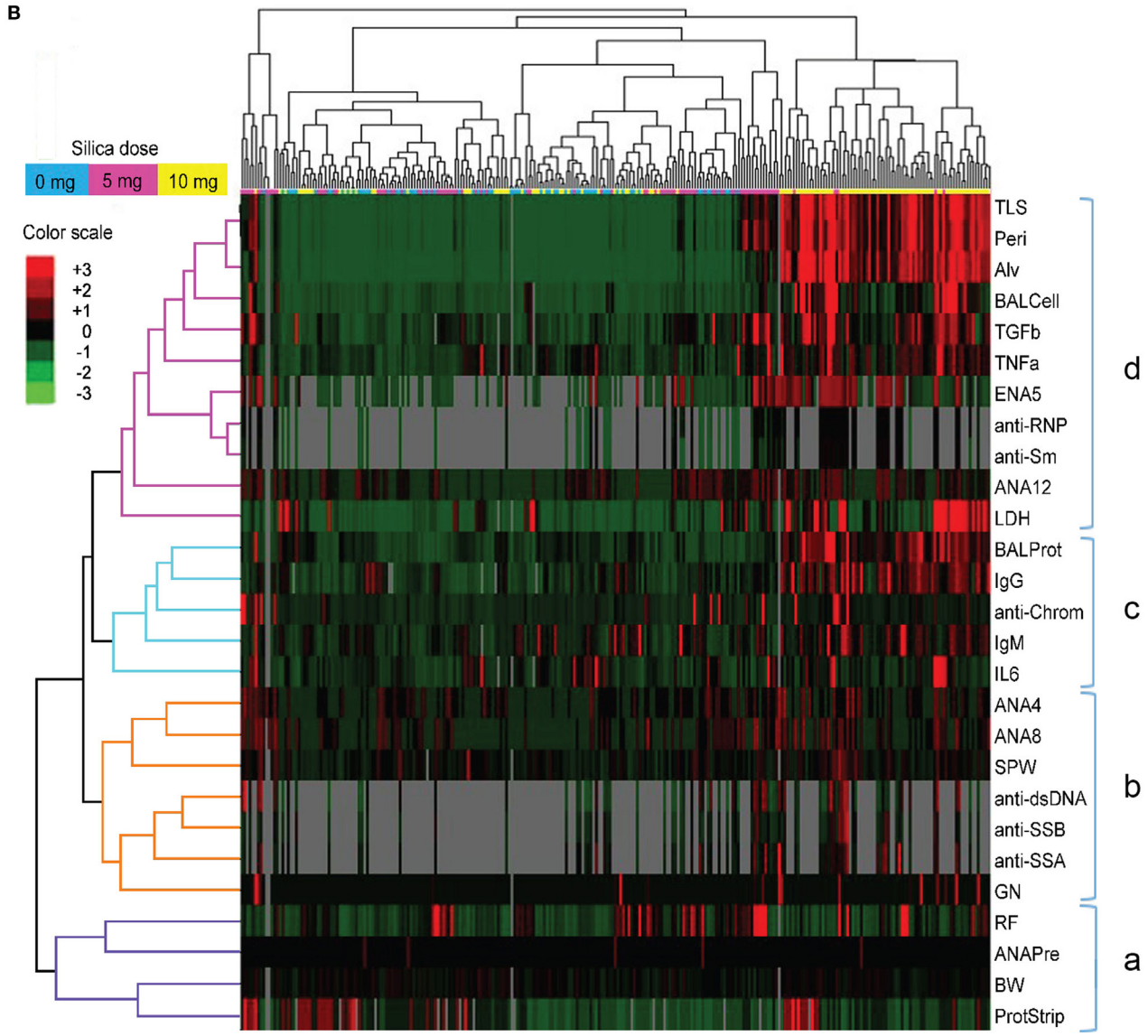

FIGURE 5 | Correlations of biomarkers in silica-exposed diversity outbred mice. **(A)** Correlation matrix of Spearman's correlation coefficient (r_s) values for mice exposed transorally to 5 or 10 mg of crystalline silica. Spearman's r_s values were calculated using pairwise deletion and represented by a color gradient scale with red = 1, yellow = 0, and green = −1. **(B)** Hierarchical cluster analysis of phenotypes and samples using a complete linkage clustering method and Spearman Rank Correlation as the similarity metric. Values are reported as relative change from the average of all samples for each phenotype with red = positive relative change, black = no difference, green = negative relative change, and gray = no data available. Dose groups are indicated by the color bar below the sample cluster with blue = 0 mg, purple = 5 mg, and yellow = 10 mg. Separate clusters are defined by a, b, c, and d. Abbreviations: TLS, total lung score; Peri, perivasculitis and peribronchitis; Alv, alveolitis; BALF cell, bronchial alveolar lavage fluid (BALF) total cell number; BALF Prot, BALF protein levels; LDH, lactate dehydrogenase (LDH) activity; SPW, spleen weight; ANA12, anti-nuclear antibody (ANA) score after 12 weeks of exposure; ENA5, designed for the detection of anti-Sm, -RNP, -SS-A (60 kDa and 52 kDa), -SS-B, and -Scl-70 IgG antibodies; RNP, anti-RNP IgG; Sm, anti-Sm IgG; SSA, anti-SSA IgG; SSB, anti-SSB IgG; dsDNA, anti-dsDNA IgG; Chrom, anti-chromatin IgG, ANA4, ANA score after 4 weeks of exposure; ANA8, ANA score after 8 weeks of exposure; ANAPre, ANA score before exposure; BW, body weight; GN, glomerulonephritis; ProtStrip, urine protein using ChemStrip assay.

such as lupus, but was more separated from silica-induced lung pathology. Thus, in DO mice certain autoimmune manifestations, such as anti-Sm and -RNP, are more strongly associated with the severity of pulmonary silicosis whereas others such as anti-dsDNA and glomerulonephritis are also dependent on other factors, possibly genetic predisposition.

Sex Effects

We next looked for potential sex effects on lung pathology, biomarkers of silicosis in BALF and autoimmunity. Using a two-way (sex and dose) ANOVA with Sidak's multiple comparisons we found a significant sex effect in BALF cell number ($p < 0.01$), ENA5 ($p < 0.05$), urine protein levels ($p < 0.0001$), and body

weight ($p < 0.0001$). Additionally, males had significantly higher alveolitis, BALF cell numbers, BALF IL-6, and ENA5 autoantibodies than females in the 10 mg dose group (**Figures 6A–D**). Therefore, major sex differences are reflected in greater lung inflammation, BALF cells and IL-6, and silica-induced anti-ENA5 autoantibodies in male DO mice.

DISCUSSION

In this study, we characterized the range of crystalline silica-associated pathology in the genetically heterogeneous DO mouse population to determine whether this model was suitable for defining causal mechanisms of both pulmonary silicosis and silica-induced autoimmunity. Indeed, a number of novel observations from this study provide strong support for that premise. First, DO mice were found to exhibit a wide variation in lung involvement, cytokine production, and importantly systemic autoimmune disease manifestations after a single inhalation exposure to silica. Second, cytokine and enzyme biomarkers associated with human pulmonary silicosis were also increased in silica-exposed mice. Third, circulating immunoglobulins and ANAs were increased with silica exposure along with the acquisition of anti-ENA specificity. Fourth, hierarchical clustering revealed that while anti-ENA5, -Sm, and -RNP responses are linked to lung pathology, other autoantibody responses (anti-DNA, -SSA, -SSB) as well as GN, are more distantly linked to the effects of silica on the lung. Additionally, about half of PBS-treated DO control mice were also ANA positive, but in contrast to silica-exposed mice, almost all lacked reactivity to common RNA and DNA antigens associated with autoimmune disease. Fifth, lupus-like glomerulonephritis although uncommon, only developed in silica-exposed mice. Finally, unlike the female bias of idiopathic systemic autoimmunity (33), sex effects of silica exposure on DO mice were more evident in males. These findings provide new insights into the effects of genetic diversity on the pathogenesis of silicosis and silica-induced autoimmunity.

In this study, a single dose of 5 and 10 mg of silica was used, which might be considered high when compared to calculated human exposures (19). However, in the absence of a standardized dose and method of administration (1, 3, 8, 16, 19, 20, 34), we selected, after comparing different routes and doses, amounts of silica in the range that produced lung pathology similar in severity to chronic human silicosis. Furthermore, the single dose by transoral instillation resulted in the most uniform presence of silica in the lung (data not shown) and reproducibility.

Silica exposure resulted in a range of lung pathologies, from mild to severe with varying degrees of peribronchial, perivascular, and alveolar inflammation even within a single dosage group. There was also a clear dose response with the 10 mg exposure group having significantly greater lung involvement and severity. These findings are consistent with previous studies in a few mouse strains that documented significant differences in the severity and type of pulmonary lesions after inhalation of silica-containing particles (9, 16, 19, 35). Less responsive strains include C57BL/6, BALB/c, and NZW while more responsive strains include C3H/HeN, MRL/MpJ, NZB, NZM2410, and (NZBxNZW) F_1 (9, 16, 20), many of which are predisposed to lupus. Among the reported strains, only the less susceptible C57BL/6 is included in the DO founders. These findings are consistent with the variations observed in human exposures (2, 4–11) and

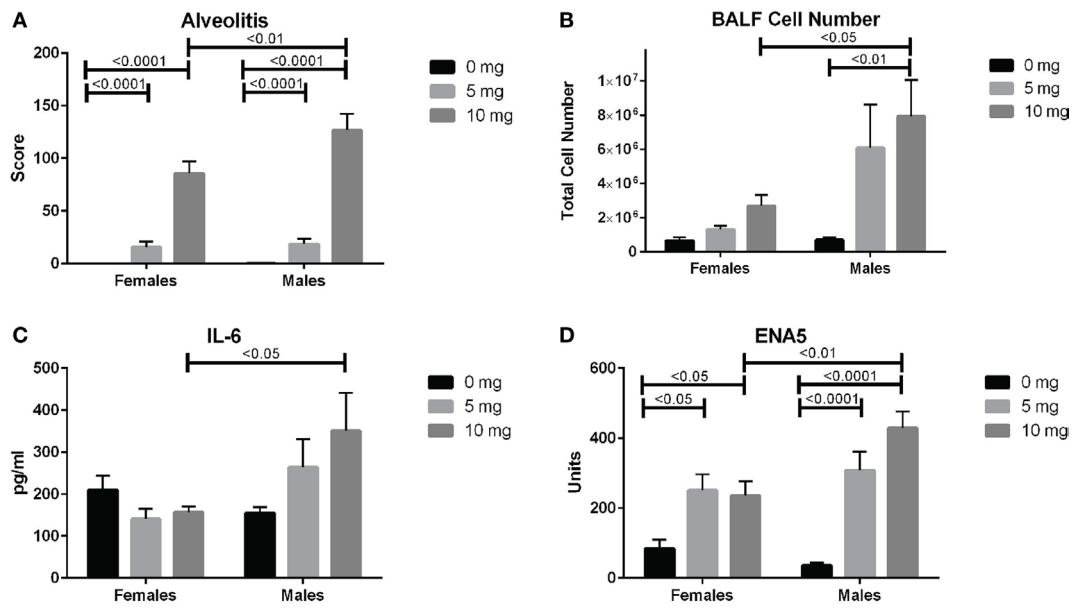

FIGURE 6 | Sex differences in silica-exposed diversity outbred mice. Mice were exposed transorally to crystalline silica in PBS (see **Figure 1**) and females and males analyzed separately for sex effects by two-way ANOVA using Sidak's multiple comparisons. Males exposed to 10 mg were found to have higher **(A)** alveolitis, **(B)** bronchoalveolar lavage fluid (BALF) cell number, **(C)** BALF IL-6, and **(D)** ENA5 autoantibodies compared to females at the same dose.

support the importance of genetic influences on susceptibility to silicosis.

Several potential biomarkers of human silicosis identified in human exposure studies, TGF-β, TNF-α and LDH (3, 32, 36), were also elevated in the BALF of silica-exposed DO mice. Among these, TGF-β appeared to be the most robust as it was increased in both low and high dose silica exposure groups and had the strongest association with lung pathology score. In contrast, IL-6, which was only elevated in a small subset of, mainly male, DO mice exposed to the higher dose, may not be a suitable marker of silicosis, but might indicate extreme exposure. Taken together, these results are consistent with similar silica-mediated inflammatory mechanisms occurring in the lungs of humans and DO mice.

Silica-induced autoimmunity in DO mice included mild splenomegaly, autoantibodies to nuclear antigens commonly detected in lupus and mixed connective tissue disease, and glomerulonephritis. Autoimmunity was slightly more severe in the lower silica dose group, with higher levels of ANA, anti-chromatin, anti-dsDNA, RF, and glomerulonephritis than both the PBS and higher dose groups. Interestingly, and of significance in studying autoimmunity in the DO mouse, was the high prevalence (~50%) of ANAs in PBS-controls, which suggests the presence of ANA-promoting variants in many of the founder strains. Indeed, although lupus is not a major characteristic of any DO founders, lupus-predisposing loci have previously been identified in three strains, B6, 129, and NOD (37, 38). Moreover, treatment of prediabetic NOD mice with a single dose of intravenous *Mycobacterium bovis* (*M. bovis*) suppresses diabetes and induces lupus-like manifestations, including autoimmune hemolytic anemia, ANAs, and immune complex-mediated glomerulonephritis (39). Consequently, as silica exposure substantially enhances lupus in mainly susceptible strains (9, 19), the aforementioned predisposing loci responsible for spontaneous and *M. bovis*-induced lupus are also likely relevant to silica-induced autoimmunity. Thus, the DO model provides the means to identify common and unique genetic variants predisposing to spontaneous and silica-induced autoimmunity spanning a broad repertoire of laboratory and wild mouse-derived genomes.

Another striking finding was the high frequency of ENA reactivity of ANAs in both silica-exposed groups compared to PBS controls (~50 vs 6%), which included antibodies to mainly RNP and Sm, but also to SSA and SSB. In contrast, nearly all ANA positive PBS-treated mice lacked reactivity to any of the common lupus-associated autoantigens tested despite only slightly lower ANA scores than mice in the silica-exposed groups. Such DNA and ENA-negative ANAs have been associated with nonpathogenic autoantibodies such as anti-DFS70 and reduced incidence of systemic autoimmune rheumatic disease (40). Thus in DO mice, silica-induced ANAs can be distinguished from spontaneous ANAs by the presence of anti-ENA specificity, which studied in mice indicate that it is primarily mediated by TLR7 signaling (41). Similarly, anti-ENA specificities analyzed in ~1,800 uranium miners exposed to silica dust found increased prevalence of anti-SSA and anti-SSB antibodies particularly in miners with SLE or heavy exposures, however, antibodies to RNP and Sm were uncommon (42). Taken together, these findings are consistent with both genetic variation and silica exposure influencing the development of ANAs and ANA specificities.

Correlation and hierarchical clustering analyses of silica-exposed DO mice further documented the connections between lung pathology and BALF biomarkers (TGF-β, TNF-α, and LDH activity) as well as the association of these pulmonary pathologies with anti-RNP and anti-Sm. The dependence of anti-ENA5 ANAs on silica exposure is not simply secondary to inflammation, since autoimmunity induced by chronic mercury exposure leads to autoantibodies to other nuclear antigens, but not anti-ENA (43). The development of anti-ENA in nearly all ANA-positive DO mice suggests a high frequency of genetic variants predisposing to this specificity among DO founders or less likely that anti-ENA induction by silica is independent of background. In contrast, other autoimmune manifestations, such as ANA, anti-dsDNA, anti-SSA/SSB, and glomerulonephritis clustered together and were less associated with silica-induced lung pathology. These autoimmune traits are likely more dependent on genetic susceptibility than anti-ENA5 in DO mice or the responsible genetic variants are less common. Nevertheless, in either situation, our findings indicate that these autoimmune manifestations are enhanced by silica exposure similar to the early induction of severe autoimmune disease in lupus-prone strains (9, 19). Moreover, these findings argue that silica exposure in itself without the development of silicosis can contribute to autoantibody production, a finding consistent with the presence of autoantibodies in silica-exposed, but silicosis-free, humans (8). Taken together, these findings establish a new definable model to investigate genetic and pathogenic mechanisms of silica-induced autoimmunity.

Here, we document a wide variation in lung inflammatory and autoimmune disease phenotypes within the DO mouse population following inhalation of crystalline silica and also define their major associations. Consequently, our results indicate the presence of both silica-specific as well as genetically imposed autoimmune manifestations, such as anti-ENA and ANA positivity. Thus, exposure of the DO mouse to silica provides a model of the diverse pathologic and autoimmune responses of the human population to environmental silica. Accordingly, the DO system provides a unique opportunity to investigate the genetic pathways and pathophysiologic mechanisms critical for promoting silica-associated autoimmune disease and supports the application of this model in investigating population wide environmental effects.

DATA AVAILABILITY STATEMENT

The dataset analyzed for this study can be found in the supplementary materials for this article.

ETHICS STATEMENT

This study was carried out in accordance with the recommendations of The Scripps Research Institute Institutional Animal Care and Use Committee (IACUC). The protocol was approved by The Scripps Research Institute IACUC.

AUTHOR CONTRIBUTIONS

JM, DK, and KP contributed to conception and design of the study. JM, GE, JC, and RP contributed to mouse maintenance, sample acquisition, execution of experiments, and data analysis. JM, DK, and KP wrote the first draft of the manuscript. All authors contributed to manuscript revision, read and approved the submitted version.

ACKNOWLEDGMENTS

This is manuscript #29625 from The Scripps Research Institute.

FUNDING

This work was supported by the National Institute of Health grant ES024485 to KMP.

SUPPLEMENTARY MATERIAL

The Supplementary Material for this article can be found online at https://www.frontiersin.org/articles/10.3389/fimmu.2018.00874/full#supplementary-material.

REFERENCES

1. Leung CC, Yu IT, Chen W. Silicosis. *Lancet* (2012) 379(9830):2008–18. doi:10.1016/S0140-6736(12)60235-9
2. Pollard KM. Silica, silicosis, and autoimmunity. *Front Immunol* (2016) 7:97. doi:10.3389/fimmu.2016.00097
3. Kawasaki H. A mechanistic review of silica-induced inhalation toxicity. *Inhal Toxicol* (2015) 27(8):363–77. doi:10.3109/08958378.2015.1066905
4. Steenland K, Brown D. Mortality study of gold miners exposed to silica and nonasbestiform amphibole minerals: an update with 14 more years of follow-up. *Am J Ind Med* (1995) 27(2):217–29. doi:10.1002/ajim.4700270207
5. Wilke RA, Salisbury S, Abdel-Rahman E, Brazy PC. Lupus-like autoimmune disease associated with silicosis. *Nephrol Dial Transplant* (1996) 11(9):1835–8. doi:10.1093/ndt/11.9.1835
6. Brown LM, Gridley G, Olsen JH, Mellemkjaer L, Linet MS, Fraumeni JF Jr. Cancer risk and mortality patterns among silicotic men in Sweden and Denmark. *J Occup Environ Med* (1997) 39(7):633–8. doi:10.1097/00043764-199707000-00008
7. Haustein UF, Anderegg U. Silica induced scleroderma – clinical and experimental aspects. *J Rheumatol* (1998) 25(10):1917–26.
8. Parks CG, Conrad K, Cooper GS. Occupational exposure to crystalline silica and autoimmune disease. *Environ Health Perspect* (1999) 107(Suppl 5): 793–802. doi:10.2307/3434342
9. Brown JM, Archer AJ, Pfau JC, Holian A. Silica accelerated systemic autoimmune disease in lupus-prone New Zealand mixed mice. *Clin Exp Immunol* (2003) 131(3):415–21. doi:10.1046/j.1365-2249.2003.02094.x
10. Steenland K. One agent, many diseases: exposure-response data and comparative risks of different outcomes following silica exposure. *Am J Ind Med* (2005) 48(1):16–23. doi:10.1002/ajim.20181
11. Miller FW, Alfredsson L, Costenbader KH, Kamen DL, Nelson LM, Norris JM, et al. Epidemiology of environmental exposures and human autoimmune diseases: findings from a national institute of environmental health sciences expert panel workshop. *J Autoimmun* (2012) 39(4):259–71. doi:10.1016/j.jaut.2012.05.002
12. Pollard KM. Gender differences in autoimmunity associated with exposure to environmental factors. *J Autoimmun* (2012) 38(2–3):J177–86. doi:10.1016/j.jaut.2011.11.007
13. Doll NJ, Stankus RP, Hughes J, Weill H, Gupta RC, Rodriguez M, et al. Immune complexes and autoantibodies in silicosis. *J Allergy Clin Immunol* (1981) 68(4):281–5. doi:10.1016/0091-6749(81)90152-4
14. Conrad K, Stahnke G, Liedvogel B, Mehlhorn J, Barth J, Blasum C, et al. Anti-CENP-B response in sera of uranium miners exposed to quartz dust and patients with possible development of systemic sclerosis (scleroderma). *J Rheumatol* (1995) 22(7):1286–94.
15. Conrad K, Mehlhorn J, Luthke K, Dorner T, Frank KH. Systemic lupus erythematosus after heavy exposure to quartz dust in uranium mines: clinical and serological characteristics. *Lupus* (1996) 5(1):62–9. doi:10.1177/096120339600500112
16. Davis GS, Leslie KO, Hemenway DR. Silicosis in mice: effects of dose, time, and genetic strain. *J Environ Pathol Toxicol Oncol* (1998) 17(2):81–97.
17. Pfau JC, Brown JM, Holian A. Silica-exposed mice generate autoantibodies to apoptotic cells. *Toxicology* (2004) 195(2–3):167–76. doi:10.1016/j.tox.2003.09.011
18. Germolec D, Kono DH, Pfau JC, Pollard KM. Animal models used to examine the role of the environment in the development of autoimmune disease: findings from an NIEHS expert panel workshop. *J Autoimmun* (2012) 39(4):285–93. doi:10.1016/j.jaut.2012.05.020
19. Bates MA, Brandenberger C, Langohr I, Kumagai K, Harkema JR, Holian A, et al. Silica triggers inflammation and ectopic lymphoid neogenesis in the lungs in parallel with accelerated onset of systemic autoimmunity and glomerulonephritis in the lupus-prone NZBWF1 mouse. *PLoS One* (2015) 10(5):e0125481. doi:10.1371/journal.pone.0125481
20. Callis AH, Sohnle PG, Mandel GS, Wiessner J, Mandel NS. Kinetics of inflammatory and fibrotic pulmonary changes in a murine model of silicosis. *J Lab Clin Med* (1985) 105(5):547–53.
21. Parker CC, Palmer AA. Dark matter: are mice the solution to missing heritability? *Front Genet* (2011) 2:32. doi:10.3389/fgene.2011.00032
22. Churchill GA, Gatti DM, Munger SC, Svenson KL. The diversity outbred mouse population. *Mamm Genome* (2012) 23(9–10):713–8. doi:10.1007/s00335-012-9414-2
23. Svenson KL, Gatti DM, Valdar W, Welsh CE, Cheng R, Chesler EJ, et al. High-resolution genetic mapping using the mouse diversity outbred population. *Genetics* (2012) 190(2):437–47. doi:10.1534/genetics.111.132597
24. Logan RW, Robledo RF, Recla JM, Philip VM, Bubier JA, Jay JJ, et al. High-precision genetic mapping of behavioral traits in the diversity outbred mouse population. *Genes Brain Behav* (2013) 12(4):424–37. doi:10.1111/gbb.12029
25. Kelly SA, Pomp D. Genetic determinants of voluntary exercise. *Trends Genet* (2013) 29(6):348–57. doi:10.1016/j.tig.2012.12.007
26. Church RJ, Gatti DM, Urban TJ, Long N, Yang X, Shi Q, et al. Sensitivity to hepatotoxicity due to epigallocatechin gallate is affected by genetic background in diversity outbred mice. *Food Chem Toxicol* (2015) 76:19–26. doi:10.1016/j.fct.2014.11.008
27. French JE, Gatti DM, Morgan DL, Kissling GE, Shockley KR, Knudsen GA, et al. Diversity outbred mice identify population-based exposure thresholds and genetic factors that influence benzene-induced genotoxicity. *Environ Health Perspect* (2015) 123(3):237–45. doi:10.1289/ehp.1408202
28. Biswas R, Trout KL, Jessop F, Harkema JR, Holian A. Imipramine blocks acute silicosis in a mouse model. *Part Fibre Toxicol* (2017) 14(1):36. doi:10.1186/s12989-017-0217-1
29. Hamilton RF Jr, Thakur SA, Mayfair JK, Holian A. MARCO mediates silica uptake and toxicity in alveolar macrophages from C57BL/6 mice. *J Biol Chem* (2006) 281(45):34218–26. doi:10.1074/jbc.M605229200
30. Toomey CB, Cauvi DM, Hamel JC, Ramirez AE, Pollard KM. Cathepsin B regulates the appearance and severity of mercury-induced inflammation and autoimmunity. *Toxicol Sci* (2014) 142(2):339–49. doi:10.1093/toxsci/kfu189
31. Koh YT, Scatizzi JC, Gahan JD, Lawson BR, Baccala R, Pollard KM, et al. Role of nucleic acid-sensing TLRs in diverse autoantibody specificities and anti-nuclear antibody-producing B cells. *J Immunol* (2013) 190(10):4982–90. doi:10.4049/jimmunol.1202986
32. Gulumian M, Borm PJ, Vallyathan V, Castranova V, Donaldson K, Nelson G, et al. Mechanistically identified suitable biomarkers of exposure, effect, and susceptibility for silicosis and coal-worker's pneumoconiosis: a comprehensive review. *J Toxicol Environ Health B Crit Rev* (2006) 9(5):357–95. doi:10.1080/15287390500196537

33. Pollard KM, Hultman P, Toomey CB, Cauvi DM, Hoffman HM, Hamel JC, et al. Definition of IFN-gamma-related pathways critical for chemically-induced systemic autoimmunity. *J Autoimmun* (2012) 39(4):323–31. doi:10.1016/j.jaut.2012.04.003
34. Barbarin V, Nihoul A, Misson P, Arras M, Delos M, Leclercq I, et al. The role of pro- and anti-inflammatory responses in silica-induced lung fibrosis. *Respir Res* (2005) 6:112. doi:10.1186/1465-9921-6-112
35. Bates MA, Brandenberger C, Langohr II, Kumagai K, Lock AL, Harkema JR, et al. Silica-triggered autoimmunity in lupus-prone mice blocked by docosahexaenoic acid consumption. *PLoS One* (2016) 11(8):e0160622. doi:10.1371/journal.pone.0160622
36. Vanhee D, Gosset P, Boitelle A, Wallaert B, Tonnel AB. Cytokines and cytokine network in silicosis and coal workers' pneumoconiosis. *Eur Respir J* (1995) 8(5):834–42.
37. Jordan MA, Silveira PA, Shepherd DP, Chu C, Kinder SJ, Chen J, et al. Linkage analysis of systemic lupus erythematosus induced in diabetes-prone nonobese diabetic mice by *Mycobacterium bovis*. *J Immunol* (2000) 165(3):1673–84. doi:10.4049/jimmunol.165.3.1673
38. Carlucci F, Cortes-Hernandez J, Fossati-Jimack L, Bygrave AE, Walport MJ, Vyse TJ, et al. Genetic dissection of spontaneous autoimmunity driven by 129-derived chromosome 1 loci when expressed on C57BL/6 mice. *J Immunol* (2007) 178(4):2352–60. doi:10.4049/jimmunol.178.4.2352
39. Baxter AG, Horsfall AC, Healey D, Ozegbe P, Day S, Williams DG, et al. Mycobacteria precipitate an SLE-like syndrome in diabetes-prone NOD mice. *Immunology* (1994) 83(2):227–31.
40. Gundin S, Irure-Ventura J, Asensio E, Ramos D, Mahler M, Martinez-Taboada V, et al. Measurement of anti-DFS70 antibodies in patients with ANA-associated autoimmune rheumatic diseases suspicion is cost-effective. *Auto Immun Highlights* (2016) 7(1):10. doi:10.1007/s13317-016-0082-1
41. Kono DH, Baccala R, Theofilopoulos AN. TLRs and interferons: a central paradigm in autoimmunity. *Curr Opin Immunol* (2013) 25(6):720–7. doi:10.1016/j.coi.2013.10.006
42. Conrad K, Mehlhorn J. Diagnostic and prognostic relevance of autoantibodies in uranium miners. *Int Arch Allergy Immunol* (2000) 123(1):77–91. doi:10.1159/000024426
43. Hultman P, Bell LJ, Enestrom S, Pollard KM. Murine susceptibility to mercury. I. Autoantibody profiles and systemic immune deposits in inbred, congenic, and intra-H-2 recombinant strains. *Clin Immunol Immunopathol* (1992) 65(2):98–109. doi:10.1016/0090-1229(92)90212-7

Conflict of Interest Statement: The authors declare that the research was conducted in the absence of any commercial or financial relationships that could be construed as a potential conflict of interest.

frontiers in Immunology

ORIGINAL RESEARCH
published: 15 March 2018
doi: 10.3389/fimmu.2018.00534

Extracellular Vesicle Subtypes Released From Activated or Apoptotic T-Lymphocytes Carry a Specific and Stimulus-Dependent Protein Cargo

Christine Tucher[1], Konrad Bode[2,3], Petra Schiller[1], Laura Claßen[1], Carolin Birr[1], Maria Margarida Souto-Carneiro[1], Norbert Blank[1], Hanns-Martin Lorenz[1,4] and Martin Schiller[1]*

[1] Division of Rheumatology, Department of Internal Medicine V, University Hospital Heidelberg, Heidelberg, Germany, [2] Department of Infectious Diseases, Medical Microbiology and Hygiene, University Hospital Heidelberg, Heidelberg, Germany, [3] Laboratory Dr. Limbach and Colleagues, Medical Care Unit, Heidelberg, Germany, [4] ACURA Center for Rheumatic Diseases, Baden-Baden, Germany

OPEN ACCESS

Edited by:
Philippe Saas, INSERM UMR1098 Interactions Hôte-Greffon-Tumeur & Ingénierie Cellulaire et Génique, France

Reviewed by:
Zsuzsa Szondy, University of Debrecen, Hungary
Adam Bruno Ceroi, Ghent University, Belgium

***Correspondence:**
Christine Tucher
christinetucher@freenet.de

Specialty section:
This article was submitted to Inflammation, a section of the journal Frontiers in Immunology

Received: *25 October 2017*
Accepted: *02 March 2018*
Published: *15 March 2018*

Citation:
Tucher C, Bode K, Schiller P, Claßen L, Birr C, Souto-Carneiro MM, Blank N, Lorenz H-M and Schiller M (2018) Extracellular Vesicle Subtypes Released From Activated or Apoptotic T-Lymphocytes Carry a Specific and Stimulus-Dependent Protein Cargo. Front. Immunol. 9:534. doi: 10.3389/fimmu.2018.00534

Extracellular vesicles (EVs) are released from nearly all mammalian cells and different EV populations have been described. Microvesicles represent large EVs (LEVs) released from the cellular surface, while exosomes are small EVs (SEVs) released from an intracellular compartment. As it is likely that different stimuli promote the release of distinct EV populations, we analyzed EVs from human lymphocytes considering the respective release stimuli (activation Vs. apoptosis induction). We could clearly separate two EV populations, namely SEVs (average diameter <200 nm) and LEVs (diameter range between 200 and 1000 nm). Morphology and size were analyzed by electron microscopy and nanoparticle tracking analysis. Apoptosis induction caused a massive release of LEVs, while activated T-cells released SEVs and LEVs in considerably lower amounts. The release of SEVs from apoptotic T-cells was comparable with LEV release from activated ones. LEVs contained signaling proteins and proteins of the actin-myosin cytoskeleton. SEVs carried cytoplasmic/endosomal proteins like the 70-kDa heat shock protein 70 (HSP70) or tumor susceptibility 101 (TSG101), microtubule-associated proteins, and ubiquitinated proteins. The protein expression profile of SEVs and LEVs changed substantially after the induction of apoptosis. After apoptosis induction, HSP70 and TSG101 (often used as exosome markers) were highly expressed within LEVs. Interestingly, in contrast to HSP70 and TSG101, gelsolin and eps15 homology domain-containing protein 3 (EHD3) turned out to be specific for SEVs irrespective of the stimulus causing the EV release. Finally, we detected several subunits of the proteasome (PSMB9, PSMB10) as well as the danger signal HMGB1 exclusively within apoptotic cell-released LEVs. Thus, we were able to identify new marker proteins that can be useful to discriminate between distinct LEV subpopulations. The mass spectrometry proteomics data are available *via* ProteomeXchange with identifier PXD009074.

Keywords: apoptosis, exosomes, extracellular vesicles, microvesicles, stimulus-dependent release

INTRODUCTION

Extracellular vesicles (EVs) are released from a variety of mammalian cells. These vesicles can be discriminated by size or molecular composition and two main EV populations have been described. To date, a population of large EVs (LEVs)—released from the cellular surface—is distinguished from a population of small EVs (SEVs), which is released from an intracellular/endosomal compartment, the multivesicular body. These EV populations have been termed microvesicles (considering LEVs) and exosomes (considering SEVs, respectively). Microvesicles are large vesicles with varying sizes in a diameter range from 200 up to 1,000 nm. These vesicles carry receptors and surface molecules from the cell of origin (1–6). The release of microvesicles results from reorganization of the actin-myosin cytoskeleton, and occurs by direct budding of the outer cellular membrane (7–9). Exosomes are vesicles smaller than 200 nm and are released from an intracellular/endosomal compartment, called multivesicular body (4, 10). Due to their endosomal origin exosomes carry endosome-associated proteins, such as Rab GTPases, Alix, or tumor susceptibility 101 (TSG101) (11–13). Exosomes and their molecular composition have intensively been studied and TSG101, the 70-kDa heat shock protein 70 (HSP70) or tetraspanins (e.g., CD63, CD81) have been reported as exosome marker proteins (14–19).

Beside analyses of their protein cargo, EVs have been reported to carry DNA or distinct RNAs and they are able to transfer genetic information from cell to cell (20–26). Thus, EVs are increasingly recognized as mediators of intercellular communication (27–30), and their role in the pathogenesis of autoimmune diseases or tumor growth has been discussed (3, 31–36). However, while the EV field is rapidly expanding, there is an urgent need to better define vesicle subpopulations. Meanwhile, the heterogeneity of EVs is a well-known fact and it has become evident that SEVs (often called exosomes) consist of diverse subpopulations. A diversity that applies for LEVs (often referred to as microvesicles or apoptotic bodies) as well (5, 17, 37).

The release of EVs can be triggered by many stimuli like cellular activation or apoptosis induction (5, 38). Thus, it seems obvious that different stimuli might favor the release of a distinct EV type. Recently, a first systematic study by Théry and co-workers analyzed and directly compared the protein content of exosomal and non-exosomal EVs released from primary human monocyte-derived dendritic cells was analyzed (39). Nevertheless, a comparative study, which systematically analyzes EVs, released after different stimulation conditions (i.e., cellular activation or apoptosis induction) is still needed. To address this issue, EVs were isolated from primary human T-lymphocytes. Activated T-lymphocytes were generated by PHA/IL-2 stimulation of PBMCs resulting in >95% CD3 positive T-cells (23, 40–42) (for details see Materials and Methods). These activated T-cells were then further stimulated with IL-2 or induced to undergo apoptosis by UV-B irradiation. LEVs were isolated by filtration following an ultracentrifugation at 10,000 × *g*. In a further ultracentrifugation step (100,000 × *g*), SEVs were isolated.

Both vesicle populations (SEVs and LEVs, respectively) were isolated either after cellular activation or after the induction of apoptosis. SEVs and LEVs were quantified, morphologically analyzed, and the protein content of each distinct EV population was investigated. We could show that apoptosis induction is the most potent stimulus for the release of LEVs. SEVs and LEVs were released in considerably lower amounts from activated T-cells. SEV release from apoptotic T-cells was comparable to LEV release from activated ones. Moreover, we demonstrated that the protein cargo of SEVs and LEVs is tightly regulated and dependent on the stimulus causing EV release, with apoptosis induction dramatically changing the protein cargo of both vesicle populations. As an example, when analyzing vesicles released from viable T-cells, TSG101 (a classically used exosome marker) is exclusively found within SEVs. After apoptosis induction, the same protein was detected within LEVs and was virtually excluded from the SEVs population. Similar changes were also observed, when we analyzed protein modifications, such as ubiquitination. By means of two dimensional difference gel electrophoresis (DIGE) followed by mass spectrometry, we were able to identify 24 proteins which are differentially expressed and regulated within SEVs and LEVs after cellular activation or apoptosis induction.

Finally, we have gained insight into the release mechanisms of EVs. We observed proteins of the actin-myosin cytoskeleton (actin, ezrin) within LEVs, whereas microtubule-associated proteins [gelsolin (GSN) or eps15 homology domain-containing protein 3] are exclusively and specifically found within SEVs. Importantly, these two proteins were specific markers for the SEV population even after the induction of apoptotic cell death. Our findings indicate that the release of LEVs is dependent on the activation of the actin-myosin cytoskeleton, suggesting a release from the cellular surface. SEVs, however, seem to be mainly released from inside the cell, and their release is associated with the microtubule apparatus. Furthermore, we observed an accumulation of proteasome subunits within LEVs and showed that the proteasome is involved in the regulation of LEV release. Interestingly, the inducible proteasomal subunits as well as the danger signal protein HMGB1 accumulated in LEVs released from apoptozing T-cells. These proteins can be used as new markers to identify distinct LEV subpopulations.

MATERIALS AND METHODS

Cell Culture

Healthy donors were participated in this study after having given informed consent. The study, approved by the ethics committee of the University of Heidelberg, was conducted according to the ethics guidelines of our institution and those of the Declaration of Helsinki.

Peripheral blood mononuclear cells (PBMCs) were isolated by density gradient centrifugation (LSM 1.077, Merck, Darmstadt, Germany) out of heparinized venous blood from normal healthy donors. PBMCs were washed twice in phosphate-buffered saline (PBS, Sigma, Taufkirchen, Germany) and were cultured in RPMI 1640 (Life Science Technologies, Darmstadt, Germany) supplemented with 10% (v/v) heat inactivated fetal calf serum (Gibco-BRL, Eggenstein, Germany) 10 mM HEPES buffer, 4 mM L-glutamine and penicillin-streptomycin (Sigma, Taufkirchen,

Germany). Cell viability was checked by trypan blue exclusion test. To generate activated T-lymphocytes 1 µg/ml phytohemagglutinine (Sigma, Taufkirchen, Germany) and 0.5 U/ml IL-2 (Roche, Mannheim, Germany) were added to the culture media for 5 days, leading to activation and marked proliferation of T-cells. These PHA/IL-2 activated lymphocytes are >95% CD3 positive (23, 40–44). Cells were then washed and stimulated with additionally 0.5 U/ml IL-2 to further expand T-cells.

Isolation of LEVs and SEVs

Extracellular vesicles-depleted culture medium was prepared overnight by centrifugation at 100,000 × *g* in a 70Ti rotor (Beckman Coulter, Krefeld Germany). To isolate EVs, T-cells were washed with PBS and plated into cell culture dishes with up to 100 × 10^6 T-cells per 30 ml EV-depleted culture medium. T-cells were either activated by the addition of IL-2 or induced to undergo apoptosis by UV-B irradiation for 30 s (90 J/cm^2). Afterward T-cells were cultured for 20 h, LEVs and SEVs were isolated by differential ultracentrifugation. Before EV isolation, cell vitality was always assessed by staining with AnnexinV (AxV, Böhringer, Mannheim, Germany) and propidiumiodide (PI, Sigma, Taufkirchen, Germany). In short, T-cells were incubated with 200 ng of AxV-FITC and 500 ng PI in 500 µl Ringer's solution (B. Braun, Melsungen, Germany) for 30 min at 4°C and analyzed by flow cytometry. To deplete whole T-cells or apoptotic cellular remnants before EV isolation the cell suspension was centrifuged at 300 × *g*, 5 min and the remaining supernatant was passed through a 1.2 µm non-pyrogenic, hydrophilic syringe filter into ultracentrifuge tubes (Beckman Coulter). Subsequently, EVs were isolated by centrifugation at 10,000 × *g* for 45 min at 10°C in a 70Ti rotor (Beckman Coulter) to receive LEV pellets. The resulting supernatant was then centrifuged at 100,000 × *g* for 45 min at 10°C to receive SEV pellets. All pellets were resuspended in either 50 µl sterile PBS for nanoparticle tracking analysis (NTA) or in 10 µl RIPA-lysis buffer (c-c-pro, Neustadt, Germany) supplemented with protease inhibitors for protein analysis (complete Mini, Böhringer, Mannheim, Germany).

Nanoparticle Tracking Analysis

A NS300 NTA machine (Malvern, Amesbury, United Kingdom) was used to analyze isolated EVs. Following camera settings were used: camera level 13/14, screen gain 1.0, and threshold 6. For each sample, a quick measurement for 60 s was performed to ensure right dilution factor and camera settings. Standard measurement was performed by taking at least three videos with 60 s, with more than 500 tracks per video.

Immunoblot Analysis

Extracellular vesicles pellets were resuspended and lysed in RIPA-lysis buffer (c-c-pro, Neustadt, Germany) supplemented with proteases inhibitor cocktail (complete Mini, Böhringer, Mannheim, Germany) for 30 min on ice. Lysates were centrifuged by 16,000 × *g* for 10 min at 4°C. Afterward, the supernatant of each probe was transferred into a new microfuge tube and the protein concentration was quantified by BCA assay (Life Technologies, Darmstadt, Germany). 15 µg protein of each probe was diluted in loading buffer and loaded onto a 12.5% SDS-PAGE. After transfer to PVDF membranes, proteins were detected by using the following antibodies:

Rabbit polyclonal anti-human: Actin (Sigma, Taufkirchen, Germany), ERK1 (K-23), HSP90 (Santa Cruz, Heidelberg, Germany), LAT (Upstate Biotechnology, New York, NY, USA), PSMA1 (clone N1C3, Biozol, Eching, Germany), ZAP70 (Epitomics, Burlingame, Canada). Goat polyclonal anti-human: Ezrin (C-19), GSN (N-18) (Santa Cruz, Heidelberg, Germany), PSMB10 (Biotechne, Wiesbaden-Nordenstadt, Germany). Mouse monoclonal anti-human: pERK (E-4), EHD3, HSP70, Ubiquitination (Santa Cruz, Heidelberg, Germany), LCK (clone 28, BD Pharmingen, Heidelberg, Germany), anti-TSG101 (clone 4A10), PSMB9 (clone 792520, Biotechne, Wiesbaden-Nordenstadt, Germany). Blots were treated with species-specific horseradish peroxidase-labeled antibodies (Dianova, Hamburg, Germany) and signals were detected with enhanced chemiluminescence (Amersham Biosiences, Freiburg, Germany).

Two Dimensional DIGE

Isolated EVs obtained from activated and apoptozing T-lymphocytes (three normal healthy donors) were lysed in THC buffer supplemented with 1 µg/ml Aprotonin, Leupeptin, Pepstatin, and 200 mM PMSF (Merck, Darmstadt, Germany). Lysates were sonicated (program: 1 s pulse and 5 s pulse off, 3 min, amplitude: 90%) two times at 4°C and centrifuged at 20,000 rpm for 15 min at 4°C. The supernatant was transferred into a new microfuge tube and protein concentration was determined by Bradford assay. Afterward each probe was divided into three parts with equal protein amounts of 5 µg. Each part was labeled with a specific dye for DIGE preparations (CYDYE DIGE Fluor CY3/CY5, VWR, Darmstadt, Germany). An internal standard was generated through mixing 5 µg protein of each probe and labeling with CY2 (CYDYE DIGE Fluor, VWR, Darmstadt, Germany). After labeling, probes were loaded onto pH stripes (VWR, Darmstadt, Germany) for the protein separation in the first dimension (isoelectric point). Then proteins were separated in the second dimension (molecular weight, standard SDS-PAGE). The experiments were performed in triplicates. Including the standards, 36 gels were obtained. To identify protein spots, 2D-gels were scanned (IPGphor3, GE Healthcare, Freiburg, Germany) and analyzed by a DIGE DeCyder machine and software (V7.0).

Mass Spectrometry

After the analysis by the DIGE DeCyder machine and software (GE Healthcare, Freiburg, Germany) we selected 24 protein spots, for identification of the proteins by mass spectrometry. Selected protein spots were picked out of the SDS-gels using an Ettan spot picker (GE Healthcare, Freiburg, Germany) and analyzed by mass spectrometry (LC-MS/MS). Mass spectrometry was performed at the Core Facility for Mass Spectrometry in the ZMBH in Heidelberg. The mass spectrometry proteomics data have been deposited to the ProteomeXchange Consortium via the PRIDE (45, 46) partner repository with the dataset identifier PXD009074 and 10.6019/PXD009074.

Transmission Electron Microscopy (TEM)

Isolated and pelleted EVs were fixed in glutaraldehyde-PBS (2% final). After washing and post-fixing in osmium tetroxide (2%) and K4[Fe(CN)6] (1.5%), samples were totally enclosed in contrast solution uranyl acetate, dehydrated with a graded dilution series of ethanol, and finally embedded into glycid-ether-100-based resin. Ultrathin sections were cut (Reichert Ultracut S ultramicrotome, Leica Microsystems). Slices were contrasted and analyzed with a Zeiss EM 10 CR electron microscope.

Proteasome Inhibition Assay

Activated T-lymphocytes were induced to undergo apoptosis by UV-B irradiation for 30 s (90 J/cm^2) in the presence or absence of 1 nM bortezomib (Santa Cruz, Heidelberg, Germany) or 10 µM Y27632 (Merck, Darmstadt, Germany). After 20 h, the amount of released LEVs was quantified by flow cytometry (FSC/SSC analysis), using an EPICS XL™ flow cytometer (Coulter, Hialeah, Fl, USA). Cell viability was assessed by AxV/PI staining as described above.

Statistics

Paired two-tailed Student's *t*-tests was used to perform statistical analysis. Experiments, in which cells of the same donor were treated with different conditions, and the respective experiment was repeated *n*-times with different donors, paired two-tailed Student's *t*-tests was performed. All statistical analyses, excluding DIGE analysis, were performed using the statistical software GraphPad Prism 5.0 (GraphPad Software, Inc., San Diego, CA, USA).

Statistical analysis for DIGE analysis was performed using DIGE DeCyder software V7.0 (GE Healthcare, Freiburg, Germany). Statistical level of significance was determined as a *p*-value of <0.05.

RESULTS

Morphologic Characterization of EVs Released From Activated or Apoptozing Human T-Lymphocytes

The morphology and molecular composition of EVs have intensively been studied since their discovery. However, vesicle preparations have been analyzed using different cellular models and distinct stimuli causing EV release (22, 47). So far, no study has analyzed different EV populations and simultaneously considered the respective release stimulus. Therefore, we characterized and compared different EV populations released either after cellular activation or after apoptosis induction.

Large EVs and SEVs were isolated from the supernatant of activated or apoptozing primary human T-lymphocytes. After apoptosis induction, the amount of AxV+ positive and PI− negative T-cells was markedly increased (90% increase, $p = 0.00004$, **Figure 1C**). The percentage of necrotic T-cells (AxV+/PI+ positive ones) was only slightly increased (8.7% increase, $p = 0.004$, **Figure 1C**). The isolation of EVs was performed by filtration followed by differential ultracentrifugation. Collected EVs were analyzed by TEM, NTA, and BCA assay. TEM preparations showed LEVs, released from viable and apoptozing T-cells, as membrane enveloped vesicles in sizes from 200 to 1000 nm in diameter (**Figure 1A**). SEVs, released from viable and apoptozing T-cells, occurred as membrane-coated vesicles, but differed dramatically in size with an average diameter from 50 to 200 nm. Isolated EVs were also analyzed by NTA as shown in **Figure 1B**. For LEVs isolated from viable T-cells a mean size of 330 nm was calculated, whereas LEVs released from apoptozing T-cells appeared somewhat larger (100–750 nm) with an average size of 390 nm. In contrast, SEVs appeared as smaller vesicles with an average size of 190 nm for SEVs released from viable T-cells. Again, SEVs released after apoptosis induction appeared somewhat larger when compared to those released from activated T-cells.

Next, we compared the amount of vesicles (SEVs and LEVs) released either after cellular activation or after apoptosis induction. The release of LEVs was massively triggered after apoptosis induction. Here, the LEV concentration rose up to a 10-fold level from 38 to 388*10^9 vesicles/ml ($p = 0.00009$, **Figure 2A**). Further, we observed a slight increase of SEVs released from apoptozing T-cells ($p = 0.045$, **Figure 2A**). Activated T-cells released slightly more LEVs when compared to SEVs ($p = 0.043$, **Figure 2A**). In parallel, we analyzed the amount of protein released within the different vesicle populations and obtained very similar results (**Figure 2B**). Further, a protein/vesicle ratio was calculated by division of protein content through the vesicle concentration (**Figure 2C**). The highest protein/vesicle ratio was found in SEVs released from activated T-cells (ratio score = 4.5, **Figure 2C**). Apoptotic SEVs and activated LEVs showed an equal protein/vesicle ratio (ratio score = 2.3, respectively 2.1, **Figure 2C**). The lowest protein/vesicle ratio was observed by the apoptotic LEVs (ratio score = 1.2, **Figure 2C**).

As suggested previously by the international society of EVs (48) we have analyzed a set of proteins, which either should be present in or excluded from distinct EV populations. Proteins associated with compartments other than plasma membrane or endosomes should not be detectable within SEVs. In fact, we were able to show, that the mitochondrial protein Bcl-2 is excluded from all EV fractions (LEVs and SEVs) and only present within whole cells. The proteins calnexin and calreticulin (endoplasmatic reticulum related) were detected in whole cells, to a lesser extent also in LEVs, but were excluded from the SEV fraction. Annexin I, a protein which is expected to be present within EVs (48), was in fact detected in whole cells as well as in all EV fractions (Figure S1 in Supplementary Material).

Protein Profile of LEVs and SEVs Released From Activated or Apoptozing Human T-Lymphocytes

After the characterization of the morphology of EVs, we were interested in the proteins present in distinct vesicle populations. To this aim, we used two dimensional DIGE and western blot analysis. For DIGE analysis, SEVs and LEVs were isolated from apoptozing or activated T-cells. One representative gel for each condition (activated LEVs, apoptotic LEVs, activated SEVs, and apoptotic SEVs) is depicted in **Figure 3A**. Using the DIGE DeCyder 2D software we could map 11,364 protein spots (100%). We identified 9,583 protein spots (84.33%) that did not significantly differ

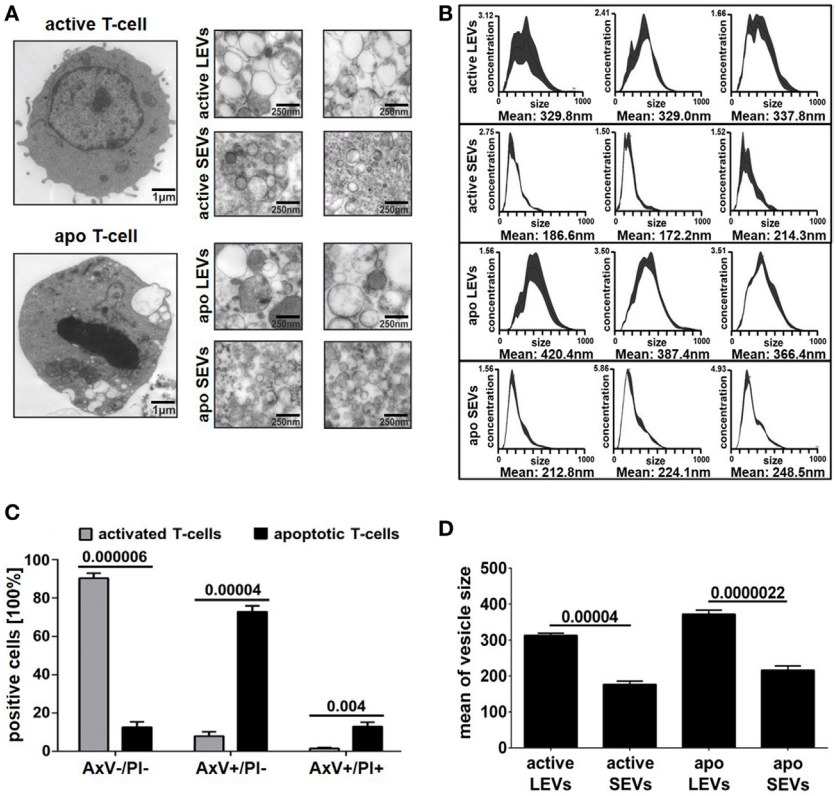

FIGURE 1 | Morphology of large EVs (LEVs) and small EVs (SEVs). **(A)** Large pictures on the left show a representative T-cell either after cellular activation (upper picture) or after apoptosis induction (lower picture). The corresponding extracellular vesicles are shown on the right side (*active* LEVs*:* LEVs released from activated T-cells; *active* SEVs: SEVs released from activated T-cells; *apo* LEVs: LEVs released from apoptozing T-cells; *apo* SEVs: SEVs released from apoptozing T-cells). **(B)** Three representative size distribution graphs with the corresponding mean values obtained by nanoparticle tracking analysis (NTA) measurements are shown. On the *x*-axis, size distribution (nm) is depicted; the *y*-axis outlines vesicle concentration (10^6 vesicles/ml). **(C)** The graph shows the percentage of viable T-cells (AxV+/PI–), apoptotic T-cells (AxV+/PI–), and necrotic T-cells (AxV+/PI+). Activated or UV-B irradiated T-cells were analyzed by flow cytometry after AxV/PI staining. Data were obtained from five independent experiments (mean values + SEM). **(D)** The graph shows mean values of vesicle size distribution (NTA analysis) obtained from 10 independent experiments. Mean values + SEM are shown. Statistical significance was calculated employing the Student's *t*-test.

in their expression levels. However, 1,781 protein spots (15.67%) showed either a different expression level in SEVs and LEVs or a significant change in expression after the induction of apoptosis. To evaluate the expression profile in a more detailed way we divided the protein spots into two major categories:

(1) Spots showing a different expression level when comparing LEVs and SEVs. Based on a p-value ≤ 0.05 we found 930 spots that were significantly higher expressed within LEVs (8.20%), while 846 protein spots showed a higher expression in SEVs (7.47%, **Figure 3B**, left pie chart).
(2) Spots that were up- or downregulated within distinct EV populations after apoptosis induction. These spots were either regulated in parallel or in opposing directions when comparing LEVs and SEVs. Here, 701 protein spots showed a simultaneous upregulation in LEVs and SEVs (39.85%), while 580 protein spots were simultaneously downregulated in both vesicle populations (32.97%, **Figure 3B**, right pie chart). 143 protein spots were upregulated in LEVs and downregulated in SEVs (8.13%) and 335 spots were regulated *vice versa* (19.04%).

Finally, we selected 24 protein spots which were either strongly regulated after the induction of apoptosis or which showed a significantly different expression in SEV and LEV preparations. Those spots were then identified by mass spectrometry (**Figure 4**).

Figure 4A shows proteins which were upregulated in LEVs and SEVs after apoptosis induction. Here we identified gamma-actin (ACTG1), beta-actin (ACTB), 14-3-3 protein theta (YWHAQ), stress-induced phosphoprotein 1, eukaryotic translation initiation factor three subunit H (EIF3H), myosin heavy chain 9 (MYH9) (**Figure 4A**).

The proteins shown in **Figure 4B** were also upregulated after apoptosis induction, but showed different expression levels when comparing LEVs and SEVs. These proteins are: protein phosphatase 1 regulatory subunit 7 (PPP1R7), major vault protein, eps15 homology domain-containing protein 3 (EHD3).

The proteins shown in **Figures 4C,D** showed a downregulation after apoptosis induction. These proteins are: proteasome subunit beta type-4 (PSMB4), enoyl-CoA hydratase 1, septin 9 (SEPT9), voltage-dependent anion-selective channel 1, guanine nucleotide-binding protein subunit beta-2-like 1 (GNB2L1),

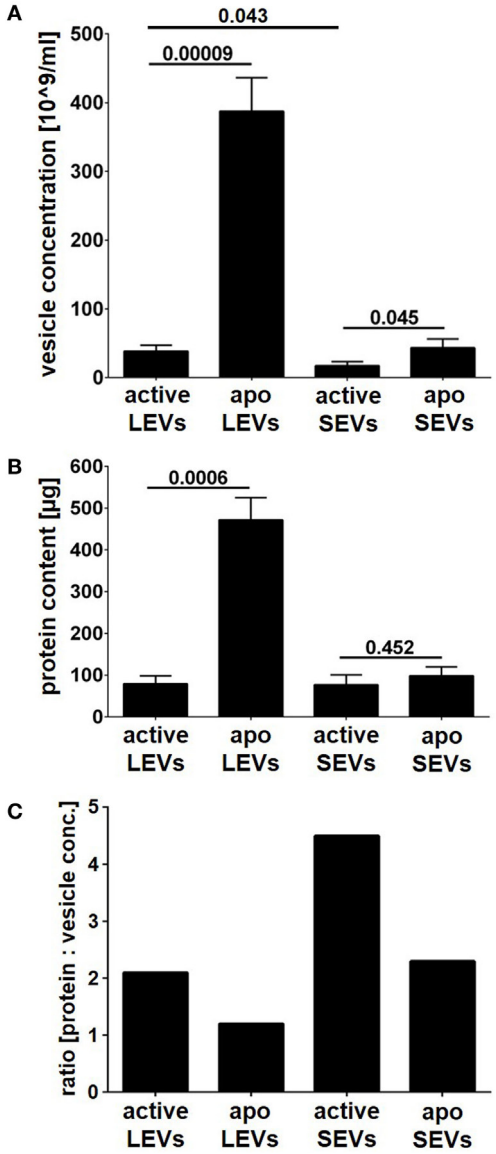

FIGURE 2 | Vesicle concentration and protein content of large EVs (LEVs) and small EVs (SEVs). LEVs and SEVs were isolated after activation of T-cells or after apoptosis induction (*active* LEVs*:* LEVs released from activated T-cells; *active* SEVs: SEVs released from activated T-cells; *apo* LEVs: LEVs released from apoptozing T-cells; *apo* SEVs: SEVs released from apoptozing T-cells). **(A)** The concentration of isolated extracellular vesicles (EVs) was quantified by nanoparticle tracking analysis (NTA). **(B)** The total protein content of isolated EVs is shown. The graphs show mean values out of eight independent experiments + SEM. Statistical significance was calculated employing the Student's *t*-test. **(C)** The graph shows the ratio calculated by division of protein content through vesicle concentration [protein content (µg) divided by vesicle concentration ($\times 10^9$ vesicles/ml)]. *Active* LEVs*:* ratio score = 2.1; *active* SEVs: ratio score = 4.5; *apo* LEVs: ratio score = 1.2; *apo* SEVs: ratio score = 2.3.

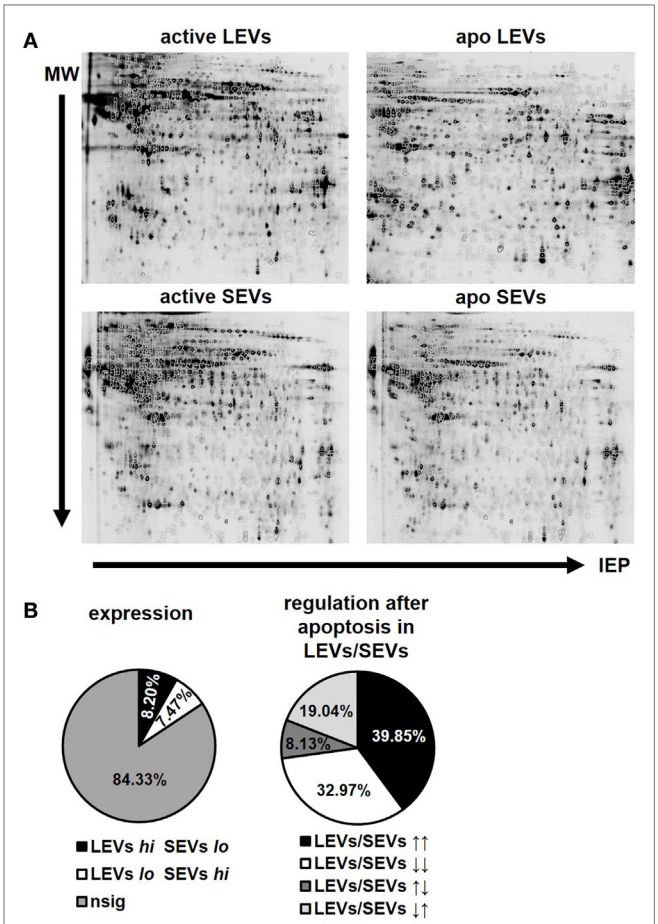

FIGURE 3 | Protein expression and regulation pattern of large EVs (LEVs) and small EVs (SEVs) after apoptosis induction. **(A)** One representative gel is shown for bidimensional electrophoresis of activated and apoptotic LEVs and SEVs. **(B)** The pie charts on the left indicate the percentage of proteins showing a different expression level within LEVs or SEVs. LEVs *high* SEVs *low* is shown in black (8.20%), LEVs *low* SEVs *high* is shown in white (7.47%). Proteins showing no significant differences in their expression within the respective EVs are shown in gray (84.33%). The right pie chart indicates the percentage of proteins which have been differentially regulated after cellular activation or apoptosis induction. LEVs *high*/SEVs *high* is shown in black (39.85%); LEVs *low*/SEVs *low* is shown in white (32.97%); LEVs *high*/SEVs *low* is shown in dark gray (8.13%); LEVs *low*/SEVs *high* is shown in light gray (19.04%). Results are calculated out of three independent experiments and statistical significance ($p \leq 0.05$) was calculated employing the Student's *t*-test.

nascent-polypeptide-associated complex alpha polypeptide (NACA), and the heat shock 60 kDa protein 1 (HSPD1).

Figures 4E,F show proteins, which are differentially regulated and expressed (comparing LEVs and SEVs) after apoptosis induction. The proteins are: adenosylhomocysteinase, leucine aminopeptidase 3, alpha-enolase 1, proteasome subunit alpha type 1 (PSMA1), phosphoglycerate kinase 1, DNA damage-binding protein 1 (DDB1), GSN, and the 40 S ribosomal protein SA.

Our findings demonstrate that the protein content of distinct EV populations is tightly regulated and dependent on the stimulus causing EV release. Apoptosis induction had a significant impact on the protein load of LEVs as well as that of SEVs. However, some proteins (DDB1, EHD3, and GSN) had a high and stable expression within SEVs despite the induction of apoptotic cell death. Thus, we suggest that distinct protein groups might be

specific for a particular EV type (e.g., EHD3 and GSN for SEVs). On the other hand, some proteins might be specific for EVs released from T-cells undergoing apoptosis (e.g., proteins of the actin-myosin cytoskeleton, like ACTG1, ACTB, and MYH9). To further substantiate this, we investigated several proteins by western blot analysis. Here, we analyzed membrane associated

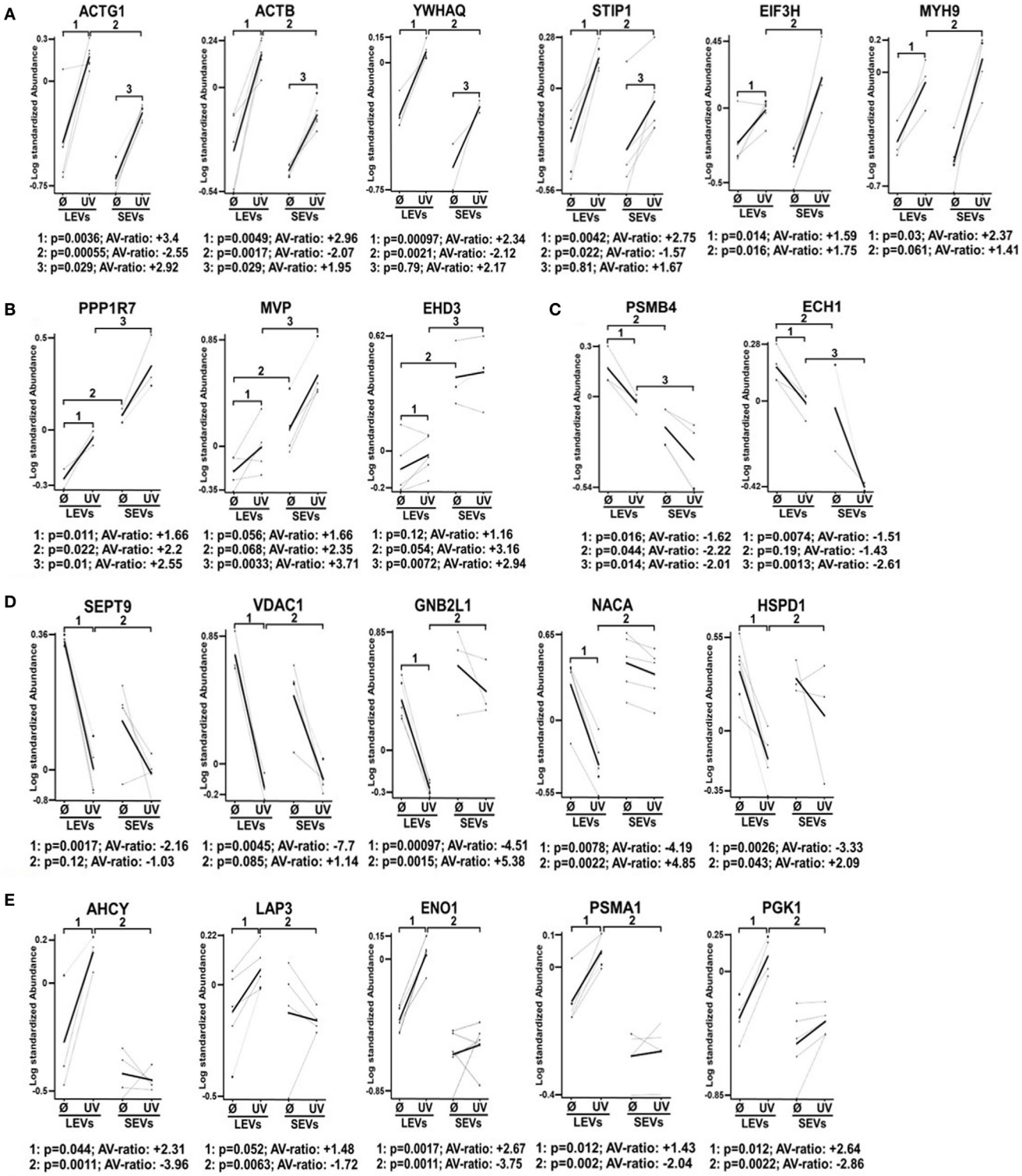

FIGURE 4 | Continued

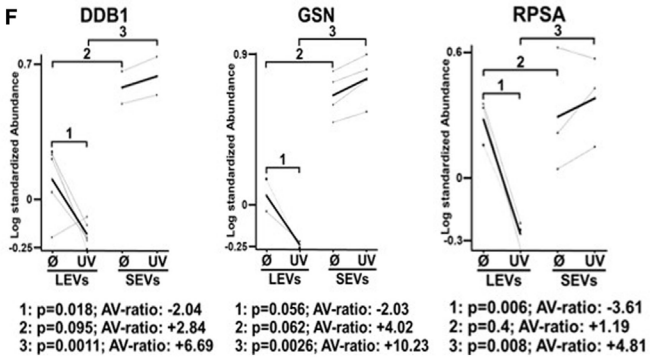

FIGURE 4 | Differential expression pattern of proteins in large EVs (LEVs) and small EVs (SEVs) isolated after cellular activation or apoptosis induction. The graphs show the expression level of proteins that have been identified by mass spectrometry. Results obtained from analysis of the 2D-gels using the difference gel electrophoresis (DIGE) DeCyder machine and software are shown (standardized protein abundance on the *y*-axis). Protein expression levels of LEVs or SEVs isolated either after cellular activation (Ø) or after the induction of apoptosis by UV-B irradiation (UV) are indicated. **(A,B)** Expression levels are shown of proteins that have been upregulated in both extracellular vesicles (EV) fractions after the induction of apoptosis. **(C,D)** Graphs show proteins that have been downregulated in LEVs and SEVs. **(E,F)** Graphs show proteins with a different expression and regulation in LEVs and SEVs. EV preparations were obtained from three healthy donors. Statistical analysis (*p*-value and AV-ratio) was done using the DIGE DeCyder software.

proteins of the T-cell receptor (TCR) signaling cascade (LAT, LCK, ZAP70, ERK1, and pERK). As shown in **Figure 5A**, these proteins turned out to be specific for LEVs. Similar results were obtained when we analyzed actin and ezrin as proteins of the actin-myosin cytoskeleton (**Figure 5B**).

In DIGE analysis, the expression of the proteasome subunits PSMA1 and PSMB4 appeared higher in LEVs when compared to SEVs. Therefore, we investigated subunits of the proteasome also by western blot analysis. As shown in **Figure 5C** PSMA1 was detected mainly in LEVs and strongly induced after induction of apoptosis (this expression profile matched with the data obtained from DIGE analysis). The proteasome subunit beta-9 (PSMB9) and proteasome subunit beta-10 (PSMB10) were specific for LEVs released from apoptozing T-cells.

A further protein that was detected within apoptotic cell-derived LEVs is the high mobility group box protein B1 (HMGB1). HMGB1 (a nuclear protein involved in structural DNA organization) can be released from necrotic cells or upon cellular activation. After this release into the extracellular space, HMGB1 serves as a mediator of inflammation (49). Interestingly, HMGB1 accumulated nearly exclusively within apoptotic cell-derived LEVs and seemed to be excluded from other EV subpopulations (**Figure 5C**).

We then analyzed cytosolic/endosomal proteins which have classically been used as exosome markers. These included the proteins TSG101 and HSP70, as well as the analysis of protein ubiquitination. When analyzing SEVs released from viable T-cells, TSG101, and HSP70 as well as ubiquitination of proteins appeared rather specific for isolated SEVs. However, after the induction of apoptosis, TSG101 and HSP70 were found mainly in LEVs, while protein ubiquitination was to be observed in both EV populations (**Figure 5D**).

Finally, as we had already observed a specific expression of the microtubule-associated proteins GSN and EHD3 in SEVs, released from activated as well as from apoptozing T-cells, we were able to validate these results by western blot analysis (**Figure 5E**).

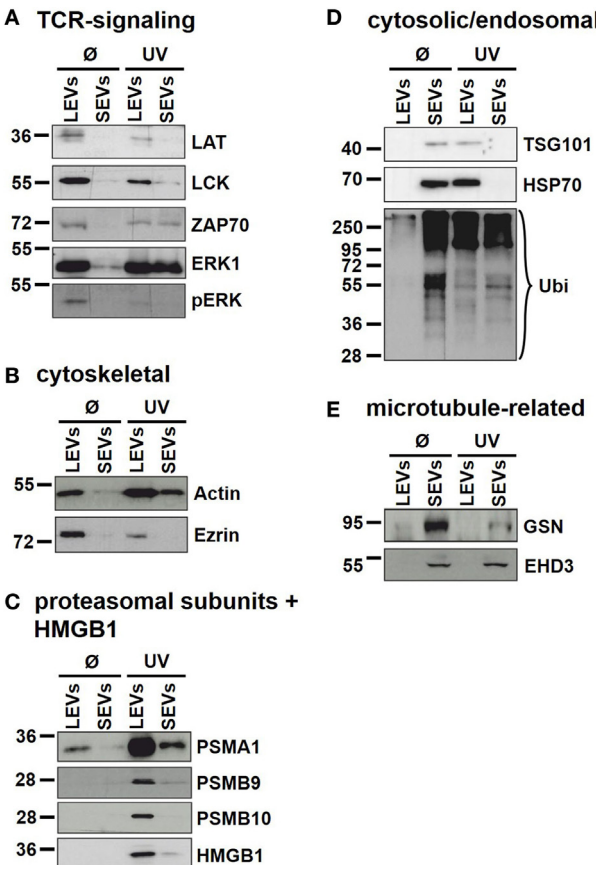

FIGURE 5 | Immunoblot analysis of proteins present in distinct extracellular vesicles (EV) populations. Large EVs (LEVs) and small EVs (SEVs) were isolated from activated T-cells (Ø) and T-cells induced to undergo apoptosis (UV). Analyzed proteins included: **(A)** proteins related to the T-cell receptor signaling, **(B)** cytoskeletal proteins, **(C)** proteasomal subunits and HMGB1, **(D)** cytosolic/endosomal proteins, and **(E)** microtubule-related proteins.

Thus, these proteins can be used as specific markers for SEVs even after the induction of apoptotic cell death.

The Proteasome Is Involved in the Regulation of LEV Release

As described above we detected the proteasome subunits PSMA1, PSMB4 within LEVs. Moreover, we could detect the functional catalytic subunits, PSMB9 and PSMB10 exclusively in LEVs released after apoptosis induction (see **Figure 5C**). Thus, we questioned whether the proteasome might play a role in the release of LEVs from apoptozing T-cells. To analyze this, T-cells were induced to undergo apoptosis in the presence of the proteasome inhibitor bortezomib. The amount of released LEVs was then quantified by flow cytometry. In parallel, we analyzed the LEV release from apoptozing T-cells treated with Y27632, a rho-kinase inhibitor known to prevent the budding of the plasma membrane and the release of LEVs (23, 50–52). FACS analyses showed a significant increase of LEV release after apoptosis induction, which was significantly reduced in the presence of bortezomib (**Figure 6A**) as well as in the presence of Y27532 (**Figure 6B**). Importantly, the total amount of apoptozing T-cells (AxV+/PI−) was not affected by the bortezomib treatment ($p = 0.07$, **Figure 6C**) and we did not observe any changes in the amount of necrotic T-cells (AxV+/PI+, $p = 0.4$, **Figure 6D**). Thus, blocking of the proteasome function in fact reduced the release of LEVs from apoptozing T-cells.

DISCUSSION

The EV research field has been rapidly growing during the past years and various EV subtypes have been described. To date, the heterogeneity of EVs is a well-known fact and it has been shown that SEVs (often called exosomes) as well as LEVs (often referred to as microvesicles or apoptotic bodies) consist of diverse EV subpopulations (5, 17, 37, 39). LEVs are mainly released from the cellular surface and distinct LEV subtypes (such as microvesicles and apopototic bodies) share similar release mechanism (e.g., blebbing of the outer cellular membrane). The discrimination between different LEV populations, however, is very difficult and well-defined discrimination markers are needed.

Distinct EVs subtypes are released in response to a variety of stimuli (5, 38) and it seems likely that a distinct stimulus can trigger the release of a typical EV subtype. As a first of its kind, in this study we systematically analyzed and compared different EV populations released either from activated or from apoptozing human T-lymphocytes.

Isolation of EVs was done by filtration followed by differential ultracentrifugation at 10,000 and 100,000 × *g*. We were able to isolate two EV populations (LEVs and SEVs) from activated or apoptozing T-cells. As expected these EV populations clearly differed in size (**Figure 1**) and apoptosis induction turned out to be the most potent stimulus for the release of LEVs (**Figure 2**). Interestingly, the amount of protein per vesicle was diminished after the induction of apoptosis when analyzing LEVs (**Figure 2C**).

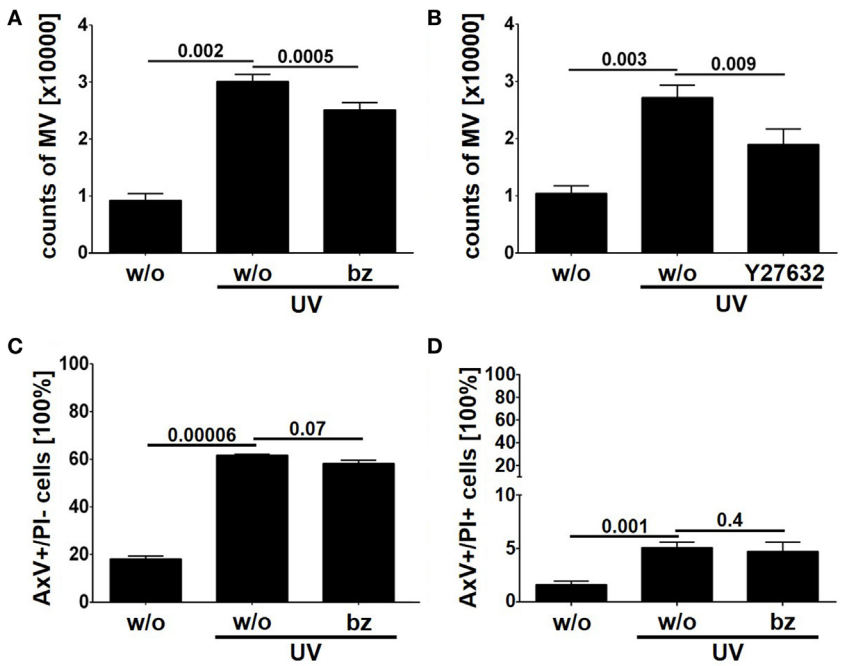

FIGURE 6 | Release of large EVs (LEVs) is impaired by bortezomib. Activated T-lymphocytes were irradiated with UV-B irradiation (90 mJ/cm^2) to induce apoptosis in presence of 1 nM bortezomib and 10 μM Y27632. After 20 h the amount of released vesicles was analyzed by flow cytometry. **(A)** The amount of released vesicles is shown in the graph. Mean values + SEM are shown. Vesicle release was inhibited by bortezomib. **(B)** The amount of released vesicles is shown (mean values + SEM). Y27632 was used to inhibit LEV release. **(C)** The graph shows the percentage of apoptozing T-cells (analyzed by AxV/PI staining). **(D)** The graph shows the percentage of necrotic T-cells (AxV+/PI+, analyzed by AxV/PI staining). Data were obtained from four independent experiments and statistical significance was calculated employing the Student's *t*-test.

This might be explained by diminution of protein synthesis and the degradation of proteins during apoptotic cell death (e.g., caspase-dependent cleavage of proteins).

Beside their characteristic differences in size we were also able to demonstrate, that each EV population carries specific proteins, schematically summarized in **Figure 7**. LEVs released from activated T-lymphocytes carried proteins associated with TCR signaling (like LAT, LCK, ZAP70, ERK1, and pERK) and proteins related to the actin-myosin cytoskeleton (actin and ezrin). SEVs released from activated T-lymphocytes carried the cytosolic and endosomal proteins TSG101 and HSP70, proteins related to the microtubule apparatus (EHD3 and GSN), and the protein DDB1. These observations support the idea, that LEVs are mainly released by budding of the plasma membrane, while SEVs are mainly released from intracellular compartments.

Importantly, the protein content of each vesicle population was dependent on the release stimulus and we observed dramatic changes in the protein profile of LEVs and SEVs after apoptosis induction. While LEVs released after apoptosis induction also carried signaling proteins as well as the cytoskeleton-related proteins, the protein pERK appeared to be rather specific for LEVs released from activated T-cells. We observed an accumulation of the proteasome subunits PSMB9 and PSMB10 exclusively within apoptotic LEVs. Another protein, which was highly specific for apoptotic LEVs, was the molecule HMGB1. This protein is a well-known danger signal, when released into the extracellular space (49). Thus, the packing of HMGB1 into membrane coated vesicles released from apoptotic T-cells might be crucial for the non-inflammatory response to apoptosis within multicellular organisms (53). This was supported by previous observations of our group, having shown, that apoptotic cell-derived membrane vesicles were engulfed by professional phagocytes without the induction of an inflammatory immune response (23, 35, 54). The release of proteasome subunits within *microvesicles* or so-called *apoptotic exosome-like vesicles* has been described previously (55, 56). Nevertheless, we herein demonstrate that apoptosis induction is a specific stimulus for the translocation of the inducible proteasome subunits, PSMB9 and PSMB10, and the danger signal protein HMGB1 into LEVs. For the first time, we present a set of proteins (PSMB9, PSMB10, and HMGB1), which were highly specific for LEVs released after the induction of apoptosis. These proteins can be used to differentiate between apoptotic cell-derived LEVs (or apoptotic bodies) and other LEV subpopulations. Moreover, we have shown that PSMB4, PSMB9 and PSMB10 are specific cargo of LEVs and cannot be found within the SEV population. Based on these findings we were interested, whether the proteasome function is also involved in the regulation of LEV release after apoptosis induction. Using the proteasome inhibitor bortezomib, we were able to demonstrate an involvement of the proteasome in the regulation of LEV release from T-cells induced to undergo apoptosis (**Figure 6**). Further studies will be needed in order to gain a deeper insight into the proteasomes role as a regulator of apoptotic cell blebbing and the subsequent release of LEVs (or apoptotic bodies).

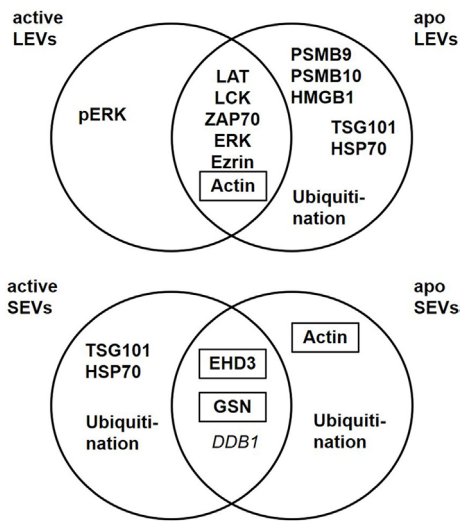

FIGURE 7 | Extracellular vesicles (EV) subtypes are characterized by distinct protein profiles. The upper diagram indicates the distribution of proteins characteristic for large EVs (LEVs), comparing activated and apoptotic LEVs. The diagram below shows the distribution of proteins characteristic for small EVs (SEVs) comparing activated and apoptotic SEVs. Proteins identified by Western blot analysis are shown in bold, proteins identified by western blot as well as mass spectrometry are shown in bold plus frame. Proteins identified by mass spectrometry are shown in italics.

When analyzing the classically used exosomal marker proteins TSG101 and HSP70 in EVs released from apoptozing T-cells we obtained very interesting results. As described above, TSG101 and HSP70 were specific for SEVs when analyzing EVs released from activated T-cells. In contrast, both proteins accumulated within the LEV fraction after the induction of apoptosis. These results are in line with some other studies, which have shown that TSG101 can be recruited to the plasma membrane and then be released within microvesicles by direct plasma membrane budding (57, 58). Only recently, another study demonstrated the release of HSP70 not only within SEVs, but also within LEVs isolated by low speed centrifugation. In this study, EVs released from human dendritic cells were analyzed (39). We demonstrate here for the first time that apoptosis induction causes the release of TSG101 and HSP70 within LEVs. Moreover, TSG101 and HSP70 are rather excluded from the SEV fraction after the induction of apoptotic cell death.

Ubiquitination has been reported to be crucial for the incorporation of proteins into exosomes (59). Thus, we analyzed the ubiquitination profile of proteins within EVs released from activated or apoptozing T-cells. Analyzing LEVs and SEVs released after cellular activation, ubiquitinated proteins were exclusively present within the SEV fractions. In contrast to this, both, SEVs as well as LEVs contained ubiquitinated proteins when EVs were isolated from apoptozing T-cells.

Beside the changes of the EV protein cargo after apoptosis induction we identified proteins specific for SEVs, regardless of the underlying release stimulus. We detected the proteins EHD3, GSN, and DDB1 in all SEV preparations. Interestingly, EHD3 and GSN have been reported to be regulators of intracellular vesicle trafficking by interacting with the microtubule apparatus

(60, 61). Moreover, other members of the EHD family (EHD1 and EHD4) have been identified as SEV-specific proteins in a recent study (39). Based on these findings EHD3 and GSN can be useful markers for the identification of SEVs which are most likely released from intracellular compartments.

Taken together, we identified several proteins which are specific for distinct EV populations released from activated or apoptozing T-cells. LEVs are characterized by proteins which are associated with the actin-myosin cytoskeleton or signaling proteins linked to the cellular membrane. We further demonstrated that proteasome subunits are present in LEV and that proteasomal function participates in the regulation of LEV release from apoptozing T-cells. SEVs, in contrast, carried proteins linked to endosomal and cytosolic compartments and some of these proteins have previously been shown to regulate intracellular vesicle trafficking. We observed substantial change of the EV protein cargo after apoptosis induction. Our findings are very important as apoptotic cell death is present in virtually all tissues as well as in cell culture conditions. Thus, when analyzing EVs, the amount of apoptozing T-cells must always be considered and some of the proteins identified here (**Figure 7**) may be useful to identify EVs released from apoptozing T-cells. Our data present an important contribution to the EV field as they provide tools for a better characterization of lymphocytic EVs. Moreover, they will substantially help to standardize isolation procedures, improve purity of EV isolates, and enable comparability of various experimental projects dealing with EVs.

ETHICS STATEMENT

This study was carried out in accordance with the recommendations of "ethics guidelines of our institution, ethics committee of the University of Heidelberg" with written informed consent from all subjects. All subjects gave written informed consent in accordance with the Declaration of Helsinki. The protocol was approved by the "ethics committee of the University of Heidelberg."

AUTHOR CONTRIBUTIONS

CT, KB, PS, and MS were participated in concept and research design. CT, KB, PS, LC, and CB conducted all experiments. CT, KB, PS, and MS analyzed data. CT, KB, PS, CB, LC, MS-C, NB, H-ML, and MS drafted and revised the work and critically discussed data for important intellectual content. CT, KB, PS, CB, LC, MS-C, NB, H-ML, and MS wrote or were contributed in writing the manuscript and had a final approve of the version to be published. All authors agreed to be accountable for all aspects of this work.

ACKNOWLEDGMENTS

We are grateful to Hilmar Bading, Department of Neurobiology and Interdisciplinary Center for Neurosciences, University of Heidelberg, for providing the opportunity to carry out the electron microscopy work in his laboratory. We thank Andrea Hellwig for her excellent technical support. NTA was performed at the Department of Virology at the University of Heidelberg. We thank D. Stammler for assistance in carrying out two dimensional DIGE experiments. Mass spectrometry analyses were conducted at the Core Facility for Mass Spectrometry at the Center for Molecular Biology of the University of Heidelberg.

FUNDING

H-ML, MS-C, and MS have been supported by grants from the German Research Foundation (Schi 1006/5-1, Lo 437/5-3, So 1402/1-1).

SUPPLEMENTARY MATERIAL

The Supplementary Material for this article can be found online at http://www.frontiersin.org/articles/10.3389/fimmu.2018.00534/full#supplementary-material.

REFERENCES

1. D'Souza-Schorey Crislyn C, Clancy JW. Tumor-derived microvesicles: shedding light on novel microenvironment modulators and prospective cancer biomarkers. *Genes Dev* (2012) 26(12):1287–99. doi:10.1101/gad.192351.112
2. Antwi-Baffour SS. Molecular characterisation of plasma membrane-derived vesicles. *J Biomed Sci* (2015) 22(1):68. doi:10.1186/s12929-015-0174-7
3. Liu M-L, Williams KJ, Werth VP. Microvesicles in autoimmune diseases. *Adv Clin Chem* (2016) 77:125–75. doi:10.1016/bs.acc.2016.06.005
4. Raposo G, Stoorvogel W. Extracellular vesicles: exosomes, microvesicles, and friends. *J Cell Biol* (2013) 200(4):373–83. doi:10.1083/jcb.201211138
5. Marcoux G, Duchez AC, Cloutier N, Provost P, Nigrovic PA, Boilard E. Revealing the diversity of extracellular vesicles using high-dimensional flow cytometry analyses. *Scientific Reports* (2016) 6(1):35928. doi:10.1038/srep35928
6. Meckes DG, Raab-Traub N. Microvesicles and viral infection. *J Virol* (2011) 85(24):12844–54. doi:10.1128/JVI.05853-11
7. Wickman GR, Julian L, Mardilovich K, Schumacher S, Munro J, Rath N, et al. Blebs produced by actin–myosin contraction during apoptosis release damage-associated molecular pattern proteins before secondary necrosis occurs. *Cell Death Differ* (2013) 20(10):1293–305. doi:10.1038/cdd.2013.69
8. Distler JHW, Pisetsky DS, Huber LC, Kalden JR, Gay S, Distler O. Microparticles as regulators of inflammation: novel players of cellular crosstalk in the rheumatic diseases. *Arthritis Rheum* (2005) 52(11):3337–48. doi:10.1002/art.21350
9. Croft DR, Coleman ML, Li S, Robertson D, Sullivan T, Stewart CL, et al. Actin-myosin-based contraction is responsible for apoptotic nuclear disintegration. *J Cell Biol* (2005) 168(2):245–55. doi:10.1083/jcb.200409049
10. Eitan E, Suire C, Zhang S, Mattson MP. Impact of lysosome status on extracellular vesicle content and release. *Ageing Res Rev* (2016) 32:65–74. doi:10.1016/j.arr.2016.05.001
11. Urbanelli L, Magini A, Buratta S, Brozzi A, Sagini K, Polchi A, et al. Signaling pathways in exosomes biogenesis, secretion and fate. *Genes (Basel)* (2013) 4(2):152–70. doi:10.3390/genes4020152
12. Thery C, Zitvogel L, Amigorena S. Exosomes: composition, biogenesis and function. *Nat Rev Immunol* (2002) 2(8):569–79. doi:10.1038/nri855
13. Kowal J, Tkach M, Théry C. Biogenesis and secretion of exosomes. *Curr Opin Cell Biol* (2014) 29:116–25. doi:10.1016/j.ceb.2014.05.004
14. Andreu Z, Yáñez-Mó M. Tetraspanins in extracellular vesicle formation and function. *Front Immunol* (2014) 5:442. doi:10.3389/fimmu.2014.00442
15. Smalheiser NR. Exosomal transfer of proteins and RNAs at synapses in the nervous system. *Biol Direct* (2007) 2:35. doi:10.1186/1745-6150-2-35
16. Kolhe R, Hunter M, Liu S, Jadeja RN, Pundkar C, Mondal AK, et al. Gender-specific differential expression of exosomal miRNA in synovial fluid of patients with osteoarthritis. *Sci Rep* (2017) 7(1):2029. doi:10.1038/s41598-017-01905-y

17. Willms E, Johansson HJ, Mäger I, Lee Y, Blomberg KE, Sadik M, et al. Cells release subpopulations of exosomes with distinct molecular and biological properties. *Sci Rep* (2016) 6:22519. doi:10.1038/srep22519
18. Yoshioka Y, Konishi Y, Kosaka N, Katsuda T, Kato T, Ochiya T. Comparative marker analysis of extracellular vesicles in different human cancer types. *J Extracell Vesicles* (2013) 2:1–9. doi:10.3402/jev.v2i0.20424
19. Zomer A, Maynard C, Verweij FJ, Kamermans A, Schäfer R, Beerling E, et al. In vivo imaging reveals extracellular vesicle-mediated phenocopying of metastatic behavior. *Cell* (2015) 161(5):1046–57. doi:10.1016/j.cell.2015.04.042
20. Kawamura Y, Yamamoto Y, Sato TA, Ochiya T. Extracellular vesicles as trans-genomic agents: emerging roles in disease and evolution. *Cancer Sci* (2017) 108(5):824–30. doi:10.1111/cas.13222
21. Cai J, Wu G, Jose PA, Zeng C. Functional transferred DNA within extracellular vesicles. *Exp Cell Res* (2016) 349(1):179–83. doi:10.1016/j.yexcr.2016.10.012
22. Kalra H, Drummen GP, Mathivanan S. Focus on extracellular vesicles: introducing the next small big thing. *Int J Mol Sci* (2016) 17(2):170. doi:10.3390/ijms17020170
23. Schiller M, Bekeredjian-Ding I, Heyder P, Blank N, Ho AD, Lorenz HM. Autoantigens are translocated into small apoptotic bodies during early stages of apoptosis. *Cell Death Differ* (2008) 15:183–91. doi:10.1038/sj.cdd.4402239
24. Schiller M, Parcina M, Heyder P, Foermer S, Ostrop J, Leo A, et al. Induction of type I IFN is a physiological immune reaction to apoptotic cell-derived membrane microparticles. *J Immunol* (2012) 189(29):1747–56. doi:10.4049/jimmunol.1100631
25. Claßen L, Tykocinski LO, Wiedmann F, Birr C, Schiller P, Tucher C, et al. Extracellular vesicles mediate intercellular communication: transfer of functionally active microRNAs by microvesicles into phagocytes. *Eur J Immunol* (2017) 47(9):1535–49. doi:10.1002/eji.201646595
26. Schiller M, Heyder P, Ziegler S, Niessen A, Claßen L, Lauffer A, et al. During apoptosis HMGB1 is translocated into apoptotic cell-derived membraneous vesicles. *Autoimmunity* (2013) 46(5):342–6. doi:10.3109/08916934.2012.750302
27. Lee TH, D'Asti E, Magnus N, Al-Nedawi K, Meehan B, Rak J. Microvesicles as mediators of intercellular communication in cancer—the emerging science of cellular 'debris'. *Semin Immunopathol* (2011) 33(5):455–67. doi:10.1007/s00281-011-0250-3
28. Rezaie J, Ajezi S, Avci ÇB, Karimipour M, Geranmayeh MH, Nourazarian A, et al. Exosomes and their application in biomedical field: difficulties and advantages. *Mol Neurobiol* (2018) 55(4):3372–93. doi:10.1007/s12035-017-0582-7
29. Börger V, Bremer M, Ferrer-Tur R, Gockeln L, Stambouli O, Becic A, et al. Mesenchymal stem/stromal cell-derived extracellular vesicles and their potential as novel immunomodulatory therapeutic agents. *Int J Mol Sci* (2017) 18(7):1450. doi:10.3390/ijms18071450
30. Garcia-Contreras M, Brooks RW, Boccuzzi L, Robbins PD, Ricordi C. Exosomes as biomarkers and therapeutic tools for type 1 diabetes mellitus. *Eur Rev Med Pharmacol Sci* (2017) 21(12):2940–56.
31. Li XL, Li H, Zhang M, Xu H, Yue LT, Zhang XX, et al. Exosomes derived from atorvastatin-modified bone marrow dendritic cells ameliorate experimental autoimmune myasthenia gravis by up-regulated levels of IDO/Treg and partly dependent on FasL/Fas pathway. *J Neuroinflammation* (2016) 13(1):8. doi:10.1186/s12974-016-0475-0
32. Cannito S, Morello E, Bocca C, Foglia B, Benetti E, Novo E, et al. Microvesicles released from fat-laden cells promote activation of hepatocellular NLRP3 inflammasome: a pro-inflammatory link between lipotoxicity and non-alcoholic steatohepatitis. *PLoS One* (2017) 12(3):e0172575. doi:10.1371/journal.pone.0172575
33. Mondal A, Kumari Singh D, Panda S, Shiras A. Extracellular vesicles as modulators of tumor microenvironment and disease progression in glioma. *Front Oncol* (2017) 7:144. doi:10.3389/fonc.2017.00144
34. Sousa C, Pereira I, Santos AC, Carbone C, Kovačević AB, Silva AM, et al. Targeting dendritic cells for the treatment of autoimmune disorders. *Colloids Surf B Biointerfaces* (2017) 158:237–48. doi:10.1016/j.colsurfb.2017.06.050
35. Fehr E-M, Spoerl S, Heyder P, Herrmann M, Bekeredjian-Ding I, Blank N, et al. Apoptotic-cell-derived membrane vesicles induce an alternative maturation of human dendritic cells which is disturbed in SLE. *J Autoimmun* (2013) 40:86–95. doi:10.1016/j.jaut.2012.08.003
36. Takasugi M, Okada R, Takahashi A, Virya Chen D, Watanabe S, Hara E. Small extracellular vesicles secreted from senescent cells promote cancer cell proliferation through EphA2. *Nat Commun* (2017) 8:15729. doi:10.1038/ncomms15728
37. Bobrie A, Colombo M, Krumeich S, Raposo G, Théry C. Diverse subpopulations of vesicles secreted by different intracellular mechanisms are present in exosome preparations obtained by differential ultracentrifugation. *J Extracell Vesicles* (2012) 1:157–64. doi:10.3402/jev.v1i0.18397
38. Robbins PD, Morelli AE. Regulation of immune responses by extracellular vesicules. *Nat Immunol* (2014) 14(3):195–208. doi:10.1038/nri3622.Regulation
39. Kowal J, Arras G, Colombo M, Jouve M, Morath JP, Primdal-Bengtson B, et al. Proteomic comparison defines novel markers to characterize heterogeneous populations of extracellular vesicle subtypes. *Proc Natl Acad Sci U S A* (2016) 113(8):E968–77. doi:10.1073/pnas.1521230113
40. Kriegel MA, Tretter T, Blank N, Schiller M, Gabler C, Winkler S, et al. Interleukin-4 supports interleukin-12-induced proliferation and interferon-G secretion in human activated lymphoblasts and T helper type 1 cells. *Immunology* (2006) 119(1):43–53. doi:10.1111/j.1365-2567.2006.02404.x
41. Nunes CT, Miners KL, Dolton G, Pepper C, Fegan C, Mason MD, et al. A novel tumor antigen derived from enhanced degradation of Bax protein in human cancers. *Cancer Res* (2011) 71(16):5435–44. doi:10.1158/0008-5472.CAN-11-0393
42. Qesari M, Richter A, Ogonek J, Mischak-Weissinger E, Wang XN, Dickinson AM, et al. Cytomegalovirus-specific T cells isolated by IFN-gamma secretion assay do not induce significant graft-versus-host reactions in vitro. *Transplantation* (2016) 100(11):2352–61. doi:10.1097/TP.0000000000001219
43. Canda-Sánchez A, Salgado FJ, Pérez-Díaz A, Varela-González C, Arias P, Nogueira M. Differential distribution of both IL-12Rβ chains in the plasma membrane of human T cells. *J Membr Biol* (2009) 227(1):1–12. doi:10.1007/s00232-008-9127-3
44. Arias AA, Perez-Velez CM, Orrego JC, Moncada-Velez M, Rojas JL, Wilches A, et al. Severe enteropathy and hypogammaglobulinemia complicating refractory *Mycobacterium tuberculosis* complex disseminated disease in a child with IL-12Rβ1 deficiency. *J Clin Immunol* (2017) 37(7):732–8. doi:10.1007/s10875-017-0435-1
45. Vizcaíno JA, Csordas A, del-Toro N, Dianes JA, Griss J, Lavidas I, et al. 2016 update of the PRIDE database and its related tools. *Nucleic Acids Res* (2016) 44(D1):D447–56. doi:10.1093/nar/gkv1145
46. Deutsch EW, Csordas A, Sun Z, Jarnuczak A, Perez-Riverol Y, Ternent T, et al. The ProteomeXchange Consortium in 2017: supporting the cultural change in proteomics public data deposition. *Nucleic Acids Res* (2017) 45(D1):D1100–6. doi:10.1093/nar/gkw936
47. Wahlgren J, Karlson Tde L, Glader P, Telemo E, Valadi H. Activated human T cells secrete exosomes that participate in IL-2 mediated immune response signaling. *PLoS One* (2012) 7(11):e49723. doi:10.1371/journal.pone.0049723
48. Lötvall J, Hill AF, Hochberg F, Buzás EI, Di Vizio D, Gardiner C, et al. Minimal experimental requirements for definition of extracellular vesicles and their functions: a position statement from the International Society for Extracellular Vesicles. *J Extracell Vesicles* (2014) 3(1):1–6. doi:10.3402/jev.v3.26913
49. Scaffidi P, Misteli T, Bianchi ME. Release of chromatin protein HMGB1 by necrotic cells triggers inflammation. *Nature* (2002) 418(6894):191–5. doi:10.1038/nature00858
50. Sebbagh M, Hamelin J, Bertoglio J, Solary E, Bréard J. Direct cleavage of ROCK II by granzyme B induces target cell membrane blebbing in a caspase-independent manner. *J Exp Med* (2005) 201(3):465–71. doi:10.1084/jem.20031877
51. Sebbagh M, Renvoizé C, Hamelin J, Riché N, Bertoglio J, Bréard J. Caspase-3-mediated cleavage of ROCK I induces MLC phosphorylation and apoptotic membrane blebbing. *Nat Cell Biol* (2001) 3(4):346–52. doi:10.1038/35070019
52. Charras GT, Hu CK, Coughlin M, Mitchison TJ. Reassembly of contractile actin cortex in cell blebs. *J Cell Biol* (2006) 175(3):477–90. doi:10.1083/jcb.200602085
53. Voll RE, Herrmann M, Roth EA, Stach C, Kalden JR, Girkontaite I. Immunosuppressive effects of apoptotic cells. *Nature* (1997) 390:350–1. doi:10.1038/37022
54. Meesmann HM, Fehr E-M, Kierschke S, Herrmann M, Bilyy R, Heyder P, et al. Decrease of sialic acid residues as an Eat-Me signal on the surface of apoptotic lymphocytes. *J Cell Sci* (2010) 123(19):3347–56. doi:10.1242/jcs.066696
55. Bochmann I, Ebstein F, Lehmann A, Wohlschlaeger J, Sixt SU, Kloetzel PM, et al. T lymphocytes export proteasomes by way of microparticles: a possible

mechanism for generation of extracellular proteasomes. *J Cell Mol Med* (2014) 18(1):59–68. doi:10.1111/jcmm.12160

56. Dieudé M, Bell C, Turgeon J, Beillevaire D, Pomerleau L, Yang B, et al. The 20S proteasome core, active within apoptotic exosome-like vesicles, induces autoantibody production and accelerates rejection. *Sci Transl Med* (2015) 7(318):318ra200. doi:10.1126/scitranslmed.aac9816
57. Nabhan JF, Hu R, Oh RS, Cohen SN, Lu Q. Formation and release of arrestin domain-containing protein 1-mediated microvesicles (ARMMs) at plasma membrane by recruitment of TSG101 protein. *Proc Natl Acad Sci U S A* (2012) 109(11):4146–51. doi:10.1073/pnas.1200448109
58. Choudhuri K, Llodrá J, Roth EW, Tsai J, Gordo S, Wucherpfennig KW, et al. Polarized release of TCR-enriched microvesicles at the T cell immunological synapse. *Nature* (2014) 507(7490):118–23. doi:10.1038/nature12951. Polarized
59. Moreno-Gonzalo O, Villarroya-Beltri C, Sánchez-Madrid F. Post-translational modifications of exosomal proteins. *Front Immunol* (2014) 5:383. doi:10.3389/fimmu.2014.00383
60. Bahl K, Xie S, Spagnol G, Sorgen P, Naslavsky N, Caplan S. EHD3 protein is required for tubular recycling endosome stabilization, and an asparagine-glutamic acid residue pair within its Eps15 homology (EH) domain dictates its selective binding to NPF peptides. *J Biol Chem* (2016) 291(26):13465–78. doi:10.1074/jbc.M116.716407
61. Mazur AJ, Radaszkiewicz T, Makowiecka A, Malicka-Błaszkiewicz M, Mannherz HG, Nowak D. Gelsolin interacts with LamR, hnRNP U, nestin, Arp3 and β-tubulin in human melanoma cells as revealed by immunoprecipitation and mass spectrometry. *Eur J Cell Biol* (2016) 95(1):26–41. doi:10.1016/j.ejcb.2015.11.001

Conflict of Interest Statement: The authors declare that the research was conducted in the absence of any commercial or financial relationships that could be construed as a potential conflict of interest.

frontiers in Immunology

REVIEW
published: 19 November 2018
doi: 10.3389/fimmu.2018.02364

Emerging Role of Immunosuppression in Diseases Induced by Micro- and Nano-Particles: Time to Revisit the Exclusive Inflammatory Scenario

*François Huaux**

Louvain Centre for Toxicology and Applied Pharmacology, Institut de Recherche Experimentale et Clinique, Université catholique de Louvain, Brussels, Belgium

Fibrosis, cancer, and autoimmunity developing upon particle exposure have been exclusively linked with uncontrolled inflammatory processes. The critical role of inflammation is now challenged by several contradictory observations indicating that the emergence of these chronic disorders may result from non-inflammatory events. A growing number of studies reveals that micro- and nano-particles can cause exaggerated and persistent immunosuppression characterized by the release of potent anti-inflammatory cytokines (IL-10 and TGF-β), and the recruitment of major regulatory immune cells (M2 macrophages, T and B regs, and MDSC). This persistent immunosuppressive environment is initially established to limit early inflammation but contributes later to fibrosis, cancer, and infection. Immunosuppression promotes fibroblast proliferation and matrix element synthesis and subverts innate and adaptive immune surveillance against tumor cells and microorganisms. This review details the contribution of immunosuppressive cells and their derived immunoregulatory mediators and delineates the mutual role of inflammatory vs. immunosuppressive mechanisms in the pathogenesis of chronic diseases induced by particles. The consideration of these new results explains how particle-related diseases can develop independently of chronic inflammation, enriches current bioassays predicting particle toxicity and suggests new clinical strategies for treating patients affected by particle-associated diseases.

Keywords: immunosuppression, inflammation, TGF-β, IL-10, immunosuppressive lymphocytes, immunosuppressive myeloid cells

OPEN ACCESS

Edited by:
Martin Herrmann, Universitätsklinikum Erlangen, Germany

Reviewed by:
Ahmed El-Fiqi, Dankook University, South Korea
Arnaud Millet, INSERM Institut pour l'Avancée des Biosciences (IAB), France

***Correspondence:**
François Huaux
francois.huaux@uclouvain.be

Specialty section:
This article was submitted to Inflammation, a section of the journal Frontiers in Immunology

Received: *04 May 2018*
Accepted: *24 September 2018*
Published: *19 November 2018*

Citation:
Huaux F (2018) Emerging Role of Immunosuppression in Diseases Induced by Micro- and Nano-Particles: Time to Revisit the Exclusive Inflammatory Scenario. Front. Immunol. 9:2364. doi: 10.3389/fimmu.2018.02364

MICRO- AND NANO-PARTICLES IN THE TWENTY-FIRST CENTURY

The toxicity of inhaled particles and the subsequent development of health diseases including fibrosis, cancer and autoimmunity are recognized since several centuries (1). Unfortunately, the available scientific knowledge is not yet adequate for monitoring particle exposure-related health problems, delivering treatment to affected patients, and devising appropriate early recognition of reactive particles and individuals at risk (2–4). For example, although silicosis has been known for

decades, exposure to dusts containing free crystalline silica remains uncontrolled in countless workplaces throughout the world and clinical cases of chronic diseases caused by inhaled particles are still frequent (5–7). Despite active research, the highly lethal disorders caused by silica inhalation continue to pose major clinical challenges because there are refractory to current therapeutic strategies (8). In addition, clinical detection of silica-associated lung diseases is currently dependent on radiological and lung function tests, which are both late manifestations of diseases (8). Therefore, effective therapeutic regimen and early disease detection have yet to be identified and developed. This problematic is not limited to naturally occurring mineral dusts. The recent ability to manipulate the structure and the morphology of particles, allowing the production of tailor-made dusts with specific size, form and function opens very attractive avenues in nanobiotechnologies and industries. However, for the successful application of these new materials now largely designed and produced worldwide, it is becoming evident that the biological fate and potential toxicity of these particles have to be actively determined (9). Hence, it is becoming vital to understand how complex pathologies (fibrosis, cancer, and autoimmune disorders) are induced by inhaled particles in order to reduce their impacts on human health.

INFLAMMATION AS THE DRIVING FORCE

The fundamental concept, usually put forward to explain the pathogenesis of particle-induced fibrosis, cancer, and autoimmune diseases, is relatively simple. An unresolved and chronic inflammatory process, characterized by marked inflammatory cell accumulation and sustained release of inflammatory molecules, damages tissues, orchestrates accumulation of mesenchymal cells and their matrix protein products, transforms normal cells to tumor cells or activates adaptive immune responses to self-antigens (10).

A precise cascade of cellular and molecular inflammatory events has been proposed from an extensive and growing number of data in human and animal exposed to particles (**Figure 1**). First, sentinel (alveolar and interstitial macrophages) and resident cells (epithelial cells and fibroblasts) actively recognize particles through sophisticated innate immune platforms (11, 12). These activated cells release various inflammatory mediators such as cytokines, chemokines, eicosanoids, and free radicals (13–16). These mediators induce a marked and persistent recruitment of inflammatory myeloid or lymphoid cells (inflammatory M1 macrophages; neutrophils, monocytes, and effector T lymphocytes) that results in tissue damages. Persistent inflammation-induced injury is subsequently followed by an exaggerated reparative phase in which polypeptide growth factors produced by inflammatory cells stimulate non-controlled fibroblast recruitment, proliferation, and matrix protein production (1). Released reactive oxygen or nitrogen species (ROS and RNS) play a major role in the genotoxic activity of particles. Under inflammatory conditions, free radicals generated from the particle itself or inflammatory cells induce DNA damage in target cell populations and participate in the carcinogenic process (17). Again, tissue damage and inflammation associated to inhaled particles are the suspected pathological pathway that leads to immune abnormalities, adaptive immunity activation, tolerance breaking, antinuclear autoantibody production and finally systemic autoimmune diseases including lupus and arthritis (10).

A myriad of inflammatory mediators accompanying inflammation are linked to scar formation, cell transformation, and autoimmunity but only few of them are definitively identified as important in the pathological processes. Among those, the master pro-inflammatory cytokines TNF-α, IL-1 (mainly produced by M1 macrophages), type I and II IFN and IL-17 (from effector T lymphocytes as Th1, γδ T cells, and Th17) are essential in the pathogenesis of particle-induced diseases (10, 18–21). These inflammatory mediators are responsible of leukocyte influx in damaged tissues and orchestrate aggregation of mature phagocytic macrophages and granuloma formation (22, 23). In addition, they promote fibroblast activation and differentiation (24), epithelial or mesothelial cell transformation (13, 25) and immune responses to self-antigens (26–28). Inflammatory cell accumulation,

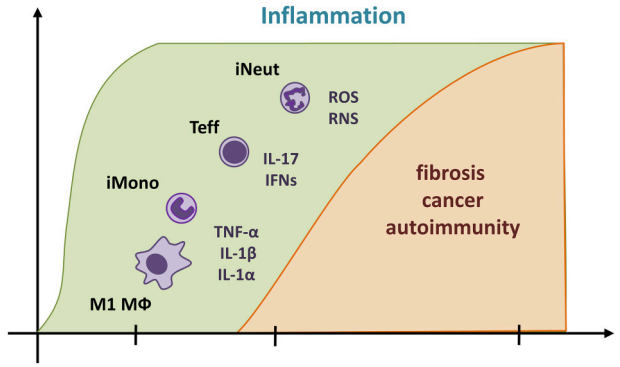

FIGURE 1 | Predominant unresolved inflammation contributes in the development of chronic diseases related to particle exposure. The pathological pathway classically described suggests that a predominant and persistent inflammatory process (in green) orchestrates fibrosis, cancer, and autoimmune diseases caused by particles (in yellow). Reactive particles induce an inflammatory cascade, which implies TNF-α, IL-1 α, and β, IFNs (IFN-γ and β), IL-17, and free radicals (ROS and RNS) and precedes the influx of inflammatory macrophages (M1 Mϕ), inflammatory myeloid cells (iMono, inflammatory monocytes; iNeut, inflammatory neutrophils), and effector T lymphocytes (T eff, comprising Th1, γδ T cells, and Th17). When immunosuppressive activities are insufficient, these pro-inflammatory mediators and cells persist and result in to uncontrolled cycle of injury. Pro-inflammatory cytokines are also considered as potent polypeptide growth factors for mesenchymal cells and ultimately induce fibrosis. Sustained production of free radicals induces irreversible DNA damage and results in carcinogenesis. Constant tissue damage and inflammation activate adaptive immunity, autoantibody production and autoimmunity.

Abbreviations: Regulatory T or B lymphocytes, T or B regs; Myeloid Derived Suppressive Cells, MDSC; Alternatively differentiated macrophages, M2 macrophages; $CD4^+$ T helper lymphocytes,Th; gamma and delta TCR chain positive T lymphocytes, γδ T cells; Interferon, IFN; Effector T lymphocytes, T eff; Carbon nanotubes, CNT.

collagen deposition, or malignant mesothelioma in silica- or asbestos-treated mice was markedly decreased by suppressing genetically or pharmacologically these key inflammatory mediators (13, 29). Increased levels of TNF-α, IL-1, IFN-γ, and IL-17 have been observed in human under conditions of developing silicosis, asbestosis or mesothelioma (30–33). These findings convincingly indicate a causal relationship between excessive or maintained accumulation of pro-inflammatory cells and cytokines and the establishment of particle-induced chronic diseases.

RECENT CLINICAL AND EXPERIMENTAL FINDINGS THAT CHALLENGE THE INFLAMMATORY DOGMA

Current treatment modalities for treating patients developing particle-related diseases have been based on the assumption that these disorders are exclusively related to chronic inflammation diseases. However, it is becoming evident that most available anti-inflammatory drugs (34, 35) or cytokine inhibitor therapy (36) are not effective for particle-exposed patients. Human validation studies have also failed to confirm the use of inflammatory mediators as biomarkers for univocally detecting the health effects of particles (37).

Besides the strong evidence of a major role of inflammation in particle-treated animals, several experimental studies did not find an evident association between inflammatory responses and experimental diseases and, thus, have also challenged this inflammatory dogma. Several studies, conducted in mice, reported that exacerbated lung inflammation is not always accompanied by a subsequent increase of fibrosis after silica or carbon nanotubes (CNT) treatment (38, 39). Inversely, limited inflammation can be associated to robust silica-induced long-term lung responses (40). More precisely, it has been found that a progressive neutrophilic inflammatory process and a sustained release of pro-inflammatory cytokines did not accompany instillation of silica or CNT in mice. In this case, a mild and non-progressive pulmonary inflammation and a transient production of pro-inflammatory cytokines such TNF-α and IL-1β was instead observed (22, 41–43). Additionally, these inflammatory components were dispensable for the development of particles-induced fibrogenesis since genetic deficiencies of these master pro-inflammatory cytokines did not completely limit lung fibrosis while they were efficient to abrogate inflammation and granuloma formation after silica or CNT (22, 44–46). Other key pro-inflammatory cytokines such as type I interferons, IL-12, IL-17, and IL-22 were also dispensable in the development of silica-induced fibrosis (21, 22, 47). The non-requirement of inflammation during experimental lung fibrosis was further supported by the fact that different treatments with anti-inflammatory molecules such as steroids, cox- or phosphodiesterase 5-inhibitors strongly reduced inflammation without modifying, however, collagen deposition (42, 43). The disconnection between inflammation and particle toxicity is not limited to fibrosis. In mice, co-exposure to silica and carcinogens from tobacco smoke resulted in rapid tumor growth in the lungs that is attenuated in the absence of leukotriene B4 axis. This mechanism is, however, independent of IL-1 activation, TNF-α production and chemokine release (48). In addition, early inflammatory reactions triggered by asbestos required NLRP3 inflammasome activation and IL-1β release, but this pathway was not critical in the chronic development of asbestos-induced mesothelioma (49). Recent investigations additionally showed that non-steroidal anti-inflammatory molecules do not reduce progression of asbestos-induced mesothelioma in animals (35, 50).

Altogether, these results strongly suggest that other pathophysiological mechanisms unrelated to inflammation are operational after particle exposure. There are now emerging studies from the literature that explain why diseases achieved by particles are not systematically related to inflammation. This review covers existing evidence supporting that immunosuppression represents an alternative pathological pathway in the development of particle-induced disorders. The most relevant studies delineating the immunosuppressive properties of (nano)particles are depicted in the following sections and commented in **Table 1**.

INVOLVEMENT OF THE ANTI-INFLAMMATORY AND IMMUNOSUPPRESSIVE CYTOKINES TGF-β AND IL-10

Indubitably, TGF-β is associated with the development of responses to particles in human and animal. Elevated TGF-β expression has been observed in patients with asbestosis or silicosis (67–71). In a variety of animal models, TGF-β activation has been demonstrated following exposure to silica, asbestos, or CNT (57, 63, 72, 73). After particles exposure, TGF-β contributes to fibroproliferative reorganization of organ tissue by orchestrating myofibroblast differentiation, collagen overproduction, and scar formation (74, 75). Previous studies have demonstrated that treatment with TGF-β inhibitors decreased lung fibrosis in animals exposed to silica (76–78). Additionally, TGF-β contributes to generate a favorable microenvironment for tumor growth and metastasis in mesothelioma, assigning this cytokine as dominant during the development of cancer induced by particles (79). It is noteworthy that the main function of TGF-β is immunosuppression since TGF-β1-deficient mice die from uncontrolled systemic inflammation and autoreactive T lymphocyte accumulation (80). The pivotal role of TGF-β argues for the development of other mechanisms than inflammation after particle exposure and supports that master immunosuppressive cytokines are also linked to particle-related diseases.

Because the anti-inflammatory cytokine IL-10 was effective in the regulation of inflammation, several authors have suggested that this cytokine could also be active in controlling inflammation in the early and late responses to mineral particles and thus plays a beneficial role based on the inflammatory paradigm (81–83). However, several lines of evidence have demonstrated that IL-10 (as TGF-β) possesses deleterious and pro-fibrotic

TABLE 1 | Historical progression of immunosuppression in particle toxicology literature: Summary of the most relevant studies supporting immunosuppressive properties of (nano) particles.

Authors	Highlighted observations	Particles	Source
Huaux et al. (51)	An experimental study revealing for the first time that lung responses to silica are unexpectedly characterized by the persistent expression of IL-10, a powerful anti-inflammatory cytokine.	silica	*Am J Respir Cell Mol Biol* 18:51-9 **1998**
	IL-10 was additionally detected after CNT exposure in murine models. Patients developing silicosis or asbestosis exhibit elevated lung levels of IL-10.	*CNT*	*references #* (37, 52, 53)
Ryan et al. (54)	This original study describes the unanticipated anti-inflammatory effects of NP by negatively regulating allergic inflammation.	fullerene NP	*J Immunol* 179:665-72
		Oxide and carbon	**2007**
	This immunosuppressive activity was confirmed in several models of inflammation with various nanoparticles.	*NP*	*references #* (16, 55, 56)
Mitchell et al. (57)	In investigating how CNT suppress immune function, this paper was the first and perhaps the most convincing to propose that nanoparticles induce immunosuppression orchestrated by IL-10 and TGF-β.	CNT	*Nat Nanotechnol* 4:451-6 **2009**
Lo Re et al. (58)	This paper was the first indicating that silica-induced lung fibrosis results from TGF-β-producing regulatory T lymphocytes (T regs).	silica	*Am J Respier Crit Care Med* 184:1270-81 **2011**
	NP also promote a selective expansion of T regs. The pathological role of T regs was confirmed in silicosis and mesothelioma.	*polystyrene NP*	*references #* (59–61)
Shvedova et al. (62)	This manuscript elegantly demonstrated that TGF-β-expressing MDSC (Myeloid Derived Suppressive Cells) are crucial for tumor development associated to CNT.	CNT	*Small* 243:320-30 **2013**
	MDSC are also implicated in silica-induced lung fibrosis and mesothelioma.	*silica*	*references #* (63, 64)
Murthy et al. (53)	A comprehensive study showing that asbestos preferentially polarized M2 macrophages during asbestosis in animal and human.	asbestos	*FASEB* 29:3527-36 **2015**
	Other particles promoted accumulation of M2 macrophages.	*silica and CNT*	*reference #* (65, 66)
Chen et al. (37)	This paper indicated that silicosis and silica-induced lung responses (see related reference #101) are associated with immunosuppressive IL-10-producing B lymphocytes (B regs).	silica	*Front Immunol* 8:110 **2017**

CNT, carbon nanotubes; NP, nanoparticles.

functions after particle exposure. First, lung expression of IL-10 was intimately associated to the development of particle-induced fibrosis and cancer and could explain the absence of chronic and progressive inflammation in human and mouse models (37, 53, 57, 84–88). Additional data supports that IL-10 participates in the extension of fibrosis since targeted overexpression of IL-10 in the murine airways caused, by itself, collagen deposition, accumulation of mesenchymal cells and airway remodeling with fibrosis (89, 90). Subsequently, it has been demonstrated that IL-10 limits inflammatory response but promotes fibrotic reaction. Indeed, mice deficient for IL-10 developed exaggerated acute inflammation but limited lung fibrosis in response to silica (51, 91). Conversely, overexpression of IL-10 in the lung, by using an adenovirus coding for this cytokine, limited the inflammatory process induced by silica, but increased the fibrotic response (92). It is now admitted that this potent immunosuppressive cytokine has direct effects on fibroblasts and matrix protein release (93). In addition, IL-10 induces the expression of pro-fibrotic mediators (i.e., TGF-β) by macrophages and limits the synthesis of anti-fibrotic mediators (i.e., prostaglandin E2) by epithelial cells (91). The deleterious effect of IL-10 is not limited to fibrosis development but is also implicated in the carcinogenic process resulting from particles. Recent results showed that asbestos exposure restricts effector T lymphocyte activation and impairs anti-tumor immunity through IL-10 release (69, 94). IL-10-expressing macrophages increased mesothelioma cell proliferation and resistance to treatment (85, 95). Collectively, these data additionally challenge the concept that only pro-inflammatory mediators and inflammation lead to fibrosis and cancer and conclusively demonstrate a key role of persistent immunosuppressive mediators in the development of particle-related disorders in the absence of inflammation (**Figure 2**).

CONTRIBUTION OF REGULATORY T AND B LYMPHOCYTES IN RESPONSE TO PARTICLES

Based on the immunosuppressive profile of silica-treated mice, the role of regulatory T lymphocytes (T regs) in the development of lung responses to particles was investigated. This specialized thymus-derived sub-population of Th lymphocytes acts to suppress immune responses, thereby maintaining homeostasis and self-tolerance. They mediate immunosuppression by producing the immunoregulatory cytokines IL-10 and TGF-β (96). Recent results indicated that T regs are progressively and specifically accumulated in lung tissue of mice treated with silica where they promote pulmonary immunosuppression and fibrosis (58, 60) (**Figure 2**). This hallmark of immunological tolerance

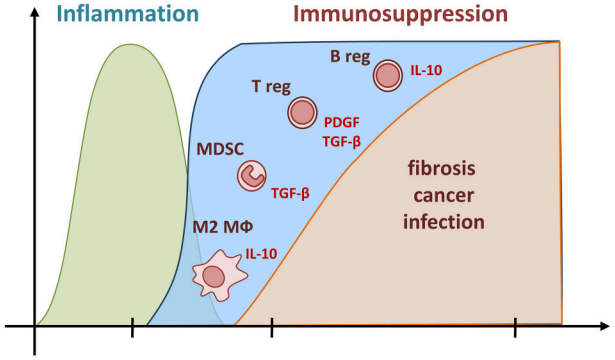

FIGURE 2 | Pathological functions of persistent immunosuppressive cells and mediators during long-term responses to particles. Unresolved Immunosuppression (in blue) represents an alternative event during the responses to particles. According to this new pathological pathway, fibrogenesis, and carcinogenesis are governed by a persistent accumulation of immunosuppressive myeloid (M2 and MDSC) and lymphoid (T and B regs) cells and a sustained production of their related cytokines (IL-10 and TGF-β). These immunoregulatory components limit both the recruitment of inflammatory cells and the activity of pro-inflammatory mediators (in green). The high amount of immunosuppressive cytokines produced can, in addition to their anti-inflammatory action, also act as profibrotic mediators, conceivably by stimulating mesenchymal cells to overproduce collagenase inhibitors and ultimately matrix elements under non-inflammatory conditions. The persistence of immunosuppressive cells and mediators is also incriminated in carcinogenesis and infection by preventing host immune responses directed against transformed cells and microorganisms.

and immunosuppressive environment was observed with other particles, detected locally and systemically, and induced by the Wnt/B-catenin pathway (57, 59, 97, 98). Lung T regs directly stimulated fibroblast proliferation and collagen deposition after transfer in non-treated mice (58). The direct profibrotic effects of T regs were reduced by inhibiting the PDGF-B/TGF-β signaling pathway, demonstrating that T regs increase tissue fibroblast numbers, and consequently, amplify collagen deposition. *In vitro* and *in vivo* studies additionally showed that mesotheliomagenic fibers such as asbestos directly enhance the immunosuppressive function of T regs and their capacity to release TGF-β and IL-10 (61, 94). In addition, the marked presence of T regs have been detected during lung carcinogenesis after silica or asbestos exposure (99, 100). From these last studies, it has been concluded that the effect of particles on T regs accumulation and function induces a maintained tolerant microenvironment counteracting anti-tumor host innate and adaptive immunity and favoring tumoral cell evasion and the occurrence of particle-induced tumors.

More recently, Chen and colleagues have identified an additional immunosuppressive subpopulation of B lymphocytes recruited in response to silica in human and animal (37, 101) (**Figure 2**). Regulatory B-lymphocytes (B regs) are immunosuppressive cells releasing IL-10 and TGF-β that support immunological tolerance and suppress immunopathology by limiting the expansion of inflammatory T cells. B regs are defined as the immunosuppressive counterpart of antibody-producing B2 lymphocytes (or conventional B cells) (102). The regulatory B-cell subpopulation has been reported to be recruited to the tumor aggregates and thereby promotes carcinogenesis by attenuating anti-tumor immune responses (103). Their pro-fibrotic functions have been attributed to their capacity to release IL-10 in silica-treated mice (101). As observed in IL-10-deficient mice, reduction of fibrosis in B reg-depleted mice was associated with an increased neutrophilic inflammation (101). Interestingly, IL-10-producing B regs convert T eff into T regs thus increasing immunological tolerance after particle exposure (104). The observation that immunosuppressive T and B-lymphocytes persistently populate damaged tissue strongly suggests that these cells are crucial immune components explaining the development of fibrotic and carcinogenic responses to particles in absence of substantial inflammation.

CRITICAL ROLES OF IMMUNOSUPPRESSIVE MYELOID CELLS

Infiltrated macrophages in cancer or asthma acquire a particular phenotype called M2, which provides an immunosuppressive microenvironment for tumor growth and allergic tolerance (105, 106). Recent studies also revealed a preferential engagement of immunosuppressive M2 macrophages after inhalation of particles (**Figure 2**). There is an increased predominance of M2-polarized macrophages in patients developing asbestosis (53). In animal, M2-related mediators such as Arginase 1, crystallizable protein YM-1 or IL-10 were all increased in response to reactive particles such as silica, ultrafine amorphous silica and CNT, appointing M2-polarized macrophages as pivotal (53, 65, 66, 107–109). Authors have recently incriminated oxidized phospholipids, IL-4 or IL-13 in the polarization of M2 macrophages that display enhanced production of TGF-β. Evidence also showed that this last cytokine explains the deleterious activities of M2 macrophages after particle treatment (43, 53, 110–112). These results therefore argue that the continuous accumulation of M2 macrophages and their products, initially for counteracting the effects of inflammatory M1 macrophages, participates in the establishment of the fibrogenic and mesotheliomagenic lesions generated by particles.

Myeloid-derived suppressor cells (MDSC) represent a heterogeneous population of immature neutrophilic and monocytic myeloid cells that displays potent immunosuppressive activities and inhibits immune effector cell functions in diverse chronic pathologies such as cancer (113). The accumulation of immature and immunosuppressive myeloid cells is also a central event during dust-induced fibrosis and cancer with predominant immunosuppression (**Figure 2**). Indeed, recent investigations have elegantly demonstrated that CNT or asbestos exposure induces a robust accumulation of MDSC that actively release TGF-β and promote cancer progression in mice (62, 64, 114). Fibrotic responses to silica also comprise an accumulation of monocytic MDSC that possess the intrinsic capacity to promote release of the collagenase inhibitor TIMP-1 by fibroblasts. The subsequent elaboration of a non-degrading matrix environment was attributed to monocytic MDSC-derived TGF-β (63). These observations newly indicate that immunoregulatory M2

macrophages and MDSC, along with T and B regs, are implicated in fibrogenesis and carcinogenesis, especially when these cells are continuously accumulated and when inflammatory activity is limited (**Figure 2**).

NANOPARTICLES INDUCE IMMUNOSUPPRESSION

The emerging concept that particles orchestrate the establishment of immunosuppressive responses is consolidated by several studies exploring the impact of nanoparticles on the immune system. As mentioned above for micrometric particles, the major concern in the field of nanotoxicology is historically related toward the capacity of nanoparticles to induce inflammation and immunostimulation (115). Nevertheless, this exclusive view has been revisited and recent attention has been given to anti-inflammatory and immunosuppressive properties of these particles (55). There is, indeed, a growing body of evidence showing that nanoparticles also display strong immunosuppressive effects (56). In 2007, Ryan and colleagues were the first to report that fullerene nanoparticles prevented mast-cell related diseases such as asthma, arthritis, and sclerosis (54). Other pioneer studies unexpectedly discovered that dendrimer nanoparticles improved disease scores in animal models of granulomatous, autoimmune, and edema diseases (116). Another example illustrating the immunosuppressive properties of nanoparticles is the study by Rajan (117). Liposomal nanoparticles possess the ability to elicit an immunosuppressive cell environment that subsequently suppress anti-tumor immunity and favor tumor progression.

The particles inducing immunosuppression mainly include metal (e.g., gold, silver, iron oxide, cerium oxide, and zinc oxide) and carbon (CNT, fullerenes) nanoparticles (56). The immunosuppressive effects of nanoparticles also depend on their physicochemical properties. For instance, small nanoparticles are more immunosuppressive than large particles (116, 118). The exact physicochemical determinants accountable for nanoparticle-induced immunosuppressive activities remain, however, unclear and require additional investigations. There is also a crucial need to determine whether molecules enrobing particles (e.g., LPS) are important for the immunosuppressive activities of (nano)particles (115).

Interestingly, research in nanotoxicology elucidated different molecular mechanisms explaining how particles promote immunosuppression. These mechanisms involve direct interference of nanoparticles with TLR-, NFκB-, or STAT1-signaling pathways (55, 119). Iron nanoparticles specifically alter IL-1β processing by preventing inflammasome assembly (120). A direct inhibitory interaction between gold nanoparticles and inflammatory cytokines have been also observed from the study of Sumbayev (118). Carbon and cerium nanomaterials exhibit potent free radical-scavenger properties and attenuate oxidant molecule production by particle-activated immune cells. These findings confer to these nanoparticles important antioxidant properties that suppress oxidative stress and inflammatory responses *in vitro* and *in vivo* (119, 121, 122).

Nanoparticles strongly and directly polarize the immune system and establish a preferentially immunosuppressive environment. CNT induce the expression of TGF-β and IL-10 (57) as observed for micrometric silica (see above). Nanoparticles also facilitate polarization of immunosuppressive T regs and anti-inflammatory Th2 lymphocytes (98, 123, 124). Mechanistic studies investigating the effects of nanoparticles on T-lymphocyte immunosuppressive lineage commitment revealed that nanoparticles (carbon, grapheme, and iron) directly interfere with autophagy, ROS production, NFκB-nuclear translocation or antigen processing by dendritic cells (124–126). While nanoparticles mainly operated through DC and T cells, they additionally target macrophages and myeloid cells. Liposomes reduced inflammatory functions of macrophages and increased anti-inflammatory mediator expression in myeloid cells (117).

The exact adverse effects of nanoparticle-induced unresolved immunosuppression are not yet delineated but fibrosis development caused by CNT or cerium has been linked to the immunosuppressive cytokines TGF-β and IL-10 (52, 72, 127, 128). Altered host resistance to infection and cancer represents another possible pathophysiological consequence of maintained immunosuppression. Administration of titanium oxide nanoparticles or liposomes inhibited lymphocyte- and macrophage-related immune responses and increased susceptibility to tumor growth (117, 129). Augmented viral and bacterial infections have also been observed after exposure to carbon nanoparticles (130, 131).

MUTUAL ROLES OF INFLAMMATION AND IMMUNOSUPPRESSION IN RESPONSES TO PARTICLES

Taken together, the studies described above and documented in **Table 1** support an additional and alternative pathological pathway, which is operative during tissue responses to particles. This new paradigm proposes that fibrogenesis, carcinogenesis, and infections can develop from persistent immunosuppressive developments induced by micro- or nano-particles under non-inflammatory conditions (**Figure 3**, below). Unresolved immunosuppression participates in the development of fibrosis by activating profibrotic factor release and inhibiting matrix degradation. The immunosuppressive milieu can also favor cancer and infection progression by facilitating tumor and microbial escape from immune surveillance.

This new pathological avenue does not overshadow the relevance of the inflammatory scenario. Indeed, the compelling findings accumulated over the years indubitably support that uncontrolled fibroblast growth and genomic instability rely upon predominant inflammation, especially when immunosuppressive activity is lacking (**Figure 3**, above). The emergence of immune complex deposition and autoimmune disorders is additionally associated to persistent inflammation in animal or human exposed to particles. The fact that particle-related autoimmune diseases are not mechanistically covered by sustained immunosuppression indicates that inflammation remains a crucial event in response to particles.

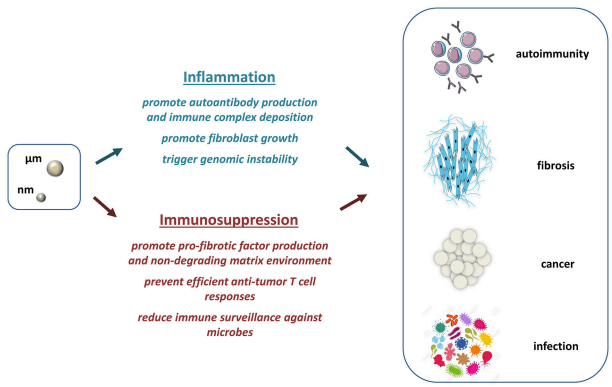

FIGURE 3 | Mutual roles of inflammatory and immunosuppressive responses in particle-induced chronic diseases. The classical scenario explaining the emergence of autoimmune diseases, fibrosis, and cancer after dust exposure mainly relies on predominant and persistent inflammation (blue). Inflammatory responses directly promote fibroblast growth and uncontrolled matrix deposition, trigger genomic instability, and cell transformation, and support autoantibody and immune complex production. An additional paradigm is now offered and comprises predominant and unresolved immunosuppression in response to particles (red). This pathway relies upon a sustained accumulation of immunosuppressive components that include mediators implicated in fibroblast activation, tumor cell and microbe evasion. The exclusive or simultaneous presence of immunoregulatory and immunostimulatory mechanisms can explain the diversity of immune responses and pathologies existing in exposed human or animal.

Importantly, the inflammatory process governs the early accumulation of immunosuppressive cells and mediators by activating several anti-inflammatory signaling pathways (e.g., IL-10) mediated predominantly by NFκB (132). This notion indicates that inflammation can predispose to a developing immunosuppressive environment and that inflammation and immunosuppression are functionally linked.

Altogether, these observations clearly argue for a more complicated mechanism in particle toxicology, wherein both types of immune responses (persistent inflammation and immunosuppression) could promote chronic diseases after particle inhalation. The mutual roles of inflammation and immunosuppression well explain the diversity of particle-induced immune polarization and pathologies (**Figure 3**). Interestingly, these apparently opposite processes are not systematically exclusive and may be, in contrast, concomitant. The view that uncontrolled immunoregulatory and immunostimulatory responses can co-exist is supported by recent human and animal studies showing mixed inflammatory and immunosuppressive elements (e.g., elevated levels of TNF-α, IL-1β, IL-10, and TGF-β) during fibrogenesis and carcinogenesis induced by particles (6, 133, 134).

TOXICOLOGICAL AND CLINICAL PERSPECTIVES

It remains, however, to learn how to extrapolate and how to benefit from these observations in predictive toxicology and translational medicine. Current bioassays testing particle reactivity are exclusively based on the appreciation of inflammatory components and suffer from a lack of specificity (135, 136). These tests could be enriched by considering the expression of immunoregulatory mediators or signatures. For instance, release of TGF-β and IL-10 and subsequent abrogation of IL-1 and TNF-α production by treated macrophages could be used to identify reactive particles as proposed by the team of Boraschi and colleagues (137). Furthermore, blockade of inflammasome machinery or antigen-presenting capacity of macrophages and DC could be considered as clear sign of immunosuppressive responses. Inhibition of inflammatory pathologies in animal models could also reflect ability of particles to trigger immunosuppression (56).

In recent years, the increase of anti-tumor responses obtained in clinic trials by blocking the immunosuppressive environment of tumors have revolutionized cancer treatment. Monoclonal antibody-based immunotherapies targeting TGF-β and IL-10 or T cell immune checkpoint receptors (PD-1 or CTLA4) are now available and confer long-term benefit for patients (138–140). Additional experimental and clinical studies are necessary to determine whether this therapeutic option inhibiting immunosuppressive responses is also promising for the treatment of patients affected by particle-associated disorders.

The existence of at least two different pathogenic routes may explain why existing therapies are controversial and disappointing with a strong differential effect in specific subgroups of patients (141, 142). The opportunity to distinguish the prevailing immune response or profile (inflammation and immunosuppression) existing in patients should also help the clinician to categorize patients, assess disease progression and select the most appropriate therapy to inhibit key effector cells and mediators of inflammation (steroids) and/or immunosuppression (immunotherapy). This possibility has been already observed in available animal models. Silica-induced lung fibrosis in rats (associated with chronic inflammation) can be reverted by anti-inflammatory treatment while in mice (developing preferentially unresolved immunosuppressive responses), silicosis is resistant to anti-inflammatory therapy but prevented by T regs neutralization (43, 60). The enthusiasm for the discovery of novel drug targets to treat particle-related diseases should be tempered as inflammation and immunosuppression are extremely imbricated with each other, leading to the fact that inhibition of one response may be compensated by the extension of the other (22, 58).

AUTHOR CONTRIBUTIONS

The author confirms being the sole contributor of this work and has approved it for publication.

FUNDING

This work was funded by the Actions de Recherche Concertées, Fédération Wallonie-Bruxelles (ARC 09/14-021 and 14/19-056), the Fondation Contre le Cancer (2012-219, 2014-148, and 150), the Fonds de la Recherche Scientifique (FNRS; Projects PDR T.0119.13 and CDR J0049.16). FH is a Senior Research Associate with the FNRS, Belgium.

REFERENCES

1. Sayan M, Mossman BT. The NLRP3 inflammasome in pathogenic particle and fibre-associated lung inflammation and diseases. *Part Fibre Toxicol.* (2016) 13:51. doi: 10.1186/s12989-016-0162-4
2. Hoy RF, Brims F. Occupational lung diseases in Australia. *Med J Aust.* (2017) 207:443–8. doi: 10.5694/mja17.00601
3. Hoet P, Desvallees L, Lison D. Do current OELs for silica protect from obstructive lung impairment? A critical review of epidemiological data. *Crit Rev Toxicol.* (2017) 47:650–77. doi: 10.1080/10408444.2017.1315363
4. Lee S, Hayashi H, Mastuzaki H, Kumagai-Takei N, Otsuki T. Silicosis and autoimmunity. *Curr Opin Allergy Clin Immunol.* (2017) 17:78–84. doi: 10.1097/ACI.0000000000000350
5. Hoy RF, Baird T, Hammerschlag G, Hart D, Johnson AR, King P, et al. Artificial stone-associated silicosis: a rapidly emerging occupational lung disease. *Occup Environ Med.* (2018) 75:3–5. doi: 10.1136/oemed-2017-104428
6. Anlar HG, Bacanli M, Iritas S, Bal C, Kurt T, Tutkun E, et al. Effects of occupational silica exposure on OXIDATIVE stress and immune system parameters in ceramic workers in TURKEY. *J Toxicol Environ Health A* (2017) 80:688–96. doi: 10.1080/15287394.2017.1286923
7. Akgun M. Denim production and silicosis. *Curr Opin Pulm Med.* (2016) 22:165–9. doi: 10.1097/MCP.0000000000000249
8. Leung CC, Yu IT, Chen W. Silicosis. *Lancet* (2012) 379:2008–18. doi: 10.1016/S0140-6736(12)60235-9
9. Ou L, Song B, Liang H, Liu J, Feng X, Deng B, et al. Toxicity of graphene-family nanoparticles: a general review of the origins and mechanisms. *Part Fibre Toxicol.* (2016) 13:57. doi: 10.1186/s12989-016-0168-y
10. Pollard KM. Silica, silicosis, and autoimmunity. *Front Immunol.* (2016) 7:97. doi: 10.3389/fimmu.2016.00097
11. Rabolli V, Lison D, Huaux F. The complex cascade of cellular events governing inflammasome activation and IL-1β processing in response to inhaled particles. *Part Fibre Toxicol.* (2016) 13:40. doi: 10.1186/s12989-016-0150-8
12. Nakayama M. Macrophage recognition of crystals and nanoparticles. *Front Immunol.* (2018) 9:103. doi: 10.3389/fimmu.2018.00103
13. Kadariya Y, Menges CW, Talarchek J, Cai KQ, Klein-Szanto AJ, Pietrofesa RA, et al. Inflammation-related IL1β/IL1R signaling promotes the development of asbestos-induced malignant mesothelioma. *Cancer Prev Res (Phila)* (2016) 9:406–14. doi: 10.1158/1940-6207.CAPR-15-0347
14. Hegde B, Bodduluri SR, Satpathy SR, Alghsham RS, Jala VR, Uriarte SM, et al. Inflammasome-independent leukotriene B4 production drives crystalline silica-induced sterile inflammation. *J Immunol.* (2018) 200:3556–67. doi: 10.4049/jimmunol.1701504
15. Chen J, Yao Y, Su X, Shi Y, Song X, Xie L, et al. Comparative RNA-Seq transcriptome analysis on silica induced pulmonary inflammation and fibrosis in mice silicosis model. *J Appl Toxicol.* (2018) 38:773–82. doi: 10.1002/jat.3587
16. Alsaleh NB, Brown JM. Immune responses to engineered nanomaterials: current understanding and challenges. *Curr Opin Toxicol.* (2018) 10:8–14. doi: 10.1016/j.cotox.2017.11.011
17. Hiraku Y, Kawanishi S, Ichinose T, Murata M. The role of iNOS-mediated DNA damage in infection- and asbestos-induced carcinogenesis. *Ann N Y Acad Sci.* (2010) 1203:15–22. doi: 10.1111/j.1749-6632.2010.05602.x
18. Mossman BT, Shukla A, Heintz NH, Verschraegen CF, Thomas A, Hassan R. New insights into understanding the mechanisms, pathogenesis, and management of malignant mesotheliomas. *Am J Pathol.* (2013) 182:1065–77. doi: 10.1016/j.ajpath.2012.12.028
19. Winkler HC, Kornprobst J, Wick P, von Moos LM, Trantakis I, Schraner EM, et al. MyD88-dependent pro-interleukin-1β induction in dendritic cells exposed to food-grade synthetic amorphous silica. *Part Fibre Toxicol.* (2017) 14:21. doi: 10.1186/s12989-017-0202-8
20. Thakur C, Wolfarth M, Sun J, Zhang Y, Lu Y, Battelli L, et al. Oncoprotein mdig contributes to silica-induced pulmonary fibrosis by altering balance between Th17 and Treg T cells. *Oncotarget* (2015) 6:3722–36. doi: 10.18632/oncotarget.2914
21. Lo Re S, Dumoutier L, Couillin I, Van Vyve C, Yakoub Y, Uwambayinema F, et al. IL-17A-producing gammadelta T and Th17 lymphocytes mediate lung inflammation but not fibrosis in experimental silicosis. *J Immunol.* (2010) 184:6367–77. doi: 10.4049/jimmunol.0900459
22. Re SL, Giordano G, Yakoub Y, Devosse R, Uwambayinema F, Couillin I, et al. Uncoupling between inflammatory and fibrotic responses to silica: evidence from MyD88 knockout mice. *PLoS ONE* (2014) 9:e99383. doi: 10.1371/journal.pone.0099383
23. Huaux F, Lo Re S, Giordano G, Uwambayinema F, Devosse R, Yakoub Y, et al. IL-1alpha induces CD11b(low) alveolar macrophage proliferation and maturation during granuloma formation. *J Pathol.* (2015) 235:698–709. doi: 10.1002/path.4487
24. Vietti G, Lison D, van den Brule S. Mechanisms of lung fibrosis induced by carbon nanotubes: towards an Adverse Outcome Pathway (AOP). *Part Fibre Toxicol.* (2016) 13:11. doi: 10.1186/s12989-016-0123-y
25. Zheng H, Hogberg J, Stenius U. ATM-activated autotaxin (ATX) propagates inflammation and DNA damage in lung epithelial cells: a new mode of action for silica-induced DNA damage? *Carcinogenesis* (2017) 38:1196–206. doi: 10.1093/carcin/bgx100
26. Ferro A, Zebedeo CN, Davis C, Ng KW, Pfau JC. Amphibole, but not chrysotile, asbestos induces anti-nuclear autoantibodies and IL-17 in C57BL/6 mice. *J Immunotoxicol.* (2014) 11:283–90. doi: 10.3109/1547691X.2013.847510
27. Zebedeo CN, Davis C, Pena C, Ng KW, Pfau JC. Erionite induces production of autoantibodies and IL-17 in C57BL/6 mice. *Toxicol Appl Pharmacol.* (2014) 275:257–64. doi: 10.1016/j.taap.2014.01.018
28. Bates MA, Brandenberger C, Langohr I, Kumagai K, Harkema JR, Holian A, et al. Silica triggers inflammation and ectopic lymphoid neogenesis in the lungs in parallel with accelerated onset of systemic autoimmunity and glomerulonephritis in the lupus-prone NZBWF1 mouse. *PLoS ONE* (2015) 10:e0125481. doi: 10.1371/journal.pone.0125481
29. Biswas R, Trout KL, Jessop F, Harkema JR, Holian A. Imipramine blocks acute silicosis in a mouse model. *Part Fibre Toxicol.* (2017) 14:36. doi: 10.1186/s12989-017-0217-1
30. Miao R, Ding B, Zhang Y, Xia Q, Li Y, Zhu B. Proteomic profiling change during the early development of silicosis disease. *J Thorac Dis.* (2016) 8:329–41. doi: 10.21037/jtd.2016.02.46
31. Comar M, Zanotta N, Bonotti A, Tognon M, Negro C, Cristaudo A, et al. Increased levels of C-C chemokine RANTES in asbestos exposed workers and in malignant mesothelioma patients from an hyperendemic area. *PLoS ONE* (2014) 9:e104848. doi: 10.1371/journal.pone.0104848
32. Polatli M, Tuna HT, Yenisey C, Serter M, Cildag O. Lung function and IFN-gamma levels in the sera of silica-exposed workers. *J Interferon Cytokine Res.* (2008) 28:311–6. doi: 10.1089/jir.2007.0093
33. Robinson BW, Rose AH, Hayes A, Musk AW. Increased pulmonary gamma interferon production in asbestosis. *Am Rev Respir Dis.* (1988) 138:278–83. doi: 10.1164/ajrccm/138.2.278
34. Greenberg MI, Waksman J, Curtis J. Silicosis: a review. *Dis Mon.* (2007) 53:394–416. doi: 10.1016/j.disamonth.2007.09.020
35. Robinson C, Alfonso H, Woo S, Olsen N, Bill Musk AW, Robinson BW, et al. Effect of NSAIDS and COX-2 inhibitors on the incidence and severity of asbestos-induced malignant mesothelioma: evidence from an animal model and a human cohort. *Lung Cancer* (2014) 86:29–34. doi: 10.1016/j.lungcan.2014.08.005
36. Baird T, Putt M, Dettrick A. A stonemason with accelerated silicosis in the setting of tumour necrosis factor alpha inhibitor therapy. *Respirol Case Rep.* (2016) 4:e00171. doi: 10.1002/rcr2.171
37. Chen Y, Li C, Lu Y, Zhuang H, Gu W, Liu B, et al. IL-10-Producing $CD1d^{hi}CD5^{+}$ regulatory B cells may play a critical role in modulating immune homeostasis in silicosis patients. *Front Immunol.* (2017) 8:110. doi: 10.3389/fimmu.2017.00110
38. Beamer CA, Seaver BP, Shepherd DM. Aryl hydrocarbon receptor (AhR) regulates silica-induced inflammation but not fibrosis. *Toxicol Sci.* (2012) 126:554–68. doi: 10.1093/toxsci/kfs024
39. Shvedova AA, Kisin ER, Murray AR, Kommineni C, Castranova V, Fadeel B, et al. Increased accumulation of neutrophils and decreased fibrosis in the lung of NADPH oxidase-deficient C57BL/6 mice exposed to carbon nanotubes. *Toxicol Appl Pharmacol.* (2008) 231:235–40. doi: 10.1016/j.taap.2008.04.018

40. Brass DM, McGee SP, Dunkel MK, Reilly SM, Tobolewski JM, Sabo-Attwood T, et al. Gender influences the response to experimental silica-induced lung fibrosis in mice. *Am J Physiol Lung Cell Mol Physiol.* (2010) 299:L664–71. doi: 10.1152/ajplung.00389.2009
41. Dong J, Porter DW, Batteli LA, Wolfarth MG, Richardson DL, Ma Q. Pathologic and molecular profiling of rapid-onset fibrosis and inflammation induced by multi-walled carbon nanotubes. *Arch Toxicol.* (2015) 89:621–33. doi: 10.1007/s00204-014-1428-y
42. Rabolli V, Lo Re S, Uwambayinema F, Yakoub Y, Lison D, Huaux F. Lung fibrosis induced by crystalline silica particles is uncoupled from lung inflammation in NMRI mice. *Toxicol Lett.* (2011) 203:127–34. doi: 10.1016/j.toxlet.2011.03.009
43. Barbarin V, Nihoul A, Misson P, Arras M, Delos M, Leclercq I, et al. The role of pro- and anti-inflammatory responses in silica-induced lung fibrosis. *Respir Res.* (2005) 6:112. doi: 10.1186/1465-9921-6-112
44. Rydman EM, Ilves M, Vanhala E, Vippola M, Lehto M, Kinaret PA, et al. A single aspiration of rod-like carbon nanotubes induces asbestos-like pulmonary inflammation mediated in part by the IL-1 receptor. *Toxicol Sci.* (2015) 147:140–55. doi: 10.1093/toxsci/kfv112
45. Song L, Weng D, Dai W, Tang W, Chen S, Li C, et al. Th17 can regulate silica-induced lung inflammation through an IL-1β-dependent mechanism. *J Cell Mol Med.* (2014) 18:1773–84. doi: 10.1111/jcmm.12341
46. Guo J, Gu N, Chen J, Shi T, Zhou Y, Rong Y, et al. Neutralization of interleukin-1 beta attenuates silica-induced lung inflammation and fibrosis in C57BL/6 mice. *Arch Toxicol.* (2013) 87:1963–73. doi: 10.1007/s00204-013-1063-z
47. Davis GS, Pfeiffer LM, Hemenway DR, Rincon M. Interleukin-12 is not essential for silicosis in mice. *Part Fibre Toxicol.* (2006) 3:2. doi: 10.1186/1743-8977-3-2
48. Satpathy SR, Jala VR, Bodduluri SR, Krishnan E, Hegde B, Hoyle GW, et al. Crystalline silica-induced leukotriene B4-dependent inflammation promotes lung tumour growth. *Nat Commun.* (2015) 6:7064. doi: 10.1038/ncomms8064
49. Chow MT, Tschopp J, Moller A, Smyth MJ. NLRP3 promotes inflammation-induced skin cancer but is dispensable for asbestos-induced mesothelioma. *Immunol Cell Biol.* (2012) 90:983–6. doi: 10.1038/icb.2012.46
50. Robinson C, Walsh A, Larma I, O'Halloran S, Nowak AK, Lake RA. MexTAg mice exposed to asbestos develop cancer that faithfully replicates key features of the pathogenesis of human mesothelioma. *Eur J Cancer* (2011) 47:151–61. doi: 10.1016/j.ejca.2010.08.015
51. Huaux F, Louahed J, Hudspith B, Meredith C, Delos M, Renauld JC, et al. Role of interleukin-10 in the lung response to silica in mice. *Am J Respir Cell Mol Biol.* (1998) 18:51–9. doi: 10.1165/ajrcmb.18.1.2911
52. Park EJ, Roh J, Kim SN, Kang MS, Han YA, Kim Y, et al. A single intratracheal instillation of single-walled carbon nanotubes induced early lung fibrosis and subchronic tissue damage in mice. *Arch Toxicol.* (2011) 85:1121–31. doi: 10.1007/s00204-011-0655-8
53. Murthy S, Larson-Casey JL, Ryan AJ, He C, Kobzik L, Carter AB. Alternative activation of macrophages and pulmonary fibrosis are modulated by scavenger receptor, macrophage receptor with collagenous structure. *FASEB J.* (2015) 29:3527–36. doi: 10.1096/fj.15-271304
54. Ryan JJ, Bateman HR, Stover A, Gomez G, Norton SK, Zhao W, et al. Fullerene nanomaterials inhibit the allergic response. *J Immunol.* (2007) 179:665–72. doi: 10.4049/jimmunol.179.1.665
55. Ilinskaya AN, Dobrovolskaia MA. Immunosuppressive and anti-inflammatory properties of engineered nanomaterials. *Br J Pharmacol.* (2014) 171:3988–4000. doi: 10.1111/bph.12722
56. Ngobili TA, Daniele MA. Nanoparticles and direct immunosuppression. *Exp Biol Med (Maywood)* (2016) 241:1064–73. doi: 10.1177/1535370216650053
57. Mitchell LA, Lauer FT, Burchiel SW, McDonald JD. Mechanisms for how inhaled multiwalled carbon nanotubes suppress systemic immune function in mice. *Nat Nanotechnol.* (2009) 4:451–6. doi: 10.1038/nnano.2009.151
58. Lo Re S, Lecocq M, Uwambayinema F, Yakoub Y, Delos M, Demoulin JB, et al. Platelet-derived growth factor-producing $CD4^+$ $Foxp3^+$ regulatory T lymphocytes promote lung fibrosis. *Am J Respir Crit Care Med.* (2011) 184:1270–81. doi: 10.1164/rccm.201103-0516OC
59. Hess KL, Oh E, Tostanoski LH, Andorko JI, Susumu K, Deschamps JR, et al. Engineering immunological tolerance using quantum dots to tune the density of self-antigen display. *Adv Funct Mater.* (2017) 27:1700290. doi: 10.1002/adfm.201700290
60. Liu F, Liu J, Weng D, Chen Y, Song L, He Q, et al. $CD4^+CD25^+Foxp3^+$ regulatory T cells depletion may attenuate the development of silica-induced lung fibrosis in mice. *PLoS ONE* (2010) 5:e15404. doi: 10.1371/journal.pone.0015404
61. Ying C, Maeda M, Nishimura Y, Kumagai-Takei N, Hayashi H, Matsuzaki H, et al. Enhancement of regulatory T cell-like suppressive function in MT-2 by long-term and low-dose exposure to asbestos. *Toxicology* (2015) 338:86–94. doi: 10.1016/j.tox.2015.10.005
62. Shvedova AA, Tkach AV, Kisin ER, Khaliullin T, Stanley S, Gutkin DW, et al. Carbon nanotubes enhance metastatic growth of lung carcinoma via up-regulation of myeloid-derived suppressor cells. *Small* (2013) 9:1691–5. doi: 10.1002/smll.201201470
63. Lebrun A, Lo Re S, Chantry M, Izquierdo Carerra X, Uwambayinema F, Ricci D, et al. $CCR2^+$ monocytic myeloid-derived suppressor cells (M-MDSCs) inhibit collagen degradation and promote lung fibrosis by producing transforming growth factor-beta1. *J Pathol.* (2017) 243:320–30. doi: 10.1002/path.4956
64. Shvedova AA, Kisin ER, Yanamala N, Tkach AV, Gutkin DW, Star A, et al. MDSC and TGFbeta are required for facilitation of tumor growth in the lungs of mice exposed to carbon nanotubes. *Cancer Res.* (2015) 75:1615–23. doi: 10.1158/0008-5472.CAN-14-2376
65. Xiang GA, Zhang YD, Su CC, Ma YQ, Li YM, Zhou X, et al. Dynamic changes of mononuclear phagocytes in circulating, pulmonary alveolar and interstitial compartments in a mouse model of experimental silicosis. *Inhal Toxicol.* (2016) 28:393–402. doi: 10.1080/08958378.2016.1188186
66. Dong J, Ma Q. Macrophage polarization and activation at the interface of multi-walled carbon nanotube-induced pulmonary inflammation and fibrosis. *Nanotoxicology* (2018) 12:153–68. doi: 10.1080/17435390.2018.1425501
67. Helmig S, Belwe A, Schneider J. Association of transforming growth factor beta1 gene polymorphisms and asbestos-induced fibrosis and tumors. *J Investig Med.* (2009) 57:655–61. doi: 10.2310/JIM.0b013e3181a4f32a
68. Jagirdar J, Begin R, Dufresne A, Goswami S, Lee TC, Rom WN. Transforming growth factor-beta (TGF-beta) in silicosis. *Am J Respir Crit Care Med.* (1996) 154(4 Pt 1):1076–81. doi: 10.1164/ajrccm.154.4.8887610
69. Matsuzaki H, Kumagai-Takei N, Lee S, Maeda M, Sada N, Hatayama T, et al. Search for biomarkers of asbestos exposure and asbestos-induced cancers in investigations of the immunological effects of asbestos. *Environ Health Prev Med.* (2017) 22:53. doi: 10.1186/s12199-017-0661-4
70. Li Y, Karjalainen A, Koskinen H, Vainio H, Pukkala E, Hemminki K, et al. Serum growth factors in asbestosis patients. *Biomarkers* (2009) 14:61–6. doi: 10.1080/13547500802676868
71. Khalil N, O'Connor RN, Flanders KC, Unruh H. TGF-beta 1, but not TGF-beta 2 or TGF-beta 3, is differentially present in epithelial cells of advanced pulmonary fibrosis: an immunohistochemical study. *Am J Respir Cell Mol Biol.* (1996) 14:131–8. doi: 10.1165/ajrcmb.14.2.8630262
72. Dong J, Ma Q. Osteopontin enhances multi-walled carbon nanotube-triggered lung fibrosis by promoting TGF-beta1 activation and myofibroblast differentiation. *Part Fibre Toxicol.* (2017) 14:18. doi: 10.1186/s12989-017-0198-0
73. Polimeni M, Gulino GR, Gazzano E, Kopecka J, Marucco A, Fenoglio I, et al. Multi-walled carbon nanotubes directly induce epithelial-mesenchymal transition in human bronchial epithelial cells via the TGF-beta-mediated Akt/GSK-3beta/SNAIL-1 signalling pathway. *Part Fibre Toxicol.* (2016) 13:27. doi: 10.1186/s12989-016-0138-4
74. Fang Y, Zhang S, Li X, Jiang F, Ye Q, Ning W. Follistatin like-1 aggravates silica-induced mouse lung injury. *Sci Rep.* (2017) 7:399. doi: 10.1038/s41598-017-00478-0
75. Wang Z, Wang C, Liu S, He W, Wang L, Gan J, et al. Specifically formed corona on silica nanoparticles enhances transforming growth factor beta1 activity in triggering lung fibrosis. *ACS Nano* (2017) 11:1659–72. doi: 10.1021/acsnano.6b07461
76. Mi S, Li Z, Yang HZ, Liu H, Wang JP, Ma YG, et al. Blocking IL-17A promotes the resolution of pulmonary inflammation and fibrosis via TGF-beta1-dependent and -independent mechanisms.

J Immunol. (2011) 187:3003–14. doi: 10.4049/jimmunol.1004081
77. Wang X, Dai W, Wang Y, Gu Q, Yang D, Zhang M. Blocking the Wnt/beta-catenin pathway by lentivirus-mediated short hairpin RNA targeting beta-catenin gene suppresses silica-induced lung fibrosis in mice. *Int J Environ Res Public Health* (2015) 12:10739–54. doi: 10.3390/ijerph120910739
78. Rong Y, Shen Y, Zhang Z, Cui X, Xiao L, Liu Y, et al. Blocking TGF-beta expression inhibits silica particle-induced epithelial-mesenchymal transition in human lung epithelial cells. *Environ Toxicol Pharmacol.* (2015) 40:861–9. doi: 10.1016/j.etap.2015.09.014
79. Neuzillet C, Tijeras-Raballand A, Cohen R, Cros J, Faivre S, Raymond E, et al. Targeting the TGFbeta pathway for cancer therapy. *Pharmacol Ther.* (2015) 147:22–31. doi: 10.1016/j.pharmthera.2014.11.001
80. Shull MM, Ormsby I, Kier AB, Pawlowski S, Diebold RJ, Yin M, et al. Targeted disruption of the mouse transforming growth factor-beta 1 gene results in multifocal inflammatory disease. *Nature* (1992) 359:693–9. doi: 10.1038/359693a0
81. Driscoll KE, Carter JM, Howard BW, Hassenbein D, Burdick M, Kunkel SL, et al. Interleukin-10 regulates quartz-induced pulmonary inflammation in rats. *Am J Physiol.* (1998) 275(5 Pt 1):L887–94. doi: 10.1152/ajplung.1998.275.5.L887
82. Hara K, Shirasuna K, Usui F, Karasawa T, Mizushina Y, Kimura H, et al. Interferon-tau attenuates uptake of nanoparticles and secretion of interleukin-1beta in macrophages. *PLoS ONE* (2014) 9:e113974. doi: 10.1371/journal.pone.0113974
83. Wang X, Coradin T, Helary C. Modulating inflammation in a cutaneous chronic wound model by IL-10 released from collagen-silica nanocomposites via gene delivery. *Biomater Sci.* (2018) 6:398–406. doi: 10.1039/c7bm01024a
84. Cohen C, Fireman E, Ganor E, Man A, Ribak J, Lerman Y. Accelerated silicosis with mixed-dust pneumoconiosis in a hard-metal grinder. *J Occup Environ Med.* (1999) 41:480–5. doi: 10.1097/00043764-199906000-00014
85. Chene AL, d'Almeida S, Blondy T, Tabiasco J, Deshayes S, Fonteneau JF, et al. Pleural effusions from patients with mesothelioma induce recruitment of monocytes and their differentiation into M2 macrophages. *J Thorac Oncol.* (2016) 11:1765–73. doi: 10.1016/j.jtho.2016.06.022
86. Jackaman C, Yeoh TL, Acuil ML, Gardner JK, Nelson DJ. Murine mesothelioma induces locally-proliferating IL-10^{+}TNF-alpha^{+}CD206^{-}CX3CR1^{+} M3 macrophages that can be selectively depleted by chemotherapy or immunotherapy. *Oncoimmunology* (2016) 5:e1173299. doi: 10.1080/2162402X.2016.1173299
87. Bode C, Kinjo T, Alvord WG, Klinman DM. Suppressive oligodeoxynucleotides reduce lung cancer susceptibility in mice with silicosis. *Carcinogenesis* (2014) 35:1078–83. doi: 10.1093/carcin/bgu005
88. Huaux F, Arras M, Vink A, Renauld JC, Lison D. Soluble tumor necrosis factor (TNF) receptors p55 and p75 and interleukin-10 downregulate TNF-alpha activity during the lung response to silica particles in NMRI mice. *Am J Respir Cell Mol Biol.* (1999) 21:137–45. doi: 10.1165/ajrcmb.21.1.3570
89. Lee CG, Homer RJ, Cohn L, Link H, Jung S, Craft JE, et al. Transgenic overexpression of interleukin (IL)-10 in the lung causes mucus metaplasia, tissue inflammation, and airway remodeling via IL-13-dependent and -independent pathways. *J Biol Chem.* (2002) 277:35466–74. doi: 10.1074/jbc.M206395200
90. Sun L, Louie MC, Vannella KM, Wilke CA, LeVine AM, Moore BB, et al. New concepts of IL-10-induced lung fibrosis: fibrocyte recruitment and M2 activation in a CCL2/CCR2 axis. *Am J Physiol Lung Cell Mol Physiol.* (2011) 300:L341–53. doi: 10.1152/ajplung.00122.2010
91. Barbarin V, Arras M, Misson P, Delos M, McGarry B, Phan SH, et al. Characterization of the effect of interleukin-10 on silica-induced lung fibrosis in mice. *Am J Respir Cell Mol Biol.* (2004) 31:78–85. doi: 10.1165/rcmb.2003-0299OC
92. Barbarin V, Xing Z, Delos M, Lison D, Huaux F. Pulmonary overexpression of IL-10 augments lung fibrosis and Th2 responses induced by silica particles. *Am J Physiol Lung Cell Mol Physiol.* (2005) 288:L841–8. doi: 10.1152/ajplung.00329.2004
93. Balaji S, Wang X, King A, Le LD, Bhattacharya SS, Moles CM, et al. Interleukin-10-mediated regenerative postnatal tissue repair is dependent on regulation of hyaluronan metabolism via fibroblast-specific STAT3 signaling. *FASEB J.* (2017) 31:868–81. doi: 10.1096/fj.201600856R
94. Miura Y, Nishimura Y, Katsuyama H, Maeda M, Hayashi H, Dong M, et al. Involvement of IL-10 and Bcl-2 in resistance against an asbestos-induced apoptosis of T cells. *Apoptosis* (2006) 11:1825–35. doi: 10.1007/s10495-006-9235-4
95. Maeda M, Miura Y, Nishimura Y, Murakami S, Hayashi H, Kumagai N, et al. Immunological changes in mesothelioma patients and their experimental detection. *Clin Med Circ Respirat Pulm Med.* (2008) 2:11–7. doi: 10.4137/ccrpm.s577
96. Shitara K, Nishikawa H. Regulatory T cells: a potential target in cancer immunotherapy. *Ann N Y Acad Sci.* (2018) 1417:104–15. doi: 10.1111/nyas.13625
97. Dai W, Liu F, Li C, Lu Y, Lu X, Du S, et al. Blockade of Wnt/beta-catenin pathway aggravated silica-induced lung inflammation through tregs regulation on Th immune responses. *Mediators Inflamm.* (2016) 2016:6235614. doi: 10.1155/2016/6235614
98. Mohamud R, LeMasurier JS, Boer JC, Sieow JL, Rolland JM, O'Hehir RE, et al. Synthetic nanoparticles that promote tumor necrosis factor receptor 2 expressing regulatory T cells in the lung and resistance to allergic airways inflammation. *Front Immunol.* (2017) 8:1812. doi: 10.3389/fimmu.2017.01812
99. Freire J, Ajona D, de Biurrun G, Agorreta J, Segura V, Guruceaga E, et al. Silica-induced chronic inflammation promotes lung carcinogenesis in the context of an immunosuppressive microenvironment. *Neoplasia* (2013) 15:913–24. doi: 10.1593/neo.13310
100. Cornelissen R, Hegmans JP, Maat AP, Kaijen-Lambers ME, Bezemer K, Hendriks RW, et al. Extended tumor control after dendritic cell vaccination with low-dose cyclophosphamide as adjuvant treatment in patients with malignant pleural mesothelioma. *Am J Respir Crit Care Med.* (2016) 193:1023–31. doi: 10.1164/rccm.201508-1573OC
101. Liu F, Dai W, Li C, Lu X, Chen Y, Weng D, et al. Role of IL-10-producing regulatory B cells in modulating T-helper cell immune responses during silica-induced lung inflammation and fibrosis. *Sci Rep.* (2016) 6:28911. doi: 10.1038/srep28911
102. Rosser EC, Mauri C. Regulatory B cells: origin, phenotype, and function. *Immunity* (2015) 42:607–12. doi: 10.1016/j.immuni.2015.04.005
103. Sarvaria A, Madrigal JA, Saudemont A. B cell regulation in cancer and anti-tumor immunity. *Cell Mol Immunol.* (2017) 14:662–74. doi: 10.1038/cmi.2017.35
104. Lu Y, Liu F, Li C, Chen Y, Weng D, Chen J. IL-10-producing B cells suppress effector T cells activation and promote regulatory T cells in crystalline silica-induced inflammatory response *in vitro*. *Mediators Inflamm.* (2017) 2017:8415094. doi: 10.1155/2017/8415094
105. Saradna A, Do DC, Kumar S, Fu QL, Gao P. Macrophage polarization and allergic asthma. *Transl Res.* (2018) 191:1–14. doi: 10.1016/j.trsl.2017.09.002
106. Fujimura T, Kambayashi Y, Fujisawa Y, Hidaka T, Aiba S. Tumor-associated macrophages: therapeutic targets for skin cancer. *Front Oncol.* (2018) 8:3. doi: 10.3389/fonc.2018.00003
107. Choi M, Cho WS, Han BS, Cho M, Kim SY, Yi JY, et al. Transient pulmonary fibrogenic effect induced by intratracheal instillation of ultrafine amorphous silica in A/J mice. *Toxicol Lett.* (2008) 182:97–101. doi: 10.1016/j.toxlet.2008.08.019
108. Misson P, van den Brule S, Barbarin V, Lison D, Huaux F. Markers of macrophage differentiation in experimental silicosis. *J Leukoc Biol.* (2004) 76:926–32. doi: 10.1189/jlb.0104019
109. Kumar S, Meena R, Paulraj R. Role of macrophage (M1 and M2) in titanium-dioxide nanoparticle-induced oxidative stress and inflammatory response in rat. *Appl Biochem Biotechnol.* (2016) 180:1257–75. doi: 10.1007/s12010-016-2165-x
110. Romero F, Shah D, Duong M, Penn RB, Fessler MB, Madenspacher J, et al. A pneumocyte-macrophage paracrine lipid axis drives the lung toward fibrosis. *Am J Respir Cell Mol Biol.* (2015) 53:74–86. doi: 10.1165/rcmb.2014-0343OC
111. Migliaccio CT, Buford MC, Jessop F, Holian A. The IL-4Ralpha pathway in macrophages and its potential role in silica-induced pulmonary fibrosis. *J Leukoc Biol.* (2008) 83:630–9. doi: 10.1189/jlb.0807533
112. Ferreira TP, de Arantes AC, do Nascimento CV, Olsen PC, Trentin PG, Rocco PR, et al. IL-13 immunotoxin accelerates resolution of lung pathological

changes triggered by silica particles in mice. *J Immunol.* (2013) 191:5220–9. doi: 10.4049/jimmunol.1203551
113. Tcyganov E, Mastio J, Chen E, Gabrilovich DI. Plasticity of myeloid-derived suppressor cells in cancer. *Curr Opin Immunol.* (2018) 51:76–82. doi: 10.1016/j.coi.2018.03.009
114. Veltman JD, Lambers ME, van Nimwegen M, Hendriks RW, Hoogsteden HC, Aerts JG, et al. COX-2 inhibition improves immunotherapy and is associated with decreased numbers of myeloid-derived suppressor cells in mesothelioma. Celecoxib influences MDSC function. *BMC Cancer* (2010) 10:464. doi: 10.1186/1471-2407-10-464
115. Boraschi D, Italiani P, Palomba R, Decuzzi P, Duschl A, Fadeel B, et al. Nanoparticles and innate immunity: new perspectives on host defence. *Semin Immunol.* (2017) 34:33–51. doi: 10.1016/j.smim.2017.08.013
116. Chauhan AS, Diwan PV, Jain NK, Tomalia DA. Unexpected *in vivo* anti-inflammatory activity observed for simple, surface functionalized poly(amidoamine) dendrimers. *Biomacromolecules* (2009) 10:1195–202. doi: 10.1021/bm9000298
117. Rajan R, Sabnani MK, Mavinkurve V, Shmeeda H, Mansouri H, Bonkoungou S, et al. Liposome-induced immunosuppression and tumor growth is mediated by macrophages and mitigated by liposome-encapsulated alendronate. *J Control Release* (2018) 271:139–48. doi: 10.1016/j.jconrel.2017.12.023
118. Sumbayev VV, Yasinska IM, Garcia CP, Gilliland D, Lall GS, Gibbs BF, et al. Gold nanoparticles downregulate interleukin-1beta-induced pro-inflammatory responses. *Small* (2013) 9:472–7. doi: 10.1002/smll.201201528
119. Ma JS, Kim WJ, Kim JJ, Kim TJ, Ye SK, Song MD, et al. Gold nanoparticles attenuate LPS-induced NO production through the inhibition of NF-kappaB and IFN-beta/STAT1 pathways in RAW264.7 cells. *Nitric Oxide* (2010) 23:214–9. doi: 10.1016/j.niox.2010.06.005
120. Wu HY, Chung MC, Wang CC, Huang CH, Liang HJ, Jan TR. Iron oxide nanoparticles suppress the production of IL-1beta via the secretory lysosomal pathway in murine microglial cells. *Part Fibre Toxicol.* (2013) 10:46. doi: 10.1186/1743-8977-10-46
121. Lee SS, Song W, Cho M, Puppala HL, Nguyen P, Zhu H, et al. Antioxidant properties of cerium oxide nanocrystals as a function of nanocrystal diameter and surface coating. *ACS Nano* (2013) 7:9693–703. doi: 10.1021/nn4026806
122. Gharbi N, Pressac M, Hadchouel M, Szwarc H, Wilson SR, Moussa F. [60]fullerene is a powerful antioxidant *in vivo* with no acute or subacute toxicity. *Nano Lett.* (2005) 5:2578–85. doi: 10.1021/nl051866b
123. Yamashita K, Sakai M, Takemoto N, Tsukimoto M, Uchida K, Yajima H, et al. Attenuation of delayed-type hypersensitivity by fullerene treatment. *Toxicology* (2009) 261:19–24. doi: 10.1016/j.tox.2009.04.034
124. Tomic S, Janjetovic K, Mihajlovic D, Milenkovic M, Kravic-Stevovic T, Markovic Z, et al. Graphene quantum dots suppress proinflammatory T cell responses via autophagy-dependent induction of tolerogenic dendritic cells. *Biomaterials* (2017) 146:13–28. doi: 10.1016/j.biomaterials.2017.08.040
125. Blank F, Gerber P, Rothen-Rutishauser B, Sakulkhu U, Salaklang J, De Peyer K, et al. Biomedical nanoparticles modulate specific $CD4^+$ T cell stimulation by inhibition of antigen processing in dendritic cells. *Nanotoxicology* (2011) 5:606–21. doi: 10.3109/17435390.2010.541293
126. Tkach AV, Shurin GV, Shurin MR, Kisin ER, Murray AR, Young SH, et al. Direct effects of carbon nanotubes on dendritic cells induce immune suppression upon pulmonary exposure. *ACS Nano* (2011) 5:5755–62. doi: 10.1021/nn2014479
127. Mishra A, Stueckle TA, Mercer RR, Derk R, Rojanasakul Y, Castranova V, et al. Identification of TGF-beta receptor-1 as a key regulator of carbon nanotube-induced fibrogenesis. *Am J Physiol Lung Cell Mol Physiol.* (2015) 309:L821–33. doi: 10.1152/ajplung.00002.2015
128. Ma J, Bishoff B, Mercer RR, Barger M, Schwegler-Berry D, Castranova V. Role of epithelial-mesenchymal transition (EMT) and fibroblast function in cerium oxide nanoparticles-induced lung fibrosis. *Toxicol Appl Pharmacol.* (2017) 323:16–25. doi: 10.1016/j.taap.2017.03.015
129. Moon EY, Yi GH, Kang JS, Lim JS, Kim HM, Pyo S. An increase in mouse tumor growth by an *in vivo* immunomodulating effect of titanium dioxide nanoparticles. *J Immunotoxicol.* (2011) 8:56–67. doi: 10.3109/1547691X.2010.543995
130. Sanpui P, Zheng X, Loeb JC, Bisesi JH Jr, Khan IA, Afrooz AR, et al. Single-walled carbon nanotubes increase pandemic influenza A H1N1 virus infectivity of lung epithelial cells. *Part Fibre Toxicol.* (2014) 11:66. doi: 10.1186/s12989-014-0066-0
131. Findlay F, Pohl J, Svoboda P, Shakamuri P, McLean K, Inglis NF, et al. Carbon nanoparticles inhibit the antimicrobial activities of the human cathelicidin LL-37 through structural alteration. *J Immunol.* (2017) 199:2483–90. doi: 10.4049/jimmunol.1700706
132. Kanterman J, Sade-Feldman M, Baniyash M. New insights into chronic inflammation-induced immunosuppression. *Semin Cancer Biol.* (2012) 22:307–18. doi: 10.1016/j.semcancer.2012.02.008
133. Rocha-Parise M, Santos LM, Damoiseaux JG, Bagatin E, Lido AV, Torello CO, et al. Lymphocyte activation in silica-exposed workers. *Int J Hyg Environ Health* (2014) 217:586–91. doi: 10.1016/j.ijheh.2013.11.002
134. Rimal B, Greenberg AK, Rom WN. Basic pathogenetic mechanisms in silicosis: current understanding. *Curr Opin Pulm Med.* (2005) 11:169–73. doi: 10.1097/01.mcp.0000152998.11335.24
135. Breznan D, Karthikeyan S, Phaneuf M, Kumarathasan P, Cakmak S, Denison MS, et al. Development of an integrated approach for comparison of *in vitro* and *in vivo* responses to particulate matter. *Part Fibre Toxicol.* (2016) 13:41. doi: 10.1186/s12989-016-0152-6
136. Kasper J, Hermanns MI, Bantz C, Maskos M, Stauber R, Pohl C, et al. Inflammatory and cytotoxic responses of an alveolar-capillary coculture model to silica nanoparticles: comparison with conventional monocultures. *Part Fibre Toxicol.* (2011) 8:6. doi: 10.1186/1743-8977-8-6
137. Italiani P, Mazza EM, Lucchesi D, Cifola I, Gemelli C, Grande A, et al. Transcriptomic profiling of the development of the inflammatory response in human monocytes *in vitro*. *PLoS ONE* (2014) 9:e87680. doi: 10.1371/journal.pone.0087680
138. Lamichhane P, Karyampudi L, Shreeder B, Krempski J, Bahr D, Daum J, et al. IL10 release upon PD-1 blockade sustains immunosuppression in ovarian cancer. *Cancer Res.* (2017) 77:6667–78. doi: 10.1158/0008-5472.CAN-17-0740
139. Stockis J, Lienart S, Colau D, Collignon A, Nishimura SL, Sheppard D, et al. Blocking immunosuppression by human tregs *in vivo* with antibodies targeting integrin αVβ8. *Proc Natl Acad Sci USA.* (2017) 114:E10161–8. doi: 10.1073/pnas.1710680114
140. Patel SA, Minn AJ. Combination cancer therapy with immune checkpoint blockade: mechanisms and strategies. *Immunity* (2018) 48:417–33. doi: 10.1016/j.immuni.2018.03.007
141. Maeda M, Nishimura Y, Kumagai N, Hayashi H, Hatayama T, Katoh M, et al. Dysregulation of the immune system caused by silica and asbestos. *J Immunotoxicol.* (2010) 7:268–78. doi: 10.3109/1547691X.2010.512579
142. Petsonk EL, Rose C, Cohen R. Coal mine dust lung disease. New lessons from old exposure. *Am J Respir Crit Care Med.* (2013) 187:1178–85. doi: 10.1164/rccm.201301-0042CI

Conflict of Interest Statement: The author declares that the research was conducted in the absence of any commercial or financial relationships that could be construed as a potential conflict of interest.

Advantages of publishing in Frontiers

OPEN ACCESS
Articles are free to read for greatest visibility and readership

FAST PUBLICATION
Around 90 days from submission to decision

HIGH QUALITY PEER-REVIEW
Rigorous, collaborative, and constructive peer-review

TRANSPARENT PEER-REVIEW
Editors and reviewers acknowledged by name on published articles

Frontiers
Avenue du Tribunal-Fédéral 34
1005 Lausanne | Switzerland

Visit us: www.frontiersin.org
Contact us: info@frontiersin.org | +41 21 510 17 00

REPRODUCIBILITY OF RESEARCH
Support open data and methods to enhance research reproducibility

DIGITAL PUBLISHING
Articles designed for optimal readership across devices

FOLLOW US
@frontiersin

IMPACT METRICS
Advanced article metrics track visibility across digital media

EXTENSIVE PROMOTION
Marketing and promotion of impactful research

LOOP RESEARCH NETWORK
Our network increases your article's readership